DTIC FILE COPY

ARO 27785.1-MS-CF

AD-A225 849

NATO Advanced Research Workshop

Toughening Mechanisms in Quasi-Brittle Materials

July 16-20, 1990

Workshop Proceedings

DTIC
ELECTE
AUG 28 1990
S D
D

DISTRIBUTION STATEMENT A
Approved for public release;
Distribution Unlimited

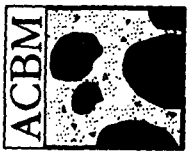

NSF Center for Science and Technology
of Advanced Cement-Based Materials
Northwestern University

90 08 27 131

MASTER COPY KEEP THIS COPY FOR REPRODUCTION PURPOSES

REPORT DOCUMENTATION PAGE

Form Approved
OMB No 0704-0188

Public reporting burden for this collection of information is estimated to average 1 hour per response, including the time for reviewing instructions, searching existing data sources, gathering and maintaining the data needed, and completing and reviewing the collection of information. Send comments regarding this burden estimate or any other aspect of this collection of information, including suggestions for reducing this burden, to Washington Headquarters Services, Directorate for information Operations and Reports, 1215 Jefferson Davis Highway, Suite 1204, Arlington, VA 22202-4302, and to the Office of Management and Budget, Paperwork Reduction Project (0704-0188), Washington, DC 20503

1. AGENCY USE ONLY (Leave blank)	2. REPORT DATE	3. REPORT TYPE AND DATES COVERED
	1990	Final 1 Jul 90-30 Jun 91

4. TITLE AND SUBTITLE
NATO Advanced Research Workshop. Toughening Mechanisms in Quasi-Brittle Materials

5. FUNDING NUMBERS
DAAL03-90-G-0179

6. AUTHOR(S)
Surendra P. Shah

7. PERFORMING ORGANIZATION NAME(S) AND ADDRESS(ES)
Northwestern University
Evanston, IL 60201

8. PERFORMING ORGANIZATION REPORT NUMBER

9. SPONSORING/MONITORING AGENCY NAME(S) AND ADDRESS(ES)
U. S. Army Research Office
P. O. Box 12211
Research Triangle Park, NC 27709-2211

10. SPONSORING/MONITORING AGENCY REPORT NUMBER
ARO 27785.1-MS-CF

11. SUPPLEMENTARY NOTES
The view, opinions and/or findings contained in this report are those of the author(s) and should not be construed as an official Department of the Army position, policy, or decision, unless so designated by other documentation.

12a. DISTRIBUTION/AVAILABILITY STATEMENT
Approved for public release; distribution unlimited.

12b. DISTRIBUTION CODE

13. ABSTRACT *(Maximum 200 words)*

This workshop brought together researchers addresssing the problem of fracture in cement, ceramics, and rock so that they could share their knowledge and develop a more general syntheses of the problem.

This preprint volume contains contributions from lectures for each of the 9 sessions. The final proceedings of this workshop will be published in a hard-cover book by Kluewer Academic Publishers (NATO ASI Series). This book will contain 36 chapters; the finalized contributions of 27 lectures and 9 reporters.

14. SUBJECT TERMS
Quasi-Brittle Materials, Toughening Mechanisms in Materials, Workshop, Cement Fracture, Ceramic Fracture, Rock Fracture

15. NUMBER OF PAGES

16. PRICE CODE

17. SECURITY CLASSIFICATION OF REPORT	18. SECURITY CLASSIFICATION OF THIS PAGE	19. SECURITY CLASSIFICATION OF ABSTRACT	20. LIMITATION OF ABSTRACT
UNCLASSIFIED	UNCLASSIFIED	UNCLASSIFIED	UL

2 7785-1-MS-CF

NATO Advanced Research Workshop

Toughening Mechanisms in Quasi-Brittle Materials

July 16-20, 1990

Workshop Proceedings Addendum

NSF Center for Science and Technology
of Advanced Cement-Based Materials
Northwestern University

90 08 27 081

Quasi-ductile behaviour of carbon-reinforced carbon

A. Wanner*, G. Rizzo**, K. Kromp*
*Max-Planck-Institut für Metallforschung
Institut fuer Werkstoffwissenschaft,
Seestraße 92, D-7000 Stuttgart, FRG
**Dipartimento di Ingegneria Chimica dei Processi e
dei Materiali, Università di Palermo
Viale delle Science, I-90128 Palermo, Italy

Abstract:

Firstly a brief review of the problem of a "ductilization" of ceramic materials by endless-fiber reinforcement is given. The problems, especially the influence of the frictional stress in the fiber-matrix interface, are pointed out for the unidirectionally reinforced CMC-system LAS/SiC, which is well documented in the literature.

Secondly displacement controlled three-point bending experiments with unloading-reloading cycles in edgewise loading (parallel to the plies) with notched specimens are presented as a means to charaterize the "quasi-ductile" behaviour of CMC laminates. The effectiveness of the method is demonstrated for C/C laminates in two different states of graphitization and for a silicon infiltrated C/C, both in a bidirectional layup.

1. Introduction

Great efforts have been made in the last years to develop tough ceramics which are not susceptible to fracture during impact or under stress in the presence of flaws or notches. In particular in the aerospace industry specific strengths, temperature resistance and failure characteristics are demanded, which cannot be fulfilled except by ceramic composites containing high performance fibrous reinforcements.

The general problem of ceramic materials is their extreme brittleness. The aim is to "ductilize" these materials, to increase their toughness. Several principles exist for increasing fracture toughness either through incorporation of particles of second phase, short whiskers or platelets or transformation toughening particles of zirconia. Such efforts increase the thoughness by typically a factor of 2-3. By far the most successful method of improving toughness is to reinforce

a matrix with strong carbon or ceramic filaments. The fracture toughness can be increased by nearly an order of magnitude and the fracture energy by two orders of magnitude with these materials.

A lot of experience has been acquired in the past with carbon fiber reinforced polymer matrix and with metal matrix composites. Efforts have been made to extend this experience to materials which can withstand high temperatures. The carbon-reinforced carbon composites (C/C) were a step in this development, although they posses the disadvantage of not being applicable in arduous surroundings without coating. Fresh impulses came from the development of new fibers, such as the organometallic derived silicon carbide yarn.

2. The problem of a "ductilization" of ceramic materials

As is already known from metal and resin matrix composites, high elastic modulus fibers have to be incorporated into lower elastic modulus matrices to achieve reinforcement and ductile behaviour.

Beside the main condition for a *ductilized ceramic matrix composite* with high toughness, that is, the failure strain of the fibers must be significantly greater than that of the matrix, the fiber should not be too strongly bonded to the matrix, it should only be frictionally bonded. In recent years, since the Nicalon-SiC fiber has widely been available [1], the general features of this "ductilization" of brittle matrix composites were studied predominantly in the LAS/SiC system, that is lithium aluminosilicate glass-ceramic matrix, reinforced with silicon carbide fibers (Nicalon-fibers). The general problems of "ductilization" will be discussed with this material, considering an unidirectional fiber reinforcement (1-D material).

3. Unidirectionally, single-fiber reinforced ceramic matrix composites

The "ductile" load response for an unidirectionally single-fiber reinforced CMC, obtained from the LAS/SiC system [2], is schematically shown in Fig. 1. In axial loading a linear elastic region ends at a stress σ_0, defined by the onset of matrix cracking. This point is similar to a "yield" point in alloys, here originated by periodic cracking of the matrix. A nonlinear region follows, which depends on the frictional behaviour of the fiber in the matrix. This region is accompanied by multiple matrix cracking, with fibers remaining intact and then by fiber pullout. At the stress σ_u, an "ultimate tensile strength", fiber bundle failure occurs. Then the load drops slowly - not a brittle, but a delayed fracture is observed.

From an energy balance analysis, given earlier [3] and a fracture mechanics approach [4,5,6] a relation between the matrix cracking stress σ_o and microstructural parameters was given:

$$\sigma_o = [6(1-\nu^2)K_{mc}{}^2\tau E_f\ f^2(1-f)(1+\eta)^2/E_m R]^{1/3}, \qquad (1)$$

where K_{mc} is the matrix toughness, ν Poisson's ratio, $\eta = E_f \cdot f/E_m(1-f)$, R the fiber radius, τ the sliding frictional stress at the interface and f the volume fraction of fibers.

This situation is not to be confused with that of unreinforced materials, in which the stress at the tip of the crack increases with increasing crack length (equation (2) does not directly depend on crack length). The important result is that in these composite systems the stress at the tip of the crack becomes independent of crack length once the crack is longer than a length c_o necessary in order to reach the equilibrium situation (Fig. 2). This holds as long as the fibers in the wake of the crack front remain intact. Thus matrix cracking is impossible below the "threshold" stress σ_o of equation (1), no matter how large a crack or a preexisting defect! The equilibrium-stress/crack-size function for straight cracks is plotted in Fig. 3 (for straight cracks $\sigma_o/\sigma_m = 1.02$ and $c_0/c_m = 1.88$). From Fig. 3 it can be seen that the stress required to propagate a matrix crack is independent of crack length for cracks larger than about $c_m/3$. The crack response in this region differs from the behaviour of cracks in unreinforced brittle materials, in which the strength decreases with $c_o^{-1/2}$, Fig. 3.

$c_m/3$ was evaluated to be several fiber spacings long and this implies that the stress for matrix cracking is not substantially reduced by introduction of larger flaws during fabrication or in service.

It is obvious from the analysis that the attainment of steady state cracking at high stress levels is restricted to a narrow range of microstructures. The limiting value is the level of σ_o that can be achieved without causing fiber failure; optimum values of all three parameters K_{mc}, τ and f increase the level of σ_o in equation (1). Additionally the influence on c_m has to be considered. A significant microstructural restriction concerns the volume fraction of fibers f because optimum properties can be achieved only in unidirectional composites whereas in multidirectional systems the volume fraction of fibers is in any case less.

In bending tests the load-deflection behaviour is similar to that in tension [2]. High failure strains and notch insensitivity are characteristic for such composites. These qualities are explicable in terms of the slip processes occurring at the fiber/matrix interface or the frictional stress τ [2,4].

Any change in the interface layer between fiber and matrix has a decisive influence on the "quasi-ductile" response of the CMC. This was proved for the system LAS/SiC, discussed as an example here. Even short exposures to high temperature can reembrittle the material: bending experiments in Ar and in air at high temperatures resulted in the some load level, but the morphology of fracture changed completely from pullout in Ar to rather brittle fracture in air [7,8]. For an unitape 2-D laminate of the same system LAS/SiC this behaviour was investigated systematically [9,10]. It was found that the reembrittlement after an exposure of 2-4 hours at high temperatures in air resulted from a change in the C-interface layer to SiO_2. This change provoked an increase in the frictional stress between fiber-matrix and thus in the pullout lengths.

4. Measurement of interfacial mechanical properties

The question is, whether only frictional forces act in the interface, as assumed for the steady state cracking in the matrix, or fiber displacement involves also debonding followed by frictional sliding. The general case will be a weak bonding and debonding in addition to frictional forces.

The frictional stresses were measured by pushing a pyramidal indenter on the end of an individual fiber and measuring the resulting displacement of the surface of the fiber below the matrix surface [2,11]. This method was refined recently by using an ultralow-load indentation instrument (Nano Instruments, Inc. Braintree, MA) to measure force and displacement continuously during loading, unloading and load cycling. Frictional sliding and combined debonding and frictional sliding at the interface were analyzed for a LAS/SiC material [12,13]. In [13] method was proposed to achieve relative frictional stress values in the special cases before and after heat treatment at 1000°C in air on the System LAS/SiC. For this purpose, specimens were cut into blocks and by erosion of a portion of the matrix, fibers were disclosed, resulting in a distribution of protruding fibers across a flat matrix surface. A load was applied by means of a sapphire hemisphere of 1 mm diameter on the protruding fibers. The load-displacement curves were measured with respect to the matrix.

5. Laminated ceramic matrix composites

It was demonstrated in Fig. 1 that when unidirectionally reinforced composites are loaded along the fiber axis, matrix cracking occurs at a stress σ_o, followed by fiber failure at the ultimate stress σ_u. The transverse properties are substantially inferior, load response is linear elastic and fracture occurs at a stress $\sigma_T << \sigma_o$, Fig. 1.

This considerable anisotropy requires that the most structural composites be laminated.

The C/C and C/SiC laminates discussed in the next chapters consist of bundles of 3000 single carbon fibers, the bundles are woven to prepregs and these plies are stapled orthogonally. Inside such a fiber bundle considerations and measurements of the frictional stress, as discussed in the last chapters may be valid. But in the laminates there also exist interbundle interfaces between parallel bundles and orthogonal bundles, in-plie delamination and inter-plie delamination will occurr.

The response in loading will depend on the loading mode to a high degree: e.g. in three-point bending with loading perpendicular to the plies, because of shear deformation, the result in general depends on the span to height ratio. For laminates with low frictional stresses such as C/C the result additionally depends on the plie thickness to height ratio [14].

6. How to characterize the "quasi-ductile" behaviour of CMC laminates?

As previously discussed the frictonal stress in the interfaces fiber-matrix has a decisive influence on the quasi-ductile behaviour of unidirectionally single fiber reinforced CMCs. For laminates not only interfaces single fiber-matrix inside a fiber bundle, but also interbundle interfaces parallel and interbundle interfaces orthogonal may influence the quasi-ductile behaviour. The methods to measure the frictional stress in the interfaces single fiber-matrix mentioned in the last chapter seem not to be applicable to those of fiber bundles. Therefore the authors tried to get information on the frictional behaviour of laminates by a special kind of experiments: prismatic specimens of rectangular cross-section were loaded edgewise in displacement controlled three-point bending experiments.

The loading principle is demonstrated schematically in Fig. 4. The chosen span was S=90mm, the displacement rate in the closed loop, measured and controlled directly at the notch by a SiC-pushrod, was $\dot{\delta}$=200µm/min. The SiC loading rods had a radius of curvature of 5mm. The experiments could be performed at high temperatures by induction heating indirectly by means of a carbon susceptor tube. The whole loading system, inside a vacuum vessel, could be evacuated to 2.10^{-5} mbar [15].

Using this equipment load-displacement curves in monotonic loading and with unloading-relcading cycles were achieved. With this kind of experiment changes in the ductile response of a C/C (carbon-reinforded carbon) laminate by silicon infiltration and the influence of the temperature of graphitization on the ductile behaviour of another C/C laminate were investigated.

7. The change in the "ductile" response of a C/C laminate after infiltration with silicon

C/C laminates of 5H-satin prepregs, woven from tows of 3000 PAN-based fibers were laminated in a [0/90°] layup. All the material was kindly supplied and the processing performed by Sintec-Keramik, Buching, FRG. The material was only carbonized but not graphitized. After the carbonization the material was not reimpregnated and was thus highly porous. This material was infiltrated by silicon as a first step for the development of an oxidation protected type. In Figs 5ab the load-displacement curves after cyclic loading are shown [16]. The enveloping curves of the unloading-reloading cycles are mearly identical to the load-displavement curves in monotonic loading.

In Fig 5a it can be seen for the C/C laminate carbonized only:

- for the enveloping curve:
  - only small deviation from linearity at a relative high level of load;
  - a sharp maximum in load;
  - subsequently rapid decay in load;
- for the unloading in successive cycles:
  - low amounts of irreversible displacement.

For the carbonized and silicon-infiltrated (C/SiC/Si) laminate in Fig. 5b:

· for the enveloping curve:
- the deviation from linearity starts already at a low level of load;
- no sharp maximum in load, but a smooth decay in sustained load (the load-displacement curve could be continued beyond the displacement range shown in Fig 5b);
· for the unloading in successive cycles:
- the displacement is nearly completely irreversible.

After the experiments the specimens were broken completely open and the pull-out behaviour was studied in the SEM, see Figs 6ab [16].
In Figs 6ab it can be observed that:

- in the only carbonized material the fiber-bundles failed in a brittle manner without pull-out of single fibers inside the bundle, but complete bundles were pulled out;
- in the siliconized material single fibers inside the bundles failed and were pulled out, but no complete bundle was pulled out;
- the surface of the single fibers appears rough because of adherent siliconized carbon matrix (see Fig 7).

This behaviour may be interpreted as follows:

· For the carbonized only material it is concluded from the shape of the load-displacement cycles and the pull-out behaviour that
- the friction in the interbundle interfaces is very low (the bonding may be not much more than van der Waals), thus resulting in good gliding behaviour of complete bundles and low irreversible displacement during cycling;
- because of the low bonding in the interfaces most of the load has to be sustained by the fiber bundles and these fail in a brittle manner and thus the load drops rapidly from a sharp maximum.
→ Because of these facts, the fracture behaviour is estimated to be brittle rather than ductile.
· For the silicon-infiltrated material it is concluded that
- the friction in the interbundle interfaces and partly between the fibers inside the bundles is high, thus the displacement during cycling is nearly completely irreversible;
- because of the relatively high bonding in the interfaces the load is distributed to the volume, thus the load drops slowly.
→ Because of these facts the fracture behaviour is estimated to be rather "quasi-ductile"

An estimation of the areas below the load-displacement curves of Figs 5ab as a measure for the work of fracture may confirm these statements.

8. The change in the "quasi-ductile" behaviour of a C/C laminate by a variation in the temperature of graphitization

C/C laminates of 8H-satin prepregs, woven from tows of 3000 PAN-based fibers were laminated in a [0/90°] layup. The materials were kindly supplied and processed by Schunk-Kohlenstofftechnik, Gießen, FRG. After four cycles of reimpregnation and carbonization the materials were graphitized at Temperatures of 2100°C ("laminate A") and 2400°C ("laminate B").

As already deceribed notched specimens of both the materials were loaded edgewise in displacement controlled experiments at room temperature and at 1000°C. In Figs 8ab load-displacement curves with numerous unloading-reloading cycles are shown for both the materials at room temperature. The dimension and the loading condition can be read from the diagrams. Again the enveloping curves of the unloading-reloading cycles are nearly identical to the load-displacement curves in monotonic loading. For both the materials the deviation from linearity occurs at a high load level, the maximum load appears sharp, followed by a rapid decay in sustained load. A difference between the materials is evident in the amount of irreversible displacement after unloading in successive cycles: material B exhibits only small amounts of irreversible displacement (Fig 8b), while material A shows remarkable amounts of irreversible displacement (Fig 8a).

Also the shape of the cycles differs: if one observes one of the cycles in Fig 8a at a low load level (high irreversible displacement), the first slope (starting the reloading) and the slope at the end of the cycle (starting the unloading) are steep, nearly as steep as the initial loading. This behaviour is sketched in Fig 9. These initial slopes also appear for material B in Fig 8b, but only slightly. These slopes are interpreted as a measure of "bonding" friction at the monents were the loading stops and changes its direction. At a certain load level this slope drops suddenly, friction turns to "gliding" friction. The same occurs in unloading, where the stored elastic energy now "loads" the specimen in the opposite direction. When the energy is exhausted, the cycle stops at a certain irreversible displacement , see Fig 9.

This difference in bonding and gliding friction nearly vanishes for material B (Fig 8b), it is supposed that the frictional stress in the interfaces is lowered by the increase

in temperature of graphitization from 2100°C to 2400°C. A look at the structure of the materials confirms these statements (Figs 10ab): Laminate B with the higher temperature of graphitization exhibits a higher content of macropores in the inter-bundle-regions (Fig 10b), compared to laminate A with the lower temperature of graphitization (Fig 10a).

After breaking open the specimens, the pullout behaviour was observed in the SEM. The appearance for both the laminates A and B was similar to that shown in Fig 6a: pull-out of complete fiber-bundles and brittle fracture of the bundles, see Figs 11ab. For the first three rows of pulled out bundles beyond the notch root (in Fig 11b from the left) the pull-out lengths of the fiber-bundles were measured. The mean pull-out length increased by 64% with increasing the temperature of graphitization.

From the response to the cycling and the estimation of the pull-out lengths it is concluded that the "quasi-ductile" behaviour decrease with increasing the temperature of graphitization from 2100°C to 2400°C.

The same cycling experiments were performed at a testing temperature of 1000°C in a vacuum of 2.10^{-5}mbar for both the laminates A and B, see Figs 12ab: The shape of the enveloping curves and that of the cycles is similar to those gained at room temperature. Except the amount of irreversible displacement seems to be higher for both the laminates, compare Figs 8ab to Figs 12ab. The pullout appearance was similar to that in Figs 11ab for the room temperature tests.

A measurement of the pull-out lengths again showed the mean pullout length to increase by 69% with increasing the temperature of graphitization from 2100°C to 2400°C. This means that the "quasi-ductile" behaviour decreases with the increase in temperature of graphitization, as for the tests performed at room temperature.

Compared to the tests at room temperature the mean pull-out lengths for the tests at 1000°C were shorter by $\sim 20\%$! The results of the measurements of the pull-out lengths are summarized in Table 1.

Table 1 : pullout lengths for laminates A and B, loaded at room temperature and at 1000°C, [µm]

	T_{graph} = 2100°C		T_{graph} = 2400°C
		+64%	
T_p = 20°C	840 ± 319 (±38%)		1381 ± 545 (±39%)
	↓ - 22%		↓ - 19%
T_p = 1000°C	657 ± 300 (±46%)	+69%	1115 ± 560 (±50%)

According to the results in Table 1 it is supposed that the frictional stress in the interbundle interfaces is increased by an increase in testing temperature for both the laminates.

To prove this the temperature dependence of the Young's modulus of laminate A parallel to the 0°-fiber direction was investigated with the resonant's beam method [17]. The modulus, at room temperature 83±2GPa, increased with increasing temperature to reach a plateau value at ~ 1000°C, see Fig 13. In the same range of temperature the material was observed in a SEM with a heating equipment- besides the macropores already shown in Fig 10a, at room temperature cracks were observed inside the bundles, see Fig 14 left. These cracks were observed to close completely in the temperature range, where the Young's modulus reaches its plateau value.

It is proposed that during the processing of the materials cooling down from the high temperatures to room temperature residual stresses in tension perpendicular to the bundles arise, which cause cracking as observed in Fig 14. Approaching the equilibrium temperature these stresses relax, cracks inside the bundles close and the friction between the bundles increases [18].

The relaxation of the residual stresses may explain the higher irreversible displacement observed in Figs 12ab at the testing temperature of 1000°C compared to Figs 5ab at the testing at room temperature and thus the decrease in the mean pull-out lengths by ~ 20% (Table 1) from room temperature to 1000°C.

It can be stated here that an increase in testing temperature (temperature of application) improves the "quasi-ductile" behaviour of the investigated C/C laminates A and B.

Summary and outlook:

Firstly a brief overview of the problem of the "ductilization" of ceramics by endless fiber-reinforement and of the importance of the frictional stress in the interface fiber-matrix was given. The problems for the unidirectionally endless-fiber reinforced LAS/SiC were dicussed, a material well documented in the literature.

A special kind of experimental procedure is proposed to characterize the "quasi-ductile" behaviour of C/C-(carbon fiber reinforced) and C/SiC-(carbon fiber reinforced silicon carbide)-laminates in [0 90°] layup: notched prismatic specimens are loaded edgewise (parallel to the plies) in displacement-controlled three-point bending experiments with intermediate unloading-reloading cycles.

A purely carbonized, porous [0 90°]-laminate and the same material in a siliconized version were loaded to demonstrate the effectiveness of the method. Two batches of another [0 90°]-laminate four times reimpregnated and carbonized, were graphitized at two different temperatures (2100°C and 2400°C) and then loaded in the same way.

Though the "quasi-ductile" behavior of laminates depends to a high degree on the mode of loading, e.g. notched-unnotched or edgewise (parallel to the plies) in summary the following statements may be made:

From the shape of the enveloping curve , the amount of irreversible displacement of successive unloading cycles, and from the shape of the cycles themselves and the pullout appearance, it is concluded that these materials exhibit "quasi-ductile" behaviour Siliconizing improves the quasi-ductility of the purely carbonized material, an increase in the temperature of graphitization decreases that of the reimpregnated material.

The proposed method seems sensitive enough to characterize the quasi-ductile behaviour of C/C and C/SiC laminates. The next steps will be to give an analytical evaluation of the unloading-reloading cycles and for the bonding and gliding friction in the individual cycles. TEM investigations of the interfacial regions are now in progress.

Literature:

[1] S. Yajima, K. Okamura, J. Hayashi, M. Omori: Synthesis of continuous SiC fibers with high tensile strength; J. Am. Ceram. Soc. **59**/7-8 (1976) 324-327.

[2] D.B. Marshall, A.G. Evans: Failure mechanisms in ceramic-fiber/ceramic-matrix composites; J. Am. Ceram. Soc. **68**/5 (1985) 225-231.

[3] J. Aveston, G.A. Cooper, A. Kelly in: The properties of fiber composites, Conf. Proc. pp.15-26; National Physical Laboratory, IPC Science and Technology Press (1971).

[4] D.B. Marshall, B.N. Cox, A.G. Evans: The mechanics of matrix cracking in brittle-matrix fiber composites; Acta metall. **33**/11 (1985) 2013-2021.

[5] B. Budiansky, J.W. Hutchinson, A.G. Evans: Matrix fracture in fiber-reinforced ceramics; J. Mech. Phys. Solids **34**/2 (1986) 167-189.

[6] L.N. McCartney: Mechanics of matrix cracking in brittle-matrix fiber-reinforced composites; Proc. R. Soc. Lond. A **409** (1987) 329-350.

[7] J.J. Brennan, K.M. Prewo: Silicon carbide fiber reinforced glass-ceramic matrix composites exhibiting high strength and toughness; J. Mater. Sci. **17** (1982) 2371-2383.

[8] K.M. Prewo: Tension and flexural strength of silicon carbide fiber-reinforced glass ceramics; J. Mater. Sci. **21** (1986) 3590-3600.

[9] E. Bischoff, M. Rühle, O. Sbaizero, A.G. Evans: Microstructural studies of the interfacial zone of a SiC-fiber-reinforced lithium aluminium silicate glass-ceramic; J. Am. Ceram. Soc. **72** (1989) 741-45.

[10] M.D. Thouless, O. Sbaizero, L.S. Sigl, A.G. Evans: Effect of interface mechanical properties on pullout in a SiC-fiber-reinforced lithium aluminium silicate glass-ceramic; J. Am. Ceram. Soc. **72** (1989) 525.

[11] D.B. Marshall: An indentation method for measuring matrix-fiber frictional stresses in ceramic composites; J. Am. Ceram. Soc. **67**/12 (1984) C259-260.

[12] D.B. Marshall, W.C. Oliver: Measurement of interfacial mechanical properties in fiber-reinforced ceramic composites; J. Am. Ceram. Soc. **70**/8 (1987) 542-548.

[13] E.Y. Luh, A.G. Evans: High-temperature mechanical properties of a ceramic matrix composite; J. Am. Ceram. Soc. **70**/7 (1987) 466-469.

[14] C. Rief, M. Lindner, K. Kromp: Experimental documentation and model calculation of damage mechanisms in loading a RCC-material in a bidirectional layup; ASTM STP (1989) 565-579.

[15] A. Bornhauser, K. Kromp R.F. Pabst: R-curve evaluation with ceramic materials at elevated temperatures by an energy approach using direct observation and compliance calculation of the crack length; J. Mater. Sci. **20** (1985) 2586-96.
[16] I. Appel: Thesis, University of Stuttgart, FRG; 1990.
[17] A. Wanner, K. Kromp: Young's and shear moduli of laminated carbon/carbon composite by a resonant beam method; in: "Brittle Matrix Composites 2", ed. by A.M. Brandt and I.H. Marshall, Elsevier Appl. Sci. Publ., London-New York (1988) 280-89.
[18] J. Jortner: Macroporosity and interface cracking in multi-directional carbon/carbons; Carbon **24**/5 (1986) 603-13.

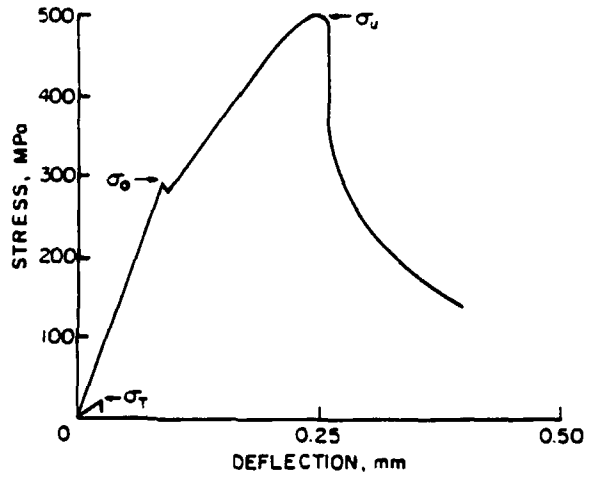

Fig. 1 Schematic graph of an uniaxially endless fiber-reinforced composite, indicating longitudinal and transverse stress-deflection behaviour [2].

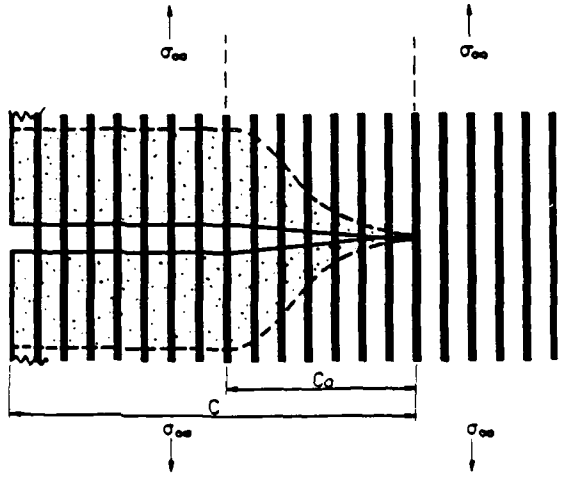

Fig. 2 Crack perpendicular to the fibers. In the dotted area, slipping between matrix and fibers has occurred (schematically).

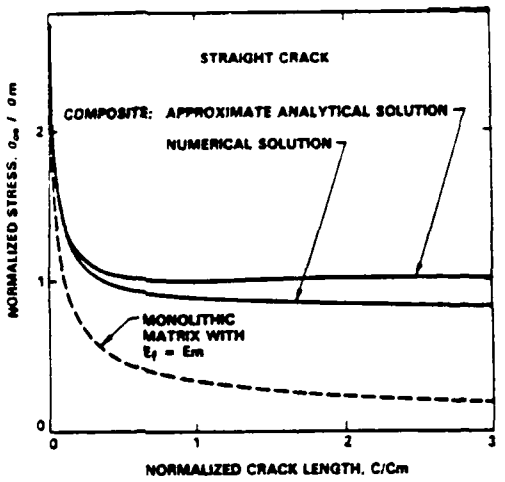

Fig. 3 Equilibrium-stress/crack size functions for matrix cracks in composites and in a monolithic ceramic [4].

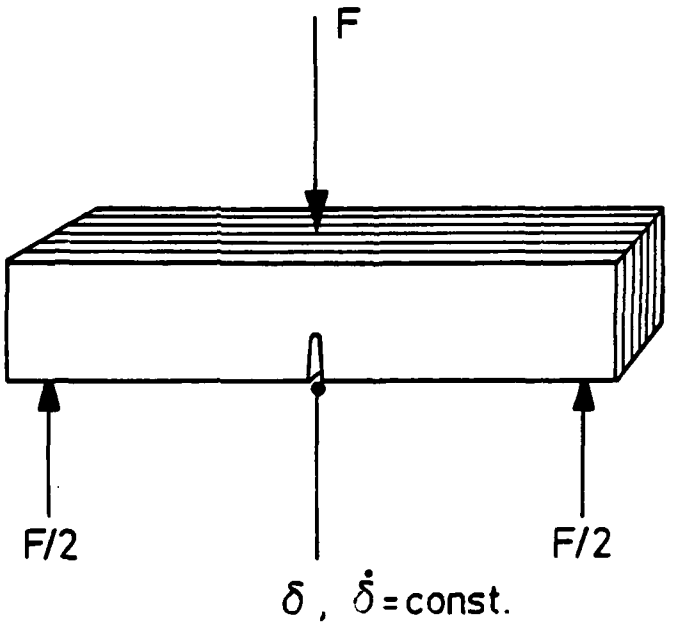

Fig 4 Edgewise loading of notched prismatic bars in displacement controlled three-point bending.

a)

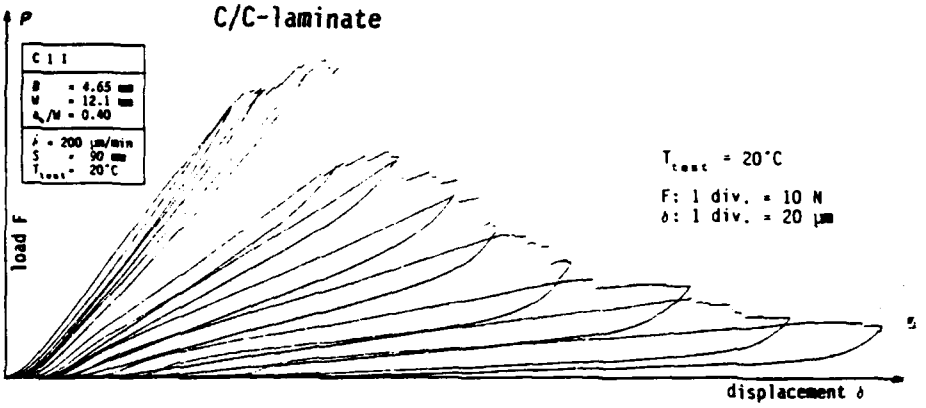

b)

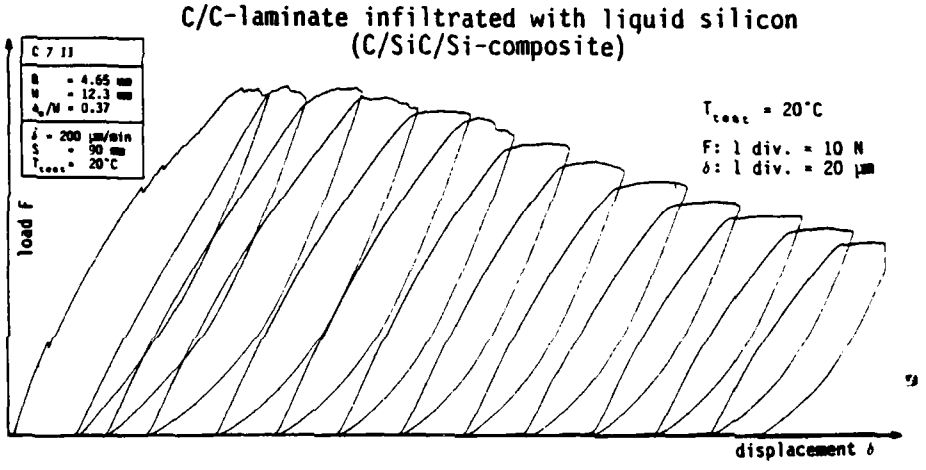

Fig 5ab Unloading-reloading cycles in displacement controlled three-point bending experiments
a) (C/C) laminate carbonized only
b) laminate carbonized + infiltratet by silicon (C/SiC/Si)

a) laminate carbonized only: pullout of complete bundles

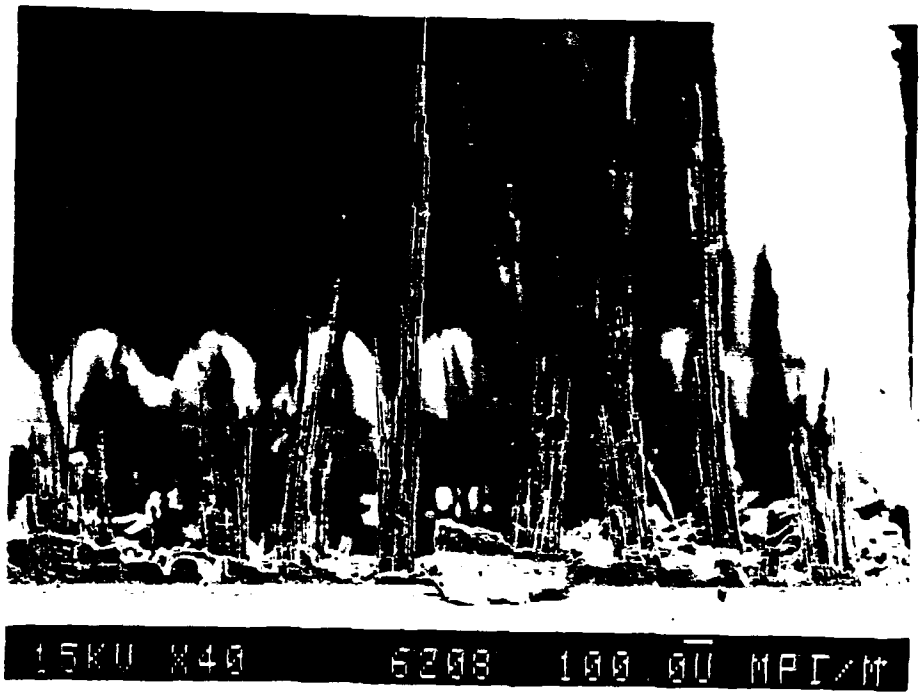

b) laminate carbonized + infiltrated by silicon: pullout of single fibers in the bundles, no pullout of complete bundles

Figs 6ab Pullout of the fracture surface of notched specimens in edgewise loading

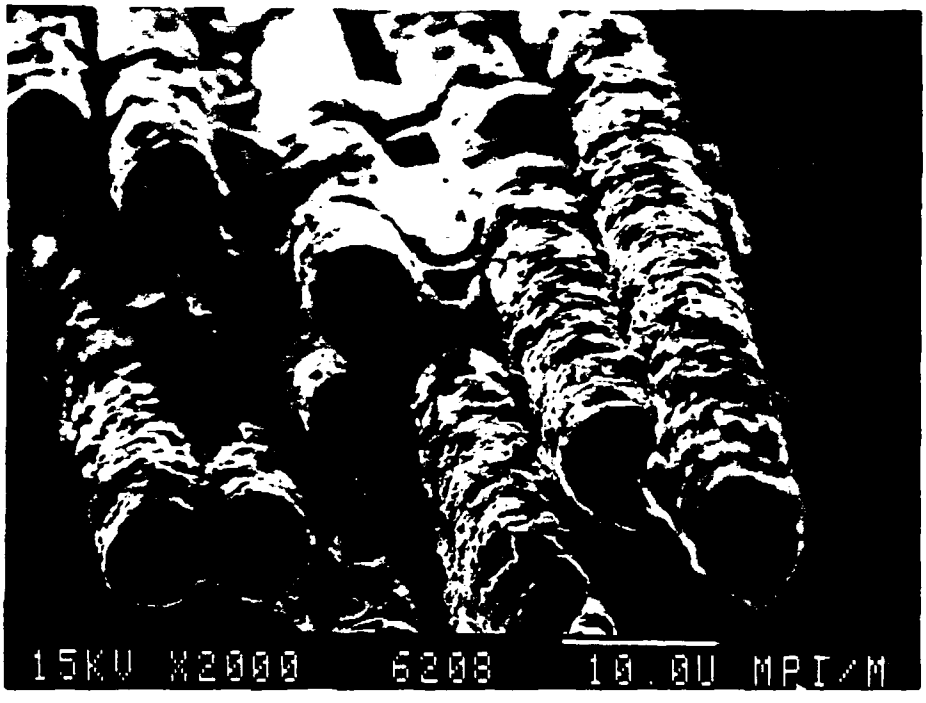

Fig 7 Laminate, carbonized + infiltrated by silicon: single fibers with adherent siliconized carbon matrix

a)

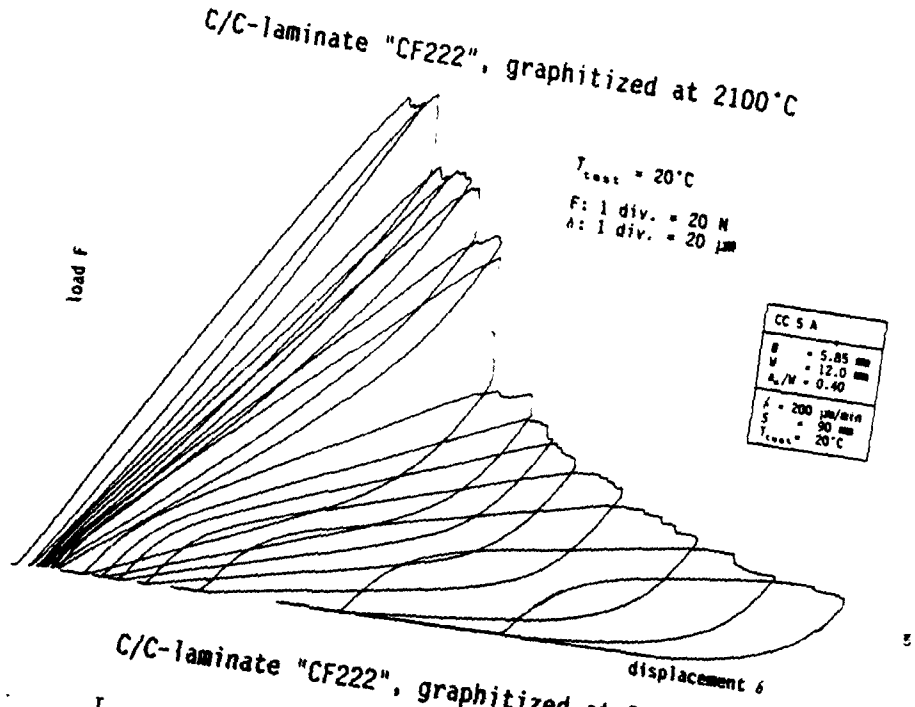

b)

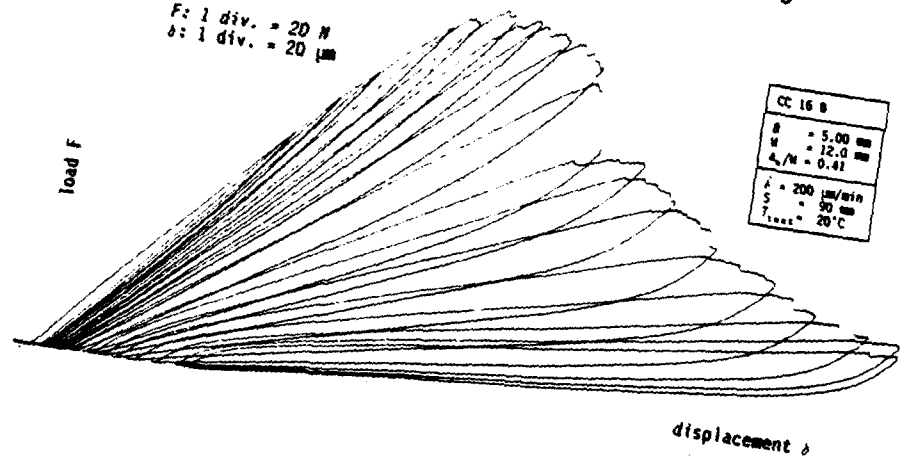

Fig 8ab Unloading-reloading cycles in displacement controlled three-point bending experiments at room temperature
a) laminate A, four times reimpregnated and carbonized, finally graphitized at 2100°C
b) laminate B, four times reimpregnated and carbonized, finally graphitized at 2400°C

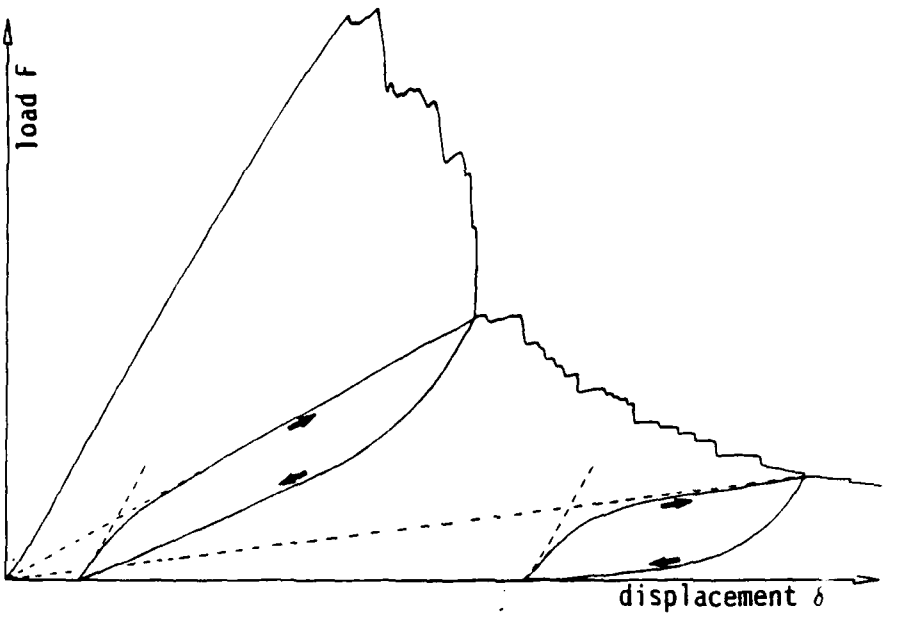

Fig 9 Change in slope of unloading-reloading cycles, schematically analogous to Fig 8a for laminate A.

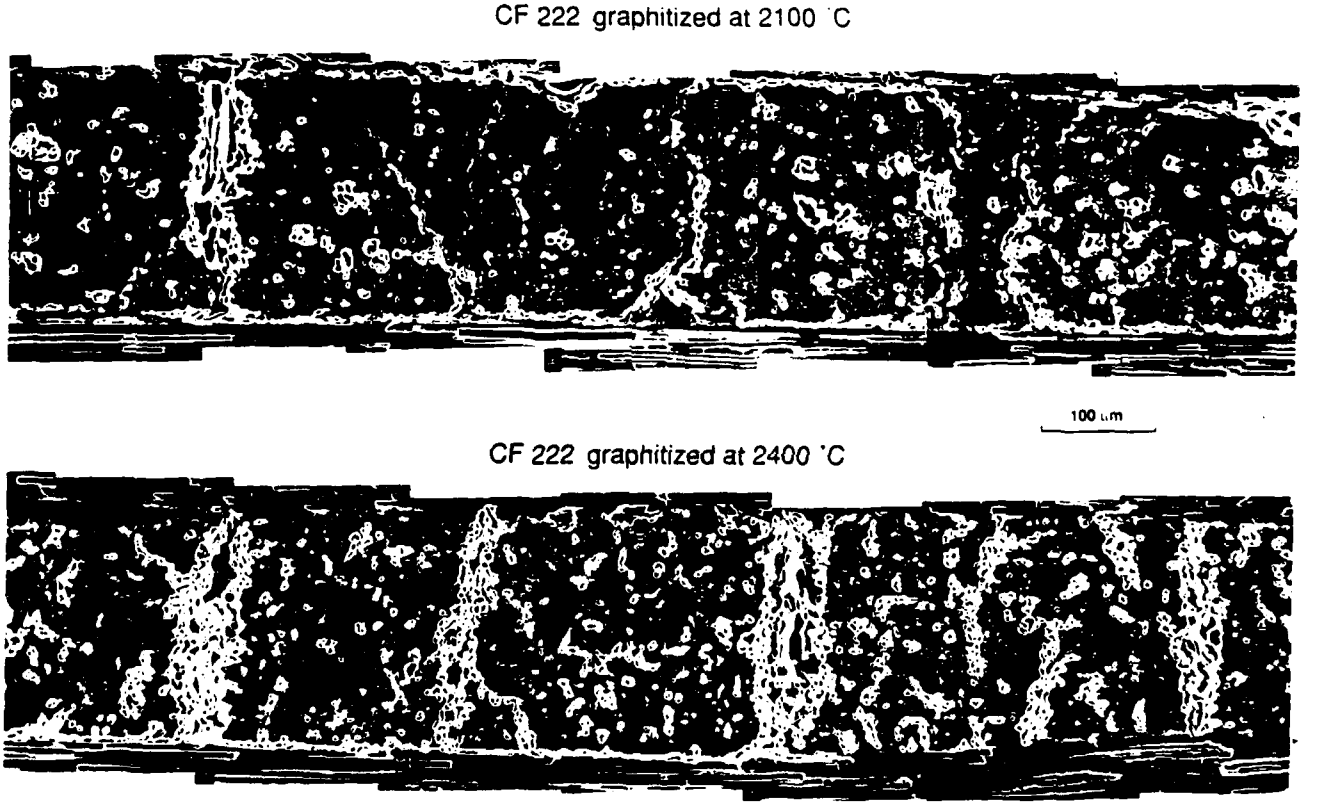

Fig 10ab Polished cut perpendicular to the plies
a) laminate A
b) laminate B

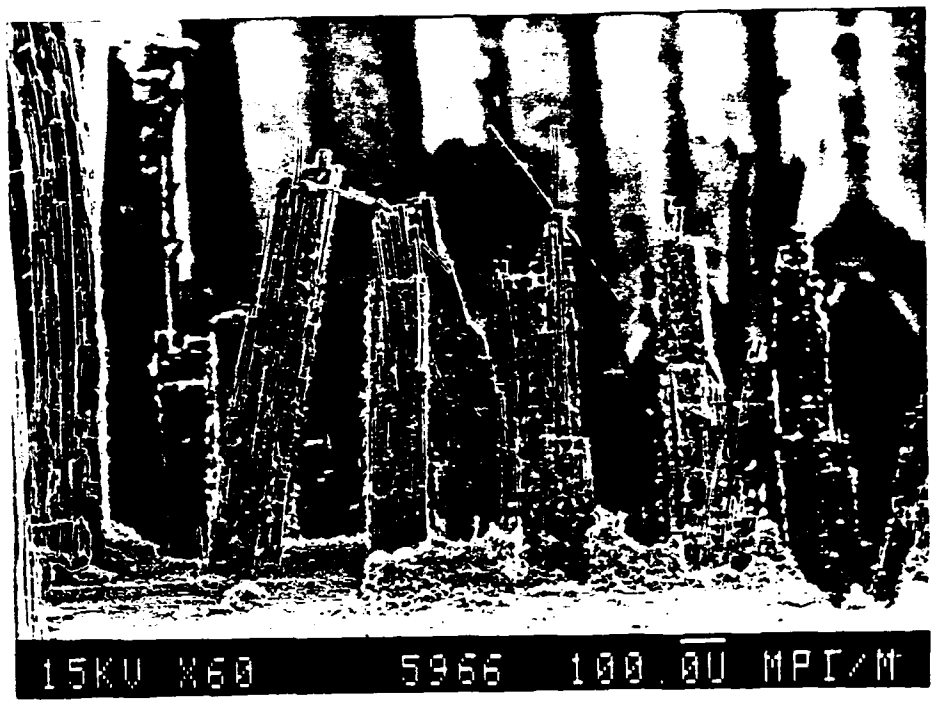

a) parallel to the fracture surface (notch root in front)

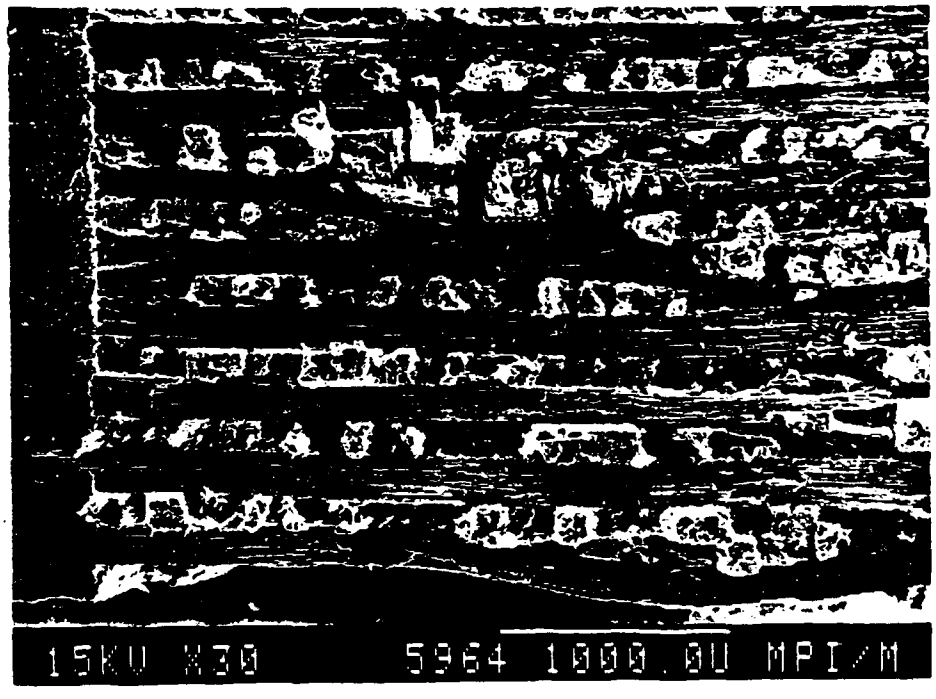

b) perpendicular to the fracture surface (notch root left)

Fig 11ab Pullout of the fracture surface of notched specimens in edgewise loading, laminate A

C/C-laminate "CF222", graphitized at 2100°C

a)

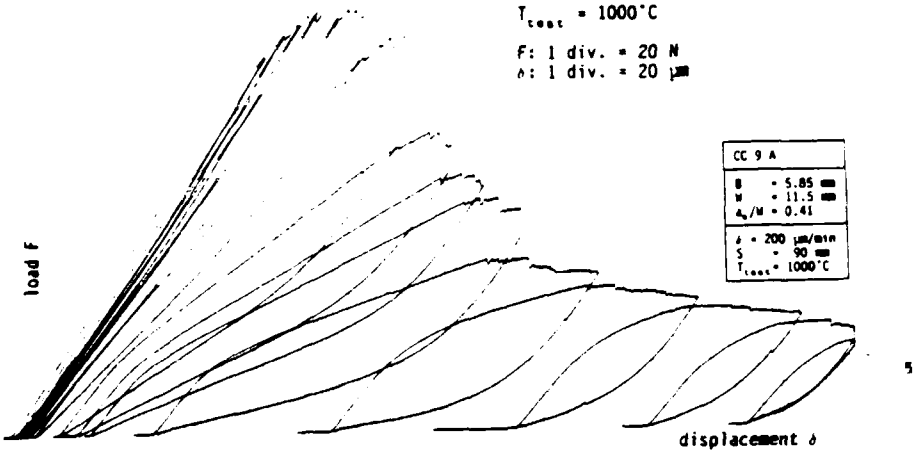

C/C-laminate "CF222", graphitized at 2400°C

b)

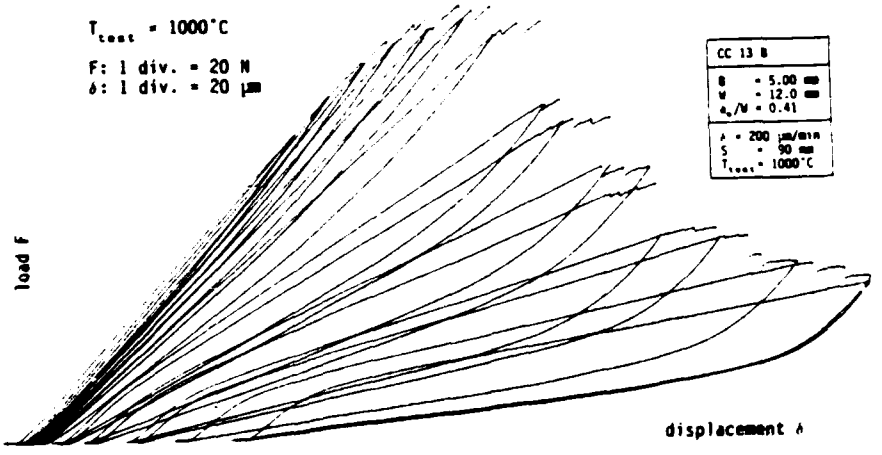

Figs 12ab Unloading-reloading cycles in displacement controlled three-point bending experiments at 1000°C
a) laminate A
b) laminate B

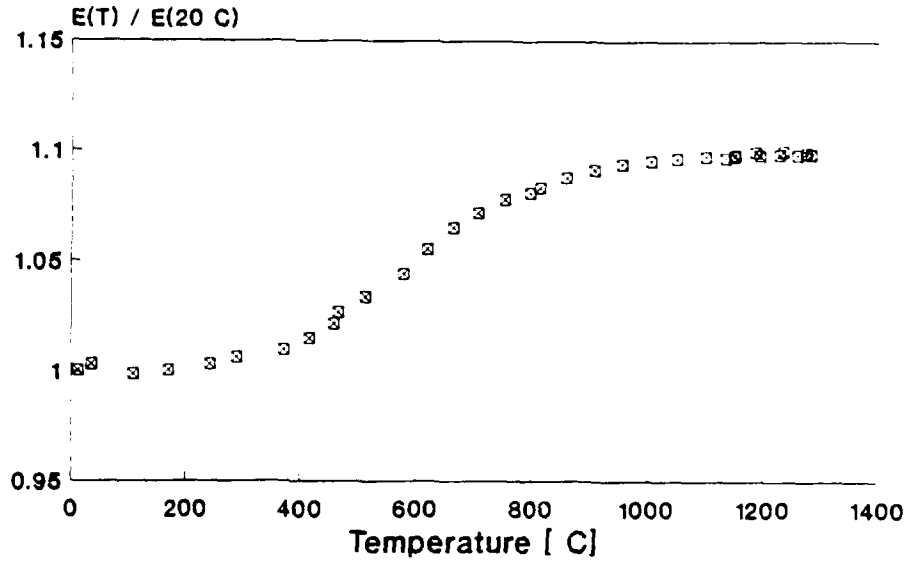

Fig 13 The dependence of Young's modulus on temperature for laminate A.

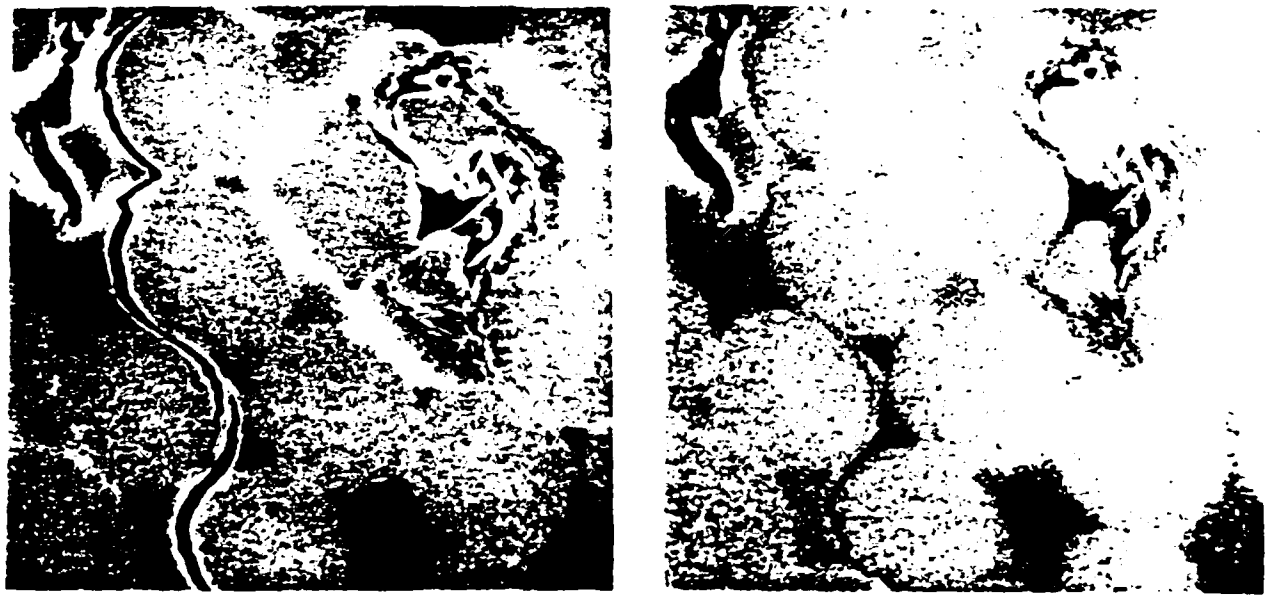

Fig 14 Cut perpendicular to the plies; pictures by SEM with heating equipment: room temperature (left), 780°C (right).

Preprints of the Proceedings

NATO Advanced Research Workshop

Toughening Mechanisms in Quasi-Brittle Materials

July 16-20, 1990

NSF Center for Advanced Cement-Based Materials
Robert R. McCormick School of Engineering and Applied Sciences
Northwestern University
Evanston, Illinois
USA

S.P. Shah, Editor

Sponsored By:

NATO Scientific Affairs Division
U.S. Air Force Office of Scientific Research
U.S. Air Force WRDC/MLLN
U.S. Army Research Office, Materials Science Division

Workshop Organizing Committee

Surendra P. Shah, Northwestern University, Director
Nils Claussen, Technical University of Hamburg
Katherine Faber, Northwestern University
Sidney Mindess, University of British Columbia
Peter Pratt, Imperial College London

Workshop Secretary

Eric Landis

Workshop Coordinator

Auria Rosenberg

Local Organizing Committee

Zdenek Bazant
Hamlin Jennings
Tianxi Tang
Mary Lynne Williams

Acknowledgements

G. A. Venturi and James Bombace, NATO Scientific Affairs Division
Spencer Wu, U.S. Air Force Office of Scientific Research
Theodore Nicholas, U.S. Air Force WRDC/MLLN
Edward Chen, Materials Research Division, U.S. Army Research Office
Jerome Cohen, Dean, Robert R. McCormick School of Engineering and Applied Sciences
Raymond Krizek, Chairman, Civil Engineering Department, Northwestern University

An additional acknowledgement is made to the ACBM center post-doctoral fellows and graduate students who spent many hours working to ensure the success of the workshop. These include:

Alberto Castro
Avraham Dancygier
Ravindra Gettu
Mustafa Karaguler
David Lange
Zongjin Li
Weiping Zhang

QUALITY INSPECTED 4

Accesion For
NTIS CRA&I ☑
DTIC TAB ☐
Unannounced ☐
Justification
By
Distribution/
Availability Codes
Dist | Avail and/or Special
A-1

PREFACE

A variety of ceramic materials has been recently shown to exhibit nonlinear stress-strain behavior. These materials include transformation-toughened zirconia which undergoes a stress-induced crystallographic transformation in the vicinity of a propagating crack, microcracking ceramics, and ceramic-fiber reinforced ceramic matrices. Since many of these materials are under consideration for structural applications, understanding fracture in these quasi-brittle materials is essential.

Portland cement concrete is a relatively brittle material. As a result mechanical behavior of concrete, conventionally reinforced concrete, prestressed concrete and fiber reinforced concrete is critically influenced by crack propagation. Crack propagation in concrete is characterized by a fracture process zone, microcracking, and aggregate-bridging. Such phenomena give concrete toughening mechanisms, and as a result, the macroscopic response of concrete can be characterized as that of a quasi-brittle material. To design super high performance cement composites, it is essential to understand the *complex fracture processes in concrete.*

A wide range of concern in design involves fracture in rock masses and rock structures. For example, prediction of the extension or initiation of fracture is important in: 1) the design of caverns (such as underground nuclear waste isolation) subjected to earthquake shaking or explosions, 2) the production of geothermal and petroleum energy, and 3) predicting and monitoring earthquakes. Depending upon the grain size and mineralogical composition, rock may also exhibit characteristics of quasi-brittle materials.

Recently, considerable interest has been developing in understanding and modeling the fracture processes in these quasi-brittle materials as well as in designing materials with improved toughness. The research activities in these groups of materials: ceramics, cement and rock can be substantially enhanced with the exchange of information between these three groups of investigators. Since the field is relatively new, it is likely that the researchers working with one set of materials are not aware of similar developments with other sets of materials. Although each material has its own set of specific

characteristics, many common aspects can be shared among these quasi-brittle materials. These include: 1) application of nonlinear fracture mechanics, 2) experimental and theoretical considerations of strain localization, 3) microscopic observation of fracture process zone, 4) non-destructive evaluation of damage, 5) models to relate microstructure with macroscopic response, and 6) development of experimental and theoretical tools.

The purpose of this workshop is to bring together researchers addressing the problem of fracture in cement, ceramics, and rock so that they can share their knowledge and develop a more general syntheses of the problem.

This preprint volume contains contributions from lecturers for each of the 9 sessions. The final proceedings of this workshop will be published in a hardcover book by Kluewer Academic Publishers (NATO ASI Series). This book will contain 36 chapters; the finalized contributions of 27 lecturers and 9 reporters.

I hope that the efforts of all who have contributed to this workshop will produce lasting and worthwhile results.

Surendra P. Shah

June 1990
Evanston, Illinois, USA

Table of Contents

Session 1: Fracture of Ceramics with Process Zone

Fracture Properties in SIC-Based Particulate Composites
K. T. Faber, W. -H. Gu, H. Cai, R. A. Winholtz and D. J. Magley....3

Crack Bridging Processes in Toughened Ceramics
Paul F. Becher....19

Fracture Process Zone in Concrete and Ceramics - A Matter of Scaling
Albert Kobayashi, Neil M. Hawkins and Richard C. Bradt....39

Session 2: Fracture in Concrete and Rock

Microcracking and Damage in Concrete
D. Francois....55

Cracking, Damage and Fracture in Stressed Rock
Philip G. Meredith....73

Test Methods for Determining Mode I Fracture Toughness of Concrete
B. L. Karihaloo and P. Nallathambi....107

Session 3: Theoretical Fracture Mechanics Considerations

Rate Effect, Size Effect and Nonlocal Concepts for Fracture of Concrete and Other Quasi-Brittle Materials
Zdenek P. Bazant....143

Micromechanics of Deformation in Rocks
John M. Kemeny and Neville G. W. Cook....167

Asymptotic Analysis of Cohesive Cracks and its Relation with Effective Elastic Cracks
J. Planas and M. Elices....217

Session 4: Experimental Observations

Microstructure, R-Curves and Mechanical Properties of Alumina-Based Ceramics (Synopsis)
Stephen J. Bennison, Srinivasarao Lathabai, Jurgen Rodel and Brian R. Lawn....235

Creep and Creep Fracture in Hot-Pressed Al_2O_3
A. Gordon Robertson, David S. Wilkinson and Carlos H. Caceres....241

Damage and Fracture Mechanisms During High Temperature Creep in Hot-Pressed Alumina
A. Gordon Robertson, David S. Wilkinson and Carlos H. Caceres....265
(Note: Presentation at Workshop will be a combination of both papers)

Study of the Fracture Process in Mortar with Laser Holographic Measurements
A. Castro-Montero, R. A. Miller and S. P. Shah....309

Session 5: Experimental Methods to Assess Damage

The Fracture Process in Concrete
Sidney Mindess....335

Characterization of the Fracture Behavior of Ceramics Through Analysis of Crack Propagation Studies
R. W. Steinbrech, R. M. Dickerson and G. Kleist....353

A Review of Experimental Methods to Assess Damage During Fracture of Rock, Concrete and Reinforced Composites
Hideaki Takahashi....377

Session 6: Theoretical Micromechanics Based Models

A Review of Some Theories of Toughening Mechanisms in Quasi-Brittle Materials
C. Atkinson....397

On the Form of Micromechanical Models of the Brittle Deformation of Solids
Dusan Krajcinovic and Michal Basista....415

On the Relationship Between Fracturing of Brittle Microcracking Solid and its Effective Elastic Properties
Mark Kachanov....439

Session 7: Fracture Process in Fiber Reinforced Ceramics

The Fracture Resistance and Strength of Brittle Matrix Composites
F. Zok....447

Session 8: Fracture Toughness of Fiber-Reinforced Cement Composites

Research Challenges in Fiber Reinforced Concrete
Victor C. Li....471

Failure Characterisation of Fibre-Reinforced Cement Composites with R-Curve Characteristics
Yiu-Wing Mai....489

Characterization of Interfacial Bond in FRC Materials
H. Stang and S.P. Shah....529

Session 9: Strain Rate, Thermal, Time and Fatigue Effects

Growth of Discrete Cracks in Concrete under Fatigue Loading
Dirk A. Hordijk and Hans W. Reinhardt.....553

Fracture of Concrete at High Strain Rate
C. Allen Ross.....571

Session 1:

Fracture of Ceramics with Process Zone

Chairs:

Leon Keer
Northwestern University
Evanston, U.S.A

Hamlin Jennings
Northwestern University
Evanston, U.S.A

Reporter:

Heinz Hübner
Technische Universitat
Hamburg, F.R.G

FRACTURE PROPERTIES IN SiC-BASED PARTICULATE COMPOSITES

K. T. Faber, W.-H. Gu, H. Cai, and R. A. Winholtz
Northwestern University
Department of Materials Science and Engineering
Evanston, Illinois 60208
U.S.A.

D. J. Magley
The Ohio State University
Department of Materials Science and Engineering
Columbus, Ohio 43210
U.S.A.

ABSTRACT. In order to evaluate the role of residual stresses in fracture toughening, a SiC-based particulate composite has been studied under uniform stressing conditions and in the near tip stress field of a pre-cracked specimen. First, residual stresses in a SiC-TiB_2 composite before and after stressing have been measured using x-ray diffraction. Tensile residual stresses in the TiB_2 drop by 50% after bending stresses of 250 MPa were applied. Likewise, the compressive residual stresses in the SiC phase decrease accordingly. Second, in the near tip stress field, a process zone of microcracks has been measured using transmission electron microscopy of thin foils taken from various locations from a fracture surface of a fracture mechanics specimen. Microcrack zones greater than 150 μm in height have been measured. Crack bridging sites of TiB_2 particles operate more than a few millimeters behind a propagating crack. Hence, the toughening in this system is comprised of both stress-induced microcracking and crack bridging. The various contributions to the toughening are discussed.

1. Introduction

The fracture toughening of ceramic materials has received a great deal of attention over the last decade. Mechanisms by which brittle materials can be toughened fall into two categories: process zone mechanisms and bridging mechanisms.[1] Process zone toughening, either by stress-induced phase transformations or stress-induced microcracking, provides shielding of a propagating crack by virtue of the microstructural changes which occur in the near vicinity of the crack. Bridging mechanisms operate behind a crack tip and provide closure forces which also act to reduce the applied stress intensity. In both cases, residual stresses may serve either as source or as a consequence of the the toughening process and should be considered in examining the toughening increment.

Residual stresses in two phase materials have long been recognized as having a significant influence on mechanical strength. In the extreme, residual stresses can result in spontaneous microcracking on cooling, destroying mechanical integrity. The conditions under which such cracking occurs are now well established.[2,3] Cracking can be avoided by maintaining a particle size distribution below some critical size, b_c, described by

$$b_c = \eta K_{Ic}^2\{(1+\nu_m)/2 + \beta(1-2\nu_p)\}/[E_m \Delta\alpha\Delta T]^2 \quad (1)$$

where η is constant ranging from 2 to 8, K_{Ic} is the fracture toughness of the microcracking site (often the interface), E is the elastic modulus, ν is Poisson's ratio, β is the modulus ratio, E_m/E_p, and the subscripts, m and p, refer to the matrix and particulate phases, respectively. The product $\Delta\alpha\Delta T$ is the thermal mismatch strain, where $\Delta\alpha$ is the difference in thermal expansion coefficients of the matrix and particulate phases, and ΔT is the difference between the temperature at which relaxation stops and the temperature of interest. However, it is below the threshold b_c where the present interest lies. It has been postulated that a regime exists whereby residually-stressed particles in the vicinity of an advancing crack will microcrack when a critical value of applied stress is reached. Such stress-induced microcracking is suggested to result in significant toughening by shielding the crack from the applied loading. [3-7] It is the intent of this paper to examine stress-induced phenomena in two-phase, non-transforming ceramics under uniform and non-uniform loading. The system chosen for study is a SiC-TiB_2 composite where residual stresses arise from a high thermal expansion mismatch.

2. The Silicon Carbide-Titanium Diboride System

Silicon carbide, although a highly refractory material, is limited by its low fracture toughness ($K_{Ic} \cong 3.22$ MPa$\sqrt{m}$). Additions of TiB_2 to SiC have provided significant increases in the fracture toughness ($\Delta K_c \cong 5.0$ MPa$\sqrt{m}$) as measured by a few investigators [8-10], although the operative toughening mechanisms were not identified. SiC-TiB_2 has also been known to exhibit R-curve behavior [10], a manifestation of both shielding and bridging processes.

The materials studied here were prepared by pressureless sintering at temperatures in excess of 2000°C and were nearly 99% dense. The materials examined in this study contained TiB_2 concentrations of 15.2%, by volume. The average TiB_2 grain size was measured to be approximately 4.5 μm, less than the critical size for spontaneous microcracking calculated using Eqn. (1). Residual stresses in this system arise from a high thermal expansion mismatch where α (SiC) $\cong 5.6 \times 10^{-6}$ °C^{-1} and α (TiB_2) $\cong 7.9 \times 10^{-6}$ °C^{-1} over the temperature range 25° to 1700°C. We may approximate the residual stress by considering a spherical TiB_2 particle in an isotropic SiC matrix by [11]:

$$\sigma^R = \frac{\Delta\alpha\Delta T}{(1+\nu_m)/(2E_m) + (1-2\nu_p)/E_p} \quad (2)$$

For the appropriate thermal and elastic properties of SiC and TiB_2, σ^R is of the order of 1.9 GPa.

3. Experimental Observations of Toughening Processes in SiC-TiB_2

In an effort to examine the potential toughening mechanisms associated with the high degree of residual stress in these SiC-based materials, a variety of experimental techniques have been utilized. First, if stress-induced microcracking is actually occurring, then some monitor of the stress relief on microcracking is warranted. Residual stress analysis via x-ray diffraction is chosen for such studies. This technique will provide

conclusive, albeit indirect, evidence for the microcracking process. Direct observation of the microcrack zone via transmission electron microscopy is also employed. Finally, additional toughening behind the crack, also associated with residual stress, is examined through interrupted fracture experiments. The three will be described herein.

3.1 Microcracking Under Uniform Stress

To establish stress-induced microcracking in a uniform stress field, residual stresses were measured by x-ray diffraction prior to stressing and upon unloading. For this investigation, the SiC-TiB_2 specimens were electrically discharge machined into bars 7.62 x 1.27 x 0.635 cm^3 and polished to a 0.25 μm finish using a sequential treatment of diamond pastes. A pressureless-sintered SiC, containing sintering aids of boron and carbon, was diamond machined with identical surface finishes and used as a standard. The reflections examined were the (121) for 6H SiC, the major SiC polytype present, and the (202) for TiB_2 at approximately 148° 2θ and 144° 2θ, respectively. Further details of the x-ray diffraction experimental set up may be found in reference 12.

During x-ray diffraction the sample was oriented according to the scheme shown in Figure 1. A General Electric quarter circle was used for both the ψ-tilts and the ϕ-rotations. Diffraction measurements were made at six ϕ values between 0 and 300° and six ψ values between 0 and 45° for each ϕ setting. Peak positions at any ϕ, ψ rotation were measured by step scanning at 0.05° 2θ increments for 100 seconds. Because peaks have a tendency to broaden as the specimen is rotated about the ψ axis due to x-ray defocussing, longer counting times were employed at large values of ψ for greater accuracy. Peak positions were determined by fitting the measured values of intensity *versus* 2θ *to a parabola.*

After the x-ray measurements were made and the residual stresses determined, the SiC-TiB_2 composite and the SiC standard were placed in a four-point bend fixture and loaded until fracture occurred. At fracture the outer fiber tensile stress reached 249 and 266 MPa for the composite and the standard, respectively. X-ray measurements were repeated in areas which experienced the maximum tensile stress to monitor any changes in the residual stress profile following stressing. Although four-point bending can hardly be considered uniform loading, the depth of penetration of the x-rays (approximately 50 μm below the surface to account for 90% of the x-ray intensity) allows examination of the stress over a nearly uniformly stressed region.

The complete stress matrix can be determined from the stress analysis, as shown by Noyan [13] and Cohen [14]. The change in the interplanar spacing related to stresses in the coordinate system in Figure 1 is

$$\frac{d_{\phi\psi}}{d_o} - \epsilon_{\phi\psi} = \frac{S_2}{2}(\sigma_{11}\cos^2\phi + \sigma_{12}\sin 2\phi + \sigma_{22}\sin^2\phi - \sigma_{33})\sin^2\psi + \frac{S_2}{2}\sigma_{33} + S_1(\sigma_{11} + \sigma_{22} + \sigma_{33}) + \frac{S_2}{2}(\sigma_{13}\cos\phi + \sigma_{23}\sin\phi)\sin 2\psi \qquad (3)$$

where d_o is the unstressed lattice spacing, ϵ represents the strain, and

S_1 and $S_2/2$ are the x-ray elastic constants $1+\nu/E$ and ν/E, respectively, for an isotropic solid. (The bulk values of ν and E were used to determine their values [15,16]). The stresses were determined from the measured d-spacings by a least-squares procedure [17] The x-ray d-spacing measurements yield the total stresses, ${}^{t}\sigma_{ij}$, associated with each phase. These must be partitioned into microstresses, ${}^{\mu}\sigma_{ij}$, (those resulting from thermal expansion mismatch and macrostresses, ${}^{m}\sigma_{ij}$, (those from machining):

$$\left\langle {}^{t}\sigma_{ij}{}^{SiC}\right\rangle = \left\langle {}^{\mu}\sigma_{ij}{}^{SiC}\right\rangle + \left\langle {}^{m}\sigma_{ij}\right\rangle \tag{4}$$

$$\left\langle {}^{t}\sigma_{ij}{}^{TiB_2}\right\rangle = \left\langle {}^{\mu}\sigma_{ij}{}^{TiB_2}\right\rangle + \left\langle {}^{m}\sigma_{ij}\right\rangle \tag{5}$$

where the macrostresses are assumed to be the same in each phase. The total microstresses must also sum to zero, such that

$$(1-f)\left\langle {}^{\mu}\sigma_{ij}{}^{SiC}\right\rangle + f\left\langle {}^{\mu}\sigma_{ij}{}^{TiB_2}\right\rangle = 0 \tag{6}$$

where f is the volume fraction of the TiB_2 phase. Solving Eqns. (4), (5) and (6) simultaneously allows the microstresses and macrostresses of each phase to be resolved:

$$\left\langle {}^{\mu}\sigma_{ij}{}^{SiC}\right\rangle = f\left[\left\langle {}^{t}\sigma_{ij}{}^{SiC}\right\rangle - \left\langle {}^{t}\sigma_{ij}{}^{TiB_2}\right\rangle\right] \tag{7}$$

$$\left\langle {}^{\mu}\sigma_{ij}{}^{TiB_2}\right\rangle = (1-f)\left[\left\langle {}^{t}\sigma_{ij}{}^{TiB_2}\right\rangle - \left\langle {}^{t}\sigma_{ij}{}^{SiC}\right\rangle\right] \tag{8}$$

$$\left\langle {}^{m}\sigma_{ij}\right\rangle = (1-f)\left\langle {}^{t}\sigma_{ij}{}^{SiC}\right\rangle + f\left\langle {}^{t}\sigma_{ij}{}^{TiB_2}\right\rangle \tag{9}$$

A difficulty of triaxial stress measurement by diffraction has been the determination of a precise valve of d_o. It has been shown that errors in d_o give rise to an error in the hydrostatic microstresses. [18] In contrast, errors of this kind will cancel out in the present measurements when comparing the pre-stressed with the post-stressed material.

Rather than examining the total stress matrices in order to compare the pre-loaded and post-loaded microstresses, the stress matrices are better analyzed by examining the hydrostatic component of the stress. However, one must first note that the stresses derived from x-ray

diffraction analysis do not provide the true internal stresses. The σ_{33} component is influenced by the near surface effect, and should necessarily be zero if stresses only at the surface are measured. However, the σ_{33} measurement represents d-spacing data collected from up to 50 microns, or approximately 10 grain diameters below the surface. To supersede these difficulties, an "effective" hydrostatic stress (defined as $(\sigma_{11} + \sigma_{22})/2$) has been calculated and it is plotted in histogram form in Figure 2.[22] It is clear that the data represents definitive evidence for residual stress relaxation on application of a stress in SiC-TiB_2 as the microstresses drop by nearly 50%. The SiC standard, in contrast, shows no significant change in the average stress after loading. The present observations demonstrate indisputable evidence for stress-induced microstress relief in a non-transforming brittle material. These results are consonant with the model of stress-induced microcracking in SiC-TiB_2.

3.2 Microcracking in the Near Crack Tip Stress Field

The near crack tip region in conventional fracture mechanics specimens provides a region to examine stress-induced process zone formation. The crack opening displacement of microcracks in SiC-TiB_2 composites is too small to be detected by either optical microscopy or scanning electron microscopy; the resolution of transmission electron microscopy is necessary to explore any microcracking. Thin sections were cut from the fracture surface of the SiC-TiB_2 composite prepared from four depths from the fracture surface of a double cantilever beam specimen. Details of the TEM sample preparation are given in reference 19.

Microcracks can be identified by Fresnel diffraction using the underfocus-overfocus process in the bright-field image.[20] Typical microcracks occur at the boundaries between TiB_2 and SiC (Figure 3(a)), due to the thermal expansion mismatch described earlier, or between TiB_2 particles (Figure 3(b)), due to thermal expansion anisotropy in the hexagonal TiB_2 structure. The former, however, are the more common. The thickness enabling the image formation is about 0.1 μm and the crack opening displacement is about 26 nm. Therefore, it is necessary to rotate the thin foil through various stereo angles to observe every microcrack. The observable fraction of the solid angle for the double tilt stage which is allowed to rotate from -30° to $+30^\circ$ is 0.29.

The distribution of microcrack lengths at different distances from the fracture surface are similar in shape and are shown in Figure 4. The number of microcracks increases dramatically as the fracture surface is approached. The microcracks located at approximately 5 mm from the fracture surface represent cracks produced during sample preparation, either occurring spontaneously during cooling (based upon the conditions in Eqn. 1) or through the ion thinning process, and will be treated as background. Since the TiB_2 particles are polyhedra and the microcracks are generally located along grain facets of the polyhedra, a microcrack can be reasonable treated as a penny-shaped crack. Hence, the microcrack density parameter, ϵ, may be defined as [21]:

$$\epsilon = \frac{3}{4\pi} N_A \langle \ell^2 \rangle \qquad (10)$$

where N_A is the number of microcracks per unit area and ℓ is the length of the microcrack measured in the thin foil. The mean microcrack diameter is approximately 2.8 μm and is independent of distance from the fracture surface. This implies that the residual stress from the thermal expansion

mismatch dominates the applied stress term. The profile of microcrack density perpendicular to the fracture surface is shown in Figure 5. These data are corrected for the fraction of the observable solid angle described above. The microcrack density is said to be saturated; that is, all TiB_2 particles have a least one microcrack associated with them, and ϵ equals 0.53 near the fracture surface. Furthermore, from the limited data, ϵ linearly decreases with increasing distance from the fracture surface. The microcrack density extrapolates to the background level at about 160 μm if a linear profile is assumed. Microcrack zones on the order of hundreds of microns in a similar SiC-TiB_2 have also been measured using small angle x-ray scattering.[22]

This quantitative examination provides unambiguous information to evaluate microcrack toughening. It provides the first direct evidence of stress-induced microcracking in a particulate non-transforming ceramic composite by demonstrating the existence of a microcrack process zone.

3.3 Crack Bridging Behind an Advancing Crack

The fracture surface of SiC-TiB_2 provides further insight into the mechanisms which give rise to enhanced toughening in this system. As in unreinforced sintered SiC [23], fracture in the SiC appears to be primarily transgranular. However, TiB_2 particles rarely fail transgranularly at the crack tip in the materials studied. Upon examination of double cantilever beam specimens interrupted during testing, there are numerous examples of TiB_2 particles acting as bridges spanning the primary crack (Figure 6). On examination of samples during testing and prior to catastrophic failure on unloading, the bridged grains were observed to be active nearly 3 mm from the crack tip. At large distances from the crack tip, breakaway generally occurs in the SiC matrix, or by complete pullout of the TiB_2 grains. Given these microstructural observations, the contribution of crack bridging to the toughening by unbroken TiB_2 grains must also be evaluated in addition to the contribution of stress-induced microcracking.

4. The Toughening Analysis

4.1 Stress-Induced Microcracking

In order to assess the contribution of stress-induced microcracking, we examine the model of Hutchinson.[24] Shielding from microcracking is comprised of two contributions: shielding due to the reduced moduli and shielding due to residual strain associated with the microcracking event. For conditions where the crack is assumed to be steadily growing with a zone of randomly-oriented microcracks induced by a critical mean stress, the shielding due to the reduced moduli can be written as

$$K_I/K_I^{\infty} = 1 - 0.608\ \delta_1 + 0.707\ \delta_2 \qquad (11)$$

where K_I is the stress intensity factor at the crack tip, K_I^{∞} is the applied stress intensity and δ_1 and δ_2 are given as

$$\delta_1 = 32\ (5-\nu)\ \epsilon_s / [45\ (2-\nu)]$$

and

$$\delta_2 = 16\nu\ (1-8\nu+3\nu^2)\ \epsilon_s / [45\ (2-\nu)]$$

where ϵ_s is the saturated microcrack density.

The shielding contribution from the residual strain is of the form

$$K_I - K_I^{\infty} = \frac{1}{3\sqrt{2\pi}} \frac{E}{(1-\nu)} \int \theta^M \frac{\cos(3\theta/2)}{r^{3/2}} dA \qquad (12)$$

where θ and r are the polar coordinates, θ^M is the dilatation strain associated with microcracking, and the integral is taken over the upper half of the microcrack zone. We approximate the microcrack which forms along a SiC-TiB_2 facet by a prototypic microcrack which forms in the center of a particle under a residual tensile stress. The dilatation strain may then be written

$$\theta^M = 16\ (1-\nu^2)\ \epsilon\ \sigma^R / 3E \qquad (13)$$

where σ^R is the residual stress. The elastic mismatch between SiC and TiB_2 is small, and therefore, neglected.

Substituting Eqn (13) into Eqn (12), we obtain

$$K_I - K_I^{\infty} = \frac{16}{6\sqrt{2\pi}} (1+\nu)\ \sigma^R \int \epsilon \frac{\cos(3\theta/2)}{r^{3/2}} dA \qquad (14)$$

The above integral was evaluated numerically using the microcrack distribution information presented in Section 3.2, and coupled with calculations of σ^R. The amount of shielding due to the residual strain contribution for the SiC-TiB_2 system is then computed to be -1.98 MPa$\sqrt{m}$. The combined effects of the modulus reduction and residual strain derive from Eqns. (11) and (14). However, to evaluate the toughening, one must recall that a crack must now propagate through a medium of microcracks. The reduced toughness of the microcracked material K_c^m ahead of the crack tip has been found to be of the form, [25]

$$K_c^m / K_c = 1 - \zeta\ \epsilon \qquad (15)$$

where K_c is the toughness of the microcrack free material and the value of ζ is 0.825. By setting $K_I = K_c^m$ in Eqn (14), and equating K_c to the toughness of monolithic SiC (3.22 MPa$\sqrt{m}$), K_I affords a prediction of the toughness due to stress-induced microcracking. For the SiC-TiB_2 examined, the toughening due to stress-induced microcracking is approximately 2.14 MPa$\sqrt{m}$, on the order of half of the observed toughening.

4.2 Crack Bridging

We use the model of Campbell et al. [26] designed for whisker-reinforced materials to examine toughening due to the bridging of TiB_2 grains. The steady state toughening can be written in terms of the critical strain energy release rate, $\mathcal{G}_c$, as

$$\Delta\mathcal{G}_c / fd \approx S^2/E - Ee_T + 4(\Gamma_i/R)/(1-f) + (\tau/d)\Sigma_i(h_i^2/R) \qquad (16)$$

where d is the debond length, e_T is the misfit strain, Γ_i is the interface fracture energy, R is the particle radius, f is the volume fraction of reinforcing particles, S is the particle strength, τ is the sliding resistance, and h_i is the pullout length. The four terms represent, respectively: the stored elastic strain energy in the reinforcement over the microcrack length prior to failure, the residual strain energy within the microcrack length, the energy needed to fracture the SiC-TiB_2 interface and the energy contribution to TiB_2 pullout.

For particles under residual tension, the last term can be neglected and we use Campbell et al.'s solution for reinforcements under tension which are oriented normal to the applied stress:

$$\Delta\mathcal{G}_c = fS^2R\,[(\lambda_1+\lambda_2 d/R)^2 - (E_p e_T/S)^2(\lambda_3 + \lambda_4 d/R)^2]/E_p(\lambda_1 + \lambda_2 d/R) + 4f\Gamma_i d/(1-f)R \qquad (17)$$

The parameters, λ_i, for i = 1 to 4 are coefficients used to describe the matrix crack opening for a given value of modulus mismatch between the reinforcement and the matrix. Any estimate of the toughening increment will represent the toughening afforded from bridging only from grains oriented parallel to the applied loading (i.e. no TiB_2 grains are subject to bending moments, and consequently, there is no effective frictional pullout contribution). Further, these estimates are limited by the reliability of our estimates of the bridge strength, S, and of the interfacial toughness, Γ_i.

For estimates of the necessary parameters, we make the following assumptions: First, the elastic strain energy component is highly sensitive to the choice of reinforcement strength, S. As the TiB_2 particles rarely fracture in the wake, one would anticipate that the interface is strength-controlling. The strength of the interfaces may then be estimated to be bounded by the average residual stress, 1.6 GPa [19], since the interfaces did not spontaneously crack on cooling. Second, the misfit strain component is reduced from its theoretical value due to microcracking ahead of the crack tip. We calculate an effective misfit strain based upon microstress results from x-ray studies. Hence, the strain e_T is approximately 50% of the microcrack-free value. Third, the interfacial fracture toughness (Γ_i) is estimated to be of the order of SiC, i.e. approximately 15 J/m^2, as an upper bound. Fourth, debonding only occurs over the grain facet length *less* the average microcrack length. TEM observations have provided data for the average microcrack length, 2.1 μm, in this case. From the above assumptions, it is clear that the energy contribution to fracture the SiC-TiB_2 interface is dominant, though not large ($\cong$ 5.6 J/m^2). The elastic strain energy and the residual strain components are of nearly equal magnitude, though opposite in sign, and nearly cancel. Converting $\Delta\mathcal{G}_c$ to ΔK_c, the toughening increment due to crack bridging is equal to approximately 2.0 $MPa\sqrt{m}$. This value is of the correct order of magnitude to account for the remainder of the fracture toughening. However, the effect of interlocking grains (not oriented parallel to the applied stress) and their effective frictional contribution to the pullout are not accounted for and could result in additional toughening.

5. Concluding Remarks

In the SiC-TiB_2 composites studies, residual stresses are of a large enough magnitude to cause stress-induced microcracking in the near vicinity of a propagating crack. Both x-ray residual stress measurements and direct transmission electron microscopy observations provide evidence for this phenomenon. The total toughening, however, cannot be explained totally in terms of stress-induced microcracking. Instead, contributions from crack bridging are of the same order of magnitude as those from microcracking. A likely scenario is one suggested by Amazigo and Budiansky [27] where the bridging and process zone mechanisms are likely to interact. Specifically, the bridged crack, which allows for a greater crack tip stress intensity, will afford larger process zones. Direct measurements of the microcracking stress are required to test this hypothesis.

Acknowledgments

Materials for this study were graciously provided by the Carborundum Company, Niagara Falls, NY. This work was supported by the National Science Foundation under Grant No. DMR-8896212.

References

1. D. R. Clarke and K. T. Faber, "Fracture of Ceramics and Glasses", J. Phys. Chem Solids, 48 [11] 1115-55 (1987).

2. R. J. Davidge and T. J. Green, "The Strength of Two-Phase Ceramic/Glass Materials", J. Mater. Sci. 3 [6] 629-39 (1968).

3. A. G. Evans and K. T. Faber, "Toughening of Ceramics by Circumferential Microcracking", J. Am. Ceram. Soc. 64 [7] 394-98 (1981).

4. D. J. Green, P. S. Nicholson and J. D. Embury, "Fracture Toughness of Partially Stabilized ZrO_2 in the System CaO-ZrO_2", J. Am. Ceram. Soc. 56 [12] 619-23 (1973).

5. R. G. Hoagland, J. D. Embury and D. J. Green, "On the Density of Microcracks Formed During the Fracture of Ceramics", Scripta metall. 9 [9] 907-09 (1975).

6. A. G. Evans, "On the Formation of a Crack Tip Microcrack Zone", Scripta. metall. 10 [1] 93-97 (1976).

7. A. G. Evans and Y. Fu, "Some Effects of Microcracks on the Mechanical Properties of Brittle Solids-II. Microcrack Toughening", Acta metall. 33 [8] 1525-31 (1985).

8. J. E. Garnier, C. H. McMurtry, and A. Zangvil. "A Microanalytical Study of a SiC-based TiB_2 Particulate Composite", unpublished work.

9. C. H. McMurtry, W. D. G. Boecker, S. G. Seshadri, J. S. Zanghi, and J. E. Garnier, "Microstructure and Material Properties of SiC-TiB_2 Particulate Composites", Am. Ceram. Soc. Bull., 66 [2] 325-29 (1987).

10. D. J. Magley, M.S. Thesis, The Ohio State University, 1989.

11. J. Selsing, "Internal Stresses in Ceramics", J. Amer. Ceram. Soc. 44, 419 (1961).

12. D. J. Magley, R. A. Winholtz and K. T. Faber, "Residual Stresses in a Two Phase Microcracking Ceramic", J. Amer. Ceram. Soc., 73 [6] (1990).

13. I. C. Noyan, "Equilibrium Conditions for the Average Stresses Measured by X-Rays", Met. Trans. A, 14A, 1907-1914 (1983).

14. J. B. Cohen, "The Measurement of Stresses in Composites", Powder Diffraction, 1 [2] 15-21 (1986).

15. G. Simmons and H. Wang, *Single Crystal Elastic Constants and Calculated Aggregate Properties*, A Handbook, 2nd Ed., M.I.T. Press, Cambridge, MA 1971.

16. V. M. Lyubimskii "Elastic Properties of Silicon Carbide Polytypes", Sov. Phys. Solid State, 18 [10] 1814-15 (1977).

17. R. A. Winholtz and J. B. Cohen, "Generalized Least-squares Determination of Triaxial Stress States by X-Ray Diffraction and the Associated Errors", Aust. J. Phys., 41, 189-199 (1988).

18. R. A. Winholtz and J. B. Cohen, "Separation of the Macro- and Micro-Stresses in Plastically Deformed 1080 Steel", Adv. in X-Ray Anal., 32, 341-53 (1989).

19. H. Cai, W.-H. Gu, and K. T. Faber, "Microcrack Toughening in a Sic-TiB_2 Composite", pp. 892-901 in Proc. Am. Soc. Composites, Fifth Technical Conference, Technomic Publishing Company, Lancaster, PA (1990).

20. D. R. Clarke, "Observation of Microcracks and Thin Intergranular Films in Ceramics by Transmission Electron Microscopy", J. Amer. Ceram. Soc., 63 [1] 104-06 (1980).

21. B. Budiansky and R. J. O'Connell, "Elastic Moduli of a Cracked Solid", Int. J. Solids Structures, 12, 81-97 (1976).

22. R. Steinbrech, personal communication.

23. K. T. Faber and A. G. Evans, "Intergranular Crack-Deflection Toughening in Silicon Carbide", J. Amer. Ceram. Soc., 66 [6] C-94-96 (1983).

24. J. W. Hutchinson, "Crack Tip Shielding by Micro-Cracking in Brittle Solids", Acta metall., 35 [7] 1605-19 (1987).

25. T.-G. Suh, M.S. Thesis, Michigan State University, 1988.

26. G. H. Campbell, M. Ruhle, B. J. Dalgleish, and A. G. Evans, "Whisker Toughening: A Comparison Between Aluminum Oxide and Silicon Nitride Toughened with Silicon Carbide", J. Amer. Ceram. Soc., 73 [3] 521-30 (1990).

27. J. C. Amazigo and B. Budiansky, "Interaction of Particulate and Transformation Toughening", J. Mech. Phys. Solids, 36 [5] 581-95 (1988).

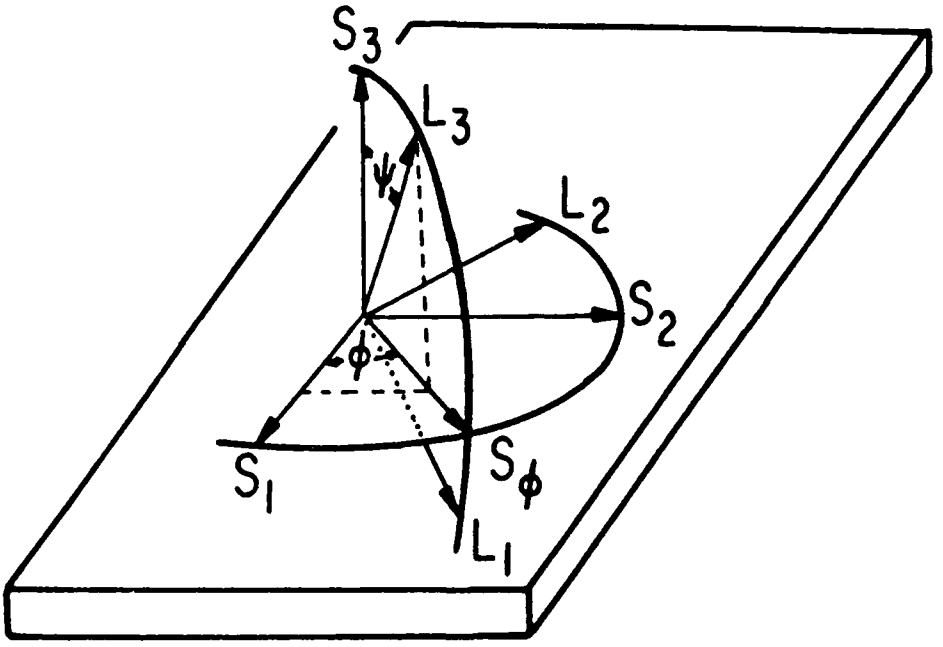

Figure 1. The coordinate system used in residual stress determinations. The S_1-S_2 surface represents the tensile surface of the SiC-TiB_2 bend bar.

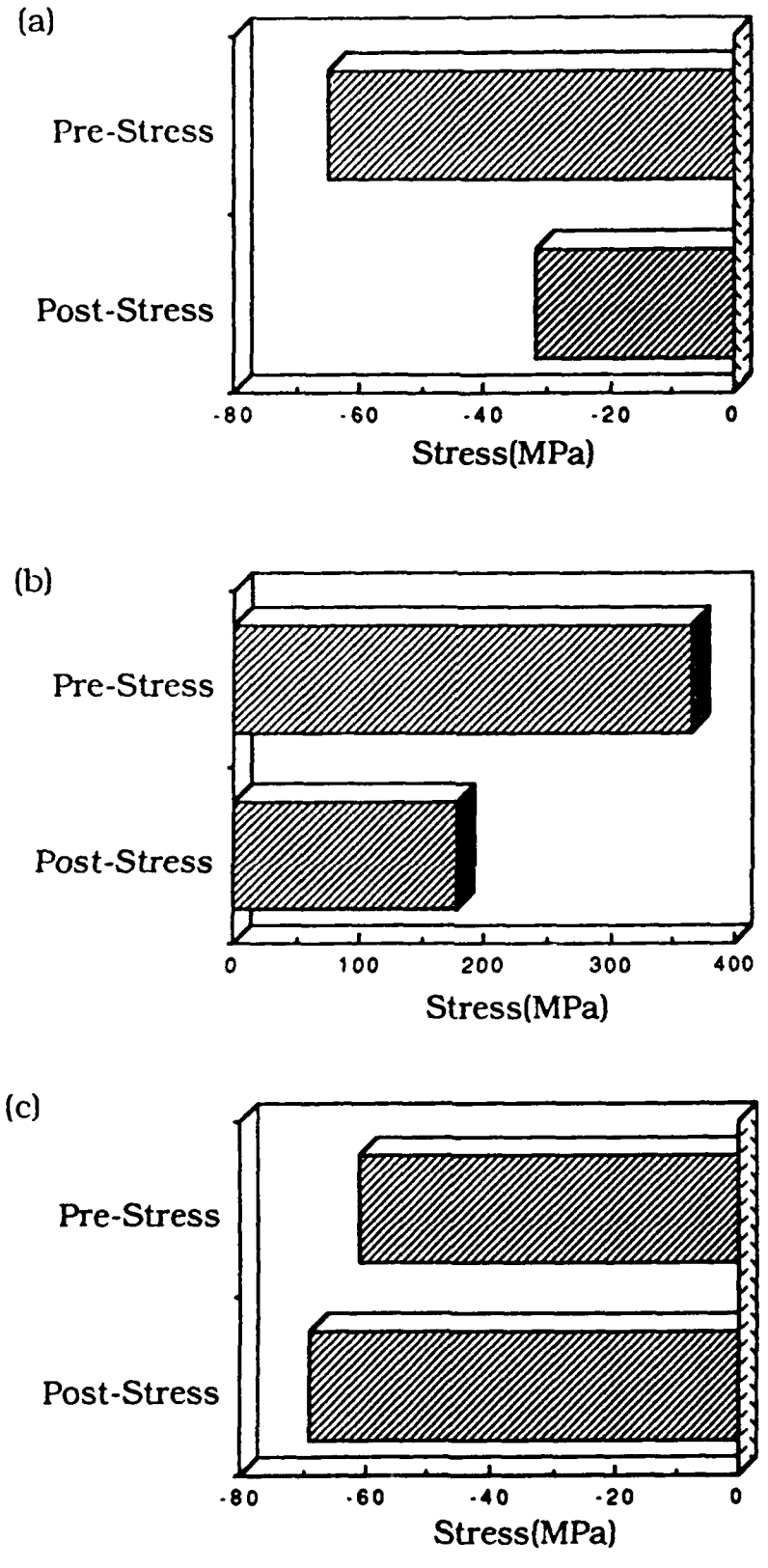

Figure 2. The effective hydrostatic stresses before and after loading for (a) the SiC phase in SiC-TiB_2, (b) the TiB_2 phase in SiC-TiB_2, and (c) the SiC standard.

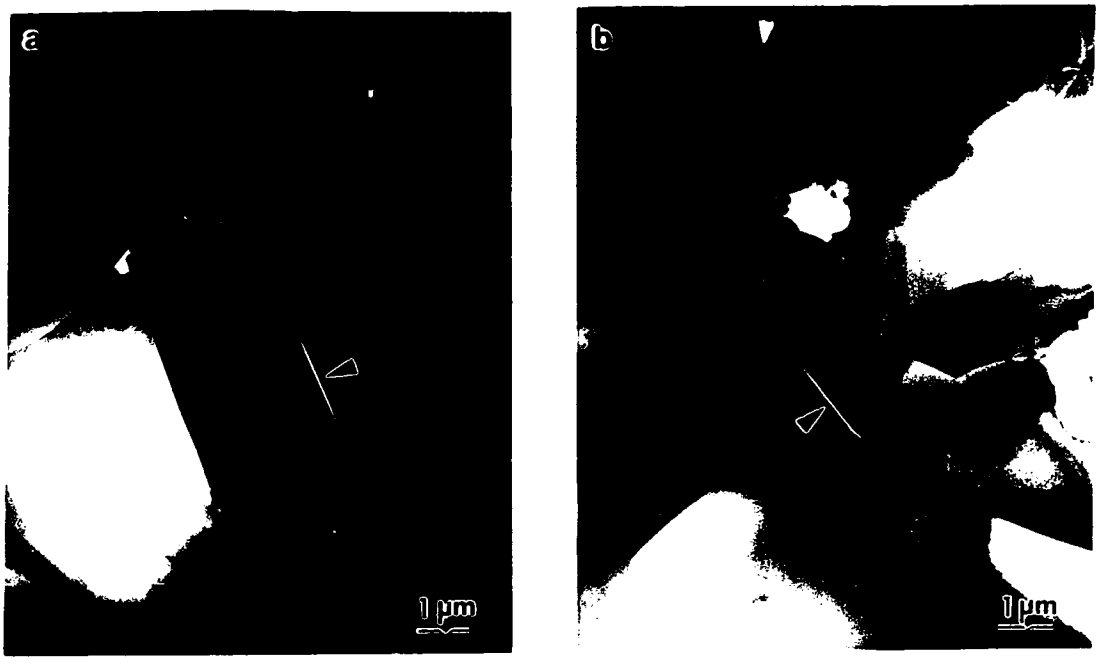

Figure 3. Transmission electron micrographs of (a) microcracks occurring on the boundary between TiB_2 and SiC and (b) a microcrack on the boundary between two TiB_2 particles.

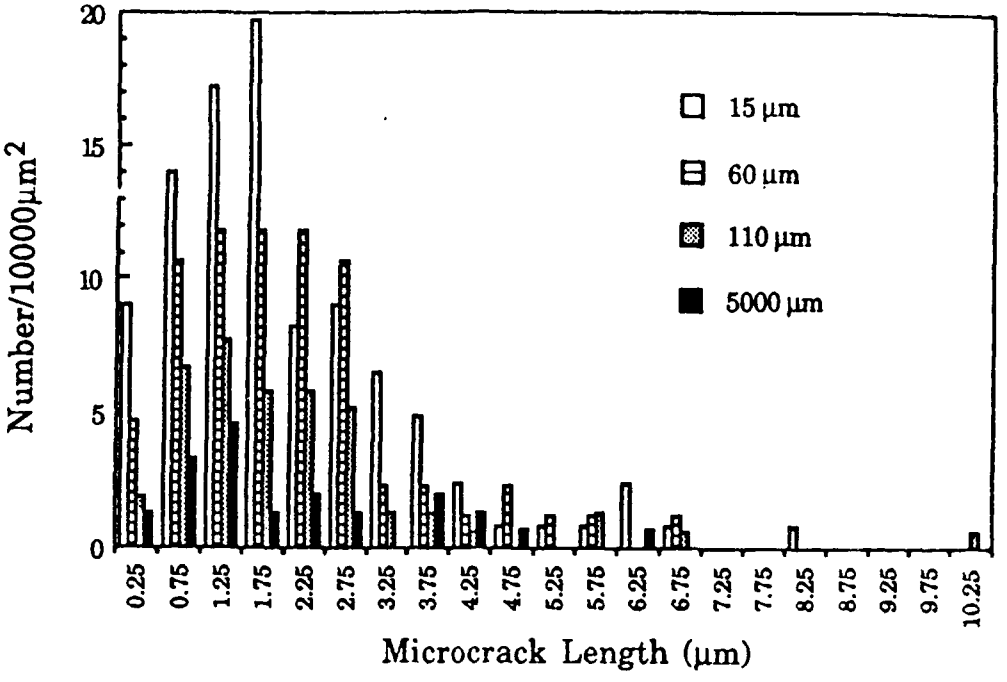

Figure 4. Microcrack distributions at different distances from the crack plane in a SiC-TiB_2 double cantilever beam specimen.

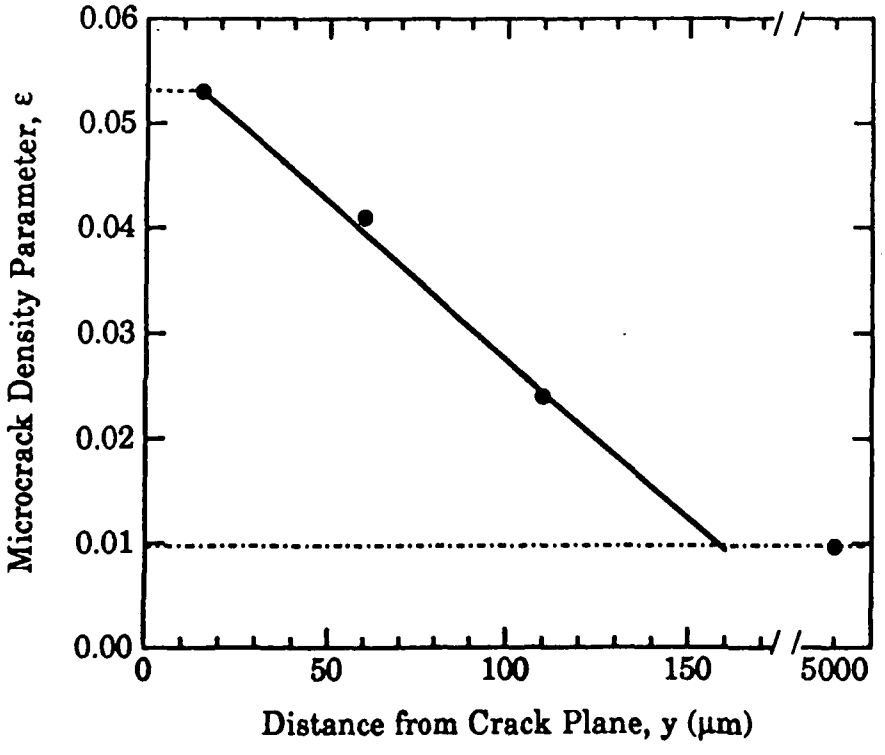

Figure 5. The microcrack density parameter, ϵ, as a function of the distance from the crack plane in a SiC-TiB_2 double cantilever beam specimen.

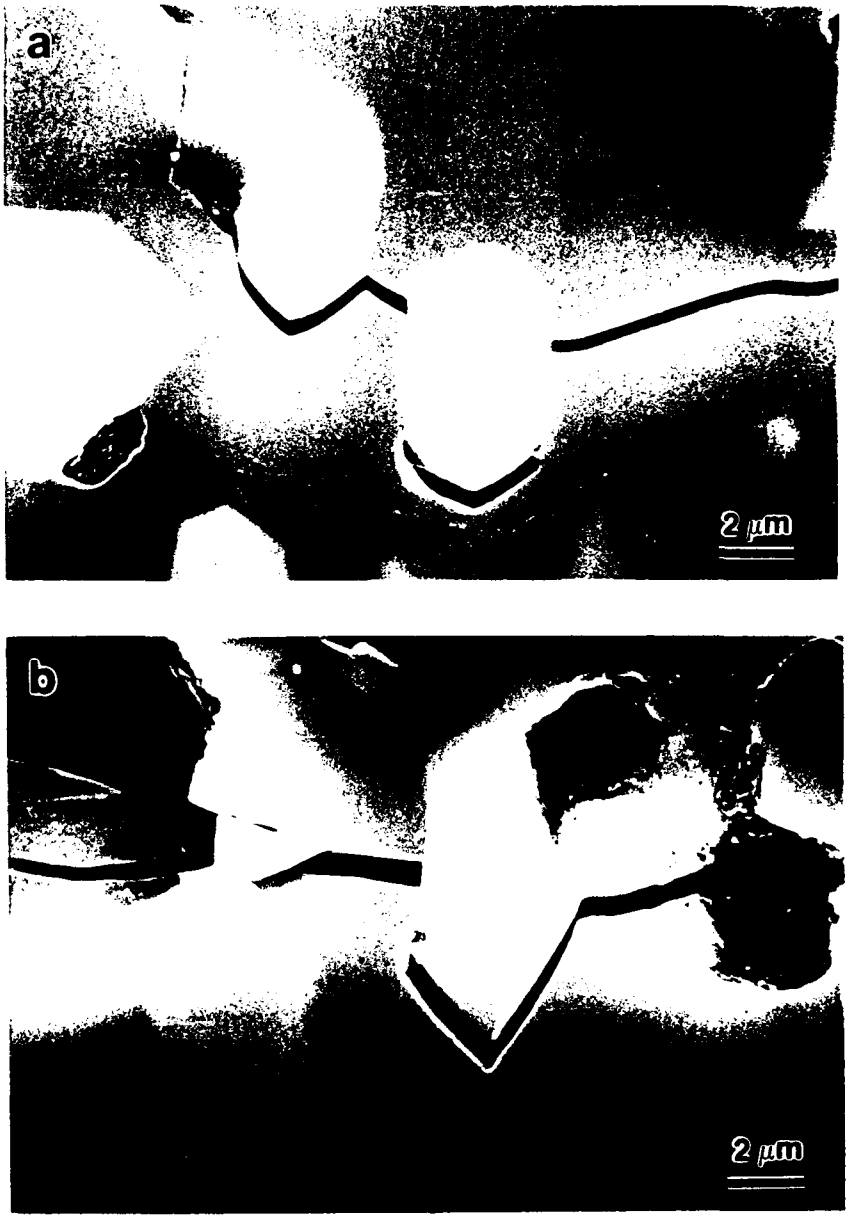

Figure 6. Scanning electron micrographs of bridging TiB_2 grains behind the crack tip in a SiC-TiB_2 composite. Micrographs were taken during an interrupted double cantilever beam test.

CRACK BRIDGING PROCESSES IN TOUGHENED CERAMICS.*

Paul F. Becher
Metals and Ceramics Division
Oak Ridge National Laboratory
P. O. Box 2008
Oak Ridge, Tennessee 37831-6068

ABSTRACT. The fracture toughness of ceramics can be improved by the incorporation of a variety brittle discontinuous reinforcing phases. Observations of crack paths in these systems indicate that these reinforcing phases bridge the crack in the region behind the crack tip. Recent developments in toughening models based on crack bridging processes in such systems are discussed and compared to the experimentally observed toughening responses with second phase whisker and self (matrix grain) reinforcement. The bridging model then can be used to optimize the toughening effects based modification of the pertinent material characteristics (e.g., microstructure and physical properties).

Introduction

The brittle nature of ceramics has, over the years, prompted us to explore a variety of approaches to increasing their fracture toughness/resistance. Initially the concern was to toughen these materials to to improve their fracture strength and/or reduce the flaw size sensitivity of the fracture strengths. Then it was recognized that resistance to damage in

---

* Invited paper to be presented at the NATO Advanced Research Workshop on Toughening Mechanisms in Quasi-Brittle Materials, Northwestern University, Evanston, IL, July 16-20, 1990

service was a further issue and that toughening these materials could enhance their damage resistance. While many issues still need to be addressed, e.g., cyclic fatigue resistance, crack size effects-R-curve behavior, improving the fracture toughness has been deemed, in general, to be quite beneficial.

One approach to toughening ceramics has been the incorporation of strong discontinuous brittle phases, e.g., whiskers [1], which is the subject of this paper. The mechanisms contributing to the increased fracture toughness are described herein in terms of crack bridging by the reinforcement. A crack bridging model is discussed which is found to accurately predict the observed toughening response in SiC whisker reinforced ceramics [2]. The results reveal that debonding of the interface between the reinforcing phase and the matrix is required to achieve significant toughening. The bridging model also illustrates how some of the properties of the matrix, interface, and reinforcing phase influence the fracture resistance of the composite. The predictive capability of the whisker bridging model then allows us to develop other approaches to achieving toughness by crack bridging. These include crack bridging by other types of second phases (platelets) and by matrix grains (self-reinforced).

Crack Bridging By Discontinuous Reinforcements

Bridging of the crack surfaces behind the crack tip by a strong discontinuous reinforcing phase which imposes a closure force on the crack is, at times, accompanied by pull out of the reinforcement [1-6]. The extent of pull out, i.e. the pull out length, brittle discontinuous reinforcing phases is generally quite limited due both to the short length of such phases and the fact that bonding and clamping stresses often discourage pull-out. However, pull-out cannot be ignored as even short pull-out lengths contribute to the toughness achieved. Crack deflection by such reinforcements has also been suggested to contribute to the fracture resistance. Often, out of plane (non mode I) crack deflections are limited in length and angle and are probably best considered as means of debonding the reinforcement-matrix interface. Such interfacial debonding is important in achieving frictional bridging (bridging by elastic ligaments which are partially debonded from the matrix) and pull-

out processes. Frictional bridging elastic ligaments can contribute significantly to the fracture toughness as is described herein.

ANALYSIS OF TOUGHENING BY DISCONTINUOUS BRIDGING PHASES

Here we will concentrate on the toughening due to crack bridging by various brittle reinforcing phases where the reinforcement simply bridges the crack surfaces and effectively pins the crack and increases the resistance to crack extension. The bridging contribution to the toughness for is:

$$\Delta K^{ur} = (E^c \Delta J)^{1/2} = K_{IC}{}^c - K_{IC}{}^m \qquad 1$$

where $K_{IC}{}^c$ is the overall toughness of the composite, $K_{IC}{}^m$ is the matrix toughness, and the term ΔJ corresponds to the energy change due to the bridging process.

The energy change associated with the bridging process is a function of the bridging stress/traction, T_u, and the crack opening displacement, u and is defined as:

$$\Delta J = \int_0^{u_{max}} T_u \, du \qquad 2$$

where u_{max} is the maximum displacement at the end of the zone [7], Figure 1.

One can equate the maximum crack opening displacement at the end of the bridging zone, u_{max}, to the tensile displacement in the bridging brittle ligament at the point of failure:

$$u_{max} = \varepsilon_f{}^l \, l_{db} \qquad 3$$

where $\varepsilon_f{}^l$ represents the strain to failure of the whisker and l_{db} is the length of the debonded matrix-whisker interface, Figure 2. The strain to failure of the

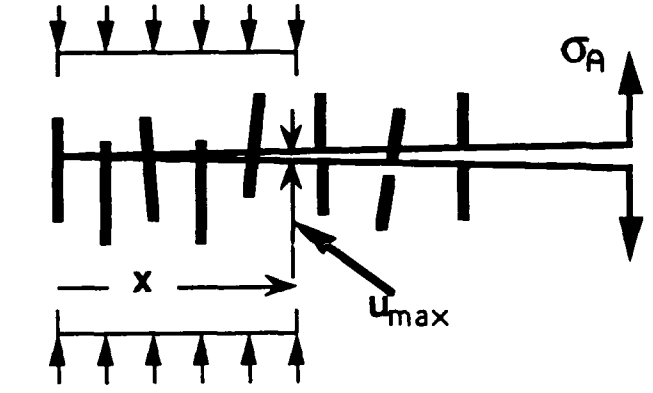

$$\Delta K^{wr} = (2E^c \Delta J)^{1/2}$$

BRIDGING STRESS
T

$$\Delta J = \int_0^{u_{max}} T\, du$$

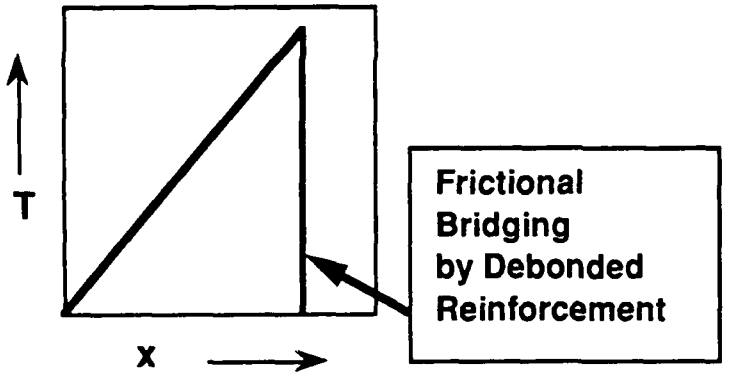

Figure 1. Crack bridging by discontinuous brittle reinforcing phases impose a closure or bridging stress in the wake of the crack tip and enhance the fracture resistance of the brittle matrix.

whisker can be defined as:

$$\varepsilon_f^{\prime} = (\sigma_f^{\prime} / E^{\prime}) \qquad 4$$

where $E^{\prime}$ is the Young's modulus of the reinforcing phase. The interfacial debond length depends on the fracture criteria for the reinforcing phase versus that of the interface and can be defined in terms of fracture stress or fracture energy. The analysis of Budiansky et al [8] yields:

$$l_{db} = (r\gamma^{\prime}/6\gamma) \qquad 5$$

where $\gamma^{\prime} / \gamma$ represents the ratio of the fracture energy of the bridging ligament to that of the reinforcement-matrix interface.

From equation 3, one quickly notices that the tensile strain displacement achieved in the bridging reinforcement and hence the maximum crack opening displacement at the end of the bridging zone increases as the debonded length/the gage length of the reinforcing ligament increases. Consideration of equations 4 and 5 show that increasing the reinforcing phase strength and/or enhancing interface debonding will contribute to greater tensile displacement within the reinforcing ligament. Increases in the crack opening displacement supported by the bridging zone will enhance the toughening achieved by such reinforcements. Therefore debonding of the matrix-reinforcement interface can be a key factor in the attainment of increased fracture toughness in these elastic systems. In fact in ceramics reinforced by strong ceramic whiskers, debonding is observed only in those systems which exhibit substantial toughening. An example of interfacial debonding associated with a bridging whisker in the wake of the crack tip is seen in Figure 3. In this case debonding is evidenced by the interfacial offsets at the leading and trailing sides of the bridging whisker.

For the case of a bridging stress which increases linearly from zero at the crack tip to a maximum at the end of the bridging zone and immediately decreases to zero, equation 2 can be reduced to $T_{max}(u_{max})/2$. The maximum closure stress T_{max} imposed by the reinforcing ligaments in the crack tip wake is the product of the fracture strength of the ligaments, $\sigma_f^{\prime}$, and the areal

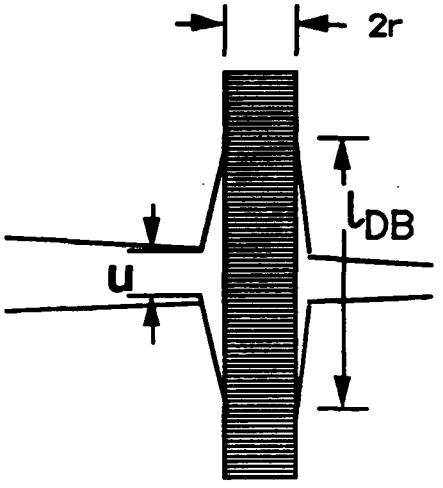

CRACK OPENING u ($=u_{max}$) AT THE END OF BRIDGING ZONE EQUATED TO MAXIMUM WHISKER TENSILE DISPLACEMENT ($l_{DB}\ \varepsilon_f^{w}$).

Figure 2. The formation of the bridging zone behind the crack tip requires that the reinforcing phase-matrix interface separate/debond (a) during fracture. The crack opening displacement associated with the bridging zone then is related to the tensile displacement in the bridging ligaments (b). At the end of the bridging zone the maximum crack opening is equivalent to the displacement in the ligament corresponding to its fracture stress.

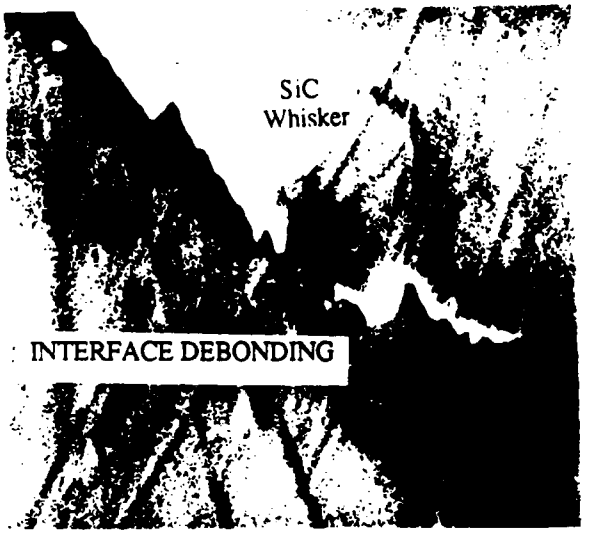

Figure 3. Debonded whisker-matrix interfaces are associated with whisker bridging in region immediately behind the crack tip in a polycrystalline aluminum oxide matrix.

fraction of ligaments intercepting the crack plane, A^l:

$$T_{max} = \sigma_f^l A^l \approx \sigma_f^l V^l \qquad 6$$

where A^l is approximated by the volume fraction, V^l, for ligaments which have large aspect ratios (e.g., $l/r \geq 30$ for whiskers). Reinforcement by frictional bridging introduces an change in energy equal to:

$$\Delta J^{flb} = [\sigma_f^l V^l (\sigma_f^l / E^l)(r\gamma^l / \gamma^j)]/12 \qquad 7.$$

From these results, the resultant toughness contribution from frictional bridging by the reinforcing phase in the crack tip wake is:

$$\Delta K^{flb} = \sigma_f^l [(r V^l/36)(E^c / E^l)(\gamma^l / \gamma^j)]^{1/2} \qquad 8.$$

The overall toughness of the composite then includes both the bridging contribution, equation 8, and that the fracture resistance of the matrix per equation 1.

MATERIAL CHARACTERISTICS INFLUENCING TOUGHNESS

The toughening contribution then can be enhanced by utilizing matrix-reinforcing phase combinations with comparable Young's moduli and by improving the strength of reinforcing phase and increasing the reinforcement content and diameter. There are obvious limits as to how large a diameter reinforcing phase can be used in systems employing a matrix with a thermal expansion coefficient greater than that of the reinforcement as the thermal contraction mismatch tensile stress intensity scales with increase in inclusion/reinforcing phase diameter. In the alumina-SiC whisker system, the larger thermal expansion coefficient of the matrix versus the whisker and the high elastic property values result in substantial hoop and longitudinal tensile strains in the matrix [3,9]. Larger diameter reinforcements can generate matrix crack during post-fabrication cooling and degrade the properties of such composite [10]. The maximum reinforcement diameter employed will depend on the elastic and thermal expansion properties of the matrix versus those of the reinforcing phase.

A critical factor in such toughening processes is interfacial debonding which can be achieved if the interfacial failure conditions are much less than those required to fracture the reinforcement. In fact, substantial toughening by such crack bridging is obtained only when the reinforcement-matrix interface debonds before or just as the main crack tip reaches the interface. The formation of a debonded interface spreads the strain displacement imposed on the bridging reinforcement ligament over a longer gage section generating a larger crack opening displacement per unit of stress supported by the ligament. As a result, the bridging traction/stress supported by the reinforcement increase more slowly with distance behind the crack tip, and a longer bridging zone is developed behind the crack tip. The resultant increase in crack opening displacement with distance behind the crack tip due to interfacial debonding, equations 3-5, significantly enhances the fracture resistance/toughness of the composite.

At this point, this model of the frictional bridging contribution by discontinuous brittle reinforcing ligaments provides a very useful means of designing such composites and analyzing their response. One can, at least, characterize those properties which are most important when selecting materials, and then systematically dissect the toughening response of composites to either uncover problem areas or to develop advanced systems. The bridging ligament model can be further refined by including a pull-out contribution and by addressing the response and contribution of whiskers which are inclined to the crack plane. In fact, the simple crack bridging model describe here and the effects of reinforcement by brittle whiskers have been successfully applied to a variety of oxide (including glasses) and nonoxide matrix ceramics.

Observed Toughening By Crack Bridging Processes

Several types of discontinuous brittle reinforcements have been successfully employed to form toughened ceramics including second phase whiskers [1-6] and platelets [11-13] and both elongated [14-17], plate-like [18] and large [3, 19-22] matrix grains. Studies of cracks in such materials reveal that, within the wake of the crack tip, the reinforcement does bridge the crack. The following sections will describe the observed toughening response in

whisker reinforced ceramics, ceramics with both elongated grains and larger grains, and when such bridging processes are combined in a composite.

Crack Bridging by Brittle Whiskers

The experimental fracture toughness results obtained to date confirm the various features of the model for crack bridging by these discontinuous brittle reinforcements [2] as shown in Figure 4 which compares experimental data with predicted curves based on equation 8. These results are based on a specific SiC whisker of a given strength and diameter. Thus Figure 4 reveals several features. First that the whisker bridging toughening contribution, $\Delta K^{wr} = \Delta K^{flb}$, does increase with volume/areal content of the reinforcing phase as predicted. Second, the toughening contribution also increases as the ratio of the composite's Young's modulus to that of the whisker increases. This best illustrated by the increase in ΔK^{wr} with increase in E^c at a given whisker content. For the examples here, E^c values were obtained by rule of mixtures [$E^c = E^m(1-V_f) + E^w V_f$]; thus at a constant volume fraction of whiskers, E^c increases in the order from glass (E^m = 80 GPa) to mullite (E^m = 210 GPa) to alumina (E^m = 400 GPa) vs SiC (E^w = 500 GPa).

These same experimental observations [2] also show that the whisker bridging toughening contribution, ΔK^{flb}, increases as (r, the whisker radius)$^{1/2}$ increases as predicted by equation 8. For example, the toughness of alumina composites containing 20 vol % SiC whiskers, increased from ≈6.5 to ≈9 to ≈12 MPa $\sqrt{m}$ when the mean diameter of the SiC whiskers increased from 0.4 to 0.75 to 1-1.5 microns, respectively. From the toughening model, we also expect the toughness to increase as the matrix-whisker interface fracture energy (strength) decreases with respect to that of the whisker (γ^w substituted for γ). While, values of the ratio of the whisker to interface fracture energy (γ^w / γ) are not available there are two observations which support the predicted behavior. First, whisker-matrix interfacial debonding and crack bridging by the whiskers are only observed in the composites exhibiting significant toughening. Second, the length of the whiskers protruding above the fracture surface increases with increased toughening

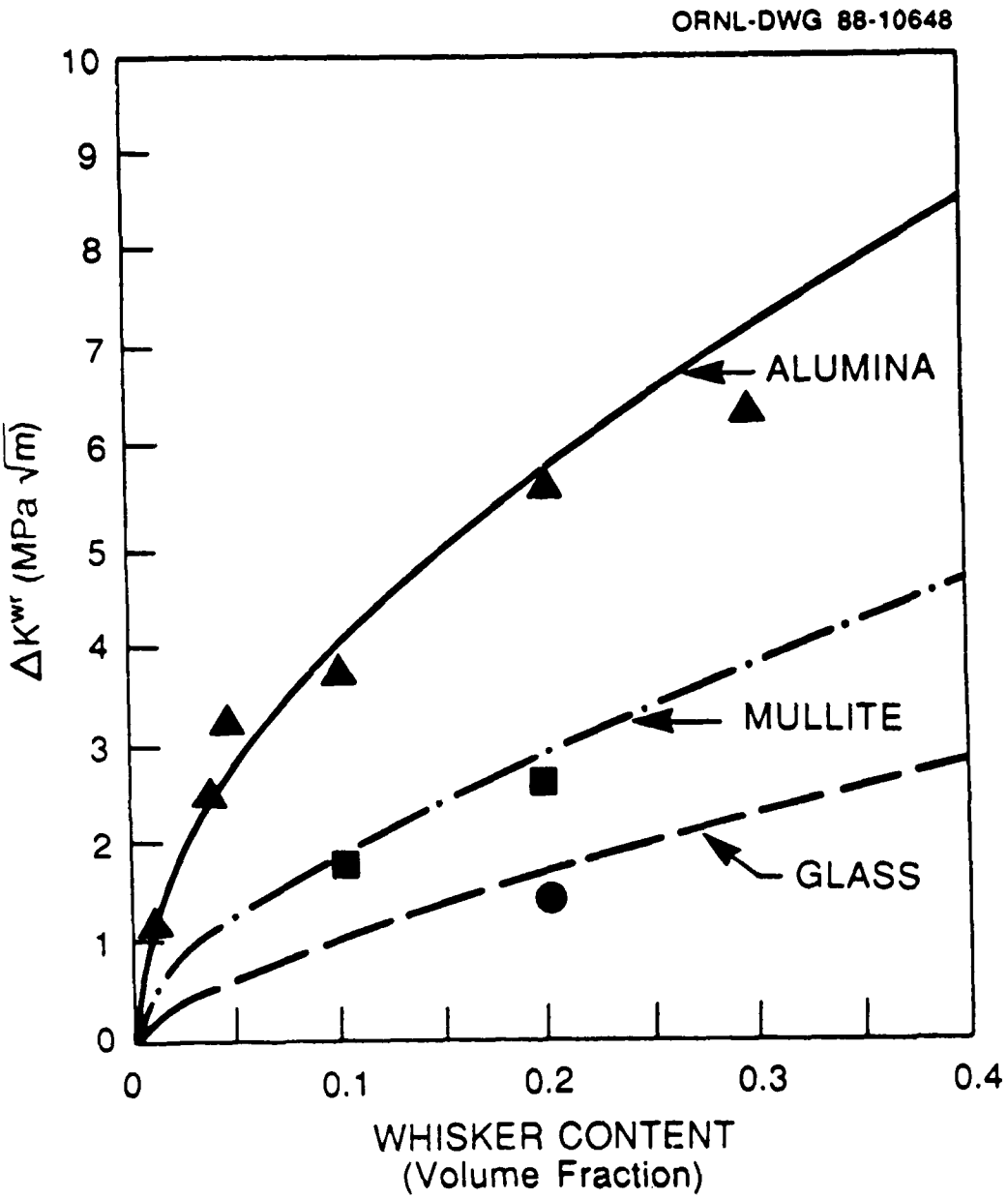

Figure 4. The Fracture Toughness Contribution from Whisker Bridging Increases with Increase in SiC Whisker Content. Curves represent predicted behavior(equation 8) for strong (10 GPa), 0.8 μm diameter SiC whisker while symbols represent experimental results.[5]

and this length can be related to the interfacial debond length. These findings indicate that the bridging contribution does indeed increase with increasing whisker diameter and when the fracture energy (and) of the interface decreases with respect to that of the whisker.

Matrix Grain Bridging: Grain Shape Effects

Crack bridging phenomena and toughening effects which are very comparable to those observed in whisker reinforced ceramics are also found in ceramics containing other reinforcing phase geometries. For example in the development of more thermal shock resistant electrical insulator, alumina ceramics which had microstructures which contain large (~100-200 μm across by ~10 μm thick) plate-like alumina grains in a medium sized (~5 micron) equiaxed grained matrix. These materials had excellent thermal shock resistance; in fact, their thermal shock resistance was much greater than any of the variety of ceramics tested including zirconias, various other oxides, silicon nitrides, and aluminas with equiaxed grains. Further examination showed that fracture toughness values were ~7 MPa $\sqrt{m}$ for samples containing ~ 25 vol % of these large single crystal alumina plates [18]. Aluminas prepared at the same time but with only equiaxed grains which were~ 5μm in size had toughness values of only 4-4.5 MPa $\sqrt{m}$. Observations of the crack paths in the alumina containing the plate-like grains revealed that cracks deflected along the interface between the matrix and the large plate-like grains. This produced plates which bridged the main crack and contributed to the high toughness in much the same manner as SiC whiskers do.

The logical extension of this is to consider whether or not crack bridging by second phase platelets contributes to fracture toughness. Composites consisting of an equiaxed polycrystalline matrix of TiO_2 in which alumina platelets are dispersed also exhibit increased fracture resistance as described by Hori et al. [11]. This work shows that under conditions where the platelet dimensions remained fairly similar that toughness increased with platelet content leading to nearly a three-fold increase at 30 vol % of alumina platelets. Initial studies also reveal that SiC platelets can produce similar

increases in toughness in alumina as do SiC whiskers [12]. Each of these composites give evidence for crack bridging by the reinforcement.

In this same vein, reinforcement of Si_3N_4 [14-16] and SiAlON [17] ceramics by the in situ growth of elongated or whisker-like grains is also a potent toughening approach resulting in toughness values of ≥10 MPa $\sqrt{m}$. Such materials have been labeled as self-reinforced and from the crack observations of Li and Yamanis [15] crack bridging by these grains contributes to the improved toughness. Sufficient additional experimental results exist to begin to test how well the current crack bridging model describes the toughening effects of such elongated grains. First, Tajima et al. results show that the toughening contribution, ΔK^{flb}, increases with increase in volume content of the elongated grains [23].

More recent observations also reveal that ΔK^{flb} increases with increase in the cross section of the elongated grains, Table 1. In fact the authors plotted the data in the form of ΔK^{flb} versus the square root of the diameter of the elongated grains [24]. The resulting plot exhibit excellent fit to the behavior predicted by equation 8. The diverse sources of observations then would support crack bridging by the elongated grains as the toughening process in these silicon nitride ceramics.

Matrix Grain Bridging: Grain Size Effects

In the present discussion, grain size effects on toughness are related to bridging ligaments formed by matrix grains which are left intact behind the crack tip [3, 19, 21, 25]. The toughening analysis is analogous to that for the whisker reinforcement described above. However here the bridging stress supported by ligaments formed by microcracking along grain boundaries is product of the frictional stress required to pull out each bridging grain times the fraction of bridging grains, $f_{gb}\,\tau_{gb}$. The grain bridging zone length is dictated by equating the crack opening displacement at the end of the zone u to that required to completely pull out the bridging grains. Assuming that half the grain must be pull out to disrupt a ligament, u will be equal to one half the grain size (d), and the incremental increase in fracture toughness due to grain bridging ΔK^{gb} is:

$$\Delta K^{gb} = [f_{gb}\, \tau_{gb}\, E^c\, (d/2)]^{1/2} \qquad 9$$

yielding a grain bridging toughening contribution consistent with experimental observations [3, 18, 21] at grain sizes below those resulting in spontaneous microcracking [18]. As noted in Figure 5, the grain size dependence of the fracture toughness of alumina ceramics is consistent with this behavior.

Table 1. Fracture Toughness of Silicon Nitride Ceramics With Elongated Grain Structures.+

Diameter of Elongated Grains, μm	Fracture Toughness, MPa √m
2.8	5.7
3.5	6.4
4.5	7.0
7	8.3
8.7	9.0
10-11	10-11

+ Data taken from results of H. Okamoto and T. Kawashima, NKK Corporation, Kawasaki, Japan.

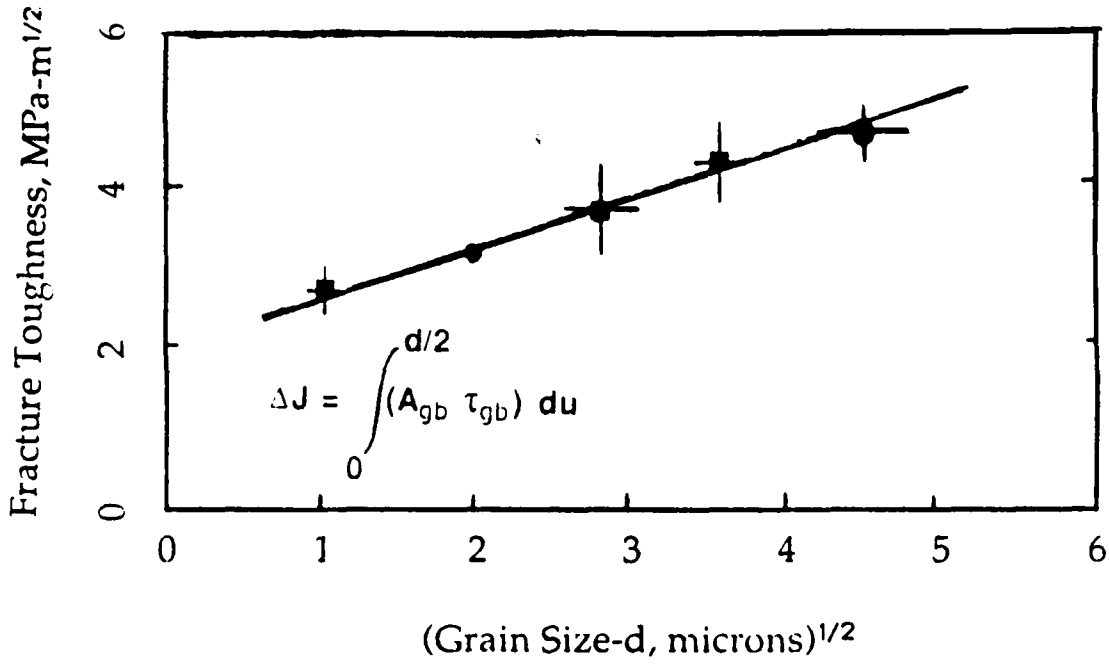

Figure 5. The fracture toughness of alumina ceramics is enhanced by increase in the matrix grain size.

Conclusions

Reinforced ceramics including reinforcement by strong whiskers initiate crack bridging processes to achieve improved fracture resistance. Similar toughening processes and effects are achieved by changes in grain size in noncubic ceramics, and/or by altering grain shape, e.g., formation of elongated grains in Si_3N_4 and SiAlON and plate-like grains in alumina ceramics. These reinforcing phases can contribute considerable toughening to brittle ceramics; factors of three increases in the fracture toughness are not uncommon.

The bridging processes involve frictional bridging where the matrix-reinforcement interface debonds which allows the reinforcement to elastically stretch over some finite gage length hindered only by frictional sliding against the matrix. The contribution of pull-out of these reinforcements to the toughness is rather limited; in part, due to their limited pull-out dimension. Enhanced interfacial debonding leads to greater toughening effects in these systems by promoting the crack opening displacement supported by the bridging zone. The amount of toughness realized is dependent upon the properties and characteristics of the reinforcing phase and the interface as described by the micromechanics models developed for these systems. The model for frictional crack bridging reveals that the bridging contribution to the toughness is a function of the whisker strength, diameter, and content, as well as the ratio of the whisker to interface fracture resistance, and the ratio of the composite to whisker Young's moduli. The predicted effect of these parameters are supported by experimental observations for SiC whisker reinforced ceramics.

Extension of the micromechanics model of toughening by crack bridging reinforcements illustrate the importance of considering other reinforcements including second phases and changes in matrix microstructure. Experimental results confirm various aspects of the toughening response due to crack bridging resulting from grain size and grain shape changes in alumina and silicon nitride ceramics. These finding suggest a variety of approaches may be possible to obtain improved fracture toughness in ceramic and other brittle systems by incorporating reinforcing phases which can generate crack bridging mechanisms. Such processes can be combined with each other or with other toughening mechanisms to develop

synergistic toughening effects. The approach described here offers a means of developing these materials by considering the material characteristics/parameters which control the crack bridging contribution.

ACKNOWLEGEMENTS

The contributions of T. N. Tiegs, C. H. Hsueh, K. B. Alexander, P. Angelini, S. B. Waters, W. H. Warwick, and L. M. Evans of ORNL and E. R. Fuller, Jr. of National Institute of Standards and Technology are gratefully acknowledged. This research was supported by the Division of Materials Sciences, Department of Energy, under Contract No. DE-AC05-84OR21400 with Martin Marietta Energy Systems, Inc.

REFERENCES

1. P. F. Becher and G. C. Wei, "Toughening Behavior in SiC-Whisker Reinforced Alumina," J. Am. Ceram. Soc. 67(12) C267-69 (1984).
2. P. F. Becher, C. H. Hsueh, P. Angelini, and T. N. Tiegs, "Toughening Behavior in Whisker Reinforced Ceramic Matrix Composites," J. Am. Ceram. Soc. 71(12) 1050-61 (1988).
3. P. F. Becher, "Recent Advances in Whisker Reinforced Ceramics," in Annual Review of Materials Science, R. A. Huggins (editor), in press.
4. N. Claussen and G. Petzow, pp. 649-62, Tailoring of Multiphase and Composite Ceramics, Vol. 20, Materials Science Research, R. E. Tressler, G. L. Messing, C. G. Pantano, R. E. Newnham (eds.), Plenum, New York 1986.
5. P. F. Becher, T. N. Tiegs, and P. Angelini, "Whisker Toughened Ceramic Composites," in Fiber Reinforced Ceramics, K. S. Mazdiyasni (editor), Noyes Publications, Park Ridge, N. J., in press.
6. R. Warren, and V. K. Sarin, "Fracture of Whisker Reinforced Ceramics," in Applications of Fracture Mechanics to Composite Materials, K. Friedrich (ed.), Elsevier, Amsterdam, in press.
7. J. R. Rice, "Mathematical Analysis in the Mechanics of Fracture," pp 191-311 in Fracture, Vol. II, H. Liebowitz (editor), Academic Press, New York, 1968.

8. B. Budiansky, J. W. Hutchinson, and A. G. Evans, "Matrix Fracture in Fiber-Reinforced Ceramics," J. Mech. Phys. Solids 34(2) 167-89 (1986).
9. P. Angelini, W. Mader, and P. F. Becher, "Strain and Fracture in Whisker Reinforced Ceramics," pp. 241-57 in Mater. Res. Soc. Symp. Proc., Vol. 78, P. F. Becher, M. V. Swain, and S. Somiya (editors), Materials Research Society, Pittsburg, PA, 1987.
10. T. N. Tiegs, "Tailoring of Properties of SiC Whisker-Oxide Matrix Composites," pp. 937-49 in Ceramic Materials and Components for Engines, V. J. Tennery (editor), Am. Ceram. Soc., Westerville, OH, 1989.
11. S. Hori, H. Kaji, M. Yoshimura, and S. Somiya, "Deflection-Toughened Corundum-Rutile Composites," pp. 283-88 in ref. 8.
12. P. F. Becher, "Microstructural Design of Toughened Ceramics," presented at the Am. Ceram. Soc. annual meeting, Dallas, Tx, April, 1990, to be published.
13. F. J. Cambier, "Processing and Properties of SiC-Platelet Silicon Nitride Ceramics," Proc. Int'l Workshop for Fine Ceramics: New Processing and Properties of Fine Ceramics," Nagoya, Japan, March 15-16, 1990 (to be published).
14. Lange, F. F., "Fracture Toughness of Si3N4 as a Function of the Initial a-Phase Content," J. Am. Ceram. Soc. 62 (7-8) 428-30 (1979).
15. C. W. Li and J. Yamanis, "Super-Tough Silicon Nitride with R-Curve Behavior," Ceram. Sci. and Engr Proc. (1989).
16. G. Himsolt, H. Knoch, H. Huebner, and F. W. Kleinlein, "Mechanical Properties of Hot-Pressed Silicon Nitride with Different Grain Structures," J. Am. Ceram. Soc. 62 (1) 29-32 (1979).
17. M. H. Lewis, pp. 713-30 in Fracture Mechanics of Ceramics, R. C. Bradt, A. G. Evans, D. P. H. Hasselman, and F. F. Lange (eds.), Plenum, New York, 1986.
18. T. N. Tiegs and P. F. Becher, "Particulate and Whisker Toughened Alumina Composites," pp. 479-85 in Proc. 22nd Auto. Tech. Dev. Contractors' Coord. Meeting, Vol. P-155, Society of Automotive Engineers, Warrendale, Pa., March, 1985.
19. R. W. Rice, S. W. Freiman, and P. F. Becher, "Grain-Size Dependence of Fracture Energy in Ceramics: I, Experiment," J. Am. Ceram. Soc. 64 (6) 345-50 (1981).

20. a. P. L. Swanson, C. J. Fairbanks, B. R. Lawn, and Y. W. Mai, J., "Crack-Interface Grain Bridging as a Fracture Resistance Mechanisms in Ceramics: I, Experimental Study of Alumina," J. Am. Ceram. Soc. 70 (4) 279-89 (1987).
b. Y. W. Mai and B. R. Lawn, "II, Theoretical Fracture Mechanics Model," ibid. 70 (4) 289-94 (1987).
21. a. B. Mussler, M. V. Swain and N. Claussen, "Dependence of Fracture Toughness of Alumina on Grain Size and Test Technique," J. Am. Ceram. Soc. 65(11) 566-72 (1982).
22. P. F. Becher, E. R. Fuller, Jr., and P. Angelini, "Matrix Grain Bridging in Whisker Reinforced Ceramics," to be published.
23. Y. Tajima, K. Urashima, M. Watanabe, and Y. Matsuo, "Fracture Toughness and Microstructure Evaluation of Silicon Nitride Ceramics," pp. 1034-41 in Ceramic Transactions, Vol. 1: Ceramic Powder Science-IIB, G. L. Messing, E. R. Fuller, Jr., and H. Hausner (editors), Am. Ceram. Soc., Westerville, OH, 1988.
24. H. Okamoto and T. Kawashima, unpublished results.
25. C. Cm. Wu, S. W. Freiman, R. W. Rice, and J. J. Mecholsky, "Microstructural Aspects of Crack Propagation in Ceramics," J. Mater. Sci. 13:2659-70 (1978).

FRACTURE PROCESS ZONE IN CONCRETE AND CERAMICS - A MATTER OF SCALING

Albert Kobayashi,* Neil M. Hawkins** and Richard C. Bradt***

University of Washington
* Department of Mechanical Engineering, Seattle, Washington 98195
** Department of Civil Engineering, Seattle, Washington 98195
*** Mackay School of Mines, University of Nevada-Reno, Reno, Nevada 89557

ABSTRACT

The crack closure stress versus crack opening displacement (COD) associated with the fracture process zone (FPZ) in concrete was determined through a hybrid experimental-numerical procedure. COD measurements, which were obtained by moire interferometry, of subcritically growing cracks were used interactively with an elastic finite element model of the concrete specimen to back out the above constitutive relation by an inverse analysis. A constitutive relation, which is similar in form but greatly different in magnitude, was also used to characterize the FPZ associated with stable crack growth in SiC_w/Al_2O_3-matrix ceramic composite. Similarity in the genesis of the FPZ's in concrete and ceramics is discussed.

INTRODUCTION

Research on concrete fracture during the past decade [1-7] has shown the existence of a fracture process zone (FPZ) ahead of a macro crack tip of concrete where microcracks form and coalesce. For mode I fracture, the behavior within the FPZ can be described by a crack closure stress, σ, vs crack opening displacement (COD), w, relationship which can be determined from the decreasing strain-softening portion of a direct tension test [3,4]. When incorporated into a finite element model, these σ-w curves can be used to predict the overall fracture strength and to simulate the progressive damage process of a fracturing concrete structure.

Crack closure stress has also been identified as the primary toughening mechanism in similar FPZ ceramic composites [8-12]. However, a constitutive relation, which quantifies the crack closure stress versus COD relation, as described above, has not been studied by others.

The authors and their colleagues have been studying the FPZ's associated with stable crack growth in concrete and ceramics using an inverse analysis based on finite element models of concrete and ceramic fracture specimens. Part of the ambiguity associated with the inverse analysis was removed in their recent studies using a hybrid analysis which incorporates the measured COD's by moire interferometry. These results are discussed in the following.

FPZ IN CONCRETE FRACTURE SPECIMENS

The theoretical background and the experimental details of the hybrid-inverse analysis used to study the FPZ of concrete fracture specimens can be found in [13-15]. Concrete specimens of two different geometries, the crack-line wedge-loaded, double-cantilever beam (CLWL-DCB) specimen shown in Figure 1(a) and the three-point bend specimen shown in Figure 1(b), were analyzed. Figures 2 and 3 show typical moire fringe patterns in the WL-DCB and three point bend specimens, respectively. Figure 4 shows the wedge load versus COD, $2V_1$, relations of four CLWL-DCB specimens. Figure 5 shows the load versus load-line displacement relations of four three-point bend specimens.

Figure 6 shows the σ versus w relation which were obtained after several iterations in the optimization process of the inverse analysis. The three line segment model, which were used in previous studies [1,2], was replaced with a smooth varying σ-w relation as shown in the caption of Figure 6. This constitutive relation with only two disposal parameters of α and β simplified the iteration process used in the inverse analysis. The coincidence between the three line segment model and the continuous model is remarkable considering the fact that the two models were derived from different concrete specimens using different computer codes.

Figures 7 and 8 show typical comparison between the COD's which were computed by using the optimized finite element model with the σ-w constitutive relation of Figure 6 and those obtained by moire interferometry. The computed load versus load line displacements and the wedge load versus COD relations are shown as data points in Figures 4 and 5, respectively. The excellent to good agreements between the measured and computed values validate the finite element model of the concrete fracture specimens with the FPZ constitutive relation of Figure 6.

FPZ OF CERAMIC COMPOSITE

A similar hybrid-inverse analysis was used to study the FPZ in three-point bend specimens machined from SiC-whisker/Al_2O_3-matrix ceramic composite [16]. Moire interferometry could not be used in high temperature testing and thus was replaced with crack mouth opening displacement (CMOD) measurements using laser interferometric displacement gages [17,18]. Figure 9 shows the specimen geometry used in this study.

Figure 10 shows the FPZ constitutive relation for $SiCw/Al_2O_3$ ceramic composite fracture specimen tested at 1200° C. Figure 11 shows the load versus CMOD relations which were obtained experimentally and from the finite element model with the FPZ constitutive of Figure 10. Again, the excellent agreement between the two results validate the FPZ model used in this study.

The same hybrid-inverse procedure was used to determine the crack growth resistance crack extension, Δa, relation for SiC-whisker/alumina-matrix composite. The specimen is a wedge-loaded, double cantilever beam (WL-DCB) specimen with a chevron notch along the entire length of its remaining ligament as shown in Figure 12. This fracture specimen is inherently rigid and is thus suitable for stable crack growth study of brittle materials. Crack growth is confined to the entire chevron notch plane without the annoying crack curving which is prevalent in ceramic DCB specimens without side grooves. The friction force at the loading pin and the location of the crack tip, which is not observable, in addition to COD variation in the FPZ, are the unknowns which cannot be measured directly.

A hybrid experimental-numerical procedure was thus developed to determine these quantities as well as the stress intensity factor of the stably growing crack. Moire interferometry was used to determine the displacement field on the side surface of the WL-DCB specimen. Figure 13 shows a typical moire pattern representing the lateral displacements on the side surface of the chevron-notched specimen. The measured horizontal displacement at the loading pin, together with the measured pin-load, were input to a three dimensional finite element model of the WL-DCB specimen. An assumed crack front, which is estimated from the moire fringe pattern, is used in the first iteration and this crack front was adjusted in subsequent numerical analyses until a reasonable match between the computed and the side-surface COD's, from the moire fringes, were obtained.

Figure 14 shows the σ versus w relation used in this study. Figure 15 shows the COD measurements and the computed COD's, one without the FPZ and identified as (LEFM) in this figure and one with the FPZ which is identified as (FPZ) on the exposed side surface of the fracture specimen. The notable difference between the computed COD's with, and without, the FPZ and the discrepancy with the measured surface displacement, is noted. These results validate the FPZ constitutive relation shown.

CONCLUSIONS

The FPZ constitutive relations for concrete and $SiCw/Al_2O_3$ ceramic composite are similar in form. The crack closure stress for $SiCw/Al_2O_3$ ceramic composite was two orders higher than that of concrete while the COD's were comparable in magnitude.

ACKNOWLEDGEMENT

FPZ studies in concrete fracture, which was conducted by Dr. Jiaji Du, was supported by National Science Foundation Grant MSM 831063 and Air Force Office of Scientific Research Contract 86-0204. Studies in ceramic fracture, which was conducted by Drs. M. G. Jenkins, K.W. White, and Mr. C. T. Yu was supported by Department of Energy Contract 86A-00209C and Office of Naval Research Contract N00014-87-K-03260.

REFERENCES

1. Liaw, B. M., Jeang, F. L., Du, J.J., Hawkins, N. M. and Kobayashi, A. S.,. "Improved Non-Linear Model for Concrete Fracture," ASCE, *J. Eng. Mech.*, 116 (2), 429-445 (1990).

2. Cho, K. Z., Kobayashi, A. S., Hawkins, N. M., Barker, D. B. and Jeang, F. L., "Fracture Process Zone of Concrete Cracks," *J. Eng. Mech.*, ASCE, 110 (8), 1174–1184 (Aug. 1984).

3. Petersson, P. E., "Crack Growth and Development of Fracture Zones in Plain Concrete and Similar Materials," Doctoral Dissertation, University of Lund, Sweden, TVBM-1006 (1981).

4. Reinhardt, H. W., Cornelissen, A. W. and Hordjik, D. A., "Tensile Tests and Failure Analysis of Concrete," *J. Struct. Eng.*, 112 (11), 2462–2477 (Nov. 1986).

5. Wecharatana, M. and Shah, S. P., "Prediction of Non-Linear Fracture Process Zone in Concrete," ASCE, *J. Eng. Mech.*, 109 (5), 1231–1246 (Oct. 1983).

6. Jenq, Y. S. and Shah, S. P., "A Fracture Toughness Criterion for Concrete," *Eng. Fract. Mech.*, 21 (5), 1055–1069 (1985).

7. Li, V. C. and Liang, E., "Fracture Processes in Concrete and Fiber Reinforced Cementitious Composites," ASCE, *J. Eng. Mech*, 112 (6), 566–586 (Jun. 1986).

8. Bazant, Z. P. and Oh, B. H. ,"Crack Band Theory for Fracture of Concrete," *Materiaux et Constructions*, 16 (93), 155–177 (1983).

9. Mori, T. and Mura, T. "An Inclusion Model for Crack Arrest in Fiber Reinforced Materials," *Mech. of Mater.* 3, 193-198 (1984).

10. Budiansky, B., Hutchinson, J.W. and Evans, A.G., "Matrix Fracture in Fiber-Reinforced Ceramics," *J. Mech. Phys Solids*, 34, 167-189 (1986).

11. Hori, M. and Nemat-Nasser, S., "Toughening by Partial or Full Bridging of Cracks in Ceramics and Fiber Reinforced Composites," *Mech. of Mater.*, 6, 24269 (1987).

12. Rose, L.R.F., "Crack Reinforcement by Distributed Springs, *J. Mech. Phys. Solids*, 35, 383-405 (1987).

13. Du, J.J., Kobayashi, A.S., and Hawkins, N.M., *Fracture of Concrete and Rock*, eds. J. P. Shah and S.E. Swartz, Springer-Verlag, 199-204 (1989).

14. Du, J.J., Kobayashi, A.S. and Hawkins, N.M., *A Hybrid Procedure for Determining the Fracture Process Zone in Concrete,* eds. S.P. Shah, S.E. Swartz and B. Barr, Elsevier Applied Science, 297-306 (1989).

15. Du, J.J., Kobayashi, A.S. and Hawkins, N.M., "An Experimental-Numerical Analysis of Fracture Process Zone in Concrete Fracture Specimens," Engineering Fracture Mechanics, 35 (1/2/3), 15-28 (1990).

16. Kobayashi, A.S., Hawkins, N.M. and Du, J.J., "An Impact Fracture Model of Concrete," *Cement-Based Composites Strain Rate Effects on Fracture,* ed. by S. Mindess and S.P. Shah, Materials Research Society Symposia proceedings, Vol. 64, 203-216 (1986).

17. Sharpe, W.N., "High Temperature Strain/Displacement Measurement," Handbook on Experimental Mechanics, ed. A.S. Kobayashi, Prentice Hall, Chapter 13, pp. 587-609, 1986.

18. Jenkins, M.G., Kobayashi, A.S., Sakai, M., White, K.W. and Bradt, R.C., "Fracture Toughness Testing of Ceramics Using Laser Interferometric Strain Gage," Bulletin of American Ceramic Society, 70(6), 393-395 (1987)..

ASK/cm

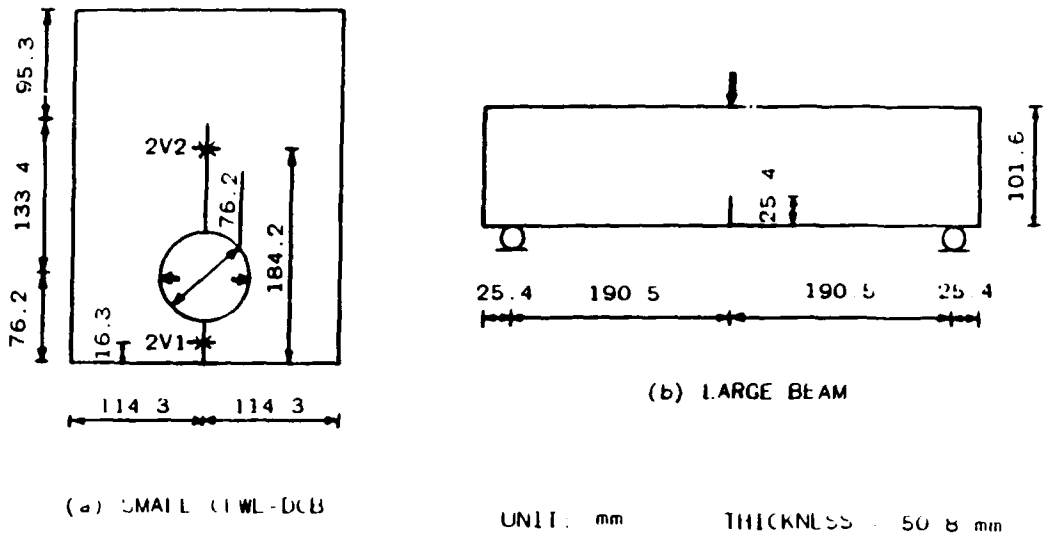

Figure 1. CLWL-DCB and Three-Point Bend Concrete Specimens.

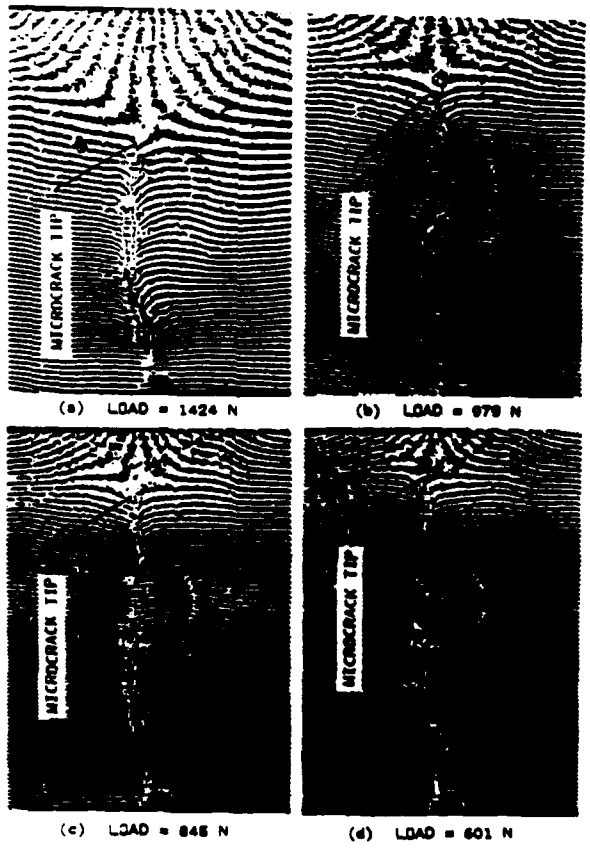

Figure 2. Sequential Moire Fringe Patterns of CLWL-DCB Specimen. Specimen No. SD-2.

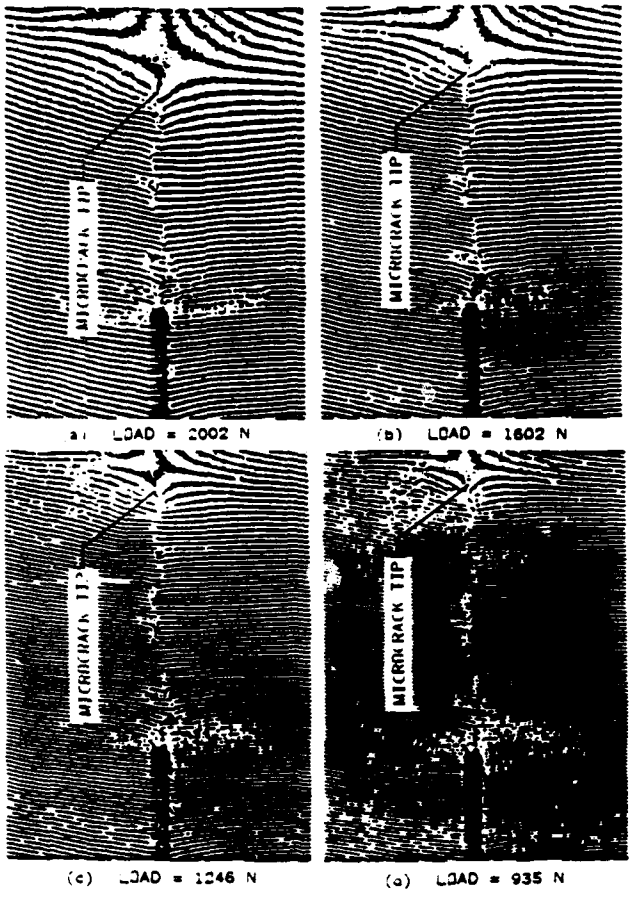

Figure 3. Sequential Moire Fringe Patterns of Three-Point Bend Specimens. Specimen No. LB-1

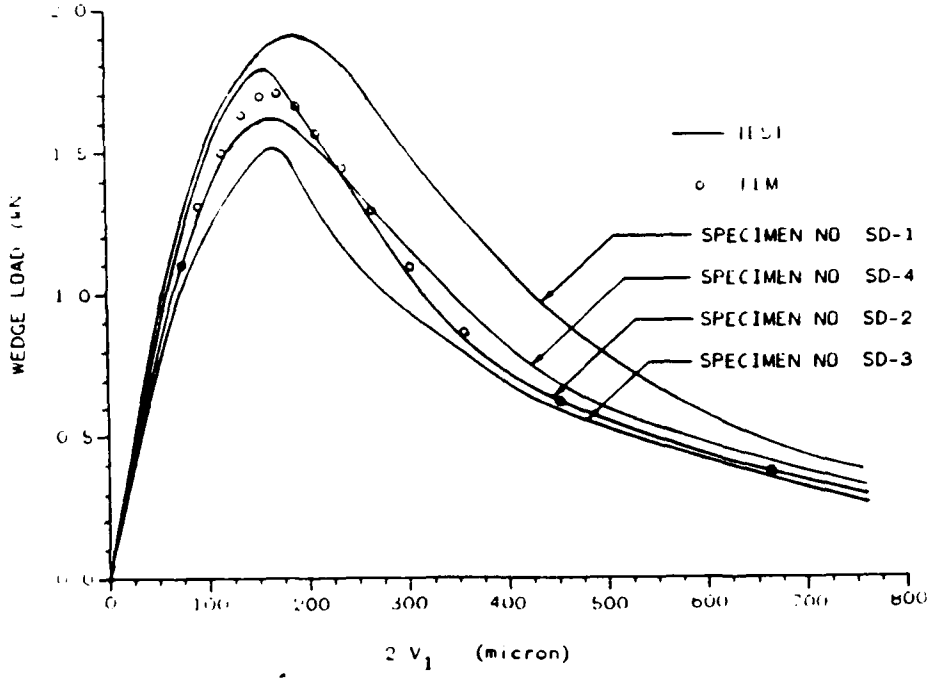

Figure 4. Wedge Load Versus $2V_1$ CLWL-DCB Specimens.

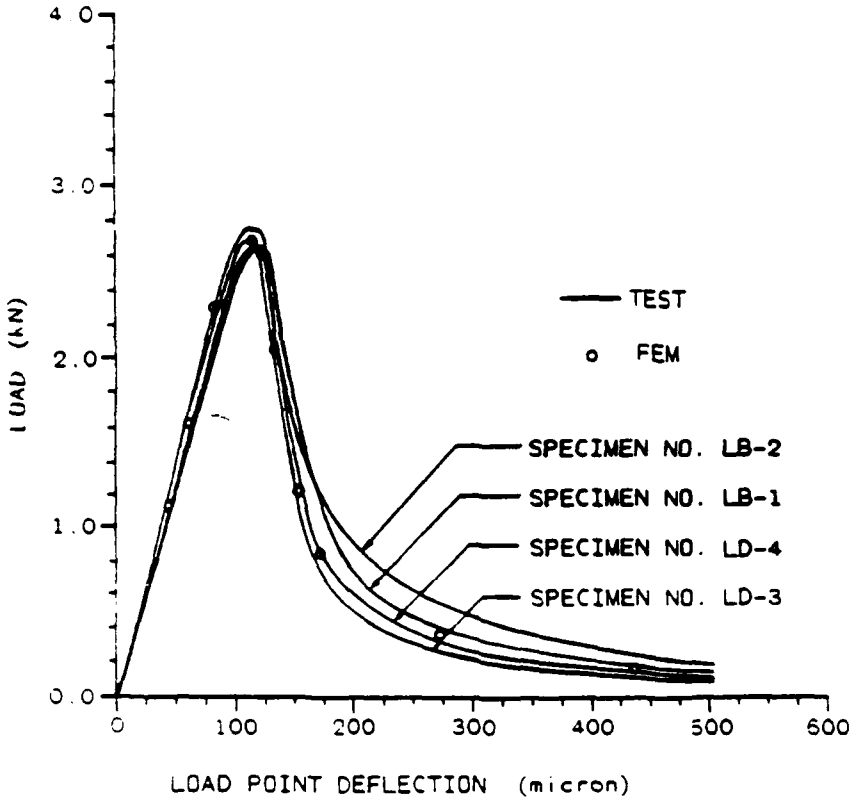

Figure 5. Load Versus Load-Line Deflection Curves, Three-Point Bend Specimens.

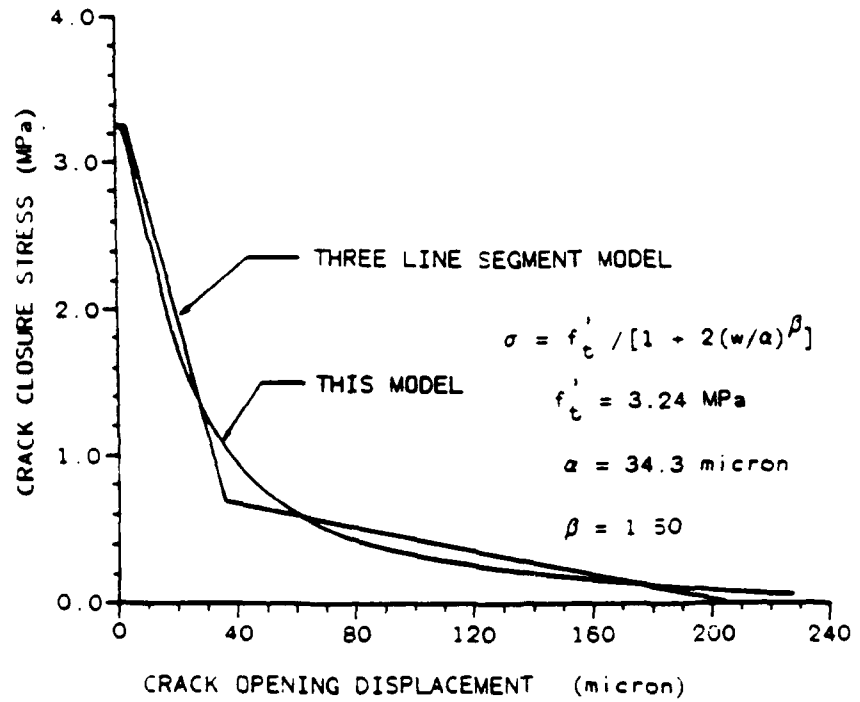

Figure 6. Crack Closure Stress Versus COD Along FPZ.

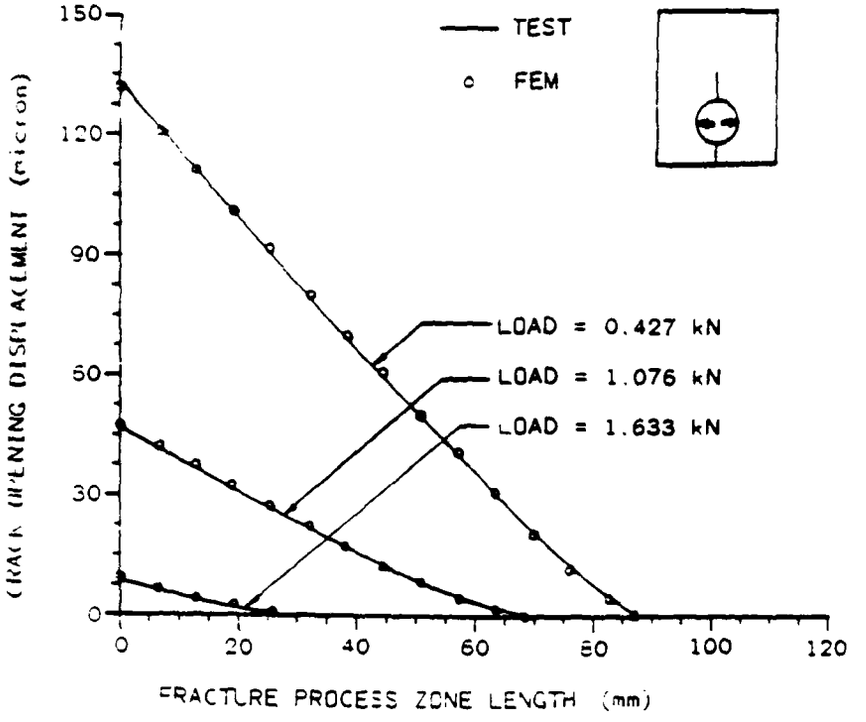

Figure 7. COD Variations along Fracture Process Zone. CLWL-DCB Specimen No. SD-4.

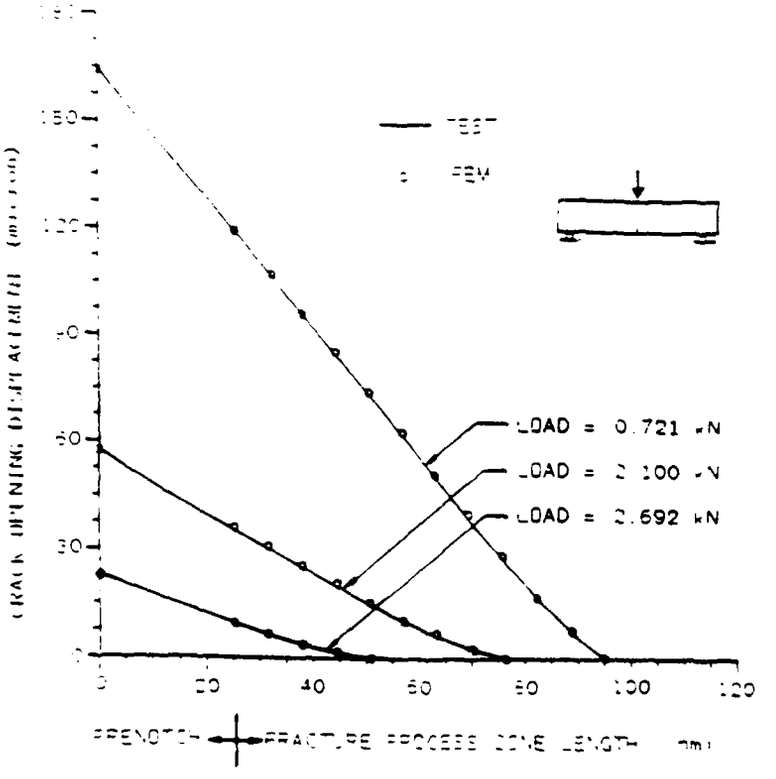

Figure 8. COD Variations along Fracture Process Zone. Three-Point Bend Specimen No. LB-4.

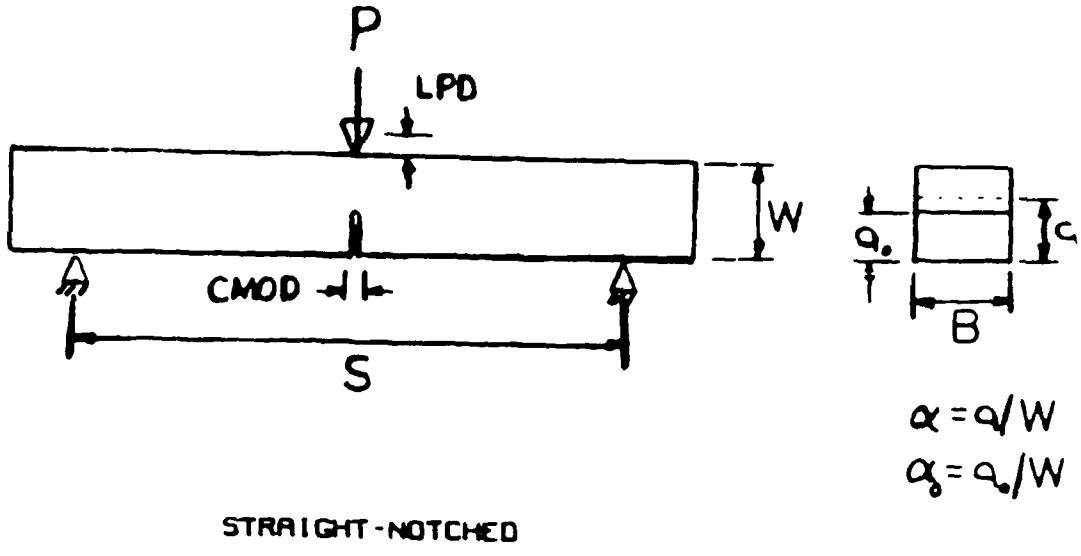

Figure 9. Three-Point Bend SiC_w/Al_2O_3 Specimen.

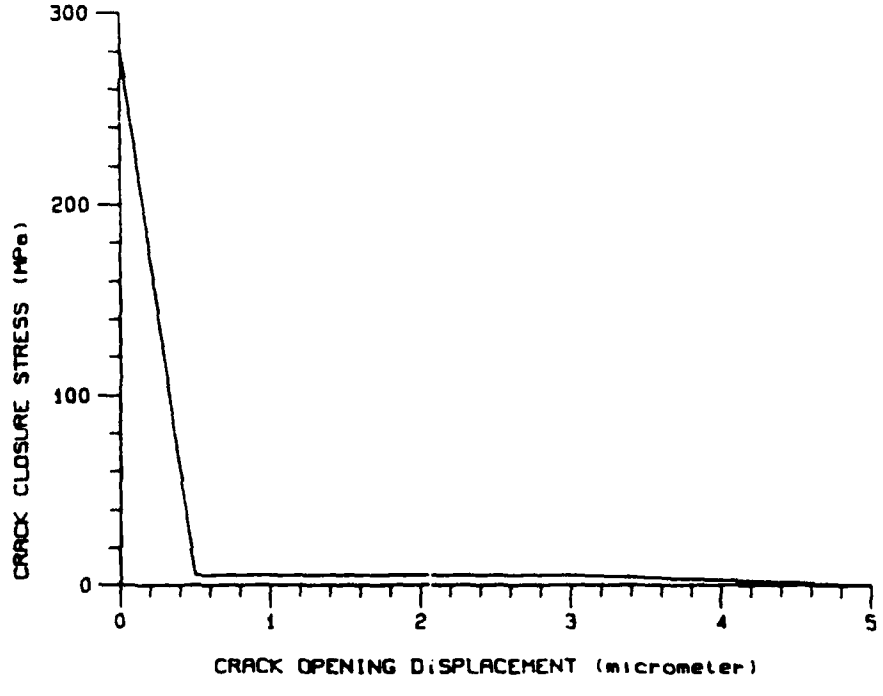

Figure 10. Crack Closure Stress Versus COD Along FPZ in Sic_w/Al_2O_3 Specimen.

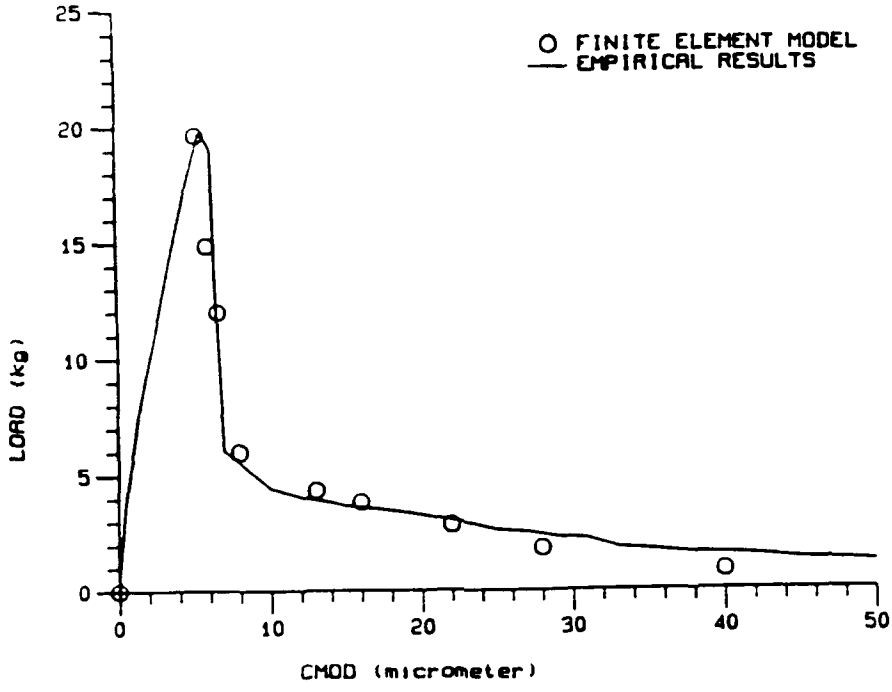

Figure 11. Load Versus CMOD Relation for a SiC Whisker/Alumina Matrix Composite Straight-Notched. Three-Point Bend Specimen.

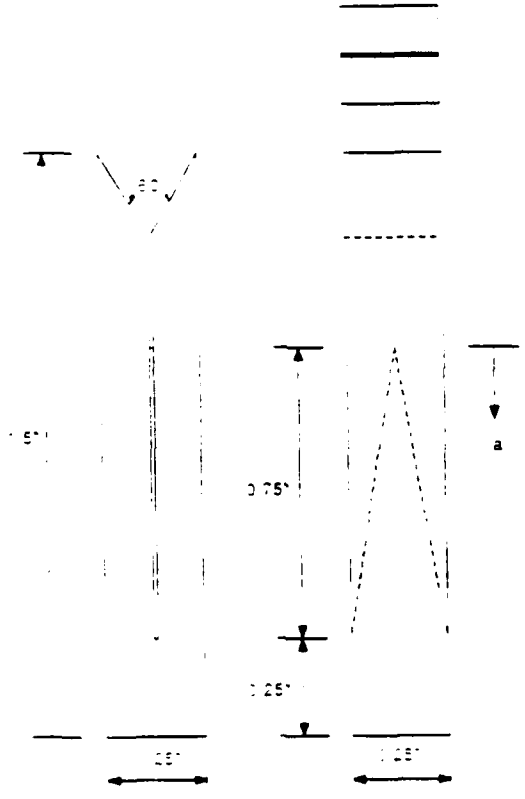

Figure 12. Chevron Notched DCB Specimen.

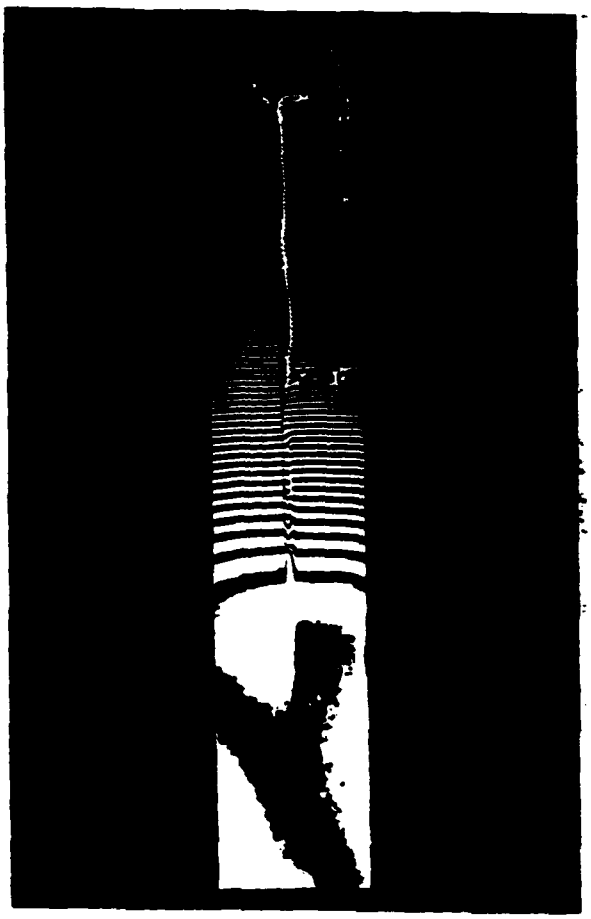

Figure 13. Moire Fringe Pattern of Chevron Notched DCB Specimen.

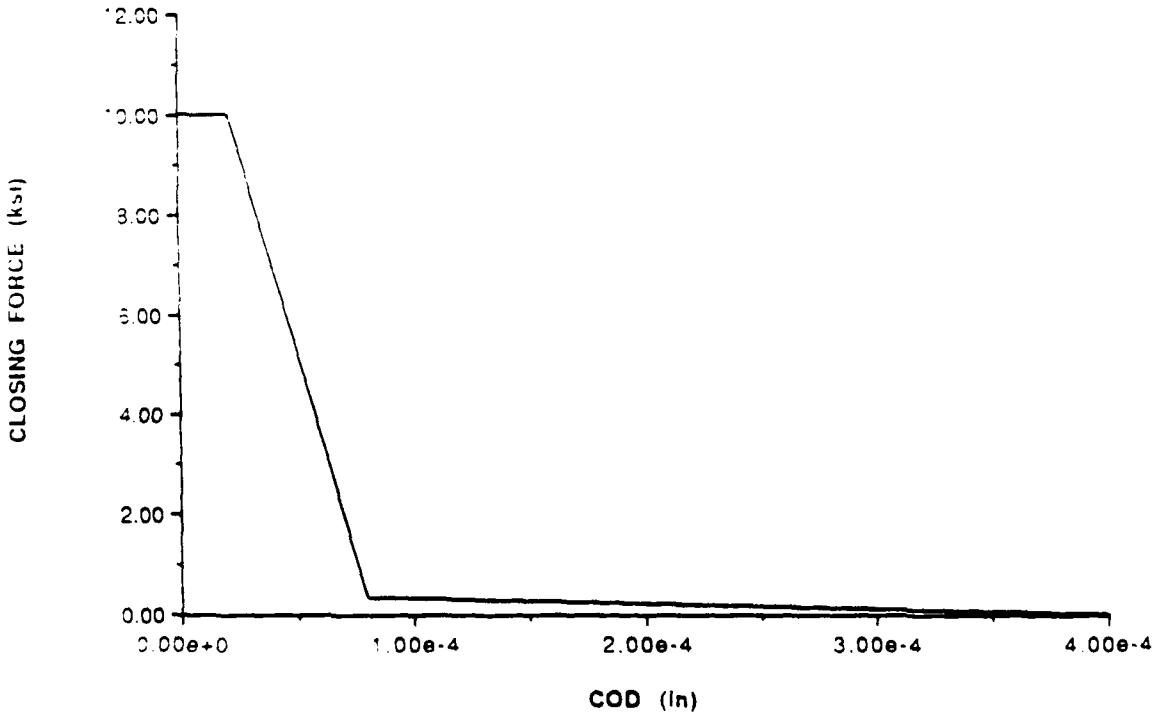

Figure 14. Crack Closure Stress Versus COD Along FPZ of Chevron Notched DCB Specimen.

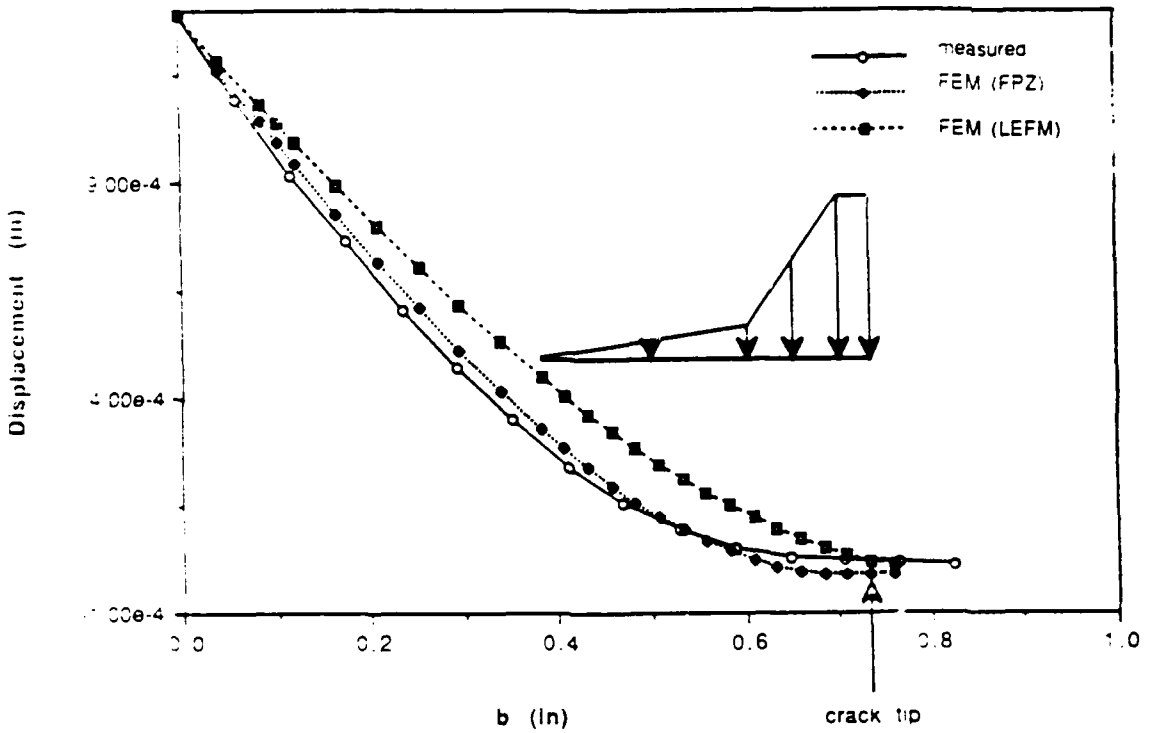

Figure 15. Crack Opening Displacement on the Surface of SiC_w/Al_2O_3 Chevron Notched DCB Specimen.

Session 2:

Fracture in Concrete and Rock

Chairs:

Toshio Mura
Northwestern University
Evanston, U.S.A

Charles Dowding
Northwestern University
Evanston, U.S.A

Reporter:

Jacky Mazars
Ecole Normale Superieure
de Cachan, France

MICROCRACKING AND DAMAGE IN CONCRETE

D.FRANCOIS. CNRS. URA 850
ECOLE CENTRALE DE PARIS. F92295 CHATENAY-MALABRY CEDEX

ABSTRECT :

Microcracks opening and propagation by successive steps provide concrete with a non linear behaviour and increase the fracture toughness with respect to the hardened cement paste. Several criteria were proposed for the propagation of microcracks Damage mechanics is an efficient tool to meodelize the behaviour of concrete. The damage is related to the strain. Various expressions were proposed for this relation. This evolution is related to the opening and to the propagation of microcracks through their influence of the compliances of the material. Extension of these models can be given in the case of fatigue, where the viscous behaviour of concrete must be taken in consideration. A new model is proposed. Lastly numerical models provide a better understanding of the behaviour of concrete and of the effect of structural parameters.

1 - Microcracking in concrete

The cracking of concrete was studied and described by many authors for instance, (Slate and Hover, 1984). Let's simply recall that before any loading this material contains many defects and microcracks. In the cement paste porosities are present. Their sizes are distributed over a wide range and when they are observed at different scales, the appearence remains the same. The cement paste is a fractal object whose dimension is equal to 2.90 to 2.97. (Regourd, 1986). The density is lower near the aggregate interface, in the "auréole de transition", and moreover this feature is accentuated under the aggregates.

Microcracks exists at the interface between the aggregate and the mortar, mostly underneath the aggregate. They are due to bleeding and to internal stresses coming from the mortar shrinkage.

There are also longer cracks at the surface which are produced by the shrinkage from drying.

When the concrete is loaded, at some critical stress the cracks at the aggregate interface, propagate through the mortar until they meet an aggregate boundary where they are stopped. It is not until further loading that they can propagate again and produce the final fracture. It is this two steps propagation which somewhat lessen the brittleness of concrete, if compared with the mortar. As the cracks are stopped before final fracture, their opening increases the deformation, producing a non linear stress strain curve and offering a way to reduce the stress concentrations at the macroscale. Furthermore this diffuse cracking absorbs energy and this increases the toughness of the material. At a smaller scale the same can be said of the mortar compared to the cement paste.

This behaviour of concrete leads quite naturally to a description in terms of damage mechanics.

If a connection is sought between the macroscopic behaviour and the physical processes of crack propagation at the microscale, a crack propagation criterion is needed.

2 - Crack propagation criteria

Cracks in concrete are loaded in mixed mode I and II. For a crack which propagates in its own plane, with no deviation, several propagation criteria can be written.

The Griffith criterion, which states that the strain energy release rate G_{Is} equal to a critical value G_{Ic} yields :

$$G = G_{Ic} \text{ or } K_I^2 + K_{II}^2 = K_{IC}^2$$

K_I and K_{II} being the stress intensity factors in mode I and II respectively, it is the criterion which is the most satisfactory from a thermodynamics point of view.

The normal stress criterion, which is based on the idea that the propagation will start when the normal stress on the propagation plane reaches a critical value yields simply

$$K_I = K_{IC}$$

because the mode II loading does not produce any normal stress on the plane of the crack.

The maximun principal stress criterion yields :

$$K_I + K_{II} = K_{IC}$$

The criterion of the strain energy density proposed by Sih (1973) yields :

$$K_I^2 + \frac{K_{II}^2}{1 - 2\nu} = K_{IC}^2$$

where n in the Poisson ratio. It is equivalent to a maximum strain criterion in that case.

The question becomes more confused when the crack is allowed to branch. The Griffith criterion is now very difficult to use because there is no simple relation between the strain energy release rate and the branching angle.

The normal stress criterion is the most likely. It gives now the following equations : (Di Tommaso, 1984)

$$K_I \sin\theta_o + K_{II}\left(3\cos\theta_o - 1\right) = 0$$

$$\cos\frac{\theta_o}{2}\cdot\left[K_I\cos^2\frac{\theta_o}{2}-\frac{3}{2}K_{II}\sin\theta_o\right]=K_{IC}$$

where θ_o is the crack branching angle.

When the normal stress on the crack is compressive, it can still propagate if the shear stress is high enough with respect to the friction force on the crack faces. The condition can be written.

$$|K_{II}| - f|K_I| = K_{IIC}$$

f being the friction coefficient.

Another complication comes from the cracks lying at the interface between two dissimilar materials. A solution to this problem exists (Di Tommaso, 1984) Depending on the ratio of the shear moduli and on the stress applied on the interface the crack propagates in the interface or branches into either the aggregate or the mortar. The tendency is for the cracks to propagate into the less rigid material. Thus in normal concrete they will not cross the aggregates, whereas this can happen in light weight concrete or in high strength concrete.

3 - Damage mechanics models.

The microcracks decrease the effective area of the material which carries the load. A damage parameter can be introduced, defined as the ratio between the effective area and the total area. It is an increasing function of the number of cracks and of their sizes. As there are cracks allready present in the concrete before any loading, there is an initial damage present. It then increases when loads are applied.

Another definition is to relate the damage parameter to the decrease of the elastic moduli, owing to the opening and to the propagation of microcracks.

In any case, the development of the cracks is not isotropic and it is obvious that the damage must be rigourously defined as a tensor.

It seens better to relate the evolution of the damage to the strain rather then to the stress. The crack propagation, whatever the

criterion used, is produced by a local stress, included in the K_I and K_{II} stress intensity factors. However on a macro scale, microcracks can propagate even when K_I and K_{II} are equal to zero. It is the case in a compression test where cracks open parallel to the load axis.

This of course is due to local stress fluctuations at the microscale and this would never happen in a perfectly homogeneous material. Back to the macroscale this damage can be related to the Poisson expansion of the concrete under compression.

But there are some thermodynamics arguments to support this idea. If the thermodynamics potential is y, the damage evolution force Y, i.e. the damage associated variable, is given by :

$$y = \frac{\partial \psi}{\partial \mathbb{D}}(\varepsilon, \mathbb{D})$$

For an elastic material such as concrete :

$$\psi = \frac{1}{2}\,\varepsilon : \sigma = \frac{1}{2}\,\mathbb{M} : \varepsilon : \varepsilon = \frac{1}{2}\mathbb{M}_o(1 - \mathbb{D}) : \varepsilon : \varepsilon$$

where $\mathbb{M}$ represents the matrix of the elastic moduli. The damage $\mathbb{D}$ is defined as an evolution of this matrix. In such a case :

$$y = \frac{-1}{2}\,\mathbb{M}_o : \varepsilon : \varepsilon$$

is purely related to the deformation and so it must be the same for the evolution of damage which is a function of Y.

Another way to look at it is to consider the strain energy release rate G which is the microcracks driving force. It can be expressed either as a function of the load or of the deformation. In the first case G is damage dependent, whereas, this parameter does not appear in the expression of G as a function of the deformation.

In a way this reflects the interaction between microcracks, an effect which is seldom taken in consideration.

The different behaviour of microcracks according to the sign of the normal stress shows that it is not possible to use a single law of evolution for the damage.

In the most general case there could be 21 components of the damage tensor as there are 21 elastic moduli. Simplifications are introduced the most stringent being to simply use a scalar.

Considering that the concrete is an orthotropic material, reduces the number of components to nine (Collombet, 1985; Pijaudier Cabot, 1985), To identify and to use such a model remains costly.

More simply Karihaloo and Fu (1990) proposed to use two parameters D_{11} and D_{22} to describe the damage in two dimensions, in the principal strains directions. Using the equivalence of complementary energy of the damaged and the equivalent elastic material these authors give the effective compliance tensor S* as :

$$S^*_{1111} = \frac{1}{E(1 - D_{11})^2}$$

$$S^*_{1212} = S_{2121} = \frac{\nu}{E(1 - D_{11})(1 - D_{22})}$$

$$S^*_{2222} = \frac{1}{E(1 - D_{22})^2}$$

They further give the evolution law as :

$$D_{11} = \left[A + B\left(\sigma_{22} / \sigma_{11}\right)\right]\left(\varepsilon_{11} - \varepsilon_{11}^{th}\right)^C$$

$$D_{22} = \left[A + B\left(\sigma_{22} / \sigma_{11}\right)\right]\left(\varepsilon_{22} - \varepsilon_{22}^{th}\right)^C$$

where A = 150 ± 10, B = 40 ± 5, and C = 0.8 ± 0.02 $\varepsilon_{11}{}^{th}$ and $\varepsilon_{22}{}^{th}$ are thresholds, which depend on the concrete and below which there is no damage. According to experiments of Kaplan (1963) who measured the strain at first cracking (in micro strain)

$$\varepsilon_{11}^{th} = 79.5\,(\pm 6) + 43.4\,V - 406.1V^2 + 707.2V^3 - 1150V^4 + 763V^5$$

where V is the volume fraction of coarse mix. This model of damage cannot describe cases where one of the stress comporment is compressive.

Mazars (1984) took this problem in consideration but taking the damage as isotropic i.e. as a scalar. In a first version (Mazars, 1986 a) an equivalent deformation threshold is introduced, this equivalent deformation being defined as $\sqrt{\langle \varepsilon_i \rangle^2}$ where ε_i are the principal

positive strains. The evolution of damage differs in tension and in compression. Another version (Mazars, 1986) introduces an unilateral damage by partitioning the stress tensor in two parts, σ^+ built with the positive eigen values and σ^- with the negative ones.

Keeping only two damage scalars D_t and D_c the behaviour of the damaged concrete is described as :

$$\varepsilon = \frac{1}{E_o(1-D_t)}\left[(1+\nu_o)\sigma^+ - \nu_o(tr\sigma)^+ 1\right] + \frac{1}{E_o(1-D_c)}\left[(1+\nu_o)\sigma^- - \nu_o(tr\sigma)^- 1\right]$$

The corresponding damage extension forces ar :

$$Y_t = \frac{1}{6E_o(1-D_t)^2}\left[(1+\nu_o)\left[3\sum_i\left(\sigma_i^+\right)^2 - \left(tr\sigma^+\right)^2\right] - (1+2\nu_o)\left(tr\sigma^+\right)^2\right]$$

and the same expression for Y_c replacing σ^+ by σ^-.

The evolutions of the damage parameters are given on loading by :

$$\frac{\dot{D}_t}{\dot{Y}_t} = \frac{\sqrt{Y_t^o}\,(1 - a_t)}{2\,(Y_t)^{3/2}} + \frac{a_t\, b_t}{2\sqrt{Y_t}\exp\left[b_t\left(\sqrt{Y_t} - \sqrt{Y_t^o}\right)\right]}$$

and a simular expression for D_c.

where $\sqrt{Y_t^o}$ and $\sqrt{Y_c^o}$ are thresholds, a_t, b_t, a_c, b_c material parameters.

The damage parameters remain constant when unloading. In such a model the material keeps the memory of the previous damage in cyclic loading.

4 - Relation between the damage and the microcracks.

The relation between the damage parameters and the microcracks comes from the influence of their propagation and of their opening on the compliances of the material.

For a penny shaped crack of radius a under a normal stress σ,

the crack discontinuity b is given by :

$$b = \left(a^2 - r^2\right)^{1/2} \cdot \frac{8\left(1 - \nu^2\right)}{\pi E} \cdot \sigma$$

whose average is :

$$\bar{b} = \frac{16\left(1 - \nu^2\right)}{3\pi E} \cdot \sigma a$$

This shows that the presence of such a crack introduces an extra strain $\pi a^2 \bar{b} / V$, V being the volume of the material. The compliance is increased proportionally to the cube of the crack size. If it propagates a strong non linear effect appears.

Karihaloo and Fu (1969) remind that the effective moduli of a material containing voids can be computed as :

$$C^*_{ijkl} = C_{ijmn}\left[I_{mnkl} - f_p\left(I_{mnkl} - S_{mnkl}\right)^{-1}\right]$$

where f is the volume frection of voids, and S_{ijkl} Elshelby's tensor, which depends on their shape. This expression can give the evolution of damage as a function of strain when there is no propagation of the defects nor nucleation of new voids. In the case of an orthotropic material under plane stress condition they find a damage evolution which displays a similar behaviour as the one given before.

$$D_{ii} = \left[A + B\sigma_{ii} + C\left(\sigma_{22} / \sigma_{33}\right)\right]\left(1 - \varepsilon_v^{th} / \varepsilon_v\right)^D$$

ε_v being the volumetric strain.

In the case of an evolution of the population of voids, the effective moduli can be computed, as a function of f and of S_{ijkl}.

In a similar fashion Krajcinovic and Fanella (1986) built a model in which initial cracks occupy a fraction of the aggregate mortar interfaces. Their sizes and orientations are randomly distributed. When the load is increased a few cracks will suddenly grow to a size equal to that of the aggregate. Then more and more cracks jump in this way until one crack will propagate in the mortar, this being

considered as the final failure. It is possible to calculate the damaged compliances which are a function of the size distribution of the aggregates and of the applied load. Similar calculations were proposed by Nobile (1986).

5 - Extension to the fatigue of concrete.

The previous models are based on the opening and on the propagation of microcracks in concrete on loading. In those models, unloading is purely elastic. When loading again the microcracks would recover exactly the same configuration as before and the cycles could then be repeated over and over without any evolution. The only way to explain the fatigue of concrete is to take in consideration its viscous behaviour. Under constant load this material creeps. This could be due to water migration in the mortar and to slow growth of the microcracks. At each cycle of loading some irreversible deformation accumulates.

Tait and Garrett (1986) showed for example that the fatigue crack propagation in mortar could be correlated to the static crack growth rate under constant stress, checking a relation established by Evans and Fuller (1974).

Hu (1990) used this idea to study the evolution of fatigue damage in concrete. He writes the evolution of the sizes of a microcrack population obeying a Weibull statistics. Each crack grows according to the law :

$$da/dt = AK_I^n$$

In this way the evolution of the fracture probability can be evaluated as a function of time. This can be done either with a constant stress or with a cyclic stress.

However this model is based on the concept of the weakest link and it should apply to a single phase material, such as hardened cement paste containing a population of cracks. For concrete the detailed description of the microcrack behaviour could be the following : slow growth of the cracks at the interfaces of the mortar and the aggregates until they reach a critical size at which time they jump accross the whole interface and stop. This critical size is a function of the local stress. This first phase produces a decreasing

demage rate because as time goes on more and more cracks have reached the critical size. The next step will be the branching of the microcracks into the mortar and their slow growth into an orientation which favours mode I. When they reach a critical size, they propagate quickly until they meet another aggregate where they stop and grow slowly. This phase will correspond to an increasing damage rate as the K_I factor on each crack keeps increasing because K_I can be written :

$$K_I = Y\sigma\sqrt{a}$$

Each crack grows according to the law :

$$\frac{1}{a_0^{\frac{n-2}{2}}} - \frac{1}{a^{\frac{n-2}{2}}} = \frac{n-2}{2} \cdot AY^n \sigma^n t$$

The time for an individual jump of a crack to the next aggregate is thus proportionnal to σ^{-n}. This would give a viscous behaviour for concrete characterized by :

$$\dot{\varepsilon} = \left(\frac{\sigma}{\sigma_o}\right)^n$$

We can now build a fatigue model for concrete having such a viscous behaviour. We consider that the material is decomposed in N elements each having a fracture strain ε_R which is distributed according to a Weibull law. For a strain ε the proportion of broken elements is :

$$N_R / N = 1 - \exp\left[-(\varepsilon / \varepsilon_o)^m\right]$$

We can take the damage parameter as this ratio N_R/N. We can now write the stress strain law as :

$$\dot{\varepsilon} = \left[\sigma / \sigma_o (1 - D)\right]^n (\sigma / \sigma_o)^n . \exp(\varepsilon / \varepsilon_o)^{mn}$$

During one fatigue cycle :

$$\int_{\varepsilon}^{\varepsilon + \Delta\varepsilon/\Delta N} \exp\left[-\left(\varepsilon / \varepsilon_o\right)^{mn}\right] d\varepsilon = \int_{t}^{t+T/2} \left(\sigma / \sigma_o\right)^{n} dt$$

This quantity is constant and equal to $(\Delta e/\Delta N)_0$ at the beginning of the test. After N cycles we will have a strain accumulation such that :

$$\int_{o}^{\varepsilon} \exp\left[-\left(\varepsilon / \varepsilon_o\right)^{mn}\right] d\varepsilon = N\left(\Delta\varepsilon / \Delta N\right)_o$$

Or else :

$$\int_{o}^{\varepsilon/\varepsilon_o} \exp\left[-x^{mn}\right] dx = \frac{N}{\varepsilon_0}\left(\Delta\varepsilon / \Delta N\right)_o$$

This function is such that for a very large number of cycles the strain per cycle remains almost constant. A very fast acceleration occurs for $\varepsilon = \varepsilon_o$, when :

$$\int_{o}^{1} \exp\left(-x^{mn}\right) dx \cong 1 = N_R\left(\Delta\varepsilon/\Delta N\right)_o/\varepsilon_o$$

This model yields a life time which varies as $e_o/(\Delta e/\Delta N)_o$. In a tensile test a strain e equal to e_o corresponds to a damage equal to 0.93, so that e_o can be considered as the fracture strain.

Experimentaly it was found that the strain increased at each cycle, in a manner which is well represented by the model (Alliche, 1990).

A simplified version consists in using a damage parameter the increase of which for one cycle is proportionnal to the increase in strain.

6 - Numerical models.

The complex structure of concrete led many authors to use numerical simulation to study the evolution of damage in concrete. The best known example is due to Zaitsev and Wittmann (1983). Other computation were published (Hu, Cotterell and Mai, 1986; Zaitsev, Kondrashenko and Arshabov, 1986; Roelfstra and Sadouki, 1986). They start from a certain distribution of initial cracks at the interfaces of the mortar and the aggregates and by introducing crack propagation criteria they follow the growth of the damage in a 2D structure. Roelfstra and Sadouki (1986) put special elements at the interfaces to simulate crack initiation.

A somewhat different numerical analysis consists in introducing random fracture resistances in the finite element mesh (Rossi and Richer, 1987).

A somewhat different approach was used by Schorn (1986) who modelized the concrete by a series of struts with random fracture resistances. This kind of model is also developped by De Arcangelis et al. so as to study the size effect. They found a master load-displacement curve if both the load and the displacement are divided by the size L of the elements to the power 3/4.(in a 2D strut system).

Besides this possibility to test the size effect, the better understanding which the visualization of damage can bring, numerical concretes constitute good models to test the influence of various parameters.

In this way for instance Zaitsev, Kondrashenko and Arshabov (1986) found that a large heterogeneity of the structure lowers the strength of light-weight concrete, that it decreases drastically when the resistance of the interfaces drops below the resistance of the mortar, and, most of all they showed the detrimental effect of the porosity of the light-weight aggregates.

7 - Conclusion.

A great deal of progress has been achieved in the understanding and in the modelization of such a complex, multiscale system as concrete. Damage mechanics, its relation with the influence of voids and microcracks on the compliances of the material, numerical modelling can help to predict its behaviour and the influence of various structural parameters. It seems that the models that are needed must incorporate a damage tensor the evolution of which is a function of strain, the viscous behaviour of concrete (or the slow crack growth) a statistical distribution of strength or of microcracks.

Experiments are still needed to better understand the fracture criteria of an individual microcrack in mixed mode, depending on its exact location, on the nature of the aggregate. A more exact knowlege of slow microcrack growth needs also to be obtained. This would allow more precise modelizations.

REFERENCES

N.ALLICHE : (1990) Thèse. Université d'Alger.

F.COLLOMBET : (1985) "Modélisation de l'endommagement anisotrope. Application au comportement du beton sous sollicitations multiaxiales". Thèse de 3ème cycle. Université Paris VI.

A.DI TOMMASO : (1984) "Evolution on Concrete Fracture" in "Fracture Mechanics of Concrete", A.Carpinteri, A.R. Ingraffea ed. Martinus Nijhoff, Pub. The Hague, pp.31-65.

A.G.EVANS and E.R.FULLER : (1974) Met. Trans, 5, pp. 27-33.

Xiao-Zhi HU : (1990) "Flaw Analysis in Time Dependent Fracture for Cemetitious Materials".

X-Z.HU, B.COTTERELL and Y.N.MAI : (1986) "Computer Simulation Models of Fracture in Concrete" in Fracture Toughness and Fracture Energy of Concrete. F.HWittmann ed. Elsevier, Amsterdam, pp. 91-100.

M.F.KAPLAN : (1963) "Strains and Stresses of Concrete at Initiation of Cracking and Near Failure". J. Am. Conc. Inst., 60, pp. 853-880.

B.L.KARIHALOO and D.FU : (1989) "A Damaged Based Constitutive law for Plain Concrete in Tension". IUTAM Congress, submitted to J. Mechanics of Materials.

B.L.KARIHALOO and D.FU : (1990) "An Anisotropic Damage Model for Plain Concrete".
In Proc. Int Conf. on Fracture and Damage of Concrete and Rock. Vienna, July 1988, Pergamon Press, Engng. Fract. Mech., 35, 205-209.
B.L.KARIHALOO and D.FU : (1990) "An Orthotrophic Damage Model for Plain Concrete in Tension". Submitted to ACI Materials J..

D.KRAJCINOVIC and D.FANELLA : (1986) "A Micromechanical Damage Model for Concrete", Engng. Fract. Mech., 25, 585-596.

J.MAZARS : (1981) "Mechanical Damage and Fracture of Concrete Structures", in Advances in Fracture Research. D.François et al, Eds. Pergamon, 4, 1499-1506.

J.MAZARS : (1984) "Application de la mécanique de l'endommagement au comportement non linéaire et à la rupture du béton de structure", Thèse de doctorat d'Etat, Université Paris VI.

J.MAZARS (a) : (1986) "A Description of Micro and Macroscale Damage of
Concrete Structures". Engng. Fract. Mech., 25, pp. 729-737.

J.MAZARS (b) : (1986) "A Model of Unilateral Elastic Damageable Material and its Application to Concrete".
in Fracture Toughness and Fracture Energy of Concrete, F.H.Wittmann, Ed. Elsevier, Amsterdam, pp. 61-71.

J.MAZARS, Y.BERTHAUD and S.RAMTANI : (1990) "The Unilateral Behaviour of Damaged Concrete", Engng. Fract. Mech., 35, 629-635.

J.MAZARS, and J.LEMAITRE : "Application of Continuous Damage Mechanics to Strain and Fracture of Concrete", Proc. of the NATO Advanced Research Worskhop on Application of Fracture Mechanics to Cementious Composites. Evanston, pp.375-388.

L.NOBILE : (1986) "A Microcrack Model of Concrete's Behaviour under Applied Load"
in Fracture Toughness and Fracture Energy of Concrete, F.H.Witmann ed. Elsevier, Amsterdam, 73-80.

G.PIJAUDIER-CABOT : (1985) "Caractérisation et modélisation du comportement du béton par un essai multiaxial automatique", thèse de 3ème cycle, Université Paris VI.

M.REGOURD : (1986) "Microstructure of Cement Blends Including Fly Ash, Silica Fume, Slag and Fillers" Proc. of the Fall Meeting Materials Research Soc., Boston.

P.E.ROELFSTRA and H.SADOUKI : (1986) "Fracture Process in Numerical Concrete"
in Fracture Toughness and Fracture Energy of Concrete. F.H.Wittmann ed. Elsevier, Amsterdam, pp. 105-116.

P.ROSSI and S.RICHER : (1987) "Stochastic Modelling of Concrete Cracking", in Constitutive Laws for Engineering Materials, C.S.Desai, ed.Tucson.

H.SCHORN : (1986) "Numerical Simulation of Composite Materials as Concrete"
in Fracture Toughness and Fracture Energy of Concrete. F.H.Wittmann, ed. Elsevier, Amsterdam, pp. 177-188.

G.C.SIH : (1973) "Some Basic Problems in Fracture Mechanics and New Concepts", Engng. fract. Mech., 5,.

F.O.SLATE and K.C.HOVER : (1984) "Microcracking of Concrete" in Fracture Mechanics of Concrete, ed. A.Carpinteri, A.R. Ingraffea, p.137, Martinus Nijhoff, Pub. the Hague.

R.B.TAIT and G.G.GARRETT : (1986) "A Fracture Mechanics Evaluation of Static and Fatigue Crack Growth Rate in Cement Mortar"
in Fracture Toughness and Fracture Energy of Concrete. F.H.Wittmann, ed. Elsevier, Amsterdam, 21-30.

F.H.WITTMANN : (1981) "Mechanisms and Mechanics of Fracture of Concrete"
in Advances in Fracture Research, ed. D.François et al, 4, 1467, Pergamon.

Y.V.ZAITSEV, V.I.KONDRASHENKO and A.A.ARSHABOV : (1986) "Simulation of Behaviour of Light-Weight Concretes under Load and its Experimental Trial".
in Fracture Toughness and Fracture Energy of Concrete. F.H.Wittmann, ed. Elsevier, Amsterdam, pp. 101-104.

Y.V.ZAITSEV and F.H.WITTMANN : (1983) "Fracture Mechanics of Concrete" Elsevier Scien. Pub., Amsterdam, 251-299.

CRACKING, DAMAGE AND FRACTURE IN STRESSED ROCK:

A HOLISTIC APPROACH

Philip G. Meredith

Rock & Ice Physics Laboratory
Department of Geological Sciences
University College London
Gower Street
London WC1E 6BT, U.K.

Draft Only

To be presented at:
NATO Advanced Research Workshop on
"Toughening Mechanisms in Quasi-Brittle Materials"

Northwestern University
16 - 20 July, 1990

1. Introduction

The quasi-brittle behaviour of crustal rocks has many aspects in common with the processes of crack growth, fracture and failure in other quasi-brittle materials such as concrete and polycrystalline ceramics. Most of these similarities arise due to the intrinsic heterogeneous, polycrystalline and commonly polyphase microstructure of these materials. However, there are also a number of fundamental differences that affect rock fracture, and which arise primarily due to their burial in the environment of the Earth's crust. Important among these are: (1) that under all but exceptional circumstances, rocks are subjected to compressive triaxial stresses in the crust; (2) that in the overwhelming majority of situations in the crustal environment, pre-existing microcracks, pores and void spaces contain fluids (especially water) which are also commonly under pressure; and (3) the average rate of natural deformation is very slow.

Since crack growth is necessarily a dilatant process (involving volume increase) it is pressure dependent, and therefore the application of compressive stresses acts to stabilize crack growth and hence to strengthen or toughen the material. Conversely, the presence of pressurized pore fluids acts to weaken rocks, both by reducing the confining effect of any applied compressive normal stress via the principle of "effective" stress (see Jaeger & Cook 1976), and also through weakening fluid-rock chemical reactions that allow subcritical crack growth processes such as "stress corrosion" to proceed. Subcritical crack growth becomes a fundamentally important deformation process in rocks because the inferred rate of natural tectonic deformation in the crust (strain rates of the order of 10^{-14}/s) is much lower than typical engineering rates of strain. This leads to a time-, environment- and deformation rate-dependence of the mechanical properties of rocks. For example, the compressive fracture stress of unconfined rock can decrease by a factor of two or three as the strain rate is reduced from those ordinarily used in laboratory tests (10^{-4}- 10^{-6}/s) to that commonly associated with natural tectonic deformation. Most rocks containing pore fluids also exhibit brittle creep behaviour (time-dependent cracking at constant stress, or "static fatigue"), especially if the applied stress is a significant fraction of the short-term fracture stress (Kranz & Scholz 1977, Kranz 1979, Costin 1987).

Furthermore, the underlying rationale behind the methodology for determining basic fracture mechanics parameters is different for rocks than for some other quasi-brittle materials (e.g. concrete), and this is reflected in the different codes of practice recently developed by ISRM and RILEM (ISRM 1988, RILEM 1985, Hillerborg 1989). In general, the size of rock masses being considered in deep engineering problems and in crustal geophysics can be considered to essentially infinite, and under these circumstances an LEFM analysis is appropriate. On the other hand, the realistic size of laboratory rock sampkes is normally many orders of magnitude smaller. Hence the ISRM approach has been to attempt to obtain valid fracture toughness values b y testing sub-size samples and then making a correction for non-LEFM bahaviour. There is, therefore, the additional

problem of the scaling effect to be considered when modelling and analysing rock fracture problems using laboratory derived data.

By contrast, the RILEM approach has been to abandon LEFM altogether and to determine the fracture energy from tension-softening measurements. This stems, at least in part, from the relatively small scale defference between test samples and real enginering structures.

In summary then, the major part of this paper is concerned with an integrated discussion of those aspects of the fracture and failure of rocks that are different from other quasi-brittle materials, i.e. compressive stress fields, the presence of pore fluids, time-dependent propereties, and scaling relations. However, it is well recognised (e.g. Kranz 1983, Meredith 1990) that even under compressive loading rock deformation proceeds by the growth, interaction and linkage of many tensile microcracks. It is apposite therefore to consider briefly the fracture of rocks under simple tensile loading before proceeding to the more complex case of compressive loading.

2. Fracture under Tensile Loading

There have been a number of comprehensive reviews published in recent years detailing different aspects of the propagation of tensile cracks in rocks (e.g. Atkinson 1982, 1984, Swanson 1984, Atkinson & Meredith 1987a, 1987b, Meredith 1989) so that only a brief summary is provided here to avoid needless repetition.

2.1 CRITICAL FRACTURE

Meredith (1989) has shown that mode I fracture toughness measurements for rocks exhibit similar treands as for many other quasi-brittle materials. The fracture toughness of polycrystalline rocks is generally found to be much higher than that of any of the rock's constituent minerals (Atkinson & Meredith 1987b, Meredith 1990), and Figure 1 also illustrates that, for rocks of similar mineralogical composition, the fracture toughness tends to increase with increasing grain size. For rocks with a large variation in grain size, it is the maximum grain size that is the controlling influence. Large grains or phenocrysts appear to act as crack "stoppers" in a similar manner to the large inclusions that are used to artificially toughen some polycrystalline ceramics.

In addition, Figure 2 shows for Merrivale granite the type of rising R-curve behaviour that is typical of many rocks (e.g. Schmidt & Lutz 1979, Ingraffea 1987, Swanson 1987, Meredith 1989) and polycrystalline ceramics (e.g. Hubner & Jillek 1977, Cook et al. 1985). The existence of R-curve behaviour is linked directly with the development of an inelastic fracture process zone that comnprises microcracking ahead of, and crack interface tractions (frictional interlocking due to the rough three-dimensional nature of crack surfaces, and ligamentary bridging between opposing crack walls) behind a macrocrack tip (Labuz et al. 1985, Ingraffea 1987, Swanson 1987, Freiman & Swanson 1990).

Crack extension resistance increases as crack length increases until the process zone is fully developed and there is at least a portion of the crack that is traction-free. Only at or beyond this critical crack length is a steady state reached, and only then can a fracture toughness value that is truly representative of the bulk material be determined.

2.2 SUBCRITICAL CRACK GROWTH

In systems where rocks are subjected to long-term loading, the classical LEFM approach does not provide an adequate description of crack growth. This is especially so at elevated temperatures and in the presence of reactive environmental species. A considerable body of evidence supports the idea that cracks can propagate in a stable, quasi-static manner at stress intensities that are substantially below the fracture toughness, albeit at velocities that are orders of magnitude lower than the terminal velocity associated with critical fracture. This phenomenon of subcritical crack growth has been observed experimentally in many quasi-brittle materials, including glass (Wiederhorn 1978), ceramics (Wiederhorn 1974), and minerals and rocks (Atkinson 1984, Atkinson & Meredith 1987a, 1987b).

The overwhelming body of experimental and observational evidence suggests that extension of pre-existing cracks and flaws by the mechanism of "stress corrosion" is likely to dominate subcritical crack growth in rocks at low homologous temperatures. Stress corrosion proceeds by the preferential weakening of strained bonds at crack tips through reactions with chemical species in the environment. Although a whole range of surfactants can contribute to stress corrosion (e.g. Dunning et al. 1984), the most active reagent for the process appears to be water.

The subcritical crack growth behaviour of many materials approximates to the classical trimodal pattern exhibited by glass in aqueous environments. This pattern of behaviour is illustrated schematically in Figure 3, where the logarithm of stress intensity (K) is plotted against the logarithm of crack velocity. In region 1, the crack extension velocity is controlled by the rate of stress corrosion reactions at crack tips. In region 2, crack growth is controlled by the rate of transport of reactive species to crack tips (Lawn & Wilshaw 1975). In region 3 the curve becomes asymptotic to the critical value (denoted by 'c'); crack growth is primarily due to thermally activated bond rupture and is relatively insensitive to the chemical environment (Freiman 1984). A lower limiting threshold is thought to exist, below which no crack growth will occur (denoted by '0'). The existence of such a subcritical crack growth limit has been demonstrated for various glass/water systems (e.g. Wiederhorn & Johnson 1973, Simmons & Freiman 1980), but has not yet been confirmed for polycrystalline ceramics or rocks. Note that because stress corrosion is a chemically-enhanced and thermally activated process, the subcritical crack growth curve should be shifted to a higher velocity for the same value of K if either the partial pressure of the active environmental reagent or the temperature is increased.

Figure 4 illustrates experimentally derived subcritical crack growth data for Westerly granite under a range of environmental conditions. All of the data of Figure 4 relate to region 1 type behaviour and may be described by a power law (Charles 1958) of the form:

$$V = V_c(K/K_c)^n \quad (1)$$

where n is known as the stress corrosion index (for the data of Figure 4, values of n lie in the range 33 - 40).

Atkinson & Meredith (1987b) provide a compilation of subcritical crack growth data for a wide range of rocks and minerals, and for polycrystalline rocks values of n in equation (1) generally lie in the range 20 - 60. Comparison of subcritical crack growth behaviour for different rock types is problematical, but an attempt is made to do this in Figure 5 (after Atkinson 1984) by normalizing stress intensity factors by the fracture toughness of each rock type. Figure 5 therefore illustrates in a broad way the relative susceptibility of different rock types (and quartz) to subcritical crack growth, bearing in mind that it is only constructed from existing experimental data. The overall trend is that the more complex the microstructure, the lower is a material's susceptibility to subcritical crack growth. Similar conclusions have been reported by Swanson (1984). These observations imply that the more heterogeneous rocks behave in a more brittle manner, at least during slow deformation. This is not what one might intuitively expect, and appears to contradict the conclusions of Cox & Scholz (1988) and Cox & Paterson (1990) that heterogeneous rocks with large initial flaw distributions tend to behave in a less brittle manner than more homogeneous rocks.

3. Fracture under Compressive Stresses

Fracture of quasi-brittle materials subjected to compressive stresses is generally much more complex than for the tensile case, since compressive failure generally involves the nucleation, propagation and interaction of a distributed array of microcracks. Direct observation of such stress-induced microcracks in rocks (e.g. Peng & Johnson 1972, Tapponier & Brace 1976, Kranz 1979, 1980, 1983, Wong & Biegel 1985) suggests strongly that they nucleate from pre-existing flaws (pores, inclusions, microcracks, etc.), and propagate in a direction parallel to the maximum principal compressive stress.

The stabilizing influence of the minimum principal compressive stress (confining stress) is illustrated in Figure 6. Where there is no confining stress (uniaxial compression) failure may be unstable, and is dominated by the propagation of a small number of axial cracks. By contrast, the application of even a modest compressive confining stress causes individual cracks to extend stably. A microcrack will extend to relieve the local stress concentration caused by an increase in the compressive stress difference, and will then arrest. In terms of fracture mechanics, neglecting for the moment any subcritical crack growth, microcracks extend once the critical tensile stress

intensity (K_{Ic}) is exceeded locally. However, since K is a decreasing function of crack length under these conditions (Tada et al. 1973, Costin 1987), individual cracks only extend until equilibrium is reached at $K = K_{Ic}$. As the compressive stress difference is increased, an increasing population of microcracks extend until their density and average size is such that they interact to produce macroscopic failure.

At moderate confining stresses, the failure mode is controlled by the interaction of numerous microcracks in a relatively narrow fracture zone to form a macroscopic shear failure (i.e. a fault); and at much higher confining stresses by distributed, near-homogeneous microcracking to cause pseudo-ductile deformation by cataclastic flow. Hence the compressive strength of rocks is very pressure dependent.

Furthermore, Main, Peacock & Meredith (1990) have noted that both seismic data from crustal earthquakes and acoustic emission data from laboratory-scale rock fracture experiments (reported in a later section) are consistent with a feedback model of compressive failure. Where a population of microcracks exists, the overall situation appears to be initially one of negative feedback. Once a crack has grown to relieve the stress locally in a high stress zone, it becomes a relatively low stress zone. It is then more likely that further stress relief will be accommodated by growth of a different crack than by further extension of the same crack. Eventually, under conditions of increasing stress, a proportion of the original population of cracks will have grown stably until their lengths are comparable to their spacing, whereupon the locally perturbed stress fields due to the presence of the cracks interact in a cooperative manner. The situation can then flip from one of negative feedback to one of positive feedback, leading to instability and failure. In terms of stress/strain relations this corresponds to a change from strain hardening to strain softening behaviour during dilatancy.

So far we have neglected any influence of time-dependent processes such as stress corrosion, but like tensile fracture, failure under compressive loading has long been recognised as a process that is dependent upon both environment and deformation rate. Therefore if we wish to use our understanding of the behaviour of individual tensile cracks to address the problem of fracture in compression it is necessary to consider the combined effects of arrays of multiple cracks in order to account for bulk material behaviour. In an attempt to address this problem, modified Griffith theories were developed to predict the shapes of failure envelopes in normal stress - shear stress space (Mohr diagrams) from consideration of the action of microcracks (modelled as elliptical flaws) at different orientations (e.g. McLintock & Walsh 1962, Murrell & Digby 1970). The essential features of this approach are illustrated in Figure 7 (after Murrell 1990). In particular, the figure shows conditions for compaction (due to crack closure), dilatancy (following crack initiation), macroscopic shear fracture, and the transitions from fracture to cataclastic flow or plastic flow (at elevated temperatures). Each of these features is associated with a particular state of crack damage.

However, a full treatment of brittle failure requires consideration of all phases of crack development including crack nucleation, crack extension and crack interaction. In recent years a number of authors have contributed to the development of a new body of theory known as "damage mechanics" that takes account of all of these phases of cracking in an attempt to explain the various aspects of non-linear, time-dependent mechanical behaviour by utilising the concept of a single variable or set of variables to describe the changing microstructural state of a material as it is deformed (e.g. Costin 1983, 1985, Horii & Nemat-Nasser 1986, Ashby & Hallam 1986, Sammis & Ashby 1986, Kemeny & Cook 1987). A brief review and comparison of the predictions of these various damage models has been provided by Gueguen et al. (1990), and so is not repeated here. Costin (1987) has pointed out that there are three basic elements required for any damage theory: (1) a definition of the state of damage; (2) an equation to describe damage evolution; and (3) a constitutive law that predicts the relation of damage to stress and strain.

It is trivial to note that any predictions derived from the models will depend crucially upon the assumed initial flaw distribution. In his comprehensive review of microcracks in rocks, Kranz (1983) points out that while a great deal of theory exists on the role of microcrack populations in rock fracture processes, there is a paucity of supporting observational data. Common assumptions include collinearity or randomness in orientation and location of the initial microcrack population, and initial length-frequency distributions that can be uniform, Gaussian, exponential or power law in form. However, the assumption of randomness in the cracking process and stochastic independence between cracks becomes increasingly untenable as stress levels increase and cracks interact and coalesce as failure is approached. Furthermore, since cracks are quasi-planar features, the growth of microcracks that are aligned with respect to principal stress directions will result in even an initially isotropic material being rapidly transformed into a mechanically anisotropic material.

4. Indirect Monitoring of Damage Development by Integrated Rock Physical Property Measurements

Where the experimental work described in this section differs from, but aims to build upon, earlier theoretical damage mechanics studies is by incorporating the diagnostic results of contemporaneous measurements of rock physical property changes during deformation experiments into the modelling process, in order to provide a physically more realistic description of crack damage development. The underlying rationale of this approach is illustrated schematically in Figure 8. In essence: (1) changes in the velocity of elastic waves pulsed through an experimental sample occur in response to changes in the cumulative density of cracks and pores, and hence indirectly describes the changing state of damage; (2) acoustic emission statistics relate to the contemporary rate of crack extensions, and hence can provide information about the rate of damage

evolution; and (3) measurement of changes in transport properties such as fluid permeability or electrolytic conductivity provides information about the interaction and linkage of dilatant microcracks leading to macroscopic fracture and failure. Currently, we are making simultaneaous measurements of elastic wave velocity changes and variations in acoustic emission parameters during our triaxial rock deformation experiments. The contemporaneous measurement of changes in connected pore volume and fluid permeability is in an active state of development.

4.1 ELASTIC WAVE VELOCITY MEASUREMENTS

Results of measurements of both P- and S-wave velocities made during triaxial deformation of dry sandstone in our laboratory have previously been reported in Sammonds et al. (1989) for all of the failure modes illustrated in Figure 6. More recent results for the cases of failure by localized shear faulting and by distributed cataclastic flow are shown in Figure 9. For both cases, the velocity of both P and S waves increases during the initial quasi-linear phase of loading, with maximum velocity occurring at about half the peak stress difference. This is interpreted as being due to the closure of cracks in response to the increasing applied stress. The most favourable oriented (i.e. those oriented normal or sub-normal to the axial stress) and most open cracks close first, and crack closure then becomes progressively more difficult. Above about half the peak stress, new dilatant cracks begin to propagate, and hence both wave velocities start to decrease. However, note that during the initial phase of deformation, the relative increase in V_1 is substantially higher than the increase in V_2, but that V_1 decreases more rapidly than V_2 in response to dilatant crack growth. Since axial P waves are more sensitive to cracks normal to the axial stress, and s waves more sensitive to cracks parallel to the axial stress, this observation supports the concept that dilatancy occurs by the growth of tensile cracks oriented parallel to the maximum compressive stress. It also shows that simultaneous measurement of changes in both velocities provides a guide to the progressive development of crack anisotropy as deformation proceeds.

A number of theories have been proposed to relate changes in elastic wave velocities to changes in effective elastic moduli, and thereby to changes in microcrack concentration or density. One of the first of these was by Walsh (1965) who calculated the excess strain energy due to the presence of an isolated penny-shaped crack in an infinite medium under stress. However, Walsh's formulation did nottake account of stress field interactions between adjacent cracks, and is therefore only applicable to low densities of relatively short cracks. O'Connell & Budiansky (1974) on the other hand specifically included crack interactions in their model which assumes that a crack is imbedded in an homogeneous medium whose effective elastic moduli are those of the cracked material. Not surprisingly, the latter theory predicts a much more rapid decrease in moduli with increase in crack density and average crack length than does the formulation that ignores interactions.

O'Connell & Budiansky's model predicts that not only both

V_p and V_s, but also the ratio V_p/V_s would decrease with increasing crack density. However, the experimental results of Figure 9, and those reported by Gupta (1973) and Sammonds et al. (1989) do not support this latter prediction. For example, Sammonds et al. note that for their experimental results, the V_p/V_s ratio initially increases with increase in stress difference. This initial increase is followed by a period where the ratio is essentially constant, before again increasing close to peak stress and beyond. Gupta (1973) reports a similar result.

Furthermore, in Figure 10 we show the results of calculations of the change in crack density from the initial unstressed state determined according to O'Connell & Budiansky's model. The crack density parameter (d) is given by

$$d = N\langle a^3 \rangle \qquad (2)$$

where N is the number of cracks per unit volume of the solid and $\langle a \rangle$ is the mean major axis of the ellipsiodal cracks. d is further defined as a function of the Poisson ratio (v) according to

$$d = [45(v_o - v)(2 - v)]/[16(1 - v^2)(10v_o - 3v_o - v)] \qquad (3)$$

where v_o is the Poisson ratio for the initial state, and v is the effective Poisson ratio of the cracked solid. From elasticity theory,

$$v = [(V_p/V_s)^2 - 2]/[2(V_p/V_s)^2 - 1] \qquad (4)$$

and hence variations in d may be determined from variations in V_p and V_s. Figure 10 shows the variations in the crack density parameter (d) calculated from the data of Figure 9. Rather than an increase in crack density, the model erroneously predicts a decrease in crack density as deformation and dilatancy proceeds. This result stems directly from the observation that the ratio V_p/V_s does not decrease during deformation as predicted by the model.

The explanation for these discrepancies between model predictions and experimental observations is that the model does not take account of the development of any crack anisotropy. As rocks deform, their compliance parallel to the axis of compression decreases due to crack closure, and that normal to the axis of compression increases due to the growth of dilatant tensile axial cracks.

More recently, Hudson (1981) and Crampin (1984) have taken crack anisotropy into account by calculating theoretically the variations in P and S wave velocities through solids containing aligned cracks. However, their formulations are only valid for crack concentrations that are low enough for no interaction to occur, and where the wavelengths of the pulsed waves are large compared with the length of the cracks.

To date, therefore, no systematic theoretical treatment exists that can take full account of both crack interactions and the development of anisotropy.

4.2 ACOUSTIC EMISSION MEASUREMENTS AND GEOMETRICAL SCALING RELATIONS

It is well documented that, for subcritical crack growth of tensile cracks, the rate of acoustic emission (AE) activity is directly related to the rate of crack propagation (e.g. Atkison & Rawlings 1981, Meredith & Atkinson 1983, Meredith 1990), and that the magnitude or amplitude of an individual AE event is related to the source dimension and the increment of crack extension that generated the emission. Meredith & Atkinson (1983) have previously reported data describing the distribution of event amplitudes as a function of stress intensity factor, from tensile tests on a range of crystalline rock types. The parameter that characterizes the amplitude distribution is the "seismic b-value" (c.f. the Gutenberg-Richter frequency-magnitude relation for earthquakes), where b is an empirical constant in the relation

$$\log N = a - bm \qquad (5)$$

where N is the number of times an event of magnitude (log scale) or peak amplitude (in dB) m occurs, and a is a constant. The data are shown in Figure 11. For these tensile experiments, the b-values are seen to lie in the range 1 - 3, and are negatively correlated and linearly related to K/K_c, the normalized stress intensity. Physically, ahigh b-value characterizes crack growth dominated by a large number of relatively small events, whereas a low b-value indicates a larger number of relatively large events. Note also that the b-value is higher in a "wet" as opposed to a "dry" environment, especially at low values of K (low crack velocity). Changes in b may therefore be due either to changes in stress intensity or to changes in the humidity of the crack tip environment.

This may be related to the observation of a trend from dominantly transgranular cracking at high crack velocity and low humidity, to dominantly intergranular cracking at low velocity and high humidity, since grain boundaries provide the main conduits for the access of water and will therefore stress corrode preferentially. At values of K close to the fracture toughness crack growth is very rapid, and hence the environment has little effect on either crack growth rate or the b-value. For either environment, the critical b-value for dynamic failure (at $K = K_{Ic}$) is unity.

The power law distribution of AE event amplitudes described by equation (5) implies that a power law distribution of flaw sizes of the form

$$N(a) = C\, a^{-D} \qquad (6)$$

is necessary to generate this range of event sizes, where C is a constant, a is the crack length, and D is the power law exponent. Furthermore, if the distribution is geometrically scale-invariant between the minimum and maximum lengths, then D is strictly defined as one aspect of the fractal dimension of the system (Mandelbrot 1982). Several authors (e.g. Caputo 1976, Aki

1981) have shown that

$$D = 3b/c \quad (7)$$

where c is a constant that depends on the relative time constants of the event and the recording system. Main et al. (1989) have shown that, for the data of Figure 11, c = 3, so that b = D; whereas for the triaxial compression experiments to be reported below, c = 3/2 and therefore b = D/2. The crack length fractal dimension (D) inferred from the above argument is also indicated on Figure 11.

It is well known that many geological structures and fabrics are often scale-invariant within well-defined characteristic limits, otherwise it would not be necessary to include scale bars or the ubiquitous geological hammer on photographs of rock samples and rock outcrops. Figure 12 (after Shaw & Gartner 1986) shows convincing evidence for the scale-invariance of shear fault systems with one dominant throughgoing fault, over a range of scales from fractions of a mm to hundreds of km. Without the scale bars and annotation it would be very difficult to distinguish laboratory shear-box experiments from plate-rupturing faults. Figure 13 superposes the size distribution of the four fault systems of Figure 12, with each normalized to the length of the dominant throughgoing fault. Two aspects emerge immediately: (1) all the fault systems have the same relative size distribution of subsidiary faults; and (2) the size distribution is a power law with a negative exponent D = 1, corresponding to critical rupture.

The most appropriate mathematical description of the size distributions of Figure 12 is the Cantor set (Mandelbrot 1982, Turcotte 1989, Main et al. 1990) which describes a dominant straight line drawn on a two-dimensional plane, with more and more identical replicas in a cascade of smaller scales, and with a power law frequency distribution of lengths. Extension to three dimensions would require a dominant fault plane with a cascade of smaller area fault planes (Main et al. 1990).

AE results from laboratory-scale triaxial compression experiments on samples of Darley Dale sandstone are shown in Figures 14 and 15. All data are plotted against time, but this is equivalent to strain for these constant strain rate tests. Details of the experimental arrangement and methodology are given in Meredith et al. (1990).

Figure 14 shows data from a test on a water-saturated sample deformed under a confining stress of 50 MPa. The stress/time curve is markedly non-linear, with peak stress followed by a significant decrease in in stress precursory to dynamic failure on a well-defined fault plane, and finally, stable sliding on the fault. Macroscopic dynamic failure occurs when the negative slope of the stress/time curve is a maximum (i.e. when the rate of stress drop is a maximum).

The AE rate increases rapidly with the onset of dilatancy, which in this case occurs at little more than 50% of the peak stress. We can usefully separate dilatancy into two phases; the

first dominated by the growth of new microcracks in the period up to peak stress, and the second dominated by the interaction and coalescence of these microcracks to form a throughgoing fault in the period of post-peak strain softening. Around peak stress, the AE rate at first flattens out and then falls dramatically to a short period of apparaent quiescence. This quiescence associated with dynamic failure is thought to be caused by saturation of the monitoring system due to a cascade of events which become indistinguishable from each other at critical crack coalescence. Similar apparent quiescence has been reported to occur close to dynamic failure by a number of other workers (Gowd 1980, Kikuchi et al. 1981, Sondergeld et al. 1984), but only when a strain softening phase preceded failure. Finally, following instability the AE rate recovers before decaying in a manner analogous to an earthquake aftershock sequence (i.e. according to Omori's law).

b-value data for this experiment exhibit the following important features: (1) during the early quasi-elastic phase of loading, where there is a low level of AE activity, the b-value remains essentially constant, with a high value close to 1.5 (and by inference D = 3). At higher levels of stress, the major trend is of a decreasing b-value, correlated with increasing AE rate and the growth of new microcracks, and which flattens out at around peak stress (b = 1, D = 2). This is followed by an inflection point leading to a much shorter time-scale b-value anomaly leading to dynamic failure close to the expected value of $b_c = 0.5$ ($D_c = 1$). Post-failure the b-value recovers as expected. Note that the error in measurement of b-values is proportional to $1/N^{1/2}$, where N is the total number of AE events in each time period for which a b-value is determined. So the variability in b-values is much greater during the relatively quiet low-stress phase of loading than during the dilatant phase where the AE rate is much increased.

Finally, Figure 15 shows the same suite of data from a test on a water-saturated sample deformed under a much higher confining stress of 200 MPa. In this case there is no stress drop, and deformation takes place quasi-statically by cataclastic flow rather than by dynamic rupture on a localized fault. Under these conditions, the AE rate again increases with the onset of microcracking, but remains at a consistently high level throughout the phase of cataclastic flow, with no indication of any period of quiescence or decay. Here, the b-value is simply negatively correlated with the level of stress, and falls from its background level of 1.5 to reach a constant value of unity (with an inferred instantaneous value of D = 2) associated with distributed microcracking during the phase of cataclastic flow. The value never falls to anywhere near the critical value of 0.5, since there is no critical stress concentration.

5. Concluding Remarks

It is clear that the geometrical distribution of flaws on all scales plays a crucial role in controlling the mechanical and physical behaviour of heterogeneous, polycrystalline, quasi-brittle materials such as rocks. It is therefore vital that

theoretical models describing the evolution of crack damage utilise physically realistic flaw distributions if predictions of the deformation response and failure of these materials are to be useful.

A whole plethora of evidence now supports the concept of a power law distribution of flaw sizes in rocks, with an exponent that varies as deformation proceeds, but that reaches a critical value for catastrophic rupture. Encouragingly, this also implies that, within certain limits, the process of fracturing is scale-invariant, which suggests that data derived from laboratory-scale samples may be able to be applied usefully to much larger scale rupture.

For the future, more detailed damage models will be required to accommodate time-dependent cracking processes and more realistic descriptions of both initial flaw distributions and the developing state of damage. This is likely to be an iterative process requiring input from the techniques that indirectly monitor damage development during progressive deformation into enhanced theoretical models.

REFERENCES

Aki K. (1981) A probabilistic synthesis of precursory phenomena, In: Earthquake Prediction: An International Review, Maurice Ewing Series 4, Amer. Geophys. Union, Washington, 566-574.

Ashby M.F. and Hallam S.D. (1986) The failure of brittle solids containing small cracks under compressive stress states, Acta Metall., 34, 497-510.

Atkinson B.K. (1982) Subcritical crack propagation in rocks: theory, experimental results and applications, J. Struct. Geol., 4, 41-56.

Atkinson B.K. (1984) Subcritical crack growth in geological materials, J. Geophys. Res., 89, 4077-4114.

Atkinson B.K. and Meredith P.G. (1987a) The theory of subcritical crack growth with application to minerals and rocks, In: Fracture Mechanics of Rock, Academic Press, London, 111-166.

Atkinson B.K. and Meredith P.G. (1987b) Experimental fracture mechanics data for rocks and minerals, In: Fracture Mechanics of Rock, Academic Press, London, 477-525.

Atkinson B.K. and Rawlings R.D. (1981) Acoustic emission during stress corrosion cracking in rocks, In: Earthquake Prediction: An International Review, Maurice Ewing Series 4, Amer. Geophys. Union, Washington, 605-616.

Caputo M. (1976) Model and observed seismicity represented in a two-dimensional space, Ann. Geophys. (Rome), 4, 277-288.

Charles R.J. (1958) Static fatigue of glass, J. Appl. Physics, 29, 1549-1560.

Cook R.F., Lawn B.R. and Fairbanks C.J. (1985) Microstructure-strength properties in ceramocs, I, Effect of crack size on toughness, J. Am. Ceram. Soc.,68, 604-615.

Costin L.S. (1983) A microcrack model for the deformation and failure of brittle rock, J. Geophys. Res., 88, 9485-9492.

Costin L.S. (1985) Damage mechanics in the post-failure regime, Mech. Mat., 4, 149-160.

Costin L.S. (1987) Time-dependent deformation and failure, In: Fracture Mechanics of Rock (ed: B.K. Atkinson), Academic, London, 167-215.

Cox S.J.D. and Paterson L. (1990) Damage development during rupture of heterogeneous brittle materials: a numerical study, In: Deformation Mechanisms, Rheology and Tectonics, (Eds: R.J. Knipe and E.H. Rutter), Geol. Soc. Lond. Spec. Pub., (in press).

Cox S.J.D. and Scholz C.H. (1988) On the formation and growth of faults: an experimental study, J. Struct. Geol., 10, 413-430.

Crampin S. (1984) Effective anisotropic elastic constants for wave propagation through cracked solids, Geophys. J.R. Astr. Soc., 76, 135-145.

Dunning J.D., Petrovski D., Schuyler J. and Owens A. (1984) The effects of aqueous chemical environments on crack propagation in quartz, J. Geophys. Res., 89, 4115-4123.

Freiman S.W. (1984) Effects of chemical environments on slow crack growth in glasses and ceramics, J. Geophys. Res., 89, 4072-4076.

Freiman S.W. and Swanson P.L. (1989) Fracture of polycrystalline ceramics, In: Deformation Processes in Minerals, Ceramics and Rocks, (Eds: D.J. Barber and P.G. Meredith), Unwin Hyman, London, (in press).

Gowd T.N. (1980) Factors affecting the acoustic emission response of triaxially compressed rock, Int. J. Rock Mech. Min. Sci. & Geomech. Abstr., 17, 219-223.

Gueguen Y., Reuschle T. and Darot M. (1989) Single crack behaviour and crack statistics, In: Deformation Processes in Minerals, Ceramics and Rocks, (Eds: D.J. Barber and P.G. Meredith), Unwin Hyman, London, (in press).

Gupta I.N. (1973) Seusmic velocities in rocks subjected to axial loading, J. Geophys. Res., 65, 1083-1102.

Hillerborg A. (1989) Existing methods to determine and evaluate fracture toughness of aggregative materials - RILEM recommendation on concrete, In: Fracture Toughness and Fracture Energy: Test Methods for Concrete and Rock, Tohoku Univ., Sendai, Japan, 121-127.

Horii H. and Nemat-Nasser S. (1986) Brittle failure in compression: splitting, faulting and brittle-ductile transition, Phil. Trans. Roy. Soc. Lond., Ser. A, 319, 337-374.

Hubner H. and Jillek W. (1977) Sub-critical crack extension and crack resistance in polycrystalline alumina, J. Mat. Sci., 12, 117-125.

Hudson J.A. (1981) Wave speeds and attenuation of elastic waves in material containing cracks, Geophys. J. R. Astr. Soc., 64, 133-150.

Ingraffea A.R. (1987) Theory of crack initiation and propagation in rock, In: Fracture Mechanics of Rock (ed: B.K. Atkinson), Academic Press, London, 71-110.

ISRM Commission on Testing Methods (1988) Suggested method for determining the fracture toughness of rock, Int. J. Rock Mech. Min. Sci. & Geomech. Abstr., 25, 71-96.

Jaeger J.C. and Cook N.G.W. (1976) Fundamentals of Rock Mechanics, 2nd. edition, Chapman and Hall, London

Kemeny J.M. and Cook N.G.W. (1987) Crack models for the failure of rocks in compression, Proc. 2nd. Int. Conf. on Constitutive Laws for Engineering Materials, Tucson, Arizona.

Kikuchi M., McNally K. and Tittman B.R. (1981) Machine stiffness appropriate for experimental simulation of earthquake processes, Geophys. Res. Lett., 8, 321-323.

Kranz R.L. (1979) Crack growth and development during creep of Barre granite, Int. J. Rock Mech. Min. Sci. & Geomech. Abstr., 16, 23-35.

Kranz R.L. (1980) The effects of confining pressure and stress difference on static fatigue of granite, J. Geophys. Res., 85, 1854-1866.

Kranz R.L. (1983) Microcracks in rocks: a review, Tectonophysics, 100, 449-480.

Kranz R.L. and Scholz C.H. (1977) Critical dilatant volume at the onset of tertiary creep, J. Geophys. Res., 82, 4893-4898.

Labuz J.F., Shah S.P. and Dowding C.H. (1985) Experimental analysis of crack propagation in granite, Int. J. Rock Mech. Min. Sci. & Geomech. Abstr., 22, 85-98.

Lawn B.R. and Wilshaw T.R. (1975) Fracture of Brittle Solids, Cambridge University Press, Cambridge, 204pp.

Main I.G., Meredith P.G. and Jones C. (1989) A reinterpretation of the precursory seismic b-value anomaly using fracture mechanics, Geophys. J., 96, 131-138.

Main I.G., Meredith P.G., Sammonds P.R. and Jones C. (1990) Influence of fractal flaw distributions on rock defromation in the brittle field, In: Deformation Mechanisms, Rheology and Tectonics, (Eds: R.J. Knipe and E.H. Rutter), Geol. Soc. Lond. Spec. Pub., (in press).

Main I.G., Peacock S. and Meredith P.G. (1990) Scattering attenuation and the fractal geometry of fracture systems, PAGEOPH., (in press).

Mandelbrot B.B. (1982) The Fractal Geometry of Nature, Freeman, New York.

McLintock F.A. and Walsh J.B. (1962) Friction on Griffith cracks in rocks under pressure, Proc. 4th. US Nat. Congr. Appl. Mech., Vol. II, Am. Soc. Mech. Eng., New York, 1015-1021.

Meredith P.G. (1989) Comparative fracture toughness testing of rocks, In: Fracture Toughness and Fracture Energy: Test Methods for Concrete and Rock, Tohoku Univ., Sendai, Japan, 211-233.

Meredith P.G. (1990) Fracture and failure of brittle polycrystals: an overview, In: Deformation Processes in Minerals, Ceramics and Rocks, (Eds: D.J. Barber and P.G. Meredith), Unwin Hyman, London, (in press).

Meredith P.G. and Atkinson B.K. (1983) Stress corrosion and acoustic emission during tensile crack propagation in Whin Sill dolerite and other basic rocks, Geophys. J. R. astr. Soc., 75, 1-21.

Meredith P.G., Main I.G. and Jones C. (1990) Temporal variations in seismicity during quasi-static and dynamic rock failure, Tectonophysics, 175, 249-268.

Murrell S.A.F. (1990) Brittle to ductile transitions in polycrystalline non-metallic materials, In: Deformation Processes in Minerals, Ceramics and Rocks, (Eds: D.J. Barber and P.G. Meredith), Unwin Hyman, London, (in press).

Murrell S.A.F. and Digby P.J. (1970) The theory of brittle fracture initiation under triaxial stress conditions, Parts I and II, Geophys. J. R. Astr. Soc., 19, 309-334 and 499-512.

Peng S.S. and Johnson A.M. (1972) Crack growth and faulting in cylindrical specimens of Chelmsford granite, Int. J. Rock Mech. Min. Sci., 9, 37-86.

O'Connell R.J. and Budiansky B. (1974) Seismic velocities in dry and saturated cracked solids, J. Geophys. Res., 79, 5412-5426.

RILEM Draft Recommendation (1985) Determination of the fracture energy of mortar and concrete by means of three-point-bend tests on notched beams, Materials and Structures, 106, 285-290.

Sammis C.G. and Ashby M.F. (1986) The failure of brittle porous solids under compressive stress states, Acta Metall., 34, 511-526.

Sammonds P.R., Ayling M.R., Jones C., Meredith P.G. and Murrell S.A.F. (1989) A laboratory investigation of acoustic emission and elastic wave velocity changes during rock failure under triaxial stresses, Proc. Int. Symp. Rock at Great Depth, Pau, France, (in press).

Schmidt R.A. and Lutz T.J. (1979) K_{Ic} and J_{Ic} of Westerly granite - effects of thickness and in-plane dimensions, In: Fracture Mechanics Applied to Brittle Materials, ASTM Spec. Tech. Pub., STP 678, 166-182.

Shaw H.R. and Gartner A.E. (1986) On the graphical interpretation of palaeoseismic data, U.S.G.S. Open File Report, 86-394.

Simmons C.J. and Freiman S.W. (1983) Effect of corrosion processes on subcritical crack growth in glass, J. Am. Ceram. Soc., 64, 683-686.

Sondergeld C.H., Granryd L.A. and Estey L.H. (1984) Acoustic emissions during compression testing of rock, In: Proc. 3rd. Conf. on Acoustic Emission/ Microseismic Activity in Geologic Structures and Materials, Trans Tech, Clausthal, 131-145.

Swanson P.L. (1984) Subcritical crack growth and other time- and environment-dependent behavior in crustal rocks, J. Geophys. Res., 89, 4137-4152.

Swanson P.L. (1987) Tensile fracture resistance mechanisms in brittle polycrystals: an ultrasonics and in-sity microscopy investigation, J. Geophys. Res., 92, 8015-8036.

Tada H., Paris P.C. and Irwin G.R. (19739 The Stress Analysis of Cracks Handbook, Del Research Corp., Hellertown, PA.

Tapponier P. and Brace W.F. (1976) Development of stress-induced microcracks in Westerly granite, Int. J. Rock Mech. Min. Sci. & Geomech. Abstr., 13, 103-112.

Tchalenko J.G. (1970) Similarities between shear zones of different magnitudes, Geol. Soc. Am. Bull., 81, 1625-1640.

Turcotte D.L. (1989) Fractals in geology and geophysics, PAGEOPH, 131, 171-196.

Walsh J.B. (1965) The effect of cracks on the compressibility of rocks, J. Geophys. Res., 70, 381-389.

Wiederhorn S.M. (1974) Subcritical crack growth in ceramics, In: Fracture Mechanics of Ceramics (eds: R.C. Bradt, D.P.H. Hasselman and F.F. Lange), Vol. 2, Plenum, New York, 613-646.

Wiederhorn S.M. (1978) Mechanisms of subcritical crack growth in glass, In: Fracture Mechanics of Ceramics (eds: R.C. Bradt, D.P.H. Hasselman and F.F. Lange), Vol. 4, Plenum, New York, 549-580.

Wiederhorn S.M. and Johnson H. (1973) Effect of electrolyte pH on crack propagation in glass, J. Am. Ceram. Soc., 56, 192-197.
Wong T.-F. and Biegel R. (1985) Effects of pressure on the micromechanics of faulting in San Marcos gabbro, J. Struct. Geol., 7, 737-749.

FIGURE CAPTIONS

FIGURE 1. Mode I fracture toughness as a function of grain size for granitic rocks. (After Meredith 1989).

FIGURE 2. Illustration of R-curve behaviour in samples of Merrivale granite. Fracture resistance (K_I) is plotted against maximum crack length at critical failure. (After Meredith 1989).

Figure 3. Schematic diagram showing the dependence of crack velocity on stress intensity (K) between the subcritical crack growth limit (0) and critical rupture (c). The influence of temperature and partial pressure of water is also indicated. The different behaviour in regions 1, 2 and 3 is discuused in the text.

FIGURE 4. Stress intensity factor - crack velocity diagram for Westerly granite at temperatures from 20' to 300'C under water vapour pressures of 2.5 and 15 kPa. Solid lines are least squares fits to the data points. (After Meredith & Atkinson 1985).

FIGURE 5. Synoptic diagram illustrating variation in subcritical crack growth behaviour with rock type. In general, polyphase rocks exhibit higher values of "n" than monominerallic rocks, with single mineral phases having the lowest values. Arrows indicate the range of data. (After Atkinson 1984).

FIGURE 6. Failure modes of quasi-brittle materials in compression, and their associated stress/strain curves: (a) axial splitting under uniaxial compression; (b) crack linkage to form a macroscopic shear failure or fault under moderate confining stress; and (c) near-homogeneous deformation by distributed cracking during cataclastic flow at high confing stress. (After Ashby & Hallam 1986).

FIGURE 7. Mohr diagram (tensile stresses taken as positive) showing envelopes for crack propagation, fracture and sliding friction, and for plastic anad cataclastic flow. Q is the intermediate principal stress. Cataclasis with dilatancy associated with new crack propagation occurs under stress conditions lying between the fracture abd crack propagation envelopes and in the cataclastic flow region of the diagram. (After Murrell 1990).

FIGURE 8. Schematic diagram illustrating the relationship between various rock physical properties and crack damage development for brittle rock.

FIGURE 9. (a) Stress difference, (b) percentage change in P-wave velocity, and (c) percentage change in S-wave velocity for triaxial deformation of dry samples of Darley Dale sandstone under confining stresses of 50 and 150 MPa.

FIGURE 10. Calculated variation in crack density from the initial unstressed state for triaxial deformation of Darley Dale sandstone. Crack densities were determined from the data of

Figure 9 according to the model of O'Connell & Budiansky (1974).

FIGURE 11. Synoptic diagram of the variation in seismic b-value and the inferred fractal dimension (D) with normalized stress intensity (K/K_c) and crack tip humidity for tensile crack propagation in a variety of crystalline rocks. Solid lines are least squares fits to the data points and converge approximately at the point ($K/K_c = 1$, $b = 1$, $D = 1$).

FIGURE 12. Geometry of shear faulting over a range of length scales (after Shaw & Gartner 1986). On the scales shown, each example is dominated by one major throughgoing fault.

FIGURE 13. Normalized discrete frequency-length distribution of the faults shown in Figure 12. All four data sets are consistent with a power law of negative slope $D = 1$ (solid line).

FIGURE 14. Contemporaneous measurements of (a) stress difference, (b) AE event rate, and (c) b-value and inferred fractal demension (D) as functions of time for a water saturated sample of Darley Dale sandstone deformed at a nominally constant strain rate of 10^{-5}/s under a confining stress (P_c) of 50 MPa. This sample failed by localized shear faulting after a dynamic stress drop. Peak stress and dynamic failure are marked by dashed vertical lines.

FIGURE 15. As for Figure 14, but for a sample of Darley Dale sandstone deformed under a confining stress of 200 MPa. In this case deformation occurred by distributed cataclastic flow, and there was no dynamic failure or stress drop.

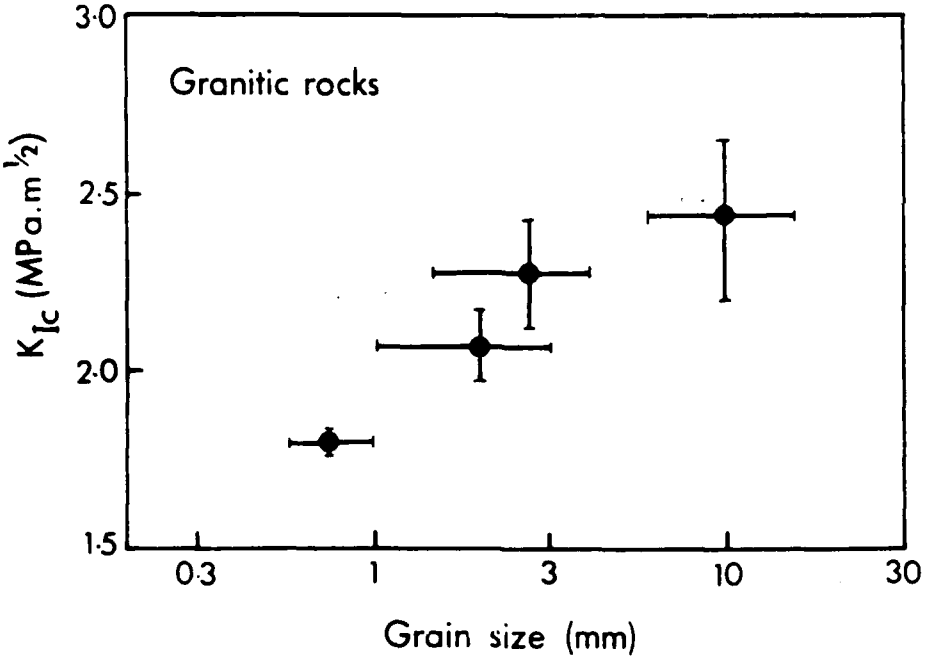

FIGURE (1)

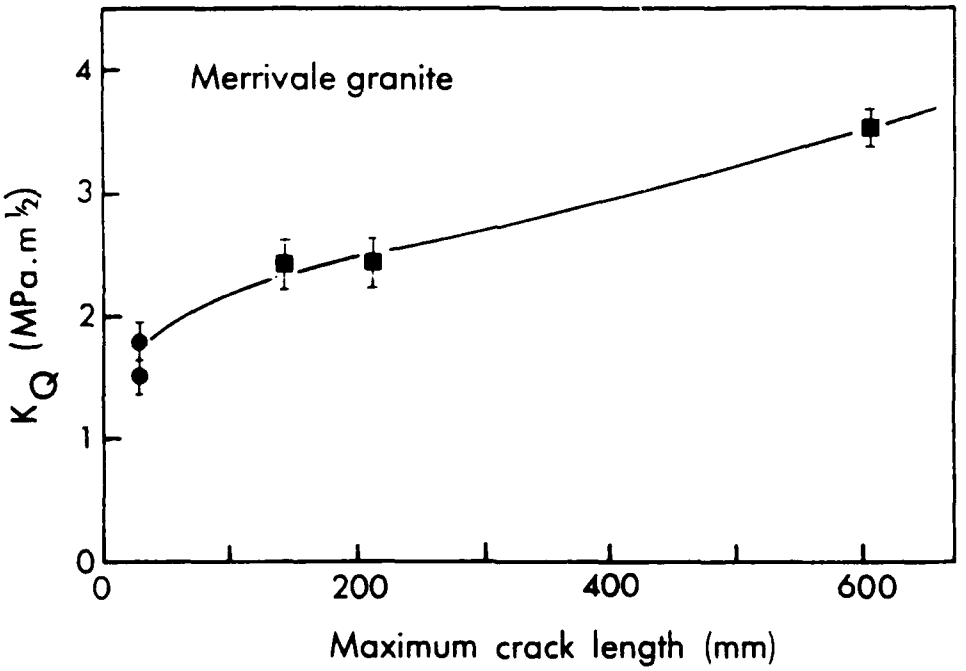

FIGURE (2)

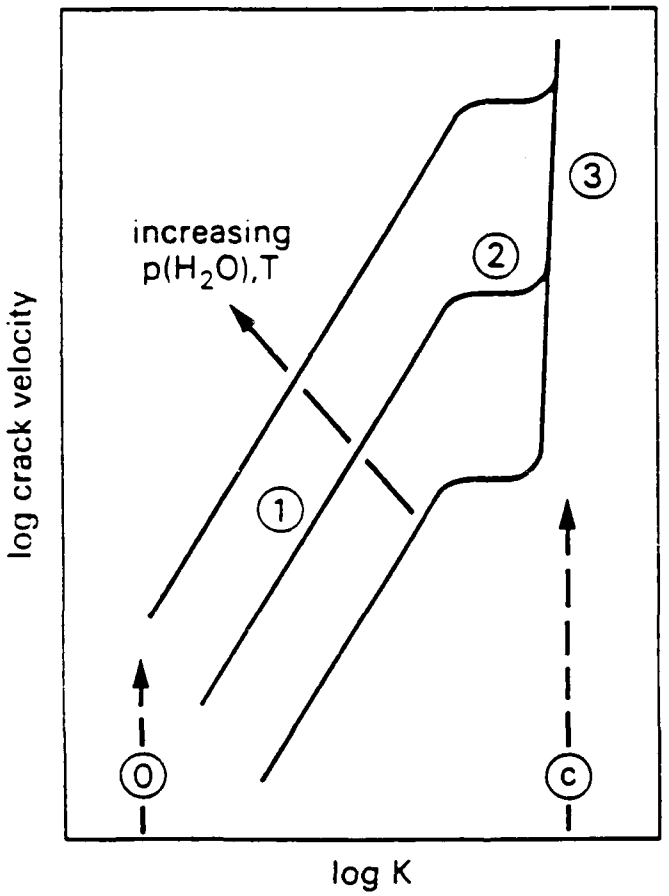

FIGURE (3)

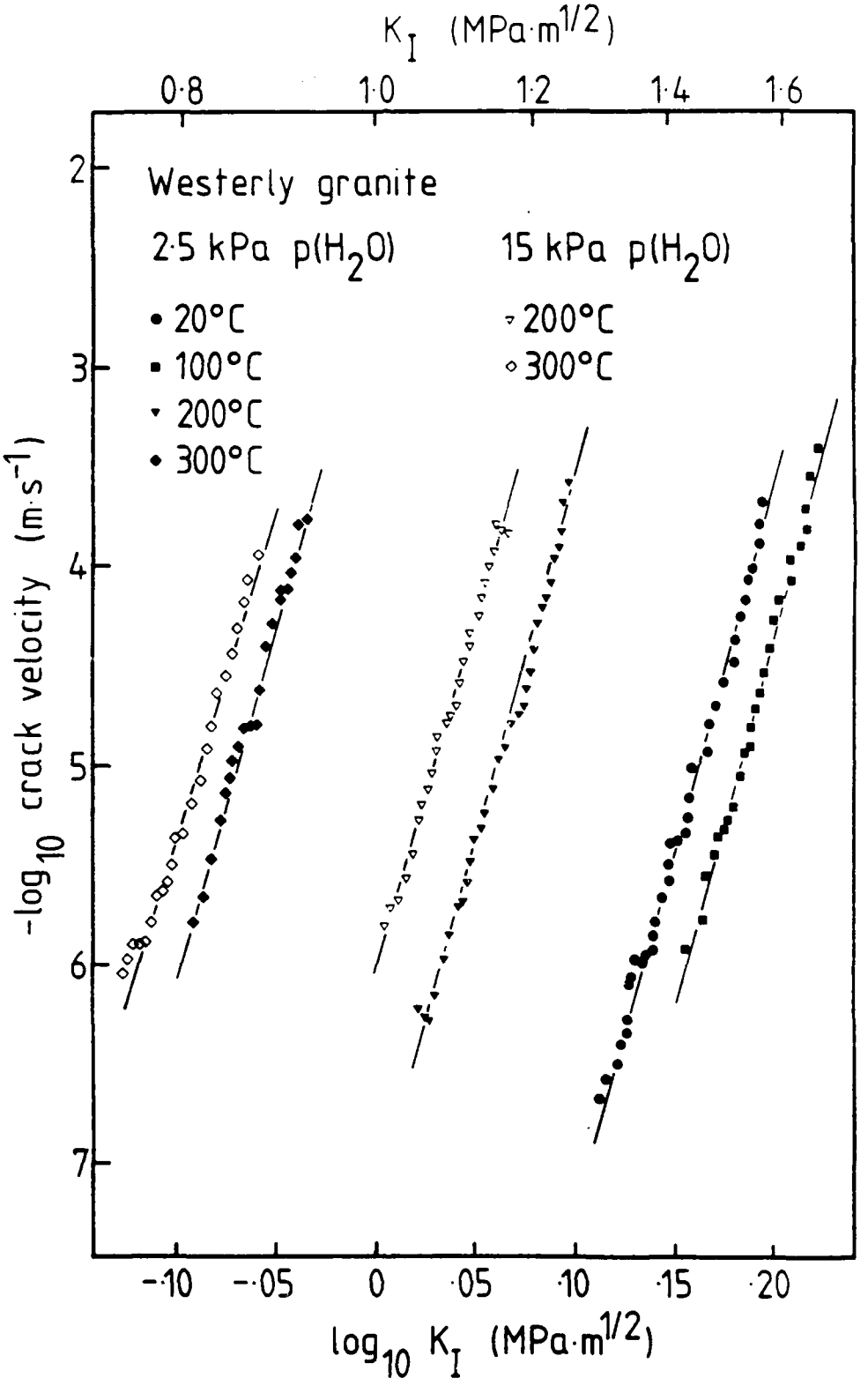
K_I (MPa·m$^{1/2}$)
0·8
1·0
1·2
1·4
1·6
Westerly granite
2·5 kPa p(H_2O)
15 kPa p(H_2O)
• 20°C
▪ 100°C
▾ 200°C
◆ 300°C
▿ 200°C
◇ 300°C
$-\log_{10}$ crack velocity (m·s^{-1})
2
3
4
5
6
7
-·10
-·05
0
·05
·10
·15
·20
$\log_{10} K_I$ (MPa·m$^{1/2}$)

FIGURE (4)

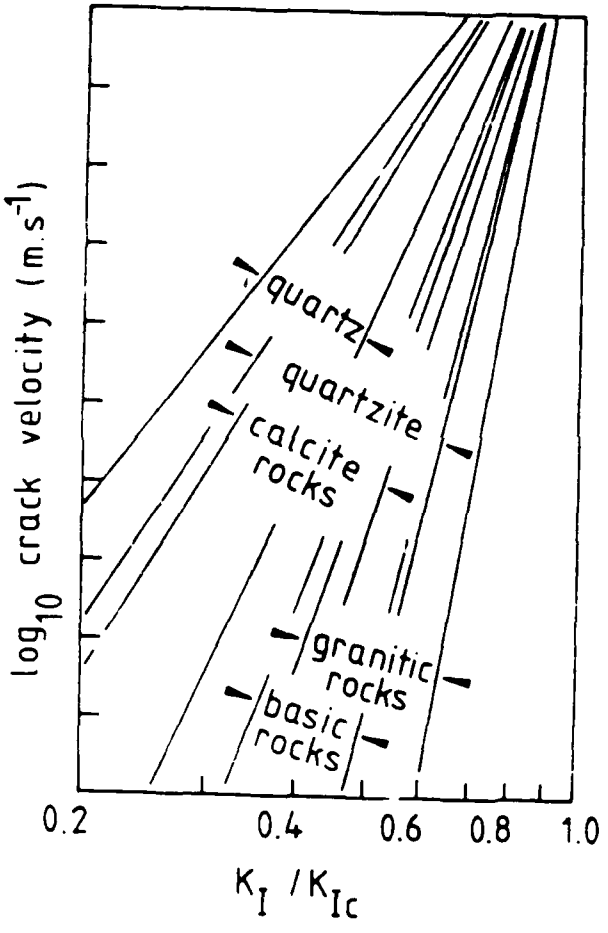
quartz
quartzite
calcite rocks
granitic rocks
basic rocks
$\log_{10}$ crack velocity ($m.s^{-1}$)
0.2
0.4
0.6
0.8
1.0
K_I / K_{Ic}

FIGURE (5)

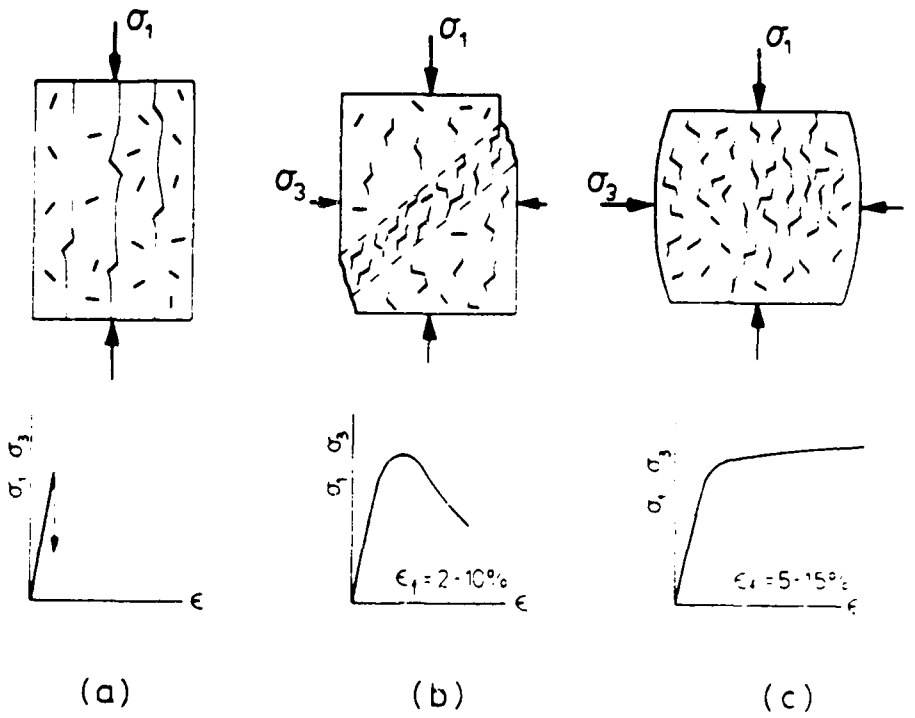

FIGURE (6)

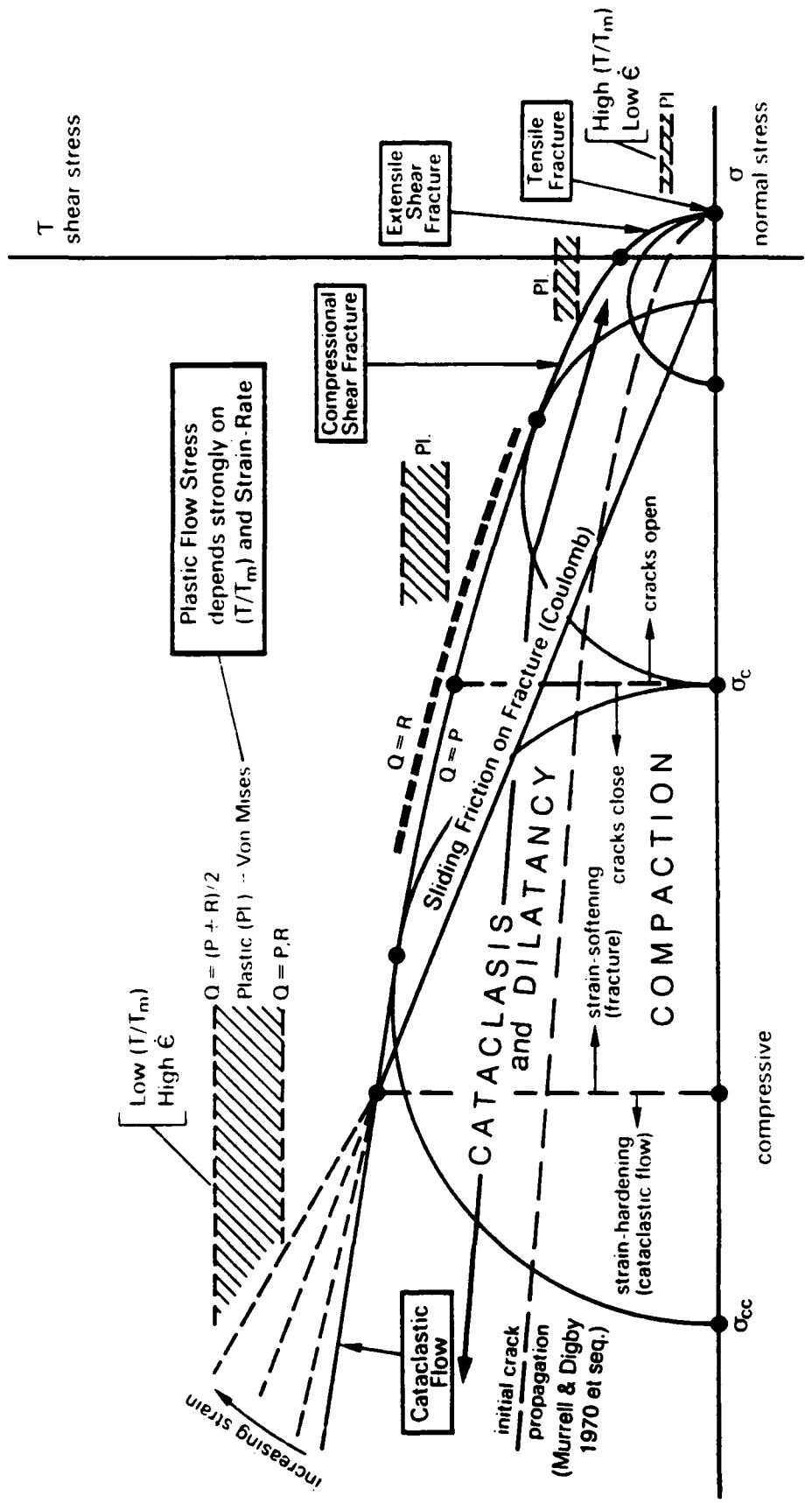
T
shear stress
σ
normal stress
Plastic Flow Stress
depends strongly on
(T/Tm) and Strain-Rate
Low (T/Tm)
High ė
Q = (P + R)/2
Plastic (Pl) -- Von Mises
Q = P,R
Compressional
Shear Fracture
Extensile
Shear
Fracture
Tensile
Fracture
High (T/Tm)
Low ė
Pl.
Pl.
Pl.
Q = R
Q = P
Sliding Friction on Fracture (Coulomb)
cracks open
cracks close
σc
CATACLASIS
and DILATANCY
strain-softening
(fracture)
COMPACTION
strain-hardening
(cataclastic flow)
σcc
compressive
Cataclastic
Flow
initial crack
propagation
(Murrell & Digby
1970 et seq.)
increasing strain

FIGURE (7)

ROCK PHYSICS - the role of cracks / pores

Isolated Cracks / Pores

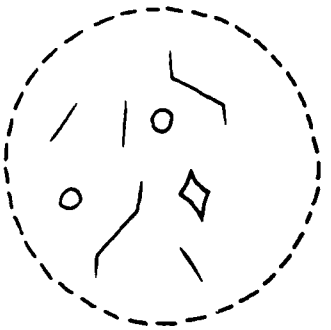

- elastic stiffness
- elastic wave propogation
- (state of damage)

Crack Growth

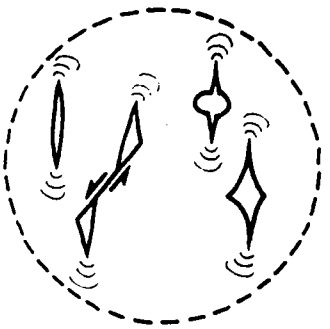

- acoustic emission / micro seismicity
- prelude to crack interaction
- (evolution of damage)

Crack Linkage

- accessible porosity
- permeability
- electrolytic conductivity
- prelude to macro fracture

Localisation

- mechanical instability
- macro fracture / failure
- (pore pressure effects)

FIGURE (8)

(c)

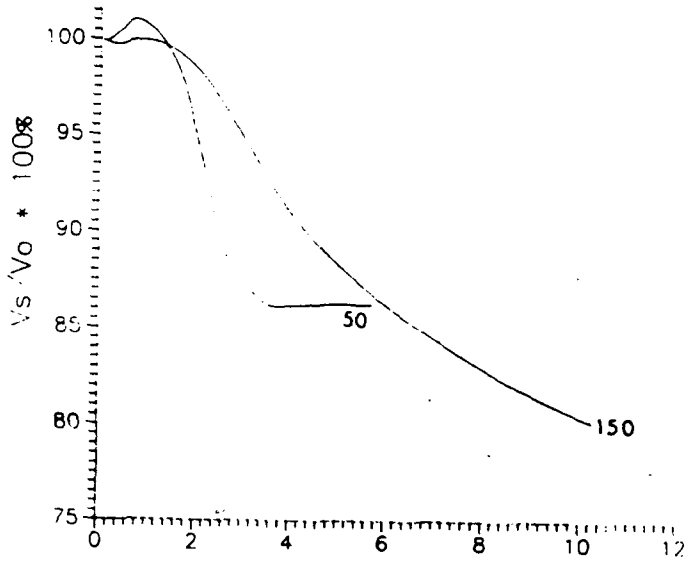
Vs/Vo * 100%
100
95
90
85
80
75
0
2
4
6
8
10
12
50
150

(b)

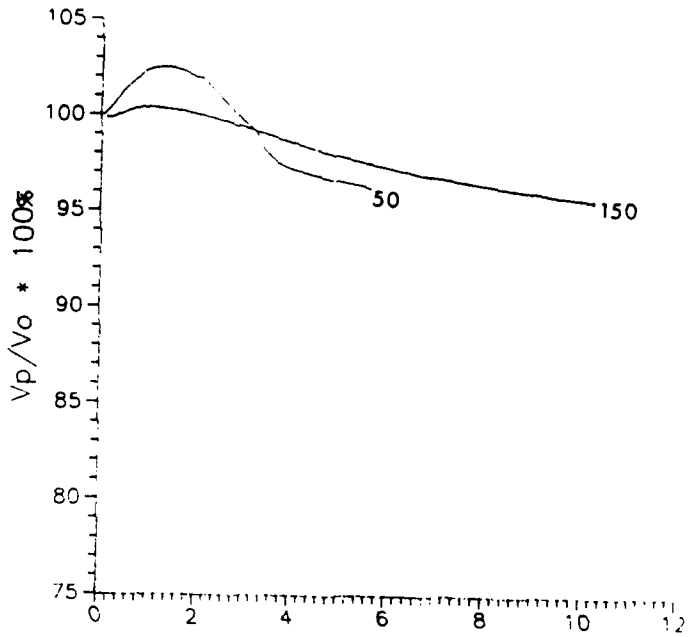
Vp/Vo * 100%
105
100
95
90
85
80
75
0
2
4
6
8
10
12
50
150

(a)

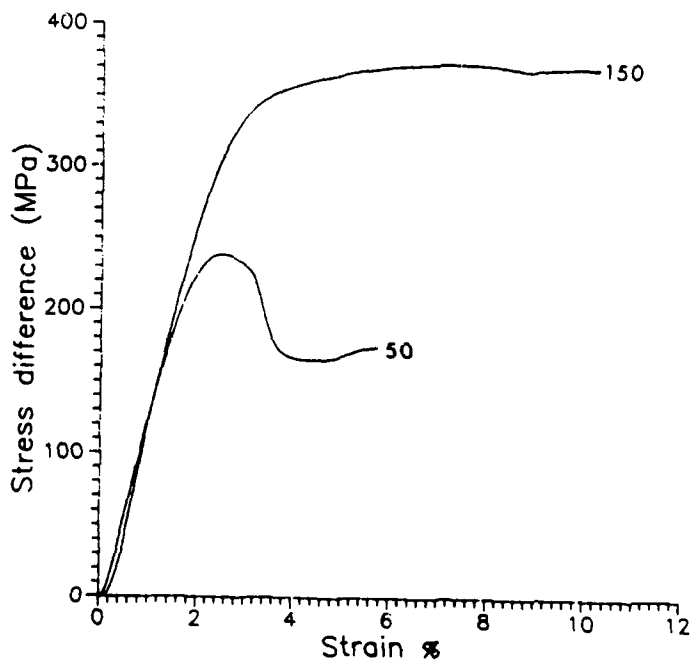
Stress difference (MPa)
400
300
200
100
0
0
2
4
6
8
10
12
Strain %
150
50

FIGURE (9)

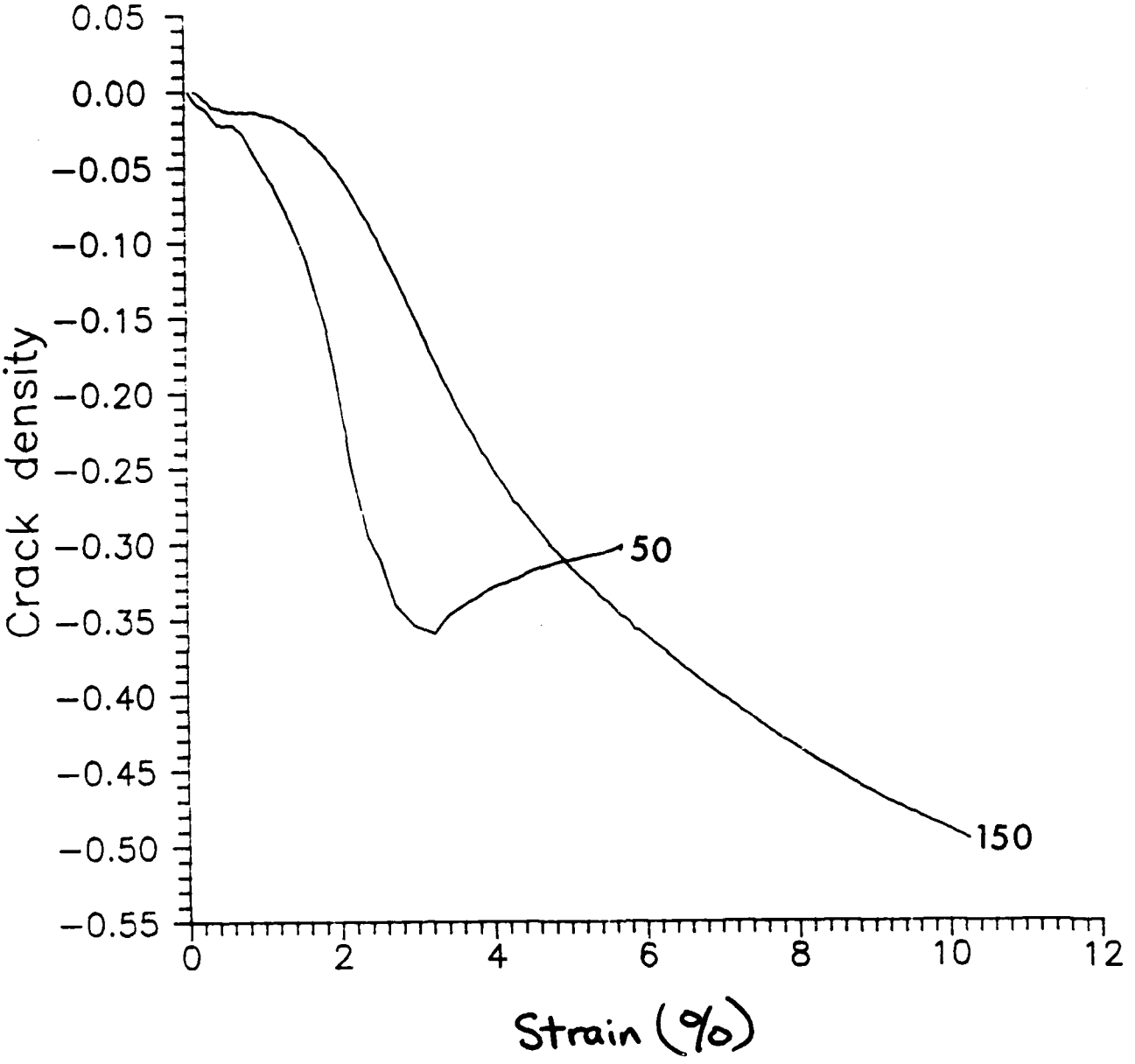
0.05
0.00
−0.05
−0.10
−0.15
−0.20
−0.25
−0.30
−0.35
−0.40
−0.45
−0.50
−0.55
Crack density
0
2
4
6
8
10
12
Strain (%)
50
150

FIGURE (10)

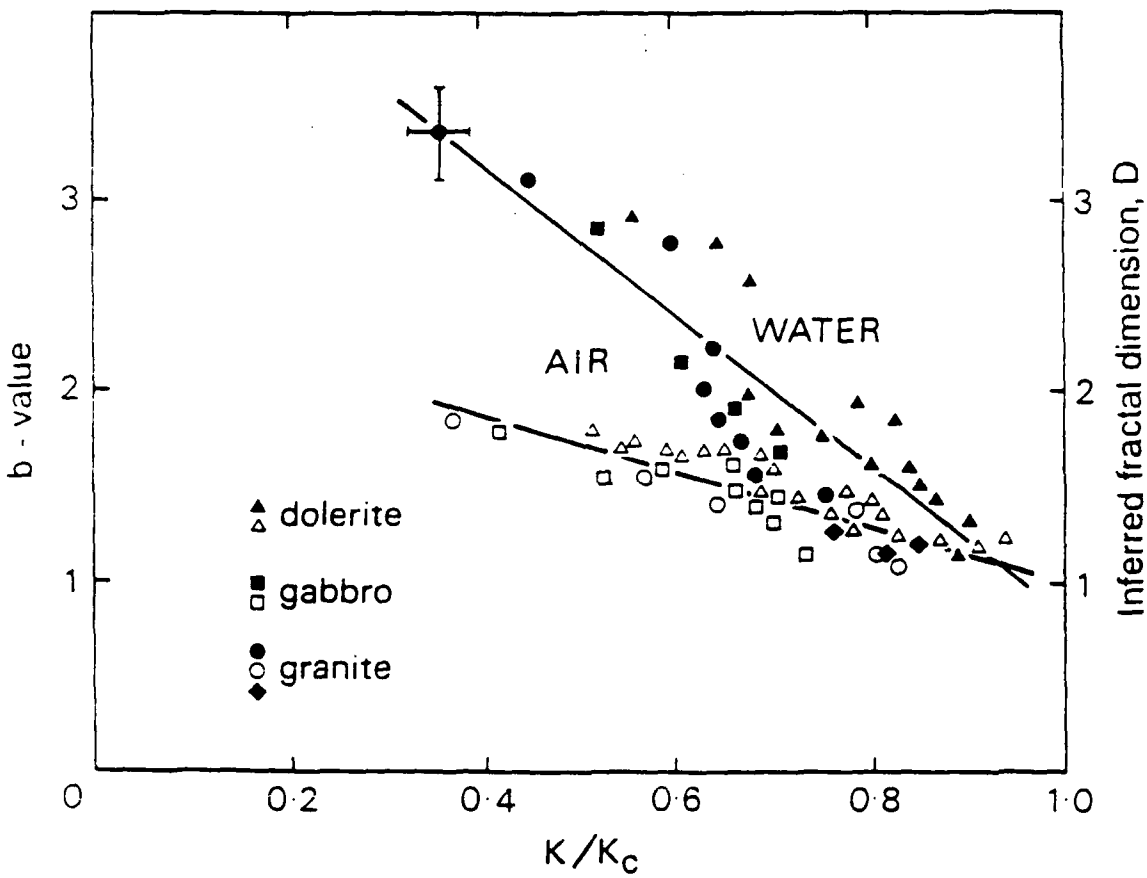
b - value
Inferred fractal dimension, D
K/Kc
0
0·2
0·4
0·6
0·8
1·0
1
2
3
WATER
AIR
dolerite
gabbro
granite

FIGURE (11)

(a) California faults showing evidence of activity in latest 15 m.y. (Howard & others, 1978)

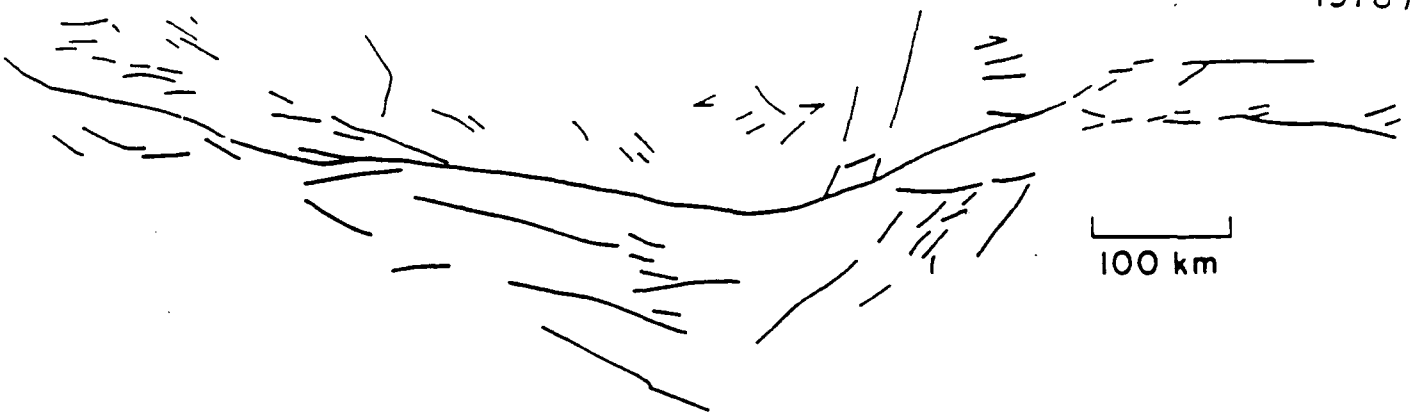

(b) Dasht-e Bayez earthquake fault, Iran (Tchalenko, 1970)

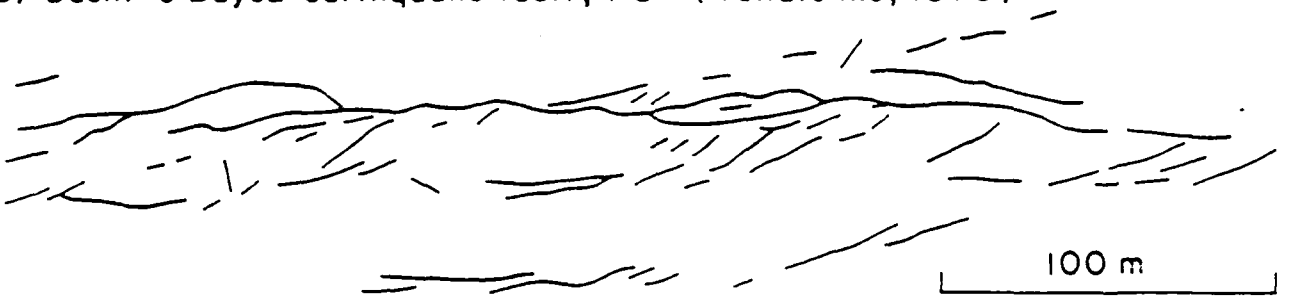

(c) Clay deformation in a Reidel shear experiment (Tchalenko, 1970)

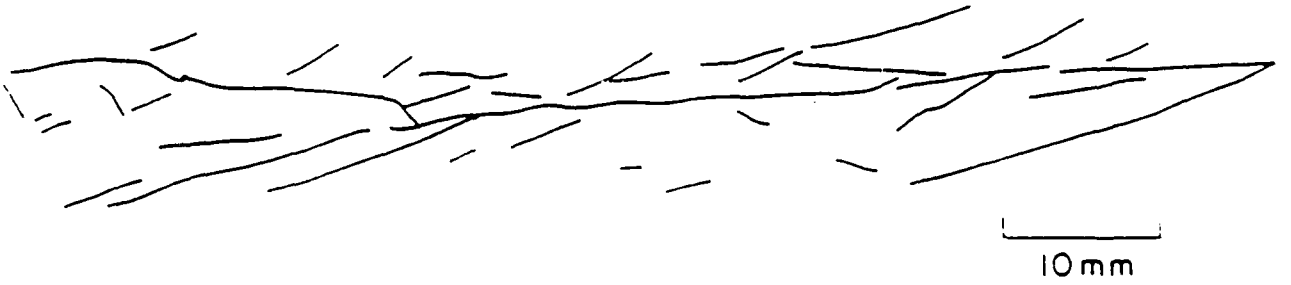

(d) Detail of shear box experiment (Tchalenko, 1970)

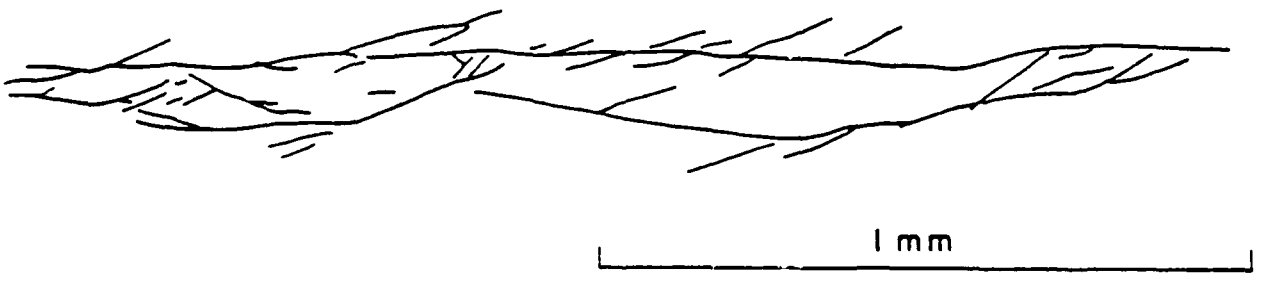

FIGURE (12)

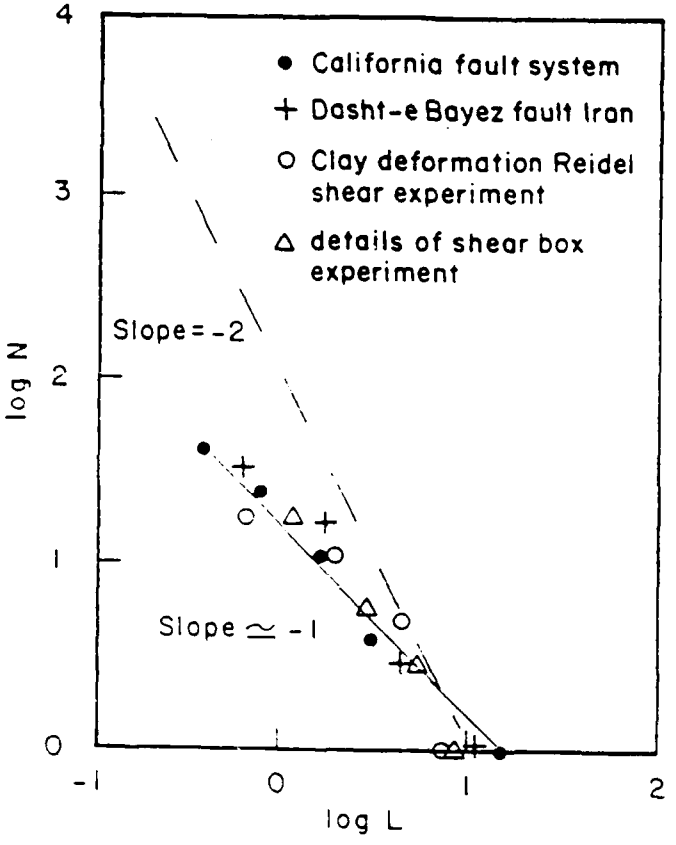
California fault system
Dasht-e Bayez fault Iran
Clay deformation Reidel shear experiment
details of shear box experiment
Slope = -2
Slope ≃ -1
log N
log L
4
3
2
1
0
-1
0
1
2

FIGURE (13)

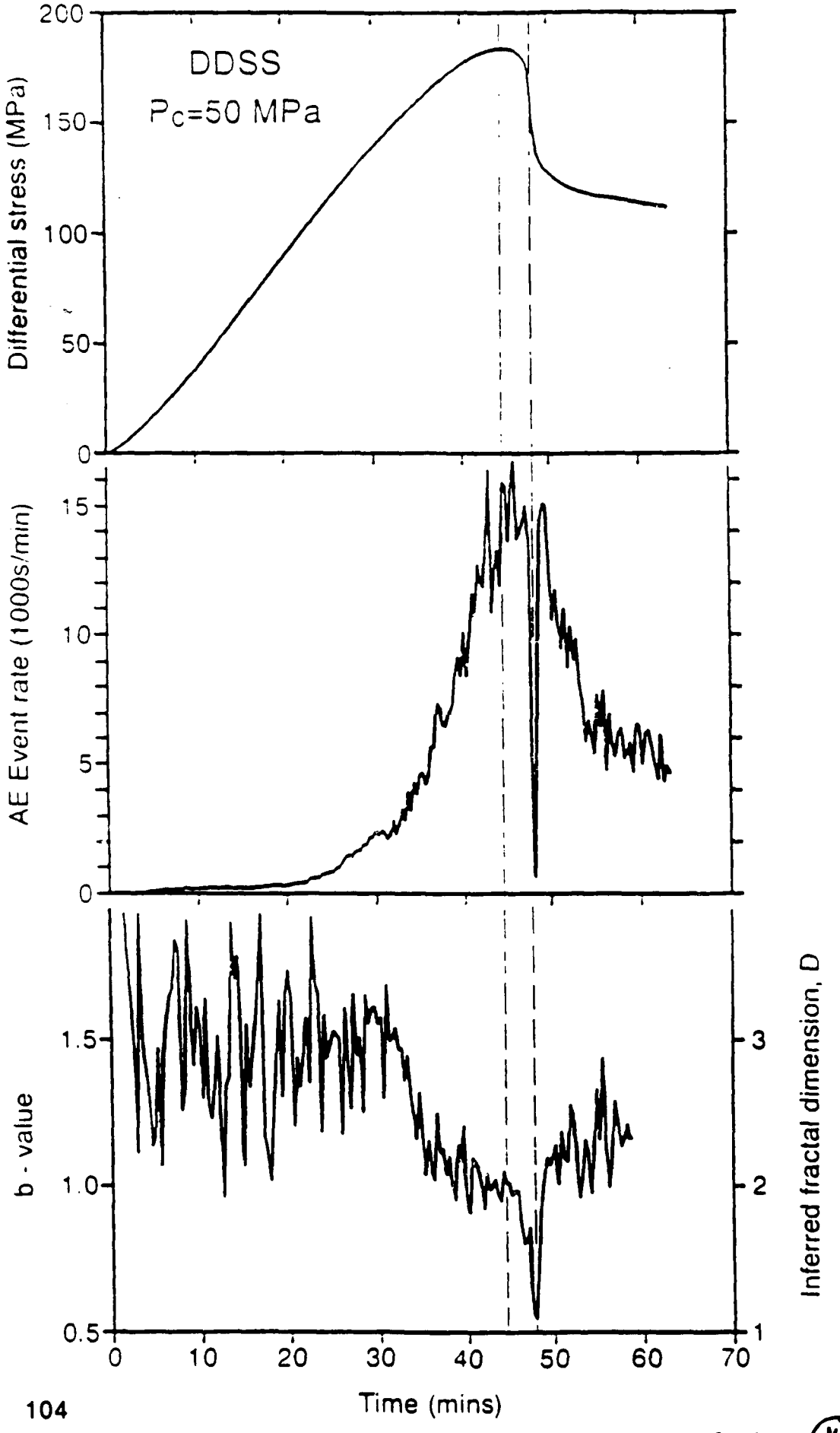
DDSS
Pc=50 MPa
Differential stress (MPa)
200
150
100
50
0
AE Event rate (1000s/min)
15
10
5
0
b - value
1.5
1.0
0.5
Inferred fractal dimension, D
3
2
1
0
10
20
30
40
50
60
70
Time (mins)

FIGURE 14

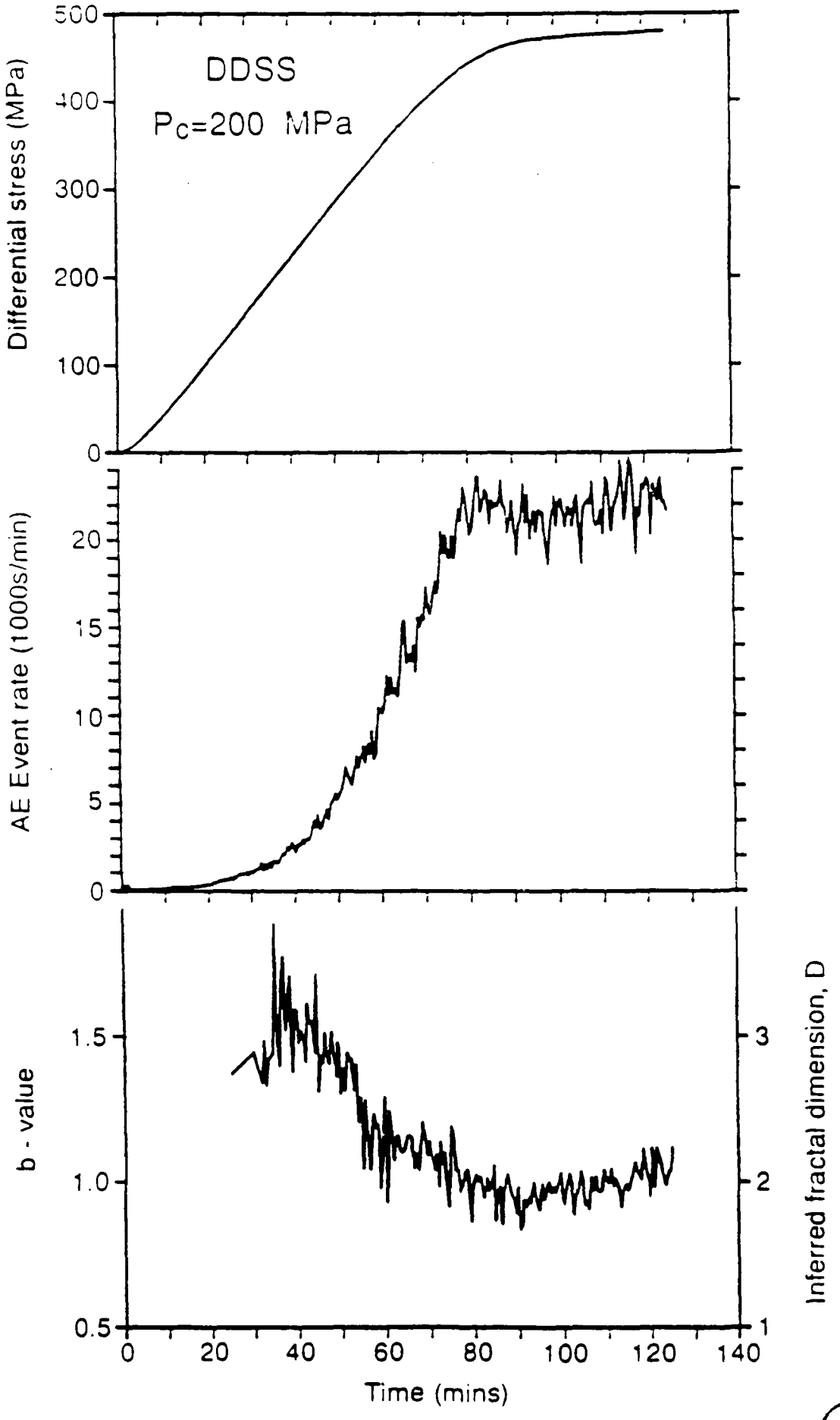
DDSS
Pc=200 MPa
Differential stress (MPa)
500
400
300
200
100
0
AE Event rate (1000s/min)
20
15
10
5
0
b - value
1.5
1.0
0.5
Inferred fractal dimension, D
3
2
1
0
20
40
60
80
100
120
140
Time (mins)

FIGURE (15)

TEST METHODS FOR DETERMINING MODE I FRACTURE TOUGHNESS OF CONCRETE

B.L. KARIHALOO and P. NALLATHAMBI
University of Sydney, Sydney, Australia.

SUMMARY

This lecture will review the various test methods considered by sub-committees *A* and *B* of RILEM TC 89-FMT for the determination of mode I fracture toughness of plain concrete. These methods have been categorized depending on the geometry of the test specimen. Thus, sub-committee *A* considered only the notched beam specimen, while sub-committee *B* considered three different compact specimen geometries. Moreover, as linear elastic fracture mechanics is fully applicable only to very large structures, three separate models have been proposed in relation to the application of LEFM to laboratory size notched beam specimens and these will be discussed . A further method considered by an earlier RILEM committee (TC-50 FMC) will also be included in the review not only because reference will often be made to this method but also to complete the presentation of all existing test methods for mode I.

INTRODUCTION

One of the earliest methods for studying the fracture behaviour of concrete was pioneered by Hillerborg et al. (1976). In this method which is based on the so-called cohesive crack model, it is assumed that fracture under monotonically increasing mode I loading occurs when the maximum (tensile) principal stress reaches the (uniaxial) tensile strength of the material f_t. It is further assumed that fracture is localized in the so-called process zone such that there is no energy dissipation in the bulk of the structure. The process zone (Fig. 1) is modelled by a displacement discontinuity with the proviso that the faces of the discontinuity are capable of transmitting certain cohesive stresses, less than f_t, such that $\sigma = F(w)$ with $F(0) = f_t$, and $F(w) \geq 0$, where $F(w)$ describes the tensile softening behaviour. In practice, $F(w)$ was approximated by a linear or bi-linear relation and was assumed to vanish when the crack opening displacement w reached a certain critical value w_c. The fracture response of concrete in this method is characterized by fracture energy G_F defined as the energy required to open a unit crack fully, or in other words, as the area under the strain-softening curve between $w = 0$ and $w = w_c$. Moreover, from the material parameters E, f_t, G_F an independent parameter with

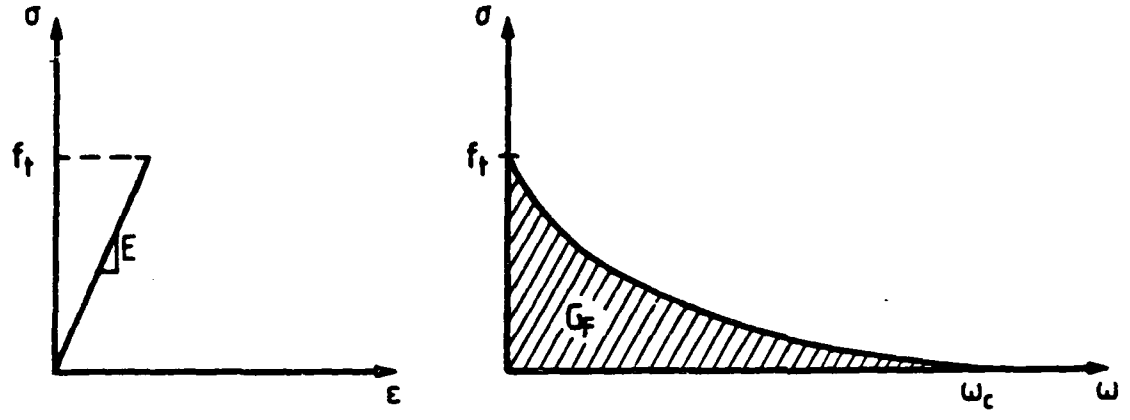

Figure 1: Pre-peak (linear) response and post-peak tension softening

the units of length $\ell_{ch} = G_F E / f_t^2$ is defined and is called the characteristic length.

An extensive round-robin testing programme organised by RILEM FMC-50 (1985) and using the same concrete mix in all participating laboratories confirmed earlier doubts that G_F varied significantly with the size of test specimens for one and the same mix. In the light of this confirmation it is somewhat surprising that this method is still widely used. It is now generally accepted that the size (scale) effect is due to curing conditions which result in cracking, to the development of microcracks at the aggregate/paste interfaces or the paste itself, to crack bridging between the aggregate particles, etc. These processes consume energy and lead to the observed non-linear load response, not only in the post-peak regime but already in the pre-peak behaviour. In the above method, the material response is assumed to be linear right up to the peak load (Fig. 1).

In order to better understand the reasons behind the observed size (scale) effect and, what is more important, to propose a reasonably size-independent test method(s) for determining the intrinsic mode I fracture toughness of concrete the RILEM TC-89 (FMT) was set up in Paris in 1986, under the chairmanship of Professor S.P. Shah. Of the several sub-committees formed at this Paris meeting, sub-committee *A* (Chair: B.L. Karihaloo) was charged with analysing available test data from three-point bend notched specimens (including the data from above-mentioned round-robin testing programme) according to the two-parameter model (Shah & Jenq 1985) and the size-effect law (Bažant & Pfeiffer 1986). These two proposals were before the committee at its inception. However, of the extensive

body of raw test data available for analysis, only a very small fraction was suitable for analysis according to these two proposals. The reasons for this were twofold. First, very few sets of data were accompanied by load-CMOD diagrams and unloading compliance figures necessary for analysis according to the two-parameter model. Secondly, even fewer sets of data met the rather strict size requirements of the size-effect law. The available data were therefore also analysed according to a third method, namely that based on effective crack model (Karihaloo & Nallathambi 1986a). This lecture will review all three methods in relation to three-point bend notched specimens on the basis of one and the same set of test data, as well as on the basis of their maximum load prediction following the methodology proposed by Planas & Elices (1987). This latter method of comparison also serves as a link between the above three methods and the earlier method due to Hillerborg *et al.* (1976).

Sub-committee *B* (Chair: P. Rossi) on the other hand, was asked to consider other, more compact specimen geometries for the determination of fracture properties of plain concrete. This lecture will review the three compact specimen geometries analysed by Sub-committee *B*, namely the tapered double cantilever beam (TDCB), the cylindrical wedge splitting specimen and the cubical wedge splitting specimen.

Both sub-committees have now finalised their reports in anticipation of their publication in October 1990. These reports have not only eased the task of preparing this review lecture, but more importantly have provided a valuable reference source. To keep this lecture within manageable length, frequent reference will be made to these reports.

THE TWO-PARAMETER MODEL (TPM)

The two-parameter model or the effective Griffith crack model (Shah & Jenq 1985) allows for both pre-critical and post-critical crack growth. The pre-critical stable crack growth is accompanied by an increasing stress intensity factor K_I (R-curve behaviour). It is assumed that the load-CMOD (Fig. 2) is more or less linear up to about half the maximum load and the corresponding crack tip opening displacement (CTOD) is zero. Significant inelastic displacement and slow crack growth occur when the load increases from about $0.5P_{max}$ on the ascending branch of the load-CMOD plot to $0.95P_{max}$ on the descending (tension-softening) branch. The latter load level is associated with the instant of growth of the original notch, i.e. with critical K_I which is designated K_{Ic}^s and with the critical value of $CTOD$ of the original notch tip which is designated $CTOD_c$.

The load-CMOD diagram is used to calculate both E and K_{Ic}^s by the traditional compliance approach. The initial compliance C_i of the load-CMOD plot (Fig. 2)

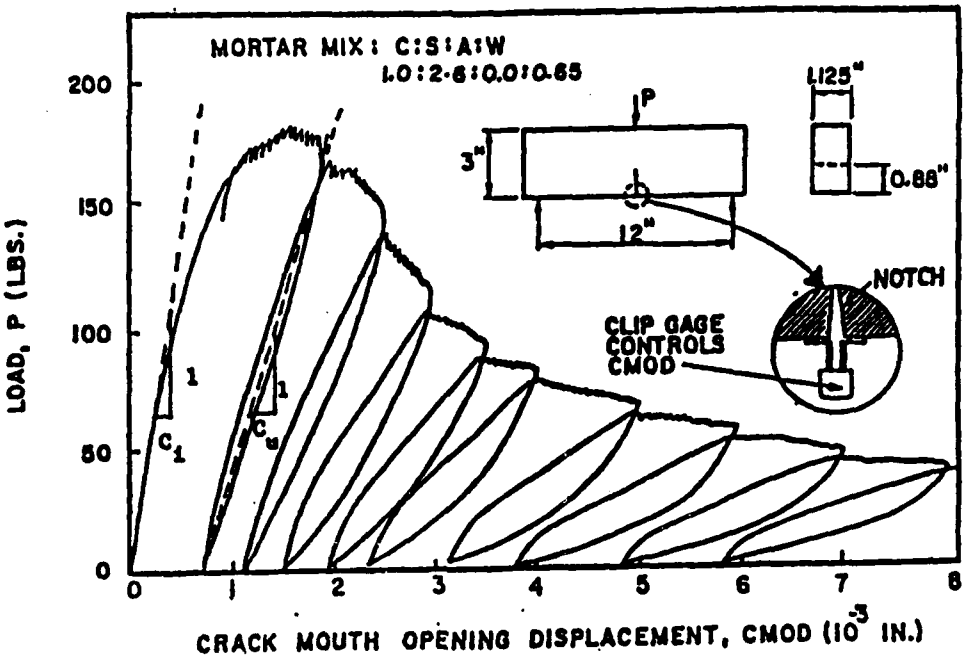

Figure 2: A typical load-CMOD plot (Jenq & Shah 1985)

is measured and used for determining the elastic modulus E of the mix.

$$E = 6S(a_0 + H_0)\, V_1\left(\frac{a_0}{W}\right)/(C_i B W^2), \tag{1}$$

where H_0 is the thickness of the knife-edge used for holding the clip gauge and the function $V_1(a_0/W)$ established from finite element calculations is

$$V_1\left(\frac{a_0}{W}\right) = 0.76 - 2.28\left(\frac{a_0}{W}\right) + 3.87\left(\frac{a_0}{W}\right)^2 - 2.04\left(\frac{a_0}{W}\right)\alpha^3 + \frac{0.66}{\left(1-\frac{a_0}{W}\right)^2}. \tag{2}$$

For a notched three-point bend specimen, B, W, S are respectively the width, depth and loaded span of the beam. It should be mentioned that the principle of two-parameter model should be applicable not only to notched beam specimens but to other geometries as well. However, recent calculations would seem to cast doubt on its applicability to geometries other than the notched beam. We shall have more to say on this subject when we discuss compact specimen geometries.

The unloading compliance C_u (Fig. 2) corresponding to $0.95P_{max}$ on the descending branch of load-CMOD plot is used to obtain an augmented traction-free notch depth $\underline{a}$ (equal to a_0 plus the effective slow crack growth size) by solving the following equation

$$E = 6S(\underline{a} + H_0)\, V_1\left(\frac{\underline{a}}{H}\right)/(C_u B W^2). \tag{3}$$

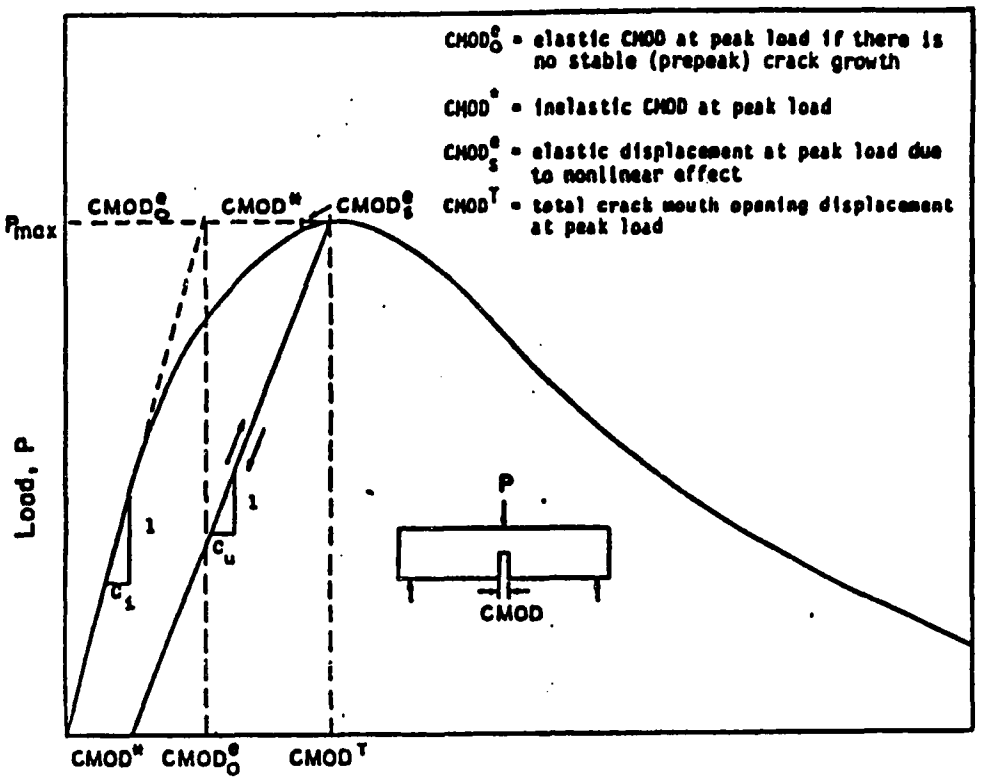

Figure 3: Decomposition of CMOD due to non-linear effect

$\underline{a}$ is determined from (3) by a trial and error procedure or from nomograms provided by John, Shah & Jenq (1987). Having calculated $\underline{a}$, the critical stress intensity factor K_{Ic}^s is determined from the LEFM formula (Srawley 1976) after replacing in it a_0 by $\underline{a}$

$$K_{Ic}^s = \frac{3P_{max}S}{2BW^2}\sqrt{\underline{a}}F(\alpha), \tag{4}$$

where $\alpha = \underline{a}/W$ and

$$F(\alpha) = \frac{1.99 - \alpha(1-\alpha)(2.15 - 3.93\alpha + 2.7\alpha^2)}{(1+2\alpha)(1-\alpha)^{3/2}}. \tag{5}$$

The effective notch depth $\underline{a}$ may also be used to calculate the critical crack tip (original notch) opening displacement $CTOD_c$

$$CTOD_c = \frac{6P_{max}S\underline{a}}{W^2BE}V_1(\alpha)\{(1-\beta)^2 + (-1.149\alpha + 1.081)(\beta - \beta^2)\}^{1/2}, \tag{6}$$

where $\alpha = \underline{a}/W$ and $\beta = a_0/\underline{a}$.

Practical difficulties are faced in unloading the specimen at precisely $0.95P_{max}$ on the descending branch of load-CMOD plot. Even in laboratories which are equipped to perform a stable bend-test, unloading the specimen at $0.95P_{max}$ is

Table 1. Summary of Results According to TPM

Sl No	g	n	f_c'	E	Range a_0/W	Range a/W	K_{Ic}^s Mean(sd)	$CTOD_c(mm)$ Mean(sd)
1	19	6	55.8	36.8	0.29-0.67	0.55-0.81	0.931(0.263)	0.0148(0.0076)
2	19	4	53.1	38.4	0.29-0.70	0.41	1.054(-)	0.0153(-)
3	19	3	54.4	39.3	0.30-0.67	0.42-0.73	1.128(0.269)	0.0200(0.0085)
4	19	25	53.1	38.4	0.25-0.61	0.44-0.83	1.146(0.014)	0.0316(0.0067)
5	19	22	54.4	39.3	0.16-0.57	0.54-0.69	1.220(0.102)	0.0312(0.0087)
6	3	12	-	36.8	0.13-0.51	0.15-0.56	0.894(0.068)	0.0042(0.0013)
7	6	2	60.7	33.5	0.20-0.21	0.25-0.28	1.141(0.095)	0.0145(0.0057)
8	13	3	45.5	31.0	0.20-0.21	0.25-0.35	1.475(0.191)	0.0220(0.0086)
9	13	3	43.4	31.0	0.20-0.21	0.24-0.28	1.530(0.022)	0.0169(0.0024)
10	19	8	25.2	27.2	0.29-0.33	0.35-0.55	0.976(0.103)	0.0170(0.0068)
11	32	17	31.0	32.3	0.50	-	0.121(-)	-
12	2	11	35.0	25.7	0.50	-	0.090(-)	-
13	8	2	110.	56.5	0.33	-	2.130(-)	0.0338(0.0039)

Notes:

1. g = Max. aggregate size (mm); n = No. of specimens tested.
2. f_c' in MPa, E in GPa, K_{Ic}^s in $MPa\sqrt{m}$
3. The entries have been grouped according to mix variables only because they do not vary with the size of test specimens. Thus entries differ only by the maximum size of coarse aggregate (g) used in the mix and other mix parameters, e.g. water/cement ratio, texture of coarse aggregate. That K_{Ic}^s (but not $CTOD_c$) is relatively insensitive to the specimen size is best judged from Fig. 4 which shows the relative K_{Ic}^s of a mix calculated by dividing the K_{Ic}^s of a particular specimen group from this mix with the K_{Ic}^s for the specimen of least depth from this group and mix. The various plots on Fig. 4 refer to different mixes.

not always successful, so that inaccuracies in the determination of C_u are unavoidable. For those laboratories which cannot perform a stable three-point bend test Shah & Jenq recommend that C_u be approximated by its value corresponding to $CMOD^* = 0$ (Fig. 3). They suggest that K_{Ic}^s and $CTOD_c$ determined under this approximation are about 10% to 25% higher than the values calculated using the C_u corresponding to $0.95P_{max}$ on the descending branch (Fig. 2). A summary of results according to TPM based on test data from several laboratories around the world (Karihaloo & Nallathambi 1990a) is given in Table 1.

The two fracture parameters K_{Ic}^s and $CTOD_c$, together with an appropriate approximation of the tension-softening behaviour may be used to calculate f_t and any other parameters required for the full description and finite element modelling of the fracture process. We shall demonstrate this calculation later in this lecture.

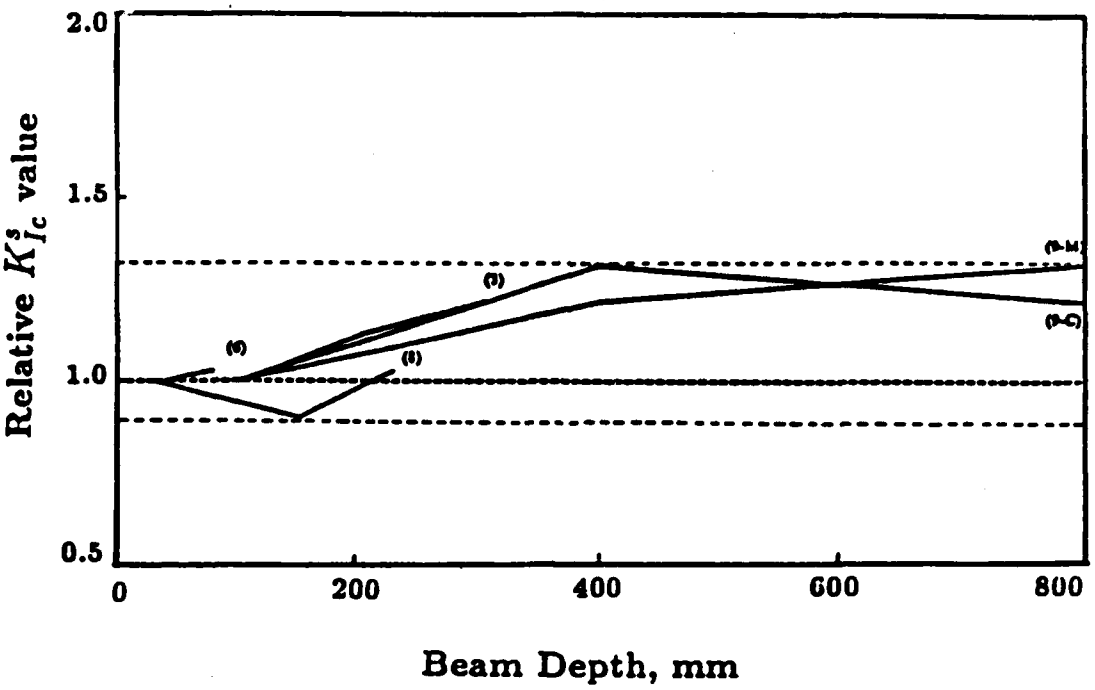

Figure 4: Variation of relative K^s_{Ic} with specimen depth

THE SIZE-EFFECT LAW (SEL)

In this model (Bažant & Pfeiffer 1986) which is applicable to materials whose fracture front is blunted by a non-linear zone of distributed cracking and damage (process zone), the fracture energy G_f (not to be confused with G_F used previously) is defined as the specific energy required for crack growth in an infinitely large structure, for which the LEFM is strictly valid. This definition is obviously independent of specimen size and geometry, provided the law for extrapolating the results of geometrically similar specimens of finite size to infinite specimen size is known and is unaffected by other size effects, such as those due to hydration heat or shrinkage.

An exact form of the scaling law for blunt fracture is not known, although an approximate form which appears to be sufficient for practical purposes was proposed by Bažant (1984)

$$\sigma_N = \beta f_t \left(1 + \frac{W}{\lambda_0 g}\right)^{-1/2}, \tag{7}$$

in which σ_N = nominal stess at failure, g = maximum size of aggregate in the mix, and β, λ_0 = empirical constants. It appears that Eqn (7) is adequate for a size range 1:30 and is not affected by alterations to the specimen geometry provided W is appropriately reinterpreted.

As applied to the notched three-point bend specimen, it is recommended that the span-to-depth ratio S/W be at least 2.5. Moreover, it is recommended that a_0/W be in the range $0.15 < a_0/W \leq 0.4$, B and W not be less than $3g$, and that the notch width be as small as possible and not exceed $0.5g$. For the scaling law to retain its validity, tests have to be performed on specimens of at least three different sizes, characterized by depths $W_1, \ldots, W_n$ and loaded spans $S_1, \ldots, S_n$. It is necessary that the smallest depth W_1 not be larger than $5g$ and the largest depth W_n not be smaller than $15g$, and that the maximum W to minimum W be at least 4. These size requirements may necessitate fabrication of very bulky specimens if large size aggregate is used in the mix. It is also recommended that the ratios of the adjacent sizes be roughly constant, with as broad a size range as feasible. Ideally, the specimens of all sizes should be geometrically similar in two dimensions, with the third dimension (width B) the same for all specimens to avoid introduction of undesirable size effects of thickness.

In actual testing, one needs to record only the maximum loads $P_1, \ldots, P_n$. This does not require the use of closed-loop systems and is thus a great advantage of this method of testing. A linear regression of the depths $X_j = W_j (j = 1, \ldots, n)$ against the inverse square of the nominal stress at failure $(= P_j^*/BW_j)$ is carried out and the slope A of the regression line is determined

$$A = \frac{\sum_j (X_j - \bar{X})(Y_j - \bar{Y})}{\sum_j (X_j - \bar{X})^2}, \tag{8}$$

where

$$\bar{X} = \frac{1}{n} \sum_j X_j, \qquad \bar{Y} = \frac{1}{n} \sum_j Y_j. \tag{9}$$

where $Y_j = (BW_j/P_j^*)$ and $(\bar{X}, \bar{Y})$ defines the centroid of all data points. P_j^* which is related to P_j takes into account the self-weight of the specimen, the effect of any overhang, i.e. if L_j is much larger than S_j, and of any geometrical dissimilarity in the specimens (Karihaloo & Nallathambi, 1990a). Having determined the slope A of the regression line (Fig. 5), the fracture energy G_f is calculated from

$$G_f = g\left(\frac{a_0}{W}\right)/(EA), \tag{10}$$

where the non-dimensional energy release rate is

$$g\left(\frac{a_0}{W}\right) = \left(\frac{S_m}{W_m}\right)^2 \left(\frac{a_0}{W}\right) [1.5F\left(\frac{a_0}{W}\right)]^2, \tag{11}$$

and $(\alpha_0 = a_0/W)$

$$F(\alpha_0) = F_4(\alpha_0) + \frac{(S_m/W_m) - 4}{4} [F_8(\alpha_0) - F_4(\alpha_0)], \tag{12}$$

$$F_4(\alpha_0) = 1.090 - 1.735\alpha_0 + 8.20\alpha_0^2 - 14.18\alpha_0^3 + 14.57\alpha_0^4, \tag{13}$$

$$F_8(\alpha_0) = 1.107 - 1.552\alpha_0 + 7.71\alpha_0^2 - 13.55\alpha_0^3 + 14.25\alpha_0^4 \tag{14}$$

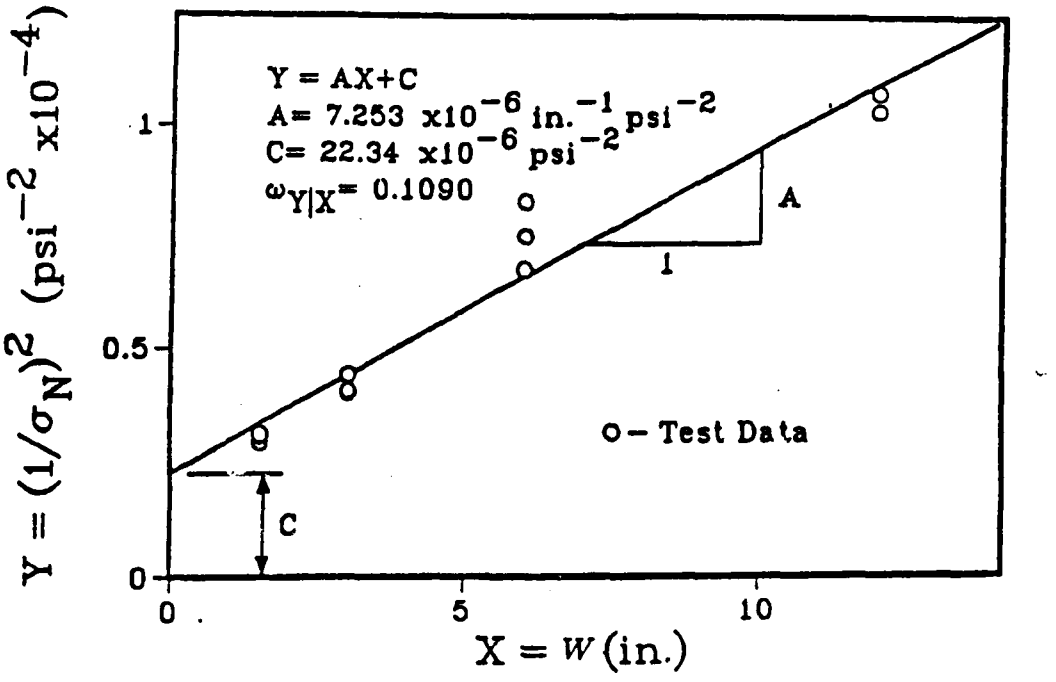

Figure 5: Linear regression plot constructed from measured maximum load values

In Eqn (11), S_m and W_m are respectively the median span and median depth of the group of geometrically similar specimens. The interpolation formula (12) is not recommended for use outside of the range $3 < S/W < 10$. Since LEFM is applicable at the limit of extrapolation, the fracture toughness may be calculated from fracture energy G_f using the plane stress relationship

$$K_{Ic}^b = \sqrt{G_f E}. \tag{15}$$

Finally, in order to establish the confidence level of calculated G_f it is necessary to perform statistical analysis of the test data. In particular, it is necessary to calculate the coefficient of variation w_A of the slope of regression line A and the relative width of scatterband m. It is suggested that w_A not exceed about 0.08 and the value of m be around 0.15. These statistical measures prevent situations in which the size range used is insufficient compared to the scatter of results. Three such situations are illustrated in Fig. 6. Fig. 6a shows the situation in which A is uncertain, while Fig. 6b illustrates the case of large scatter necessitating the use of a very broad range of sizes. Fig. 6c on the other hand illustrates the case of small scatter permitting the use of a narrow range of sizes.

It should however be borne in mind that since the value of w_A can be reduced by increasing the number of test specimens even with a wide scatterband, it is necessary also to limit the value of m, in addition to limiting the value of w_A.

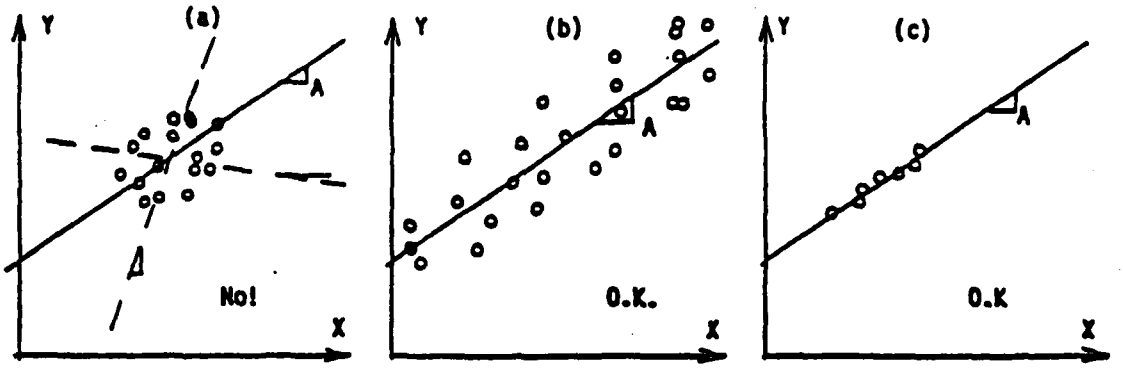

Figure 6: Examples of correct and incorrect regression plots

A summary of results according to SEL based on test data from several laboratories (Karihaloo & Nallathambi 1990a) is given in Table 2.

THE EFFECTIVE CRACK MODEL (ECM)

The effective crack model (Karihaloo & Nallathambi 1986a, 1989a) is based on the assumption that the effect of various (non-linear) energy consuming processes taking place in the fracture process zone can be represented by a supplementary traction-free crack (Fig. 7). The latter, when added to the pre-existing notch depth a_0 gives the size of the effective notch a_e. It is evident that this assumption is also made in the TPM. However, as will become clear in the sequel, the method of determining a_e differs from that of $\underline{a}$ in TPM. What is more important, it is much easier to determine a_e accurately than it is to determine $\underline{a}$ without the use of a servo-hydraulic testing machine. That is the major advantage of ECM over TPM, otherwise in principle they are very similar.

It is also obvious from Fig. 7 that the size of the traction-free supplementary crack $\Delta a_e = a_e - a_0$ cannot be equal to the size of the fracture process zone which has residual stress carrying capacity.

The application of ECM to notched three-point bend specimen (Fig. 8) does not require any load/deflection information past the peak load. However, if a closed-loop testing machine is available, then CMOD or load-point displacement may be used as a feed-back signal to achieve stable failure.

The Young modulus (E) of the mix is calculated from the initial, linear segment of the continous load-deflection plot. However, if such a plot cannot be obtained, E may be determined by testing cylindrical specimens, preferably using two electrical strain gauges with gauge length at least $3g$ glued opposite to each other at mid-height.

Table 2. Summary of Results According to SEL

Sl. No.	g	n	Size, mm S B W	a_0/W	A	G_f (J/m)	K_{Ic}^b	ω_A	m
1		6	0600 80 076						
2		4	1000 80 140						
3	20	4	1200 80 200	0.200	0.759E-01	22.986	0.874	0.144	0.161
4		4	1500 80 240						
5		4	1800 80 300						
6		6	0600 80 076						
7		4	1000 80 140						
8	20	4	1200 80 200	0.300	0.123E-00	23.989	0.892	0.185	0.211
9		4	1500 80 240						
10		4	1800 80 300						
11		6	0600 80 076						
12		4	1000 80 140						
13	20	4	1200 80 200	0.400	0.231E-00	21.600	0.847	0.102	0.121
14		4	1500 80 240						
15		4	1800 80 300						
16		3	095 38 038						
17		3	191 38 076						
18	13	3	381 38 152	0.167	0.578E-02	42.531	1.084	0.133	0.146
19		3	762 38 305						
20		3	095 38 038						
21		3	191 38 076						
22	5	3	381 38 152	0.167	0.873E-02	23.670	0.883	0.031	0.048
23		3	762 38 305						
24		3	0400 100 100						
25	19	2	0800 100 200	0.400	0.270E-01	71.059	1.520	0.537	0.585
26		2	2000 100 500						
27		8	0400 100 100						
28		2	0800 100 200						
29	19	2	1200 100 300	0.200	0.709E-02	94.058	1.751	0.331	0.435
30		1	2000 100 500						
31		1	3200 100 800						

1. g = Max. aggregate size in mm; n = Number of specimens tested.
2. Of the hundreds of specimen groups for which peak load values were available only the above few groups satisfied the rather strict size requirements of SEL. Even for these few groups, statistical measures (ω_A should be less than 0.08 and m should be about 0.15) point towards poor quality of results.
3. Extreme care should be exercised in determining slope of regression line A. A slight error in its determination can significantly alter G_f.

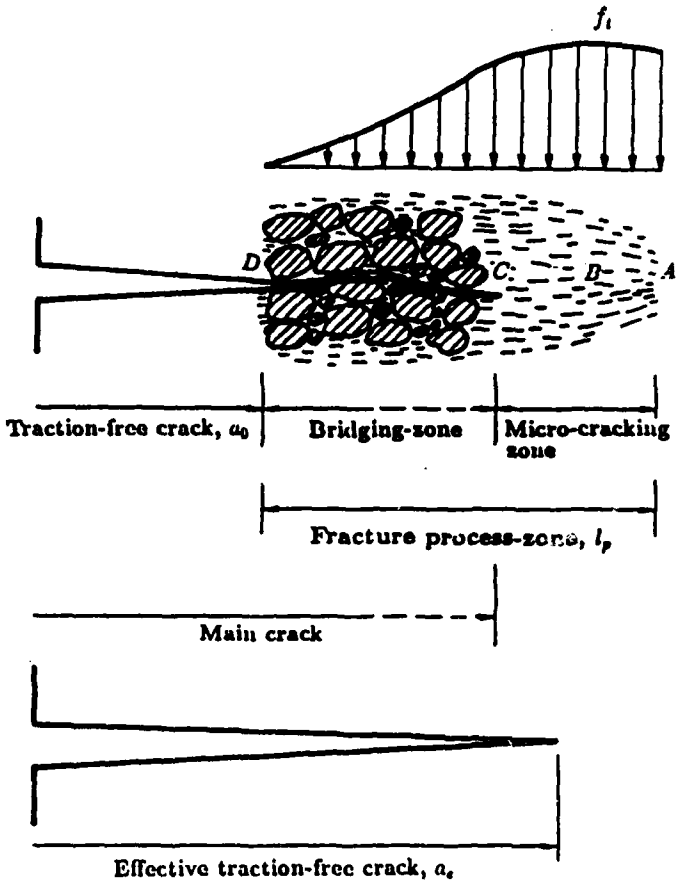

Figure 7: Schematic illustration of process zone and effective notch depth

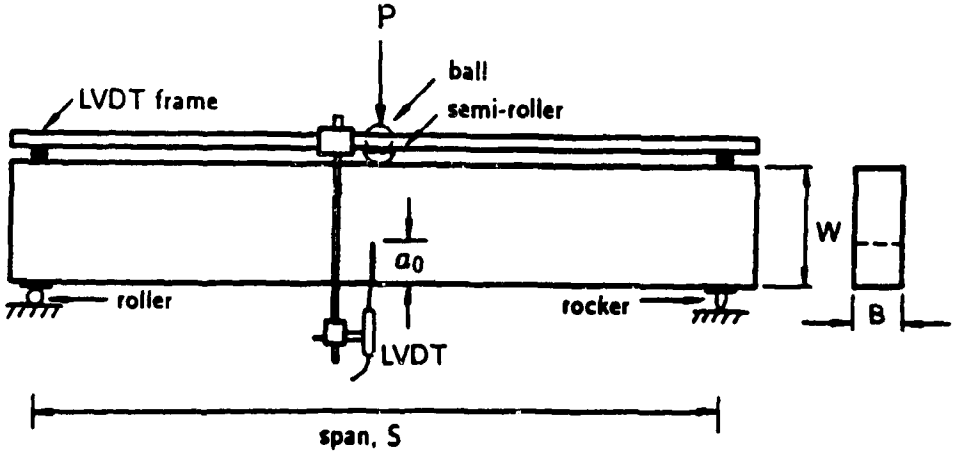

Figure 8: Loading apparatus and LVDT fixing arrangement

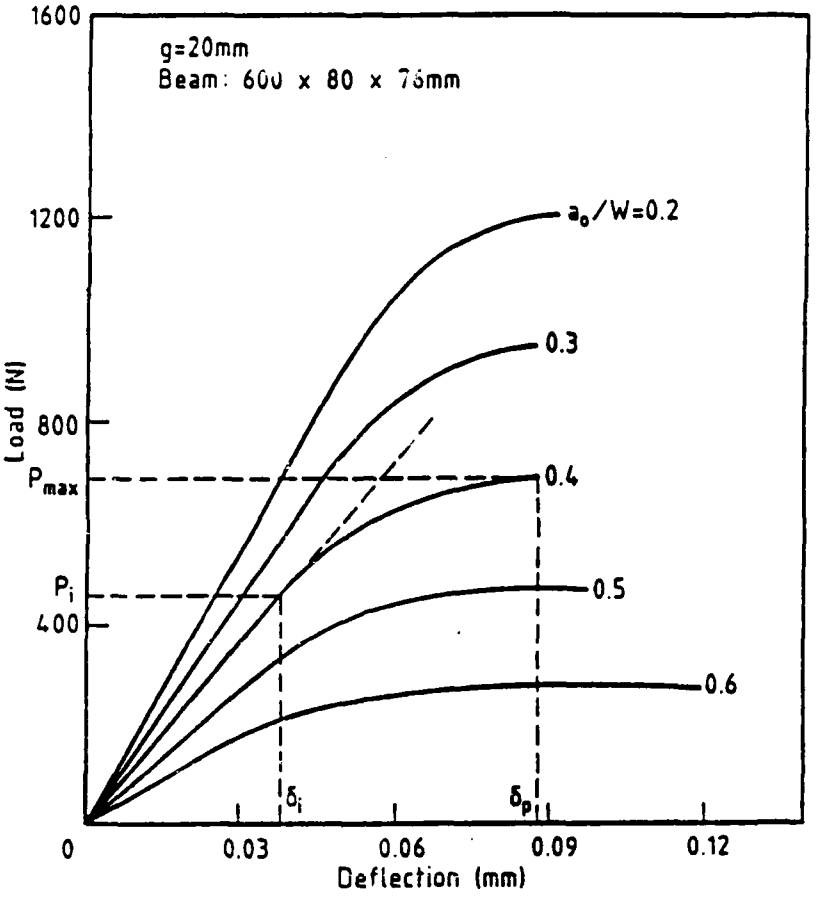

Figure 9: Typical load-deflection plots up to peak load for various a_0/W ratios

Typical load-deflection plots up to the peak load are shown in Fig. 9, for various a_0/W ratios. It should be emphasized that these plots need not be drawn continuously; it is sufficient to measure mid-span load-point deflection at several load levels up to the peak load. From these plots, P_i, P_{max} (P_i in linear range) and the corresponding mid-span deflections δ_i, δ_p are read, and E calculated from the following equation (Karihaloo & Nallathambi 1989a)

$$E = \frac{P_i}{4B\delta_i}\left(\frac{S}{W}\right)^3\left[1+\frac{5qS}{8P_i}+\left(\frac{W}{S}\right)^2\left\{2.70+1.35\frac{qS}{P_i}\right\}-0.84\left(\frac{W}{S}\right)^3\right] + \frac{9}{2}\frac{P_i}{B\delta_i}\left(1+\frac{qS}{2P_i}\right)\left(\frac{S}{W}\right)^2 F_2(\alpha_0), \tag{16}$$

where q is the self-weight of the beam per unit length, and

$$F_2(\alpha_0) = \int_0^{\alpha_0} \beta\, F_1^2(\beta)\, d\beta, \tag{17}$$

with $\alpha_0 = a_0/W$, and for $S/W = 4$, $F_1(\beta)$ is given by Eqn (5). A slightly less accurate expression (error $< 1\%$) for $F_1(\beta)$ is available in the range $0.1 < \beta < 0.6$

for two span to depth ratios ($S/W = 4$ and 8) with linear interpolation permitted within, and outside of, these ratios

$$F_1(\beta) = A_0 + A_1\beta + A_2\beta^2 + A_3\beta^3 + A_4\beta^4 \tag{18}$$

where

$$\begin{aligned} A_0 &= +0.0075\frac{S}{W} + 1.90 \\ A_1 &= +0.0800\frac{S}{W} - 3.39 \\ A_2 &= -0.2175\frac{S}{W} + 15.40 \\ A_3 &= +0.2825\frac{S}{W} - 26.24 \\ A_4 &= -0.1450\frac{S}{W} + 26.38 \end{aligned} \tag{19}$$

The coefficients $A_i (i = 0, 1, ..., 4)$ have been obtained by linear interpolation from the coefficients given by Brown & Srawley (1966) for $S/W = 4$ and 8.

The reduction in the stiffness of the beam (Fig. 8) is a result of both the stable crack growth and the formation of the discontinuous process zone ahead of the visible crack. It is however difficult to separate these two causes. Therefore it is assumed that the critical notch depth a_e may be calculated by introducing a fictitious beam containing a notch a_e whose unchanged stiffness (proportional to E) would be equal to the reduced stiffness of the real beam containing a notch of depth a_0, i.e.

$$\begin{aligned} \delta_p &= \frac{P_{max}}{4BE}\left(\frac{S}{W}\right)^3\left[1 + \frac{5qS}{8P_{max}} + \left(\frac{W}{S}\right)^2\left\{2.70 + 1.35\frac{qS}{P_{max}}\right\} - 0.84\left(\frac{W}{S}\right)^3\right] \\ &\quad + \frac{9}{2}\frac{P_{max}}{BE}\left(1 + \frac{qS}{2P_{max}}\right)\left(\frac{S}{W}\right)^2 F_2(\alpha_e), \end{aligned} \tag{20}$$

where

$$F_2(\alpha_e) = \int_0^{\alpha_e} \beta F_1^2(\beta)\, d\beta \tag{21}$$

Here $\alpha_e = a_e/W$ and $F_1(\beta)$ is again given by Eqn (5) or Eqn (18). It will be noticed that Eqn (20) equates the stiffnesses and not the energies, as should be done in the ECM. Later in this lecture, we shall use the actual comparison of energies and shall show that a_e thus calculated is indeed very close to that calculated from Eqn (20).

$\alpha_e = a_e/W$ is calculated from Eqn (20) by a trial and error procedure described by Karihaloo & Nallathambi (1989a). This procedure was applied to all notched three-point bend test data available to the authors from various laboratories (Karihaloo & Nallathambi 1990a) and the corresponding a_e/W was calculated. The

following regression equation gave the best fit

$$\frac{a_e}{W} = \gamma_1 \left(\frac{\sigma_n}{E}\right)^{\gamma_2} \left(\frac{a_0}{W}\right)^{\gamma_3} \left(1 + \frac{g}{W}\right)^{\gamma_4}, \tag{22}$$

where, as before, g is the maximum size of the aggregate used in the mix, $\sigma_n = 6M/(BW^2)$, $M = (P_{max} + qS/2)S/4$, and $\gamma_1 = 0.088 \pm 0.004$, $\gamma_2 = -0.208 \pm 0.010$, $\gamma_3 = 0.451 \pm 0.013$ and $\gamma_4 = 1.653 \pm 0.109$. The elastic modulus E in Eqn (22) was determined from the initial, linear segment of the load-deflection plot using Eqn (16). This method of determining E is more consistent with the ECM. Having determined the effective crack length a_e, the critical stress intensity factor according to the ECM is calculated using

$$K_{Ic}^e = \sigma_n \sqrt{a_e} F_1(a_e/W), \tag{23}$$

where $F_1(a_e/W)$ is given by Eqn (5) or Eqn (18).

It is possible to improve the above expression K_{Ic}^e by considering the true state of stress at the front of a pre-crack in a three-point bend specimen. Elastic finite element calculations show (Nallathambi & Karihaloo 1986b) that this stress field consists not only of a tensile stress normal to the crack plane (as assumed in the derivation of Eqn (23)) but also of a significant (tensile) stress in the crack plane and of a shear stress. By making an allowance for the true stress state ahead of the existing crack front, Eqn (23) becomes

$$\bar{K}_{Ic}^e = \sigma_n \sqrt{a_e}\, Y_1(\alpha)\, Y_2(\alpha, \beta), \tag{24}$$

where as before $\alpha = a_e/W$, $\beta = S/W$, and

$$Y_1(\alpha) = A_0 + A_1\alpha + A_2\alpha^2 + A_3\alpha^3 + A_4\alpha^4 \tag{25}$$

$$Y_2(\alpha, \beta) = B_0 + B_1\beta + B_2\beta^2 + B_3\beta^3 + B_4\alpha\beta + B_5\alpha\beta^2 \tag{26}$$

Regression coefficients A_i, B_j, $(i = 0, ..., 4;\ j = 0, 1, ..., 5)$ are given in Table 3.

Table 3. Regression coefficients A_i, $B_j (i = 0, ..., 4;\ j = 0, ..., 5)$

i/j	0	1	2	3	4	5
A_i	3.6460	-6.7890	39.2400	-76.8200	74.3300	-
B_j	0.4607	0.0484	-0.0063	0.0003	-0.0059	0.0033

Fig. 10 shows the relative variation of K_{Ic}^e with specimen depth. The plots refer to different mixes. It is clear that K_{Ic}^e is reasonably independent of the size of the specimen. Further decrease in variation is expected when the tests are conducted in strict accordance with the requirements of the ECM.

Tables 4 and 5 compare the fracture parameters K_{Ic}^e, Δa_e predicted by the ECM with the predictions from the TPM and SEL (Nallathambi & Karihaloo, 1990a)

Table 4. Summary of Results According to (ECM) & (TPM)

Sl No	n	g	f_c'	E	Range a_0/W	Range a_c/W	Range g/W	K_{Ic}^s Mean(sd)	K_{Ic}^s Mean(sd)	$CTOD_c$ Mean(sd)
1	90	2	44.3	26.3	.20-.60	.27-.63	-	0.633(.065)	-	-
2	84	5	42.1	29.3	.20-.60	.27-.64	-	0.641(.057)	-	-
3	60	10	40.3	32.0	.20-.50	.28-.56	-	0.706(.046)	-	-
4	30	14	40.9	32.6	.20-.40	.28-.47	-	0.728(.018)	-	-
5	30	20	37.6	33.0	.20-.40	.29-.49	-	0.776(.028)	-	-
6	76	20	38.0	33.2	.20-.60	.29-.69	-	0.884(.057)	-	-
7	6	19	55.8	36.8	.29-.67	-	.55-.81	-	0.931(.263)	.0148(.0076)
8	3	19	53.1	38.4	.29-.50	.36-.55	.41	0.965(.045)	1.054(-)	.0200(.0085)
9	3	19	54.4	39.3	.30-.67	.37-.73	.42-.73	1.145(.098)	1.128(.269)	.0316(.0067)
10	20	19	53.1	38.4	.15-.61	.23-.68	.44-.83	0.797(.075)	1.146(.014)	.0312(.0087)
11	20	19	54.4	39.3	.19-.57	.27-.63	.40-.71	0.971(.078)	1.220(.102)	.0042(.0013)
12	12	10	29.0	21.7	.50-.50	.54-.55	-	0.760(.039)	-	-
13	8	10	58.9	24.5	.30-.50	.37-.55	-	0.908(.068)	-	-
14	8	10	33.1	19.7	.50-.50	.54-.55	-	0.859(.091)	-	-
15	15	10	55.5	29.8	.20-.50	.27-.55	-	1.023(.052)	-	-
16	14	20	36.2	24.0	.50-.50	.53-.55	-	1.031(.129)	-	-
17	15	16	38.3	34.1	.33-.33	.40-.41	-	1.120(.217)	-	-
18	8	19	29.0	32.5	.20-.40	.27-.47	-	1.413(.272)	-	-
19	4	19	34.3	33.2	.20-.40	.28-.48	-	1.759(.172)	-	-
20	16	19	26.3	32.0	.20-.40	.28-.48	-	1.232(.147)	-	-
21	12	3	-	36.8	.13-.50	.18-.56	.15-.56	0.926(.061)	0.894(.068)	.0042(.0013)
22	2	6	60.7	33.5	.19-.21	.28-.29	.25-.28	1.221(.061)	1.141(.095)	.0145(.0057)
23	3	13	45.5	31.0	.19-.21	.27-.29	.25-.35	1.429(.046)	1.475(.191)	.0220(.0086)
24	3	13	43.4	31.0	.20-.21	.28-.29	.24-.28	1.610(.026)	1.530(.022)	.0169(.0024)
25	12	13	34.1	27.7	-	-	-	0.975(.150)	-	-
26	12	5	48.4	32.9	-	-	-	1.004(.068)	-	-
27	8	19	25.2	27.2	.29-.33	.36-.40	.35-.55	0.982(.169)	0.976(.103)	.0170(.0068)
28	6	13	48.5	33.3	.50-.51	.62-.73	-	0.421(.091)	-	-
29	11	8	93.0	32.0	.50-.50	.53-.54	-	1.198(.199)	-	-
30	11	8	28.0	31.0	.50-.50	.55-.57	-	0.830(.117)	-	-
31	6	12	68.0	39.0	.50-.50	.55-.57	-	1.356(.101)	-	-
32	6	12	21.0	26.0	.50-.50	.57-.58	-	0.727(.038)	-	-
33	17	32	31.0	32.3	.50-.50	.56-.57		1.585(.210)	1.211(.121)	-
34	11	2	35.0	25.7	.50-.50	.53-.58	-	1.102(.098)	0.790(.090)	-
35	2	8	110.	56.6	.33-.33	.37-.38	-	1.896(.064)	2.130(-)	.0338(.0039)

Notes:

1. g = Max. aggregate size in mm; n = No. of specimens tested.
2. f_c' in MPa, E in GPa, K_{Ic} in $MPa\sqrt{m}$, $CTOD_c$ in mm.
3. Absence of an entry in K_{Ic}^s and $CTOD_c$ columns means that load-CMOD plot was not available.

Table 5. Summary of Results According to ECM & SEL

Sl No	g	n	Size, mm S B W	a_0/W	A	G_f (J/m)	K^b_{Ic}	ω_A	m	K^s_{Ic} Mean(sd)
1		6	0600 80 076							
2		4	1000 80 140							
3	20	4	1200 80 200	0.200	0.07590	22.986	0.874	0.144	0.161	
4		4	1500 80 240							
5		4	1800 80 300							
6		6	0600 80 076							
7		4	1000 80 140							
8	20	4	1200 80 200	0.300	0.12300	23.989	0.892	0.185	0.211	0.867(.063)
9		4	1500 80 240							
10		4	1800 80 300							
11		6	0600 80 076							
12		4	1000 80 140							
13	20	4	1200 80 200	0.400	0.23100	21.600	0.847	0.102	0.121	
14		4	1500 80 240							
15		4	1800 80 300							
16		3	095 38 038							
17		3	191 38 076							
18	13	3	381 38 152	0.167	0.00578	42.531	1.084	0.133	0.146	0.975(.150)
19		3	762 38 305							
20		3	095 38 038							
21		3	191 38 076							
22	5	3	381 38 152	0.167	0.00873	23.670	0.883	0.031	0.048	1.004(.068)
23		3	762 38 305							
24		3	0400 100 100							
25	19	2	0800 100 200	0.400	0.02700	71.059	1.520	0.537	0.585	1.264(.293)
26		2	2000 100 500							
27		8	0400 100 100							
28		2	0800 100 200							
29	19	2	1200 100 300	0.200	0.00709	94.058	1.751	0.331	0.435	1.208(.260)
30		1	2000 100 500							
31		1	3200 100 800							

Notes:

1. g = Max. aggregate size in mm; n = Number of specimens tested.
2. All K_{Ic} values are given in $MPa\sqrt{m}$.
3. For the purposes of comparison G_f has been converted to an equivalent fracture toughness value K^b_{Ic} using the LEFM plane stress relationship $K^b_{Ic} = \sqrt{G_f E}$.
4. See also notes 2, 3 appearing after Table 2.

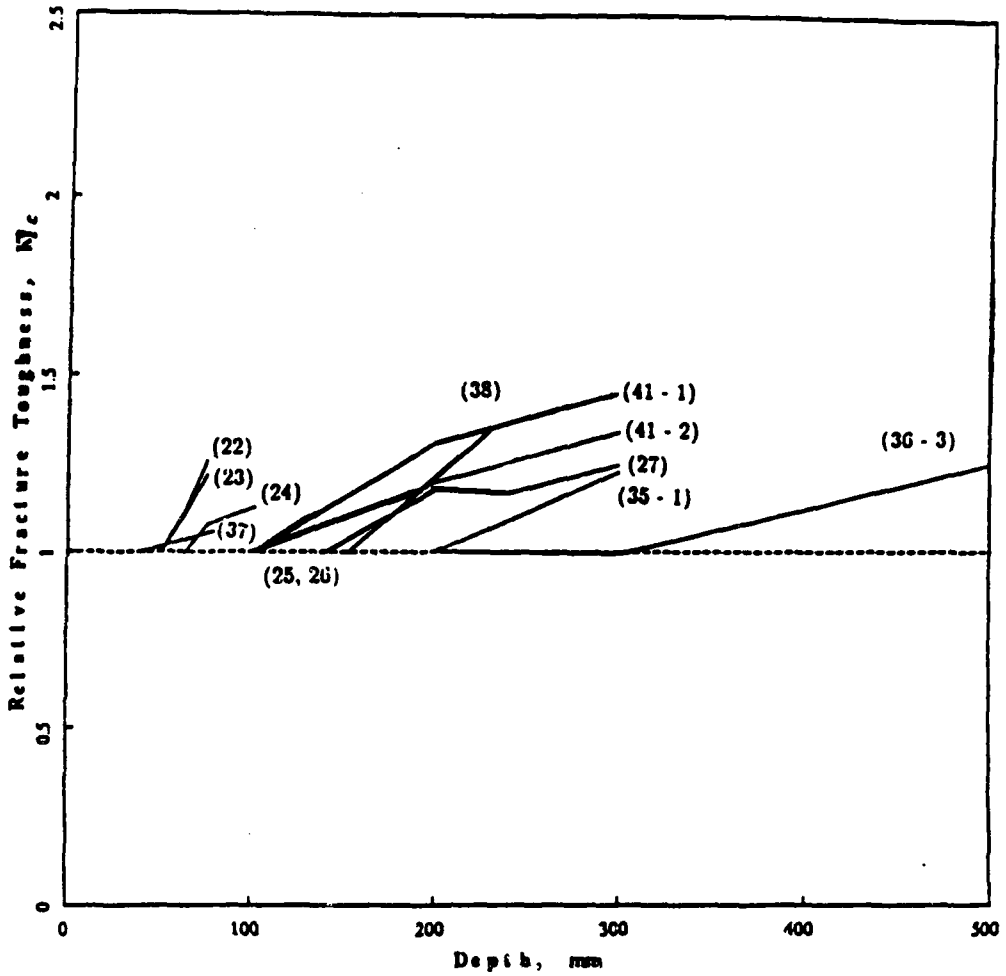

Figure 10: Variation of relative K_{Ic}^s with specimen depth

COMPARISON OF ECM WITH TPM

As seen from Table 4 the fracture parameters of plain concrete calculated using the effective crack model(ECM) and the two parameter model(TPM) are in good agreement despite the fact that they were determined from essentially separate series of test data. This was because of the paucity of simultaneous load-displacement and load-CMOD measurements from one and the same three-point bend specimen.

An investigation was conducted (Nallathambi & Karihaloo, 1990a) to compare the results of the two models using the necessary data from the same test specimens. To achieve this aim, both load-displacement and load-CMOD plots are simultaneously recorded for all notched specimens tested in three-point bending. A further aim of this investigation was to make this comparison for a wide variety of concrete mixes, ranging in (cylinder) compressive strength from about $25MPa$ to nearly $80MPa$.

It is found that irrespective of the concrete strength, the fracture parameters calculated using the effective crack model (namely, the effective fracture toughness K_{Ic}^{s} and the effective traction-free notch length a_e) are practically indistinguishable from the corresponding parameters calculated using the two parameter model (namely, the fracture toughness K_{Ic}^{s} and the notch iength a; the latter being also used to determine the critical crack tip opening displacement($CTOD_c$)).

Table 6 shows selected mix properties and the elastic modulus E calculated in four different ways, both direct and indirect. It will be appreciated that all four values of E for each of the mixes are in very good agreement with one another. This proves conclusively that any variations in fracture parameters between various models (Hillerborg's cohesive crack, ECM, TPM and SEL) cannot be attributed to differences in the measurement of E.

Table 6. Mix Properties

Mix	Compressive Strength $f_c(MPa)$	Elastic Modulus, (GPa)				Tensile Strength $f_t^{\odot}(MPa)$
		E^{*}	E_c^{**}	$E^{\dagger}$	$E^{\ddagger}$	
C1	26.8	24.62	24.51	25.56(.35)	25.04(.29)	2.58
C2	39.0	33.80	29.56	29.87(.21)	31.56(.64)	3.11
C3	49.4	34.65	33.27	33.28(.22)	32.96(.24)	3.50
C4	67.5	37.20	38.89	37.13(.23)	38.39(.82)	4.09
C5	78.2	40.30	41.86	40.99(.60)	40.26(.99)	4.41

Notes:
- * Determined from separate cylinder tests (using strain gauges)
- ** Estimated from the relationship, $E_c = 4734\sqrt{f_c}MPa$ (=$57000\sqrt{f_c}psi$)
- † Calculated from $P-\delta$ plot
- ‡ Calculated from $P-CMOD$ plot
- $^{\odot}$ Estimated from the relationship, $f_t = 0.4983\sqrt{f_c}\ MPa$ (=$6\sqrt{f_c}psi$)

Table 7 shows the fracture parameters calculated according to ECM and TPM. As mentioned above, the agreement between the two models is excellent. It should however be mentioned that the regression formula (Eqn 22) overestimates slightly the values of a_e/W (see Table 7). It is therefore recommended that a_e be calculated from Eqn (20) using the trial and error procedure given by Karihaloo & Nallathambi (1989a).

Another approach to comparing ECM with TPM is by calculating the tensile strength f_t, the total work of fracture W_d, and/or the critical crack opening w_c using the pair of fracture parameters defined by these models. These additional (but dependent) parameters are in any case required for a full description and finite element implementation of the fracture process. As an additional benefit this comparison approach allows us to put Δa_e on a sound physical foundation. It will be recalled that Δa_e was calculated above from a comparison of stiffnesses, whereas

Table 7. Fracture Parameters for Various Mixes

Mix/ Data	C1 Mean(sd)	C2 Mean(sd)	C3 Mean(sd)	C4 Mean(sd)	C5 Mean(sd)
a_0/W	0.295(.001)	0.296(.000)	0.295(.001)	0.293(.003)	0.293(.003)
$a_e/W^{\dagger}$	0.443(.005)	0.441(.001)	0.435(.004)	0.428(.002)	0.419(.006)
$a_e/W^{\ddagger}$	0.447(.003)	0.454(.001)	0.446(.003)	0.442(.004)	0.426(.008)
$a/W^{\odot}$	0.443(.015)	0.442(.006)	0.436(.001)	0.430(.002)	0.413(.006)
K_{Ic}^{e}	0.992(.015)	1.265(.013)	1.376(.020)	1.502(.046)	1.881(.095)
K_{Ic}^{s}	0.993(.054)	1.269(.028)	1.381(.031)	1.509(.040)	1.847(.098)
$CTOD_c$	0.033(.010)	0.026(.001)	0.026(.001)	0.024(.001)	0.026(.001)

Notes: † ECM
‡ Eqn 22
$^{\odot}$ TPM
K_{Ic} in $MPa\sqrt{m}$, $CTOD_c$ in mm

the basic assumption in ECM is that it be determined by equating the actual work of fracture W_d with the energy required to create a hypothetical supplementary traction-free crack $\Delta a_e = a_e - a_0$. This will be done in the sequel.

For the above comparison approach to work, it is necessary to judiciously approximate the post-peak tension softening diagram. For simplicity this diagram is usually approximated by a linear segment, although the present authors have recently given an analytical solution (Karihaloo & Nallathambi, 1989b)[1] for a highly non-linear law that better approximates the observed post-peak behaviour (Fig. 11) particularly at P_{max} (horizontal tangent at $\sigma = f_t$).

The transmitted stress-displacement law in the post-peak region is approximated as follows:

$$\frac{\sigma}{f_t} = 1 - \frac{w}{w_c} \quad (Linear) \tag{27}$$

$$\frac{\sigma}{f_t} = \left[1 - 9.2431\beta^2 + 33.8259\beta^3 - 59.4248\beta^4 + 49.3000\beta^5 - 15.4722\beta^6\right] \quad (Non\text{-}lin), \tag{28}$$

where $\beta = w/w_c$.

For the assumed $\sigma - w$ laws it was shown by Nallathambi & Karihaloo, (1990b) that

$$K_{Ic}^{e} = 0.7071\sqrt{E' w_c f_t}$$

$$W_d = \int_0^{\ell_{pc}} \int_0^{w_s} f^{-1}(w)\, dw\, ds = 0.1050 E' w_c^2. \quad (Linear\ law) \tag{29}$$

[1]Several unfortunate errors in this paper have been corrected in (Nallathambi & Karihaloo 1990b).

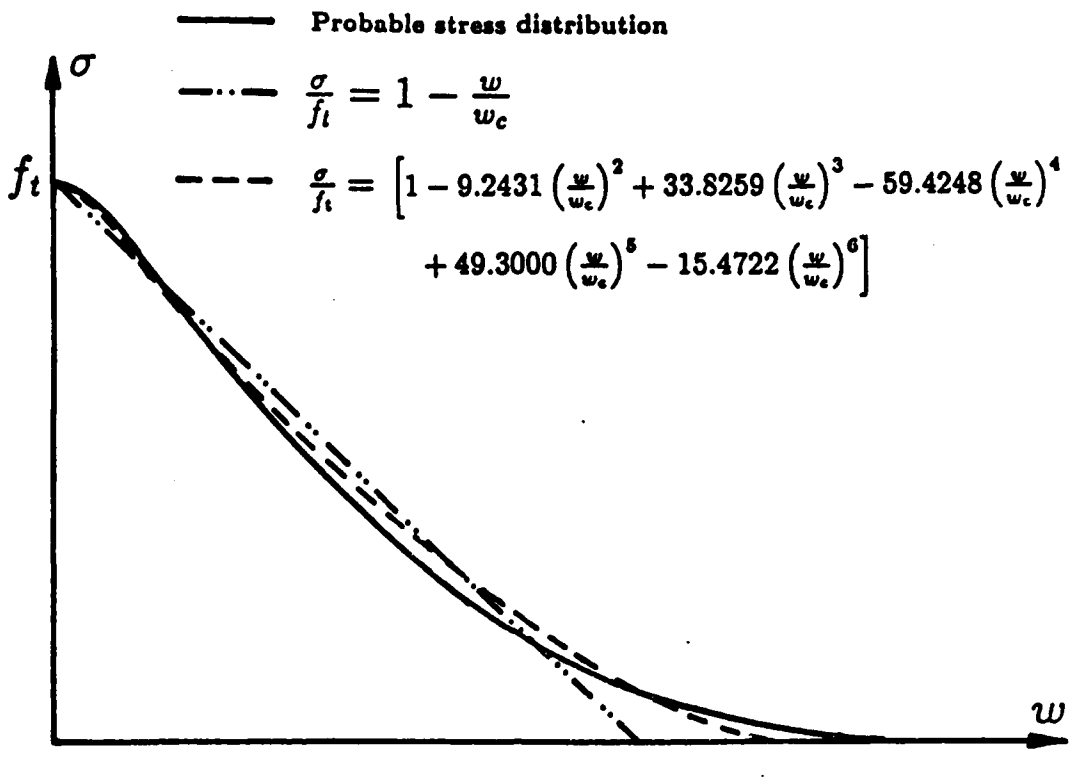

Figure 11: Approximations to tension-softening diagram

and

$$K_{Ic}^e = 0.7043\sqrt{E' w_c f_t}$$

$$W_d = \int_0^{\ell_{pc}} \int_0^{w_c} f^{-1}(w)\, dw\, ds = 0.0521 E' w_c^2. \quad \textit{(Non-linear law)} \qquad (30)$$

where $f^{-1}(w)$ represents the right hand side of Eqns. (27, 28). Equating W_d to $({K_{Ic}^e}^2/E)\Delta a_e$ gives

$$\Delta a_e = 0.210 E w_c / f_t \quad \textit{(Linear law)}$$
$$\Delta a_e = 0.105 E w_c / f_t \quad \textit{(Non-linear law)}$$

Finally, one may also calculate the critical process zone size ℓ_{pc} corresponding to the two assumed $\sigma - w$ laws:

$$\ell_{pc} = 0.366 E w_c / f_t \quad \textit{(Linear law)}$$
$$= 0.359 E w_c / f_t \quad \textit{(Non-linear law)} \qquad (31)$$

Using the pair of fracture parameters (K_{Ic}^e, Δa_e) or (K_{Ic}^e,$\Delta \underline{a}$) from Table 7 in Eqs. (29)-(31) one can calculate w_c without knowing f_t and compare it with the $CTOD_c$ of the TPM (Table 7). The results are given in Table 8.

Table 8. Additional Material Parameters Calculated From ECM and TPM

	$CTOD_c$	$w_c(mm)$		$f_t^\dagger$	$f_t(MPa)$		$\ell_{pc}(mm)$	
Mix	(mm)	Lin	Non-lin		Lin	Non-lin	Lin	Non-lin
C1	0.0332	0.0208	0.0296	2.58	3.70	2.63	52.6	103.1
C2	0.0263	0.0213	0.0318	3.11	4.78	3.39	51.2	100.4
C3	0.0261	0.0219	0.0305	3.50	5.29	3.76	49.5	97.0
C4	0.0242	0.0202	0.0293	4.09	5.88	4.18	47.7	93.6
C5	0.0261	0.0221	0.0322	4.41	7.61	5.40	44.8	87.8
mean	0.0272	0.0216	0.0307					

Note: † calculated from the empirical relationship $f_t = 0.4983\sqrt{f_c(MPa)}$

It is evident from Table 8 that the $CTOD_c$ according to TPM agrees better with the authors' non-linear approximation. The same is true, if one now uses the calculated values of w_c to determine f_t and ℓ_{pc} (Eqn 31) and compares the resulting f_t with that given by the well-known empirical formula (Table 8). It is worth noting that f_t is the only material parameter for which an independent formula, albeit an empirical one, exists. There is at present no similar independent way of checking the accuracy of $CTOD_c$ or ℓ_{pc}. It would seem though that the linear $\sigma - w$ approximation underestimates both w_c and ℓ_{pc}.

COMPARISON OF FCM, ECM, TPM AND SEL

The above comparison was restricted to two methods, namely TPM and ECM. Moreover, the comparison was based on the fracture parameters determined using these methods. To the extent that both these methods approximate the actual pre-peak behaviour and use LEFM, albeit after accounting for the stable slow crack growth, it is advisable to compare them at the asymptotic limit of large size structures when LEFM is strictly applicable. The comparison will not be restricted to TPM and ECM but will also include SEL and fictitious cohesive crack model (FCM) of Hillerborg *et al.* (1976).

The methodology for such a comparison was proposed by Planas & Elices (1987) and will not be repeated here. Readers will find a succinct account in the report by Karihaloo & Nallathambi (1990a). It will suffice here to summarize the major conclusion reached by Planas & Elices. It should be mentioned though that Planas & Elices did not include ECM in their comparison. However, their methodology was recently followed by Karihaloo & Nallathambi (1990b) and applied also to ECM.

The major conclusion flowing from this extensive comparative study is that all four models are able to predict accurately the maximum load carrying capacity of concrete specimens in the practical range of sizes used in the laboratory but that

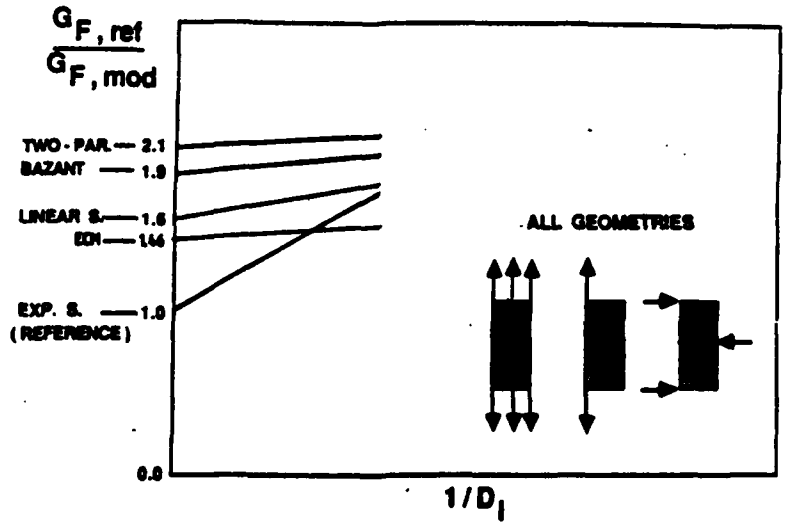

Figure 12: Ratio of $G_{F,reference}$ (FCM with quasi-exponential softening) to $G_{F,model}$ predicted for large sizes by ECM, TPM, SEL and FCM with linear softening

the predictions for large size structures are less accurate. The latter part of this conclusion is illustrated on Fig. 12 which compares the predictions of the various models in the limit as the representative size of the structure (D_i) tends to infinity. It should be mentioned that the comparison for ECM is only applicable to notched beam geometry and not to the other two geometries shown in Fig. 12.

Planas & Elices argue that the reason for the discrepancy among the models at large sizes is due to the inconsistency in the definition of size effect in the various models and therefore in that of the fracture energy based on this effect. It should however be mentioned that the prediction of ECM is the least conservative of the models studied.

MODE I FRACTURE TOUGHNESS FROM COMPACT SPECIMEN GEOMETRIES

In the foregoing we analysed and compared four methods (models) for determining mode I fracture toughness of concrete from notched three-point bend specimens. Only three of these models (TPM, SEL, ECM) were considered by Sub-Committee *A*. FCM was included in the above discussion for completeness of presentation. Except for ECM which is applicable only to notched three-point bend geometry, it is claimed that TPM, SEL and FCM can be applied to any geometry. We shall however see in the sequel that their applicability to geometries other than the notched three-point bend is not fully validated. In fact, it would seem that $CTOD_c$ of TPM is particularly susceptible to geometry and cannot therefore be

regarded as a material parameter without further validation. K_{Ic}^{s} on the other hand, would seem to be relatively insensitive to geometry changes.

Sub-committee *B* which analysed three compact geometries did not choose any of the above models *per se* as a starting point. Nevertheless, it is clear that its approach can be regarded as a judicious mix of the effective Griffith crack model (which forms the basis of TPM and ECM) and the scaling law (extrapolation to infinite size specimens) implied in SEL (Rossi *et al.* 1990). They started from the same premise as SEL, namely that LEFM is strictly applicable in the asymptotic limit of very large concrete structure (representative size $D \rightarrow \infty$). They claim that it is possible to obtain the intrinsic K_{Ic} for ordinary concrete using a DCB test specimen $3.5m$ long and $1.1m$ wide. They recognized however the difficulty associated with handling and testing such a specimen in a *normal* laboratory and proposed to carry out parallel tests on small specimens. The latter will yield *non-objective* K_{Ic} (i.e. size-dependent K_{Ic}), whilst the large specimens would yield the *objective* K_{Ic}. Their aim is to find an analytical relation between these two K_{Ic} with a view to establishing the scaling law (scale factor). If this aim is attained, then it would be possible to determine the intrinsic fracture toughness of 'in-situ' concrete from core samples.

With these two broad objectives in mind Rossi *et al.* (1990) chose the tapered DCB (Fig. 13) as the *infinitely* large specimen for determining the *objective* K_{Ic} and cylindrical and cubical wedge splitting geometries (Fig. 14) as the small specimens for determining the *non-objective* K_{Ic}. The choice of the last two geometries was dictated by the desire to accommodate on the one hand core samples drilled from existing concrete structures and dams and on the other fresh concrete specimens prepared using large aggregate (Jenq & Shah 1988).

The crack opening displacement was used as the feedback signal to obtain stable failure. Loading and unloading were performed during the test to determine the compliance function that was approximated by only four data points (crack lengths) resulting in a surprising inflexion point in the compliance function. Rossi *et al.*, (1990) are aware of the inaccuracies so caused and have also used the program FRANC to improve the accuracy. A sample calibration curve is shown in Fig 15 for the cubical WS specimen.

Typical load-COD plots for the three geometries are shown in Figs. 16-18, respectively. Concrete *A* refers to a mix with f_c = 51 *MPa*, E=36.6 *GPa* and indirect tensile strength = 3.7 *MPa*, whereas concrete *B* refers to a mix with the corresponding properties 55 *MPa*, 36 *GPa* and 4.5 *MPa*, respectively. The maximum size of aggregate used in concrete *A* was $20mm$ and that in concrete *B* was $12.5mm$.

Finite element calculations were performed to establish the compliance function $C(a)$ for each geometry. However, the above remark regarding the accuracy should be borne in mind in the practical use of these functions.

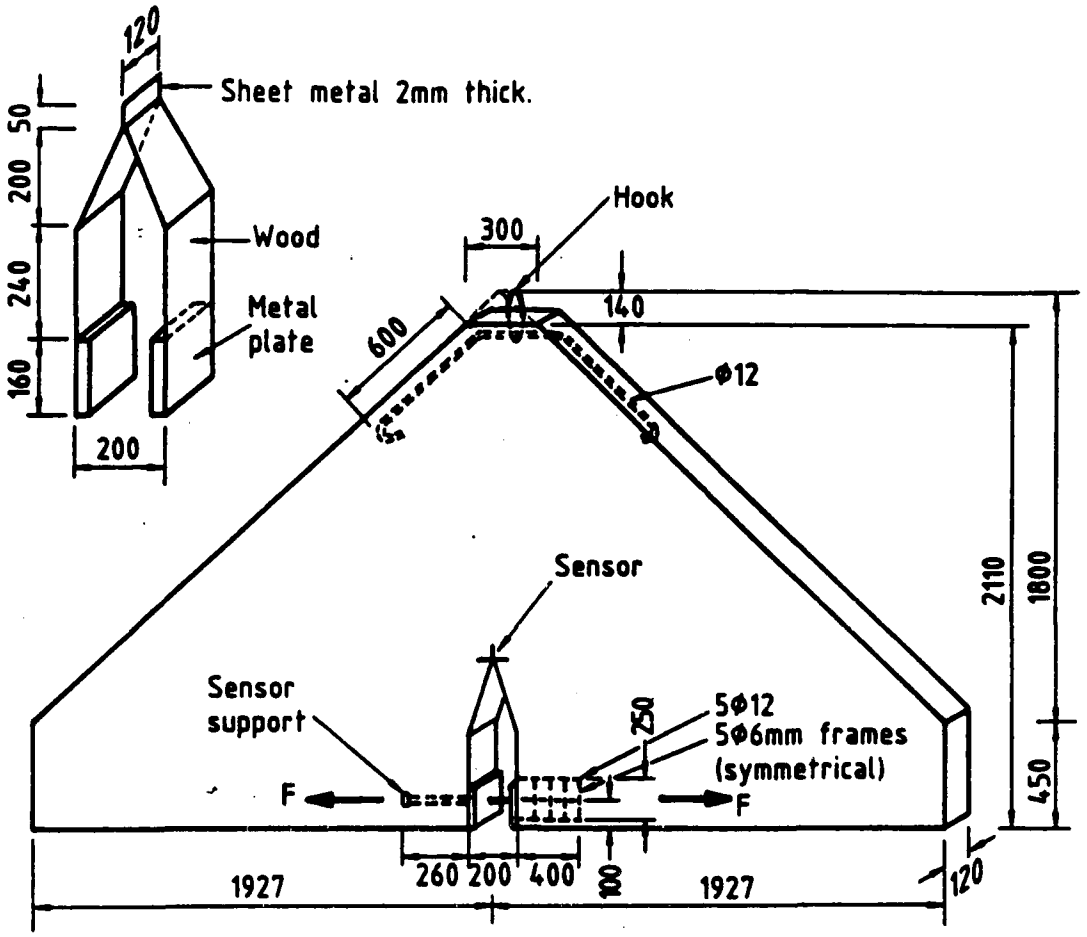

Figure 13: The tapered double cantilever beam (TDCB) specimen.

TDCB Specimen ($0.55 \leq a \leq 1.55m$):

$$C(a) = \frac{1}{E}(3410.75a^3 - 7470.05a^2 + 5700.1a - 1281)\ (m/N) \tag{32}$$

Cubical WS Specimen ($0.059 \leq a \leq 0.15m$):

$$C(a) = \frac{10^4}{E}(268.1a^3 - 58.7a^2 + 4.4a - 0.1)\ (m/N) \tag{33}$$

Cylindrical WS Specimen ($0.047 \leq a \leq 0.09m$):

$$C(a) = \frac{10^6}{E}(33.03a^3 - 5.19a^2 + 0.28a - 0.005)\ (m/N) \tag{34}$$

Then from the standard plane stress relationship between the stress intensity factor and rate of change of compliance with crack growth the following expressions for the R-curve result:
TDCB Specimen ($0.55 \leq a \leq 1.55m$):

$$K_I(a) = \frac{1}{\sqrt{2}\,B}(10232.25a^2 - 14940.1a + 5700.1)^{1/2}\,F\ (MPa\sqrt{m}), \tag{35}$$

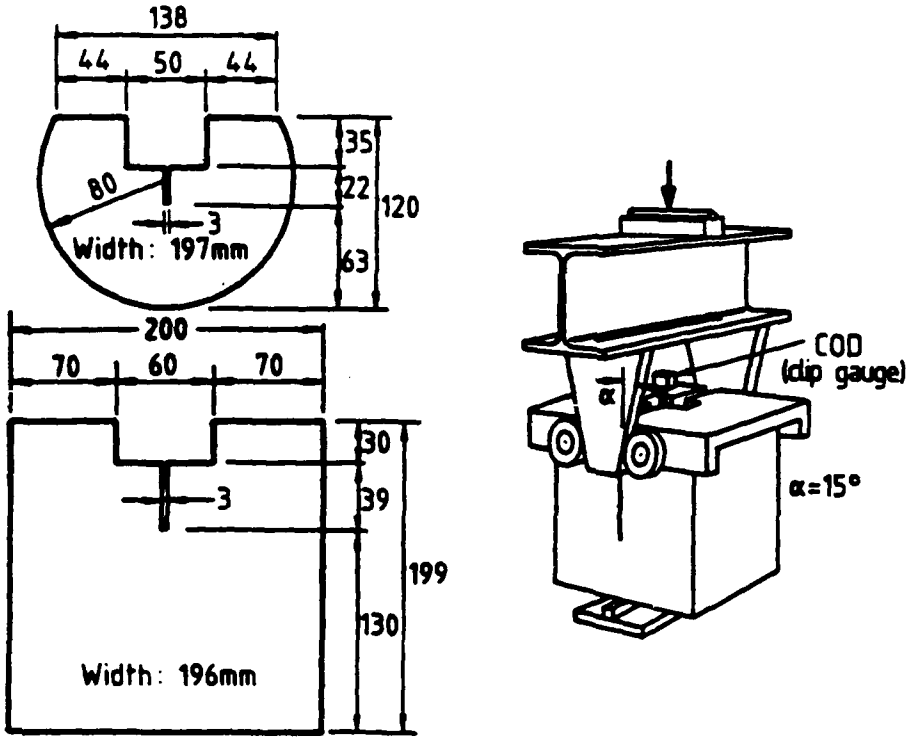

Figure 14: The cylindrical and cubical wedge splitting specimens, showing the load application device.

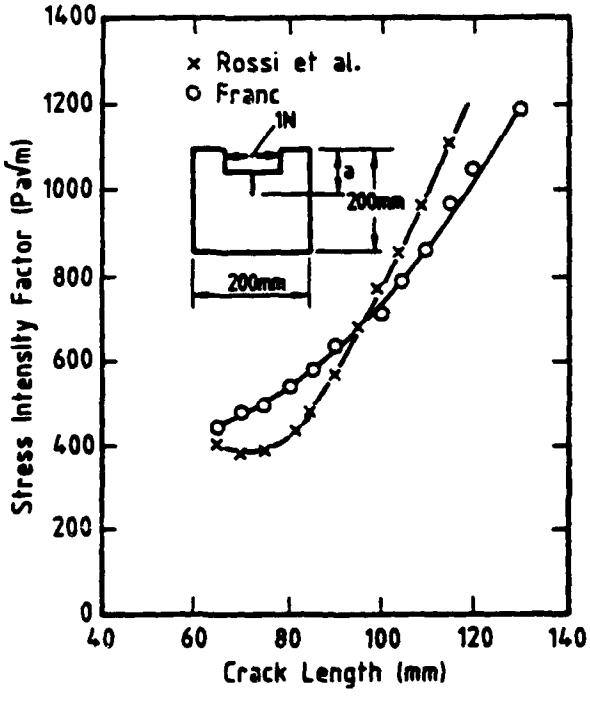

Figure 15: Stress intensity factor per unit applied force *vs* the crack length for the cubical WS specimen

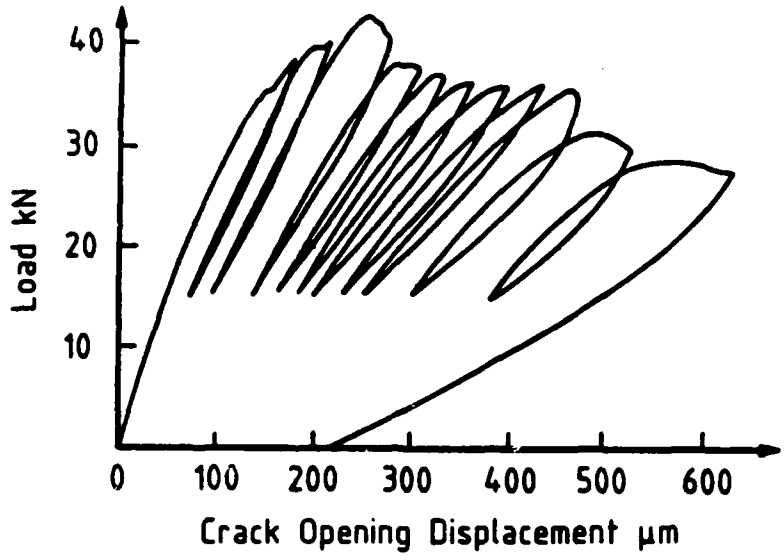

Figure 16: Load-COD plot for TDCB specimen from concrete A

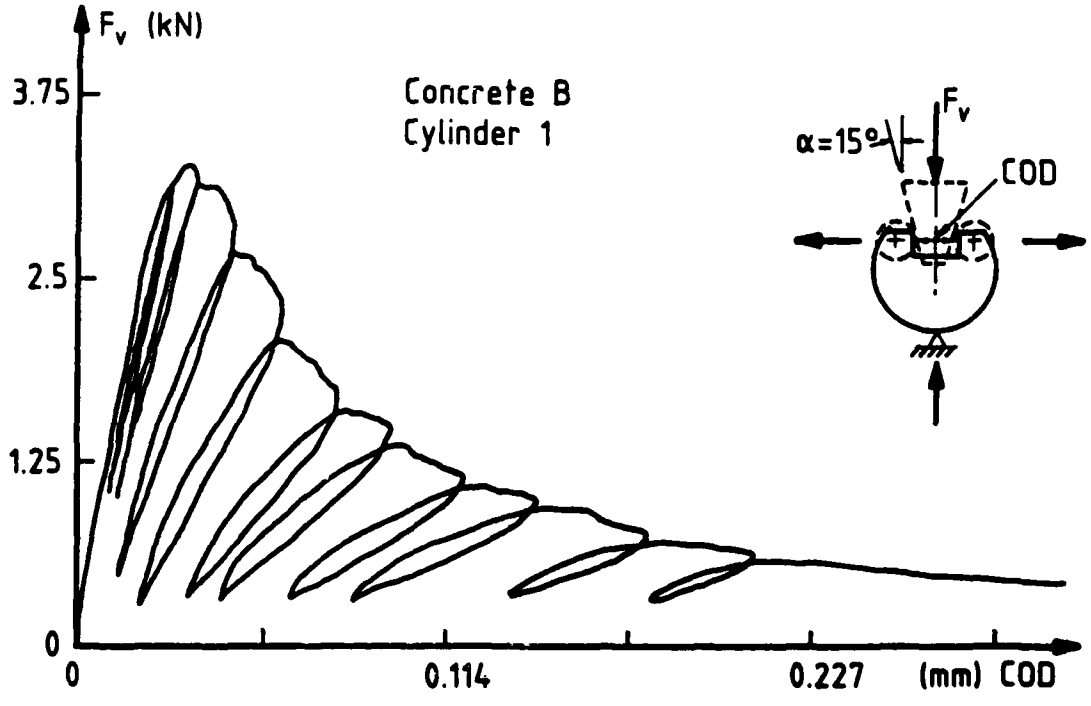

Figure 17: Load-COD plot for cylindrical WS specimen from concrete B

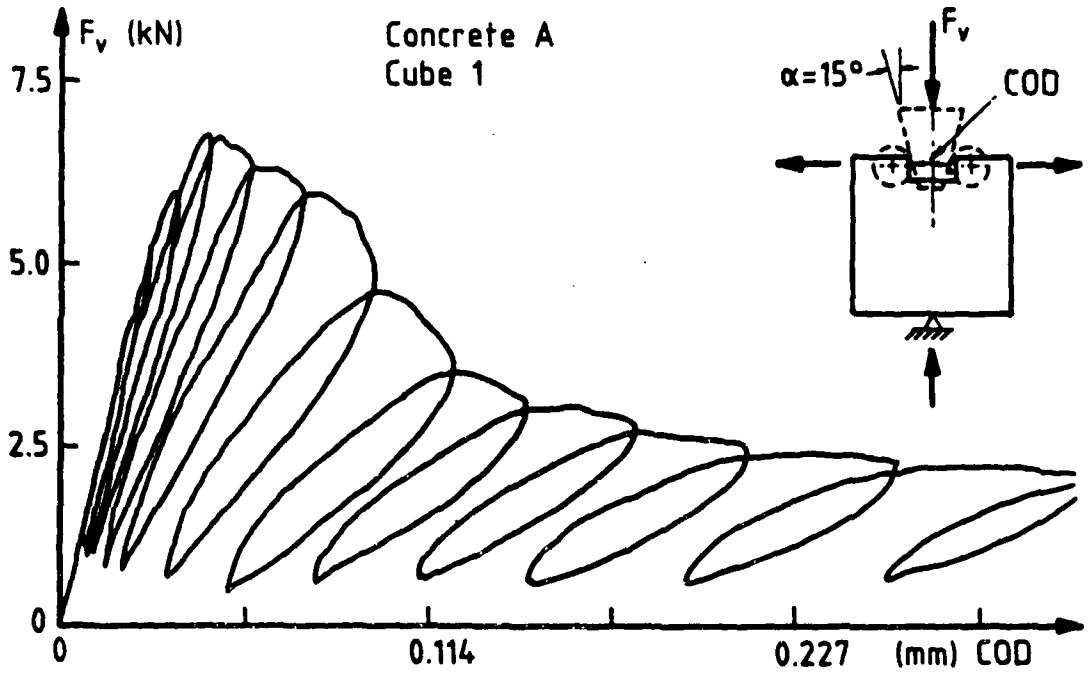

Figure 18: Load-COD plot for cubical WS specimen from concrete A

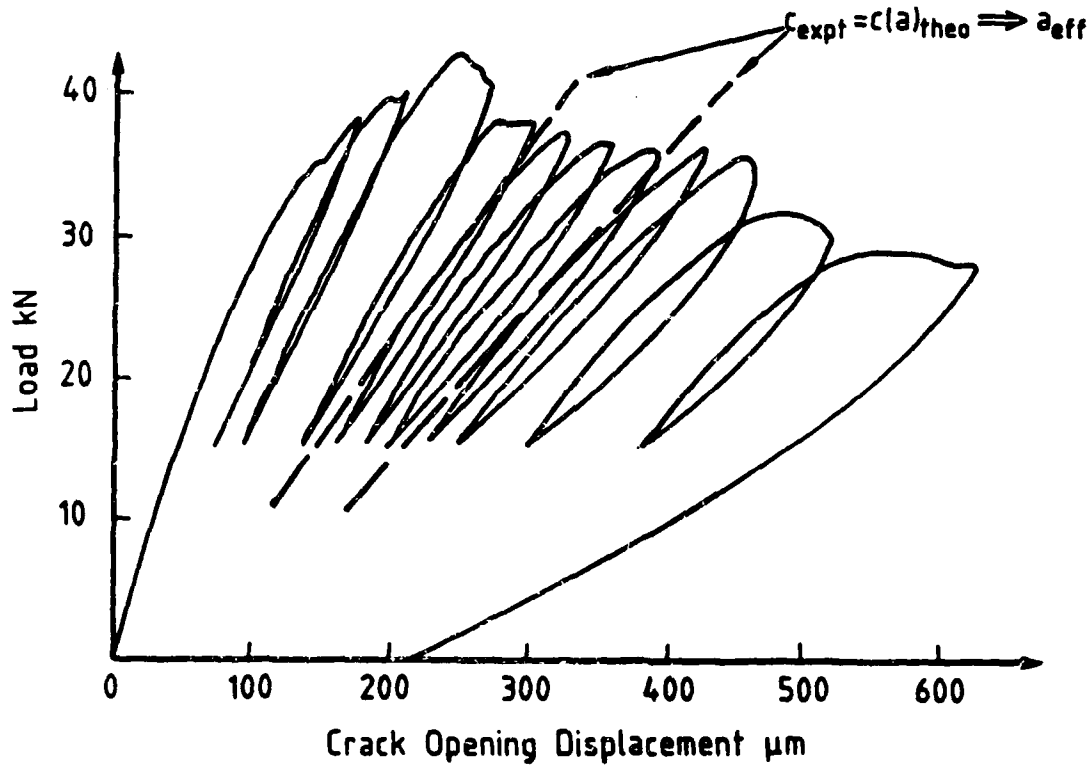

Figure 19: Determination of a_{eff}

Cubical WS Specimen ($0.059 \leq a \leq 0.15m$):

$$K_I(a) = \frac{100}{\sqrt{2}\,B}(804.3a^2 - 117.4a + 4.4)^{1/2}\,F_s\ (MPa\sqrt{m}), \tag{36}$$

Cylindrical WS Specimen ($0.047 \leq a \leq 0.09m$):

$$K_I(a) = \frac{1000}{\sqrt{2}\,B}(99.09a^2 - 10.38a + 0.28)^{1/2}\,F_s\ (MPa\sqrt{m}), \tag{37}$$

where B = thickness of the specimen.

To avoid having to use unreliable surface observations of crack advance, Rossi *et al.* (1990) use the notion of effective crack. The length of this crack a_{eff} is determined by equating the experimental compliance of the real crack having an irregular front preceded by a microcracked zone with that of an effective crack with a regular front (Fig. 19).

They also calculate an effective elastic modulus E_{eff} for use in compliance expressions (32)-(34). It is calculated by matching the theoretical compliance corresponding to a_0 with the experimental compliance during the first loading (i.e. in the elastic domain before the formation of any microcracks at the notch tip). The critical stress intensity factor K_{Ic} for each geometry is then calculated from (35)-(37) with a replaced a_{eff} and E by E_{eff}.

Typical $K_{Ic} - a_{eff}$ curves for the three geometries are shown in Fig. 20-22 respectively.

It is claimed that the mean value of the *objective* K_{Ic} following from the TDCB specimen is 2.21 and 2.11 $MPa\sqrt{m}$ for mixes A and B respectively, whereas the mean value and variation $= (K_{Ic})_{max} - (K_{Ic})_{min}/(K_{Ic})_{max}$ of the *non-objective* K_{Ic} determined from cylindrical WS specimen is 1.44 (33.7%) and 1.52 (14.3%) for mixes A and B, and from cubical WS specimen is 1.82 (17.4%) and 1.97 (11.8%), respectively.

Rossi *et al.* (1990) have shown that as the TDCB specimen is tested in a vertical position, the influence of the self-weight upon K_{Ic} is negligible. They also claim that the influence of the reinforcing bar (required for suspending the specimen) on the energy consumption is negligible. This is a rather doubtful claim in the light of the stiffening effect of the reinforcing bar on the TDCB system as a whole. It would be helpful if Rossi *et al.* could provide some quantitative estimate of this stiffening effect. Until such further evidence is forthcoming, the *objective* K_{Ic} determined from the TDCB must be regarded with caution.

They also propose the following regression equations for calculating the *objective* K_{Ic} of plain concrete from the results of small specimens

$$K_{Ic}(\text{Cubical WS}) = K_{Ic}(\text{TDCB})(1.075 - 0.075\frac{g}{g^*}) \tag{38}$$

$$K_{Ic}(\text{Cylindrical WS}) = K_{Ic}(\text{TDCB})(0.802 - 0.042\frac{g}{g^*}) \tag{39}$$

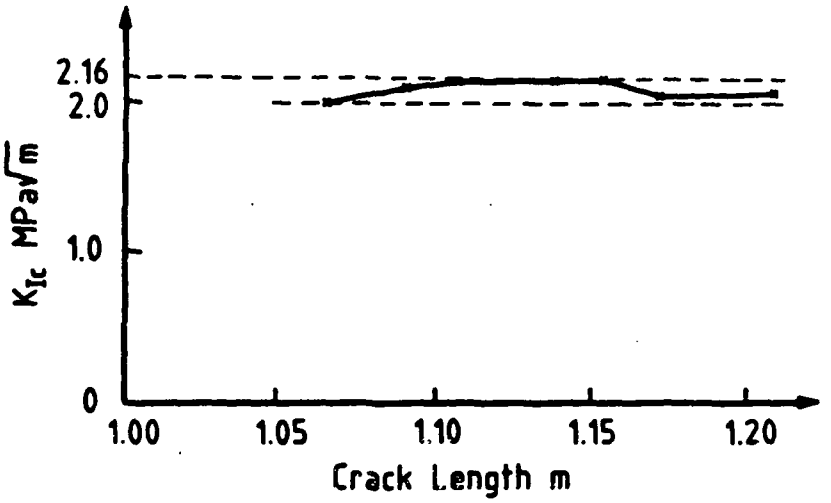

Figure 20: K_{Ic} *vs* a_{eff} for TDCB specimen from concrete A

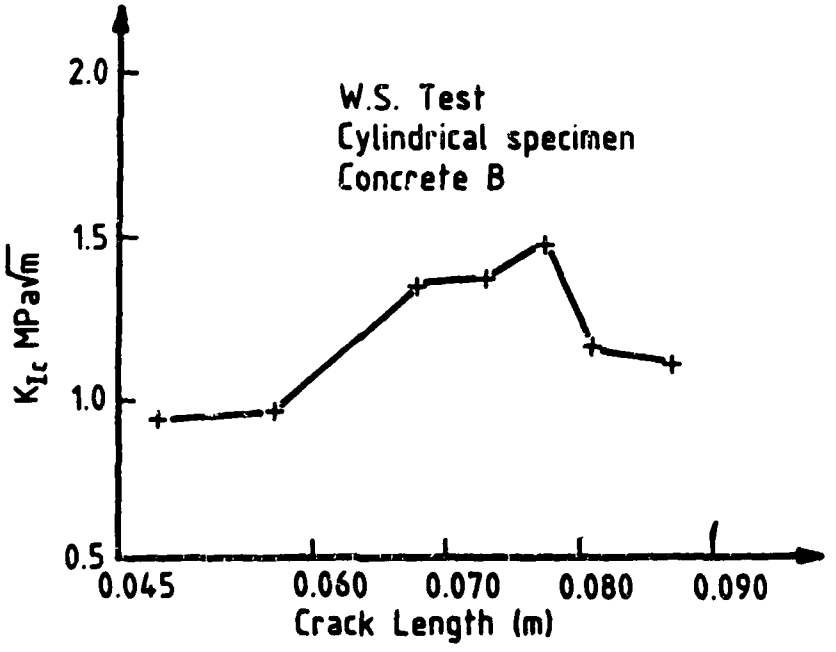

Figure 21: K_{Ic} *vs* a_{eff} for cylindrical WS specimen from concrete B

where $g^* = 6mm$ and $6 \leq g(mm) \leq 20$.

They have also calculated the specific fracture energy G_F as a function of the ligament length and found that it increases with increasing h, besides the maximum aggregate size, g. It is reasoned that the increase in G_F with h (Fig. 23) is because of the changes in the width and length of the fracture process zone as it propagates along the ligament, so that the longer the ligament, the more energy is expended outside of the localized fracture process zone.

Based on G_F and K_{Ic}, the Sub-committee report ends with the finite element evaluation of the maximum load based on a bilinear approximation to the tension-softening diagram, in much the same manner as it has been done by Petersson (1981).

CONCLUDING REMARK

The aim of this lecture was to review the various test methods and models considered by sub-committees *A* and *B* of RILEM TC-89 (FMT) and to present the results as they appear in the final reports of these sub-committees, with very occasional remarks on the drawbacks of one method or the other. In a general review of this nature it is very tempting to criticise methods or models which may be competing with one's own. It is to be hoped that this reviewer has avoided that temptation, and that the presentation will result in a lively debate and discussion which will be included in the final version of this paper.

REFERENCES

Bažant, Z.P., (1984) Size effect in blunt fracture: concrete, rock, metal, *J. of Eng. Mech., ASCE*, **110**, pp. 518-535.

Bažant, Z.P., Kim, J.K. and Pfeiffer, P.A., (1986) Determination of fracture properties from size effect tests, *J. of Struct. Eng., ASCE*, **112**, No.2, pp. 289-307.

Brown, W.F. and Srawley, J.E., (1966) Crack toughness testing of high strength matallic matyerials, *ASTM-STP No. 410*, p. 130.

Hillerborg, A., Modeer, M. and Petersson, P.E. (1976), Analysis of Crack Formation and Crack Growth in Concrete by Means of Fracture Mechanics and Finite Elements, *Cement Concr. Res.*, **6**, pp. 773-782.

Jenq, Y.-S. and Shah, S.P., (1985) Two parameter fracture model for concrete, *ASCE, J. Eng. Mech.*, **111**, pp. 1227-1241.

Jenq, Y.-S. and Shah, S.P., (1988) On the concrete fracture testing methods, *Proceedings of the International Workshop on Fracture Toughness & Fracture Energy*, Sendai, pp. 443-463.

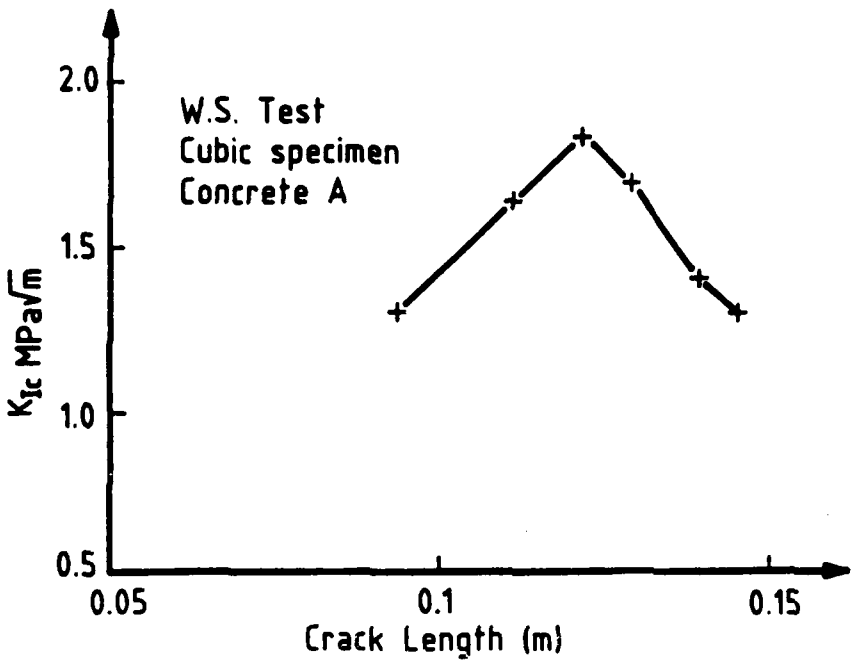

Figure 22: K_{Ic} vs a_{eff} for cubical WS specimen from concrete A

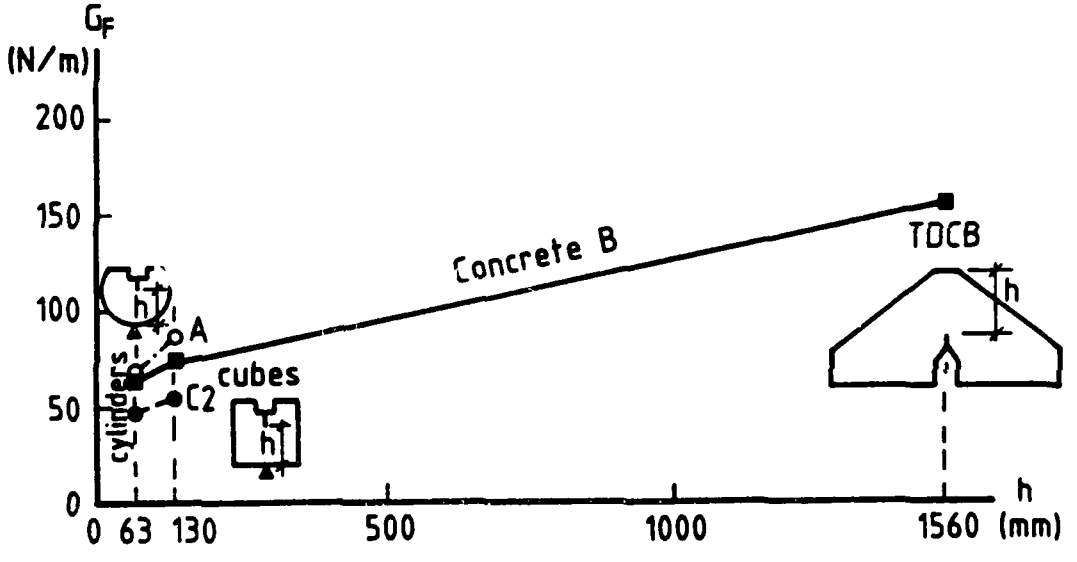

Figure 23: Specific fracture energy G_F *vs* ligament length

John, R., Shah, S.P. and Jenq, Y.-S., (1987) A fracture mechanics model to predict the rate sensitivity of mode I fracture for concrete, *Cem. and Conc. Research*, **17**, pp. 249-262.

Karihaloo, B.L. and Nallathambi, P., (1989 a) An improved effective crack model for the determination of Fracture toughness of concrete, *Cem. and Conc. Research*, **19**, pp. 603-610.

Karihaloo, B.L. and Nallathambi, P., (1989 b) Effective crack model and tension-softening models, ***Fracture of Concrete and Rock: Recent Developments*** (Eds: S. P. Shah, S. E. Swartz and B. Barr), Elsevier Science., pp. 701-710.

Karihaloo, B.L. and Nallathambi, P., (1990 a) Final report of Sub-committee *A* (Chairman B. L. Karihaloo) notched beam test: mode I fracture toughness of ***RILEM TC89-FMT***, (Chairman: S. P. Shah), p.86. To be published by Chapman & Hall, Oct. 1990.

Karihaloo, B.L. and Nallathambi, P., (1990 b) Size effect prediction from effective crack model for plain concrete, *Matériaux et Constructions*, (in press).

Nallathambi, P. and Karihaloo, B.L., (1986 a) Determination of specimen-size independent fracture toughness of plain concrete, *Magazine of Concrete Research*, **38**, pp. 67-76.

Nallathambi, P. and Karihaloo, B.L., (1986 b) Stress intensity factor and energy release rate for three-point bend specimens, *Engineering Fracture Mechanics*, **25**, pp. 315-321.

Nallathambi, P. and Karihaloo, B.L., (1990a) Performance of effective crack and two-parameter models, *ASCE, J. of Eng. Mech.*, (submitted for publication).

Nallathambi, P. and Karihaloo, B.L., (1990b) Fracture of concrete: application of effective crack model, *Proc. of the 9th Int. Conf. on Expt. Mech.*, Lyngby, Denmark.

Petersson, P.E. (1981), Crack Growth and Development of Fracture Zones in Plain Concrete and Similar Materails, *Report TVBM 1006*, University of Lund, Sweden.

Planas, J. and Elices, M. (1987), Asymptotic Analysis of the Development of a Cohesive Crack Zone in Mode I Loading for Arbitrary Softening Curves, *Proceedings SEM-RILEM International Conference*, Houston, Eds: S. P. Shah and S. E. Swartz, pp. 384.

RILEM FMC-50 (1985), Determination of the fracture energy of mortar and concrete by means of three-point bending tests on notched beams, *RILEM, Matériux et Constructions*, **18**, pp. 287-290.

Rossi, P, Brühwiler, E, and Chhuy, S., (1990) Fracture mechanics of concrete: Test methods, *Sub-committee B, RILEM TC89-FMT*, Compact Specimen Testing, p. 33. To be published by Chapman & Hall, Oct. 1990.

Srawley, J. E., (1976) Wide-range stress intensity factor expressions for ASTM E399 standard fracture toughness specimens, *Int. J. of Fracture*, **12**, pp. 475-476.

Session 3:

Theoretical Fracture Mechanics Considerations

Chairs:

David Darwin
University of Kansas
Lawrence, U.S.A

Brian Moran
Northwestern University
Evanston, U.S.A

Reporter:

John Rudnicki
Northwestern University
Evanston, U.S.A

RATE EFFECT, SIZE EFFECT AND NONLOCAL CONCEPTS FOR FRACTURE OF CONCRETE AND OTHER QUASI-BRITTLE MATERIALS

Zdeněk P. Bažant
Walter P. Murphy Professor of Civil Engineering
Northwestern University, Evanston, Illinois 60208, USA

ABSTRACT. The lecture reviews several recent results achieved at Northwestern University in the problem of size effects and nonlocal concepts for concrete and other brittle heterogeneous materials, and presents a new method for calculating the load-deflection curves of fracture specimens or structures with time-dependent crack growth and viscoelastic material behavior. The results reviewed deal with the size effect law in fracture and its exploitation for determining material fracture characteristics, statistical generalization of the size effect law with a nonlinear reformulation of Weibull's weakest-link theory, determination of the size dependence of the fracture energy determined by work-of-fracture method, nonlocal models for smeared cracking and damage, microstructural determination of the nonlocal material properties and fracture process zone behavior, size effect in fatigue fracture of concrete, and use of the size effect for determining the fracture properties of high-strength concrete.

1. Introduction

Fracture analysis of concrete structures has to deal with two important complicating characteristics: the distributive nature of cracking and damage in concrete, which causes the fracture process zone to be relatively large and engenders a size effect, and time dependence of both the crack growth and the material behavior. The nonlinear behavior caused by the existence of a large fracture process zone has been in the focus of attention for some time and its treatment is becoming quite well understood [1-3, etc.]. Attention to the size effect is more recent [8] but it has already led to some useful extensions of fracture theory and a new method for determining material fracture properties [4-7, 9-12]. The existence of the rate effect has been known for a long time and has been studied extensively with regard to dynamic fracture. However, the nonlinear fracture aspects of the rate effect, which are manifested in interaction with the size effect, have not received attention until recently, although they are no doubt very important for predicting the response of structures.

The present lecture intends: (1) to present a new effective and relatively simple method for calculating the load-deflection response of a structure with a large fracture process zone, time-dependent fracture growth, and viscoelastic material properties; and (2) to review several recent results achieved at Northwestern University. No claims for exhaustive or even balanced coverage of the latest developments are made. Due to exploding research

activity, this would be beyond the scope of the present paper.

2. Review of Some Recent Results

2.1 A REVIEW OF SIZE-EFFECT - THE SALIENT CHARACTERISTIC OF FRACTURE

The structural size-effect is the most important characteristic and the easiest measurable consequence of nonlinear fracture behavior. Considerable attention has been devoted at Northwestern University to the phenomenologic description of the size effect [8-12] as well as its physical mechanism. We will begin by a brief overview of the latest phenomenologic characterization of fracture in terms of the size effect and the consequences for the measurement of fracture properties.

The size effect may be defined in terms of the nominal strength $\sigma_N = c_n P_u/bd$ (for 2D) or $c_n P_u/d^2$ (for 3D) in which P_u = maximum load of geometrically similar specimens of size d (dimension) and, in case of two dimensions, thickness b; c_n = factor chosen for convenience. Under the assumption that there is a large fracture process zone that is not negligible compared to d, and that the crack at failure of geometrically similar structures of different sizes is also geometrically similar, the nominal strength approximately obeys the size effect law [8]:

$$\sigma_N = B f_u (1+\beta)^{-1/2}, \qquad \beta = d/d_0 \tag{1}$$

in which f_u = any measure of material strength, e.g., the tensile strength, and B, d_0 = empirical constants. This law describes a smooth transition from plastic limit analysis, for which there is no size effect (σ_N = constant) to linear elastic fracture mechanics (LEFM), for which the size effect is the maximum possible, given by $\sigma_N \propto \beta^{-1/2}$. The plot of Eq.1 is shown in Fig.1. The horizontal asymptote represents the limiting case of plastic limit analysis, and the inclined asymptote of slope - 1/2 the limiting case of LEFM. Parameter d_0, called the transitional size, corresponds to the intersection of these two asymptotes. Eq.1 has originally been derived by dimensional analysis and similitude arguments, based on the hypothesis that the energy release due to fracture depends not only on the fracture length but also on a second length characteristic that is approximately a material property and characterizes either the effective length or the effective width of the fracture process zone, or the nonlocal properties of an equivalent continuum.

Under certain further simplifying assumptions based on equivalent LEFM, it has been shown [11] that the size effect law from Eq.1 can also be written in the form

$$\sigma_N = c_n \left(\frac{E G_f}{g'(\alpha_0) c_f + g(\alpha_0) d} \right)^{1/2} \tag{2}$$

in which G_f = fracture energy of the material, defined as the energy required for crack propagation in an infinitely large specimen, E = Young's elastic modulus, c_f = effective length of the fracture process zone in an infinitely large specimen (a material constant), $\alpha_0 = a_0/d$, a_0 = length of initial notch of crack, and $g(\alpha)$ = non-dimensionalized energy release rate of the specimen of the given geometry, which is obtained by writing the LEFM solution

for the energy release rate in the form $G = P^2 g(\alpha)/E\,b^2\,d$ where P is the applied load or reaction, $\alpha = a/d$, $a = a_0 + c$, c = crack extension from the notch or initial crack tip. These formulas are valid for plain stress. For plain strain or axisymetric propagation, E must be replaced by $E/(1-\nu^2)$. Defining the so-called intrinsic strength $\tau_N = (P_u/bd)g'(\alpha_0)$ and intrinsic size $\bar{d} = g(\alpha_0)d/g'(\alpha_0)$, one can rewrite Eq.2 in the form

$$\tau_N = \left(\frac{E\,G_f}{c_f + \bar{d}}\right)^{1/2} \tag{3}$$

which involves only material constants EG_f and c_f. Comparing Eq.2 or 3 with Eq.1, one gets the following expressions for material fracture constants

$$G_f = \frac{B^2 f_u^2}{c_n^2 E} d_0 g(\alpha_0), \qquad c_f = d_0 \frac{g(\alpha_0)}{g'(\alpha_0)} \tag{4}$$

Thus, after measuring the maximum loads for geometrically similar specimens of sufficiently different sizes, one can determine B and d_0 by least-square fitting all the data (Eq.1 can be rearranged to a linear regression plot), and then evaluate the fracture energy and the effective process zone length from Eq.4 (strictly on the basis of maximum load data). This method is probably the easiest to implement in the laboratory (even a soft testing machine is adequate and no measurements of displacements or crack lengths are required). The method has been verified by numerous tests on concrete and rock. The results are, by definition, size independent and they were also proven to be approximately shape independent, since very different fracture specimen geometries furnished approximately the same results, as expected theoretically.

The ratio β, which may be calculated by one of the following two expressions,

$$\beta = \frac{g(\alpha_0)}{g'(\alpha_0)} \frac{d}{c_f}, \qquad \beta = \frac{B^2 g(\alpha_0)}{c_n^2} \frac{d\,f_u^2}{E\,G_f} \tag{5}$$

is called the brittleness number. For $\beta \to 0$, plasticity applies, and for $\beta \to \infty$, LEFM applies. For $\beta < 0.1$ it is possible to use plasticity as an approximation, and for $\beta > 10$ it is possible to use LEFM. For the intermediate β-values, nonlinear fracture mechanics must be used. However, if the transitional size d_0 is determined, an approximate prediction of maximum load can be obtained by interpolating between the solutions of plasticity and LEFM according to Eq.1. This should be useful for design; proposals to modify the existing design formulas for diagonal shear failure of beams (without or with stirrups, unprestressed or prestressed), punching shear failure of slabs, torsional failure of beams, pullout failures of bars and of studded anchors have been made and verified by extensive tests [14-22].

Based on size effect measurements, other basic nonlinear fracture characteristics can also be obtained. The critical crack-tip opening displacement may be determined as

$$\delta_c = \frac{8\,K_{If}}{E}\sqrt{\frac{c_f}{2\pi}}, \qquad \text{with} \quad K_{If} = \sqrt{E\,G_f} \tag{6}$$

Furthermore, the R-curve (resistance curve) for the specimen or structure can be calculated as

$$R(c) = G_f \frac{g'(\alpha_1)}{g'(\alpha_0)} \frac{c}{c_f}, \quad \text{with} \quad \frac{c}{c_f} = \frac{g'(\alpha_0)}{g(\alpha_0)} \left(\frac{g(\alpha_1)}{g'(\alpha_1)} - \alpha_1 + \alpha_0 \right) \tag{7}$$

in which α_1 is a dummy parameter representing the relative crack length for structure size for which $R(c)$ corresponds to the maximum load (Fig.2). Choosing various values of α_1, the values of R (critical G-value required for further crack growth) and c can be calculated from Eq.7, and thus the $R(c)$-curve defined parametrically. This curve is by definition size independent but depends on the geometry of the structure. For very different geometries, very different R-curves can be obtained. Eq.7 defines the master R-curve for an infinitely large specimen. For a specimen of finite size, the R-curve given by Eq.7 is followed only up to the maximum load P_u, and after that the actual R-curve is constant (horizontal), with the R-value equal to that attained at the peak load [23, 24]. The reason is that for prepeak loading the fracture process zone grows in size while remaining attached to the crack or notch tip (provided structures with $g'(\alpha_0) > 0$ are considered), whereas in post-peak softening the fracture process zone gets detached from the notch tip and travels ahead retaining approximately a constant size.

Using the equivalent LEFM approach, the curve of load or reaction P versus the load-point displacement u may be calculated from the equations

$$u = P \left(C_0 + \frac{2}{bE} \int_0^\alpha g(\alpha') d\alpha' \right), \qquad P = b \frac{Ed}{g(\alpha)} R(c), \tag{8}$$

in which C_0 is the compliance for a specimen without any crack. Choosing various values of c, with $\alpha = (a_0 + c)/d$, the values of P and u can be evaluated from Eq.8, defining the load-deflection curve parametrically.

Eq.8 provided a strong verification of the size effect method of determining fracture properties. The material fracture parameters were determined solely from the maximum loads measured on geometrically similar rock fracture specimens of very different sizes [23]; then the R-curve was calculated from Eq.7, and from that the load-deflection diagram shown in Fig.3 from Eq.8 was computed. The results showed excellent agreement with the measured load deflection curve (Fig.3). Similar agreement has been obtained for concrete [13].

2.2. STATISTICAL GENERALIZATION AND WEIBULL'S EFFECT

The fact that Eq.1 or Eq.3 can be algebraically rearranged to a linear regression plot of $Y = \tau_N^{-2}$ versus $X = \bar{d}$ makes it possible to obtain easily the statistics of the material fracture parameters. The coefficients of variation of fracture toughness (defined for a specimen of infinite size), the effective length of the fracture process zone, and the fracture energy may be approximately obtained as

$$\omega_{K_{If}} = \frac{1}{2}\omega_A, \omega_{c_f} = (\omega_A^2 = \omega_c^2)^{1/2}, \omega_{G_f} = (4\omega_{K_{If}}^2 + \omega_E^2)^{1/2} \tag{9}$$

in which ω_A and ω_C are the coefficients of variation of the aforementioned slope and of the

Y-intercept of the linear regression plot, and ω_E is the coefficient of variation of the elastic modulus of concrete [11].

Eq.9 takes care only of the uncertainty of the material parameter values in the foregoing deterministic model. More realistically, one should note that the failure process in itself is stochastic, and the simplest vehicle to take that into account is Weibull's reasoning. However, the classical Weibull-type formulations do not apply to concrete structures because they exhibit stable growth of cracking with significant stress redistributions prior to maximum load. Good results, however, can be obtained with a nonlocal generalization of Weibull approach [25], in which the survival probability of the structure is calculated as the joint probability of survival of all the material elements based on the stress distribution just prior to failure, in which the material failure probability is determined from Weibull distribution using the nonlocal stress average, $\bar{\sigma}_i$;

$$-\ln(1-P_f)=\int_V \sum_{i=1}^{n}\left(\frac{\bar{\sigma}_i}{\sigma_0}\right)^m \frac{dV}{V_0}, \quad \bar{\sigma}_i(\underset{\sim}{x})=\int_V \alpha(\underset{\sim}{s}-\underset{\sim}{x})\sigma_i(\underset{\sim}{s})dV(s) \tag{10}$$

in which P_f = failure probability of the structure, σ_i = principal stresses ($i=1,2,3$), V = volume of the structure, V_0 = volume of a small representative volume of the material, $\underset{\sim}{x}, \underset{\sim}{s}$ = coordinate vectors, $\alpha(\underset{\sim}{s}-\underset{\sim}{x})$ = given weighting function of a nonlocal material model (based on characteristic length ℓ); and m, σ_0 = Weibull modulus and scale parameter determined by fitting Weibull distribution to direct tensile test data (assuming a zero Weibull threshold). It has recently been found [25] that the nonlocal Weibull concept leads, under certain approximations, to the following generalization of the size effect law (Fig.4).

$$\bar{\sigma}_N = B\, f_u(\beta^{2n/m}+\beta)^{-1/2} \tag{11}$$

in which the overbar denotes the mean nominal strength, $\bar{\sigma}_N$; and $n = 2$ or 3 for two- or three-dimensional similarity. For concrete, typically $m = 12$. For large structure sizes, Eq.11 aproaches LEFM, same as Eq.1. For small structure sizes, $\beta \to 0$, Eq.11 asyptotically approaches the classical Weibull size effect, $\bar{\sigma}_N = \beta^{-n/m}$, which gives a rather weak size effect, $\bar{\sigma}_N = \beta^{-1/6}$ for two-dimensional similarity. Thus, Eq.11 represents a smooth transition from the classical Weibull size effect to LEFM. Eq.11 has been shown to agree with the data for concrete somewhat better than Eq.1, but the difference is rather small except when dealing with very small structure sizes. The formulation in Eq.2-7 can be generalized in accordance with Eq.11.

2.3. SIZE DEPENDENCE OF FRACTURE ENERGY OBTAINED BY CURRENT RILEM METHOD

The fact that the size effect method based on the maximum load yields excellent predictions of the load-deflection curves, in good agreement with measurements, makes it possible to exploit this formulation for examining the fracture energy determined from the area under the load-deflection curve, which represents the work-of-fracture method proposed for ceramics by Nakayama [26], and by Tattersall and Tappin [27], and introduced for concrete by [28,29]. The work of fracture has been calculated for concrete specimens on the basis

of the load-deflection curve obtained from the R-curve (Eqs.7 and 8), keeping the R-value constant for the post-peak softening (area in Fig.2c). This calculation indicates a size effect on the value of the fracture energy G_f^R, due to the fact that the peak load occurs at different points of the R-curve for specimens of different sizes. The calculation results are shown in Fig.2d; note that the size dependence of G_f^R is quite strong, in fact stronger than that of the R-curve, although not as strong as that of the apparent fracture energy G_c determined by LEFM method. This agrees with the conclusions of Planas and Elices [4], who showed that the fracture energy measurements according to the RILEM standard, which is based on the work-of- fracture method, must be extrapolated to a specimen of infinite size in order to obtain consistent (size independent) results.

2.4. NONLOCAL DAMAGE MODELS

In finite element analysis of damage and cracking in concrete structures, the size effect has long been neglected. Unfortunately, most of the existing models are based on plasticity or its modifications and exhibit no size effect, which is unacceptable for concrete structures. Modeling of the size effect should be accepted as the basic criterion for correctness of a finite element code. The only way to achieve a correct size effect in agreement with Eq.1 is to either use some type of a nonlinear fracture model for a line crack with cohesive crack-bridging zone, or a nonlocal form of a finite element code for distributed damage of smeared cracking. The latter approach is more versatile and perhaps somewhat more realistic due to the diffuse nature of cracking in reinforced concrete structures. A nonlocal generalization of the classical smeared cracking formulation has been introduced in [30], and a good agreement with size effect data and with Eq.1 has been demonstrated. A more realistic constitutive flaw for the evolution of damage or cracking in the fracture process zone is the microplane model, in which the material properties are characterized separately on planes of various orientation in the material. This model has recently been generalized to a nonlocal form, and it was again demonstrated that such a generalization agrees well with size effect fracture data as well as Eq.1 (Fig.5); see [31].

2.5. MICROMECHANICS MODELING

It is very difficult to identify the strain-softening constitutive relations for the fracture process zone on the basis of measurements alone. Therefore, micromechanics modeling could be of great help. Micromechanics models need to represent systems of microcracks that are observed experimentally. Therefore, initial studies of micromechanics of fracture of concrete concentrated on the analysis of an array of cracks in a homogeneous elastic matrix. Some observed features could be reproduced with such models, particularly the strain-softening behavior. This was, for example, demonstrated for an array of parallel microcracks spaced on a cubic lattice and subjected to a microscopic uniaxial stress field. Application of the homogenization conditions to such a crack array also showed that the corresponding macroscopic smoothing continuum is nonlocal, and of the nonlocal damage type. Stability analysis of the interacting crack systems, however, indicated that such a model is unrealistic because only one of the cracks can grow in a stable manner, which is of course not what is seen in

experiments. The reason for this discrepancy no doubt consists in the micro-inhomogeneity of the material, especially the presence of harder inclusions.

Interaction of cracks and inclusions in an elastic matrix has been studied in [32], using a Green's function approach (Fig.6). Approximate solutions have been obtained for a crack interacting with many inclusions, for various geometric configurations. The solution was used to obtain an apparent R-curve of a microcrack in a smoothed homogeneous matrix such that its growth is the same as the growth of the actual crack interacting with inclusions. It was found that in many situations the apparent R-curve is rising, which has a stabilizing effect on the system of cracks. The apparent rising R-curve can stabilize a system of many cracks, such that many cracks can grow simultaneously, in agreement with observations.

As a conclusion from this study, it appears that a study of crack arrays in a homogenous continuum is in general insufficient, and the presence of inhomogeneities representing the aggregate pieces must be considered simultaneously in the analysis. It should be also noted that this result is simular to that of Gao and Rice [33], who however considered only the case when the elastic moduli of matrix and inclusions differ very little, using perturbation method. A special problem of this type has also been solved by Mori et al. [34].

2.6. SIZE EFFECT CORRECTION TO PARIS LAW FOR FATIGUE FRACTURE

Under repeated loading, cracks tend to grow, which is described by the well-known Paris law [35, 36]. Applicability of this law to fatigue crack growth in concrete has been verified by Swartz et al. [37]. Since Paris law describes the crack growth as a function of the amplitude of the stress intensity factor, a question arises with respect to the size effect. In monotonic loading, the stress intensity factor does not provide sufficient characterization of fracture when different sizes are considered, as is known from the previously discussed size effect law. The same phenomenon must be expected for cyclic fracture, especially since fracture under monotonic loading can be regarded as a limiting case of fracture under cyclic loading. Recent fatigue fracture experiments on notched concrete beams at Northwestern University [38] have shown that the fatigue crack growth in geometrically similar specimens of different sizes can be described by the following law:

$$\frac{\Delta a}{\Delta N} = C\left(\frac{\Delta K_I}{K_{I_c}}\right)^n, \qquad K_{I_c} = K_{I_f}\left(\frac{\beta}{1+\beta}\right)^{1/2} \tag{12}$$

in which K_{I_f} = fracture toughness for an infinitely large specimen, ΔK_I = amplitude of the stress intensity factor, $\Delta a/\Delta N$ = crack length extension per cycle; and C, n = constants. For $\beta \to \infty$, this equation reduces to the well-known Paris law. For normal size concrete specimens, however, the deviations from Paris law are quite significant. This is revealed by the experimental results in Fig.7 for three different sizes in the ratio 1:2:4. In this plot, the Paris law gives an inclined straight line of slope n, but it is seen from Fig.7 that for each size one obtains a different straight line. The solid straight lines represent Eq.12.

2.7. FRACTURE OF HIGH STRENGTH CONCRETE

It has already been well established that high strength concrete is more brittle than

normal strength concrete. This question has been investigated at Northwestern University using the size effect method of determining material fracture properties [13]. Concrete of 28-day standard compression strength 12,000 psi, typical for high-rise construction in the Chicago area, has been used. The results are summarized in Fig.8, which shows the relative values of various material properties compared to the normal strength concrete, particularly the compression strength f'_c, modulus of rupture f_r, Young's modulus E, fracture toughness K_{I_c} and fracture energy G_f (both for an infinitely large specimen), effective length of the fracture process zone c_f, and Irwin's characteristic size of the nonlinear zone ℓ_0. Whereas the compression strength is 2.6-times higher than that of normal-strength concrete, the fracture toughness is increased only by about 25%, fracture energy by about 15%, and the effective lengths of the fracture process zone is decreased 2.5 times and the characteristic size of the nonlinear zone is *decreased* approximately 5-times. Consequently, the brittleness number of the high strength concrete structure is approximately 2.5-times *higher* than the brittleness of an identical structure made of normal-strength concrete. This aspect of high strength concrete is unfavorable for design and requires special attention.

3. Effect of Rate of Loading and Creep

Fracture of rocks as well as ceramics is known to exhibit a significant sensitivity to the rate of loading. For concrete, the influence of the rate of loading on fracture propagation is even more pronounced and is further compounded by viscoelasticity of the material in the entire structure. To calculate the response of a structure, as well as to be able to evaluate laboratory measurements, the most important is the determination of the load or reaction P as a function of the load-point displacement u and time t for a prescribed loading regime. The following simple method has been formulated for this purpose.

We begin by rewriting Eq.8 for a structure with rate-independent fracture as follows

$$u = C(a)P, \qquad C(a) = C_0 + \frac{2}{bE}\varphi(\alpha), \qquad P = b\sqrt{d}\frac{K_{IR}(c)}{k(\alpha)} \tag{13}$$

in which $C(a)$ is the secant compliance of the structure at growing crack length a, C_0 is the elastic compliance of the same structure without crack, $K_{IR}(c) = \sqrt{ER(c)}$ = R-curve of fracture toughness (material property), $c = a - a_0$ = crack extension from the notch or initial crack of length a_0, d = characteristic dimension of the structure, $\alpha = a/d, b$ = structure thickness, $\varphi(\alpha) = \int_0^\alpha g(\alpha')d\alpha'$, $k(\alpha) = \sqrt{g(\alpha)}$. When both the load and the crack length are varying (and $\dot{a} = da/dt \geq 0$) are varying, differentiation of Eq.12 yields

$$\dot{u} = C(a)\dot{P} + P\frac{dC(a)}{da}\dot{a} \tag{14}$$

$$\dot{a} = \Phi(a)\dot{P} \tag{15}$$

in which we introduce the notation

$$\Phi(a) = \frac{1}{b\sqrt{d}}\left[\frac{K'_{IR}(c)}{k(\alpha)} - \frac{K_{IR}(c)}{k(\alpha)^2}\frac{k'(\alpha)}{d}\right]^{-1} \tag{16}$$

Materials which under a constant fast rate of loading follow linear elastic fracture mechanics exhibit crack growth that approximately obeys the following equation

$$\dot{a} = \kappa_c \left(\frac{K_I(P)}{K_{IJ}}\right)^n \exp\left[-\frac{U}{R_0}\left(\frac{1}{T} - \frac{1}{T_0}\right)\right] \tag{17}$$

in which K_I = stress intensity factor, U = activation energy of crack growth, R_0 = gas constant, T = absolute temperature, T_0 = reference temperature, and κ_c, n = empirical constants. The applicability of this well-known equation to concrete has been verified in [39]. For materials which under constant fast rate of loading exhibit nonlinear fracture properties, the proper generalization of Eq.16 is as follows:

$$\dot{a} = \kappa_c \left(\frac{K_I(P)}{K_{IR}(c)}\right)^n \exp\left[-\frac{U}{R_0}\left(\frac{1}{T} - \frac{1}{T_0}\right)\right] \tag{18}$$

in which

$$\tilde{K}_{IR}(c) = K_{IR}(c) \quad \text{if} \quad \dot{P} \geq 0; \quad \text{otherwise } \tilde{K}_{IR}(c) = K_{IR}(c_p) \tag{19}$$

When the loading rate is approximately constant and temperature is constant, Eq.17 automatically yields the size effect in agreement with the size effect law.

Outside the fracture process zone, concrete behaves as a linearly viscoelastic material described by the stress-strain relation

$$\epsilon(t) = \int_0^t J(t,t')d\sigma(t') \tag{20}$$

assuming that the [illegible] strain ϵ_{sh} and the delayed thermal expansion are zero; here ϵ, σ = strain and s[illegible] $J(t,t')$ = compl[illegible] function for creep, representing the strain at a[illegible] t caused by a unit uniaxial stress appl[illegible] age t'. Based on Eq.20, the elastic-viscoelastic analogy yields for the load-displacement relation the following Volterra integral equation

$$u(t) = \int_0^t J(t,t')\bar{C}[a(t')]dP(t') \tag{21}$$

in which $\bar{C}(a) = EC(a)$ = compliance of the structure for a unit value of the elastic modulus (i.e., for E = 1). This equation results by noting that the delayed viscoelastic displacement at time t caused by load increment $dP(t')$ occuring at time t' on homogeneous a structure with crack length a(t') is $J(t,t')\bar{C}[a/(t')]dP(t')$. Differentiating Eq.21, one obtains

$$\dot{u} = C[a(t)]\dot{P}(t) + \dot{u}_v(t) \tag{22}$$

in which

$$\dot{u}_v(t) = \int_0^t \dot{J}(t,t')\bar{C}[a(t')]dP(t') \tag{23}$$

Here $\dot{J}(t,t') = \partial J(t,t')/\partial t$ = material compliance rate.

The problem of solving the response of a viscoelastic structure with rate-dependent crack growth under a given controlled displacement history $u(t)$ consists of solving functions $a(t)$

and $P(t)$ from Eq.17 and 21 (with Eq.22). This represents a system of two integro-differential equations of Volterra type. The initial conditions are $a = a_0$ and $P = 0$ at $t = t_0$. The problem can be solved by finite difference approximations in small time steps $\Delta t = t_{j+1} - t_j$ where $j = 1, 2, 3, \ldots$ = subscripts for chosen discrete times. With the notation denote $f(P,a) = \kappa_c \frac{P_{k(a)}}{b\sqrt{d}K_{IR}(c)}^{n} \exp - \frac{U}{R_0}\frac{1}{T} \cdots \frac{1}{T_0}$ the finite difference approximations of Eqs.17, 21 and 22 are as follows

$$\Delta a = f(P,a)\Delta t + \Phi(a)\Delta P \tag{24}$$

$$\Delta u = P\frac{dC(a)}{da}\Delta a + C(a)\Delta P + \Delta u_v \tag{25}$$

$$\Delta u_v = \sum_{j=1}^{i-1}[J(t_{i+1}, t_{j+\frac{1}{2}}) - J(t_i, t_{j+\frac{1}{2}})]\bar{C}[a(t_{j+\frac{1}{2}})]\Delta P_j \tag{26}$$

in which Δ denotes the increments over the time step Δt. In each time step, the solution algorithm may proceed as follows:

1. Loop on iterations.

2. For the first iteration, use the P- and a -values from the end of the previous step, and for the next iterations, use the P and a values for the midstep as determined from the previous iteration of this step. Evaluate $f(P,a), C(a), \bar{C}(a)$and $\Phi(a)$. Then evaluate $dC(a)/da \simeq \Delta C/\Delta a$ based on the final a-value in the previous step, for the first iteration, or on the average value of a as determined in the previous iteration of this step. Then calculate Δu_v from the load increments and crack lengths at previous discrete times and time steps, using Eq.27.

3. Solve ΔP and Δa from Eqs. 25 and 26, which represent a system of two linear algebraic equations. Check for convergence according to the given tolerance. If the tolerance criterion is not met, return to step 2 above and start the next iteration. Otherwise begin the first iteration of the next time step.

The most important simplification in the preceding solution is the approximation of a crack with a finite fracture process zone and cohesive crack bridging zone by an equivalent sharp crack which supposedly gives about the same overall response of the specimen. This is no doubt adequate for a sufficiently large structure but inadequate for a sufficiently small structure. For smaller structures it is necessary to solve the problem taking at least into account a crack bridging zone of a finite length, which requires postulating a relationship between the crack bridging stress and the crack opening displacement as a material property. This relationship involves both instantaneous response and crack bridging creep. A solution of this type has recently been formulated.

The rate-of-loading effect on fracture has been studied experimentally by the size effect method. The most interesting result [40] is that the effective length of the fracture process zone decreases as the loading rate increases, and thus the response is getting more brittle, closer to LEFM. This is seen in Fig.9 which shows that, for specimens of 3 sizes (1:2:4), for

max σ_N-points shift to the right (i.e., toward a higher brittleness β) as the time to reach the peak load increases (tests at constant displacements rates). Measurements are continuing.

4. Closing Remarks

As a final comment on the rate and creep effects, many concrete structures, (for example dams), develop large cracks over a long period of time. Taking the rate effects in fracture growth as well as material creep (and shrinkage) farther away from the fracture process zone into account is essential for realistic predictions. To present the mathematical groundwork representing perhaps the simplest possible formulation has been one goal of the present workshop contribution. The other goal has been to review a host of recent developments which all exploit in some way a knowledge of the size effect due to fracture This effect itself is a consequence of the nonlocal character of damage in this type of materials.

Acknowledgement

Partial financial support from NSF Center for Science and Technology of Cement-Based Materials at Northwestern University is gratefully acknowledged. Ravindra Gettu of Northwestern University deserves thanks for some expert help in preparation of this manuscript.

References

1. A. Hillerborg, M. Modéer, and P.-E. Petersson, "Analysis of Crack Formation and Crack Growth in Concrete by Means of Fracture Mechanics and Finite Elements," *Cement and Concrete Research* 6(6) (1976), 773-782.

2. Y. S. Jenq and S. P. Shah, "A Fracture Toughness Criterion for Concrete," *Engineering Fracture Mechanics* 21(5) (1985), 1055-1069.

3. S. E. Swartz and T. M. E. Refai, "Influence of Size Effects on Opening Mode Fracture Parameters for Precracked Concrete Beams in Bending," in *Fracture of Concrete and Rock, Proceedings of SEM-RILEM Int. Conf.*, Houston, June 1987, edited by S. P. Shah and S. E. Swartz, Springer-Verlag, NY (1989), 242-254.

4. J. Planas and M. Elices, "Conceptual and Experimental Problems in the Determination of the Fracture Energy of Concrete," in *Fracture Toughness and Fracture Energy, Test Methods for Concrete and Rock*, Preprints of the Proceedings of an Int. Workshop Sendai, Japan, October, 1988, edited by M. Izumi, Tohoku Univ., Sendai, Japan (1988), 1-18.

5. J. Planas and M. Elices, "Size Effect in Concrete Structures: Mathematical Approximations and Experimental Validation," in *Cracking and Damage, Strain Localization and Size Effect*, Proceedings of France-U.S. Workshop, Cachan, France, 1988, edited by J. Mazars and Z. P. Bažant, Elsevier, London (1989), 462-476.

6. H. Horii, Z. Shi, and S.-X. Gong, "Models of fracture process zone in concrete, rock and ceramics," in *Cracking and Damage, Strain Localization and Size Effect*, Proceedings of France-US Workshop, Cachan, France, 1988, edited by J. Mazars and Z. P. Bažant, Elsevier, London (1989), 104-115.

7. M. Elices and J. Planas, "Material Models," in *Fracture Mechanics of Concrete Structures*, RILEM TC90-FMA, edited by L. Elfgren, Chapman and Hall, London, (1989), 16-66.

8. Z. P. Bažant, "Size Effect in Blunt Fracture: Concrete, Rock, Metal," *J. Engng. Mech.*, ASCE, Vol. 110, No. 4 (April 1984), 518-535.

9. Z. P. Bažant and P. A. Pfeiffer, "Determination of Fracture Energy from Size Effect and Brittleness Number," *ACI Mater. J.*, Vol. 84, No. 6, (Nov.-Dec. 1987), pp. 463-480.

10. Z. P. Bažant, "Fracture Energy of Heterogeneous Materials and Similitude," *Preprints, SEM/RILEM Int. Conf. on Fracture of Concrete and Rock* (Houston), edited by S. P. Shah and S. E. Swartz, Soc. for Exp. Mech., 1987; also in *Fracture of Concrete and Rock SEM-RILEM Int. Conf.*, edited by S. P. Shah and S. E. Swartz, Springer-Verlag, New York, (1989), 229-241.

11. Z. P. Bažant and M. T. Kazemi, "Size Effect in Fracture of Ceramics and Its Use for Determining Fracture Energy and Effective Process Zone Length," Report No. 89-6/498s, (1989) ACBM Center, Northwestern University; *J. of American Ceramic Soc.*, in press.

12. Z. P. Bažant, "Mechanics of distributed cracking," *Appl. Mech. Reviews ASME.* 39 (1986), 675-705.

13. R. Gettu, Z. P. Bažant, and M. E. Karr, Fracture Properties and Brittleness of High Strength Concrete, Report No. 89-10/B627f, Center for Advanced Cement-Based Materials, Northwestern University (1989); also *ACI Materials Journal*, in press.

14. Z. P. Bažant and M. T. Kazemi, "Size Effect Tests of Diagonal Shear Fracture," *ACI Materials Journal* (1990), in press.

15. Z. P. Bažant and Hsu-Huei Sun, "Size Effect in Diagonal Shear Failure: Influence of Aggregate Size and Stirrups," *ACI Materials Journal* 84(4) (1987), 259-272.

16. Z. P. Bažant and J. K. Kim, "Size Effect in Shear Failure of Longitudinally Reinforced Beams," *Am. Concrete Institute Journal* 81 (1984), 456-468; Disc. 796 & Closure 83 (1985), 579-583.

17. Z. P. Bažant and Z. Cao, "Size Effect in Shear Failure of Prestressed Concrete Beams," *Am. Concrete Inst. Journal* 83 (1986), 260-268.

18. Z. P. Bažant and Z. Cao, "Size Effect in Punching Shear Failure of Slabs," *ACI Structural Journal* (Am. Concrete Inst.) 84 (1987), 44-53.

19. Z. P. Bažant and S. Sener, "Size Effect in Pullout Tests," *ACI Materials Journal* 85 (1988), 347-351.

20. Z. P. Bažant, S. Sener, and P. C. Prat, "Size Effect Tests of Torsional Failure of Plain and Reinforced Concrete Beams," *Materials and Structures* RILEM, Paris, (1988), 425-430.

21. P. Marti, "Size Effect in Double-Punch Tests on Concrete Cylinders," *ACI Materials Journal* 86(6) (1989), 597-601.

22. R. Eligehausen and J. Ožbolt, "Size Effect in Anchorage Behavior," Proc., ECF8, "Fracture Behavior and Design of Materials and Structures," (1990), 2671-2677.

23. Z. P. Bažant, R. Gettu, and M. T. Kazemi, Identification of Nonlinear Fracture Properties from Size Effect Tests and Structural Analysis Based on Geometry-Dependent R-Curve, Report No. 89-3/498p, Center for Advanced Cement-Based Materials, Northwestern Univ., Evanston, IL., 1989.

24. Z. P. Bažant and M. T. Kazemi, "Size Dependence of Concrete Fracture Energy Determined by RILEM Work-of-Fracture Method," Report No. 89-12/B623s, (1989), NSF Center for Science and Technology of Advanced Cement-Based Materials, Northwestern University, Evanston, IL; also *Int. J. of Fracture*, in press.

25. Z. P. Bažant and Y. Xi, "Statistical Size Effect in Concrete Structures: Nonlocal Theory," Report No. 90-5/616s, (1990), Center for advanced Cement-Based Materials, Northwestern University, Evanston, IL.

26. J. Nakayama, "Direct Measurement of Fracture Energies of Brittle Heterogeneous Materials," *Journal of American Ceramics Society* 48(11) (1965), 583-87.

27. H. G. Tattersall and G. Tappin, "The Work of Fracture and Its Measurement in Metals, Ceramics and Other Materials," *Journal of Material Science* 1(3) (1966), 296-301.

28. A. Hillerborg, "The Theoretical Basis of a Method to Determine the Fracture Energy G_F of Concrete," *Materials and Structures* 18(106) (1986), 291-96.

29. A. Hillerborg, "Results of Three Comparative Test Series for Determining the Fracture Energy G_F of Concrete," *Materials and Structures* 18(107) (1986), 407-13.

30. Z. P. Bažant and F.-B. Lin, "Nonlocal Smeared Cracking Model for Concrete Fracture," *J. of Struct. Eng. ASCE* 114(11) (1988), 2493-2510.

31. Z. P. Bažant and J. Ožbolt, "Nonlocal Microplane Model for Fracture, Damage and Size Effect in Structures," *J. of Eng. Mech. ASCE*, (1990), in press.

32. J. Pijaudier-Cabot, Z. P. Bažant and Y. Berthaud, "Interacting Crack Systems in Particulate or Fiber-Reinforced Composites," Proc., 6th Int. Conf. on Numerical Methods on Fracture Mechanics (1990), held in Freiburg, West Germany, April 1990.

33. H. Gao and J. R. Rice, "A First order Perturbation Analysis on Crack Trapping by Arrays of Obstacles," Report Division of Appl. Sciences, Harvard Univ., Cambridge MA, Nov. 1988.

34. T. Mori, K. Saito and T. Mura, "An Inclusion Model for Crack Arrest in a Composite Reinforced by Sliding Fibers," *Mech. of Materials* Vol. 7 (1988), 49-58.

35. P. C. Paris, M. P. Gomez, and W. E. Anderson, "A Rational Analytic Theory of Fatigue," *The Trend in Engineering* 13(1) (Jan. 1961).

36. P. C. Paris and F. Erdogan, "A Critical Analysis of Propagation Laws," *Transactions of ASME, J. of Basic Engrg.* 85 (1963), 528-534.

37. S. E. Swartz and C. G. Go, "Validity of Compliance Calibration to Cracked Beams in Bonding," J. of Experimental Mech. 24(2) (June 1984), 129-134.

38. Z. P. Bažant and K. Xu, "Size Effect in Fatigue Fracture of Concrete," Report No. 89-12/623s, (1989), ACBM Center, Northwestern University; submitted to *ACI Mat. J.*.

39. Z. P. Bažant and P. C. Prat, "Effect of Temperature and humidity on fracture energy of concrete," *ACI Materials J.* 84 (July 1988), 262-271.

40. Z. P. Bažant and R. Gettu, "Determination of Nonlinear Fracture Characteristics and Time Dependence from Size Effect," in *Fracture of Concrete and Rock: Recent Developments*, Proc. Int. Conf. in Cardiff, UK, edited by S. P. Shah, S. E. Swartz and B. Barr, Elsevier Applied Science, London, (1989), 549-565.

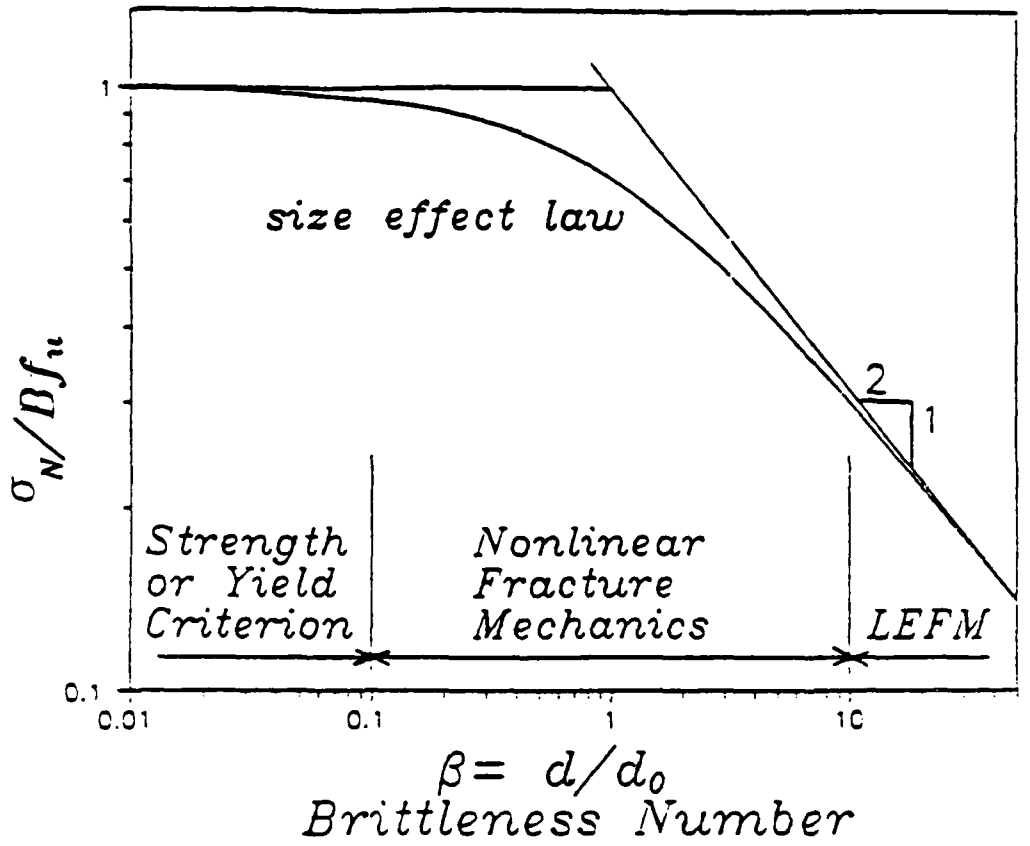

Fig.1. Size effect law for quasi-brittle structures.

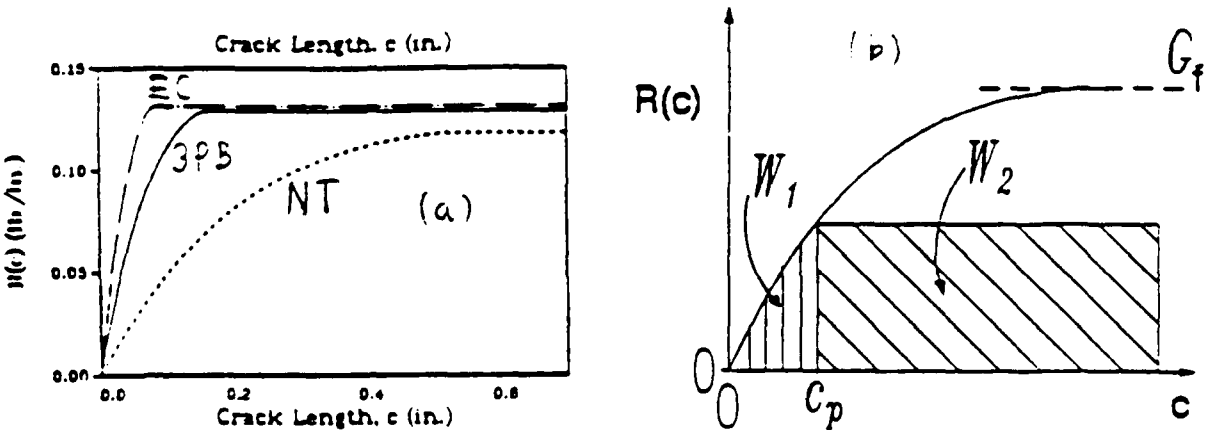

Fig.2. R-curves and effect of size on fracture energy, along with an idealized picture of the evolution and movement of fracture process zone.

(c)

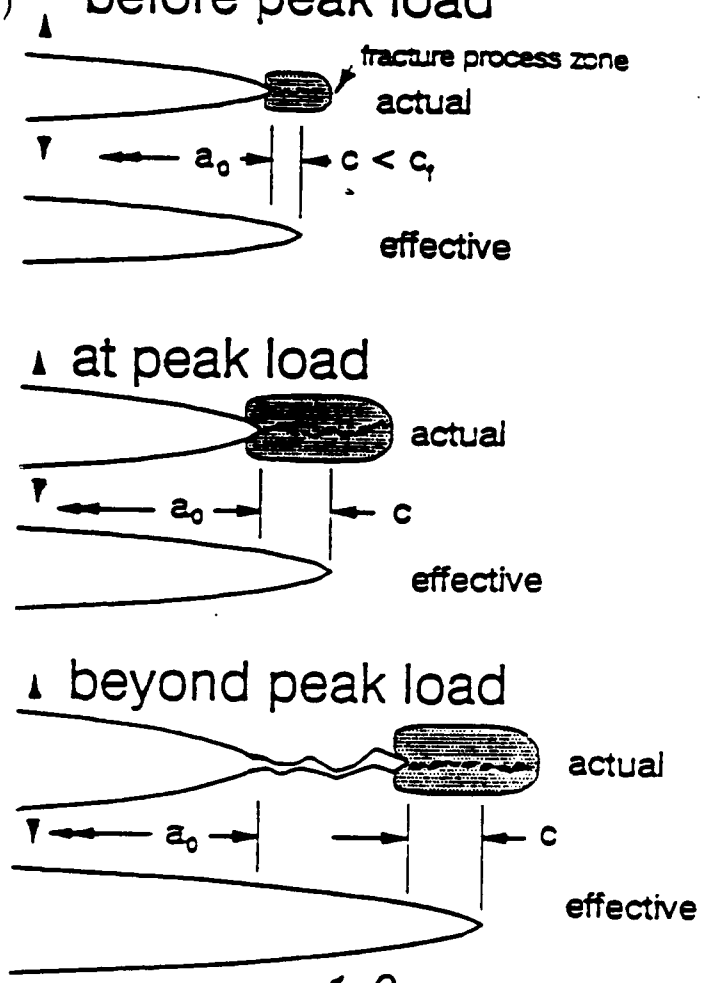
before peak load
fracture process zone
actual
a_0
$c < c_f$
effective
at peak load
actual
a_0
c
effective
beyond peak load
actual
a_0
c
effective

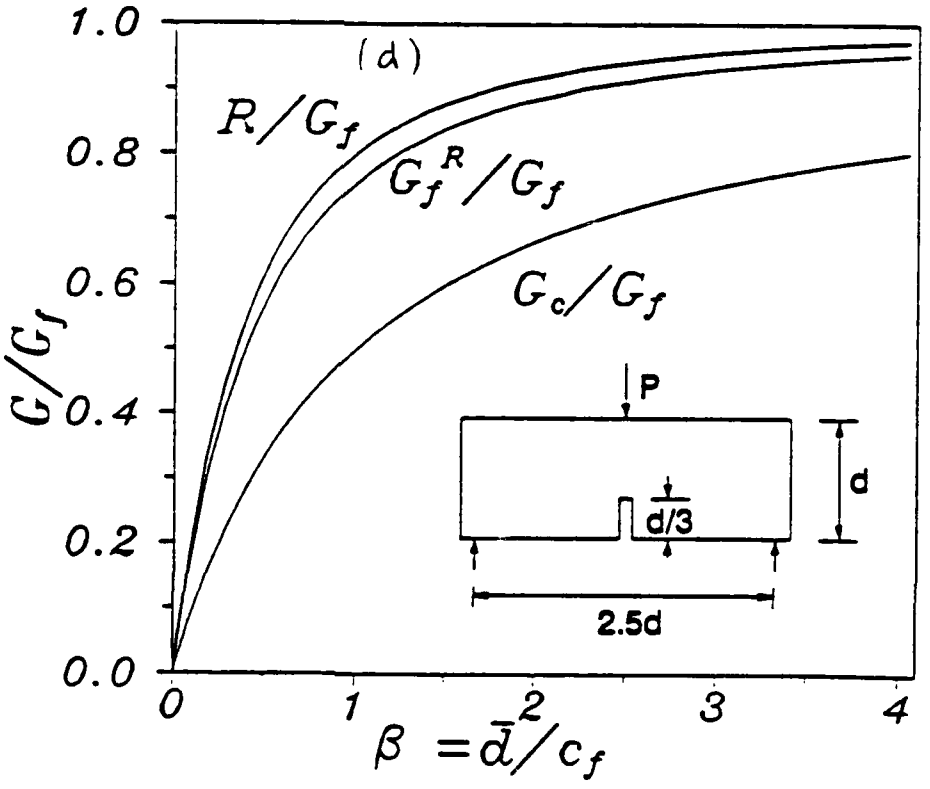
(d)
R/G_f
G_f^R/G_f
G_c/G_f
G/G_f
1.0
0.8
0.6
0.4
0.2
0.0
0
1
2
3
4
$\beta = \bar{d}/c_f$
P
d
d/3
2.5d

Fig. 2

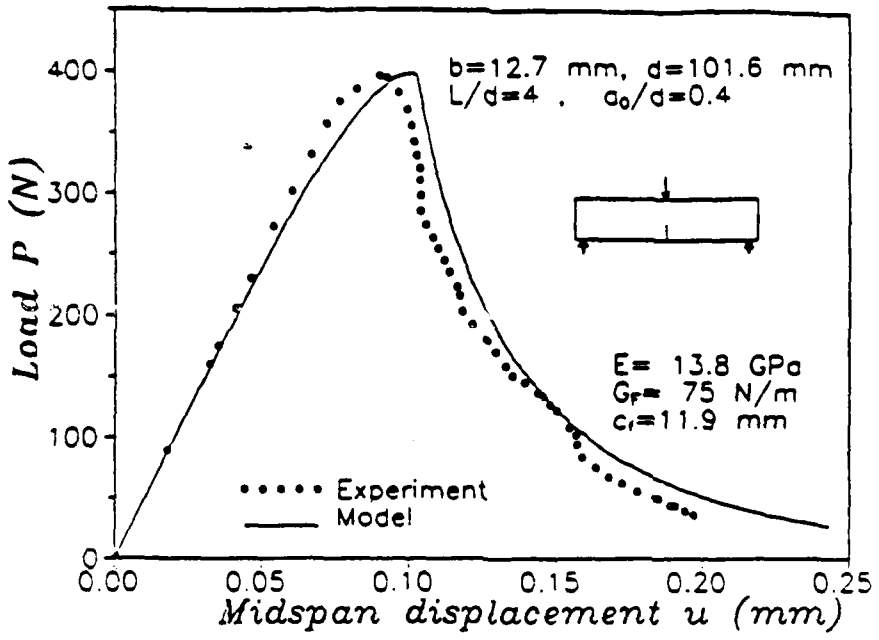

Fig.3. Prediction of the load-deflection curve from measured maximum loads of rock fracture specimens of different sizes, in comparison with the load- deflection curve measured by Bažant, Gettu, and Kazemi [23].

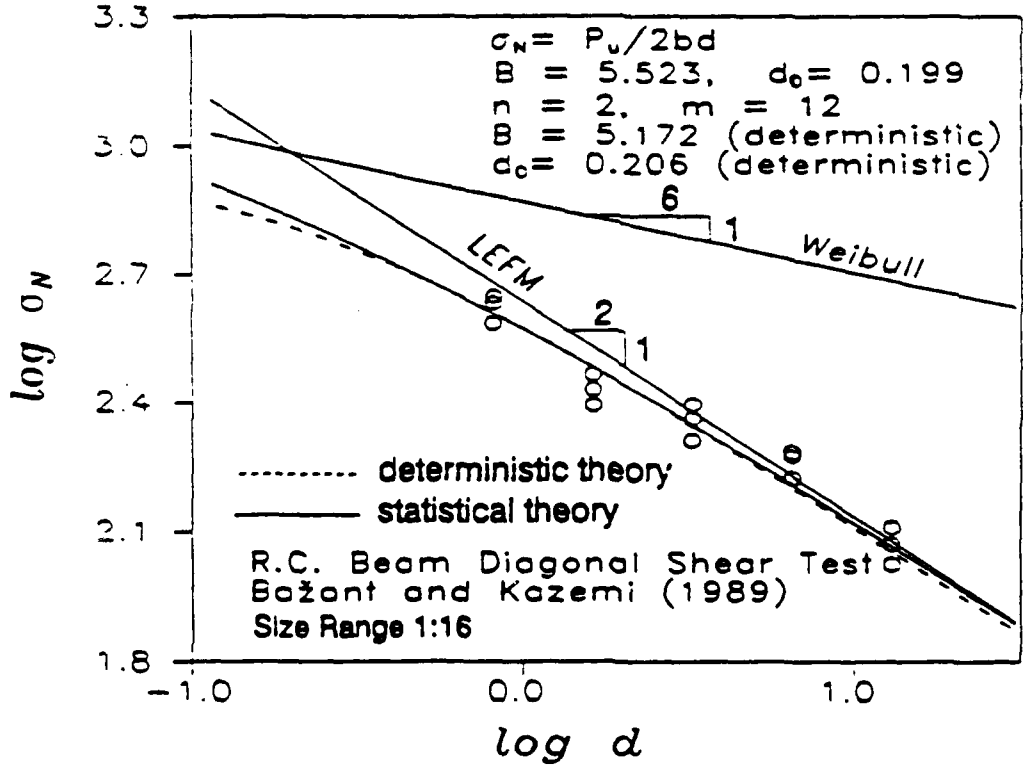

Fig.4. Statistical generalization of the size effect law.

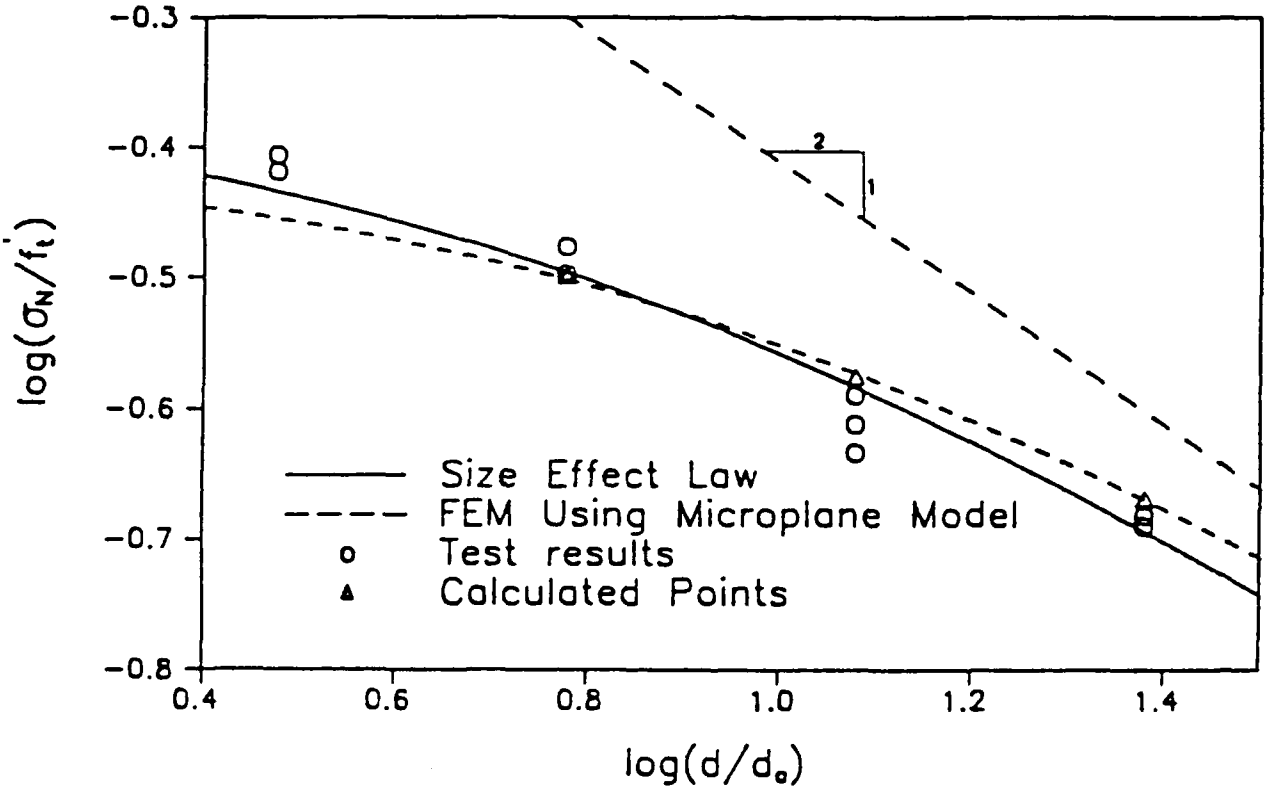

Fig.5. Nominal strengths of fracture specimens of different sizes calculated by a finite element program based on nonlocal microplane material model, compared with the size effect law and with experimental measurements of Bažant and Pfeiffer [9].

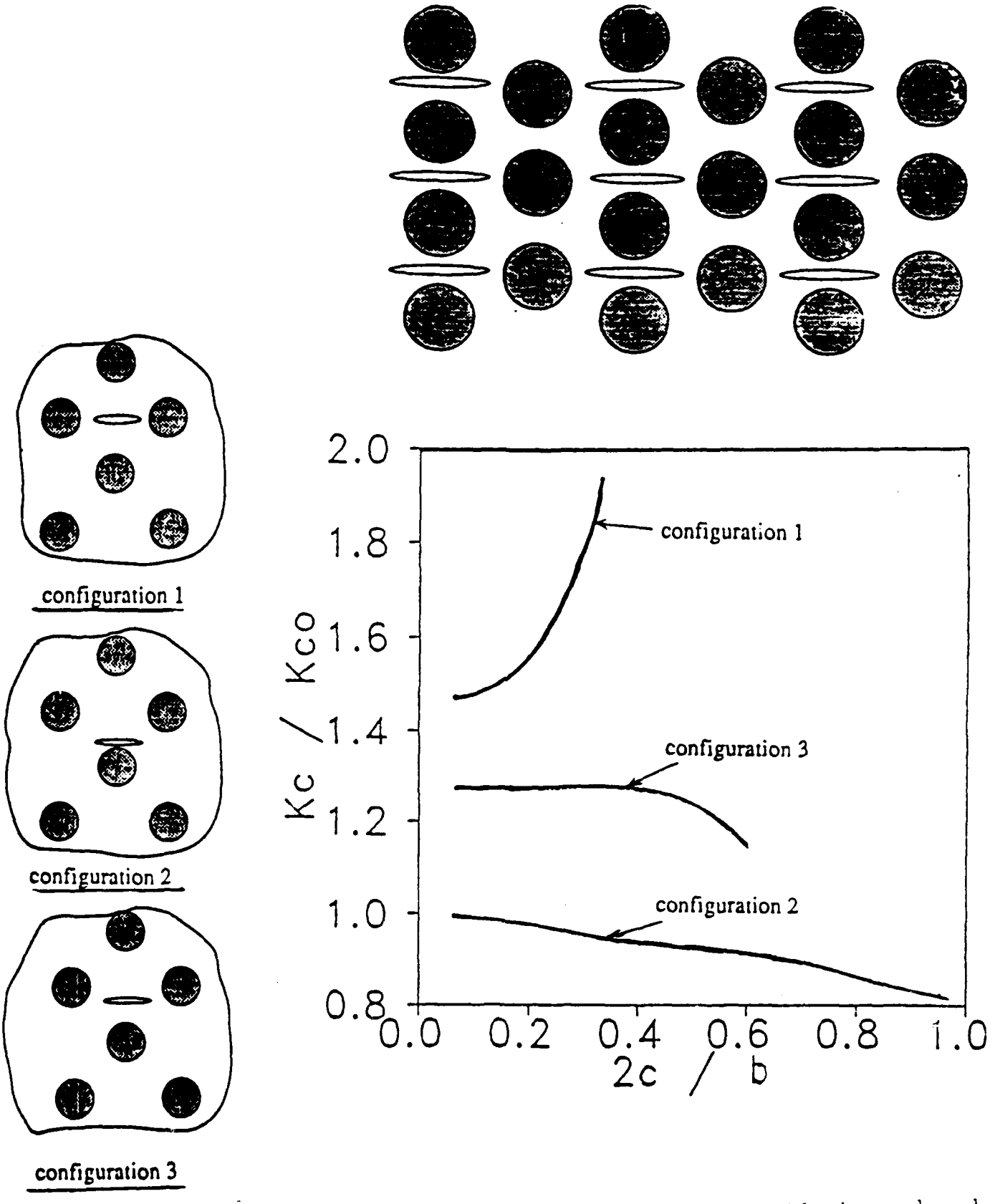

Fig.6. Approximation of fracture process zone by an elastic matrix with microcracks and inclusions, and apparent R-curves for the microcracks calculated by Pijaudier Cabot, Bažant and Berthaud [32].

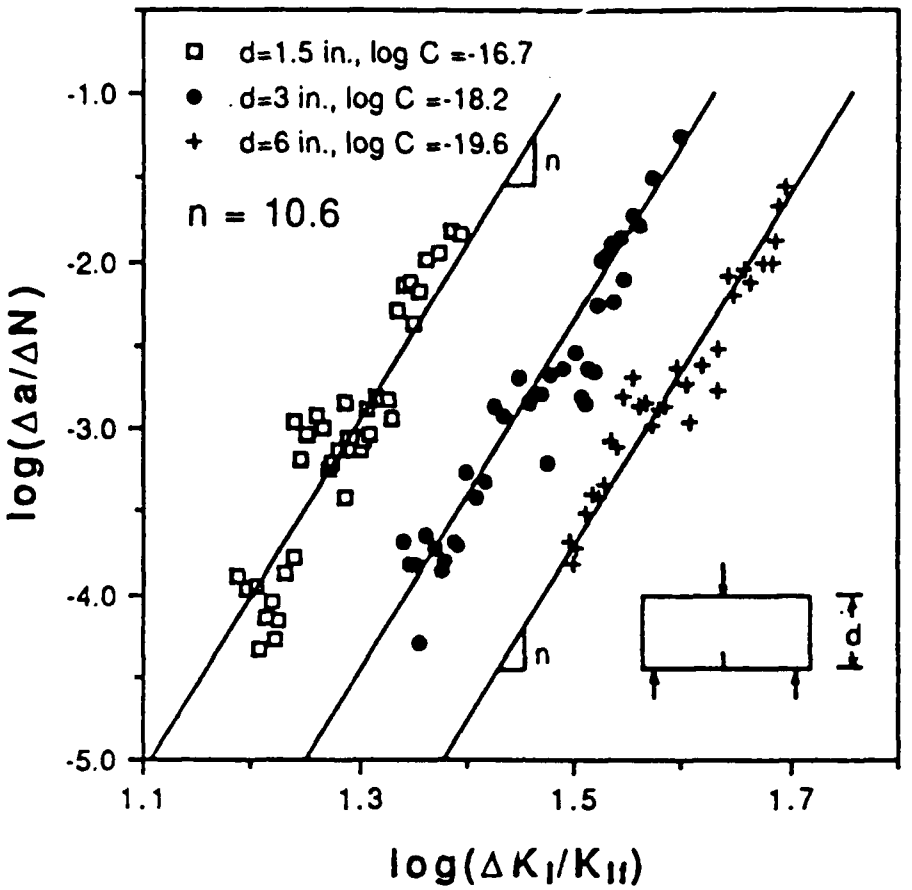

Fig.7. Test results of Bažant and Xu [38] on fatigue fracture of concrete specimens of three different sizes and their comparison with size-adjusted Paris law.

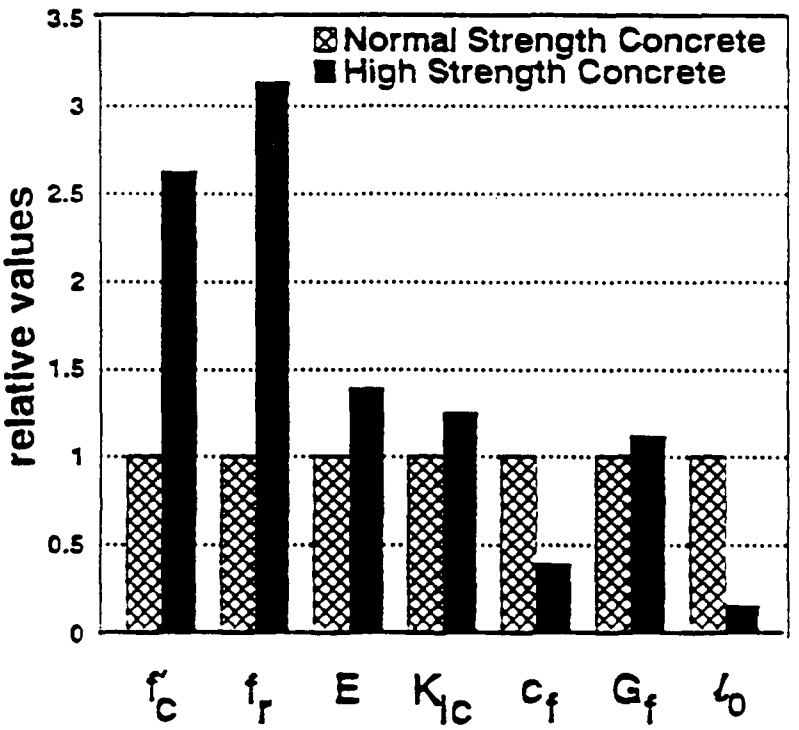

Fig.8. Comparison of nonlinear fracture characteristics of high strength concrete and normal concrete [13].

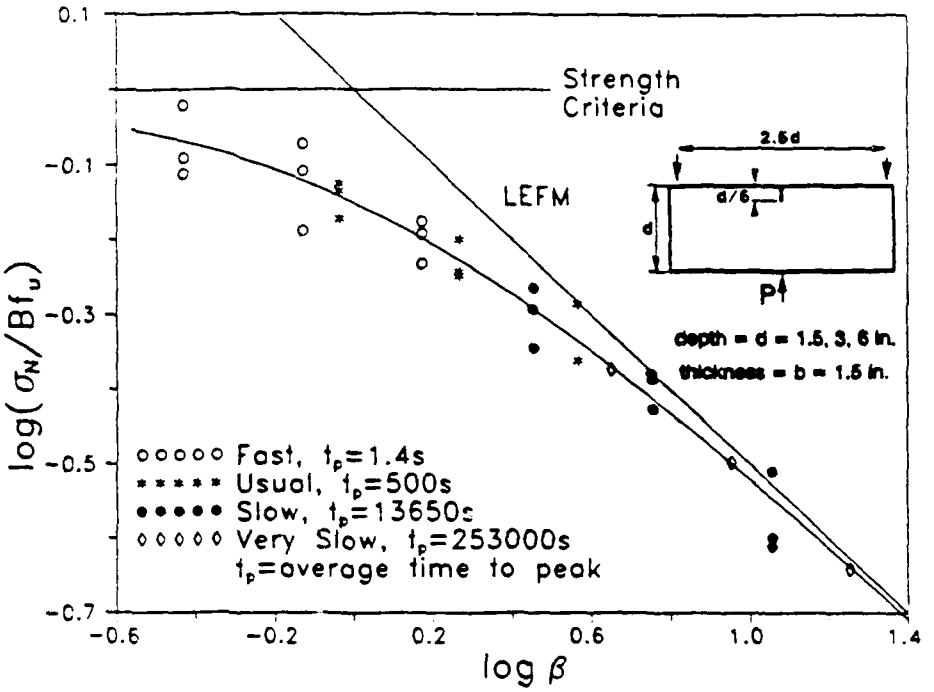

Fig.9. Size effect on nominal strengths at different loading rates, reported by Bažant and Gettu [40].

Micromechanics of Deformation in Rocks

John M. Kemeny
Department of Mining and Geological Engineering
University of Arizona
Tucson, AZ 85718

Neville G. W. Cook
Earth Sciences Division
Lawrence Berkeley Laboratory
and
Department of Materials Science and Mineral Engineering
University of California, Berkeley, CA 94720

Abstract

Laboratory testing of rocks subjected to differential compression have revealed many different mechanisms for extensile crack growth, including pore crushing, sliding along pre-existing cracks, elastic mismatch between grains, dislocation movement, and hertzian contact. Micromechanical models based on fracture mechanics have been developed for these different mechanisms by many different researchers. In this paper, the K_I solutions for these micromechanical models are reviewed. Because of the similarity in rock behavior under compression in a wide range of rock types, it is not surprising that the micromechanical models discussed in the previous sections have many similarities. This may explain the success of models based on certain micromechanisms in spite of the lack of evidence for these mechanisms in microscopic studies. Based on these similarities, a generic micromechanical model is proposed that in some way takes into account all of the above phenomena. It is demonstrated how the K_I solutions from the micromechanical models can be used to derive nonlinear stress-strain curves that exhibit strain-hardening and strain-softening, dilatation, σ_2 sensitivity, and rate dependence. By using subcritical crack growth, transient and tertiary creep behavior can also be predicted. Also, it is shown how these micromechanical models can form the basis for continuum damage models using the finite element method.

1 Introduction

Rock is a very heterogeneous material, containing different and often anisotropic crystals, as well as structural weaknesses at all scales. These weaknesses include grain boundaries, pores, and cracks on the small scale, and joints, faults, and bedding planes on the larger scale. When rock is subjected to differential compressive stresses, extensile, opening-mode microcracks grow from these flaws and degrade the properties of the rock. Our understanding of the fundamental mechanisms involved in the micromechanics of brittle and semi-brittle rock deformation has increased greatly in the past decade, due to the many microscopic studies that have been carried out on rocks subjected to compressive stresses in the laboratory. It has been found, for instance, that microcrack growth occurs preferentially in the direction of the maximum principal stress, and this results in stress-induced anisotropic rock properties (Wong, 1985; Fredrich et al., 1989; Zheng, 1989). As more cracks grow and the cracks increase in length, crack interaction becomes important, and cracks can coalesce to form large scale splitting or shear fractures. The growth of cracks has been shown to be closely associated with the macroscopic constitutive behavior of the rock. For instance, the initial, stable growth of microcracks is associated with strain-hardening stress-strain behavior, and the interaction and coalescence of cracks is associated with unstable strain-softening stress-strain behavior (Hallbauer et al., 1973). Both strain-hardening and strain-softening behavior exhibit dilatation as a result of extensile crack growth. Also, experiments have shown that for tests conducted at higher confining pressures, the average length of the cracks is reduced, promoting the transition from brittle to semi-brittle behavior (Fredrich et al., 1989; Zheng, 1989). Microstructural parameters such as grain size, porosity, and initial crack density play an important role in rock deformation, and recent experimental studies have helped elucidate their effects (Zhang et al., 1989; Fredrich et al., 1989). An example of microcrack growth in Indiana limestone is presented in Figure 1, revealing several of the different mechanisms that can cause crack growth under compression (from Zheng, 1989).

Another aspect of rock deformation and failure of great importance is the time and rate-dependence of rock deformation. Recent experimental studies have shown that both time and rate dependent behavior in brittle rocks can be the result of rate-controlled processes acting at the tips of cracks where stress concentrations exist (Sano et al., 1981; Carter et al., 1981; Atkinson, 1984). This time-dependent crack growth occurs at values of the stress intensity factor below the fracture toughness of the material, and is referred to as sub-critical crack growth. Subcritical crack growth is the result of several mechanisms that

can occur simultaneously, including stress corrosion, diffusion, dissolution, ion exchange, and microplasticity (Atkinson, 1984).

Fracture mechanics theory (i.e., Lawn and Wilshaw, 1975) is now routinely being applied to many different aspects of the micromechanics of rock deformation and failure. Fracture mechanics models have been developed to analyse crack growth under compressive stresses due to grain crushing (Zhang et al., 1989), sliding along pre-existing cracks (Nemat-Nasser and Horii, 1982; Steif, 1984; Ashby and Hallum, 1986; Horii and Nemat-Nasser, 1986; Kemeny and Cook, 1987a,b), stress concentrations around pores (Sammis and Ashby, 1986), elastic mismatch between grains (Dey and Wang, 1981), dislocation movement (Krajcinovic, 1989), and combinations of these mechanisms (Costin, 1985). One of the important aspects of these models is that even though they are based on linear elastic fracture mechanics (LEFM), nonlinear stress-strain behavior can be predicted due to the growth of the cracks in an otherwise linear-elastic solid. For instance, the models predict that the initial growth of cracks results in strain-hardening stress-strain behavior. Also, the models that include crack interaction show that crack interaction can cause a transition from strain-hardening to strain-softening stress-strain behavior. Several fracture mechanics models have been able to predict the transition from axial splitting to shear faulting as the confining pressure is increased (Horii and Nemat-Nasser, 1986; Kemeny and Cook, 1987a). Also, a few of the models have implemented a crack growth criterion based on subcritical crack growth, and these models are able to predict the creep and rate dependence in rock (Costin, 1985; Kemeny, 1990).

The experiments and theoretical models described above are in general based on the standard triaxial test consisting of an axial stress and a confining pressure. Ideally, under these boundary conditions the stress state is constant throughout the body, and a rotation of the principal stresses does not occur during loading. In actual field situation where rock deformation and failure are occurring in a rock mass, stress gradients occur due to the complicated boundary conditions imposed. These stress gradients play an important role in the fracture systems that develop, and in rock mass stability. Experimental studies have been conducted looking at the effects of stress gradients on rock deformation and fracture formation (Guenot, 1989; Gough and Bell, 1982; Haimson and Herrick, 1985; Santerelli, 1987; Ewy, 1989). Fracture mechanics models based on the micromechanics of crack growth, interaction, and coalescence are now being developed that can take into account complicated boundary value problems with stress gradients. These models are formulated by implementing micromechanical models into an elastic finite element code. In each of the

elements, the micromechanical models are utilized to calculate the effects of crack growth, interaction, and coalescence, and the stress gradient effects are accounted for by the finite element calculations. Examples of finite element damage models that have been developed in this way are given in Costin and Stone (1987), Krajcinovic (1989), and Kemeny and Tang (1990).

This paper discusses the use of fracture mechanics in modelling the deformation and failure of rocks subjected to differential compressive stresses. In section 2 that follows, linear elastic fracture mechanics theory is briefly reviewed. Then, in section 3, some of the micromechanical models that have been developed to model the different mechanisms for crack growth under compression are reviewed. In section 4, it is shown how these models can used to develop nonlinear constitutive relations for rock. This includes micromechanical models for nonlinear constitutive relations based on the rate-independent fracture toughness, rate dependent models based on subcritical crack growth, and creep due to subcritical crack growth. In section 5, these micromechanical models are implemented into an elastic finite element code, to look at the effects of microcrack growth on complicated boundary value problems. As an example, we look at borehole breakout using both the rate-independent and subcritical crack growth models.

2 Fracture Mechanics Preliminaries

The analyses in this paper are limited to two-dimensional, linear-elastic bodies subjected to compressive principal stresses σ_1 and σ_2, and containing simple configurations of cracks. In this section, some of the important aspects of linear elastic fracture mechanics are briefly discussed. The discussion is limited to those topics that will be used in later sections of this paper. For a complete discussion of linear elastic fracture mechanics theory, see Liebowitz (1968), Lawn and Wilshaw (1975), or others.

Following the usual notation in linear elastic fracture mechanics, three types of stress intensity factors, K_I, K_{II}, K_{III}, are distinguished, which relate to the three types of crack displacements: mode I (opening), mode II (sliding), and mode III (tearing). The stresses near the crack tip then have the following form (Lawn and Wilshaw, 1975):

$$\begin{Bmatrix} \sigma_1 \\ \sigma_2 \\ \tau_{12} \end{Bmatrix} = \frac{K_Q}{\sqrt{2\pi r}} \begin{Bmatrix} f_1^Q \\ f_2^Q \\ f_{12}^Q \end{Bmatrix} \qquad (1)$$

where r is the radial distance from the crack tip, θ is the angle measured from the plane of the crack, Q takes on the values I, II, and III for the three cracking modes, and $f(\theta)$ are smooth functions of θ. The stress intensity factors take into account the crack geometry and boundary conditions, and can be extremely simple for simple crack configurations (e.g., Rooke and Cartwright, 1976). For instance, for a single flat crack of length $2l$ oriented along the x axis in an infinite body subjected to normal crack face tractions $\sigma(x)$, the mode I stress intensity factor at the tip $x=l$ is given by (Cherepanov, 1979):

$$K_I = \frac{1}{\sqrt{\pi l}} \int_{-l}^{l} \sigma(x) \sqrt{\frac{l+x}{x-x}} \, dx \qquad (2)$$

Much of the usefulness of the stress intensity factors for rock deformation lies in their relationship to the strain energy of the body that contains the cracks. The energy release rate, G, is defined as:

$$2G = \frac{\partial U_e}{\partial l} \qquad (3)$$

where U_e is the elastic strain energy of the solid that contains the crack, and $2l$ is the crack length. The relationship between G and the stress intensity factors is given by:

$$G = \frac{K_I^2}{E'} + \frac{K_{II}^2}{E'} + \frac{K_{III}^2}{E}(1+\nu) \qquad (4)$$

where $E' = E$ for plane stress and $E' = E/(1 - \nu^2)$ for plane strain. By integrating 2G from zero to the given crack length, the additional strain energy due to the crack, U_e, can be calculated.

A convenient method for calculating the displacements of an elastic body containing cracks is Castigliano's theorem (Sokolnikoff, 1956). From Castigliano's theorem the

displacement x_i that occurs under a load P_i when a linear elastic body is subjected to loads $P_1, P_2, \ldots P_n$ is given by:

$$X_i = x_i(\text{uncracked body}) + \partial U_e/\partial P_i \qquad (5)$$

The displacements due to the uncracked body are already known for the simple configurations considered in this paper. Equations (3) to (5) give the procedure for calculating the additional displacements due to the cracks once the stress intensity factor solutions are known.

Two criteria for crack growth will be considered in this paper. The first crack growth criterion (rate-independent) is based on the work of Griffith (1920) and others, and states that crack growth occurs when:

$$K_I = K_{Ic} \qquad (6)$$

where K_{IC} is the fracture toughness. Assuming that K_{IC} does not change with crack growth, the criterion for unstable crack growth is:

$$K_I \geq K_{Ic} \quad \text{and} \quad \partial K_I/\partial a > 0 \qquad (7)$$

A second crack growth criterion (rate-dependent) is based on crack growth that occurs below K_{IC} and is referred to as subcritical crack growth. A common empirical equation used to describe subcritical crack growth is based on the power law formulation of Charles(1958), and in given by:

$$\dot{a} = da/dt = A(K_I)^n \qquad (8)$$

where A and n are material constants.

Micromechanical Models for Crack Growth Under Compression

As discussed in the introduction, microcrack growth under compression occurs by many different mechanisms, and in the past few years, mechanical models have been developed for many of these mechanisms. In this section we review the stress intensity factor solutions for several of these micromechanical models. The discussion is limited to the axial growth of extensile cracks, i.e., the formation of shear bands or faults is not considered. It is found that the micromechanical models for crack growth under compression have many similarities, and at the end of this section we introduce a generic model for crack growth under compression that encompasses all the models. The stress intensity factor solutions discussed here will be used in section 3 to derive nonlinear constitutive relations.

Cylindrical Pore Model

A two-dimensional cylindrical pore is subjected to maximum and minimum principal stresses σ_1 and σ_2, respectively, as shown in Figure 2. For $\sigma_1 > 3\sigma_2$, tension will occur at the boundary of the pore in the direction of the maximum principal stress. As $\sigma_1 - 3\sigma_2$ increases, eventually a pair of tensile stresses will initiate and grow in the direction of σ_1. When the length of the tensile crack, l, is small compared with the radius of the pore, R, i.e., $l \ll R$, a small-crack approximation to the stress intensity factor is appropriate, given by:

$$K_I = 1.12(\sigma_1 - 3\sigma_2)\sqrt{\pi l} \qquad (9)$$

This solution is based on the edge crack subjected to a uniform tensile far field stress (Rooke and Cartwright, 1976). Notice that K_I for this configuration increases with increasing crack length, and for a fixed σ_1, equation (7) predicts that the crack will grow in an unstable manner.

When the tensile cracks are long in relation to the size of the pore, i.e., $R \ll l$, the stress intensity factor can be approximated by a straight crack oriented in the direction of σ_1 with a set of point forces at the center of the crack. The stress intensity factor for this configuration is given by:

$$K_I = \frac{CR(\sigma_1 - 3\sigma_2)}{\sqrt{\pi l}} - \sigma_2\sqrt{\pi l} \qquad (10)$$

where C is a constant. Note that this solution takes into account the opening force due to σ_1 and the closing effect that σ_2 has on the long crack of length $2l$. Also note that from equation (7), this solution predicts stable crack growth (K_I decreases for increasing l for fixed σ_1 and σ_2. Thus equations (9) and (10) together predict that the tensile cracks will initially grow in an unstable fashion, and stabilize at some crack length.

In order to determine the length of crack at which the crack stabilizes, a solution is needed that is valid at all crack lengths. A stress intensity factor solution that encompasses both the small and large crack behavior is given by Sammis and Ashby (1986):

$$K_I = \left[\frac{1.1(\sigma_1 - 2.1\sigma_2)}{(1 + l/R)^{3.3}} - \sigma_2\right]\sqrt{\pi l} \qquad (11)$$

The K_I vs. l behavior for this solution is shown in Figure 3, for various values of σ_2/σ_1. K_I initially increases with increasing l, reaches a maximum, and thereafter decreases with increasing l. The maximum represents the transition from stable to unstable crack growth. Figure 4 shows that the maximum occurs at a length $l<R$, and decreases with increasing σ_2/σ_1.

Sliding Crack Model

Consider an initial straight crack of length $2l_0$, at an angle β to the principal stresses σ_1 and σ_2, as shown in Figure 4. The shear stress along the crack over and above that due to friction (assuming a linear coefficient of friction, μ) is given by:

$$\tau^* = \frac{1}{2}\left[(\sigma_1 - \sigma_2)\sin 2\beta - \mu(\sigma_1 + \sigma_2 + (\sigma_1 - \sigma_2)\cos 2\beta\right] \qquad (12)$$

The stress intensity factors for the initial configuration are given by:

$$K_I = 0$$
$$K_{II} = \tau^* \sqrt{\pi l_o} \qquad (13)$$

Assuming that crack growth will occur in the direction such that $\sigma_{\theta\theta}$ at the crack tip is maximized, crack growth will occur at an angle of about 70° from the plane of the crack. These out of plane cracks are referred to as wing cracks. When the wing cracks are small, i.e., $l << l_o$, the stress intensity factors are given by (Cotterell and Rice, 1980):

$$K_I = 3/4 \left(\sin \beta/2 + \sin 3\beta/2 \right) \tau^* \sqrt{\pi l_o}$$
$$K_{II} = 1/4 \left(\cos \beta/2 + 3 \cos 3\beta/2 \right) \tau^* \sqrt{\pi l_o} \qquad 14$$

This solution cannot be used for stability analysis, since $\partial K_I / \partial l$ is identically equal to zero.

As the crack grows longer, it grows in the direction of σ_1, and the stress intensity factors at the tip of the wing cracks becomes predominantly K_I. A long crack approximation for the sliding crack for $l >> l_o$ is given by (Kemeny and Cook, 1987a):

$$K_I = \frac{2 l_o \tau^* \cos \beta}{\sqrt{\pi l}} - \sigma_2 \sqrt{\pi l} \qquad 15$$

The long crack approximation to the sliding crack is similar to the long crack approximation for the cylindrical pore model, when $l_o = R$, where R is the radius of the pore. Compared with the Sammis and Ashby approximation to the pore model (equation 11), K_I in equation (15) above decreases much less rapidly.

One approximation to the sliding crack valid at all crack lengths is given by Horii and Nemat-Nasser (1986). This model considers an initial crack length $2l_o$ at angle β with

straight wing cracks of length l which are at an angle α from the direction of the initial crack, where α varies with the length of the wing cracks:

$$K_I = \frac{2 l_o \tau^* \sin\alpha}{\sqrt{\pi(l+l^*)}} - \frac{\sqrt{\pi l}}{2}\left[\sigma_1 + \sigma_2 + (\sigma_1 - \sigma_2)\cos 2(\alpha+\beta)\right] \quad (16)$$

where $l^* = 0.27 l_o$. The stress intensity factor for a given wing crack length is given by the value of α that maximizes K_I. This model predicts stable crack growth for σ_2 compressive, but shows a transition to unstable crack growth when σ_2 is only slightly tensile (Horii and Nemat-Nasser, 1986).

Elastic Mismatch Model

Consider a body containing two materials (or one material with a change in anisotropy orientation) and subjected to principal stresses σ_1 and σ_2, as shown in Figure 5. In two dimensions, each material can be described by a compressibility matrix, as given by:

$$\begin{Bmatrix} \epsilon_1 \\ \epsilon_2 \\ \epsilon_{12} \end{Bmatrix} = [S] \begin{Bmatrix} \sigma_1 \\ \sigma_2 \\ \sigma_{12} \end{Bmatrix} \quad (17)$$

where, for instance, S_{21} gives the strain in the 2 direction due to a stress σ_1. The S_{ij} can, for instance, take into account the strong anisotropy that occurs within individual grains.

For $\sigma_1 > \sigma_2$, differential expansion will occur in the 2 direction, and a tensile stress will develop at the interface in the material with the smaller lateral expansion. For a small crack in this material at the interface, the stress intensity factor can be approximated by the edge crack with point forces P at the edge (Rooke and Cartwright, 1976):

$$K_I = 2.6 \frac{P}{\sqrt{\pi l}} \quad (18)$$

Dey and Wang (1981) give an approximate solution for the point force P in terms of the S matrix and the width of the body, d:

$$P = \frac{0.45\sigma_1 d}{\pi}\left[\frac{\sigma_1(S_{12}^2 - S_{12}^1) - \sigma_2(S_{22}^2 - S_{22}^1)}{\sigma_1 S_{12}^2}\right] \qquad (19)$$

where the superscript indicates material 1 or 2. Under a uniaxial stress ($\sigma_2 = 0$) and for a large contrast in compressibility between materials 1 and 2, this reduces to:

$$K_I = \frac{1.04\sigma_1 d}{\pi\sqrt{\pi l}} \qquad (20)$$

If we take d to be the grain size, then this result is very similar to the results for the long-crack approximations to the pore and sliding crack models when $d/2 = R = l_0$. One drawback with this model is that the growth of the crack will significantly reduce the compressibility of material 1, essentially shutting down all crack growth when the compressibility reduces to that of material 2 (see Dey and Wang, 1980).

Dislocation Pile-up Model

When a solid is stressed beyond its yield point, dislocations will be created, giving rise to plastic slip. The yield point for different minerals can differ by orders of magnitude, causing grain boundaries to become barriers to dislocation movement. At such a barrier, a dislocation pile-up can occur. As the strength of the pile-up increases, a tensile crack can develop at the edge of the pile-up, referred to as a Zener-Stroh crack.

Consider a slip plane subjected to a resolved shear stress τ_r, as shown in Figure 6. This stress has to exceed the lattice friction stress τ_f before the dislocations can move. If there are n edge dislocations of Burgers vector magnitude $\bar{b}$ in a pile-up of length L, the driving stress τ^* is given by:

$$\tau^* = \frac{n\bar{b}G}{L\pi(1-\nu)} \qquad (21)$$

The stress distribution due to the pile-up at a distance x and angle θ is given by (Krajcinovic, 1989):

$$\sigma_r = \frac{G}{2\pi(1-\nu)} \frac{n\bar{b}\sin\theta}{x} \qquad (22)$$

Using the stress distribution in equation (22), and using the formula for K_I for a variable stress as given in (2), this gives:

$$K_I = \sqrt{\pi/2}\, \tau^* \sin\theta\, L/\sqrt{l} \qquad 23)$$

Note that this solution has the same form as the stress intensity factor for the sliding crack model given in equation (15).

Herztian Crack Model

Consider the simple model of two spheres of radius R in contact and under a compressive force P. Using Herztian contact theory (e.g., Johnson, 1985), the pressure distribution along the contacting portions of the spheres is given by:

$$P(r) = P_0 \left[1 - (r/a)^2 \right]^{1/2} \qquad 24$$

where a is the radius of contact given by:

$$a = \frac{\pi P_0 R(1-\nu^2)}{E} \qquad (25$$

and P_0 is the maximum pressure at the center of the circle of contact given by:

$$P_0 = 3/2 \frac{P}{\pi a^2} \qquad 26)$$

At the edge of the contact area, a tensile stress σ_r exists, the maximum value of which is given by:

$$\sigma_r = \frac{(1-2\nu)}{2} \frac{P}{\pi a^2} \qquad (27)$$

Based on this tension, the stress intensity factor for a small crack in this tension region is given by (Zhang et al., 1989):

$$K_I = 1.12 \sigma_r \sqrt{\pi \ell}$$

$$= \left\{ \frac{1.12(1-2\nu)P}{2\pi \left[\frac{3PR(1-\nu^2)}{2E} \right]^{2/3}} \right\} \sqrt{\pi \ell} \qquad (28)$$

This model predicts unstable crack growth and is only valid for l<<a. A tensile stress will also develop in the sphere similar to that in a Brazilian test (Sternberg and Rosenthal, 1952). A small flaw in the center of the sphere will be subjected to a mode I stress intensity factor which for a two dimensional disk of radius R can be approximated by (Rooke and Cartwright, 1976):

$$K_I = \frac{P}{R} \sqrt{\frac{\ell}{\pi}} \left[1 + \frac{3}{2} \left(\frac{a}{R} \right)^2 \right] \qquad (29)$$

Again this solution predicts unstable crack growth.

Generic Model

Because of the similarity in rock behavior under compression in a wide range of rock types, it is not surprising that the micromechanical models discussed in the previous sections have many similarities. This may explain the success of certain models such as the

sliding crack and pore models, in spite of the lack of evidence for these models in microscopic studies. The similarities in behavior between the different models include:

1. Crack growth predominantly in the σ_1 direction.
2. K_I proportional to a distance parameter such as pore size, grain size, initial crack length, etc.
3. Crack growth unstable when the crack length on the order of the small parameter.
4. Crack growth stable when the crack length is large compared with the small parameter.
5. K_I very sensitive to σ_2.
6. K_I linearly proportional to $\sigma_1 - C\sigma_2$, where C is a constant.

Because of these similarities, is seems appropriate to develop a 'generic' micromechanical model that in some way takes into account all of the above phenomena. Here a generic model is proposed, which consists of a crack of length $2l$ oriented in the direction of σ_1, and subjected to a tensile stress σ_0 over a region of length 2a, as shown in Figure 7. The length of this tensile region remains fixed as the crack grows. Initially the crack length $2l$ can be smaller than the length 2a, and for this case the behavior should be described by the small-crack approximations. As the crack grows and becomes long compared with a, the model should behave like the long-crack approximations. Based on item 6 above, we take σ_0 to be linearly proportional to $\sigma_1 - C\sigma_2$, i.e.:

$$\sigma_0 = C_1(\sigma_1 - C_2\sigma_2) \qquad (30)$$

where C_1 and C_2 are constants. A closed form solution for K_I for this configuration can be derived from the Green's function solution given in equation (2). The stress distribution is given by:

$$\sigma(x) = \begin{cases} C_1(\sigma_1 - C_2\sigma_2) & |x| \le a \\ 0 & l \le |x| > a \end{cases} \qquad (31)$$

Thus K_I for this configuration is given by:

$$K_I = \frac{C_1(\sigma_1 - C_2\sigma_2)}{\sqrt{\pi l}} \int_{-a}^{a} \sqrt{\frac{l+x}{l-x}}\, dx - \sigma_2\sqrt{\pi l}$$

$$= \frac{2C_1(\sigma_1 - C_2\sigma_2)\sqrt{l}}{\sqrt{\pi}} \sin^{-1} a/l - \sigma_2\sqrt{\pi l} \qquad (32)$$

Note we have added the effect of σ_2 closing the crack. The results of this equation with C_2 = 3 are shown in Figure 8, at different values of σ_2/σ_1. Figure 8 shows that initially K_I increases with increasing crack length, and starts to decrease as soon as l >a. Thus initial unstable behavior is predicted, followed by stable crack growth for l>a. The model has three free parameters, a, C_1 and C_2.

Consider a slightly more realistic configuration where the stress σ_0 is not constant over the region 2a but decreases linearly as shown in Figure 7. K_I for this case can be calculated in the same manner and gives:

$$K_I = \frac{C_1(\sigma_1 - C_2\sigma_2)\sqrt{l}}{\sqrt{\pi}} \left[(2 - l/a)\sin^{-1} a/l + \sqrt{1 - a^2/l^2} \right] - \sigma_2\sqrt{\pi l} \qquad (33)$$

The results of this equation with C_2 = 3 are shown in Figure 9, at different values of σ_2/σ_1. In contrast with the results in Figure 8, the peak in the K_I vs. l curves in Figure 9 decreases with increasing σ_2/σ_1. This matches closely with the Sammis and Ashby (1986) model shown in Figure 3.

Crack Interaction

The effects of crack interaction were not considered in any of the models described above. In general the two extremes of crack interaction effects (in two dimensions) are collinear interaction and parallel interaction. Simple models for the effects of collinear and parallel crack interaction are considered here. Recall that many of the long-crack approximations are based on a crack oriented in the direction of σ_1 and subjected to point normal forces P at the center of the crack. Collinear crack interaction can be included by considering a collinear array of cracks, each containing center point forces P. The stress intensity solution for this is given by (Rooke and Cartwright, 1976):

$$K_I = \frac{P}{\sqrt{b \sin \frac{\pi \ell}{b}}} - \sqrt{2}\sqrt{2b \tan \frac{\pi \ell}{2b}} \qquad (34)$$

where b is the center-to-center distance between the cracks. This solution can form the basis for interaction effects in the models described above. For instance, for the long-crack approximation to the sliding crack as given in equation (15), the inclusion of crack interaction gives:

$$K_I = \frac{2\ell_o \tau^* \cos\beta}{\sqrt{b \sin \frac{\pi \ell}{b}}} - \sqrt{2}\sqrt{2b \tan \frac{\pi \ell}{2b}} \qquad (35)$$

The intensity of crack interaction is a function of l/b, which varies from l_o/b initially to 1 when the cracks have coalesced into a splitting fracture. Similarly, the effects of parallel interaction can be included by considering a doubly periodic array of cracks, each containing center point forces P. For the sliding crack model, the K_I solution becomes (Kemeny and Cook, 1987a):

$$K_I = \frac{\tau^* 2\ell_o \cos\beta}{\sqrt{b \sin \frac{\pi \ell}{b}}} \left[1 - 2\sin\left(\frac{\pi \ell}{2b}\right) \frac{\ln\left[\frac{\tan \frac{\pi f}{2b}}{\tan \frac{\pi \ell_o}{2b}}\right]}{\frac{\pi f}{4b} + \ln\left[\frac{\cos \frac{\pi \ell_o}{2b}}{\cos \frac{\pi \ell}{2b}}\right]} \right] \qquad (36)$$

$2f$ = spacing between parallel cracks

Derivation of Nonlinear Stress-Strain Curves

The K_I solutions as given in the previous section can be used to derive nonlinear stress-strain curves due to the growth of cracks under compressive stresses. Experiments have indicated a close relationship between nonlinear constitutive rock behavior and the growth,

interaction, and coalescence of microcracks (e.g., Hallbauer et al., 1973). In general, the initial growth of cracks is associated with strain-hardening behavior, and the interaction and coalescence of cracks is associated with strain-softening behavior. These results also agree with experiments on plexiglass sheets containing slits and subjected to compressive stresses (Horii and Nemat-Nasser, 1986). In addition to the K_I solutions given in last section, we have the choice of the crack growth criterion to use, namely:

$K_I = K_{IC}$ crack growth criterion

or

Subcritical crack growth criterion - $\partial l/\partial t = A(K_I)^n$

If the $K_I = K_{IC}$ criterion is used, then rate-independent stress-strain curves can be derived. If the subcritical crack growth criterion is used, then rate-dependent stress-strain curves and creep behavior can be derived. In this section we demonstrate how these three deformation phenomena can be derived, using first the K_I solution for the long-crack approximation to the sliding crack without crack interaction (equation 15), and secondly, using the long-crack approximation to the sliding crack with crack interaction (equation 35). The results show that without crack interaction, the following characteristics of rock behavior can be modelled:

1. Strain-hardening
2. Sensitivity of stress-strain curves to σ_2.
3. Rate-dependence of strength
4. Transient creep behavior

With crack interaction, the following two additional characteristics of rock behavior can be modelled:

5. Strain-softening
6. Creep Rupture

Also, it is found that using realistic material parameters, the models give an excellent match with laboratory data.

Nonlinear Stress-Strain Curves - $K_I = K_{IC}$ Criterion

Consider a body of width 2w, height 2h, and unit thickness, containing a single sliding crack, and subjected to principal stresses σ_1 and σ_2. The displacement at the boundary of the body will consist of the displacement of the body if the crack was not present plus the additional displacement due to the crack. The displacement due to the body with no crack is simply given by:

$$\delta_e = \frac{\sigma_1 \cdot 2h}{E'} \qquad (37)$$

The additional displacement due to the crack can be calculated using Castigliano's theorem, as given in equation (5), and using the K_I solution for the non-interacting sliding crack as given in equation (15). This gives:

$$\delta_c = \frac{\partial U_0}{\partial P} = \frac{\partial}{\partial P}\left\{ 2\int_{\ell_0}^{\ell} \frac{K_I^2}{E} d\ell \right\}$$

$$= \frac{8\ell_0^2 c(sc - \mu c^2)}{2wE}\left[\frac{2\tau^* c}{\pi} \ln \frac{\ell}{\ell_0} - \frac{\sigma_2}{\sigma_1}\left(\frac{\ell}{\ell_0} - 1\right)\right] \qquad (38)$$

where throughout the rest of this section c and s are used for $\cos\beta$ and $\sin\beta$, respectively. At this point we consider the displacement due to N non-interacting sliding cracks, which will be N times the displacement given above. The total strain is calculated from the total displacement (elastic plus crack displacements) and gives:

$$\epsilon_1 = \frac{\sigma_1}{E}\left[1 + 8\chi c(sc - \mu c^2)\left(\frac{2\tau^* c}{\sigma_1 \pi} \ln \frac{\ell}{\ell_0} - \frac{\sigma_2}{\sigma_1}\left(\frac{\ell}{\ell_0} - 1\right)\right)\right] \qquad (39)$$

where we define χ as the initial crack density, given by:

$$\chi = \frac{N\ell_0^2}{V} \qquad (40)$$

V is the volume which is equal to 2w x 2h for a two dimensional body of unit thickness. For a fixed crack length, equation (39) represents a linear relationship between stress and strain. On a plot of stress vs. strain, this represents a series of straight lines with different slopes for different values of l, as shown on Figure 10. These lines would be the effective moduli for proportional loading, $\sigma_1 = k\sigma_2$.

The crack growth criterion $K_I = K_{IC}$ is now introduced. On each of the straight lines (i.e., for a given crack length $2l$), there will be a point on the line where the $K_I = K_{IC}$ criterion is met, which is given by:

$$K_{IC} = \frac{2\ell_o \tau^* \cos\beta}{\sqrt{\pi \ell}} - T_2\sqrt{\pi \ell} \qquad (41)$$

This equation can be solved for σ_1 (τ^* is a function of σ_1, see equation 12), which gives the stress at which cracking will occur along any of the straight lines on Figure 10. Initially, the crack has a length l_o, and as the stress is increased loading will initially follow this line. When equation (41) above is satisfied for $l = l_o$, the crack will start to grow, and the stress and strain values will follow the nonlinear curve defined by the locus of points calculated from the stresses in equation (41) and the strains from equation (39). The results of this procedure are plotted in Figure 11 for material parameters representing Westerly granite (material properties given in Table 1), for different values of σ_2. Note that this model predicts initial linear loading, followed by strain hardening. Also, the results are very sensitive to small increases in σ_2.

For the case of uniaxial loading ($\sigma_2 = 0$), a closed form solution for this nonlinear curve can be derived by eliminating the crack length a from the two equations, which gives:

$$\epsilon_1 = \frac{T_1}{E}\left[1 + 8\chi c(sc - \mu c^2)\left[\frac{2\tau^* c}{T_1 \pi} \ln\left(\frac{4\ell_o \tau^{*2} c^2}{K_{IC}^2 \pi}\right)\right]\right] \qquad (42)$$

This analysis is now repeated, using the K_I solution for the model with crack interaction as given in equation (35). First the linear stress-strain behavior is calculated for a body

containing N cracks, where collinear crack interaction is included. Using Castigliano's theorem, the total strain is given by:

$$\epsilon_1 = \frac{\sigma_1}{E}\left[1 + \frac{16\chi(1-\mu^2)}{\pi}\left[\frac{\sigma_c}{\sigma_1}\ln\left(\frac{\tan\frac{\pi\ell}{2b}}{\tan\frac{\pi\ell_0}{2b}}\right) - \frac{\sigma_2}{\sigma_1}\frac{b}{\ell_0}\ln\left(\frac{\tan\frac{\pi}{4}\left(1+\frac{\ell}{b}\right)}{\tan\frac{\pi}{4}\left(1+\frac{\ell_0}{b}\right)}\right)\right]\right] \quad (43)$$

Again the crack density parameter χ has been used as given in equation (40). The second equation that is needed is the crack growth criterion, given by:

$$K_{Ic} = \frac{2\sigma_c\sqrt{\ell}\cos\beta}{\sqrt{b\sin\frac{\pi\ell}{b}}} - \sigma_2\sqrt{2b\tan\frac{\pi\ell}{2b}} \quad (44)$$

Taken together, equations (43) and (44) represent the nonlinear stress-strain behavior, i.e., the stress-strain curve is the locus of stresses calculated from equation (44) and strains calculated from equation (43) for crack lengths that vary from l_0/b to 1. Nonlinear stress-strain curves calculated for different values of σ_2 are presented in Figure 12. The material properties used are that of Westerly Granite, as given in Table 1. Also in Figure 12, these results are compared with experimental results from Wawersik and Brace (1971). The model results are able to reproduce many of the features of the stress-strain behavior of Westerly granite. This includes the initial strain-hardening due to the initial stable growth of the wing cracks before crack interaction, and the strain-softening behavior due to crack interaction. Also, the model predicts the large increase in strength with very small increases in confining stress. The model predicts that ultimate failure occurs by the wing cracks coalescing to form a single, macroscopic axial-splitting crack. The model does not predict the transition to shear faulting that occurs at higher values of confining stress. More sophisticated results could be produced by considering more complex crack interaction effects.

Nonlinear Stress-Strain Curves - Subcritical Crack Growth Criterion

Consider a body of width 2w, height 2h, and unit thickness containing N noninteracting sliding cracks, and subjected to uniaxial loading ($\sigma_2 = 0$). On the boundary of the body, a fixed uniaxial strain rate $\dot{\epsilon}_0$ is applied. Assuming the strain at t=0 is equal to zero, this gives:

$$\epsilon_1 = \dot{\epsilon}_0 t \qquad (45)$$

Using the value for the stress intensity factor from equation (15), the subcritical crack growth equation becomes:

$$\frac{dl}{dt} = A\left[\frac{2\sigma_0 \tau^* \cos\beta}{\sqrt{\pi l}}\right]^n \qquad (46)$$

The linear stress-strain relation for this configuration is the same as equation (39) that was derived in the previous section (and setting $\sigma_2 = 0$). Equation (39) can be solved for σ_1 and along with equations (45) and (46), this gives:

$$\frac{dl}{dt} = A\left[\frac{2\lambda_1 \dot{\epsilon}_0 t E (sc - \mu c^2) c}{\sqrt{\pi l}\left[1 + \frac{16\chi c^2 (sc - \mu c^2)^2}{\pi} \ln\frac{l}{l_0}\right]}\right]^n \qquad (47)$$

This nonlinear ordinary differential equation, along with the initial condition that $l = l_0$ at t=0, can be solved numerically to give crack length as a function of time ($l(t)$). This, along with equation (39), gives σ_1 as a function of time:

$$\sigma_1(t) = \frac{E \dot{\epsilon}_0 t}{1 + \frac{16\chi c^2 (sc - \mu c^2)^2}{\pi} \ln\frac{l(t)}{l_0}} \qquad (48)$$

The strain as a function of time is given by equation (45), and the nonlinear stress-strain curve is the plot of these $\sigma(t)$, $\varepsilon(t)$ pairs for different times. Some numerical results are shown in Figure 13, using the properties of Oshima granite as given in Table 2. The results are shown for two values of the loading rate that differ by an order of magnitude. As shown in Figure 13, the stress-strain curve is sensitive to the loading rate. Initially, the cracks grow at extremely small rates due to the n value of 30. and this region the results for the two loading rates follow the same elastic slope. As the cracks start to grow at higher rates, the case with the higher loading rate results in higher stresses, which agrees with experimental data (Jaeger and Cook, 1979).

The analysis is now repeated, using the stress intensity factor solution that includes collinear crack interaction (equation 35). This solution is used in the subcritical crack growth equation, along with the linear stress-strain relation for the case of collinear crack interaction as given in equation (43). As before, this results in a nonlinear ordinary differential equation. Using the initial condition that $l/b = l_o/b$ at t=0, this equation can be integrated to give $l/b(t)$. This along with equation (43) can be used to give σ_1 as a function of time. These results are presented for the material properties of Oshima granite (Table 2) in Figure 14a for four values of applied strain rate. The results are compared with the experimental data of Sano et al. (1981) at the same strain rates in Figure 14b. The results show several interesting features. Initially, the behavior is linear, and this is due to the region when the cracks are growing at a very low rate. As the crack velocity increases, strain-hardening behavior is initially predicted, followed by strain-softening behavior. The volume strain is initially compressional, dominated by the solid matrix before the cracks begin to grow. As the cracks grow, the volume strain becomes dilatational. The stresses at which this occurs, and the amount of dilatation, match closely with the results of Sano et al. (1981), as shown in Figure 14b. The results show an increase in strength with increasing loading rate, which is in agreement with experimental results.

Creep

For the case with no crack interaction, consider the same two equations as before, i.e., the linear stress-strain equation as given in equation (39), and the crack velocity equation as given in equation (46). To model the creep behavior of crack growth under compression, we now consider the boundary conditions of a constant uniaxial stress σ_1. In this case, using the initial condition that $l = l_0$ at t=0, equation (46) can be integrated analytically to give:

$$\ell = \left[A \frac{(2\ell_o \tau^* \cos\beta)^n}{\pi^{n/2}} (1 + n/2) + \ell_o^{1+n/2} \right]^{\frac{1}{1+n/2}} \qquad 49$$

and the strain as a function of time becomes:

$$\epsilon_1 = \frac{T_1}{E} \left[1 + \frac{16 K_{IC}^2 (SC - \mu C^2)^2}{\pi (1+n/2)} \ln \left(1 + \frac{A (2\ell_o \tau^* \cos\beta)^n t (1+n/2)}{\pi^{n/2}} \right) \right] \qquad 50$$

This can be rewritten into the form:

$$\epsilon_1 = \epsilon_0 - C_1 \ln (1 - C_2 t) \qquad 51$$

where

$$\epsilon_0 = \bar{T}_1 / E$$

$$C_1 = \bar{T}_1 / E \; \frac{16 K_{IC}^2 (SC - \mu C^2)^2}{\pi (1+n/2)}$$

$$C_2 = \frac{A (2\ell_o \tau^* \cos\beta)^n (1+n/2)}{\pi^{n/2}}$$

Equation (51) predicts transient creep and is of the exact form that is often used to describe the transient creep in brittle rocks from experimental studies (Jaeger and Cook, 1979).

The above analysis can be repeated using the stress intensity factor solution that includes collinear crack interaction, equation (35). When this solution is used in the subcritical crack growth equation, it can be integrated to give *l*/b(t), and using equation (43), ε(t). The

results for different values of creep stress are presented in Figure 15. For small times for all values of σ_1 and for all times for low values of σ_1, the results agree with the results with no crack interaction, i.e., transient creep. For values of σ_1 close to the failure stress, a transition from transient creep to creep rupture is seen.

Continuum Damage Modelling

The nonlinear results derived in the previous section were made under the assumption that the principal stresses σ_1 and σ_2 are uniform throughout the body (no end effects or stress gradients). Using the finite element method, these results can be extended to complicated boundary conditions that contain stress gradients. This is accomplished by implementing the procedures described in the previous section into an elastic finite element code on an element by element basis, where in each element it is assumed that the principal stresses are uniform. Like the results in the previous section, nonlinear behavior is predicted due to crack growth in an otherwise linearly elastic body. Also as in the previous section, two relationships are needed, the first being the linear stress-strain relationship for each element as a function of its crack density, and the second being a crack growth criterion. If the $K_I = K_{IC}$ crack growth criterion is used, then rate-independent nonlinear behavior will be predicted. If the subcritical crack growth criterion is used, then rate-dependent nonlinear behavior and creep will predicted. Results using both the $K_I = K_{IC}$ and subcritical crack growth criteria are presented in the following sections. First the issue of stress-induced anisotropy is discussed.

Stress-Induced Anisotropy

The micromechanical models reviewed in section 2 predict that crack growth under compression occurs primarily in the direction of σ_1. For a body that is initially isotropic, crack growth in the direction of σ_1 will result in stress-induced anisotropic rock properties, and this must be taken into account in the finite element calculations. In the case of an initially isotropic body, crack growth in the direction of the maximum principal stress will render the material transversely isotropic. The linear stress-strain relations under the assumption of transverse isotropy are given by:

$$\epsilon_x = \frac{\sigma_x}{E_1} - \frac{\nu_2 \sigma_y}{E_2} - \frac{\nu_1 \sigma_z}{E_1}$$

$$\epsilon_y = -\frac{\nu_2 \sigma_x}{E_2} + \frac{\sigma_y}{E_2} - \frac{\nu_2 \sigma_z}{E_2}$$

$$\epsilon_z = -\frac{\nu_1 \sigma_x}{E_1} - \frac{\nu_2 \sigma_y}{E_2} + \frac{\sigma_z}{E_1}$$

$$\epsilon_{xz} = \frac{2(1+\nu_1)}{E_1}\tau_{xz}$$

$$\epsilon_{xy} = \frac{1}{G_2}\tau_{xy} \qquad (52)$$

$$\epsilon_{yz} = \frac{1}{G_2}\tau_{yz}$$

Note that there are five independent elastic constants, E_1, E_2, ν_1, ν_2, and G_2. In two dimensions, the linear stress-strain relationship can be put into the form (plain strain):

$$\begin{Bmatrix} \sigma_x \\ \sigma_y \\ \tau_{xy} \end{Bmatrix} = D \begin{Bmatrix} \epsilon_x \\ \epsilon_y \\ \epsilon_{xy} \end{Bmatrix} \qquad (53)$$

where the D matrix is given by:

$$D = \frac{E_2}{(1+\nu_1)(1-\nu_1-2n\nu_2^2)} \begin{bmatrix} n(1-n\nu_2^2) & n\nu_2(1+\nu_1) & 0 \\ n(1+\nu_1)\nu_2 & (1-\nu_1^2) & 0 \\ 0 & 0 & m(1+\nu_1)(1-\nu_1-2n\nu_2^2) \end{bmatrix} \qquad (54)$$

where $n=E_1/E_2$ and $m=G_2/E_2$. The above formula assume that the cracks grow parallel to the x axis. If crack growth is inclined relative to the x axis, then the D matrix can be transformed by a matrix containing the direction cosines (Zienkiewicz and Taylor, 1989). Using equation (52), Castigliano's theorem, and one of the K_I solutions for crack growth under compression from section 2, the five independent elastic constants for stress-induced anisotropy can be determined. For instance, for the sliding crack model with collinear crack interaction (equation 35), this gives:

$$E_1 = \frac{E}{1 + \frac{16\chi}{\pi}\left[(sc-\mu c^2) - \frac{\sigma_2}{\sigma_1}(sc+\mu c^2)\right] c^2 (sc-\mu c^2) \ln\left[\frac{\tan\frac{\pi\ell}{2b}}{\tan\frac{\pi\ell_0}{2b}}\right]}$$

$$E_2 = \frac{E}{1 + \frac{16\chi}{\pi}\left(\frac{b}{\ell_0}\right)^2 \ln\sec\frac{\pi\ell}{2b}}$$

$$\nu_1 = \frac{E_1}{E} \cdot \nu$$

$$\nu_2 = \frac{E_2}{E}\left[\nu + \frac{16\chi}{\pi}(sc-\mu c^2) c\left[c(sc+\mu c^2)\ln\left[\frac{\tan\frac{\pi\ell}{2b}}{\tan\frac{\pi\ell_0}{2b}}\right] + \frac{b}{\ell_0}\ln\left[\frac{\tan\frac{\pi}{4}\left(1+\frac{\ell}{b}\right)}{\tan\frac{\pi}{4}\left(1+\frac{\ell_0}{b}\right)}\right]\right]\right]$$

$$G_1 = \frac{E}{2(1+\nu) + \frac{16\chi}{\pi}\left(\frac{b}{\ell_0}\right)^2 \ln\sec\frac{\pi\ell}{2b}}$$

55

Finite Element Damage Model - $K_I = K_{IC}$ Criterion

The D matrix for stress-induced anisotropy discussed above is a measure of the damage that occurs in each of the elements due to crack growth and interaction. This damage measure, along with the $K_I = K_{IC}$ crack growth criterion, has been implemented into an elastic finite element code to produce a nonlinear damage model. Details of this damage model are presented in Kemeny and Tang (1990). Results of this model for the geometry of a thick walled cylinder are presented in Figure 16. The thick walled cylinder is subjected to a vertical external stress of 260 MPa and a horizontal stress of 130 MPa. The properties assumed are that of Westerly granite given in Table 1, and the sliding crack model with crack interaction was used. As shown in Figure 16, crack growth stabilizes with only a minimum amount of damage occurring around the boundary of the specimen. An addition to the model was made to account for the presence of isotropic damage in addition to the anisotropic damage due to the growth of axial extensile cracks. This allows for the many additional sources of damage such as the linking of axial cracks via a shear crack. The results when isotropic damage is added are shown in Figure 17. Figure 17 shows a much more well developed breakout shape, which agrees with the numerical results of Zheng et al. (1989) and experimental results of Ewy (1989) and others. It is interesting to note that damage progresses into the rock without completely failing the rock in the damage zone.

For instance, at the boundary of the hole, the damage variable, *l*/b, reaches a value of 0.508 (*l*/b=1 is complete failure). This agrees with experimental results (e.g., Ewy, 1989).

Finite Element Damage Model - Subcritical Crack Growth Criterion

Here the subcritical crack growth criterion is used as the basis for a finite element damage model. Details are given in Kemeny and Tang (1990). Implementing the subcritical crack growth criterion rather than the $K_I = K_{IC}$ criterion results in several improvements in the damage model. One improvement is that the increase in crack length in each element at each time increment is calculated explicitly from the subcritical crack growth equation. Another improvement is the sensitivity of the results to the applied rate of loading. This rate dependence plays an important role in actual problems in geomechanics. In drilling, for instance, stress concentrations around the borehole can occur almost simultaneously with the drilling. In laboratory experiments, however, rock samples are usually pre-drilled, followed by the application of load at slower loading rates. These differences can be examined using the rate-dependent damage model. Some results of the rate-dependent damage model are presented in Figure 18. A thick walled cylinder is subjected to vertical and horizontal stresses of 50 and 25 MPa, respectively. The properties used are that of Oshima granite (table 2). In this creep test, the loads are applied instantaneously at t=0, and held constant. Figure 18 presents the results __ hours after the loads have been applied.

Conclusions

Linear elastic fracture mechanics is an important tool in understanding the nonlinear deformation of rocks. There are many different mechanisms for extensile crack growth in rocks due to differential compression, including pore crushing, sliding along pre-existing cracks, elastic mismatch between grains, dislocation movement, and hertzian contact. We have reviewed several fracture mechanics models for these different mechanisms, and many similarities between the models are evident. Based on these similarities, a generic model is proposed that encompasses the different models. Models to take into account the effects of crack interaction are also discussed. From the micromechanical models, nonlinear stress-strain curves are derived that exhibit strain-hardening and strain-softening, dilatation, σ_2 sensitivity, and rate dependence. Also, it is shown how these models can form the basis for continuum damage models using the finite element method.

Acknowledgements

This work was supported, in part, by the Director, Office of Basic Energy Sciences, Division of Engineering, Mathematics, and Geosciences, of the U.S, Department of Energy under contract DE-AC03-76SF00098. Special thanks are given to Dr. Ziqiong Zheng for allowing us to use the photograph shown in Figure 1, and to F. F. Tang for providing the rate-dependent finite element damage results.

References

Ashby, M.F. and Hallam, S.D. 1986. The failure of brittle solids containing small cracks under compressive stress. Acta Metall. 34:497-510.

Atkinson, B. K. 1984. Subcritical crack growth in geologic materials. J. Geophys. Res., 89:4077-4114.

Atkinson, B. K., and Meredith, P. G. 1987. The theory of subcritical crack growth with applications to minerals and rocks, In: Fracture Mechanics of Rock, edited by B. K. Atkinson, Academic Press, London, pp 111-166.

Carter, N.L., Anderson, D.A., Hansen, F.D., and Kranz, R.L. 1981. Creep and creep rupture of granitic rocks, In The Mechanical Behavior of Crustal Rocks, Geophysical Monograph 24, AGU, Washington, D.C.

Charles, R.J. 1958. Static fatigue of glass, J. Appl. Phys. 29:1549-1560.

Cherepanov, G.P. 1979. Mechanics of Brittle Fracture, McGraw-Hill, NY.

Costin, L.S. 1985. Damage mechanics in the post-failure regime. Mech. Mat. 4:149-160.

Costin, L.S. and Stone, C.M. 1987. Implementation of a finite element damage model for rock. Proc. 2nd Int. Conf. Constitutive Laws for Eng. Mat. 2:829-840.

Dey, T.N. and Wang, C.Y. 1981. Some mechanisms of microcrack growth and interaction in compressive rock failure, Int. J. Rock Mech. & Min. Sci., 18:199-209.

Evans, B. and Wong, T.-f. 1985. Shear localization in rocks induced by tectonic deformation, in Mechanics of Geomaterials, edited by Z. Bazant, John Wiley, pp189-210, New York.

Ewy, R. 1989. Ph.D. thesis, University of California, Berkeley.

Fredrich, J.T., Evans, B. and Wong, T.-f. 1989. Micromechanics of the brittle to plastic transition in Carrara marble. J. Geophys. Res. 94:4129-4145.

Fredrich, J.T.. and Wong, T.-f. 1986. Micromechanics of thermally induced cracking in three crustal rocks. J. Geophys. Res. 91:12743-12764.

Guenot, A. 1989. Borehole breakouts and stress fields. Int. J. Rock Mech. 26:185-195.

Haimson, B.C. and Herrick, C.G. 1985. In situ stress evaluation form borehole breakouts experimental studies, Proc. U.S. Symp. Rock Mech. 26th, 1207-1218.

Haimson, B.C. and Herrick, C.G. 1989. Borehole Breakouts and In Situ Stress. Proceedings, Energy-Source Technology Conference, Houston, TX.

Hallbauer, D.K., Wagner, H., and Cook, N.G.W. 1973. Some observations concerning the microscopic and mechanical behavior of quartzite specimens in stiff, triaxial compression tests. Int. J. Rock Mech. Min. Sci. 10:713-726.

Horii, H. and Nemat-Nasser, S. 1986. Brittle failure in compression: splitting, faulting, and brittle-ductile transition. Phil. Trans. Royal Soc. London. 319:337-374.

Jaeger, J.C., and Cook, N.G.W. 1979. Fundamentals of Rock Mechanics, 3rd Edition, Chapman and Hall, London.

Johnson, K.L. 1985. Contact Mechanics. Cambridge University Press, Cambridge.

Kemeny, J. M., and Cook, N. G. W. 1987a. Crack models for the failure of rock under compression. Proc. 2nd Int. Conf. Constitutive Laws for Eng. Mat. 2:879-887.

Kemeny, J.M. and Cook, N.G.W. 1987b. Determination of rock fracture parameters from crack models for failure in compression. Proc. 28th US Symposium on Rock Mechanics, 1:367-374.

Kemeny, J. M. 1990. A model for nonlinear rock deformation under compression due to subcritical crack growth, To appear.

Kemeny, J.M. and Tang, F.F. 1990. A Numerical Damage Model for Rock Based on Microcrack Growth, Interaction, and Coalescence, To appear, Symposium on Damage Mechanics in Engineering Materials at the ASME Winter Annual Meeting, Nov. 25-30, 1990, Dallas, Tex.

Krajcinovic, D. 1989. Damage mechanics, Mech. Mats., 8:117-197.

Kranz, R. L. 1983. Microcracks in rocks: a review. Tectonophysics. 100:449-480.

Lawn, B.R. and Wilshaw, T.R. 1975. Fracture of Brittle Solids. Cambridge University Press, Cambridge.

Nemat-Nasser, S. and Horii, H. 1982. Compression-induced nonplanar crack extension with application to splitting, exfoliation, and rock burst. J. Geophys. Res. 87:6805-6822.

Rooke, D.P., and Cartwright, D.J. 1976. Compendium of Stress Intensity Factors, The Hillingdon Press, Middx.

Sammis, C.G. and Ashby, M.F. 1986. The failure of brittle porous solids under compressive stress states. Acta Metall. 34:511-526.

Sano, O., Ito, I., and Terada, M. 1981. Influence of strain rate on dilatancy and strength of Oshima granite under uniaxial compression, J. Geophys. Res., 86:9299-9311.

Sokolnikoff, I.S. 1956. Mathematical Theory of Elasticity, McGraw-Hill, NY.

Steif, P.S. 1984. Crack extension under compressive loading. Eng. Fract. Mech. 20:463-473.

Sternberg, E. and Rosenthal, F. 1952. The elastic sphere under concentrated loads, J. Appl. Mech. 19:413-21.

Wawersik, W. R. and Brace, W. F. 1971. Post-failure behavior of a granite and diabase. Rock Mech. 3:61-85.

Wong, T.-f. 1982. Micromechanics of faulting in Westerly granite. Int. J. Rock Mech. Min. Sci. 19:49-64.

Wong, T.-f. 1985. Geometric probability approach to the characterization and analysis of microcracking in rocks. Mech. of Mat. 4:261-276.

Zhang, J., Wong, T.-f., and Davis, D.M. 1989. Micromechanics of pressure-induced grain crushing in porous rocks. J. Geophys. Res., in press.

Zheng, Z., Kemeny, J. M., and Cook, N. G. W. 1989. Analysis of wellbore breakouts. J. Geophys. Res. 94:7171-7182.

Zheng, Z. 1989. Ph.D. thesis, University of California, Berkeley.

Zienkiewicz, O.C. and Taylor, R.L. 1989. The Finite Element Method. McGraw-Hill, London.

Zoback, M.D., Moos, D., and Mastin, L. 1985. Wellbore breakouts and in situ stress, J. Geophys. Res., 90:5523-5530.

Figure Captions

Figure 1. SEM micrograph of Berea sandstone subjected to uniaxial compression (σ_1 vertical) showing stress-induced microcracks formed by several different micro-mechanisms, from Zheng (1989).

Figure 2. a) Cylindrical pore model for crack growth under compression. b) small-crack approximation. c) long-crack approximation.

Figure 3. Results from the pore model of Sammis and Ashby for different values of σ_2/σ_1.

Figure 4. Sliding crack model for crack growth under compression.

Figure 5. Elastic mismatch model.

Figure 6. Dislocation pile-up model.

Figure 7. Generic model for crack growth under compression. a) constant stress σ_0 over a distance a at the crack center. b) linearly decreasing stress at the crack center.

Figure 8. Results of the generic model in Figure 7a for different values of σ_2/σ_1, and taking $C_2 = 3$.

Figure 9. Results of the generic model in Figure 7b for different values of σ_2/σ_1, and taking $C_2 = 3$.

Figure 10. Illustration of the derivation of nonlinear stress-strain curves using the effective moduli for the body containing cracks of different lengths (straight lines), along with the $K_I = K_{IC}$ criterion for crack growth for each of these crack lengths (solid points). Nonlinear stress-strain relation is the curve connecting these points.

Figure 11. Nonlinear stress-strain curves calculated from the sliding crack model without crack interaction using the $K_I = K_{IC}$ crack growth criterion. Parameter values used for Westerly granite (see Table 1).

Figure 12. Nonlinear stress-strain curves calculated from the sliding crack model with crack interaction using the $K_I = K_{IC}$ crack growth criterion. Parameter values used for Westerly granite (see Table 1). Experimental results by Wawersik and Brace (1971) at the same confining stresses (dashed lines).

Figure 13. Nonlinear stress-strain curves from the sliding crack model without crack interaction using the subcritical crack growth criterion. Parameter values for Oshima granite (see Table 2).

Figure 14. a) Nonlinear stress-strain curves from the sliding crack model with crack interaction using the subcritical crack growth criterion, at four values of applied strain rate. Parameter values for Oshima granite (see Table 2). b) Experimental results by Sano et al. (1981) at the same strain rates.

Figure 15. Creep vs. time using the sliding crack model with crack interaction and using the subcritical crack growth criterion, at three values of creep stress. Parameter values for Oshima granite (see table 2).

Figure 16. Contours of damage for a thick-walled cylinder subjected to horizontal and vertical stresses of 260 and 130 MPa, respectively. Damage model based on $K_I = K_{IC}$ crack growth criterion and sliding crack model with crack interaction.

Figure 17. Contours of damage for a thick-walled cylinder subjected to horizontal and vertical stresses of 260 and 130 MPa, respectively. Damage model based on $K_I = K_{IC}$ crack growth criterion and sliding crack model with crack interaction. Isotropic damage also added.

Figure 18. Contours of damage for a thick-walled cylinder subjected to horizontal and vertical stresses of 50 and 25 MPa, respectively. Damage model based on subcritical crack growth criterion, and results are shown after loads have been applied for __ hours.

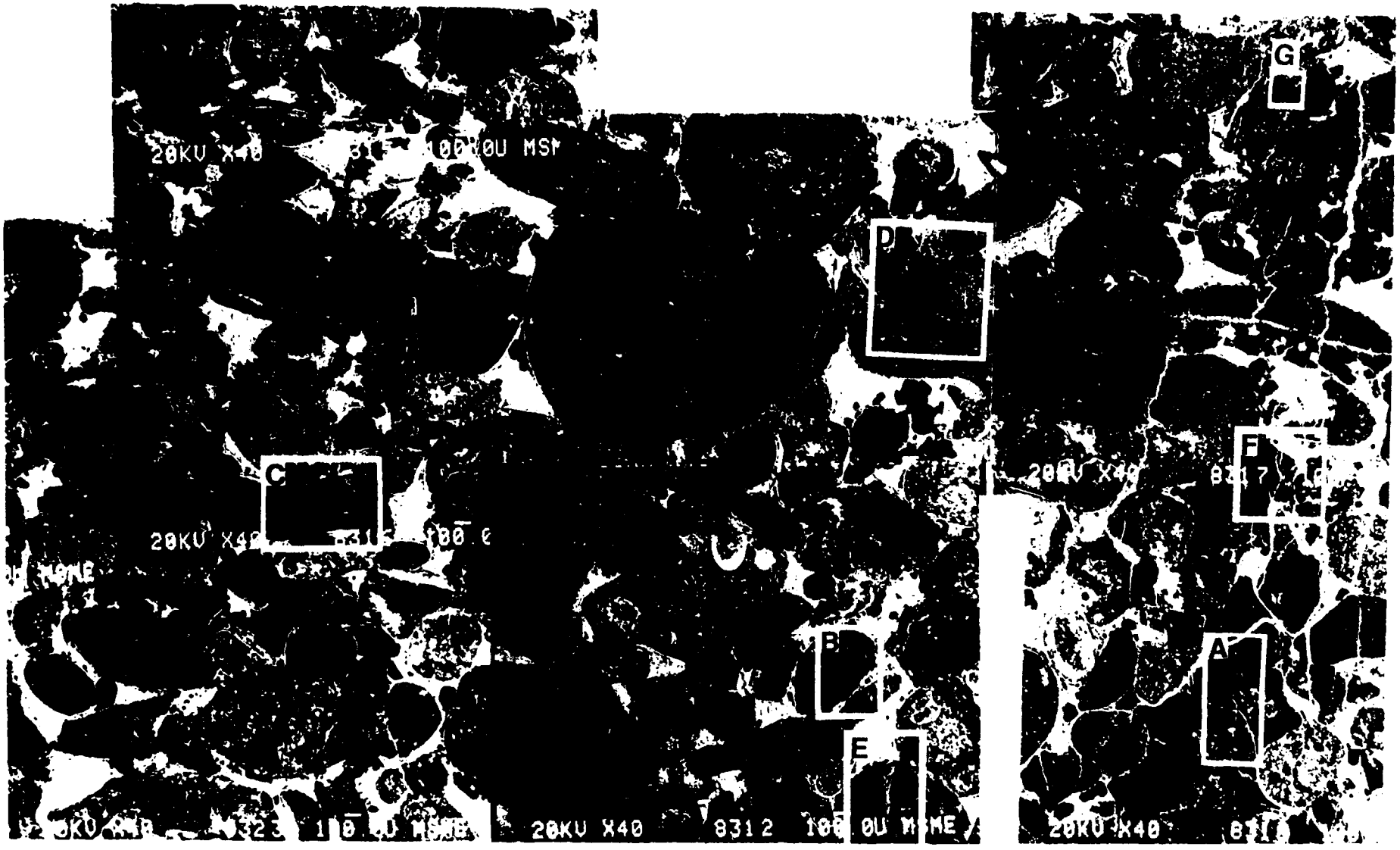

Fig. 1

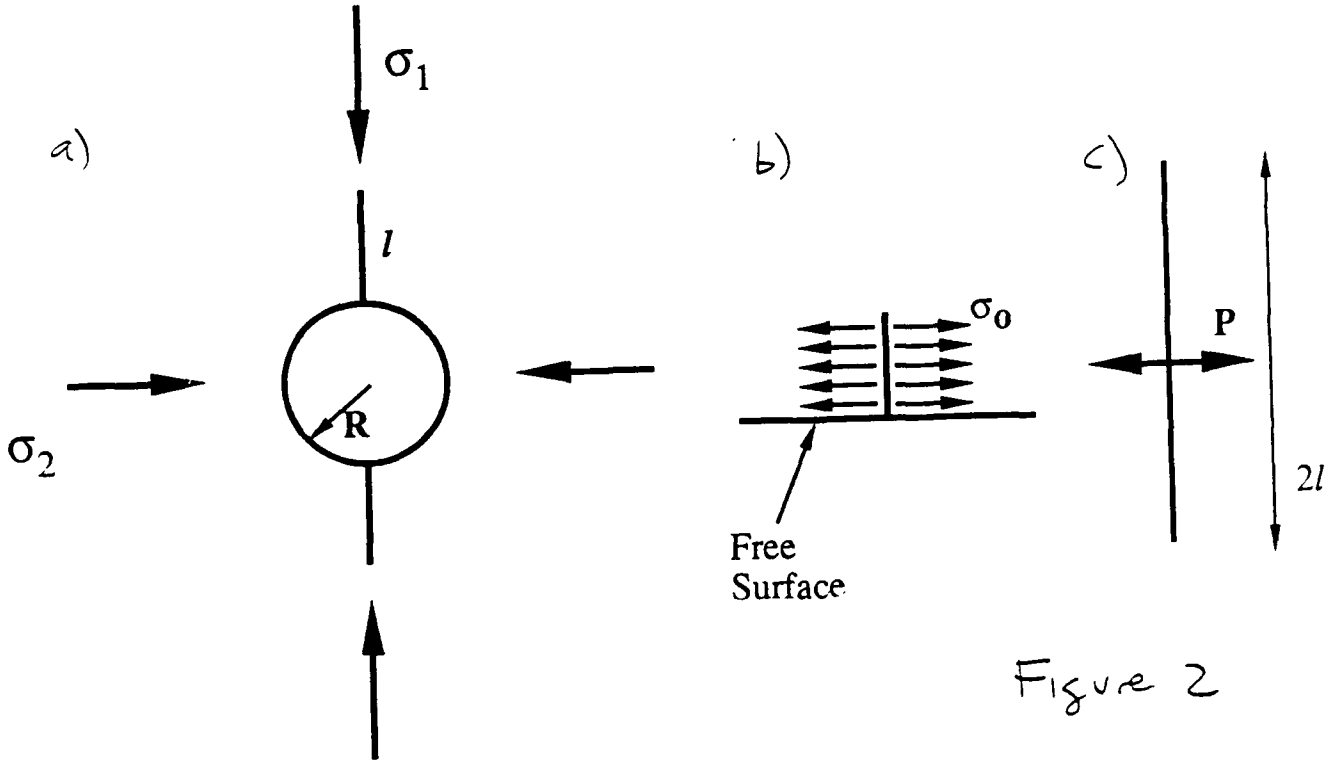

Figure 2

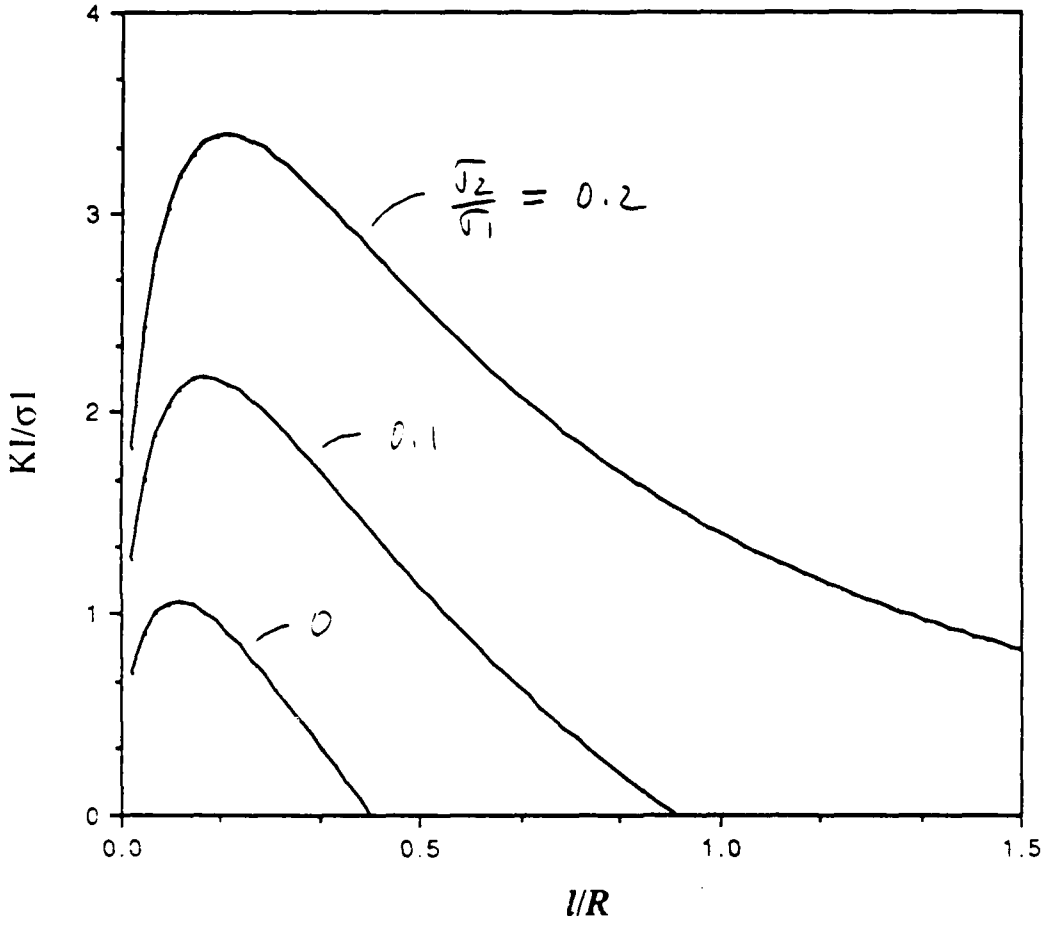

Figure 3

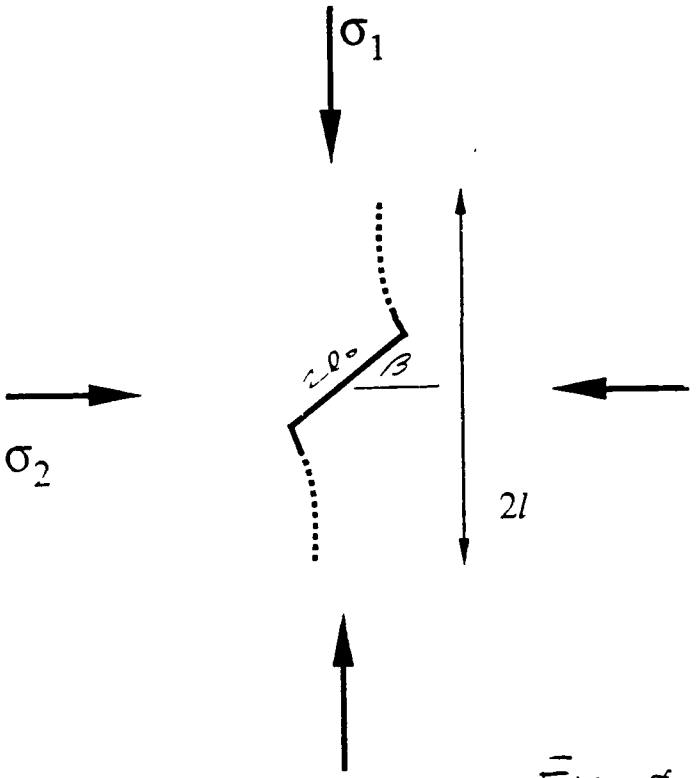

Figure 4

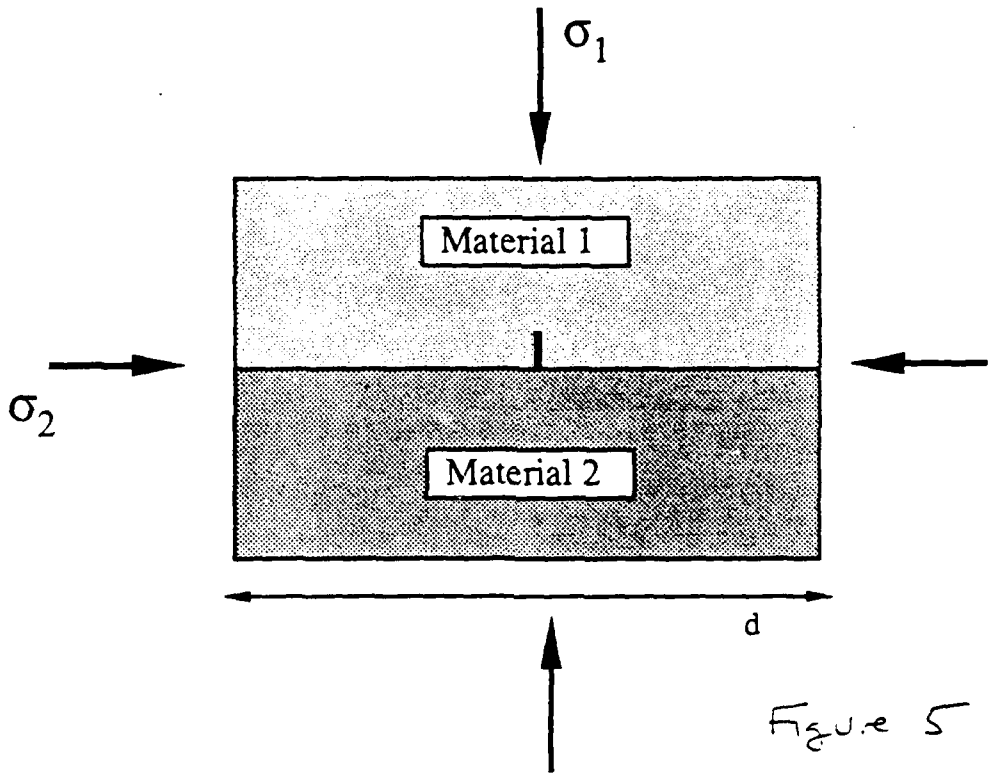

Figure 5

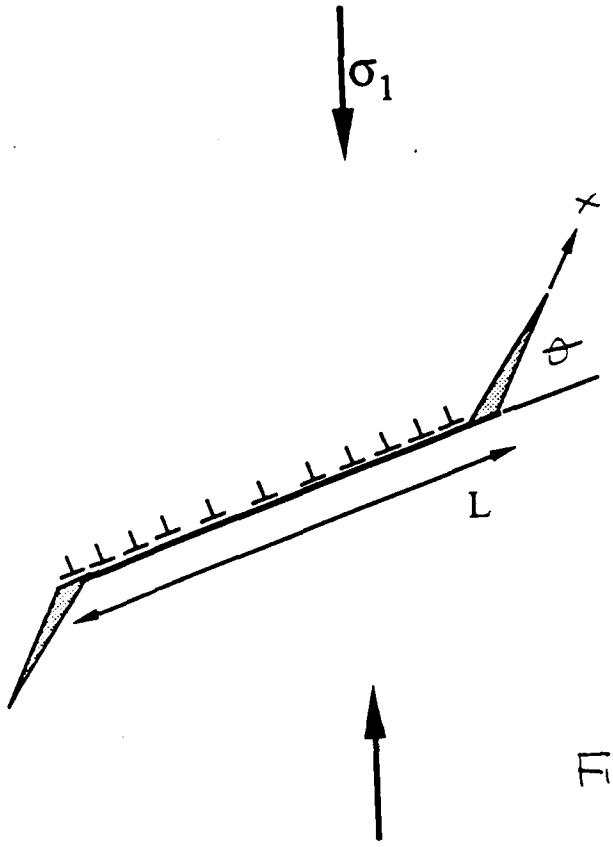

Figure 6

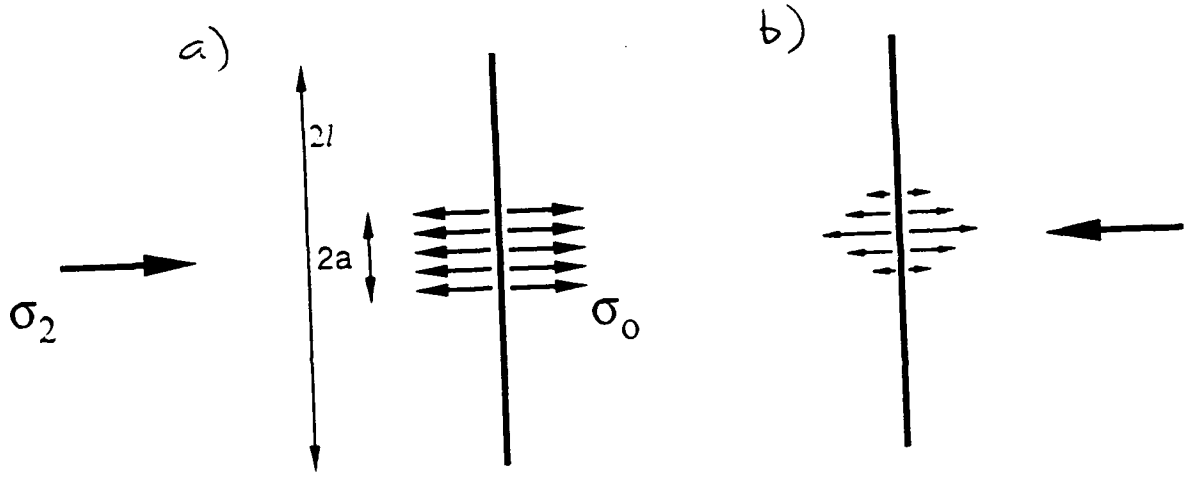

Figure 7

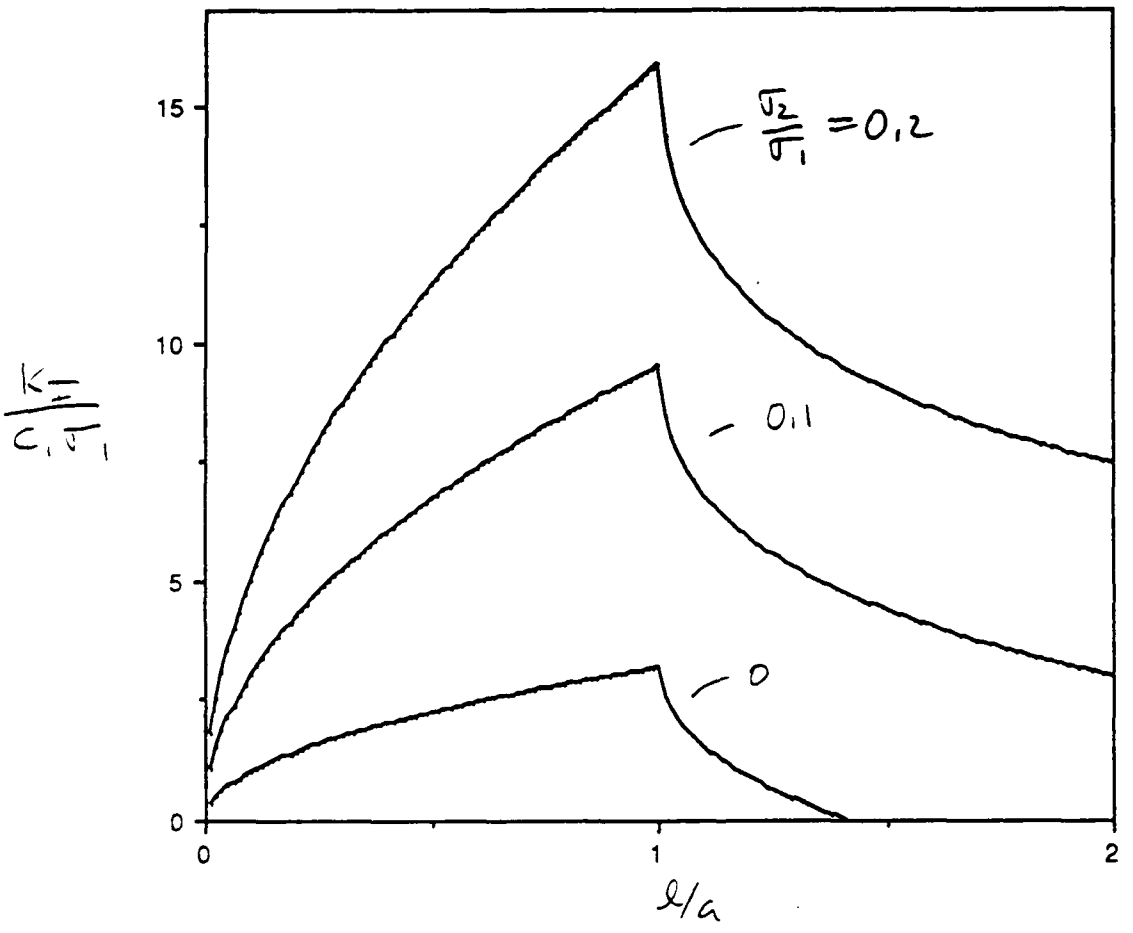

Figure 8

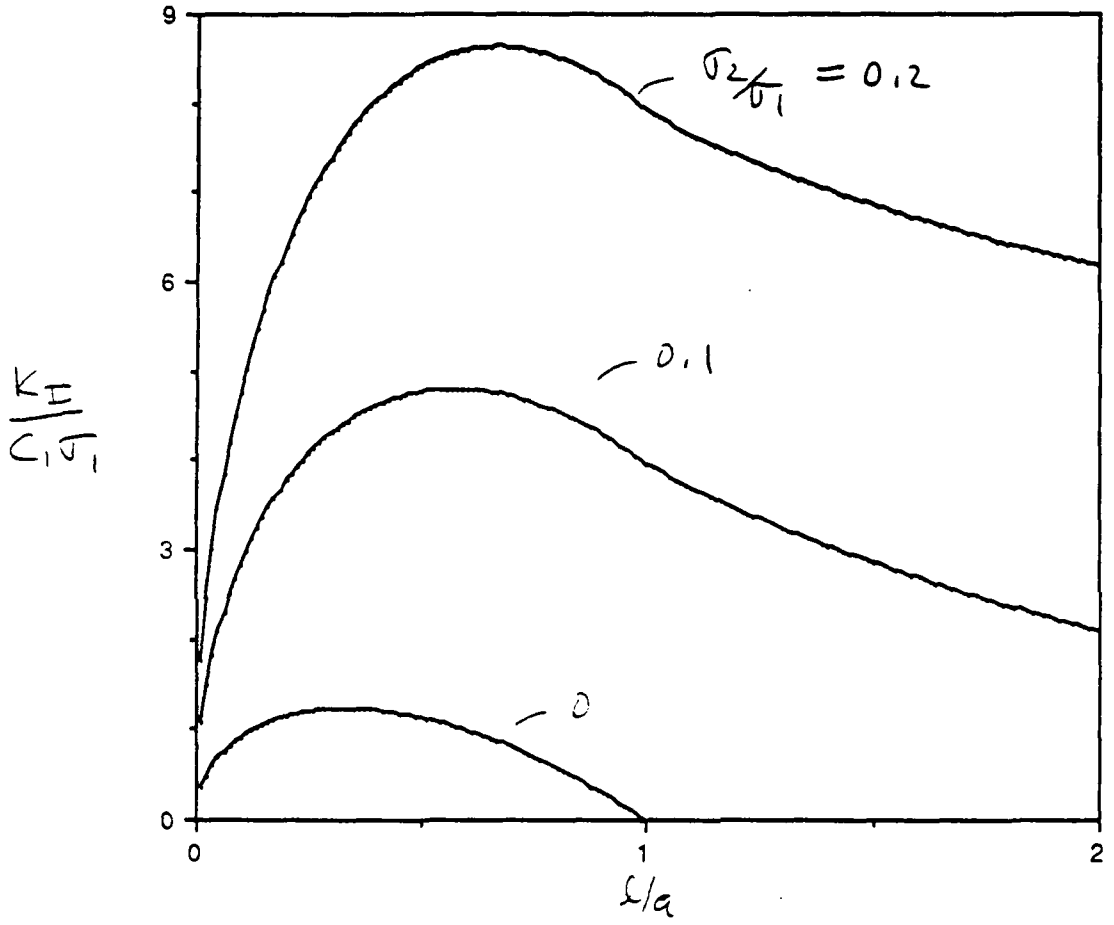

Figure 9

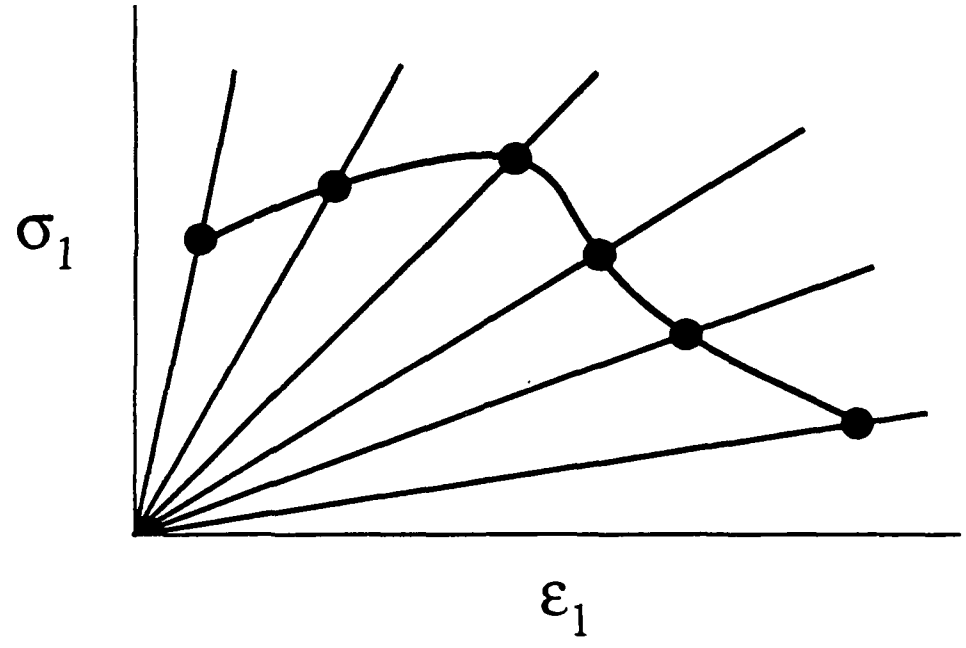

Figure 10

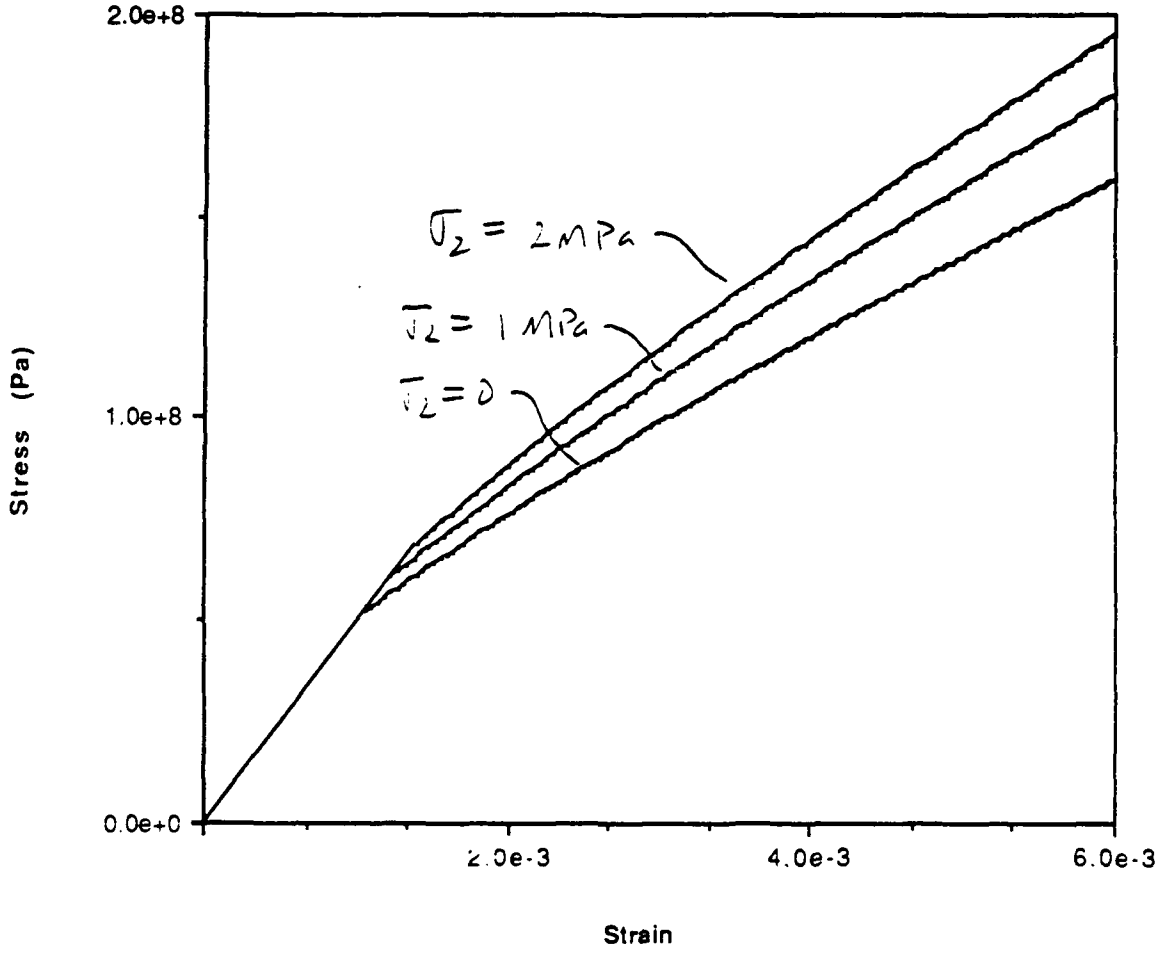
2.0e+8
1.0e+8
0.0e+0
Stress (Pa)
σ_2 = 2 MPa
σ_2 = 1 MPa
σ_2 = 0
2.0e-3
4.0e-3
6.0e-3
Strain

Figure 11

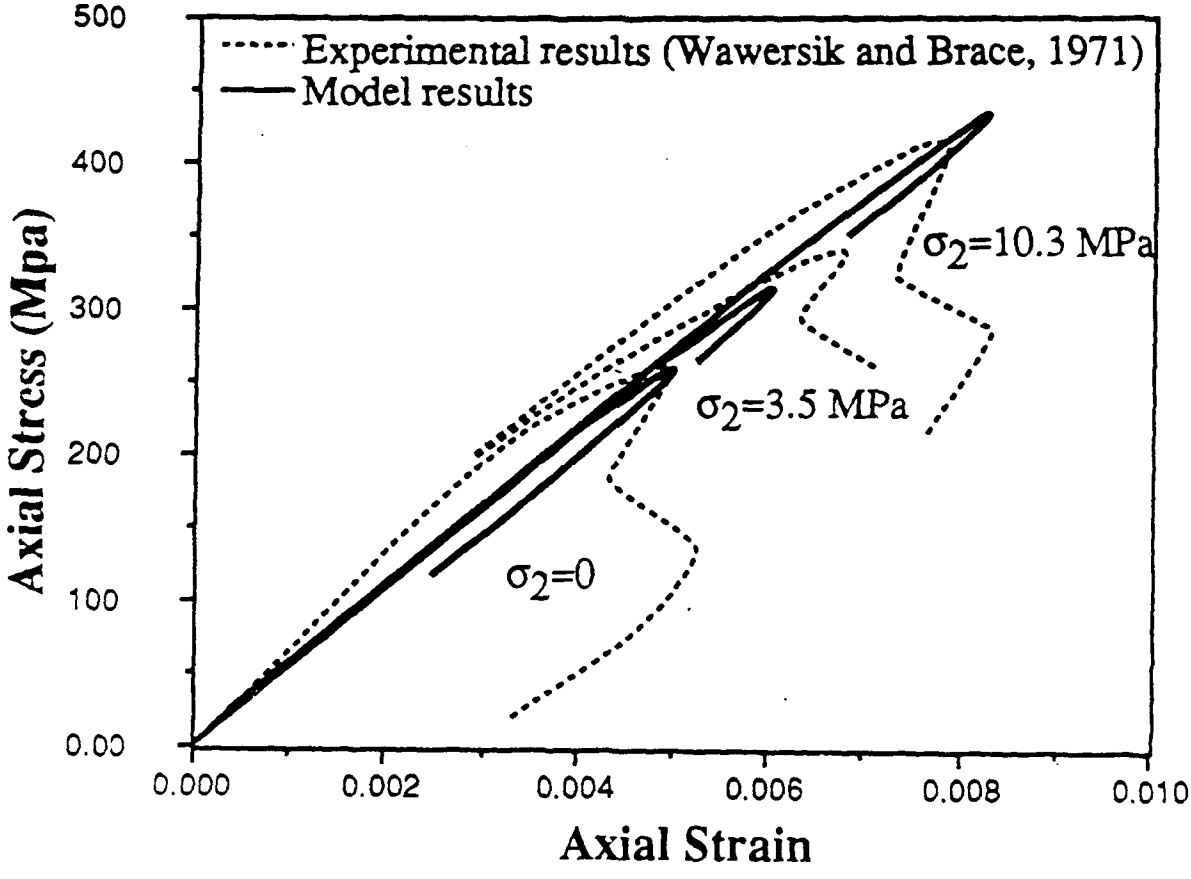
Experimental results (Wawersik and Brace, 1971)
Model results
σ2=10.3 MPa
σ2=3.5 MPa
σ2=0
Axial Stress (Mpa)
Axial Strain
500
400
300
200
100
0.00
0.000
0.002
0.004
0.006
0.008
0.010

Figure 12

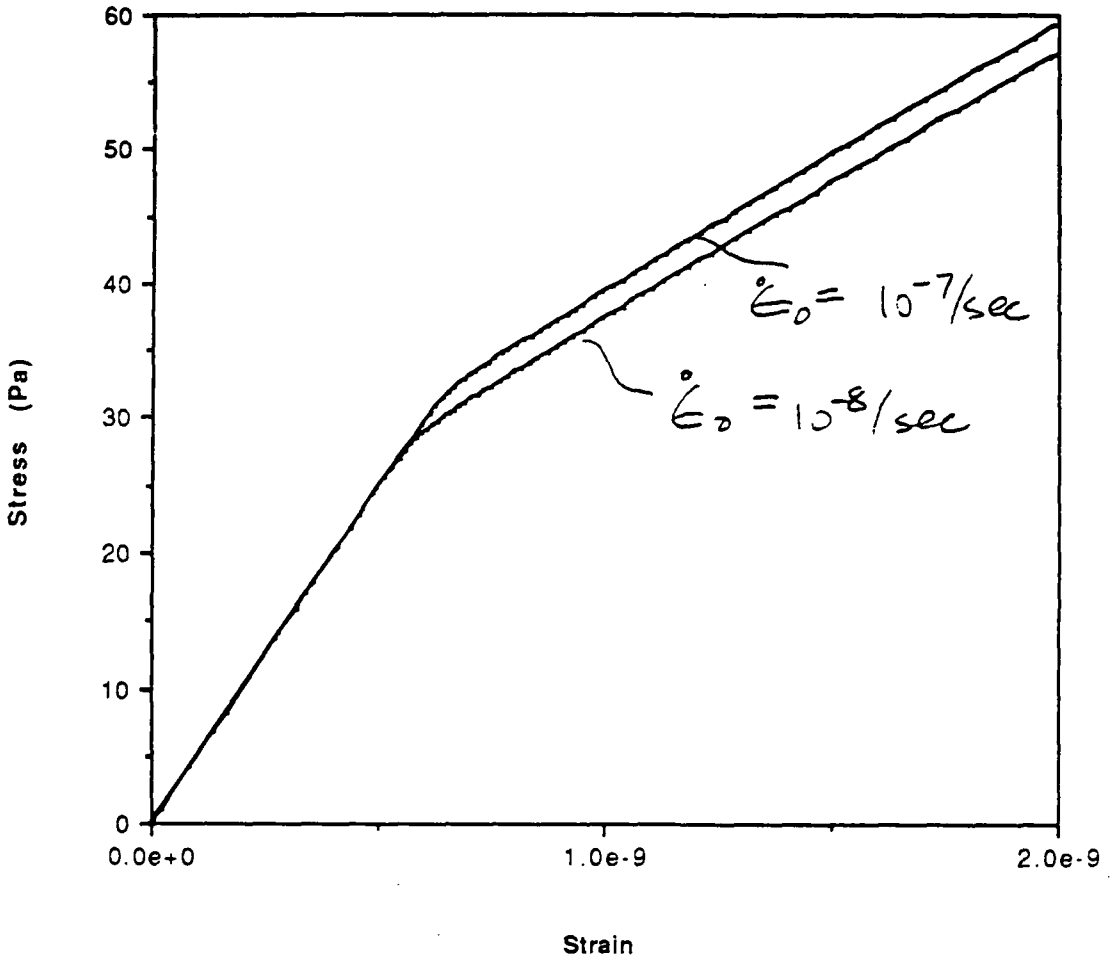
60
50
40
30
20
10
0
Stress (Pa)
0.0e+0
1.0e-9
2.0e-9
Strain
$\dot{\epsilon}_0 = 10^{-7}$/sec
$\dot{\epsilon}_0 = 10^{-8}$/sec

Figure 13.

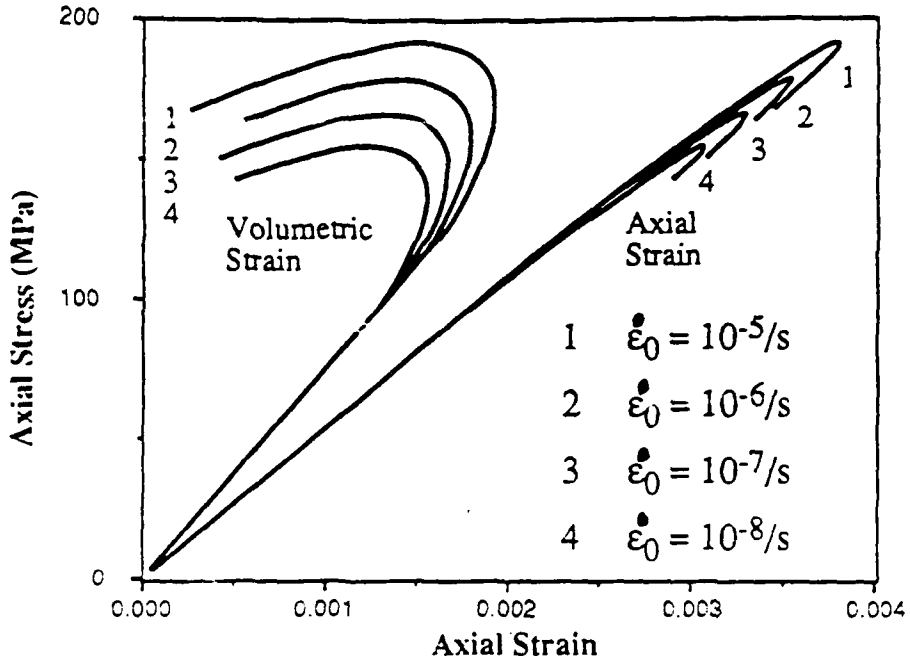
200
100
0
Axial Stress (MPa)
0.000
0.001
0.002
0.003
0.004
Axial Strain
1
2
3
4
Volumetric Strain
Axial Strain
1 $\dot{\varepsilon}_0 = 10^{-5}/s$
2 $\dot{\varepsilon}_0 = 10^{-6}/s$
3 $\dot{\varepsilon}_0 = 10^{-7}/s$
4 $\dot{\varepsilon}_0 = 10^{-8}/s$

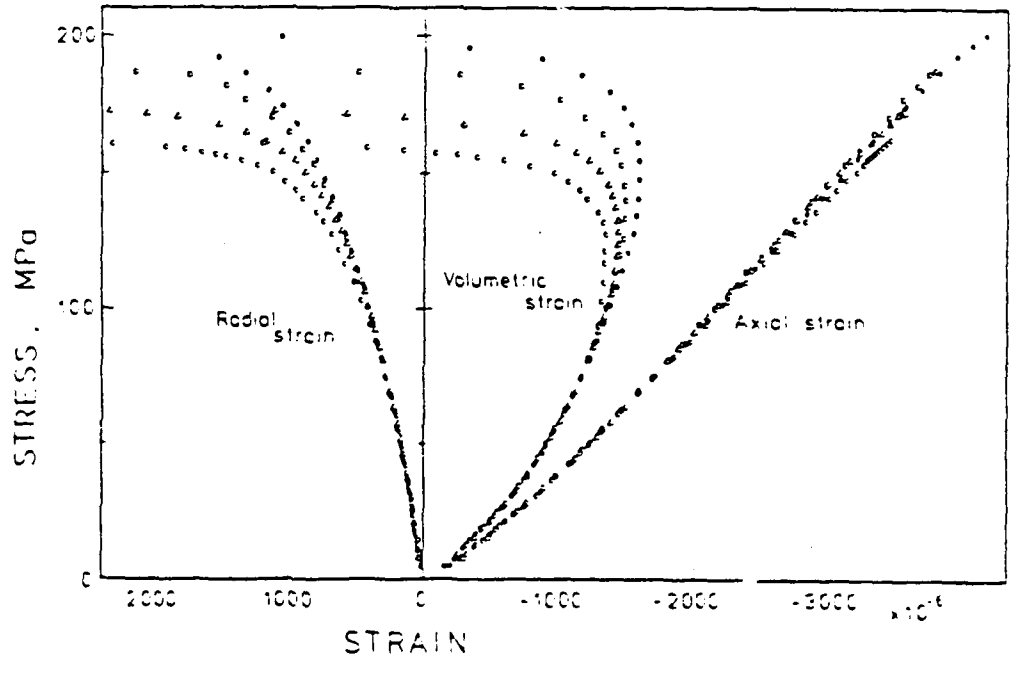
200
100
0
STRESS, MPa
Radial strain
Volumetric strain
Axial strain
2000
1000
0
-1000
-2000
-3000
STRAIN

Fig 14

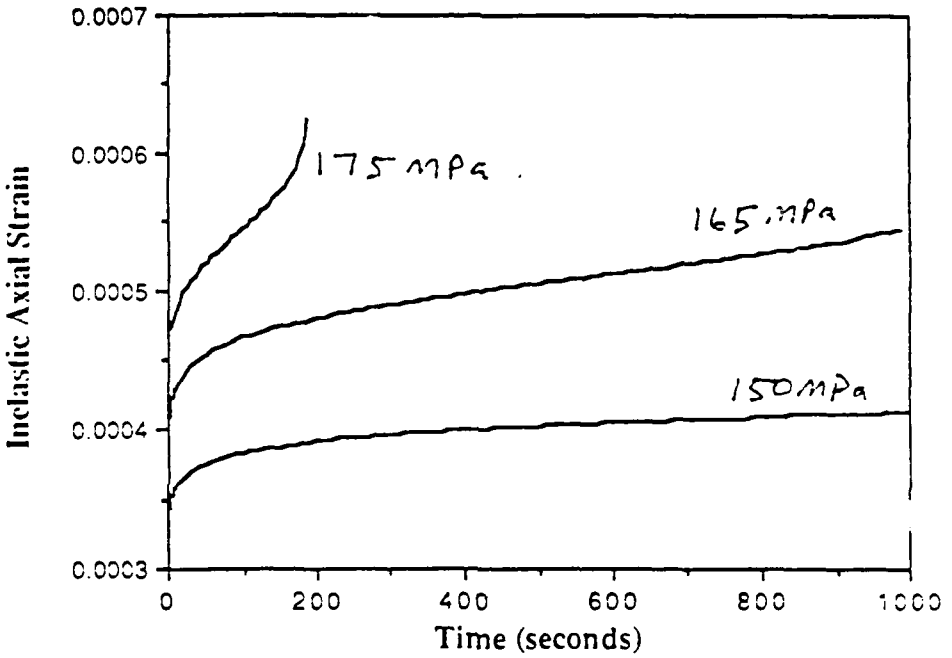
0.0007
0.0006
0.0005
0.0004
0.0003
Inelastic Axial Strain
175 mPa
165 mPa
150 mPa
0
200
400
600
800
1000
Time (seconds)

Fig. 15

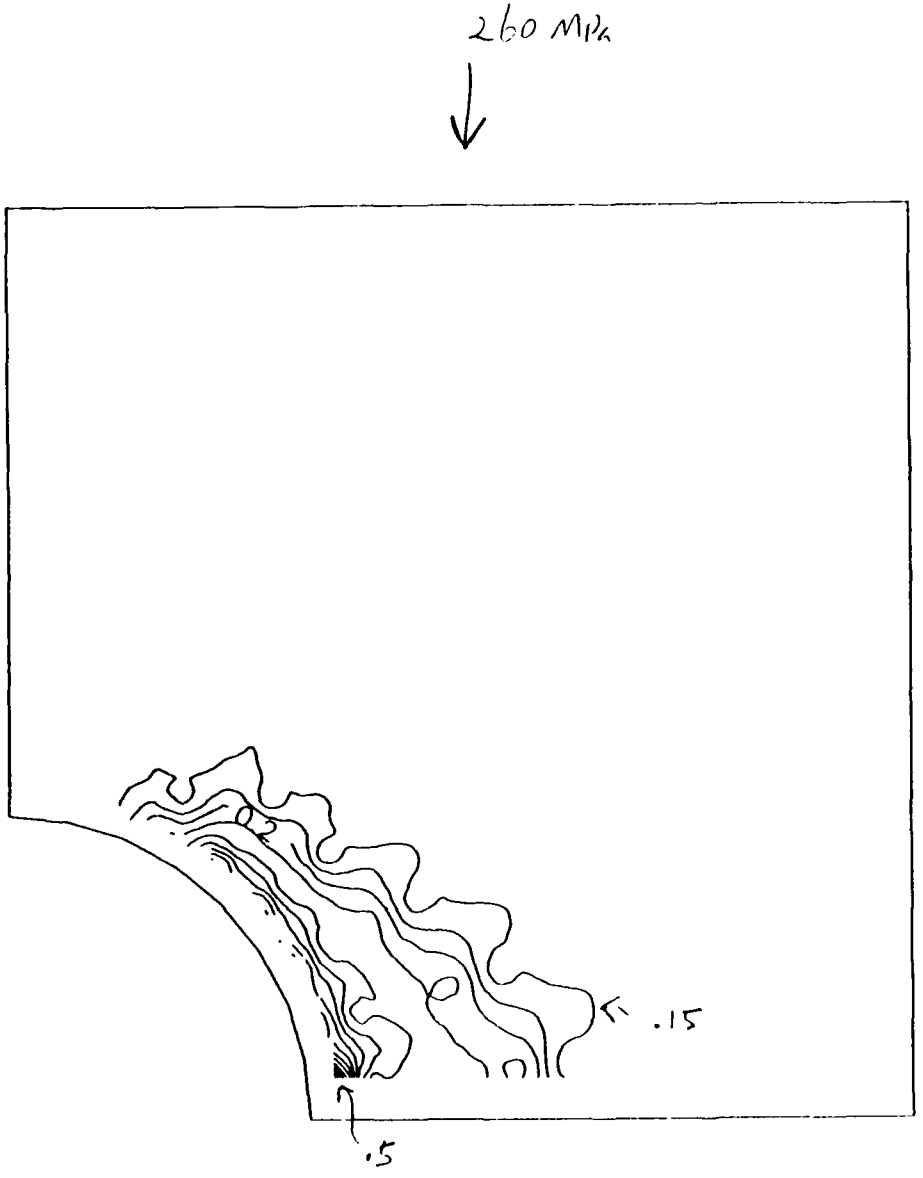

Figure 17

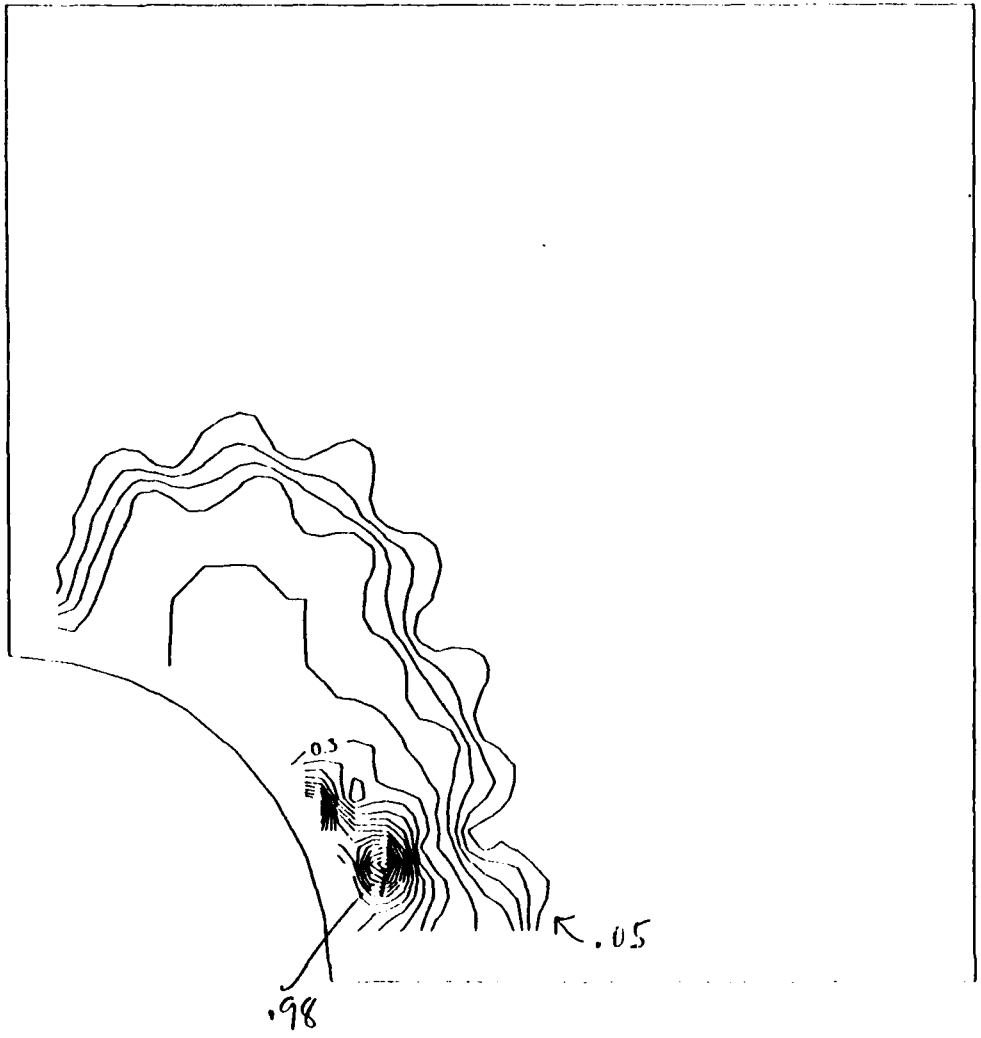

Figure 18

ASYMPTOTIC ANALYSIS OF COHESIVE CRACKS AND ITS RELATION WITH EFFECTIVE ELASTIC CRACKS

J. Planas and M. Elices
Department of Materials Science. Escuela de Ingenieros de Caminos.
Universidad Politécnica de Madrid. Ciudad Universitaria. 28040-Madrid. Spain.

ABSTRACT

Replacement of a cohesive crack problem by an approximate linear elastic problem was proven useful in some instances. This contribution provides a unified treatment of a wide class of equivalences between such problems and sets limiting conditions for the effective crack models. After reviewing the cohesive crack model, the concept of *equivalent crack* is introduced and some examples of equivalences are discussed. Finally, the equivalences are analyzed in the limit of very large sizes, and it is shown that some equivalences, different for small sizes, merge when the specimen size is increased. Some equivalences, however, remain different, particularly the equivalence which is at the root of the *R-CTOD-curve* model. Equations to improve the predictions of this model are given for large sizes.

1. INTRODUCTION

Modelling crack initiation and propagation in cohesive materials leads to solving a non linear fracture mechanics problem and, with a few exceptions, one has to resort to numerical analysis. Under these circumstances it is quite natural to look for approximate solutions based on Linear Elastic Fracture Mechanics (LEFM), a field where computation is easier and more experience is available.

The substitution of an actual fracture process —with a plastic or non-linear zone surrounding the crack tip— by an effective or equivalent crack was probably the first approximation to non-linear fracture problems. In the early approaches the effective crack extension was mildly related to the size of the plastic zone in quite an intuitive way, but the ability of the effective crack to represent the actual behaviour was not deeply investigated at a theoretical level, although it was extensively used in experiment interpretation and in design.

The *equivalent* linear elastic problem has to be solved in conjunction with an associate R-curve or, otherwise stated, a crack growth rule has to be independently stated as a relationship between the effective crack growth resistance and the effective crack extension. This is not the only price one has to pay for simplifying the cohesive crack; it was proven that the R-curve is geometry and size dependent —i.e., is not a material property— and, consequently, the equivalence becomes severely restricted.

In spite of these shortcomings there is some evidence [1] showing that for usual geometries and available sizes, differences among R-curves (when adequately formulated) are well inside the experimental scatter and, in this respect, they may be considered a material property for practical purposes, as long as peak-load versus size prediction is concerned.

However, there is no way to know *a priori* whether this R-curve which fits very well the peak-load size effect will be equally accurate in describing other aspects of the behavior, for example the load-displacement curve, or any other curve.

The aim of this contribution is to deepen in this research line and provide limits of validity of the effective elastic crack models as approximations of cohesive crack models. In this paper the concept of effective elastic crack is discussed first and afterwards the equivalence for large sizes is explored with the help of the asymptotic method, already developed by the authors [2, 3, 4].

2. THE EQUIVALENT ELASTIC CRACK

We shall restrict to a class of cohesive materials and loading according to the following hypothesis:

H.1.- *Loading*: Loading is assumed to consist in monotonic mode I crack growth, achieved by symmetric proportional loading of an initially symmetric specimen.

H.2.- *Bulk Behaviour*: The material displays linear elastic bulk behaviour —with Young modulus E and Poisson's ratio ν— as long as the major principal stress does not reach a critical value σ_R.

H.3.- *Crack Initiation*: When the maximum principal stress reaches σ_R (the tensile strength) fracture is initiated and strain localization takes place in what is called the Fracture Process Zone (FPZ). The FPZ is modelled as a cohesive crack where the strain localization is idealized as a displacement jump or crack opening, while cohesive stresses simulate the softening behaviour.

H.4.- *Crack Evolution*: Once the cohesive crack has formed, the stress transferred through the crack faces is assumed to depend upon the relative displacement of the crack faces.

For these loading conditions, the stress normal to the crack plane, σ, is supposed to be given by a single-valued, non-negative function of the crack opening w, i.e.:

$$\sigma = F(w) \qquad \text{where} \qquad F(0) = \sigma_R \qquad \text{and} \qquad F(w) \geq 0 \tag{2.1}$$

The material function $F(w)$, together with E and ν, suffice to characterize the cohesive material behaviour, as far as monotonic mode I is concerned. Based on this function, usually called the softening curve, several definitions were done:

a.- The work needed to monotonically open a crack of unit surface up to w, the *specific work supply*, is a material function given by

$$W_F(w) = \int_0^w F(w')dw' \tag{2.2}$$

b.- The specific work supply needed to fully open a unit surface is also a material property called the *specific fracture energy* G_F (or, simply, fracture energy), i.e.,

$$G_F = \int_0^{w_c} F(w')dw' \tag{2.3}$$

where, it is assumed that the value of $F(w)$ is zero for crack openings exceeding w_c.

Now, let us go back to the concept of *equivalent crack*, and consider a particular equivalence —the force-displacement equivalence— to fix the idea. Two geometrically identical cracked samples, as shown in figure 1, are loaded under displacement control u.

One sample is made with a cohesive material, as defined above, and the other is made with a linear elastic material. The measured response of the two samples —i.e. the loads P and P_{eq} — for every displacement u will be different, but we can force the responses to match each other, $P = P_{eq}$, by choosing a suitable *equivalent crack length* a_{eq} and a suitable *equivalent crack growth resistance* R_{eq} at each deformation level.

In doing so, we force both samples to exhibit the same P-u behaviour, but in general, the equivalence ends here; stress or displacement fields, or relevant parameters like *CMOD* or *CTOD*, are not the same. Moreover, the price paid for the equivalence is that the linear elastic material has not a constant crack growth resistance. Instead, a changing value with crack length is needed in order to keep the P-u equivalence. Moreover the R-Δa curve obtained is not a material property, it depends on the geometry and specimen size.

At first sight, the advantages of using this equivalence are not obvious since there are not simple rules for the generation of the R-curves for every geometry and size. However, in some circumstances this can be done as we shall see later.

In a general equivalence, the equivalent resistance to crack growth may be obtained (for a monotonic process), by using the classical concepts of LEFM, because the equivalent specimen is, by construction, linear elastic. Given the equivalent load P_{eq} and the equivalent crack length a_{eq}, we may compute the stress intensity factor for the equivalent crack, which will always take the form:

$$K_{Ieq} := K_{Ieq}(P_{eq}, a_{eq}) = \frac{P_{eq}}{B\sqrt{D}} S\left(\frac{a_{eq}}{D}\right) \tag{2.4}$$

where B is the specimen thickness, D one of its characteristic in-plane dimensions, and $S(a/D)$ is the geometrical shape factor.

Owing to the postulated linearity of the material of the equivalent specimen, the resistance to crack growth may be written in any of the following equally valid forms:

$$R_{eq} := G_{Req} = J_{Req} = \frac{K_{Req}^2}{E'} \tag{2.5}$$

where G_R is the resistant-energy release rate, J_R the resistant-J integral, and K_R the resistant-stress intensity factor, and E' is the effective elastic modulus for generalized plane stress or plane strain. Since the equivalent crack is on the monotonic quasi-static loading curve, hence in a state of incipient growth, the resistant-K must be equal to the driving-K in Eq. (2.4), and then

$$R_{eq} := \frac{[K_{Ieq}(P_{eq}, a_{eq})]^2}{E'} \tag{2.6}$$

2.1. P-Y Equivalences

This kind of equivalence is shown in figure 1. The actual sample is sketched on the left, its cohesive zone has grown monotonically up to C, and the corresponding load is $P(C)$. The equivalent sample, made with an elastic non cohesive material, is sketched on the right and it is loaded with *same* P value (hence the P equivalence labeling). Notice that the crack length is not a_0 but $a^{P\text{-}Y} = a_0 + \Delta a^{P\text{-}Y}$, where P stands for the imposed load and Y for the magnitude related with the second degree of freedom. One should realize that the stress and displacement fields of the right hand sample are known when the load and the crack length are known. Since load is fixed, only one degree of freedom remains.

2.1.1. P-u Equivalence

When load point displacement u is chosen as a second variable, one arrives at the load-displacement equivalence. If P and u are measured in the actual sample, the *P-u equivalent elastic crack length* $a^{P\text{-}u}$ can be computed from:

$$C_{eq}(a^{P\text{-}u}) = \frac{u}{P} \tag{2.7}$$

where $C_{eq}(a)$ is the expression for the compliance of the equivalent specimen for a crack length a, which may be obtained from linear elastic analyses.

Equation (2.7) determines the equivalent crack length at each loading step, from which, and the known load, other magnitudes may be computed for the P-u equivalent specimen. In particular, the *P-u equivalent crack growth resistance* $R^{P\text{-}u}$ may be obtained from equations (2.6) and (2.4) substituting $R_{eq} = R^{P\text{-}u}$, $a_{eq} = a^{P\text{-}u}$ and $P_{eq} = P$. The resultant R-curve will be geometry and size dependent because of the implicit size and geometry dependence of both members of equation (2.7)

2.1.2. P-CMOD Equivalence

When *CMOD* (Crack Mouth Opening Displacement) is chosen instead of the displacement associated to the load, one has a *P-CMOD* equivalence. The *P-CMOD equivalent elastic crack length* $a^{P\text{-}CMOD}$ can be computed from an equation entirely similar to (2.7),

$$C_{eq}^{CMOD}(a^{P\text{-}CMOD}) = \frac{CMOD}{P} \tag{2.8}$$

where $C_{eq}^{CMOD}(a)$ is the expression for the compliance associated to *CMOD* for a non cohesive sample with a crack of length a.

The *P-CMOD crack growth resistance* may be obtained —after computing the equivalent crack length from (2.8)— from (2.6) and (2.4) with the adequate change of indices as done before for the P-u equivalence. The same comments as before, regarding size and geometry dependence of R-curves, can be done.

It can not be stated, at first sight, that equations (2.7) and (2.8) are equivalent and, hence, there is no reason for $a^{P\text{-}u}$ and $a^{P\text{-}CMOD}$ to take the same value.

2.2. X-Y Equivalences

The above reasoning used to set P-X equivalences can be generalized to any couple of variables X-Y. Now, the actual specimen and the equivalent (or *virtual*) specimen are not bearing the same load, in general, and the equivalent load $P^{X\text{-}Y}$ and equivalent crack length $a^{X\text{-}Y}$ corresponding to the virtual specimen can be computed by equating X and Y in both specimens:

$$X_{eq}(P^{X\text{-}Y}, a^{X\text{-}Y}) = X \tag{2.9}$$

$$Y_{eq}(P^{X\text{-}Y}, a^{X\text{-}Y}) = Y \tag{2.10}$$

where the left hand members are the elastic expressions for magnitudes X and Y in the equivalent specimen and the right hand members the actual values of X and Y (either measured or computed using the cohesive model).

Equations (2.9) and (2.10) determine the equivalent load and crack length, from which any other magnitude can be found for the equivalent specimen. In particular, the equivalent crack growth resistance is, again, obtained from (2.4) and (2.6) with the obvious equivalence specifiers: $R_{eq} = R^{X\text{-}Y}$, $a_{eq} = a^{X\text{-}Y}$ and $P_{eq} = P^{X\text{-}Y}$.

2.2.1. J-CTOD Equivalence

The couple *J-CTOD* is an example of the generalized *X-Y* equivalence The variable *J* stands for the J-integral, with the essential remark that when the cohesive sample is considered,the J-integral has to be taken over a path always surrounding the cohesive zone. Under such circumstances it was shown [5] that:

$$J = W_F(CTOD) \tag{2.11}$$

where W_F, the specific work supply, was defined in (2.2). For the non-cohesive sample, J is equal to K_I^2/E' as stated before in Eq. (2.5). The variable *CTOD* is the crack opening at the initial crack tip.

The couple of equations (2.9) and (2.10) for this particular equivalence are, after use of (2.6) and (2.11):

$$\frac{[K_{Ieq}(P^{J\text{-}CTOD}, a^{J\text{-}CTOD})]^2}{E'} = W_F(CTOD) \tag{2.12}$$

$$w_{eq}(P^{J\text{-}CTOD}, a^{J\text{-}CTOD}, a_0) = CTOD \tag{2.13}$$

where $w_{eq}(P, a, a_0)$ is the crack opening at the initial crack tip location a_0 of the equivalent specimen subject to load P when the crack length is a.
These two equations may be used in different ways. We first notice that once expressions for K_I and w —depending only on geometry and loading— and for W_F —depending only on material— are given, (2.12) and (2.13) provide the parametric representation of the *P-a* curve, with parameter *CTOD*. We further notice that the LH member of (2.12) is the equivalent crack growth resistance (2.6) which, according to (2.12) is a unique function of *CTOD*. This equivalence results, then, in a *R-CTOD* curve model, previously analyzed by the authors on different grounds [1].

Equation (2.13) may be made more explicit by writing the *CTOD* of the elastic sample (LH member of 2.13) in the form derived in [6]

$$w_{eq}(P^{J\text{-}CTOD}, a^{J\text{-}CTOD}, a_0) = \frac{8}{\sqrt{2\pi E'}} K_{Ieq}(P^{J\text{-}CTOD}, a^{J\text{-}CTOD}) (\Delta a^{J\text{-}CTOD})^{1/2} L\left(\frac{\Delta a^{J\text{-}CTOD}}{D}\right) \tag{2.14}$$

where $L(\Delta a/D)$ is a dimensionless function implicitly depending on shape and initial crack length and D is a characteristic structural length (for example, beam depth). The function $L(\Delta a/D)$ satisfies the condition $L(0) = 1$ for any geometry.

The use of this equation in (2.12) and (2.13) allows the elimination of the load, and further use of (2.6) reduces the equations to:

$$R^{J\text{-}CTOD} = W_F(CTOD) \tag{2.15}$$

$$\Delta a^{J\text{-}CTOD}\ L^2\left(\frac{\Delta a^{J\text{-}CTOD}}{D}\right) = \frac{\pi}{32}\frac{E'\ CTOD^2}{W_F(CTOD)} \tag{2.16}$$

The first of this equations is no more than the *R-CTOD* equation, linked to the material softening curve by (2.2). The second equation (2.16) gives the *J-CTOD* equivalent crack extension. The set of the two equations is the parametric representation of the R-Δa curve which must be noted to be size and geometry dependent, because of the presence of the function $L(\Delta a/D)$. Only for $D \to \infty$ the R-Δa curve becomes geometry independent because then $\Delta a/D \to 0$ and $L \to 1$.

From these equations and the relationships (2.6) and (2.4) the load $P^{J\text{-}CTOD}$ acting on the equivalent specimen for a given *CTOD* may be obtained. There is no reason to expect that this load coincide with the actual load P. However, it was found that the maximum load can be accurately predicted using the equivalent sample, at least for notched beams. As an example, for concrete beams (where $l_{ch} = EG_F/\sigma_R^2$ was supposed equal to 0.3 m), the error was less tnan 5% for beam depths larger than 8 cm [1].

2.2.2. Bazant Size-Independent R-Δa Equivalence

As already stated, any of the above equivalences lead, at least in principle, to size dependent R-Δa curves. Bazant has put forward a method to determine a size-independent —but geometry-dependent— R-Δa curve from the knowledge of the size-effect curve, or variation of peak load P_{peak} with size D for geometrically similar precracked structures [7, 8, 9].

Bazant's approach is a general X-Y equivalence in the sense that two conditions are imposed. The first condition is that the peak load must be the same on the actual and on the equivalent elastic specimen for every size D. The second condition is that the R-Δa curve must be size independent. The only input is the size effect curve, which may be written as a function $P_{peak}(D)$, known from experiments or by computation. The unknowns are the equivalent resistance and the equivalent crack extension at peak load for every size. When the size is eliminated, the R-Δa curve appears. The result, derived and used by Bazant in many papers, is that the R-curve is the envelope of the following uniparametric family of functions, with parameter D:

$$R^{B\text{-}G} = \frac{1}{E'}\left(\frac{P_{peak}(D)}{B\sqrt{D}}\, S\left(\alpha_0 + \frac{\Delta a^{B\text{-}G}}{D}\right)\right)^2 \qquad (2.17)$$

where $\alpha_0 = a_0/D$ is constant because of geometrical similarity, and superindex B-G stand for Bazant and General, because no special size effect curve is postulated here. The size effect may come from a cohesive model, from Bazant's size effect law, or from any other imaginable model. The result depends of course on the size effect behaviour and also, at least in principle, on α_0 and on other hidden geometrical parameters in the shape function S. It is size-independent, but geometry-dependent.

3. ASYMPTOTIC ANALYSIS OF THE EQUIVALENT CRACK

Let us explore, now, the *equivalences* for large specimen sizes. The authors developed a method particularly appropriate for analyzing cohesive crack models when the specimen size is large [2, 3, 4] and some results will be briefly summarized here.

It is assumed that the size of the cohesive zone, c, remains bounded as the specimen size (characterized by D) grows and that the stress and displacement fields can be developed in series of c/D. The zeroth order asymptotic approach is obtained when terms of the order of c/D or higher are neglected. When the terms linear in c/D are also retained —neglecting terms of the order of $(c/D)^2$— the first order approach is obtained.

For zeroth order approach, the stress and displacement fields *far from the cohesive crack tip* are the same as the corresponding fields of an elastic crack of length a_0. This is a well known far field property. In this approximation, the solution is written as a weighted sum of elastic solutions, with a dimensionless density function $k^*(x)$ defined on $(0,1)$ the values of which for every cohesive crack length c are determined from the equation:

$$\int_0^x k^*(u)\,(x-u)^{-1/2}\,du - F^*\left(8c^*\int_x^1 k^*(u)\,(u-x)^{1/2}\,du\right) = 0 \qquad (3.1)$$

with
$$c^* = \frac{c}{l_{ch}} = \frac{c\,\sigma_R^2}{E'\,G_F} \qquad (3.2)$$

and
$$F^*(w^*) = \frac{1}{\sigma_R} F\left(\frac{G_F}{\sigma_R} w^*\right) \qquad (3.3)$$

where x and u are relative positions on the cohesive zone, so that x and $u = 0$ at the initial crack tip and x and $u = 1$ at the cohesive crack tip; c^* and $F^*(w^*)$ are dimensionless forms of the cohesive zone size c and of the softening function $F(w)$ in Eq. (2.1).

Once the density function $k^*(x)$ has been obtained for a given c, the J-integral, the load expressed as nominal intensity factor (SIF for the initial crack length and the actual load), and the *CTOD* may be found to be:

$$J = 2\pi c^*\,G_F\left(\int_0^1 k^*(u)\,du\right)^2 + O\left(\frac{c}{D}\right) \qquad (3.4)$$

$$K_{IN} = \sqrt{2\pi c^*\,E'G_F}\int_0^1 k^*(u)\,du + O\left(\frac{c}{D}\right) \qquad (3.5)$$

$$CTOD = \frac{G_F}{\sigma_R} 8c^* \int_0^1 k^*(u)\,u^{1/2}\,du + O\left(\frac{c}{D}\right) \qquad (3.6)$$

where $O(c/D)$ stands for a function of the same order of its argument, and it is explicited to remember that we are in the zeroth order approach. Since Eq. (2.11) is always valid, we may use this and Eqs. (3.4) and (3.6) to find the following essential relationship between the cohesive zone size and the *CTOD:*

$$c = \frac{\pi}{32}\,\frac{E'\,CTOD^2}{W_F(CTOD)}\langle u^{1/2}\rangle^{-2} + O\left(\frac{c}{D}\right) \qquad (3.7)$$

where $\langle f(u)\rangle$ is the *k^*-weighted average* value of any given function $f(u)$ on the $(0,1)$ interval:

$$\langle f(u)\rangle = R\,\frac{\int_0^1 f(u)\,k^*(u)\,du}{\int_0^1 k^*(u)\,du} \qquad (3.8)$$

When the approximation is extended to first order, a new far field property —not so obvious— was deduced (restrictedly in [3], a complete proof will be published elsewhere):

For a cohesive material and a general geometry under mode I loading, every far field may be approximated, up to and including order c/D, by the corresponding elastic field of a crack of length $a_0 + \Delta a^{FF}{}_\infty$ where $\Delta a^{FF}{}_\infty$ is the Full Far Field effective (or equivalent) crack extension given, for each cohesive crack size, by the following equation

$$\Delta a^{FF}_{\infty} = c \langle u \rangle \tag{3.9}$$

where $\langle\ \rangle$ has the same meaning as before. Notice that this equation is based only on the zero order solution, and has a meaning only for first order approximation. The existence of a full far field equivalence for higher orders of approximation.is dubious.

It is possible to express Δa^{FF}_{∞} in terms of the *CTOD* and to derive a lower bound for it. Substituting c from (3.7) into (3.9) we get:

$$\Delta a^{FF}_{\infty} = \frac{\pi}{32} \frac{E' CTOD^2}{W_F(CTOD)} \frac{\langle u \rangle}{\langle u^{1/2} \rangle^2} + O\left(\frac{c}{D}\right) \tag{3.10}$$

Use of the Bunyakovsky-Schwarz inequality in the first term of the RH member of this equation, and the fact that the second term vanishes as D grows to infinite, delivers the lower bound theorem:

$$\Delta a^{FF}_{\infty} > \frac{\pi E}{32} \frac{CTOD^2}{W_F(CTOD)} \qquad \text{for c/D small enough.} \tag{3.11}$$

3.1. Far Field (FF) Equivalences

Let us consider the equivalences based on variables associated with fields far away from the cohesive zone (*FF*, far fields), and this limited to very large sizes for which the full far field equivalence exists to a given degree of accuracy. Several among the variables used to define equivalences in the previous section are far field variables. This is obviously the case for P, u and *CTOD* , but also for J. The later is a very special case because it comes from a path independent integral that may be performed along any contour. Hence, if two specimens have identical far fields they also have identical J-integrals, eventhough their near fields may be essentially different . This is in fact the dual of a reasoning frequently used in LEFM (equal near fields imply equal Js even if far fields are essentially different).

According to the preceding, the equivalences in which both indices correspond to far fields are then mutually equivalent, and we have for a given situation (a given cohesive zone size):

$$\Delta a^{FF}_{\infty} = \Delta a^{P\text{-}u}_{\infty} = \Delta a^{P\text{-}CMOD}_{\infty} \tag{3.12}$$

where subscript ∞ means infinite (very large) size.

The R-Δa curve for zero order approximation is expressed parametrically by the first term of Eq. (3.4) for R and (3.9) for Δa. To get a first order approximation, the linear term in Eq. (3.4) has to be included which requires the solution of a further integral equation similar to (3.1).

It is intersting to comment Bazant Equivalence for a Cohesive model at this point *(B-C)*. Bazant equivalence is based on the knowledge of the peak load over a certain range of sizes. The peak load is a far field property, but the necessity of having a range of sizes to find the R-curve limites the analysis for large sizes. Indeed, if we know the size effect for only one size, no information at all about the R-curve can be obtained. If we know the size effect in the neigborhood of a size (peak load and its derivative with respect to size) only one point of the R-curve — and the slope at this point— may be obtained, wich corresponds to the peak for this particular size. From the asymptotic size effect equation previously obtained by the authors, and the definition of the *B-C* equivalence, it may be easily proved that the *B-C* equivalence is also far field at the peak:

$$\Delta a^{B\text{-}C}_{\infty peak} = \Delta a^{FF}_{\infty peak} \qquad \text{and} \qquad R^{B\text{-}C}_{\infty peak} = R^{FF}_{\infty peak} = G_F \tag{3.13}$$

3.2. The J-CTOD Equivalence

When the variables chosen for the equivalence are related with the cohesive zone the far field property can not be directly exploited. This happens, for example, with the variable *CTOD* and with the equivalence *J-CTOD*. In principle, there is no reason to suspect that $\Delta a^{J\text{-}CTOD}$ and Δa^{FF} coincide for very large sizes, and we will see that they do not.

Consider first the *J-CTOD* equivalence in the limit of large sizes. Putting $L = l$ for $D \to \infty$ in Eq. (2.16) one inmediately obtains

$$\Delta a^{J\text{-}CTOD}_{\infty} = \frac{\pi}{32}\frac{E'\,CTOD^2}{W_F(CTOD)} \tag{3.14}$$

which is obviously the approximation of order zero of fthe *J-CTOD* equivalent crack extension , so that in a neigborhood of $c/D = 0$ one has

$$\Delta a^{J\text{-}CTOD} = \Delta a^{J\text{-}CTOD}_{\infty} + O\left(\frac{\Delta a^{J\text{-}CTOD}_{\infty}}{D}\right) \tag{3.15}$$

It appears that the RH member of equations (3.11) and (3.14) coincide, so that the lower bound theorem above turns out to state that the the *FF* equivalent crack extension is always larger than the *J-CTOD* equivalent crack extension in the limit of large sizes:

$$\Delta a^{FF}_{\infty} > \Delta a^{J\text{-}CTOD}_{\infty} \tag{3.16}$$

One may use the Full Far Field equivalence for large sizes to find first order relationships between the actual load P and displacement u and those determined through the *J-CTOD* equivalence, $P^{J\text{-}CTOD}$ and $u^{J\text{-}CTOD}$.

To obtain the relationship between the loads we just write that, by the very definitions of FF and J-CTOD equivalences

$$J = J^{FF} = J^{J\text{-}CTOD} \tag{3.17}$$

The second equality obviously imply that the stress intensity factors at the equivalent crack tips must be equal in *FF* and *J-CTOD* equivalences. Using then the expression (2.4) one finds

$$P\,S\left(\alpha_0 + \frac{\Delta a^{FF}}{D}\right) = P^{J\text{-}CTOD}.S\left(\alpha_0 + \frac{\Delta a^{J\text{-}CTOD}}{D}\right) \tag{3.18}$$

from which one obtains, accurate to first order:

$$P^{J\text{-}CTOD} = P\left(1 + \frac{S_0'}{S_0}\frac{\Delta a^{FF}_{\infty} - \Delta a^{J\text{-}CTOD}_{\infty}}{D}\right) + o\left(\frac{\Delta a^{FF}_{\infty}}{D}\right) \tag{3.19}$$

where $o(\Delta a/D)$ stands for a function vanishing faster than its argument.

To obtain the relationship between the displacemens, we first recall that the displacement in an equivalent elastic specimen may be always written as

$$u_{eq} = C_{eq} P_{eq} = C^*\left(\frac{a_{eq}}{D}\right)\frac{P_{eq}}{B\ E'} \tag{3.20}$$

where C_{eq} is the compliance and $C^*(a/D)$ a dimensionless compliance, related to the shape factor for the stress intensity factor $S(a/D)$ in (2.4) by the relationship

$$2\ S^2\left(\frac{a_{eq}}{D}\right) = C^{*\prime}\left(\frac{a_{eq}}{D}\right) \tag{3.21}$$

where $C^{*\prime}$ indicates the first derivative of C^* with respect to its argument. This equation follows easily from the well known relationship of LEFM between G and the derivative with respect to crack length of the elastic energy.

Writting now $a_{eq} = a_0 + \Delta a_{eq}$, $a_0/D = \alpha_0 =$ constant, and using (3.21) for the first derivative of C^*, we may find the first order expansion of (3.20) as

$$u_{eq} = C^*_0 \frac{P_{eq}}{B\ E'}\left(1 + \frac{2S_0^2\ \Delta a_{eq}}{C^*_0\ D}\right) + o\left(\frac{\Delta a_{eq}}{D}\right) \tag{3.22}$$

where subindex *0* for C^* and S means values for the initial crack length

According to the far field equivalence theorem, at a given instant the load and displacement in the actual specimen are equal (to first order) than those in the FF equivalent specimen, hence:

$$u = C^*_0 \frac{P}{B\ E'}\left(1 + \frac{2S_0^2\ \Delta a^{FF}_{\infty}}{C^*_0\ D}\right) + o\left(\frac{\Delta a^{FF}_{\infty}}{D}\right) \tag{3.23}$$

For the J-CTOD equivalence the analogous result is found as

$$u^{J\text{-}CTOD} = C^*_0 \frac{P^{J\text{-}CTOD}}{B\ E'}\left(1 + \frac{2S_0^2\ \Delta a^{J\text{-}CTOD}_{\infty}}{C^*_0\ D}\right) + o\left(\frac{\Delta a^{J\text{-}CTOD}_{\infty}}{D}\right) \tag{3.24}$$

The relationship between displacements is now found by eliminating P and $P^{J\text{-}CTOD}$ from (3.23), (3.24) and (3.19):

$$u^{J\text{-}CTOD} = u\left(1 + \left(\frac{S_0'}{S_0} - \frac{2S_0^2}{C^*_0}\right)\frac{\Delta a^{FF}_{\infty} - \Delta a^{J\text{-}CTOD}_{\infty}}{D}\right) + o\left(\frac{\Delta a^{FF}_{\infty}}{D}\right) \tag{3.25}$$

It appears, then, that up to first order the *J-CTOD* equivalence may be used to find estimates of load and displacement that can be further corrected using (3.19) and (3.25) if an estimate of the difference between the two effective crack extensions is available. In the next section some numerical results are presented regarding this difference.

3.3. Numerical results for the FF and J-CTOD equivalences at infinite size

To have a feeling of the trend of the equivalences for large sizes, a numerical analysis was performed and three softening curves, depicted in Fig. 2, were investigated; a rectangular softening (or Dugdale softening), a linear softening, and a quasi-exponential softening. The numerical method described in [3] was used to solve the integral equation (3.1) for a number of cohesive zone sizes.

At each step, the equivalent resistance to crack growth for *FF* and *J-CTOD* equivalences was obtained from equation (3.4) since in these equivalences $R_{eq} = J_{eq} = J$. The *FF* equivalent crack extension was obtained from Eq. (3.9) and the *J-CTOD* equivalent crack extension from Eq. (3.14), after obtention of the *CTOD* from (3.6). The resulting R-Δa curves for the two equivalences and different softening curves are given in Fig. 3.

For a given softening curve, we observe in Fig. 3 that although there is a neat difference between the two R-curves at a numerical level, it seems that they would be hardly distinguishable at the experimental level since both curves would fit into the usual experimental scatter band. Hence, at least for very large sizes, the *J-CTOD* equivalence provides a relatively easy-to-apply approximation of the actual overall behaviour (remember that for this equivalence the R curve is known in parametric closed form).

As far as the P-u curve (one of the basic experimental "observables") is concerned, the predictions from the *J-CTOD* equivalence can be improved by using the relationships (3.19) and (3.25) which depend basically on the difference between the equivalent crack extensions for the *FF* and *J-CTOD* approximations. Fig. 4 gives a picture of this difference for the three softening curves previously envisaged. It shows a proportional rising at the begining of loading and ends in a plateau after the peak load, where steady-state crack growth takes place (only for infinite size, which is our case). We notice that the plateau values are very close for the progressively softening models, and may be a constan value of 2.7 % of the characteristic size l_{ch} could be a good general estimate for the difference for any reasonably smooth softening curve.

ACKNOWLEDGEMENTS

The authors gratefully acknowledge financial support for this research provided by CICYT, Spain, under grants PB86-0494 and CE89-0012.

REFERENCES

[1] Planas, J., Elices, M. and Toribio, J., "Approximation of Cohesive Models by R-CTOD Curves", In *Fracture of Concrete and Rock* (S.P. Shah, S.E. Swartz and B. Barr, Eds.), pp. 203-212 (1989).

[2] Planas, J. and Elices, M., "Un Nuevo Método de Análisis del Comportamiento Asintótico de la Propagación de una Fisura Cohesiva en Modo I", *Anales de Mecánica de la Fractura,* **3**, pp. 219-227 (1986).

[3] Planas, J. and Elices, M., "A new method of asymptotic analysis of the development of a cohesive crack in mode I loading", Report 87-02, Departamento de Ciencia de Materiales, ETS de Ingenieros de Caminos, Ciudad Universitaria, 28040 Madrid, Spain (1987)

[4] Planas, J. and Elices, M., "Nonlinear Fracture of Cohesive Materials", *International Journal of Fracture,* Special Issue, edited by Z. P. Bazant, in press.

[5] Rice, J., "Mathematical Analysis in the Mechanics of Fracture, In *Fracture*, Vol. 2 (H. Liebowitz, Ed.), Academic Press, pp. 192-311 (1968).

[6] Planas, J. and Elices, M., "Fracture Criteria for Concrete: Mathematical Approximations and Experimental Validation", *Engineering Fracture Mechanics,* **35**, pp. 87-94 (1990).

[7] Bazant, Z. P., Kim, J-K., and Pfeiffer, P. A., "Nonlinear Size Effect Properties from Size Effect Tests", *Journal of Structural Engineering*, ASCE, **112**, No. 2, pp. 289-307, 1986.

[8] Bazant, Z. P., and Pfeiffer, P. A., "Determination of Fracture Energy from Size Effect and Brittleness Number", *ACI Materials Journal*, **84**, No. 6, pp 463-480, 1987

[9] Bazant, Z. P., Gettu, R., and Kazemi, M. T., "Identification of Nonlinear Fracture Properties from Size Effect Tests and Structural Analysis Based on Geometry-Dependent R-Curves", Report No. 89-3/498p, Center for Advanced Cement-Based Materials, The Technological Institute, Northwestern University, Evanston, Illinois 60208, 1989.

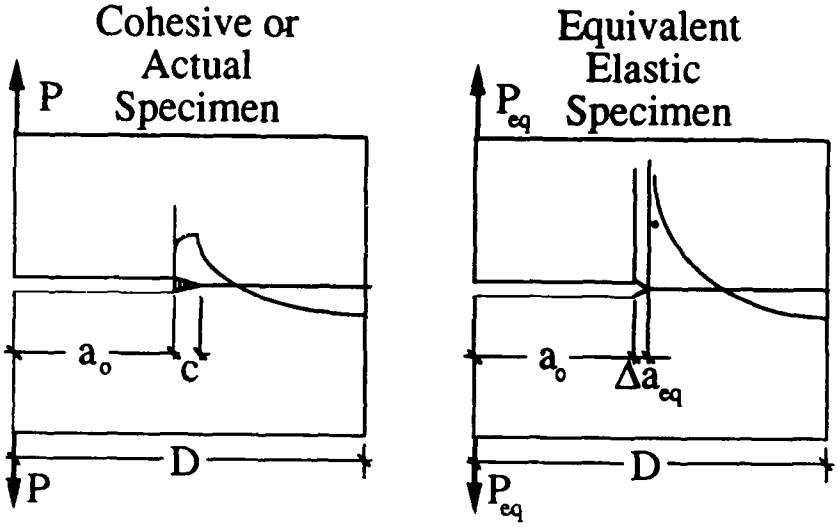

Figure 1. Definition of equivalent elastic specimen.

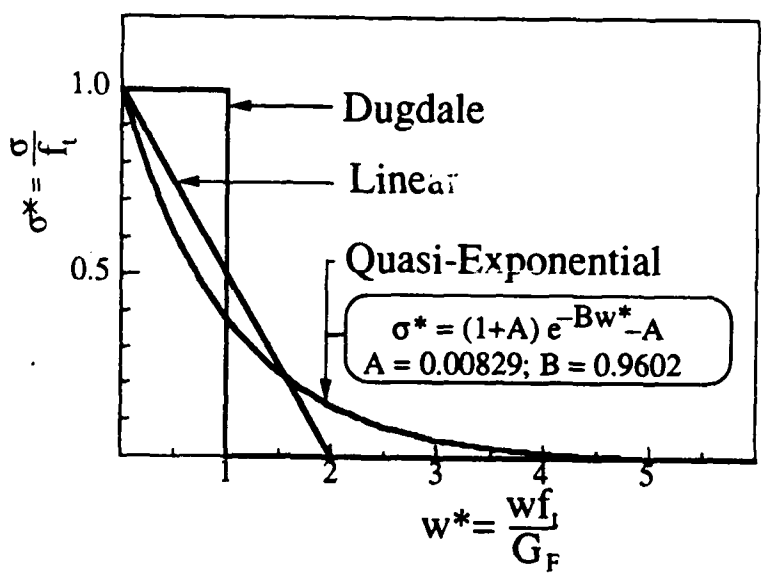

Figure 2. Softening curves analyzed in this work.

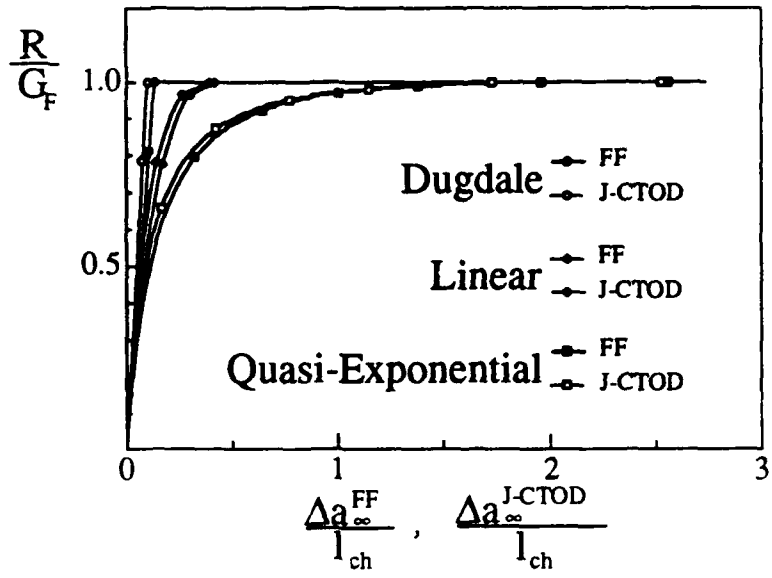

Figure 3. R-Δa curves for the FF(Far Field) equivalence and for the J-CTOD equivalence, for infinite size.

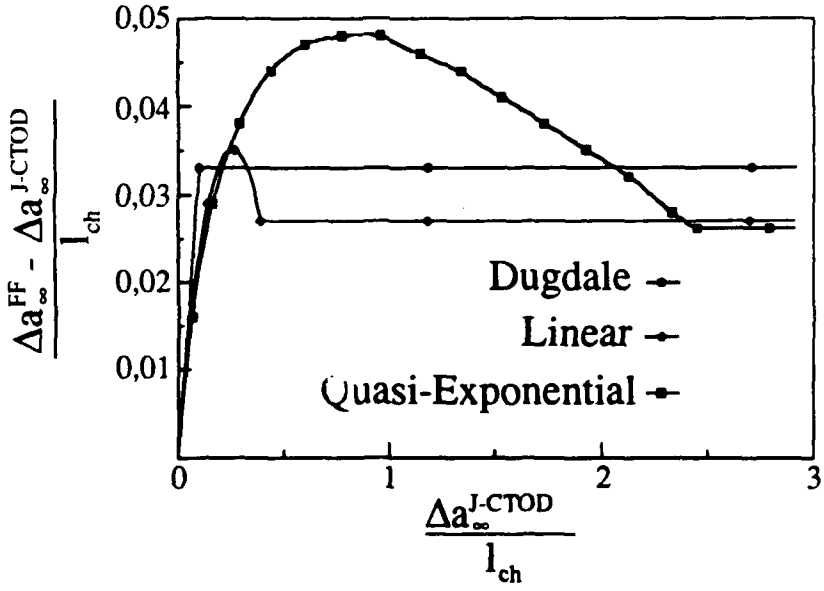

Figure 4. Difference between the equivalent crack extension of FF and J-CTOD equivalences, for infinite size.

Session 4:

Experimental Observations

Chairs:

Morris E. Fine
Northwestern University
Evanston, U.S.A

Peter L. Swanson
Denver Research Center,
U.S.A.

Reporter:

Joseph Homeny
University of Illinois,
Urbana, U.S.A.

MICROSTRUCTURE, R-CURVES AND MECHANICAL PROPERTIES OF ALUMINA-BASED CERAMICS

Stephen J. Bennison*, Srinivasarao Lathabai*, Jurgen Rödel* and Brian R. Lawn

Ceramics Division
National Institute of Standards and Technology
Gaithersburg, MD 20899
USA

For: NATO Advanced Research Workshop on Toughening Mechanisms in Quasi-Brittle Materials, July 16-20, 1990. Northwestern University.

---

* Guest Scientist on leave from the Department of Materials Science and Engineering, Lehigh University, Bethlehem, PA 18015 USA.

SYNOPSIS

It now well established that many monolithic ceramics exhibit the property of rising crack resistance with crack extension; i.e. R-curve or T-curve behavior. The magnitude of the toughness increase can be respectable, up to factors of three to four in some systems, occurring over crack extensions of several millimeters or hundreds of grain dimensions. The R-curve characteristic determines mechanical behavior. For example, the stabilizing effect on crack growth can lead to the property of flaw tolerance i.e. a decreased dependence of the strength on flaw size, which is a desireable property for structural applications in which the component is subject to damage.

The magnitude and form of the R-curve is sensitive to detailed characteristics of the microstructure such as grain size and shape, second phases, grain boundary toughness and intensity of residual stresses. The strong influence of microstructure leads to potential manipulation of crack-resistance properties through controlled processing. Opportunities for the development of improved structural ceramics rest with a proper understanding of the influence of R-curves on properties, an appreciation of the role of microstructure in crack-resistance characteristics, and the development of novel microstructures which exploit the operative toughening mechanism(s).

A substantial body of evidence has been gathered which demonstrates that the principal mechanism of R-curve behavior in monolithic ceramics, such as alumina, is grain-localized bridging at the crack interface behind the advancing tip. Bridging grains exert closure forces across the crack interface and shield the tip from the applied stress-intensity field. The accumulation of bridges with crack propagation leads to increased toughness

with extensions over many grain diameters.

In the present work we examine the phenomenon of crack-resistance behavior due to grain bridging using alumina-based ceramics as a model system. The paper is divided into four sections. In the first a model for grain bridging, formulated in terms of microstructural parameters, is reviewed and discussed [1]. Particular emphasis is placed upon the role of microstructural elements and suggestions for adjustments of R-curves through thoughtful processing are given. The second section deals with the influences of an R-curve on a variety of mechanical properties. This latter section is subdivided into three domains of crack size: short - concerning wear properties [2]; intermediate - strength [3,4] and fatigue (static, dynamic, cyclic) [5,6]; long - cyclic fatigue. The links between microstructure, R-curves and properties will be further stressed in the discussion of properties. The third section presents results of a more detailed investigation of grain bridging in the form of in situ SEM observations of crack-microstructure interactions [7]. Measurements of crack profiles demonstrate directly the closure forces exerted by the bridges on the crack. The final section presents some general conclusions and recommendations for future work.

REFERENCES

1. S.J. Bennison and B.R. Lawn, "Role of Interfacial Grain-Bridging Sliding Friction in the Crack-Resistance and Strength Properties of Nontransforming Ceramics," Acta Metall., 37[10] 2659-71 (1989).

2. S-J. Cho, B.J. Hockey, B.R. Lawn and S.J. Bennison, "Grain-Size and R-Curve Effects in the Abrasive Wear of Alumina," J. Am. Ceram. Soc., 72[7] 1249-52 (1989).

3. S.J. Bennison and B.R. Lawn, "Flaw Tolerance in Ceramics With Rising Crack-Resistance Characteristics" J. Mater. Sci. 24 3169-75 (1989).

4. P. Chantikul, S.J. Bennison and B.R. Lawn, "Role of Grain Size in the Strength and R-curve Properties of Alumina," J. Am. Ceram. Soc., in press (1990).

5. S. Lathabai and B.R. Lawn, "Fatigue Limits in Noncyclic Loading of Ceramics with Crack-Resistance Curves," J. Mat. Sci., 24 4298-4306 (1989).

6. S. Lathabai, Y-W. Mai and B.R. Lawn, J. Am. Ceram. Soc., "Cyclic Fatigue Behavior of an Alumina Ceramic with Crack-Resistance Characteristics," J. Am. Ceram. Soc., 72[9] 1760-63 (1989).

7. J. Rödel, J.F. Kelly and B.R. Lawn, "In Situ Measurement of Bridged Crack Interfaces in the SEM," J. Am. Ceram. Soc., in press (1990).

CREEP AND CREEP FRACTURE IN HOT-PRESSED Al_2O_3

A.Gordon Robertson*, David S. Wilkinson and Carlos H. Cáceres+
Department of Materials Science and Engineering
McMaster University
Hamilton, Ontario, Canada L8S 4L7

* current address:
PAPRIVAN
3800 Westbrook Mall
Vancouver, BC
V6S 2L9
Canada

+ on leave from:
INVAP SE
8400 Bariloche
Argentina.

ABSTRACT

The creep and creep fracture behaviour of two hot-pressed aluminas are presented, for both flexure and tension testing. Steady-state power-law creep is observed with a stress exponent of about 2 for each material. Three distinct fracture regimes are found. At high stress in flexure, fracture occurs by slow crack growth with a high stress dependence of the failure time. At intermediate stresses, in both flexure and tension, creep fracture occurs by multiple microcracking after modest strains. Failure times exhibit a modest stress dependence (stress exponent of 2 in tension and 3 in flexure). Thus, the Monkman-Grant is observed in tension, with a constant equal to 0.09. The failure times are considerably longer in flexure than in tension, due to the constraint imposed on crack growth by the bending geometry. We conclude that flexure cannot be used for creep lifetime assessment, even in simple, single phase materials such as Al_2O_3. At low stresses in tension, failure also exhibits Monkman-Grant behaviour, but with a much higher constant 0.21. The material shows the onset of superplastic behaviour.

1. INTRODUCTION

The increasing emphasis on the development of structural ceramics for high temperature applications has led to a greater need for understanding creep fracture in these materials. Typical operating lives for engine components, for example, will be several thousand hours. It is therefore inappropriate to design components for such applications using only data drawn from short-term tests. Long term testing however, is costly. Therefore, a fundamental understanding of the processes which control creep fracture is imperative. In this study, a model material, hot-pressed Al_2O_3, has been used. Although Al_2O_3 itself is not suitable as a high temperature structural material, its behaviour is representative of "dry grain boundary" ceramics (i.e. ceramics without significant amounts of glass between the grains). Moreover, it is a potential matrix material for some structural composites with high temperature capability. Other structural ceramics with high temperature strength such as silicon nitride contain extensive glass as a second phase. Moreover, they are microstructurally unstable at high temperature[1]. Creep fracture data for these materials are therefore more difficult to interpret.

Creep fracture in hot-pressed alumina has been studied previously[2-6], using 3-point flexure testing. The temperatures used in these tests were fairly high (1300-1400°C) with very short failure times (<3 hours). Two failure regimes have been identified. In the first, failure is by slow crack growth. In the second, general damage is associated with the growth and linkage of microcracks. In keeping with previous work on metals, Dalgleish et al.[6] attempt to analyze their results in the general damage region, using the Monkman-Grant relationship which suggests that the product of steady-state strain rate and failure time should be constant, independent of the applied stress. They find, however, that the Monkman-Grant product is stress-dependent, and suggest that this is due to the stress dependence of the crack coalescence processes. They also caution[6] that their results may be related to testing geometry.

In the current program, lower temperatures and strain rates, and thus larger failure times, have been studied. In addition, the use of tensile testing is explored, in order to avoid the ambiguities inherent due to stress redistribution in bending. Finally, the effect of impurities is invertigated by studying two separate hot-pressed aluminas.

2. EXPERIMENTAL

2.1 Materials

Two commercially available hot-pressed aluminas were used in this study. The first, manufactured by AVCO* in 1983, contained about 0.3 wt% MgO as a sintering aid. The second, manufactured by ARCO# in 1986 contained only 200 ppm (by weight) MgO, but had about 800 ppm Y. Both materials were obtained in the form of hot-pressed billets. Both were of high density with residual porosity <0.05% in each case. Both contained equiaxed grains with a mean linear intercept grain size of 1.6 μm for AVCO and 1.0 μm for ARCO. Electron microscopy did not reveal any grain boundary glass in either material.

2.2 Flexure Testing

Flexure bars 65? mm long were machined from the billets, using a prescribed machining schedule (Robertson, 1989). Most bars had a fixed cross-section of 4x6 mm. However, some were deeper (5x10 mm), thus enabling larger strains to be achieved. The tensile face was always that taken from closest to the centre of the billet. The tensile axis was perpendicular to the hot pressing direction. The tensile edges were bevelled on a 600 mesh resin-bonded polishing plate. The tensile faces and the bevels were then lapped to a 0.25 μm diamond finish.

---

* AVCO, Systems Division, Wilmington, MA

ARCO, Silag Division, Greer, SC.

Samples were tested in air, using one of two four-point bend rigs, with 20 and 28.5 mm inner span, and 40 and 54.0 mm outer span, respectively. Deformation was monitored continuously using 3 probe extensometers.

2.3 Tensile Testing

Creep fracture testing under tension eliminates the uncertainties associated with the time-dependent stresses which develop during bend tests. We have therefore designed a simple tensile creep tester for this work. It uses hot grips so as to minimize specimen material requirements and machining costs. Thus, pin-loaded specimens, as shown in Fig. 1, were designed. Provided that care is taken to align the loading holes accurately, this specimen provides for minimal bending.

Tests were conducted under dead load in a clamshell furnace, using SiC pull rods and load pins. Strain measurements were made using a long focal length telescope. This was sighted on knife edges machined into each of the four shoulders of the specimen (see Fig. 1). In order to allow for this, a sighting tunnel with a sliding glass window was placed on one side of the creep furnace. Opposite the window, a rectangular wall was machined into the furnace insulation. This was necessary to produce a dark background, against which the specimen was visible. The precision with which flag-to-flag displacements could be measured was found to be ± 5 μm.

In converting the displacements to strains, it is necessary to divide by the length of the deformation zone. However, for the configuration used here, this is not known exactly. Deformation is uniform within the 12.5 mm gauge section. However, because of the need for gradual flares out to the specimen shoulder, a reduced but significant rate of deformation occurs outside the gauge section. We have therefore normalized the displacements by a nominal gauge length of 20 mm, a value intermediate between the reduced gauge length and the shoulder-to-shoulder separation. This value also

produces strains which are consistent with those measured on failed specimens.

The flat faces of each specimen were lapped by hand prior to testing, to a 3 μm diamond finish. Edges were bevelled longitudinally so as to reduce the risk of edge failure. The loading holes were also bevelled in order to minimize bending due to any small misalignment of the SiC loading pins. A more complete description of the tensile test facility is available elsewhere[7].

Most samples were tested at a single stress to fracture. In a few cases however, incremental stress change tests were conducted to determine the creep stress exponent. Similarly, a few samples were tested in compression in an MTS servohydraulic machine. In this case the samples had a 4x4 mm square section and a height of 7 mm. The samples were compressed between SiC platens and the strain was determined by a differential extensometer measuring the relative displacements of the platens.

3. RESULTS

3.1 Preliminary Results

Initial work was performed at 1350°C on the AVCO material, in flexure. In these early tests, larger bend bars with a 5x10 mm cross-section were used. Outer fibre strains of up to 7% were possible with this configuration. Tests with nominal outer fibre stresses between 12 and 39 Mpa were performed. No fracture occurred. Indeed, no microcracking was visible on the tensile face. Moreover, it was discovered[8,9] that this material swells at 1350°C; i.e. cavity growth occurs due to the pressure exerted by trapped gas in residual porosity, even in the absence of an applied stress. Further testing was therefore constrained to temperatures of 1250°C and below, in which case swelling rates are found to be negligible.

3.2 Flexural Results

Flexural tests were performed on both materials over a range of temperatures. However, the majority of tests were performed at 1250°C for ARCO alumina and at 1150°C for AVCO alumina. Typical creep curves are shown in Fig. 2, for AVCO tested at 1150°C. Outer fibre tensile strain ϵ, is calculated from the 3-point probe displacements using the analysis of Hollenberg et al.[10]. The stresses listed are the nominal outer fibre stress at steady-state*. These are obtained from the applied elastic stresses using the formulation of Cohrt et al.[11]

$$\sigma = \frac{2n+1}{3n}\sigma_{el}$$

where the stress exponent n, for this material, is 1.8. The creep rate data are plotted in Fig. 3 for both the ARCO and AVCO materials. Strain rates were measured at a strain of about 0.02.

For tests conducted at stresses above 175 MPa for the AVCO material (or 180 MPa for the ARCO material)#, steady-state is never achieved due to short time fracture of the samples, and creep data is not reliable. At lower stresses, however, steady-state creep does occur. Power-law creep behaviour is apparent with a stress exponent of 1.8±0.2 for ARCO, and 2.0±0.2 for AVCO. The activation energies, estimated from the data are 390 kJ/mole for ARCO, and 480 kJ/mole for AVCO.

The transition in creep behaviour at about 175 MPa is accompanied by a dramatic change in the fracture behaviour. This is clearly shown in Fig. 4 in which the failure strain is plotted as a function of stress. At stresses above the transition stress, in both the ARCO and AVCO aluminas, fracture occurred at very low strains, under 1%, and in very short times, typically less than 2 hr. At lower stresses, fracture occurred in the AVCO samples only

---

* Since the estimated time to relax to steady-state (a few minutes at 1250°C) is considerably shorter than most of the tests, we use this as the most reasonable indicator of stress level.

A steady-state stress of 170 MPa corresponds to an initial elastic stress of 200 MPa.

after strains about 12% were reached, while in the ARCO samples fracture did not occur out to the maximum strain attainable using deep bend bars, near 18%. The stress rupture data are plotted in Fig. 5. They also give clear evidence of a change in behaviour at about 175 MPa steady-state stress.

3.3 Tensile Tests

Tensile tests were performed only on ARCO alumina at 1250°C. Most samples were crept to failure. The creep curves are shown in Fig. 6. Very little primary creep is observed as compared with the bend tests. There is also very little evidence of tertiary creep prior to failure. The small increase in strain rate at large strain is due largely to the influence of increased stress during creep at constant applied load.

The steady-state creep data are summarized in Fig. 7. These data were obtained from both fixed stress and from stress-change tests. The stress exponent for tensile creep is 1.8, the same as that obtained from the compression and flexural tests. Scatter in strain rate between individual samples was significant (see Fig. 7). However, when incremental stress tests were conducted, the results were very consistent; i.e., the stress exponent was constant and close to 1.8. The scatter between tests is thought to be due in part to billet to billet variations in the material.

Failure strain increases rapidly as the stress decreases. This is shown in Fig. 8 in which both the true failure strain $\epsilon_f = \ln(A_o/A_f)$ and the longitudinal strain $e_f = \ln(l_f/l_o)$ are plotted. At the higher stresses, above 80 MPa, the failure strain is relatively constant, around 9%. However, it increases rapidly at lower stresses, rising to 17% at 40MPa.

The stress rupture data are shown in Fig. 9. Once again, there are two different regions. At the two highest stresses, the data fit a relationship of the form $t_f \sim \sigma^{-m}$, where the stress exponent m is about 2. For the lower stresses, below 55 MPa a stress

exponent of between 1.5 and 2 is appropriate, but at much longer times. Between these two regimes lies a region in which the time to failure increases rapidly with decreasing stress. This, along with the rapid increase in failure strain at the lower stresses, suggests a transition in failure mechanism between 80 and 55 MPa.

4. DISCUSSION

4.1 Creep Behaviour

Primary Creep

Stress redistribution during flexural tests complicates the analysis of primary creep. However, the tensile tests on ARCO also show primary creep. At 1250°C, we find primary creep strains of about 1%. This compares with strains of about 0.5% in a somewhat different hot-pressed alumina, observed by Chokshi and Porter[12].

Several explanations for primary creep have been suggested. Gruffel et al.[13] explain their primary creep in hot-pressed alumina as due to concurrent grain growth. However, we have done extensive grain growth measurements in our material and find no significant grain growth at 1250°C, although grain growth is substantial at temperatures of 1350°C and above[8,9]. Frost and Ashby[14] have modelled primary creep due to diffusion creep transients. For ARCO at 1250°C, their model predicts strains of about 0.1% with a time constant of 0.6 h. This is much less (both in time and strain) than what is observed. Thus, the physical basis for the observed primary creep is not clear. There may however, be effects due to grain size distribution on primary creep. The dominant mode of deformation at low strains is thought to be grain boundary sliding. Both grain boundary sliding rates and its accommodation by diffusion are grain-size dependent processes. Moreover, the material contains grains of variable size. There must therefore exist a transient, in which load is redistributed from the fine-grained regions which deform the most readily to the coarser-grained regions. No quantitative estimate of the strain required

by this process has been made. However, it must be greater than that predicted by uniform grain size models of the type developed by Frost and Ashby[14]. Moreover, elastic anisotropy is likely to play a role in modifying local stresses at small strains.

Steady-State Creep

Steady-state creep was established for both materials, and in both types of tests. The stress exponents measured were close to 2 in all cases. Similar values have been measured for a range of hot-pressed aluminas[4,12,15]. The significance of this exponent has not been firmly established. However, it is similar to that associated with superplastic deformation in metallic systems and some ceramics[16].

The activation energy measured for flexural creep in AVCO is 480 kJ/mole. This is very close to that measured by Porter et al.[15] of 460 kJ/mole, and by Johnson et al.[4] of 480 kJ/mole on similar MgO-doped AVCO aluminas (but not with the value of 635 kJ/mole reported by Chokshi and Porter[12], also for a similar material). Moreover, these values all lie within the range of reported activation energies for Al diffusion in Al_2O_3, which extends from 420 kJ/mole (ref.14, pp. 99- 102), to 684 kJ/mole[17]. The activation energy for creep in the ARCO alumina of 390 kJ/mole is considerably lower. This may indicate O diffusion control. For example, in a study of neck growth between alumina spheres at 1500-1900°C, Dynys et al.[17] found Al control of boundary diffusion at high temperature and O control at low. Given the different impurity levels in the ARCO and AVCO materials, a difference in the diffusion process is certainly possible.

The overall creep resistance of the ARCO alumina is greater, by a factor of about 15, than that of AVCO (see Fig. 3). Thus, the rate of creep of ARCO at 1250°C, is roughly equivalent to that of AVCO at the same stress, but 100°C cooler. Microstructurally, the materials are very similar. The small difference in grain size is insufficient to account for the difference in creep rate. We therefore suggest that differences in impurity and dopant levels[18]

lead to significant differences in diffusion coefficient and the creep rate. This is consistent with the difference in activation energy just noted. It is also consistent with our observations of swelling in these two materials at higher temperatures[8,9], in which swelling rates are considerably higher in the AVCO material. Swelling is again thought to be due to grain boundary diffusion.

4.2 Creep Fracture

Using a combination of flexural and tensile tests, two transitions in creep fracture behaviour are observed. At high stress (above about 175 MPa in flexure), failure is very rapid (≤2 hour) and at low strain (≤1%). Thus, failure occurs before steady-state creep is established. For a given stress, the scatter in time to failure is large (2 orders of magnitude). Thus, it is difficult to determine a stress exponent for stress rupture. However, it is clearly high, about 40. At stresses below 175 MPa, in flexure, a transition occurs. The failure strain is much greater (12-16% for AVCO, >18% for ARCO), and the stress exponent is between 2 and 3.

A second transition occurs within the stress range covered by the tensile data, for ARCO alumina. For stresses between 82 and 120 MPa, a stress rupture exponent of 2 is observed, while failure strains remain constant at around 9%. On further reducing the stress below 55 MPa, the failure strain increases sharply. The stress exponent remains near two. However, the time to failure jumps by about a factor of 3 on crossing the transition. It therefore appears that three distinct failure regions exist, depending on stress, for creep fracture in ARCO alumina at 1250°C.

The high stress exponent observed following high stresses in flexure is indicative of failure by slow crack growth, and this is consistent with fracture surface observations[18]. Below the first transition, in AVCO alumina, failure also occurs by crack growth. However, multiple cracks are observed with their eventual linkage causing failure. In ARCO, the material develops only a few

microcracks and cavities up to high strains. These are insufficient to induce fracture. In tension, ARCO alumina develops the same type of microdamage but in this case fracture is observed. The stress exponent for rupture is ≈3 in flexure and ≈2 in tension.

The creep rupture stress exponent has often been used to interpret the damage mechanism. An exponent of 3 for example, has been associated with crack growth controlled by surface diffusion[19], while an exponent of 2 in this case would correspond to Monkman-Grant behaviour. However, interpretation of damage mechanisms based on creep fracture exponents can be misleading, partly because of possible time dependent nucleation effects[20,21] and partly due to the effect of the stress redistribution in flexural specimens. Thus, a more detailed assessment of deformation and damage processes is required to identify the responsible mechanism for fracture. The analysis of creep damage in these materials is the subject of a subsequent paper[18], while the effect of stress redistribution will be discussed next.

Stress redistribution during bending results from a variety of processes. The first, and most commonly considered is the non-linear nature of creep which results in load shedding from the outer fibres[10]. Microcracking and cavitation, which effectively increase the strain in the outer tensile region, also increase load shedding from regions under tension. This effect may also result in a shift in the neutral axis towards the compressive side of the flexure bar. Finally, at large strains, movement of the load points occurs due to rotation. This reduces the moment applied to the central portion of a flexure bar, resulting in a decrease in the overall creep rate. This effect occurs only at large strains and is therefore not of concern unless the ductility of the material is significant (as it is here). Therefore, it would seem that evaluation of the fracture mechanism on the basis of rupture data using flexural specimens may be misleading when cavitation and large strains are possible.

It is for this reason that tensile testing is of value and may

even be essential in evaluating the creep fracture behaviour of ceramics. A comparison of the creep rupture plots in flexure and tension (Figs. 5 and 9) reveals a much shorter creep life for the same nominal stress in tension. This difference cannot be rationalized simply in terms of the lower outer tensile stress after stress redistribution. The explanation lies in the nature of crack propagation and the local stress fields surrounding cracks. Figure 10 shows the stress intensity factors K_{Ic}, at failure, for both tensile and flexure specimens. These have been determined by measuring the size of the dominant crack on the fracture surface of each specimen. Using this and the known nominal stress on each specimen, K_{Ic} can be estimated. The value of K_{Ic} so determined is constant and equal to about 3 MPa $m^{1/2}$ for all of the tensile specimens and for the flexure specimens in the high stress, slow crack growth regime. However, a considerably higher value is estimated for the flexure specimens at lower stresses. Since the toughness of the material is not a function of geometry, this suggests that below the first transition in flexure considerable stress relaxation must occur in the vicinity of the crack tips, invalidating the K_{Ic} calculation. This is apparently not the case in tension. Crack propagation is less stable in tension. As the cracks grow they accelerate. This sharpens the crack tips and restors anelastic crack tip stress field. Thus, fast fracture occurs at the expected value of K_{Ic}. In flexure however, the geometry tends to stabilize the crack, extending the life considerably. Thus, while flexure may be a valid test geometry when failure is by slow crack growth of a single flaw at short times (i.e when an elastic stress field is maintained in the vicinity of the crack), it is not valid for determining rupture life when creep effects become important. In these instances tensile testing is required.

On the basis of the K_{Ic} measurements, we conclude that the failure times above the first transition stress would be the same in tension and in flexure. We have therefore replotted the tensile stress rupture data including the high stress flexure data (Fig. 11). It is clear that the large increase in failure time below the first transition in flexure is largely an artifact of the

constraints imposed by the geometry of testing.

Another indicator of failure mechanism is the failure strain. In the intermediate failure regime, in flexure, we find a very small increase in ϵ_f with decreasing stress. Dalgleish et al.[6] however, observed a much larger increase in the strain to failure over the same stress range. This may be due to differences in loading configuration. The 3-point bend geometry used by Dalgleish et al. places a much smaller volume of material under high stress.

A constant failure strain is one indication of Monkman-Grant behaviour. In its usual form, the Monkman-Grant relationship is:

$$\dot{\epsilon}_{ss} t_f = C_{MG}$$

where C_{MG} is a constant. Fulfilling this equation over a range of stress requires that the stress exponents for creep and fracture be equal. This is approximately true for the tensile data in both the intermediate and low stress regimes. However, C_{MG} is different - 0.09 at intermediate stress, and 0.21 at low stress. The Monkman-Grant relationship indicate that failure is deformation-controlled. This is consistent with the microstructural observations[18] in both stress regimes.

Further macroscopic evidence of the change of fracture behaviour with stress is given by the difference between the longitudinal and cross-sectional strains observed at failure. From Fig. 6 the longitudinal strains, as measured by optical extensometry, can be calculated. These values are plotted in Fig. 8, together with the failure strains measured from the cross-sections of the failed specimens. The two values agree at high stress. However, at low stresses, the longitudinal strains are much larger. The difference is due to the contribution of cavitation and microcracking to the longitudinal strain. The magnitude of this difference suggests a very high degree of damage tolerance in this material at the lower stresses. Indeed, the material verges on superplastic behaviour.

5. SUMMARY

1. Creep in both ARCO and AVCO hot-pressed aluminas exhibit power-law behaviour with a stress exponent of 1.8 for ARCO and 2.0 for AVCO.

2. The creep resistance of ARCO is about 15 times greater than that of the AVCO. This is thought to be due to the effect of minor impurities on grain boundary diffusion coefficients.

3. Primary creep transients in tension are larger than that predicted by existing models. This is most likely due to the effect of stress redistribution within the polycrystal due to the distribution of grain size.

4. Creep fracture exhibits three distinct regimes, depending on the stress applied.

5. At high stress, failure by slow crack growth with a high stress rupture exponent of about 40. Failure occurs when the K_{Ic} for failure, estimated to be 3 MPa $m^{1/2}$, is reached.

6. At intermediate stresses, failure exhibits a modest stress dependence with an exponent near 3 in flexure and 2 in tension, and with a constant fracture strain. Thus, the Monkman-Grant law is valid in this regime. The times to failure are considerably lower in tension than in flexure, while only the tensile tests give realistic K_{Ic} values from fracture surface observations. This suggests that flexure testing cannot be used for estimating failure lives.

7. At low stress, failure also obeys the Monkman-Grant relationship, but with a much higher failure strain.

ACKNOWLEDGEMENT

We wish to acknowledge the financial support of the Natural Sciences and Engineering Research Council of Canada. In addition,

partial support in the form of a fellowship to one of us (C.H.C.) from the Consejo Nacional de Investigaciones de la República Argentina is gratefully acknowledged.

REFERENCES

1-D.S. Wilkinson, M.M. Chadwick and A.G. Robertson,"High Temperature Stability of Structural Ceramics",,pp. 131-138, in Proc. Intl. Symp. on Advanced Structural Materials, Edited by D.S. Wilkinson, Pergamon Press, New York, 1989.

2-B.J. Dalgleish, S.M. Johnson and A.G. Evans, "High-Temperature Failure of Polycrystalline Alumina: I, Crack nucleation", J. Am. Ceram. Soc., **67**, 741-750 (1984).

3-W. Blumenthal and A.G. Evans,"High-Temperature Failure of Polycrystalline Alumina: II. Creep Crack growth and Blunting", J. Amer. Ceram. Soc., **67**, 751-759 (1984).

4-S.M. Johnson, B.J. Dalgleish and A.G. Evans,"High-Temperature Failure of Polycrystalline Alumina: III. Failure Times", J. Am. Ceram. Soc., **67**, 759-763 (1984).

5-B.J. Dalgleish and A.G. Evans, "Influence of Shear Bands on Creep Rupture in Ceramics", J. Am. Ceram. Soc., **68**, 44-48 (1985).

6-B.J. Dalgleish, E.B. Slamovich and A.G. Evans, "Duality in the Creep Rupture of a Polycrystalline Alumina", J. Am. Ceram. Soc., **68**, 575-581 (1985).

7-A.G. Robertson,"Swelling and Creep Damage Accumulation in Hot-Pressed Alumina", *Ph.D. thesis, McMaster University* (1989).

8-A.G. Robertson and D.S. Wilkinson, "Swelling in Hot- Pressed Aluminas: I. Theory", to be published, (1989).

9-A.G. Robertson and D.S. Wilkinson,"Swelling in Hot- Pressed Aluminas: II. Experimental", to be published, (1989).

10-G.W. Hollenberg, G.R. Terwilliger and R.S. Gordon, "Calculation of Stresses and Strains in Four Point Bending Creep Tests", J.Am.Ceram.Soc., **54**, 196-199, (1971).

11-H. Cohrt, G. Grathwohl and F. Thummler, "Non-Stationary Stress Distribution in a Ceramic Bending Beam During Constant Load Creep", Res.Mech., **10**, 55-71 (1984).

12-A.H. Chokshi and J.R. Porter,"High Temperature Mechanical Properties of Single Phase Alumina", J. Mater. Sci., **21**, 705-710 (1986).

13-P. Gruffel, P. Carry and A. Mocellin, "Effect of Testing Conditions on Superplastic Creep of Alumina Doped with Ti and Y", Science of Ceramics, **14**, 587-592 (1988).

14-H.J. Frost and M.F. Ashby, "Deformation-Mechanism Maps", Pergamon, Oxford, 1982.

15-J.R. Porter, W. Blumenthal and A.G. Evans, "Creep Fracture in Ceramic Polycrystals. I. Creep Cavitation Effects in Polycrystalline Alumina", Acta. Metall., **29**, 1899-1906 (1981).

16-A.K. Mukherjee, T.R. Bieler and A.H. Chokshi, "Superplasticity in Metals and Ceramics"; pp. 207-231, in Proc.of the 10th RISO Intl. Symp. on Metallurgy and Materials Science. Edited by J.B. Bilde-Sorensen, N. Hansen, D. Juul Jensen, T. Leffers, H. Lilholt and O.B. Pedersen., RISO National Lab., Roskilde, Denmark,, 1989.

17-J.M. Dynys, R.L. Coble, W.S. Coblenz and R.M. Cannon, "Mechanisms of Atom Transport During Initial Stage Sintering of Al_2O_3", pp. 391-404, in Sintering Processes, Edited by G.C. Kuczynski, Mater. Sci. Res. V13, Plenum, New York, 1980.

18-D.S. Wilkinson, A.G. Robertson and C.H. Cáceres, "Damage Mechanisms During High Temperature Creep in Hot-Pressed Alumina", to be published (1990).

19-T-J. Chuang and J.R. Rice, "The Shape of Intergranular Creep Cracks Growing by Surface Diffusion", Acta Metall., **21**, 1625-1628 (1973).

20-D.S. Wilkinson, "The Effect of Time-Dependent Void Density on Grain Boundary Creep Fracture. I. Continuous Void Coalescence", Acta Metall., **35**, 1251-1259 (1987).

21-D.S. Wilkinson, "The Effect of Time-Dependent Void Density on Grain Boundary Creep Fracture. I. Continuous Void Coalescence", Acta Metall., **35**, 2791-2799 (1987).

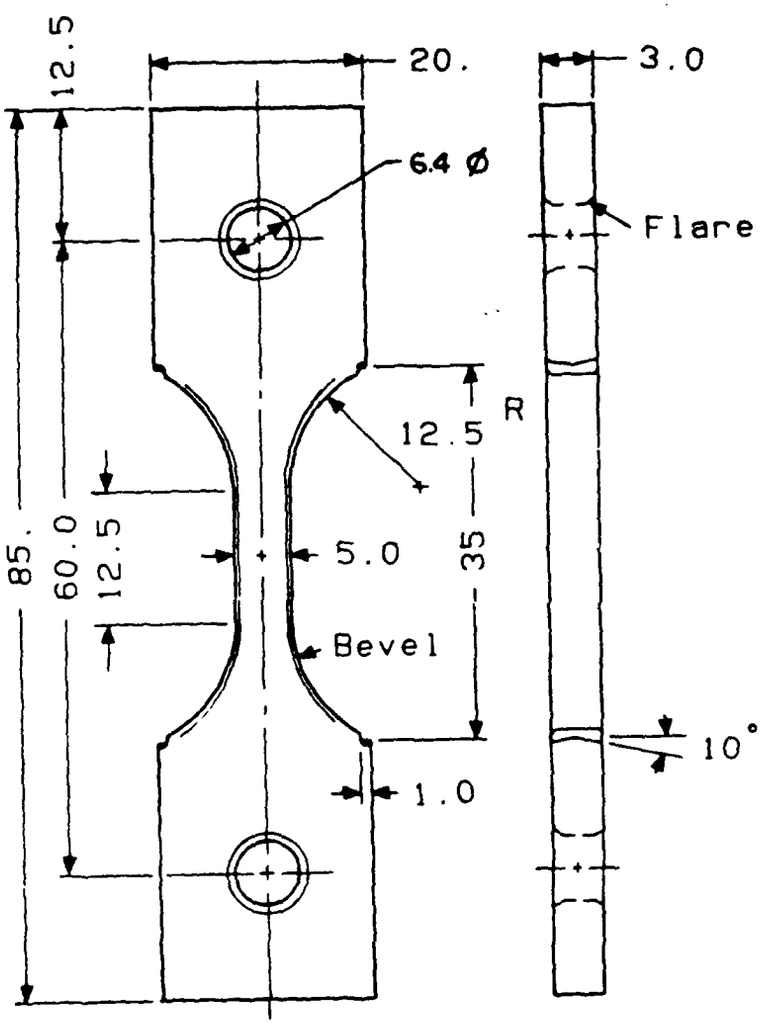

Fig. 1: Tensile test specimen, (dimensions in mm).

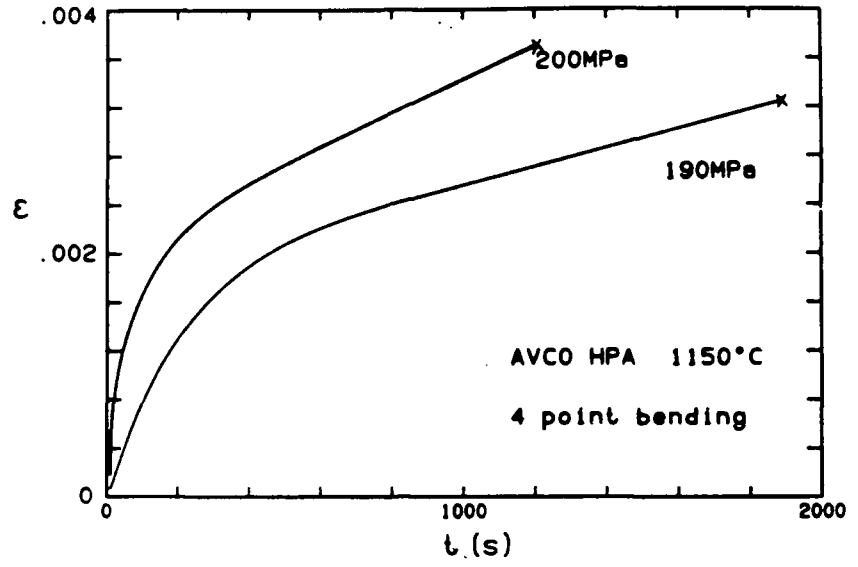

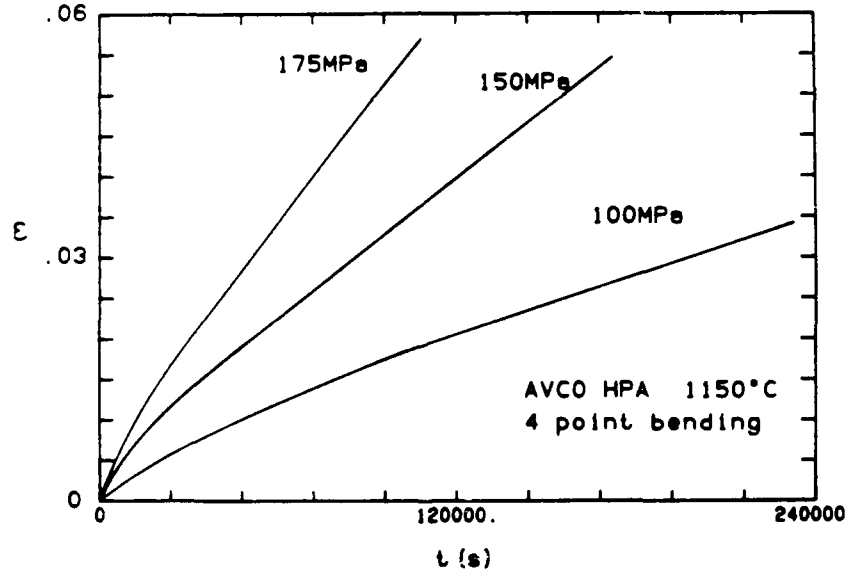

Fig. 2: Flexural creep curves in AVCO alumina at (a) high stresses and (b) intermediate stresses. The strain and steady state stresses are calculated for a stable neutral axis and a stress exponent of 2.0.

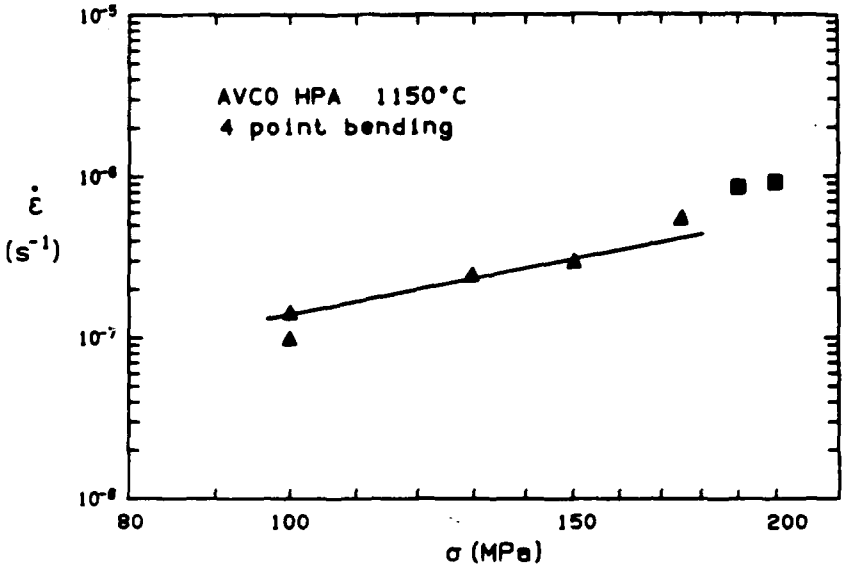

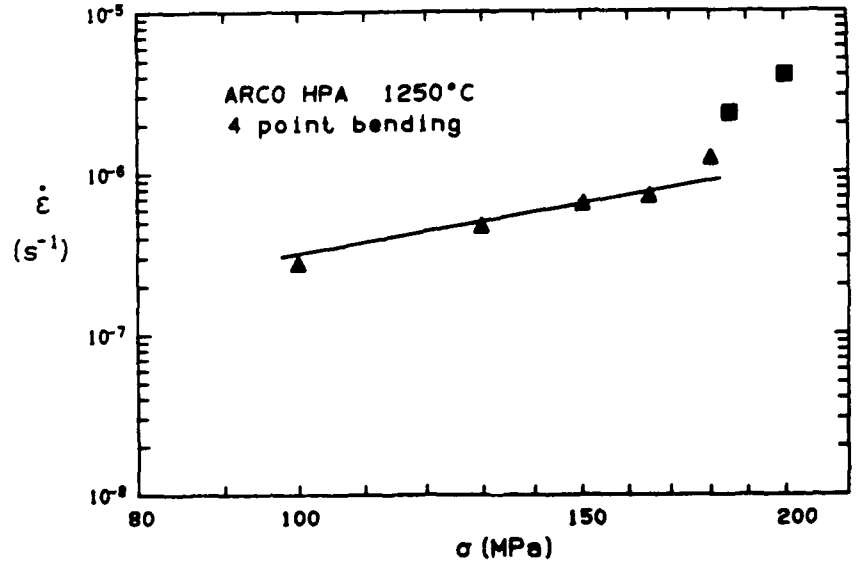

Fig. 3: Flexural creep rates in (a)AVCO and (b)ARCO alumina as a function of steady state stress and temperature. Solid squares are for samples that failed before attaining steady state creep.

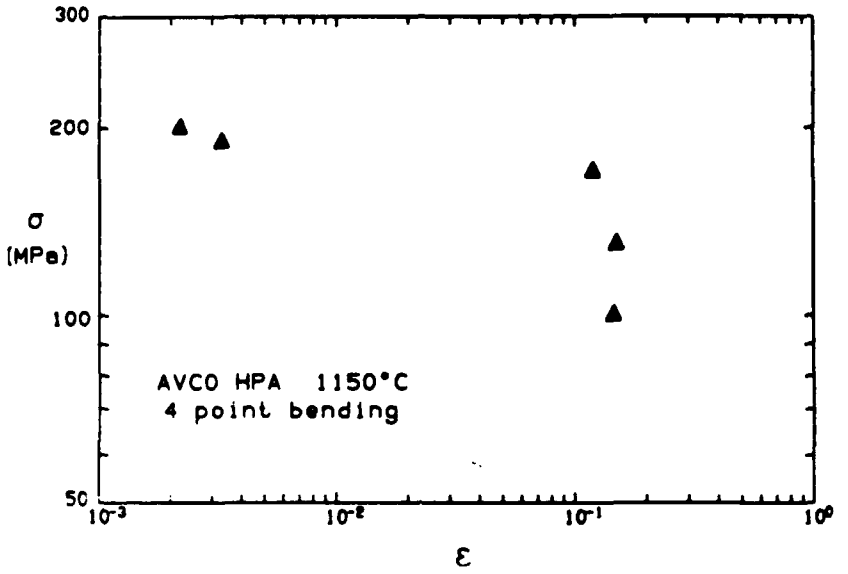

Fig. 4: The failure strain ϵ_f as a function of the steady state stress for flexure tests in AVCO alumina.

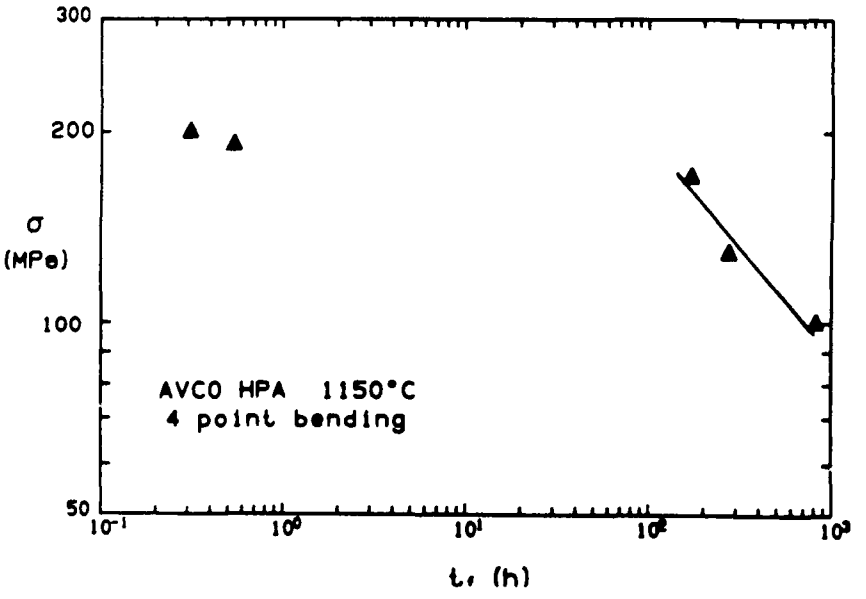

Fig. 5: Flexural stress rupture data for AVCO alumina.

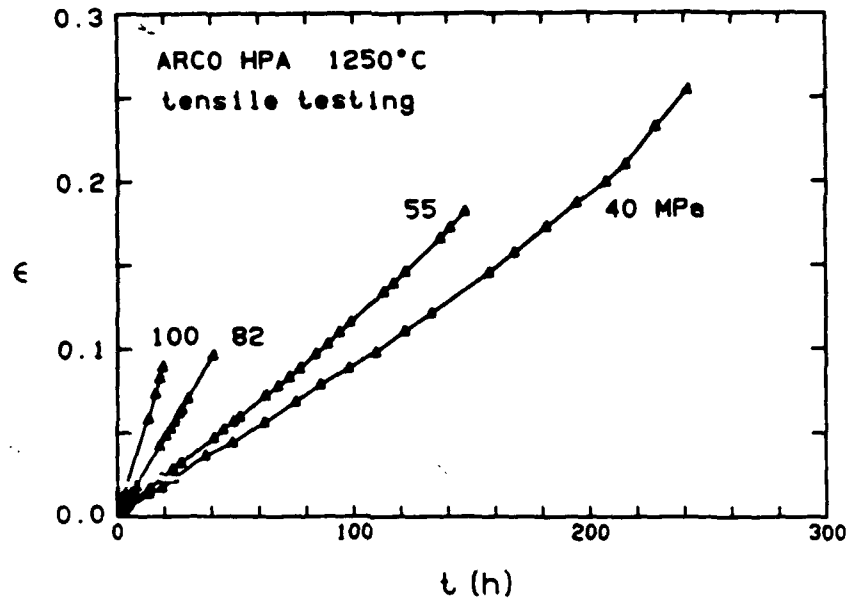

Fig. 6: Creep curves for ARCO alumina in tension.

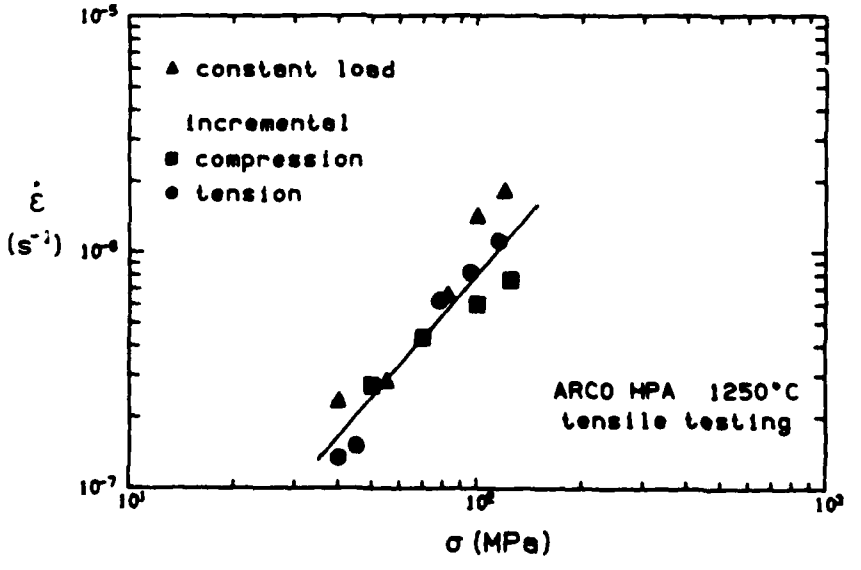

Fig. 7: Steady-state creep data for ARCO alumina in tension.

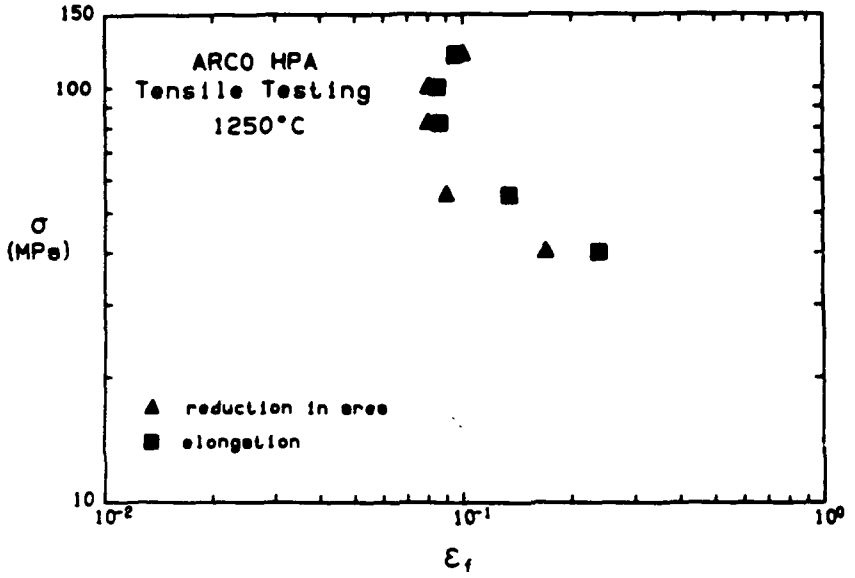

Fig. 8: Failure strains in ARCO alumina deformed in tension, as a function of applied stress.

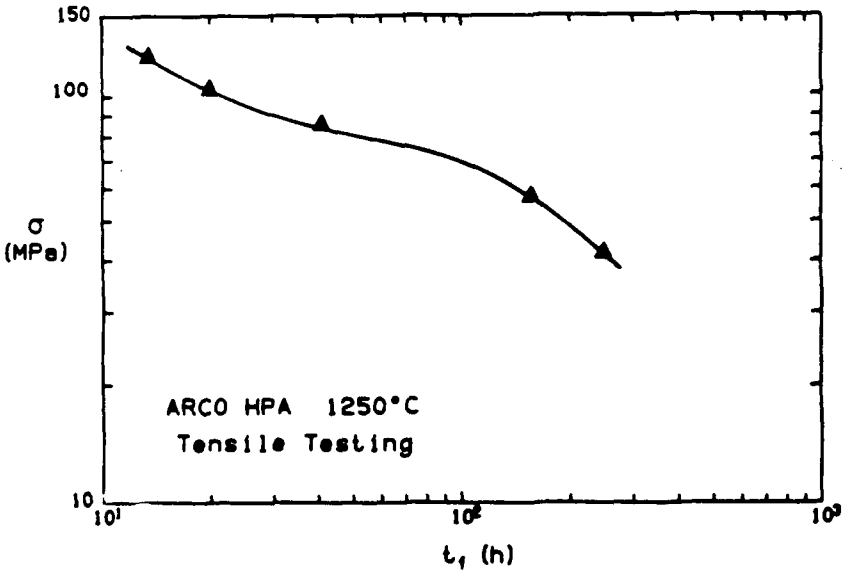

Fig. 9: The time to failure as a function of applied stress for ARCO alumina tested in tension.

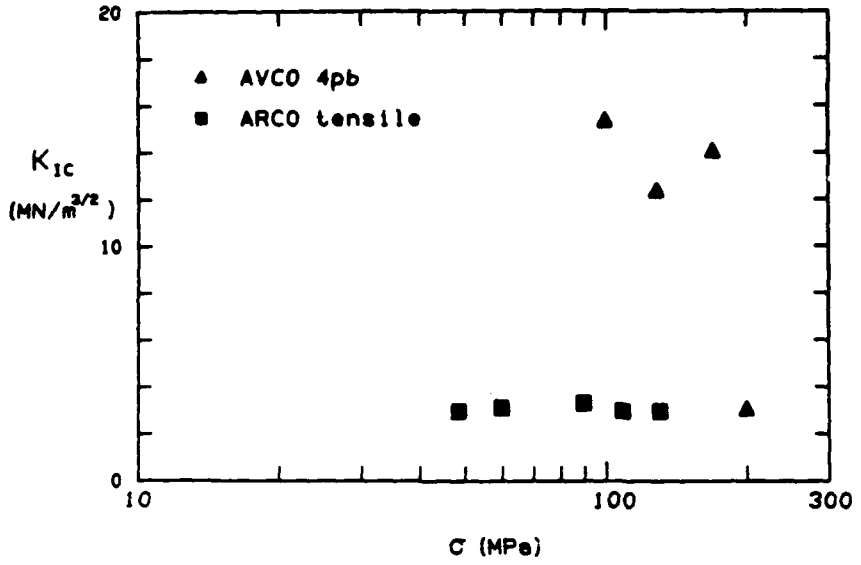

Fig. 10: Estimates of the stress intensity factor K_{Ic} from the fracture surface of both flexure and tensile specimens.

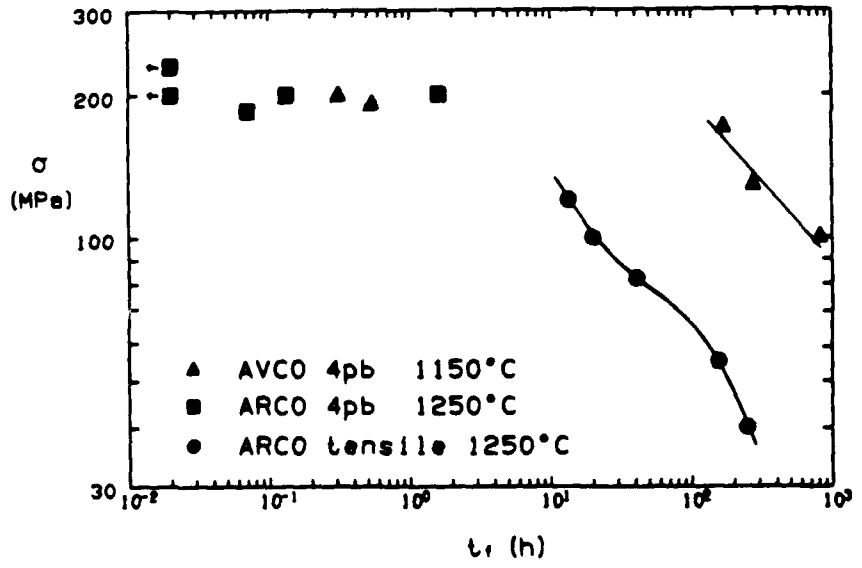

Fig. 11: The stress rupture data of Figs.5 and 9 replotted including the high stress flexure data for ARCO alumina. The arrows refer to points which failed upon loading.

DAMAGE AND FRACTURE MECHANISMS DURING HIGH TEMPERATURE CREEP IN HOT-PRESSED ALUMINA

David S. Wilkinson, A. Gordon Robertson* and Carlos H. Cáceres+

Department of Materials Science and Engineering
McMaster University
Hamilton, Ontario, Canada L8S 4L7

* current address:
PAPRIVAN
3800 Westbrook Mall
Vancouver, BC
V6S 2L9
Canada

+ on leave from:
INVAP SE
8400 Bariloche RN
Argentina

ABSTRACT

The mechanisms responsible for creep damage accumulation and fracture have been examined in two commercial hot-pressed aluminas. Differences between the two materials can be ascribed to minor compositional variations. Three damage regimes have been identified, depending on stress. At high stress, a single crack nucleated at a processing flaw controls failure. These cracks grow in a linear elastic stress field. At intermediate stresses, crack tip stresses relax, and many microcracks are observed. These are also nucleated at flaws. They grow and link under strain control. However, the details of this process are different under tension and bending, thus invalidating the flexure test as a means of established creep life, even in simple, single phase materials. At the lowest stress, extensive cavitation, with relatively little microcrack development is observed. The material is damage tolerant, and can be thought of as superplastic. We find that processing flaws control the creep strength at all stresses. These should therefore be carefully controlled in materials aimed at high temperature structural applications.

1. INTRODUCTION

The failure of ceramic polycrystals can generally be related to pre-existing flaws or (in the case of high temperature failure) to flaws which are generated during service[1,2]. At high temperatures, these defects can propagate under the influence of an applied stress, coupled with creep deformation, leading to failure. Alternatively, the applied stress can induce the nucleation of creep cavities at grain boundary triple junctions. These cavities grow and link to form microcracks which upon coalescence lead to fracture. This is an overly simplistic view of the creep fracture process however. Moreover, there are several aspects of the process that are not well understood, mostly due to the lack of experimental data. This paper therefore explores the mechanisms responsible for creep damage in a microstructurally simple ceramic, namely hot-pressed alumina.

Creep deformation of fine grained alumina can occur by several competing mechanisms - basal slip, diffusional creep, grain boundary sliding, and cavitation. Cavity growth can be thought of as just another competitive deformation mechanism[3,4]. All deformation mechanisms occur simultaneously during the irreversible deformation of alumina, the contribution of each one depending on the applied stress and temperature[3,4]. When cavities nucleate at stress concentrations such as grain boundary triple junctions, particles or slip band/grain boundary intersections, they may grow by diffusion or grain boundary sliding, contributing to the overall strain. Cavitation can thus be viewed as a stress relieving, geometrically necessary feature of the deforming structure. Since the dominant deformation mechanism is a function of stress, the need for stress relief by cavitation may also depend on the stress, leading to a stress dependent fracture behaviour.

In a companion paper[5] we have shown that fine-grained alumina exhibits three distinct fracture regimes. At high stresses (above 175 MPa for AVCO alumina, 180MPa for ARCO), fracture occurs by slow crack growth with very little strain and a high (of order 40)

stress exponent of the failure time. At intermediate stresses, fracture occurs following modest strains, and the stress exponent in tension is 2, the same as that for creep deformation in this material. Thus, the material exhibits Monkman-Grant behaviour in this regime. For the lowest stresses, fracture also obeys the Monkman-Grant relationship, but with much larger failure strains. The main concern of this paper is to examine the micromechanisms of creep damage at the intermediate and low stress regimes in fine grained hot-pressed Al_2O_3.

2. EXPERIMENTAL

2.1 Mechanical Testing

The mechanical test procedures are described in some detail elsewhere[5,6]. Both 4-point flexural testing and tensile testing have been performed, in air, under constant load conditions. While both materials have been tested in flexure, only the ARCO material has undergone tensile testing. In all cases, the surfaces relevant to subsequent microstructural and surface damage observations were polished prior to testing. In the case of flexural tests, a 0.25μm diamond finish was achieved on the tensile face. In the tensile specimens, a 3μm diamond finish was achieved on the flat faces along the gauge length. Specimen edges were bevelled to avoid premature damage initiation at these locations.

2.2 Microstructural Characterization

Test specimens were examined extensively using scanning electron microscopy. In addition to the examination of fracture surfaces and of the external faces of test specimens, internal polished sections were examined. In this case, samples were sectioned near the centerline of the test piece parallel to the loading direction of the flexure bar or tensile sample. This plane was polished to a 0.25 μm diamond finish and thermally etched[6]. Specimens were gold-coated prior to SEM examination. In some cases, by taking

special care, both an internal polished plane and a specimen face could be examined simultaneously. This made it possible to assess the internal penetration of cracks initiated at the surface.

3. RESULTS

3.1 Material Characterization

Two commercially available hot-pressed aluminas were used in this study, one manufactured by AVCO (from 1983)*, the other by ARCO (from 1986)#. Both of these materials have fine-grained (≈1 μm) equiaxed microstructures. Both swell upon exposure in air at temperatures of 1350°C and above[7,8]. This is accompanied by grain growth. However, at temperatures of interest in this study, namely 1250°C and below, both swelling and grain growth are negligible. The materials differ somewhat in their chemical composition, as outlined in Table I. The AVCO material contains about 0.3 wt% MgO introduced as a sintering addition. ARCO however, contains only 200 ppm MgO, but 800 ppm Y. The ARCO material also contains substantially more carbon.

TABLE I: Chemical Analysis

	C	Fe_2O_3	K_2O	MgO	MnO	S	SiO_2	TiO_2	Y	Zn
ARCO	250	90	4	200	3	16	200	25	800	19
AVCO	140	130	6	3000	2	17	140	25	10	17

Values are p.p.m. by weight.
Carbon data obtained by combustion analysis; all other analyses by X-ray fluorescence.

* AVCO, Systems Division, Wilmington, MA

ARCO, Silag Division, Greer, SC.

The porosity of each of the as-received materials is very low, about 0.01%. However, as revealed by TEM (Fig. 1), it is distributed differently in the two materials. The AVCO alumina contains almost exclusively intergranular pores at three-grain junctions, with a mean radius of 0.12 μm. The ARCO alumina contains mostly intragranular porosity, typically in the form of clusters. The average pore radius is about 15 nm.

Thermally etched, polished sections of as-received material do not reveal many microstructural defects. However, subsequent creep testing exposes defects in the form of porous regions, regions of large grain size, and regions of chemical inhomogeneity. The defects were more numerous and more severe in the ARCO material.

3.2 Failure Times and Strains

Data for time to failure and failure strain have been presented elsewhere for both flexure and tensile testing[5]. The behaviour of the two materials is similar. They show three regimes. For both materials, at high stress (above about 175 MPa steady-state stress), in flexure, failure occurs by slow crack. The creep fracture exponent m ($t_f \sim \sigma^{-m}$) is difficult to determine but it is very large, at least 40. The failure strains are low, less than 1%. This we call the *slow crack growth* regime. Below about 175 MPa there is an abrupt transition to the *microcrack growth regime*. Moderate failure strains are observed (12-16% in flexure for AVCO, 8-10% in tension for ARCO), and the stress exponent is about 2 (in tension). The ARCO alumina does not fail in flexure for strains of up to 18%, either at 1200 or 1250°C. At low stresses (below 55 MPa in tension), a third regime is observed, the *creep fracture regime*. Monkman-Grant behaviour is observed (with the stress exponent for creep and creep rupture both equal to about 1.8). The failure strain is large, about 17%.

The overall creep behaviour of the AVCO material parallels that of ARCO, but at a temperature about 100°C lower. Thus, most of the

AVCO data was collected at 1150°C while the ARCO data was collected at 1250°C.

3.3 Slow Crack Growth Failures

Both materials fail very quickly above a threshold stress in flexure*. In all cases, a single crack is found to originate at or near the tensile surface, and propagate to failure. Only a single crack is visible on the tensile face of these specimens. It therefore appears that a crack propagates from the single most damaging flaw in the specimen, accelerating rapidly as it grows.

Typical failure origins are shown in Fig. 2. These include internal processing flaws in the form of penny-shaped cracks perpendicular to the hot pressing direction (Fig. 2a); regions of abnormal grain growth, generally with many large grains in a cluster (Fig. 2b,c); and amorphous regions (Fig. 2c). The first two types of flaws are generally subsurface, and are clearly present in the material prior to testing. Amorphous regions are generally connected to the surface and may result from deposits which develop on the surface during specimen heat-up prior to testing. The types of failure origins observed are similar for both materials.

3.4 Microcrack Growth Regime

Both materials exhibit considerable damage tolerance in this regime. Failure occurs by the development of several microcracks that grow simultaneously until one becomes critical. Details of the process depend on the geometry of testing. This regime has been explored using both tensile and flexure testing.

---

* This does not mean that such failures do not occur in tension. However, the tensile creep rig we have used is incapable of applying sufficient loads to produce such failures.

In *ARCO alumina,* in flexure, the samples develop relatively few microcracks. These are mostly nucleated at chemical inhomogeneities (Fig. 3a). They do not propagate easily through the material. Rather, they blunt or bifurcate after propagating some distance (Fig. 3b). Other microcrack origins include large grains, either isolated (Fig. 3c) or in clusters (Fig. 3d). For the maximum strains available in the bend rig (about 18%), the larger cracks which develop never propagate to the point of failure.

In tensile specimens, the outer surface is heavily decorated with microcracks (Fig. 4). These are also nucleated at chemical inhomogeneities or other microstructural defects. An example is shown in Fig. 5 of a crack on a polished internal section. A large grain is just visible inside the crack near its centre. Another large grain is visible ahead of the crack (right-hand side). The boundary of this grain is decorated by a set of cavities which have linked together. Thus large grains appear to act as preferential sites for cavity nucleation. Internal microcrack and cavity nucleation is more widely distributed in tensile than in flexure samples, because of the uniform stress. Microcracks remain sharp while growing (Fig. 6a) while cavities are flat or crack-like, and cover a single grain facet in most cases (Fig. 6b). Failure occurs by the competitive growth of several microcracks until one becomes critical. Figure 7 shows the fracture surface of a sample following creep at 82 MPa. The failure origin is a well-defined semi-circular crack emanating from a large-grained region. Only a single crack is visible on the fracture surface (although several cracks exist away from the fracture surface as shown in Fig. 5). As the stress is lowered and the lowest stress regime is approached, the failure origin becomes less distinct (section 3.5).

In *AVCO alumina*, samples deformed in flexure develop a large number of microcracks on the tensile face. A variety of crack origins can be identified, some of which are different from those responsible for the slow crack growth failures discussed in the previous section. The microcracks appear to be organized in "shear" bands (Fig. 8a) that extend under the surface forming a 3D pattern (Fig.

8b). The number of shear bands observed does not vary significantly with increasing stress (Fig. 9). Observation at higher magnifications reveals an extensive array of individuals cavities besides the larger cracks. In many cases, it is clear that microcracks have formed through a process of cavity coalescence (Fig. 10).

The main difference between the two aluminas studied, in this regime, lies in the amount of microcracking and cavitation observed, which is much more extensive in the AVCO material. The higher density of microcracks in AVCO leads to the development of "shear" bands. The development of these bands through microcrack coalescence in flexure is illustrated in Fig. 11. This, in turn, leads to the development of large cracks as described by Dalgleish et al.[9,10]. These large cracks delineate a sort of slip line field which becomes the dominant feature in the tensile face of AVCO samples. Several large cracks develop at the same time and compete with each other until one of them reaches a critical size and induces failure.

3.5 Creep Fracture Regime

In this regime, observed only in the tensile specimens of ARCO for stresses below 55 MPa, the outer surface appears almost featureless with virtually no cracks (Fig.12-a), despite the very large elongations involved (27%)[5]. High magnification imaging of polished internal surfaces reveals a large density of cavities (Fig. 13), whose eventual coalescence leads to the development of microcracks. The cavities are all intergranular, crack like or with angular shapes, suggesting surface diffusion or grain boundary sliding as growth mechanisms.

Fig. 14 shows the fracture surface of a sample crept at 40 MPa. The fracture origin is clearly defined (Fig.14-b), but several microcracks have grown independently on this plane. The final fracture involves extensive microcrack coalescence. The latter is

illustrated in Fig. 12-b. As two microcracks grow towards one another but on different planes, additional small microcracks are nucleated in the field of stress concentration between them. All of these grow perpendicular to the applied stress axis. However, as the two main microcracks approach one another, the region between them undergoes local bending and the local stress axis rotates. Crack growth in this regime is associated with large crack opening displacements, as shown in Fig. 15.

Crack propagation is by cavity linkage in the vicinity of the crack tip. However, the number and size of the cavities is much greater than in the intermediate stress regime. There appears to be almost a cavity cloud at the crack tip (Fig. 16). This accounts for the large crack tip opening displacements, and is further evidence of the extensive ductility and damage resistance of the material.

4. DISCUSSION

In this section we discuss the various processes which control failure in the three regimes we have identified. The slow crack growth regime has not been extensively studied here, and only a few remarks are warranted. However, the lower stress regimes which involve failure through a process of widely distributed damage accumulation will be discussed in greater detail.

4.1 Slow crack growth regime

In this regime, a single microcrack is able to propagate sufficiently rapidly to avoid the creep relaxation processes which occur at lower stresses. Crack propagation is so rapid that very few, if any, additional microcracks are observed, other than the one which causes the failure. Thus failure in this regime is crack growth controlled. Since the cracks grow from preexisting flaws which vary widely in both type and size, the large scatter in lifetimes is not unexpected.

The transition stress between this and the microcrack regime is essentially independent of temperature, at about 17/180 MPa (steady state stress). This is seen by comparing the present results for AVCO alumina with those of Dalgleish et al.[10], also on AVCO alumina (although of a slightly different vintage). The transition stress is the same for both, despite the higher temperature range used(1200-1300°C). A similar transition stress is found in the ARCO alumina. The transition stress is determined almost exclusively by that required to cause early fracture by slow crack growth. As noted earlier, this process is extremely stress sensitive ($t_f \sim \sigma^{-m}$, with m greater than 40). It is also relatively temperature insensitive. Thus even though the position of the stress rupture curve for the microcrack regime does change with temperature, the transition stress does not.

The very high stress sensitivity of the failure time in this regime suggests a competition between crack growth and stress relaxation processes. Crack growth in an unrelaxed solid is controlled by the elastic stress intensity factor K_I. Models for this process[11] predict a power-law relationship of the form

$$\dot{a} \sim K_I^{\alpha/2} D^{1-\alpha/2}$$

where D is the size of the damage zone ahead of the crack. The exponent α depends on the damage mechanism involved in the crack growth process; however, it is always in the range from 1 to 3. As relaxation occurs around the crack however, the crack tip stress fields and thus crack growth, are no longer controlled by K_I. Instead, a different parameter such as C^*, the creep analogue to the J-integral, must be used. Models for creep crack growth in this regime[11] lead to crack growth relationships of the form

$$\dot{a} \sim (C^*)^{\beta/(n+1)}$$

where β is usually between 1 and 3 and n is the creep exponent. The time to failure in either of these two regimes can be estimated by integrating the crack growth rate equations over the range of expected crack length (i.e. from nucleation to the onset of fast fracture). In either case, a modest stress dependence is predicted, in contradiction to the experimental results. The most likely reason for this is that crack growth is occurring during the period in which the stress field relaxes from linear elastic to C^*. The time required for this has been estimated by Riedel[12] for a stationary crack. It is

$$t_1 \approx \frac{K_I^2(1-\nu^2)}{(n+1)EC^*}$$

where E is the elastic modulus and ν is Poisson's ratio. An estimate of this time for the current study gives values of the order of 5-30 min. However, the transition from the slow crack growth regime to microcracking occurs after several hours[5]. The explanation for this apparent discrepancy lies in the effect of crack propagation on crack tip stress fields. Finite element simulations of creep crack propagation[13] indicate that crack tip stress relaxation is impeded by propagation, while Hui and Riedel[14] have shown that the severity of the crack tip singularity is increased by crack propagation. Indeed, for $n<3$, as is the case here, they show that the elastic stress field dominates at the crack tip of a growing crack. Thus a fully relaxed stress field can only be expected for a stationary crack, or one which is highly constrained and grows very slowly. This is the case for cracks growing in flexure at intermediate stresses. The transition from slow crack growth of a dominant crack therefore represents the onset of stress relaxation as the rate of crack propagation decreases.

4.2 Microcrack regime

There are a number of significant differences in the behaviour of the two aluminas studied. Both have a fine equiaxed grain structure with very similar grain size. However, ARCO alumina has the greater density and severity of flaws (large grained regions in particular). We might therefore expect that the low temperature strength of this material will be lower than that of the AVCO alumina. On the other hand, the creep resistance of the ARCO material is considerably greater[5]. This is attributable to differences in chemical composition (see Table I), and is consistent with swelling data for the same materials[7,8]. An extensive study of creep in alumina[3,4] indicates that grain boundary sliding accommodated by grain boundary diffusion is the dominant mechanism over a wide range of conditions (1.4 to 310 MPa and 1200 to 1550°C). Grain boundary diffusion is also thought to be rate controlling in the swelling experiments[8].

The microcracking behaviour also differs substantially between the two materials. However, the reasons for this are less obvious. The AVCO material develops a uniform distribution of shear bands and profuse cavitation on, and for a substantial distance below, the tensile face of the flexure bars. Dalgleish et al.[9,10], found similar results, including the development of shear bands and failure following strains of between 10-20%. The stress range used by Dalgleish et al. was the same (170-100 MPa) as ours. However, the temperatures (1200-1300°C) and strain rates ($10^{-5}s^{-1}$) were higher. Thus, it appears that the microcrack growth failure regime extends over a wide range of temperature and deformation rate in this material.

The ARCO alumina also develops microcracks at intermediate stresses, but they grow much less readily than in AVCO alumina. In flexure, samples did not fail even after 18% strain on the tensile face. This high ductility occurs despite the presence of large flaws which help to nucleate microcracks. In part, this is due to crack blunting and bifurcation (see Fig.3-b). In tension, ARCO alumina does fail after moderate strains. Extensive microcracking is observed, both internally and surface nucleated, throughout the

gauge length of each specimen. Microcrack linkage involves a similar process to that observed in the AVCO flexure specimens. This suggests that the apparent ductility of ARCO alumina is due to load shedding around microcracks and stress concentrations. Indeed, polished internal sections from flexure specimens indicate that damage extends only a short distance below the tensile surface.

The development of "shear bands" is much less evident in the ARCO tensile specimens than in the AVCO flexure bars. This mode of crack propagation and linkage is peculiar to the bend geometry, and probably accounts for the much greater times to failure in flexure than in tension. That is, the development of extensive zones of damage in shear bands are an effective load shedding mechanism which is not available in tension.

In summary, we conclude that while there are differences in the ductility of the two materials studied, their fracture behaviour in the microcrack regime is broadly similar and involves the same set of sequential processes - namely, the nucleation and growth of microcracks from microstructural flaws, followed by linkage and failure. The propagation of microcracks can be described using models developed for the growth of isolated cracks under steady state creep, such as those by Wilkinson and Vitek[11], at least until the microcracks approach one another and begin to interact. The microcrack linkage process is complex. However, this is only likely to control the lifetime in a constrained geometry such as flexure. The creep lives in this regime obey the Monkman-Grant equation with a constant of 0.09. This suggests that the propagation of the microcracks is controlled by creep deformation.

4.3. Creep Fracture Regime

At stresses between 82 and 55 MPa, in tension, ARCO alumina undergoes a second transition. This is readily apparent from the creep rupture and failure strain data[5]. There is also a detectable

difference in the damage accumulation process. Below the transition, relatively little microcracking is evident. Cracks which do develop grow slowly and are blunt (Fig. 15). Crack growth is accompanied by broad damage zones at the crack tip (Fig. 16). This type of behaviour is similar to that found in metallic alloys which undergo superplastic deformation[15]. Moreover, the large failure strains and a stress exponent close to 2 are all consistent with superplasticity.

The transition in time to failure at 55 MPa is not associated with any change in creep deformation mechanism. In addition, Monkman-Grant behaviour is observed both above and below the transition. There is simply an increase in the Monkman-Grant constant or failure strain. This is associated with an increase in damage tolerance.

The observed cavitation and microcracking morphology give some indication of changes to the mechanism of damage growth with decreasing stress. In the microcrack growth regime, cavities are predominantly flat, i.e. crack-like, even in the vicinity of crack tips. They lie on grain boundary facets, normal to the stress axis, and quite often occupy an entire facet. As the stress is lowered, cavities become angular or blocky in shape. This suggests that cavities grow initially by surface diffusion until they occupy a full grain facet. At this point their rate of growth slows down and further growth requires grain boundary sliding (leading to an angular shape). This is apparently possible only at the higher strains achieved in the lower stress regime.

As noted earlier, the creep deformation mechanism in Al_2O_3 is thought to involve extensive grain boundary sliding[3,4]. However, sliding is not in itself a self-sufficient deformation mechanism. It must either be accommodated by deformation (diffusion or dislocation motion) or else by cavity formation at triple junctions. Heuer et al.[4] refer to this latter process as non-accommodated grain boundary sliding. In the absence of cavitation, it is the accommodation mechanism which controls creep kinetics[16].

However, even when void formation does occur, unless it occurs uniformly at most triple junctions, most sliding is accommodated by deformation. In the current study, it is apparent that cavitation is inhomogeneously distributed throughout the material.

The accommodation of grain boundary sliding is most difficult at regions of locally abnormal grain size, since this requires diffusional accommodation over a larger distance. Thus cavities form preferentially on these grains (Fig.5), which act as nucleation sites for microcracks. As the stress is lowered diffusional accommodation becomes possible at isolated large grains and only large grain clusters are able to nucleate microcracks. Thus the density of microcracks decreases with stress. The extreme example of this behaviour is found in experiments on AVCO alumina tested in flexure at 1350°C[17], unpublished research]. After 7% outer fibre strain no microcracks, and no cavity larger than a single grain boundary facet (about 1 μm) was found. The large grains play no role at this temperature.

Mechanistic models for intergranular cavitation usually assume that an array of voids sits on a large, flat grain boundary, oriented normally to the stress axis. This is in contrast with fine grained materials in which the grain size is comparable to the cavity spacing. For cavities growing by surface diffusion, the grain size limits the maximum cavity length[18]. Once the cavity covers a full grain facet, further growth requires the development of negative surfaces curvatures which are only tenable for low values of the $D_s\delta_s/D_b\delta_b$ ratio and/or high stress. For alumina, in the temperature range of concern here, this ratio is close to 1. This explains why we rarely see isolated cavities longer than a single grain facet (Figs.6 and 13).

It is possible to estimate the time required for cavities to grow to full facet size based on current models[19]. This is done in Appendix I. Since there is considerable uncertainty in the value of the surface diffusivity in alumina, we have obtained an upper bound on the time by using the lowest reasonable value for the diffusion

coefficient. We find nevertheless that cavities grow rather quickly by this mechanism, and reach facet size in less than 0.2 of the measured life (Fig. 17). In addition, the predicted stress dependence of this time is stronger ($t_f \sim \sigma^{-3}$), than that for the measured time to failure. Thus, we conclude that surface diffusion controls the initial growth of isolated cavities up to full facet size. However, this process does not control the lifetime, in either the microcrack or creep fracture regimes.

Creep life appears therefore to be limited by the rate of crack propagation, in both regimes. The increased ductility observed at low stress is due to the increased resistance to cavity linkage at crack tips which slows crack propagation. This is evident from Fig. 16, showing the large number of blunted cavities ahead of a growing crack. In contrast with the intermediate stress regime, crack advance appears to occur only after the development of a zone of intense damage near the crack tip. The development of widespread damage throughout the material prior to crack propagation appears to be important to this process, as it enables cavities to blunt rapidly by grain boundary sliding as the crack tip approaches. On a continuum level, this process has been modelled by treating the region ahead of the crack as having a failure strain ϵ_f^*, not necessarily equal to the macroscopic failure strain ϵ_f, at which the ligament at the crack tip fails[20]. The rate of crack propagation due to this process is

$$\dot{a} = \frac{\dot{\epsilon}_o}{\epsilon_f^*} \left[\frac{C^*}{I_n \sigma_o \dot{\epsilon}_o}\right]^{\frac{1}{(n+1)}} D^{\frac{n}{(n+1)}}$$

where ϵ_o, σ_o and n are material parameters, D is the size of the damage zone, and I_n is a dimensionless constant. Thus, as the ductility of the crack tip ligaments increase crack growth slows down.

Finally, the possible effect of preexisting cavities in the crack path on crack propagation needs to be addressed. This could result

in increased crack velocity[21]. However, the effect in this case is likely to be modest. In particular, there is very little evidence of tertiary creep in this material. Thus, creep damage does not affect the creep behaviour.

5. SUMMARY

1. The micromechanisms of creep fracture of 2 commercial hot-pressed aluminas have been examined in the range of 40 to 200 MPa. Three failure regimes have been identified.

2. At the highest stress, fracture occurs by the growth of a single dominant crack, which is nucleated at a processing flaw. The stress required to produce this mode of failure is insensitive to temperature.

3. Below a critical stress (about 175/180 MPa), a stationary stress field is able to develop at microcracks which enable them to grow more slowly. Failure in this regime involves the growth and linkage of multiple microcracks at chemical inhomogeneities and large grained regions. The crack density and morphology depends on both test geometry and the material. In bending extensive coalescence of microcracks on different planes takes place through a shear band type process. This substantially increases the failure time with respect to tensile testing, thus raising serious questions about the validity of such tests for lifetime assessment, even in simple materials.

4. At the lower stresses, damage accumulation is dominated by isolated cavities growing by a combination of surface diffusion and grain boundary sliding. The eventual development of microcracks occurs at large grains and grain clusters in the structure. These cracks grow through a material containing a high density of cavities which however blunt by sliding as the crack approaches. The material becomes very damage tolerant, and can be thought of as superplastic.

5. Isolated cavities grow quickly by surface diffusion to the limiting size of a grain facet at low and intermediate stresses. However, the propagation of cracks in a creeping solid controls the final fracture process. Consequently, failure is strain controlled at both the intermediate and low stress regimes, in correlation with the observed Monkman-Grant behaviour. The Monkman-Grant strain is different in the two regimes.

6. Failure is flaw related in all regimes. These should therefore be carefully controlled in materials intended for high temperature applications.

ACKNOWLEDGEMENTS

We wish to acknowledge the financial support of the Natural Sciences and Engineering Research Council of Canada. In addition, partial support in the form of a fellowship to one of us (C.H.C.) from the Consejo de Investigaciones de la República Argentina is gratefully acknowledged.

REFERENCES

1-B.J. Dalgleish, S.M. Johnson and A.G. Evans, "High-Temperature Failure of Polycrystalline Alumina: I, Crack nucleation", J. Am. Ceram. Soc., **67**, 741-750 (1984).

2-A.G. Evans, "Structural Reliability: A Processing Dependant Phenomenon", J. Am. Ceram. Soc. **65**, 127-137 (1982).

3-R.M. Cannon, W.H. Rhodes and A.H. Heuer," Plastic Deformation of Fine Grained Alumina (Al_2O_3):I, Interface Controlled Diffusional Creep".J.Amer.Ceram.Soc. 63, 46-53 (1980).

4-A.H. Heuer, N.J. Tighe and R.M. Cannon," Plastic Deformation of Fine Grained Alumina(Al_2O_3):II, Basal Slip and Non Accommodated Grain Boundary Sliding", J.Amer.Ceram.Soc. 63, 53-58 (1980).

5-D.S. Wilkinson, A.G. Robertson and C.H. Cáceres, "Damage Mechanisms During High Temperature Creep in Hot-Pressed Alumina", to be published (1990).

6-A.G. Robertson,"Swelling and Creep Damage Accumulation in Hot-Pressed Alumina", Ph.D. thesis, McMaster University (1989).

7-A.G. Robertson and D.S. Wilkinson, "Swelling in Hot- Pressed Aluminas: I. Theory", to be published, (1989).

8-A.G. Robertson and D.S. Wilkinson,"Swelling in Hot- Pressed Aluminas: II. Experimental", to be published, (1989).

9-B.J. Dalgleish and A.G. Evans, "Influence of Shear Bands on Creep Rupture in Ceramics", J. Am. Ceram. Soc., **68**, 44-48 (1985).

10-B.J. Dalgleish, E.B. Slamovich and A.G. Evans, "Duality in the Creep Rupture of a Polycrystalline Alumina", J. Am. Ceram. Soc., **68**, 575-581 (1985).

11-D.S. Wilkinson and V. Vitek, "The Propagation of Cracks by Cavitation: A General Theory", Acta Metall., 30, 1723-1732 (1982).

12-H. Riedel, in "Fracture at High Temperatures", p.308, Springer Verlag, 1986.

13-S.B. Biner and D.S. Wilkinson, "Creep Crack Growth Simulation under Transient Stress Fields", Met.Trans.A, 19, 829-835 (1988).

14-C.Y. Hui and H. Riedel,"The Asymptotic Stress and Strain Field Near the Tip of a Growing Crak Under Creep Conditions", Intl.J.Fracture, 17, 409-425 (1981).

15-C.H. Caceres and D.S. Wilkinson, "Large Strain Behaviour of a Superplastic Copper Alloy-II: Cavitation and Fracture", Acta metall., 32, 423-434 (1984).

16- R. Raj and M.F. Ashby, "On Grain Boundary Sliding and Diffusional Creep", Met. Trans.A, 2, 1113-1127 (1972).

17-A.G. Robertson and D.S. Wilkinson, unpublished research (1988).

18-A.G. Evans and W. Blumenthal, "High Temperature Failure in Ceramics", in Fracture Mechanics of Ceramics, pp.423-448, Vol.6, ed.R.C.Bradt, A.G.Evans, D.P.H.Hasselman and F.F.Lange, Plenum Press, 1983.

19-A.C.F. Cocks and M.F. Ashby,"On Creep Fracture by Void Growth", Prog.Mater.Sci., 27, 190-244 (1982).

20- G. A. Webster, "Crack Growth at High Temperatures", in Engineering Appraoches to High Temperature Design (eds. B. Wilshire and D. R. J. Owen, Pineridge Press, 1983), 1-55.

21-A.C.F. Cocks and M.F. Ashby, "The Growth of a Dominant Crack in a Creeping Material", Scripta Metall. 16, 109-114 (1982).

FIGURE CAPTIONS

Fig. 1: Transmission electron micrograph of the as-received microstructure for the a) AVCO and b) ARCO materials.

Fig. 2: Typical failure origins at high stress - a) an internal processing flaw (ARCO, tested at 1250°C, 200 MPa steady-state stress); b) a large grain size region (ARCO, 1250°C, 185 MPa); c) another large grain size region (AVCO, 1100°C, 200 MPa); and d) an amorphous surface deposit (AVCO, 1150°C, 200 MPa). 100 μm bars.

Fig. 3: The origins of microcracks include a) chemical deposits (ARCO, 1250°C, 140 MPa, flexure); b) chemical deposits leading to crack bifurcation (ARCO, 1250°C, 140 MPa, flexure); c) isolated large grains (ARCO, 1200°C, 125 MPa, flexure); and d) clustered large grains (ARCO 1250°C, 170 MPa, flexure). 10μm bars.

Fig. 4: Extensive microcracking is visible at intermediate stresses on the side of a tensile specimen of ARCO deformed at 100 MPa and 1250°C.

Fig. 5: Internal crack in a tensile specimen nucleated at a large grain in ARCO at 1250°C and 55 MPa.

Fig. 6: High magnification view of creep damage in an internal section of a tensile sample fractured of ARCO at 82 MPa and 1250°C a) near a microcrack; and b) typical general cavitation damage.

Fig. 7: The fracture surface of a tensile specimen of ARCO tested at 82 MPa and 1250°C.

Fig. 8: Microcracking at intermediate stresses on a) the tensile surface of a bend bar, and b) on an internal section, showing the same morphology of damage. AVCO, 100 MPa, 1150°C. Stress axis is vertical.

Fig. 9: Extensive microcracking on tensile surface of a bend bar of AVCO at 1150°C, at a higher stress (170 MPa) than in Fig. 7. Stress axis is vertical.

Fig. 10: Cavitation and microcracking on an internal section of a bend bar of AVCO,tested at 100 MPa and 1150°C. Tensile face is on the left, with the stress axis vertical.

Fig. 11: Microcrack coalescence through shear band formation is a major form of crack propagation at intermediate stresses on the tensile surface of a bend bar. Stress axis is vertical. AVCO, 100 MPa, 1150°C.

Fig. 12: Microcracking at low stresses a) on the side of a tensile specimen; and b) an enlarged view showing the coalescence process. Tensile axis is vertical. ARCO, 40MPa, 1250°C.

Fig. 13: General cavitation damage and the generation of a microcrack by cavity coalescence, in a tensile specimen of ARCO deformed at 40 MPa and 1250°C. Tensile axis is vertical.

Fig. 14: The a) fracture surface and b) the origin of the microcrak on a tensile specimen of ARCO tested at 40 MPa and 1250°C.

Fig. 15: Microcracking at low stresses on an internal section of a tensile sample tested at 55MPa. Note the large crack opening displacement and the blunting of the crack tip. Tensile axis is vertical. ARCO, 1250°C.

Fig. 16: The tip of a crack and its damage zone in an internal section of a tensile sample of ARCO alumina. 40MPa, 1250°C.

Fig. 17: The experimentally determined time to fracture as a function of applied stress for ARCO alumina in tension, as compared to predicted failure times by cavitation under surface diffusion control (Solid line, Equation A-2).

APPENDIX I. The growth of cavities by surface diffusion

Surface diffusion controls cavity growth when surface diffusion is slower than boundary diffusion. This results in flat, crack-like cavities. Assuming the extreme case of $D_s\delta_s << D_b\delta_b$, the void rate of growth can be expressed as[A1]:

$$\frac{dr}{dt} = \frac{2}{\pi}\frac{D_s\delta_s\omega}{T\gamma_s^2(1-f_b)^3}\sigma^3 \qquad (A\text{-}1)$$

where the material parameters are defined, along with appropriate values, in Appendix II. This mechanism gives an essentially constant rate of growth. Thus, the final size of cavities growing by this mechanism up to the time of fracture can be readily estimated. Calculations were performed for two stress levels - 100MPa (for which t_f = 19.5h), and 40MPa (for which t_f = 249h). Using the smallest reasonable value for surface diffusivity ($D_s\delta_s$ = 4 $10^{-25}m^3/s$) we find that the cavity radius at the time of fracture would be 4.5 μm at 100 MPa and 3.6 μm at 40 MPa. These values are actually larger than the observed cavity sizes (compare with figs.6 and 12). This difference is related to the limit imposed by the grain size on cavity growth. The same type of calculations for grain boundary diffusion and plastic growth of cavities yielded very small cavity sizes at the time of fracture.

By integrating eq. (A-1), the time to fracture for cavities growing by surface diffusion can be estimated [A1]:

$$t_f = t_n + \sqrt{2}(1-2f_i)\frac{kTl\gamma_s^2}{D_s\delta_s\omega}\sigma^{-3} \qquad (A\text{-}2)$$

where t_n is the nucleation time (assumed to be zero). We have used this equation to determine the time for cavities to grow by surface diffusion across a single grain boundary facet. We have therefore assumed that the cavity spacing l is 6μm, which corresponds to a situation of cavities 1.5μm long (i.e the facet length), separated by a distance 4 times their length to give a volume fraction at fracture of 25%). We have again used the lower diffusion coefficient in order to provide an upper bound on the time of cavity growth. The results are plotted in Fig.17. They show clearly that the time required for facet sized cavities to develop is considerable less than the measured life, even using the most favourable diffusion coeficient possible.

APPENDIX II. Material parameters

The following values of the material parameters for ARCO alumina are used in the calculations of Appendix I:

T=1523K, test temperature.
d=1.5μm, grain size.
γ=1J/m^2, surface tension.
l, centre to centre cavity spacing,(=6μm in equation A-2).
ω= 2.12 10^{-29} m^3, atomic volume (assuming Al-control).
$r_o=2\gamma/\sigma$, initial void size.
f_i, initial volume fraction (~0 in equation A-2).

Surface diffusion coefficients are of the form

$$D_s\delta_s = D_s^o\delta_s \exp(-Q_s/RT)$$

Several measurements are available for surface diffusivity, as follows:

TABLE A-I: Surface Diffusion Data for Al_2O_3 at 1250°C

Q_s (kJ/mol)	$D_s^o\delta_s$ (m^3/s)	$D_s\delta_s$ (m^3/s)	Reference
650	7.5 10^{-3}	4 10^{-25}	A2
418	8.6 10^{-10}	4 10^{-24}	A3
547	6.0 10^{-6}	1 10^{-24}	A4

In the calculations we have used the data which gives the lowest diffusion coefficient, so as to obtain an upper bound on the rate of cavity growth.

REFERENCES

A1-A.C.F. Cocks and M.F. Ashby,"On Creep Fracture by Void Growth", Prog.Mater.Sci., 27, 190-244 (1982).

A2-A.G. Robertson and D.S. Wilkinson,"Swelling in Hot- Pressed Aluminas: II. Experimental", to be published, (1989).

A3-R.M. Cannon, W.H. Rhodes and A.H. Heuer,"Plastic Deformation of Fine Grained alumina (Al_2O_3):I, Interface Controlled Diffusional Creep".J.Amer.Ceram.Soc. 63, 46-53 (1980).

A4-J.M. Dynys, R.L. Coble, W.S. Coblenz and R.M. Cannon, "Mechanisms of Atom Transport During Initial Stage Sintering of Al_2O_3", pp. 391-404, in Sintering Processes, Edited by G.C. Kuczynski, Mater. Sci. Res. V13, Plenum, New York, 1980.

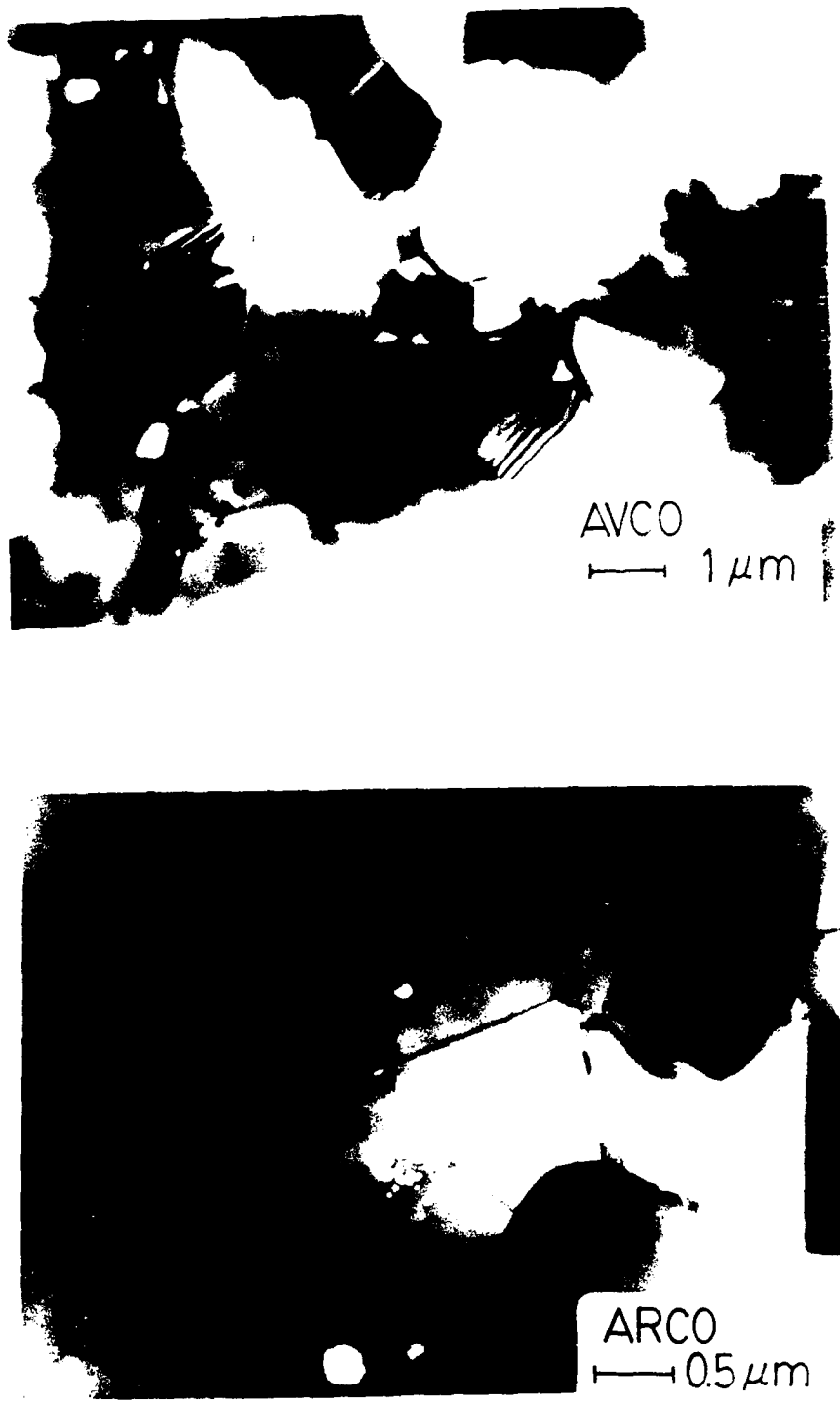

Fig. 1: Transmission electron micrograph of the as-received microstructure for the a) AVCO and b) ARCO materials.

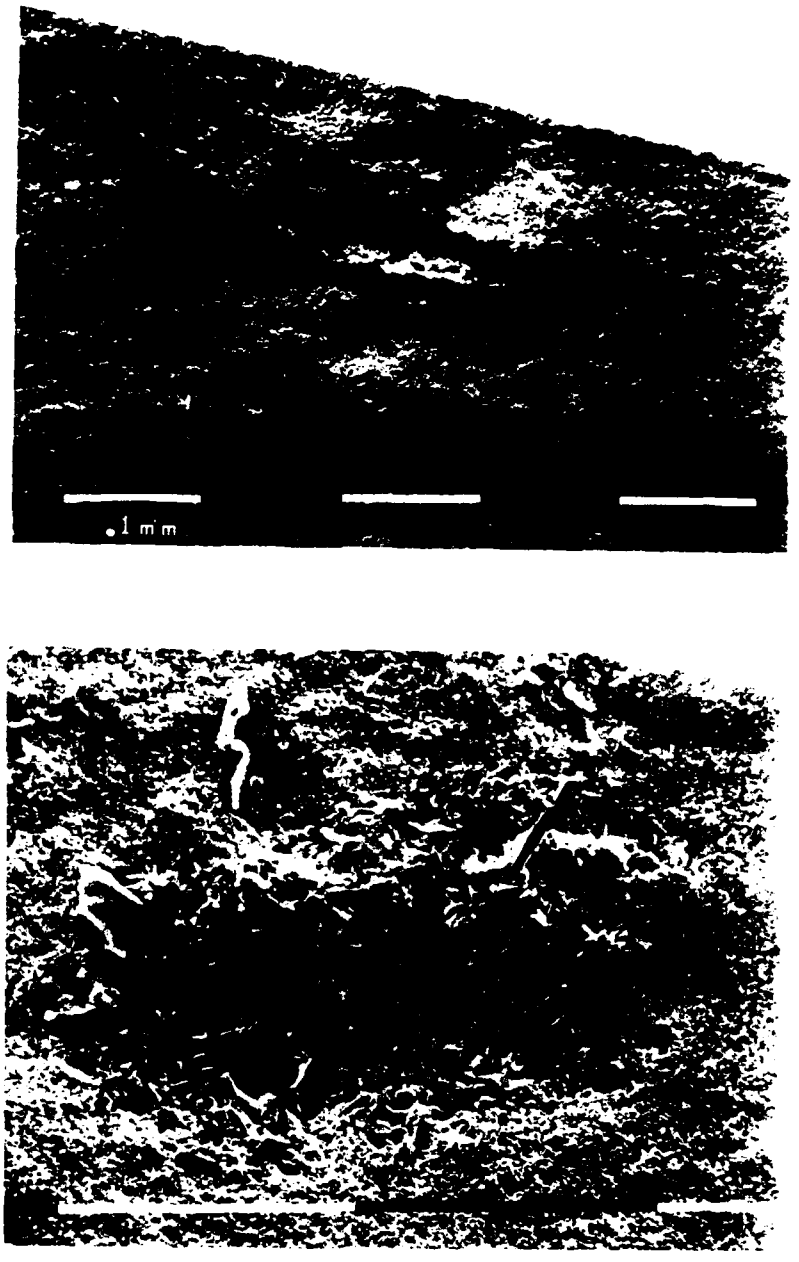

Fig. 2: Typical failure origins at high stress - a) an internal processing flaw (ARCO, tested at 1250°C, 200 MPa steady-state stress); b) a large grain size region (ARCO, 1250°C, 185 MPa).

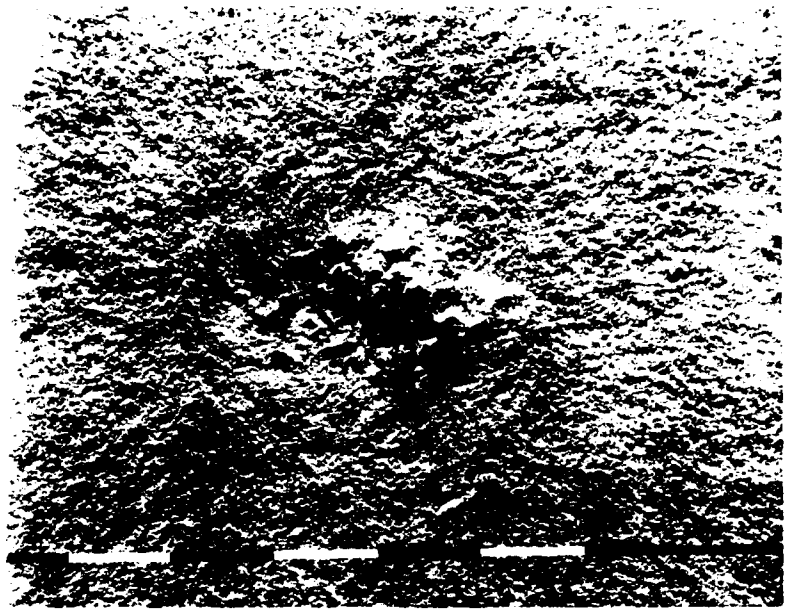

Fig. 2: c) another large grain size region (AVCO, 1100°C, 200 MPa); and d) an amorphous surface deposit (AVCO, 1150°C, 200 MPa).

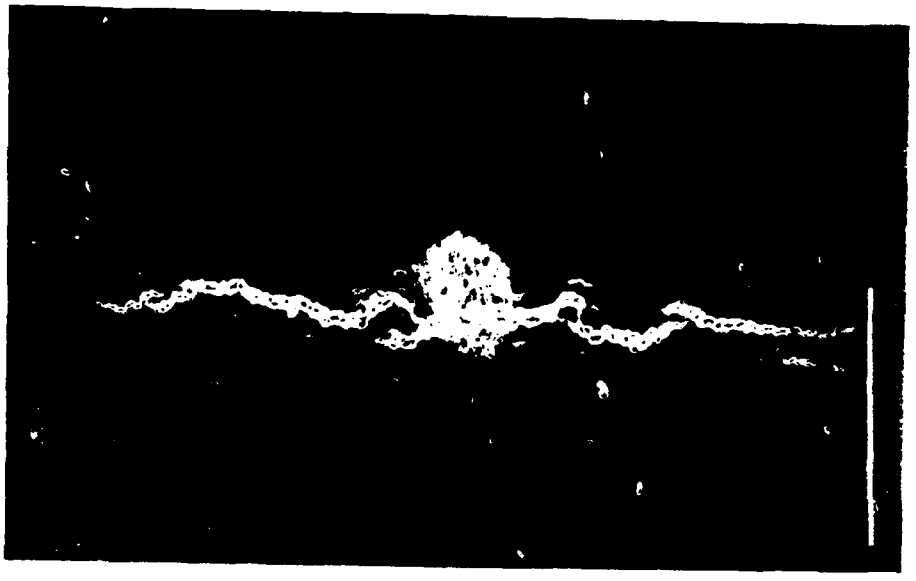

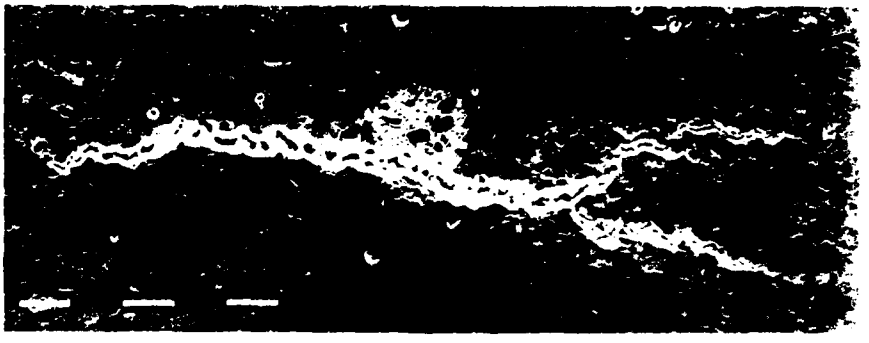

Fig. 3: The origins of microcracks include a) chemical deposits (ARCO, 1250°C, 140 MPa, flexure); b) chemical deposits leading to crack bifurcation (ARCO, 1250°C, 140 MPa, flexure).

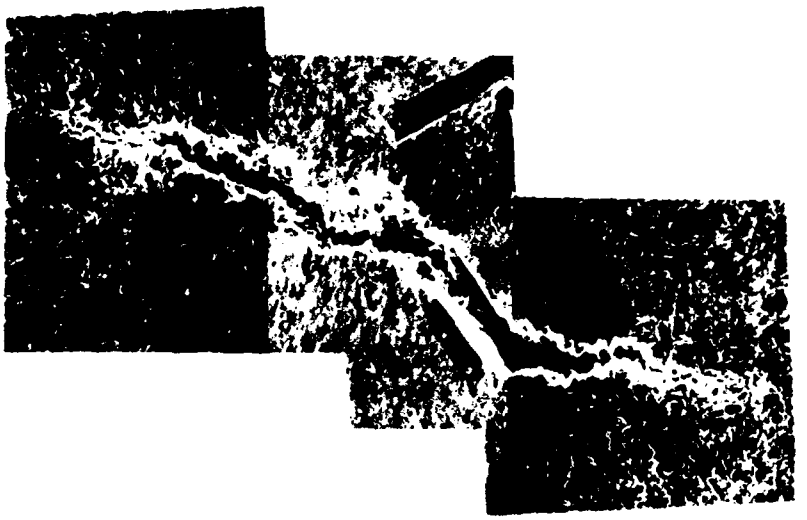

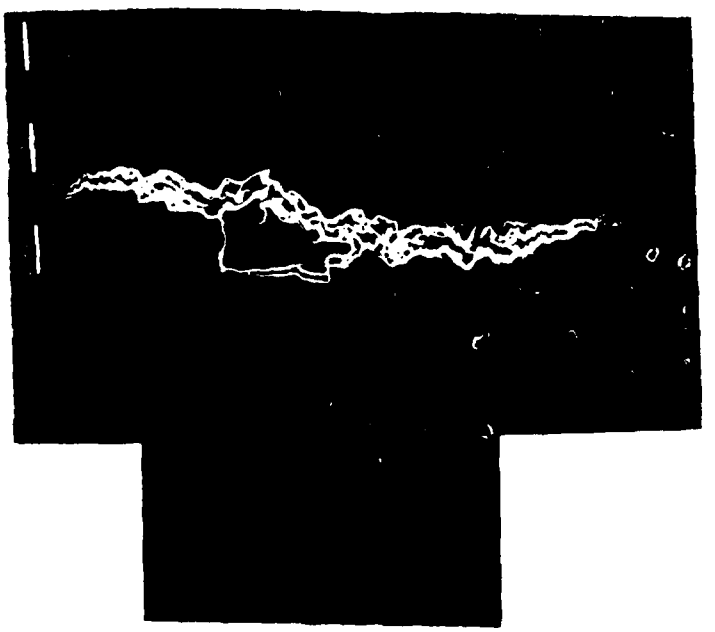

Fig. 3: c) isolated large grains (ARCO, 1200°C, 125 MPa, flexure); and d) clustered large grains (ARCO 1250°C, 170 MPa, flexure; 10μm bars)

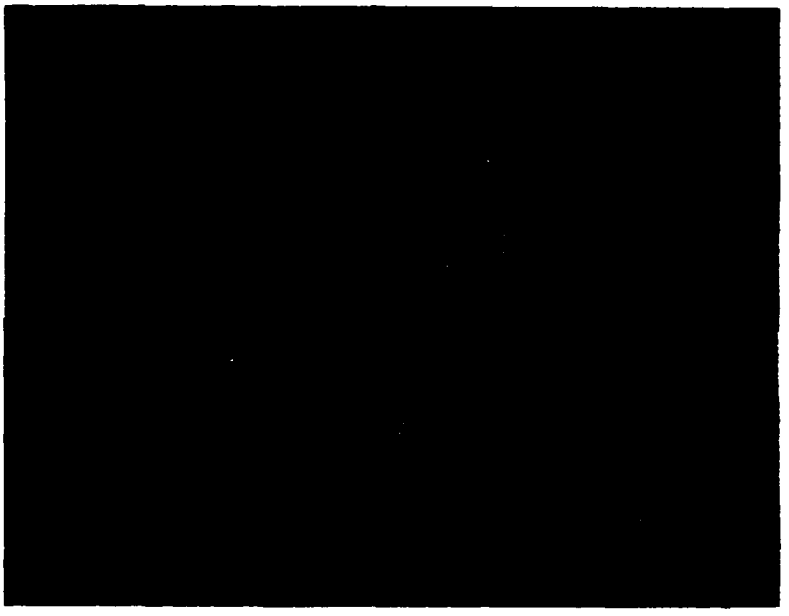

Fig. 4: Extensive microcracking is visible at intermediate stresses on the side of a tensile specimen of ARCO deformed at 100 MPa and 1250°C.

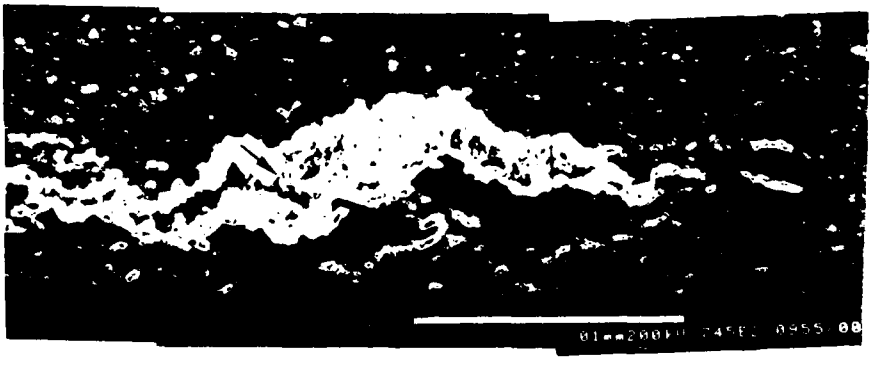

Fig. 5: Internal crack in a tensile specimen nucleated at a large grain in ARCO at 1250°C and 55 MPa.

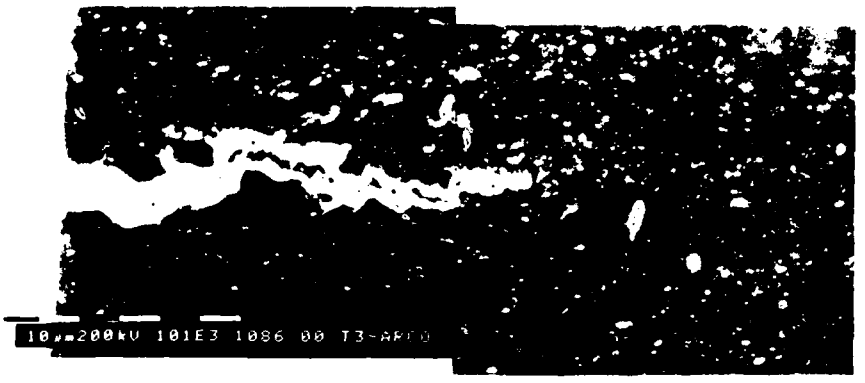

Fig. 6: High magnification view of creep damage in an internal section of a tensile sample fractured of ARCO at 82 MPa and 1250°C a) near a microcrack; and b) typical general cavitation damage.

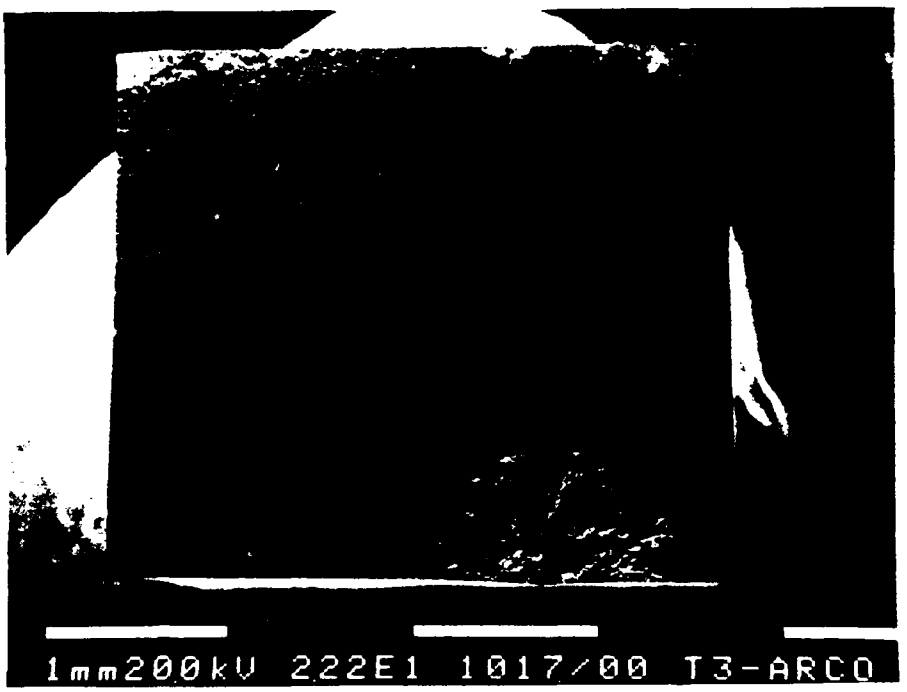

Fig. 7: The fracture surface of a tensile specimen of ARCO tested at 82 MPa and 1250°C.

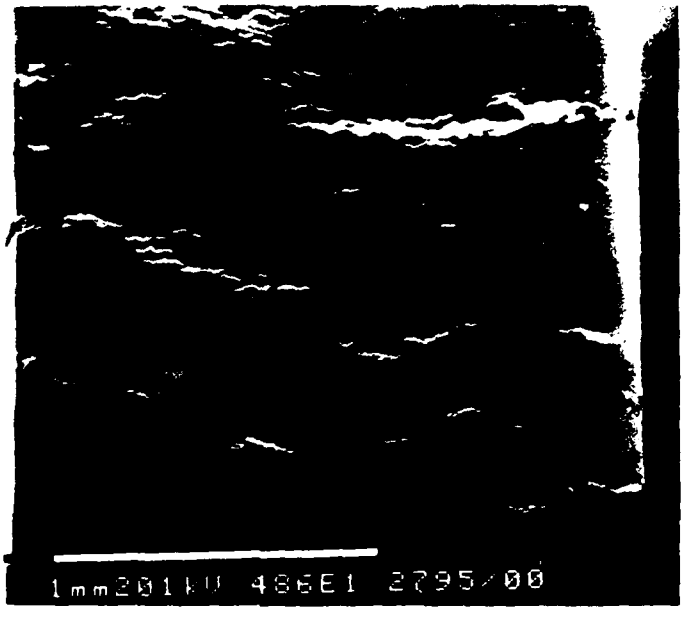

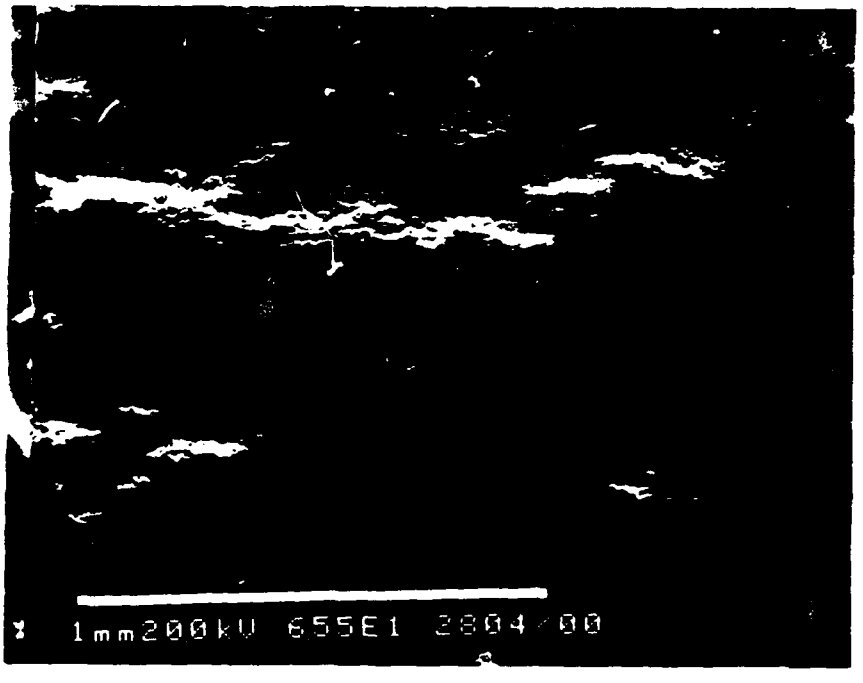

Fig. 8: Microcracking at intermediate stresses on a) the tensile surface of a bend bar, and b) on an internal section, showing the same morphology of damage. AVCO, 100 MPa, 1150°C. Stress axis is vertical.

Fig. 9: Extensive microcracking on tensile surface of a bend bar of AVCO at 1150°C, at a higher stress (170 MPa) than in Fig. 7. Stress axis is vertical.

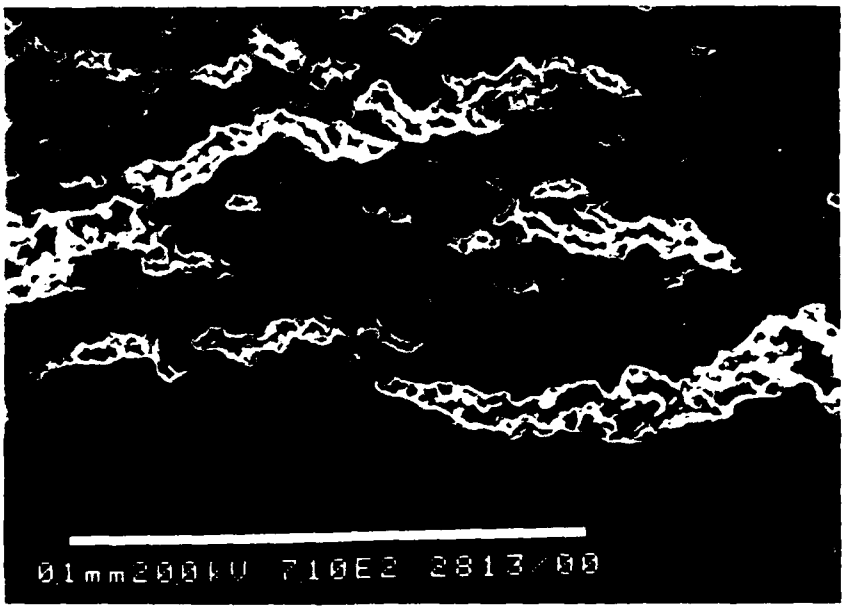

Fig. 10: Cavitation and microcracking on an internal section of a bend bar of AVCO,tested at 100 MPa and 1150°C. Tensile face is on the left, with the stress axis vertical.

Fig. 11: Microcrack coalescence through shear band formation is a major form of crack propagation at intermediate stresses on the tensile surface of a bend bar. Stress axis is vertical. AVCO, 100 MPa, 1150°C.

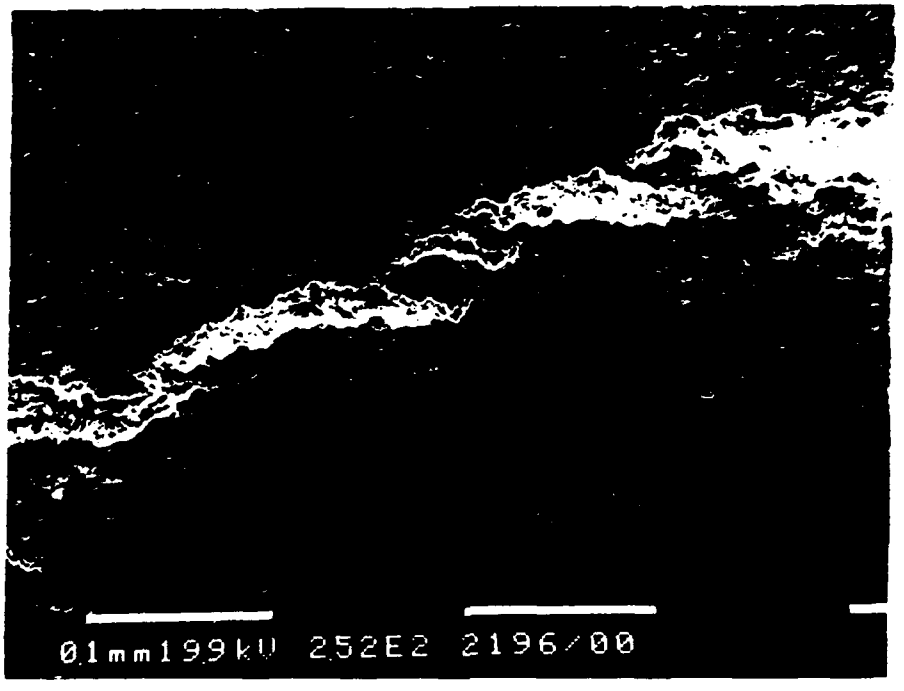

Fig. 12: Microcracking at low stresses a) on the side of a tensile specimen; and b) an enlarged view showing the coalescence process. Tensile axis is vertical. ARCO, 40MPa, 1250°C.

Fig. 13: General cavitation damage and the generation of a microcrack by cavity coalescence, in a tensile specimen of ARCO deformed at 40 MPa and 1250°C. Tensile axis is vertical.

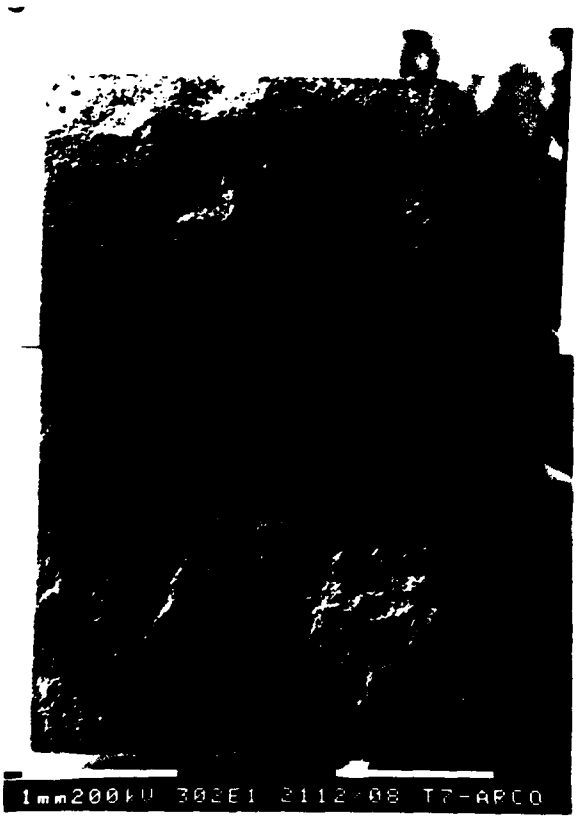

Fig. 14: The a) fracture surface and b) the origin of the microcrak on a tensile specimen of ARCO tested at 40 MPa and 1250°C.

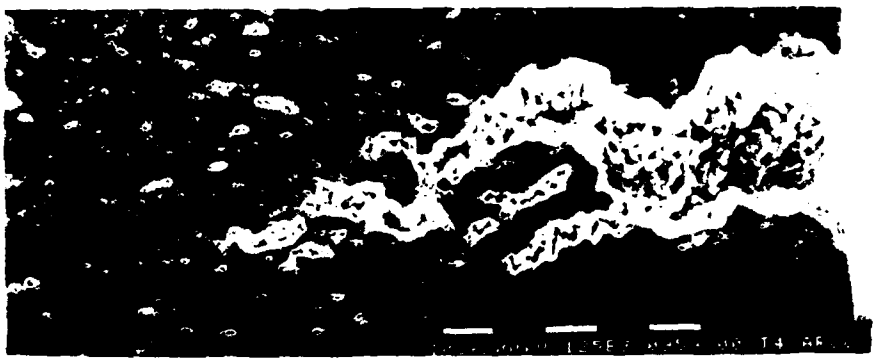

Fig. 15: Microcracking at low stresses on an internal section of a tensile sample tested at 55MPa. Note the large crack opening displacement and the blunting of the crack tip. Tensile axis is vertical. ARCO, 1250°C.

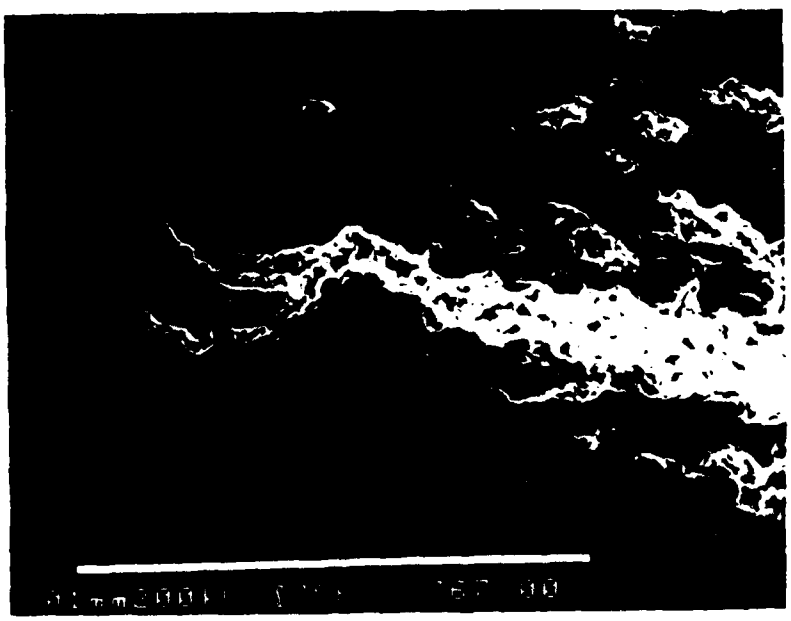

Fig. 16: The tip of a crack and its damage zone in an internal section of a tensile sample of ARCO alumina. 40MPa, 1250°C.

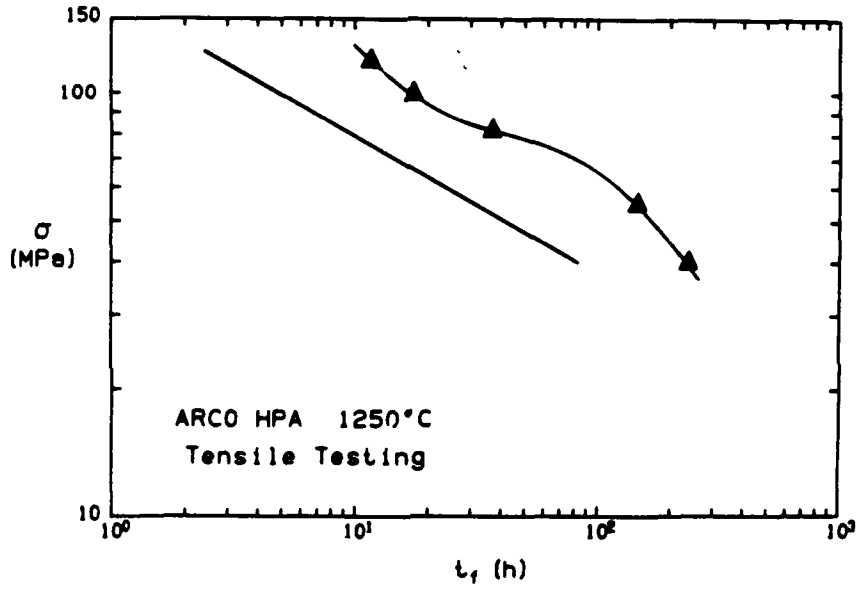

Fig. 17: The experimentally determined time to fracture as a function of applied stress for ARCO alumina in tension, as compared to predicted failure times by cavitation under surface diffusion control (Solid line, Equation A-2).

STUDY OF THE FRACTURE PROCESS IN MORTAR WITH LASER HOLOGRAPHIC MEASUREMENTS

by A. Castro-Montero[1], R. A. Miller[2] and S. P. Shah[3]

ABSTRACT

Center notched plate mortar specimens were loaded in tension. A multiple sensitivity vector holographic setup was developed to record several deformation stages during the stable crack propagation range. The three sensitivity vector setup enabled the calculation of both crack opening displacements and strain fields around the crack trajectories. An image analysis system was used to isolate the interferometric effect from the sandwich holograms resulting in fringe patterns with perfect contrast. Image analysis was also used as a faster, more accurate and more consistent method for fringe count.

After evaluation of the holograms, the existence of tensile forces transmitted through the crack faces was associated to the presence of tensile strain behind the crack tip. Existing cohesive crack models were evaluated base on experimental crack profile measurements. A crack length dependent cohesive crack model with a bilinear closing pressure was proposed. A definition of the fracture process zone (FPZ) is proposed based on the difference between experimentally observed and linear elastic fracture mechanics (LEFM) strain fields.

INTRODUCTION

The fracture of concrete is characterized by formation and propagation of fracture process zone. Several phenomena have been associated with fracture process zone including microcracking around the crack tip, localization and strain softening and crack bridging (often also termed aggregate interlock). A key to a better understanding of fracture mechanics of concrete is the accurate observation of fracture process zone on a microscopic s' 'e.

1 Graduate Research Assistant, Department of Civil Engineering, Northwestern University, Evanston, Illinois 60208
2 Assistant Professor of Civil and Environmental Engineering, University of Cincinnati, Cincinnati, Ohio 45221.
3 Professor of Civil Engineering and Director of the National Science Foundation Center for Advanced Cement Based Materials, Northwestern University, Evanston, Illinois 60208

This paper will examine the cohesive crack model which proposes that fracture in concrete can be modeled using linear elastic fracture mechanics (LEFM) and applying a closing pressure to the crack faces. Using experimentally measured crack opening displacements, four closing pressures proposed in literature were tested as were the basic underlying assumptions of the cohesive crack model.

In the technique described in this paper, three simultaneous holograms were taken by illuminating the specimen from three different directions. In addition, digital image analysis techniques were developed to accurately evaluate wide field in plane deformation. The results of the strain field calculation obtained using this newly developed technique for mortar center notched plate specimens are discussed in this paper.

HOLOGRAPHIC INTERFEROMETRY TEST

Each interference pattern represents the component of the displacements onto the sensitivity vector k (Abramson, 1981). In order to obtain a two dimensional displacement field (in plane and out of plane), in principle, two interferograms are required. However, since there is no sign associated to the fringe counts a third interferogram is necessary. These requirements are discussed in more detail by Castro-Montero, Shah and Miller[1]. Figure 1 is a schematic view of the optical set-up with three illumination directions (R,L and C) used for this study.

For each load step a different hologram is recorded from each illumination direction (holograms R,L and C).

FRINGE COUNT

The holographic interferograms were acquired into an image analysis system using a slow scan high resolution camera. The image is represented by a 512x512 2-d array of integers, each corresponding to the average light intensity across an element area referred to as pixel (Picture Element). The size of a pixel determines the spatial resolution.

The bright and dark bands of the holographic fringes can be represented as a binary image. In a binary image the pixel intensities assume only two values, ON (or 1) for perfect white and OFF (or 0) for perfect black.

Figure 2 is the enhanced interferometric image in which the intensity value is zero for dark bands and one for bright bands. Further image processing allows to assign intensity values to each fringe corresponding to the fringe order.

A pixel P is selected on the binary image (Fig. 2). A flooding procedure which assigns an arbitrarily selected intensity value (Y) to all the pixels connected to pixel P is performed. Thus, all the pixels on the band containing P are assigned the intensity value Y. The same procedure is repeated for consecutive bands. The intensity value Y is incremented by one for each band.

Figure 3 shows a fully processed interferogram in which same intensity values correspond to same fringe orders. Note that there is a different intensity level for each half a fringe (i.e., different intensity for dark and bright bands). The fringe count between any two points can now be easily obtained by computing half the difference of the corresponding intensity levels (e.g., fringe count between A and B in Fig. 3 is (90 - 65)/2 = 12.5).

Even though the use of the image analysis system results in very fast fringe counts, speed is not the main advantage of this technique. The isolation of the interferometric effect on the holographic images and the binarization process result in accurate and objective fringe counts. The gradual change in intensity from a dark to a bright band make it very difficult to obtain consistent fringe counts when conventional (by hand) methods are used.

EVALUATION OF HOLOGRAMS

Crack Profiles.

For the computation of the crack opening displacements (COD) the modified Nelson and McCrickerd (Nelson and McCrickerd, 1986, Miller, Shah and Bjelkhagen, 1988) method was used. This method assumes the out of plane motion to be negligible (i.e. COD is the main component of the displacement) and that displacements are small. Since the direction of motion is assumed, one hologram is sufficient. Equation 1 gives the magnitude of the COD in terms the fringe count and the geometry of the optical set-up.

$$COD = \frac{n\lambda}{4 \cos\alpha \cos\psi} \qquad (1)$$

where:

COD = Crack Opening Displacement. Displacement of one point on the crack face with respect to the point across the crack.

n = fringe count from a point on the crack face to the point across the cross the crack.

α = angle between illumination direction and sensitivity vector (**k**)

ψ = angle between direction of motion and sensitivity vector (**k**)

Typical crack profiles are shown in Fig. 4. Miller, Shah and Bjelkhagen[2] showed that short cracks have profiles which are basically the same as LEFM profiles. Longer cracks have profiles which are much thinner than LEFM crack, suggesting that applying a closing pressure to the LEFM profile may provide the correct final profile.

Strain Fields.

Fringe counts relative to the left face of the crack, or the symmetry line for points beyond the crack tip, were taken at every point on a 3 in x 3 in (76 mm x 76 mm) grid (1.5 in on each side of the crack line and 3 in in front of the notch tip) every 1/8 in (3 mm)for all three holographic images (R,L and C). A computer program was used to calculate the displacement of every point relative to the left face of the crack by locating the intersection point of the holodiagrams corresponding to each illumination direction. A third order best fit polynomial was obtained for the displacements along lines perpendicular to the crack line. For the sections crossing the crack a different polynomial was obtained for the left and right side of the crack. The strain field was obtained by differentiation and was evaluated from $x = -1$ in to $x = +1$ in every 1/8 in (3 mm) at every cross section, where x is the distance from the crack line and is positive to the right. Figure 5 shows the strain field (ϵ_{xx}) around the bottom crack for crack lengths of 1.375 in (35 mm), 1.875 in (48 mm) and 2.25 in (57 mm), corresponding to 1324 lb (6.0 KN), 1461 lb (6.6 KN) and 1601 lb (7.2 KN) of applied load. The strain fields shown in Fig. 5 include only the measured additional strain after the initial preload state.

In general, a high strain ($>100\mu\epsilon$) region can be found around and in front of the crack tip with a maximum value of approximately 300 $\mu\epsilon$. Behind the crack tip there is a zone of negative strain which suggests relaxation of tensile strain with respect to the initial preload stage. Also, note that there is a gradual descent of the strain level behind the crack tip as opposed to the sharp drop corresponding to the LEFM solution.

ANALYSIS OF THE CLOSING PRESSURE MODELS WITH $K_I=0$

Cohesive zone models based on the Dugdale-Barrenblatt approach of placing a closing pressure on the faces of a discrete crack could be used to account for the non-linear effects of the fracture process zone (FPZ) and aggregate interlock. Hillerborg, et. al.[3] proposed a cohesive crack model to account for the complex fracture mechanisms in concrete. Figure 6 is a summary of the closing pressure relationships studied. The following four closing pressures were chosen for this study: An exponential closing pressure proposed by Gopalaratanam and Shah[4]; a bilinear curve proposed by Roelfstra and Wittmann[5]; a trilinear closing pressure proposed by Liaw, Jeang, Hawkins and Kobayashi[6]; and a linear relationship proposed by Cedolin, Iori, and DeiPoli[7].

The applied load and the criterion $K_I=0$ were specified and then the necessary crack length was computed as indicated by Castro-Montero, Shah and Miller[8]. This was done applying the experimental load to the FEM mesh and then propagating the crack length 3 mm (1/8 in) at a time.

Many previous studies calibrate the closing pressure vs. w relationship by comparing the theoretically predicted load-displacement relationship vs. the experimental values. Such a comparison for one of the specimens tested during the holographic study is shown in Fig. 7. The holographically measured notch tip opening displacements are compared with those obtained from the finite element analysis and with four different closing pressure vs. w relationships. It is observed that all four closing pressures give essentially the same load vs. NTOD curves. This means that a unique closing pressure vs. w relationship can not be asserted when a discrete displacement measurement is used for calibration. A similar observation was also made when the computed crack length ($K_I=0$) is compared with the holographically measured crack length.

The authors believe that a better evaluation of the different closing pressures results from comparing the experimental crack profiles vs. predicted crack profiles. In order to provide an objective comparison, an error definition was proposed. A positive error means the closing pressure was not large enough to close the LEFM crack profile down to the holographic profile while a negative error means the closing pressure was too strong and closed the LEFM crack profile down too much.

In Fig. 8 it can be seen that there is a substantial difference between the observed and predicted crack profiles regardless of the closing pressure vs. w relationship used.

A CRACK LENGTH DEPENDENT COHESIVE CRACK MODEL

A more objective method of determining closing pressure vs. crack opening relationship is not to assume any a priori shape. This was done using a Green's function type of approach. The necessary closing pressure distribution to match the holographically measured crack profiles was calculated. Three observations are pertinent from this analysis: (1) the closing pressure vs w relationship may not be invariant with respect to crack length, (2) a bilinear curve may be sufficient to approximate the closing pressure vs. w relationship and (3) as noted before, closing pressure vs w relationship appears to be a function of compressive strength.

Based on these observations a bilinear relationship was determined using the crack length dependent model proposed by Cook[9]. It was assumed that for crack lengths shorter than a given length d there is no closing pressure. For longer crack lengths a bilinear function was used. A finite difference Levenberg-Marquardt algorithm was applied to optimize the closing pressure function for each specimen. A proposed bilinear closing pressure, based on the optimization procedure is shown in Fig. 9.

For the proposed bilinear closing pressure there is a good prediction of the crack opening displacements although the crack lengths are over estimated including a segment close to the crack tip with either small or null predicted crack opening.

Jenq and Shah and Cook, et. al. suggested that K_I did not need to be equal to 0. The above bilinear closing pressure was applied and K_I corresponding to the experimentally observed crack length was calculated. When the calculated K_I values include closing pressure, an essentially constant value for the specimens with the same compressive strength

is obtained regardless of crack length. In contrast, when cracks are assumed to be traction free (LEFM) the value of K_I increases with crack length. Thus, it seems that the cohesive type of model can explain the R-curve type of response reported for quasi-brittle materials. Figure 10 shows the relative error plots and typical profiles corresponding to the calculated value of K_I. Note that the predicted profiles match well with the measured ones.

DEFINITION OF FRACTURE PROCESS ZONE

In Fig. 11, the differences in strain fields between the LEFM solution and the experimentally measured values are shown. It is arbitrarily assumed that the differences are significant when they exceed the strain value of 60 $\mu\epsilon$. Positive differences mean that the tensile strain predicted by LEFM was higher while the negative values mean that the LEFM predicted lower tensile strain than the holographically measured values. The zones marked A in Fig. 11 are the regions where the LEFM solution predicts tensile strain values of 60 $\mu\epsilon$ or more higher than those measured holographically. Note that zone A remains essentially constant regardless of crack length. Since this zone is relatively small and does not change with crack length a model based on modified LEFM may be a possible approach. Zones B, with negative values, typically found behind the crack tip show that the relaxation of the observed strain is 60 $\mu\epsilon$ less than that in the elastic solution. Zones B can be defined as the wake of the fracture process zone (WFPZ) and they enclose the area where extensive microcracking has been developed and tensile forces are still transmitted through the crack. Behind this zone, the fracture process approaches a traction free condition.

Figures 12 shows the difference between the predicted response using the bilinear closing pressure and the holographic measurements. Note that there is a good correlation of the results and the zones with significant deviation from the experimental results are practically eliminated.

CONCLUSIONS

a. Sandwich hologram interferometry with multiple sensitivity vectors can be used to measure crack opening displacements and strain fields in mortar specimens under

tensile stress. When holographic interferometry is used to measure Mode I crack opening displacements the effect of out of plane motion should be taken into account.

b. Digital image analysis facility provided a faster, more consistent and more accurate method of fringe count than the manual method.

c. There is a region of high tensile strain that moves with the tip of the propagating crack. The material behind the crack tip experiences strain relaxation. However, the gradual nature of the strain relaxation demonstrates the existence of tensile force transmitted through the crack faces.

d. Zones of nonlinear behavior can be located by computing strain field deviations form the linear elastic solution.

e. A bilinear closing pressure vs. COD cohesive crack model has been proposed to predict both crack profiles and strain field, fully characterizing the material behavior.

ACKNOWLEDGMENTS

Professor Hans Bjelkhegan's advice in the development of the holographic setup is greatly appreciated. The authors thank Mr. John Schmidt for his valuable contributions in the development of the experiments. This study was made possible through the support of the Air Force Office of Scientific Research (AFOSR) (Grant No. 88-C-018P00001) Program Manager Dr. Spencer Wu). Partial support from the National Science Foundation (Grant No. NSF-DMR-8808432 Program Manager: Dr. Lance Haworth) is also appreciated.

REFERENCES

1. Castro-Montero, A., Shah, S.P. and Miller, R.A. "Strain field measurement in fracture process zone," to be published in Engineering Mechanics, ASCE, Nov. 1990.

2. Miller, R.A., Shah, S.P., and Bjelkhagen, H. (1988) "Measurement of crack profiles in mortar using laser holographic interferometry," Experimental Mechanics, Vol 28(4), 388-394.

3. Hillerborg, A., Modeer, M. and Petersson, P. E., "Analysis of a crack formation and growth in concrete by means of fracture mechanics and finite elements," Cement and Concrete Research, Vol. 6, No. 6, pp 773-782, 1977.

4. Gopalaratanam, V. S. and Shah, S. P., "Softening response of plain concrete in direct tension," ACI Journal, Proceedings, Vol. 82, No. 3, pp. 345-356, 1987.

5. Roelfstra, R. E. and Wittmann, F. H., "A numerical method to link strain softening with fracture in concrete," Fracture Toughness and Fracture Energy in Concrete, F. H. Wittmann, ed. Elsevier Science Publishers, B. V., Amsterdam, 1986.

6. Jeang, F. L. and Hawkins, N. M., Nonlinear analysis of concrete fracture, Structures and Mechanics Report, Department of Civil Engineering, University of Washington, Seattle, WA, 1985.

7. Cedolin, L., DeiPoli, S. and Iori, I., "Tensile behavior of concrete," Journal of the Engineering Mechanics Division, ASCE, Vol. 113, No. 3, p. 431, 1987.

8. Miller, R.A., Castro-Montero, A. and Shah, S.P. "Cohesive crack models examined with laser holographic measurements," submitted for publication in the Journal of the American Ceramic Society, 1990.

9. Cook, R.F., Fairbanks, C.J., Lawn, B.R. and Mai, Y-W. (1987) "Crack resistance by interfacial bridging: its role in determining strength characteristics," Journal of Materials Research, Vol. 2(3), 345-356.

FIGURES

Figure 1. Holographic set up with three sensitivity directions.

Figure 2. Typical holographic interferogram after isolation of interferometric effect.

Figure 3. Fully processed interferogram for automatic fringe count.

Figure 4. Typical crack profiles.

Figure 5. Holographic strain fields.

Figure 6. Comparison of closing pressures.

Figure 7. Load vs. Notch Tip Opening Displacement (NTOD).

Figure 8. Crack profile comparison.

Figure 9. Proposed bilinear closing press ·:.

Figure 10. Crack profile comparison for proposed bilinear closing pressure.

Figure 11. Difference between experimental and LEFM strain fields.

Figure 12. Difference between experimental and LEFM with bilinear closing pressure strain fields.

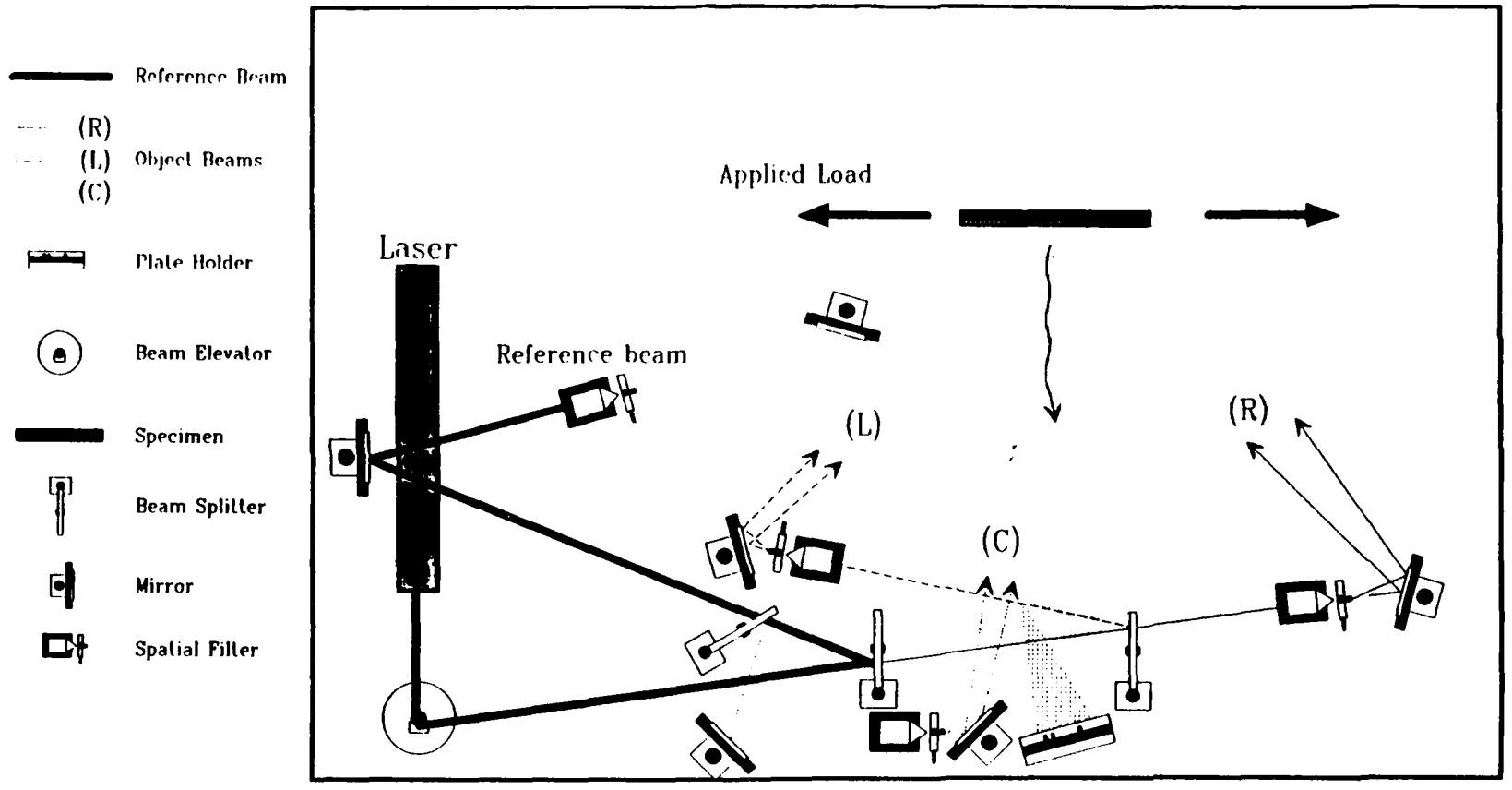

Figure 1. Holographic set up with three sensitivity directions.

Figure 2. Typical holographic interferogram after isolation of interferometric effect.

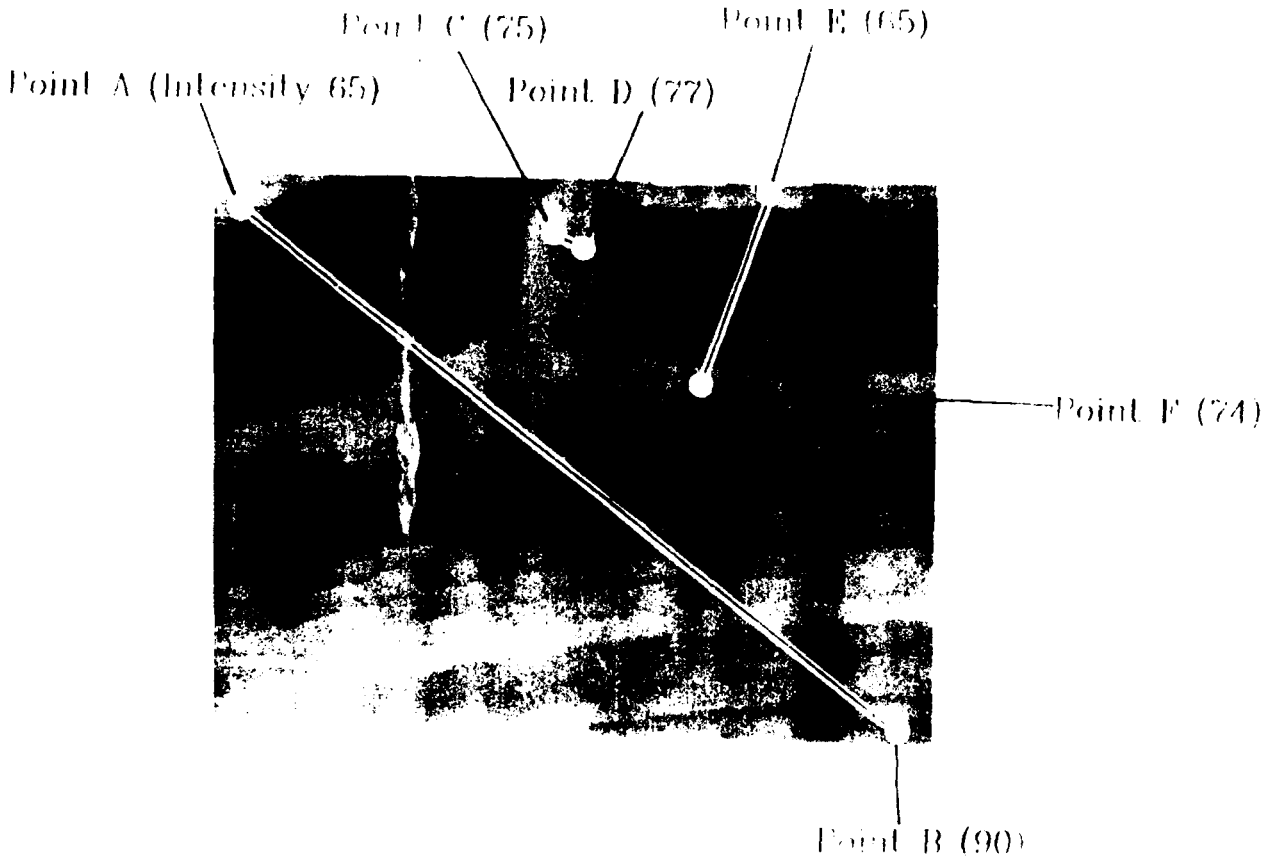

Figure 3. Fully processed interferogram for automatic fringe count.

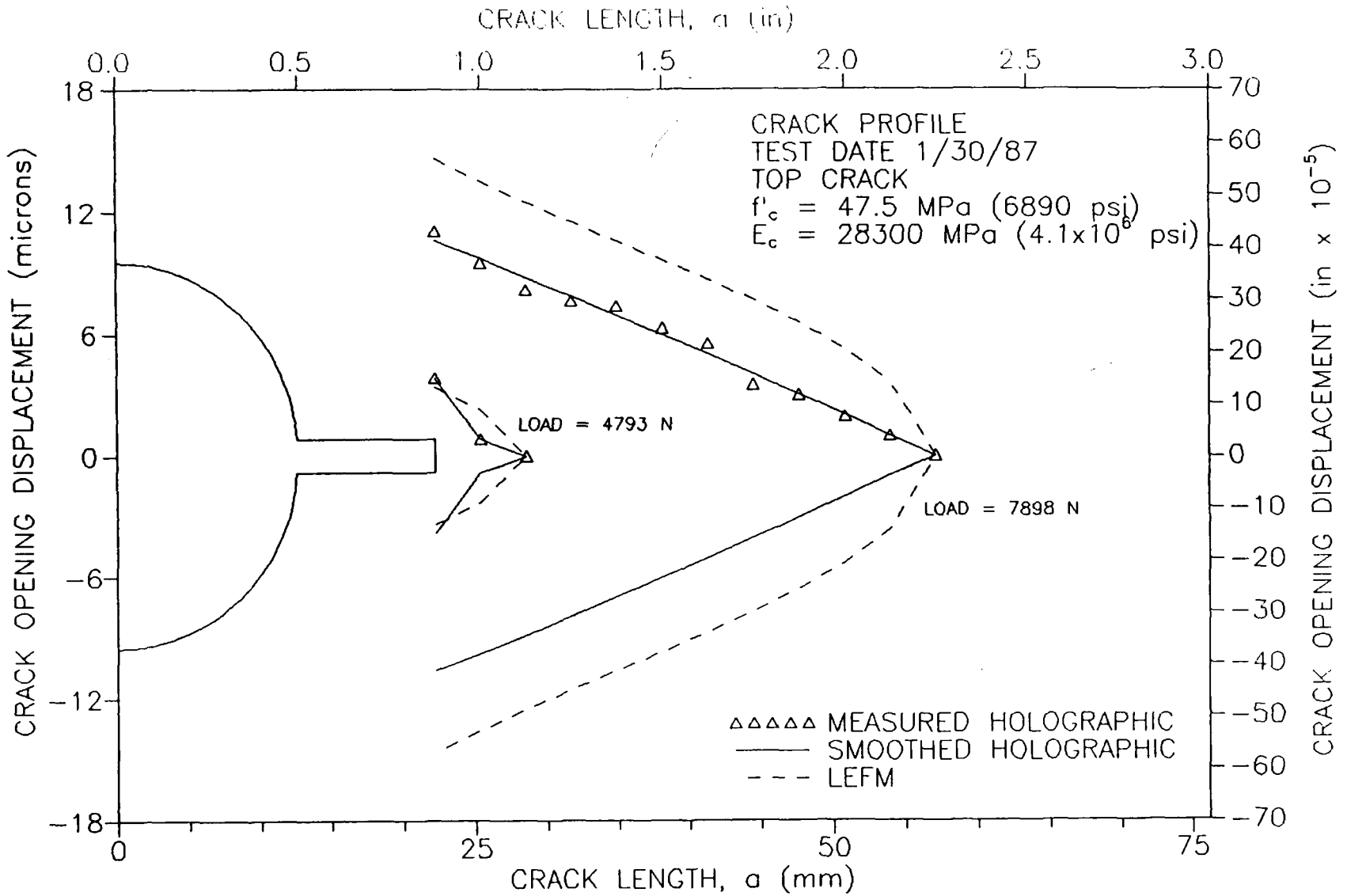

Figure 4. Typical crack profiles.

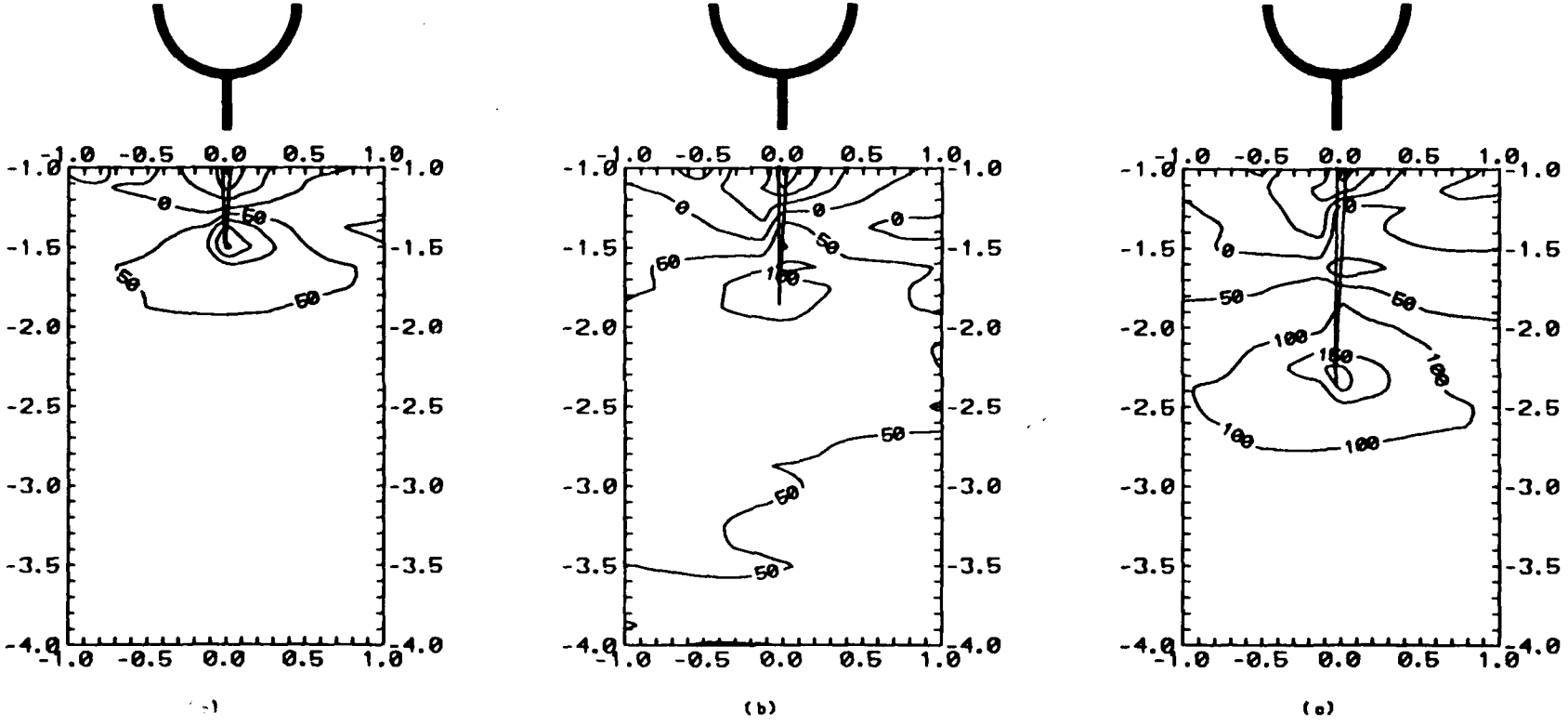

Figure 5. Holographic strain fields.

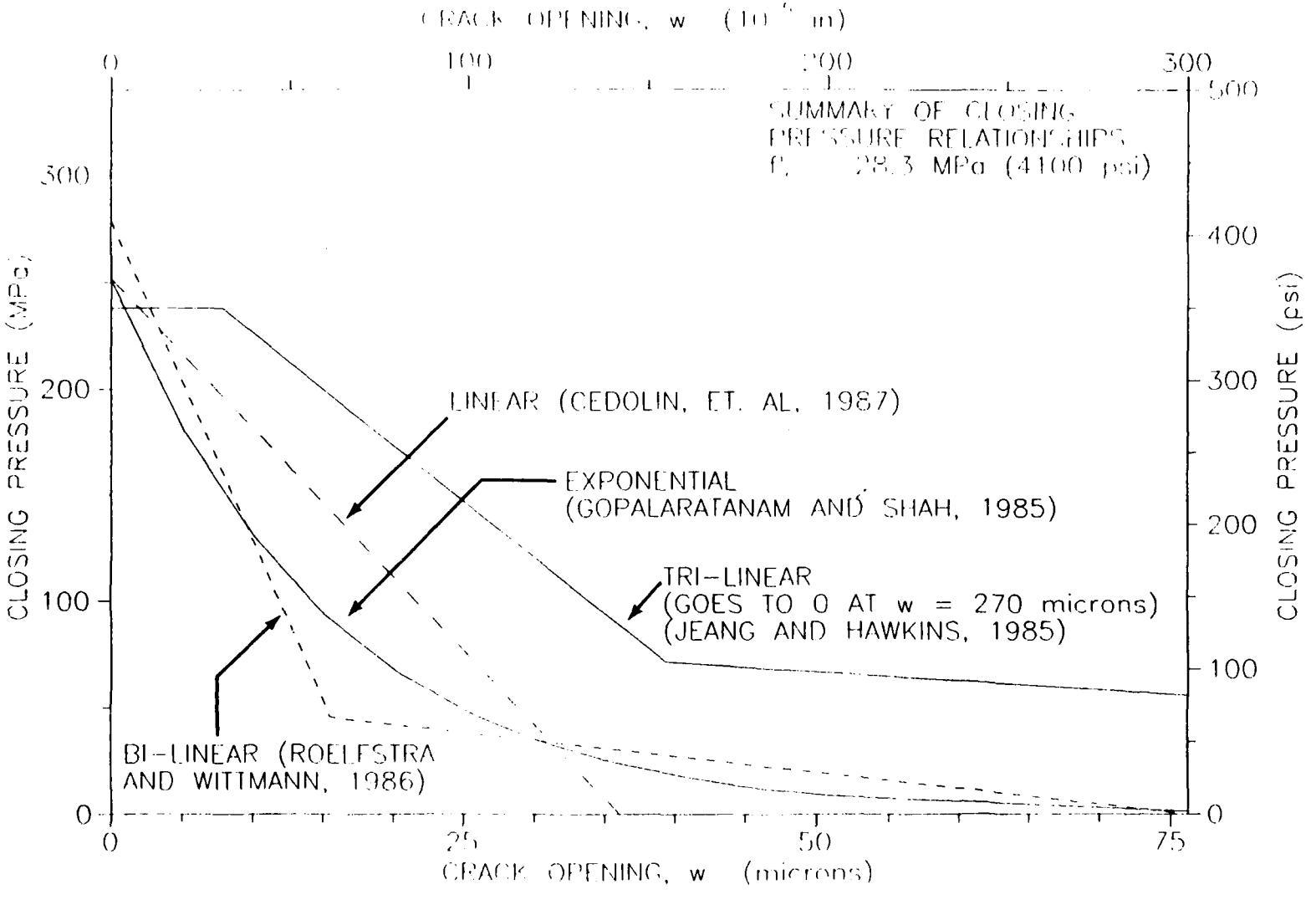

Figure 6. Comparison of closing pressures.

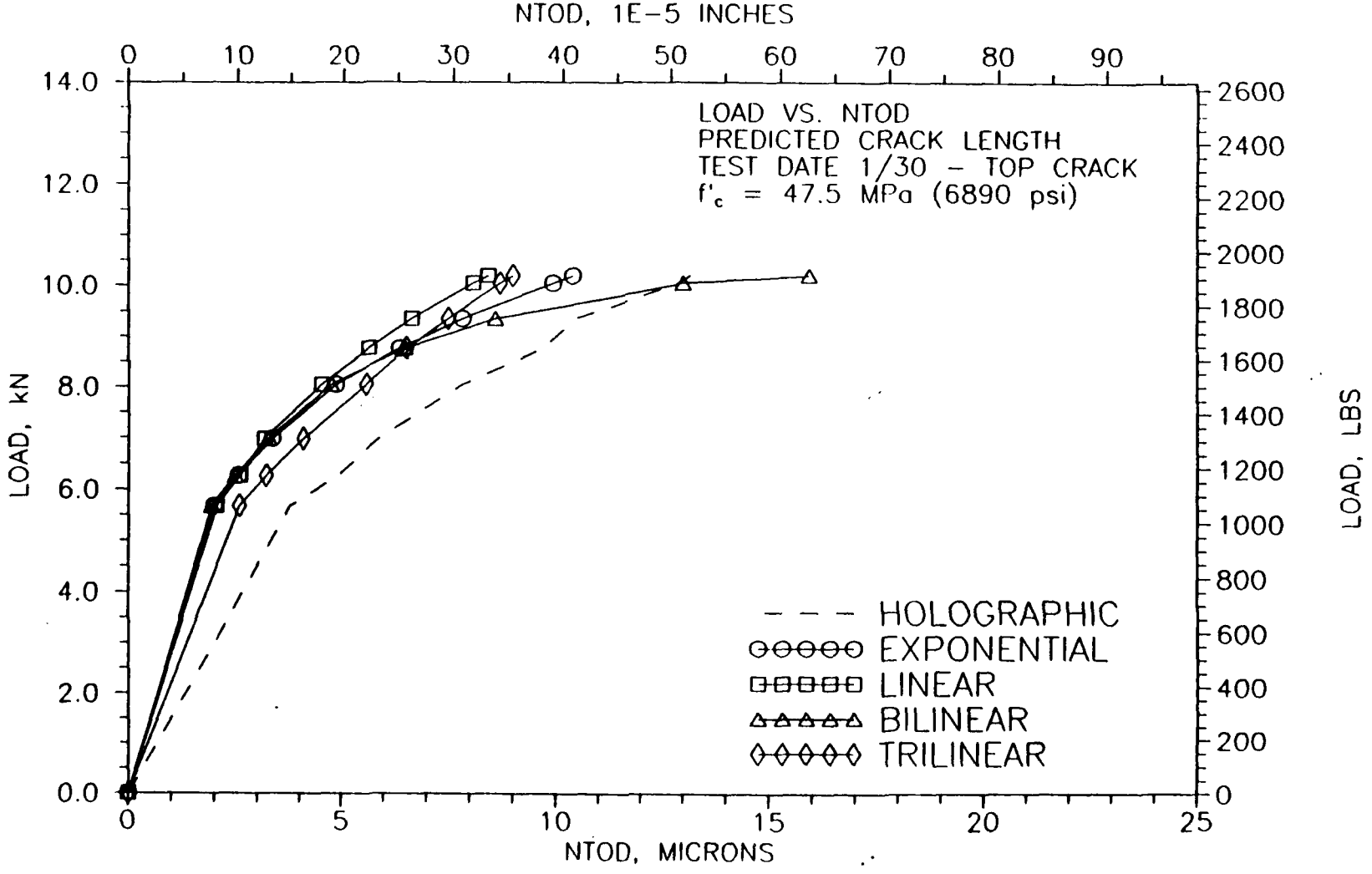

Figure 7. Load vs. Notch Tip Opnening Displacement (NTOD).

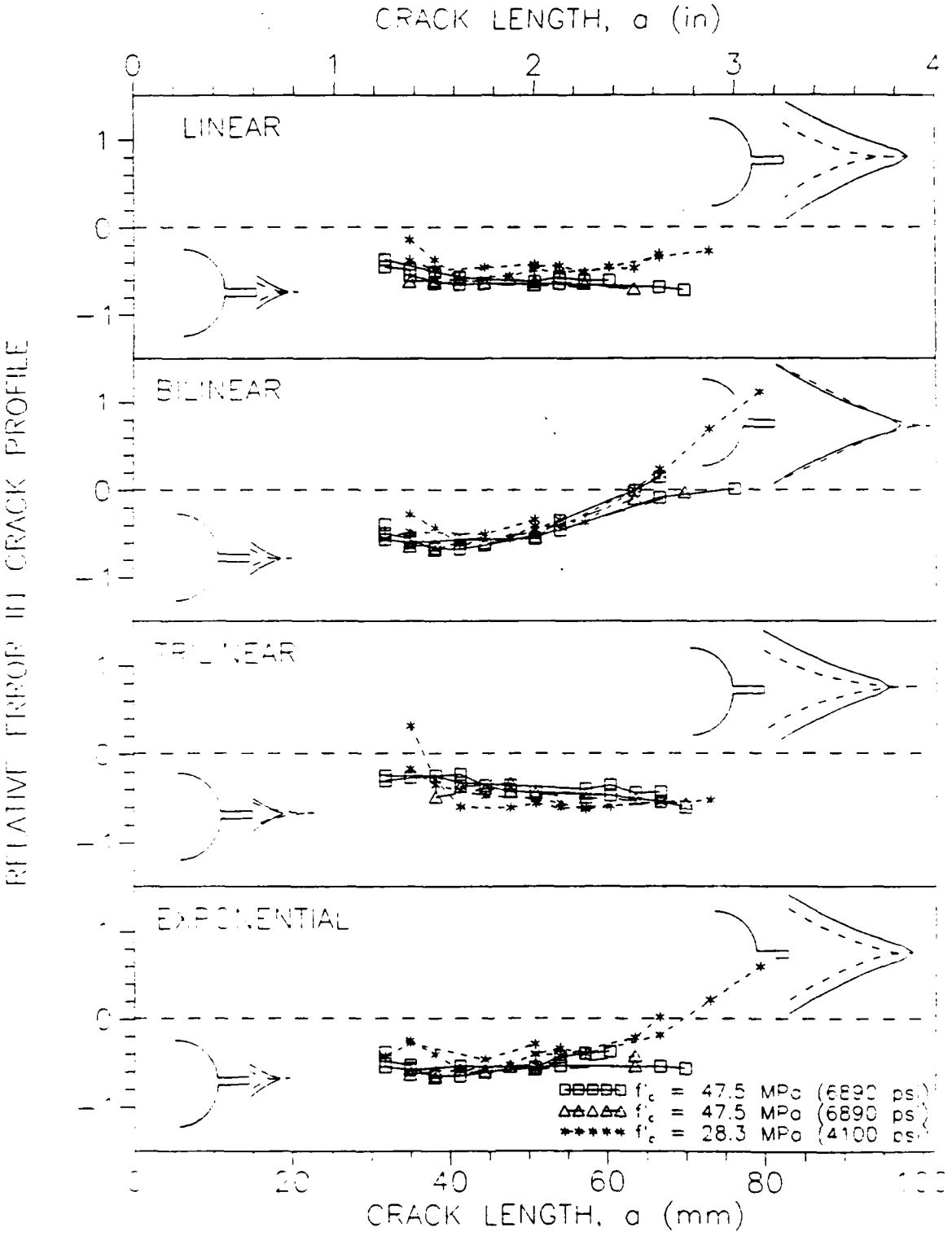

Figure 8. Crack profile comparison.

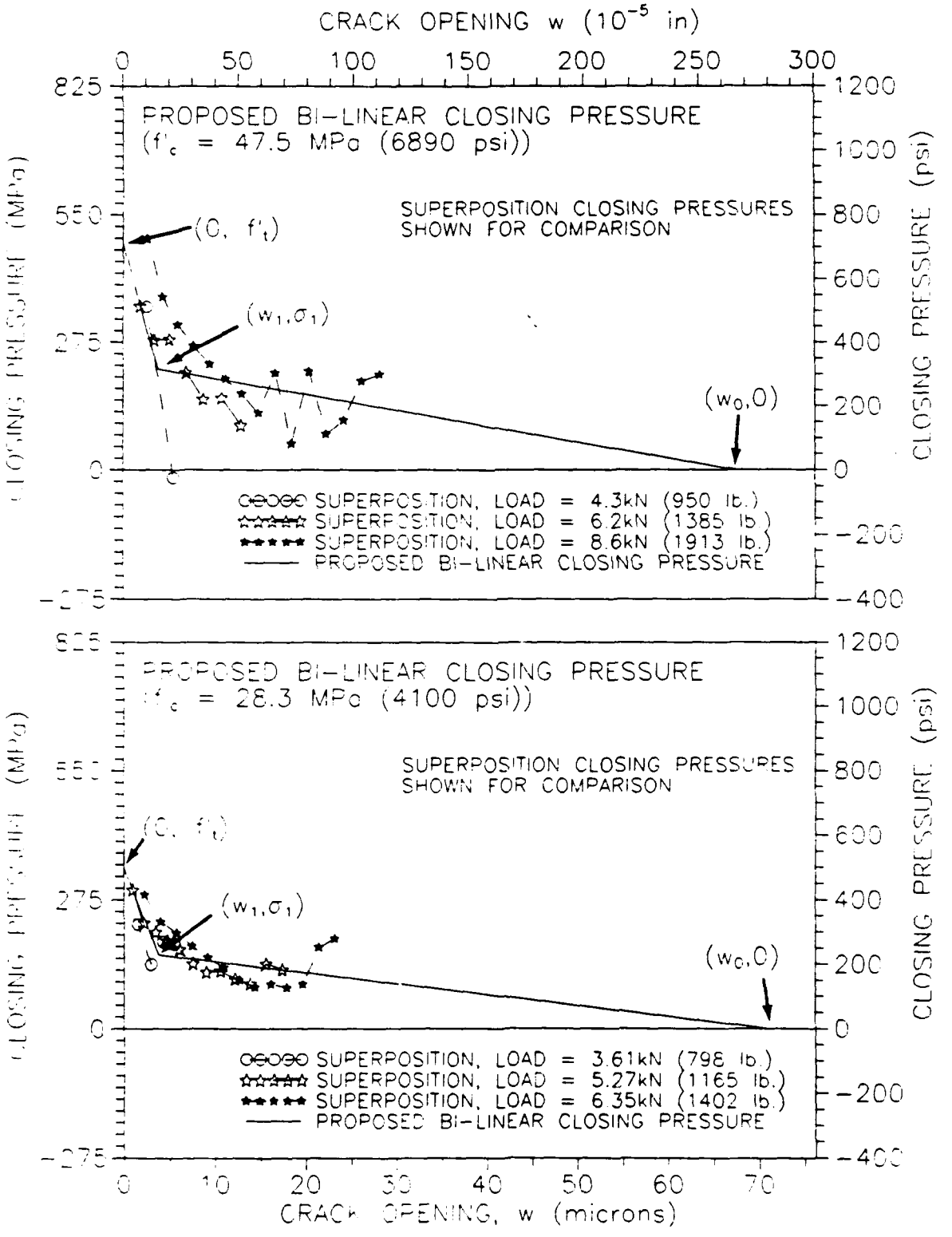

Figure 9. Proposed bilinear closing pressure.

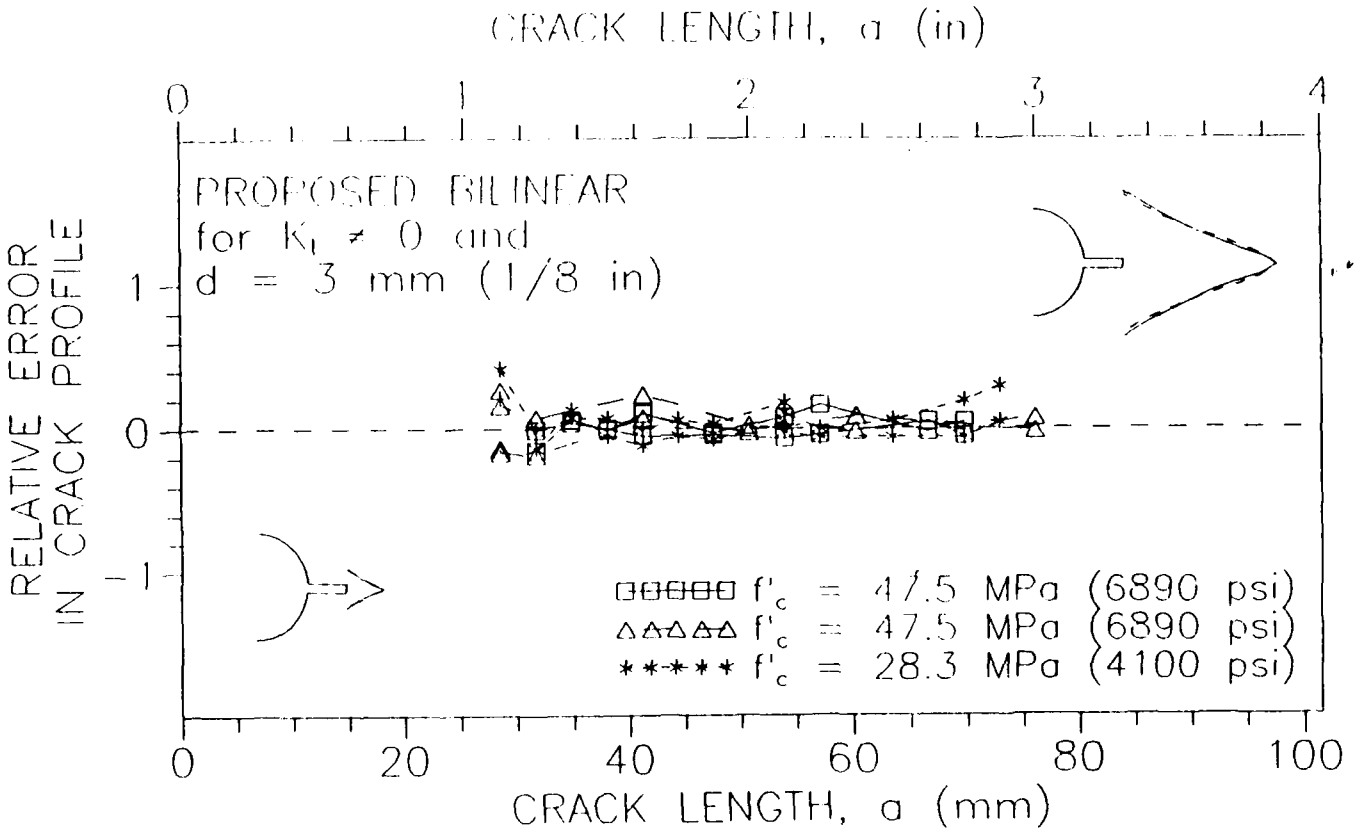

Figure 10. Crack profile comparison for proposed bilinear closing pressure.

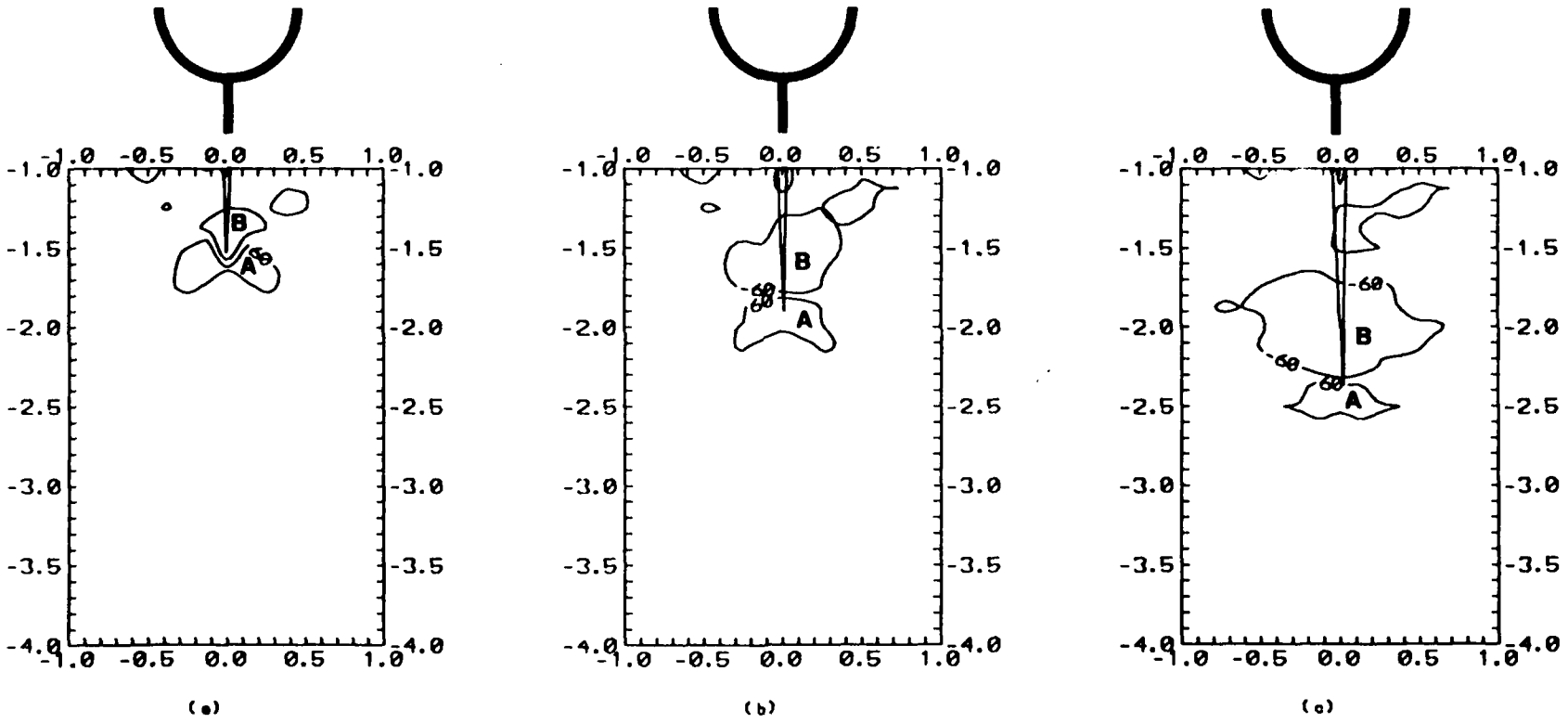

Figure 11. Difference between experimental and LEFM strain fields.

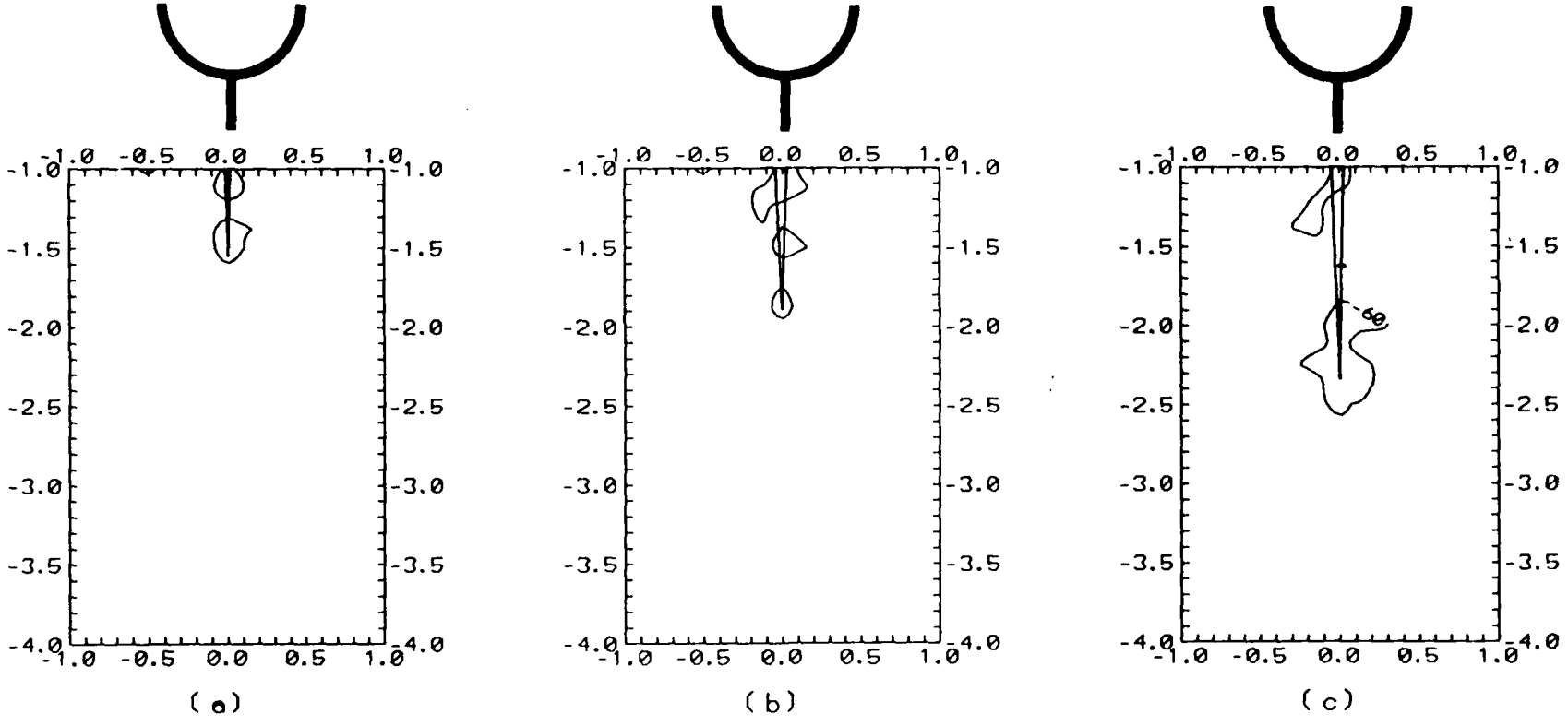

Figure 12. Difference between experimental and LEFM with bilinear closing pressure strain fields.

Session 5:

Experimental Methods to Assess Damage

Chairs:

Piet Stroeven
Delft University of Technology,
The Neterlands

Peter Pratt
Imperial College
London, U.K.

Reporter:

Jan van Mier
Delft University of Technology,
The Neterlands

THE FRACTURE PROCESS ZONE IN CONCRETE

SIDNEY MINDESS
Department of Civil Engineering
University of British Columbia
2324 Main Mall
Vancouver, British Columbia V6T 1W5
Canada

ABSTRACT. A number of different experimental techniques have been used to try to determine: (1) whether a process zone exists in concrete; (2) if it does, what its dimensions might be; and (3) whether it is a fundamental material property. From an extensive review of the literature, it would seem that not only the apparent size of the process zone, but its very existence, are strongly dependent on both the specimen geometry and on the methods of measurement. It is difficult to avoid the conclusion that the process zone is not a fundamental material property for cementitious composites.

1. Introduction

When a brittle material containing a crack is subjected to stress, the stress distribution ahead of the crack has the form shown in Fig. 1. That is, for a sharp crack, there are very high stress concentrations in the immediate vicinity of the crack tip. Because of the heterogeneity of concrete at both the macrostructural and microstructural levels, including discontinuities and pre-existing microcracks, there will be many highly localized areas of relative weakness in this highly stressed zone. Therefore, as a crack propagates in concrete, one would expect a great deal of microcracking to occur, largely (but not exclusively) in this highly stressed region. This region of discontinuous microcracking ahead of the continuous (visible) crack is generally referred to as the fracture process zone.

It must be emphasized, as will be seen below, that not all investigators have found such a process zone. However, if there is a true fracture process zone, or even simply random microcracking associated with crack propagation, it is important to try to quantify the amount of damage that occurs during the fracture of concrete.

There are a number of conceptual problems to be dealt with in any discussion of fracture process zones in concrete. First, as Thouless [1] has pointed out (Fig. 2), instead of looking for a process zone ahead of the crack tip, one can as easily consider a bridging zone

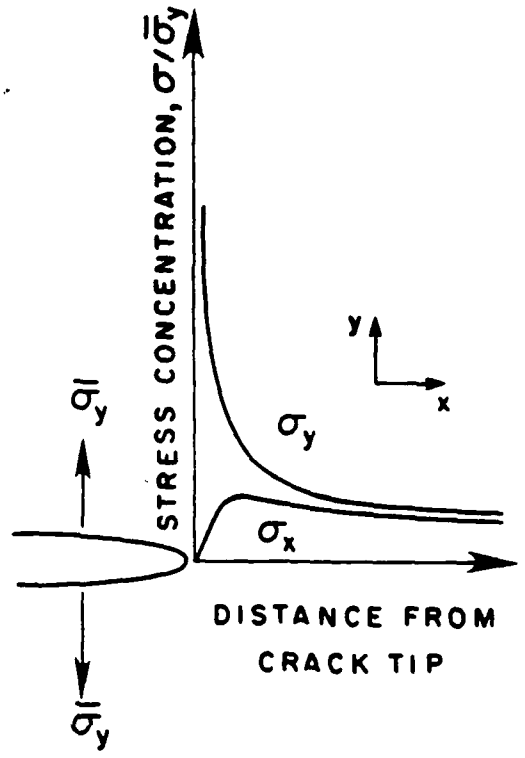

Figure 1. Stress field ahead of a crack tip.

behind the crack tip. Either assumption leads to similar results when applied to the problem of crack tip propagation. Second, it appears to be impossible to define, in an unequivocal fashion, the "true" crack length in concrete [2]; the position of the tip of a propagating crack is uncertain. Since, as mentioned above, there are already pre-existing microcracks in virgin concrete, it is necessary to distinguish between these and the additional microcracks caused by the imposed stresses. At the moment, it is not possible to do this. Third, investigators such as Bazant [3] are not really concerned with the size of the fracture process zone as determined by direct observation. They are simply interested in an elastically equivalent crack system, which yields the correct energy dissipation and correct stress vs. displacement relationships in a concrete specimen. Finally, it has been shown [4,5] that the crack length appears to vary across the width or thickness of the specimen. Thus, surface crack measurements cannot accurately indicate the extent of the process zone. In view of these complexities, it is then not surprising that there is a great deal of controversy about the process zone in concrete.

In this paper, some of the experimental techniques used to identify the process zone, and the results of these studies, will be discussed.

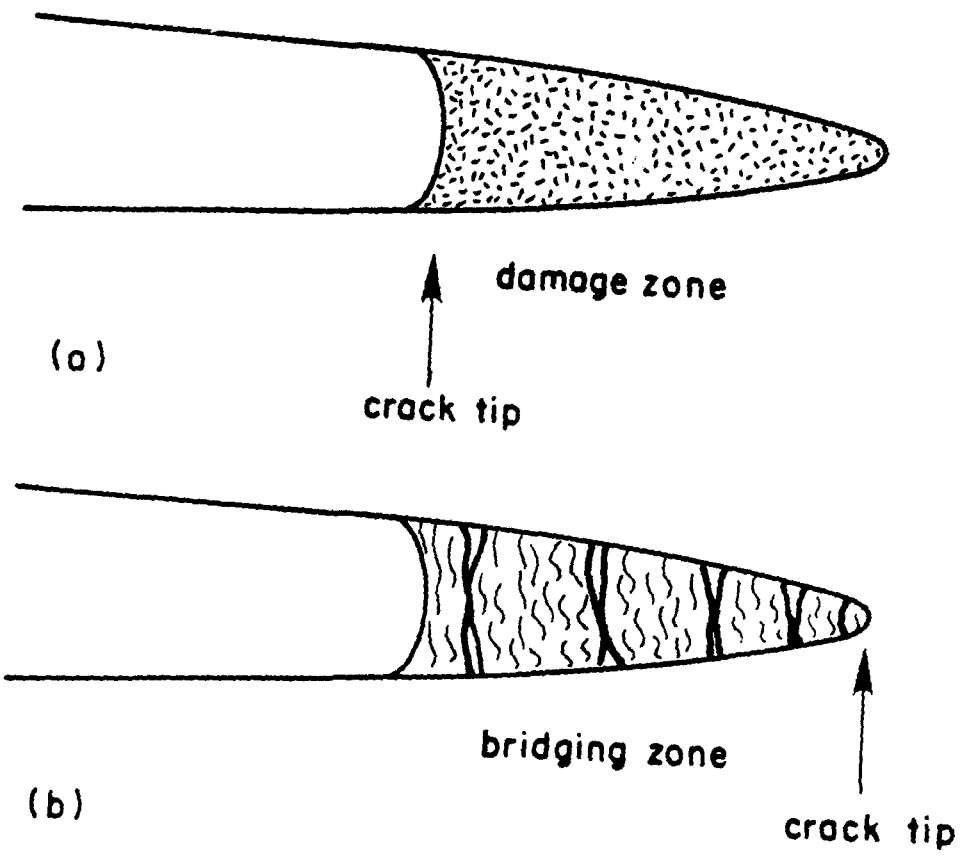

Figure 2. Schematic illustration of a crack tip, and either the (a) damage zone, or (b) bridging zone, after Thouless [1].

2. Experimental Techniques

Over the years, a great many different experimental techniques have been employed to try to find the extent of the process zone. These may be divided roughly into three categories:

Surface techniques:
- optical microscopy
- scanning electron microscopy
- electric resistance strain gauges
- photoelastic methods
- interferometry techniques

Measurements involving the specimen interior:
- X-ray techniques
- mercury penetration measurements
- dye penetrants
- infrared vibrothermography
- ultrasonic pulse velocity
- acoustic emission

Indirect methods:
- compliance measurements
- Demec gauges
- numerical methods

As indicated above, these techniques tend to measure rather different properties of the material. Some involve only the surface characteristics of the specimen, and some include an indication of what is happening in the interior of the specimen. Still others consider the system as a kind of "black box", where the physical details of the cracking are not considered directly, as long as an assumed crack system yields the correct stress vs strain and/or energy relationships. Thus, it is sometimes difficuilt to reconcile the very different conclusions that various researchers have come to with regard to the process zone.

It must also be noted that some techniques involve first loading the specimen to some stress or strain, but then unloading the specimen before the cracks are examined. Others, however, permit observations of the cracking while the specimens are still under load. Since the fine cracks tend to close and become virtually invisible on unloading, it is clear that valid measurements can only be made with those techniques which do not involve unloading the specimens before measurements are made.

3. Surface Techniques

The earliest attempts to examine cracking in concrete, such as the very extensive studies carried out at Cornell University using both **optical microscopy** [6,7] and **X-ray techniques** [6,8,9] were not really sensitive enough to reveal the presence of a process zone.

However, more sophisticated techniques have also not always revealed a process zone. On the one hand, Tait and Garrett [10], using in situ observations of cracking in pastes in the sample chamber of a **scanning electron microscope** (SEM), did identify a process zone in the vicinity of the crack tip, 1-4 mm in extent. Baldie and Pratt [11] used **backscattered electron imaging** on polished sections of cement paste. They found that crack growth seemed to occur by first the formation, and then the coalescence of microcracks ahead of the crack tip, but they identified "only a limited formation of ar actual process zone".

On the other hand, extensive in situ observation in an SEM by Mindess et al. [12-14] showed no evidence of a process zone. Using similar techniques, Diamond and Bentur [15] concluded that while there was crack subdivision and branching near the visible crack tip, "there is no physical distinction corresponding to separate lengths of 'straight, open crack' behind a crack tip and 'process zone microcracking' ahead of a crack tip".

Using a **replica technique** in conjunction with an SEM, Bascoul and his co-workers [16,17] also found extensive microcracking near the

crack tip, but not a well-defined process zone. They concluded [17] that "Nothing allows... (us)... to think that there is a damaged zone ahead of the macrocrack except at the beginning of crack branching".

Other, more sophisticated optical microscopy techniques have also been contradictory. Eden and Bailey [18] used **diffuse illumination** with a reflected light microscope, and concluded that stable crack growth involves the formation of a process zone which grows to some characteristic size before the crack becomes unstable. Stroeven [19, 20] however, used **fluorescent oils** to help delineate the cracks in concrete. Typical results are shown in Fig. 3 [19], which represents the crack pattern of an axial section of a grooved concrete specimen subjected to direct tension, slightly beyond the ultimate load. While there is very extensive cracking, much of this was already present in the virgin specimen as a result of shrinkage. Stroeven found that the cracks developed, and grew together, in a stochastic way. Certainly, there is no "process zone" in evidence.

Still other techniques have yielded different results. **Electric resistance strain gauges** have been used to identify relatively large process zones [21,22], of the order of 10 to 15 mm wide and lengths of up to 100 mm. However, these "process zones" were defined in terms of the surface strain exceeding, typically, $3x10^{-4}$ rather than by direct observation of cracks. In spite of these rather large dimensions, the process zone could not, surprisingly, be identified by optical methods. **Photoelastic techniques** were also ambiguous; Van Mier [23] and Van Mier and Nooru-Mohamed [24] could not define a fracture process zone, while Stys [25] did find one.

Perhaps the most sensitive of the surface techniques for identifying cracks in concrete are the interferometry techniques: **holographic interferometry** and **speckle interferometry**. These technqiues can achieve a sensitivity down to about 1 μm. Even with this sensitivity in measuring surface displacements, however, the results are uncertain. Most studies, as with electric strain gauges, define the process zone in terms of some limiting strain [26-28]. Thus, a fairly large process zone can be identified ahead of the crack tip, as in Fig. 4 [29], even though it cannot be defined optically. On the other hand, Ferrara and Morabito [30] could not with certainty specify a well- defined process zone, while Regnault and Bruhwiler [28] could not locate, or even define, the tip of the tension-free crack.

Similarly, white light **Moiré interferometry** was used to identify rather large (20-100 mm) process zones [31-33]. Again, one wonders why zones this large could nto be observed directly by microscopic techniques.

4. Measurements Involving the Specimen Interior

In principle, measurements involving the interior of the specimen, i.e. the bulk of the material, should provide a better indication of the extent of the process zone. Unfortunately, since we cannot directly

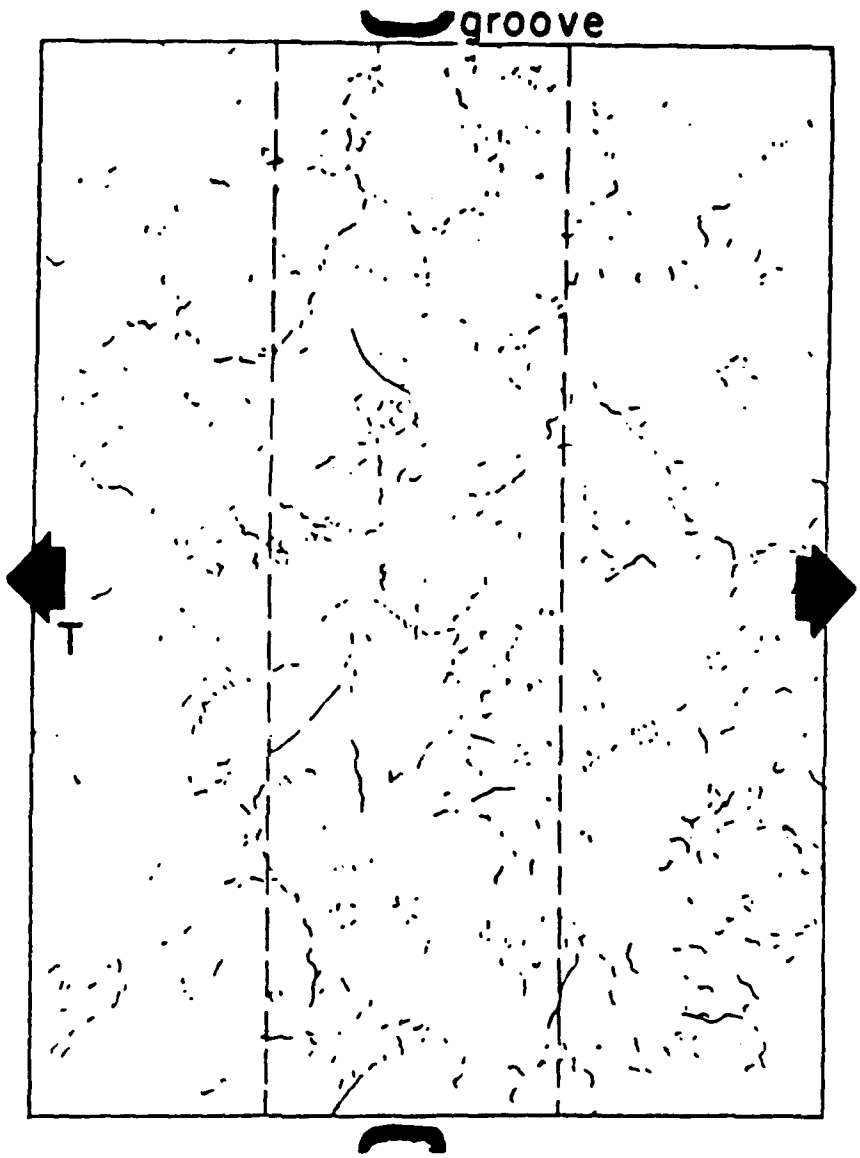

Figure 3. Manually copied crack pattern of axial section of two-sided grooved specimen subjected to direct tension slightly beyond the ultimate, after Stroeven [19].

see the interior of a specimen indirect means of locating cracks must be used for this purpose.

As indicated above, X-ray techniques [6,8,9] are not really sensitive enough for this purpose. Mercury penetration measurements [34] can only indicate crack widths and volumes, but cannot define the location of the microcracked region. Similarly, dye penetrants [35-37] can reveal the shape of the crack front, but cannot reveal the extent of the process zone.

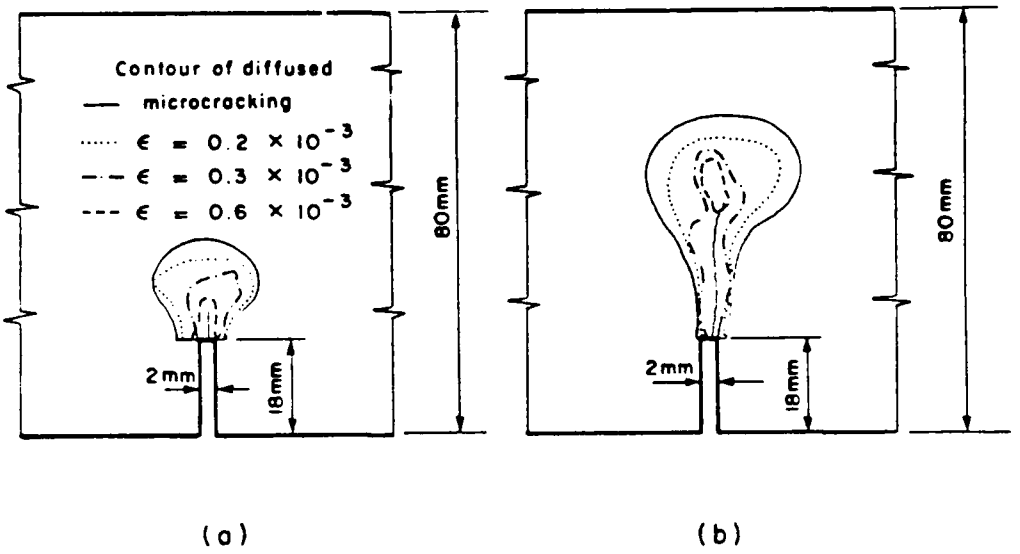

Figure 4. Equal strain contours and the developing crack, as measured using optical interferometry with laser light: (a) intermediate load level; (b) load level close to failure, after Cedolin, Dei Poli and Iori [27].

Infrared vibrothermography is based on the principle that heat is generated when there is energy dissipation in a material subjected to vibratory excitation beyond its stable reversible limit. This technique has been used [38] to observe progressive damage in a concrete specimen under compressive loading. This is an averaging technique, which shows the global damage within the specimen; whether this can be equated with the microcrack patterns that occur during the growth of a single crack under monotonically increasing loading is not certain.

Ultrasonic pulse velocity measurements have long been used to try to assess damage in concrete. This too is an averaging technique, which is affected by the total damage (or cracking) between the transducers. Extensive work using this technique carried out by Alexander and his co-workers [39-43] showed that the main crack would not propagate until a microcracked zone had developed in front of it, typically about 1/2 of the residual beam depth in size. Similarly, Chhuy et al. [21] found a damage zone about 100 mm long ahead of the crack tip. On the other hand, Berthaud [44,45] found it difficult to deduce the size of the process zone using ultrasonic pulse velocities, and Reinhardt

and Hordijk [22] concluded that such measurements do not lead to a geometrical description of the process zone.

Acoustic emission (AE) techniques have been used very extensively to try to assess the nature of the process zone. AE events occur when transient elastic waves are generated by the rapid release of energy that occurs upon cracking, and can be measured using piezoelectric transducers [46]. Maji and Shah [47-51], in a very detailed series of tests, found that beyond the peak load most of the AE events occurred near the crack tip; they deduced a process zone extending about 25 mm ahead of the crack tip, and a longer distance behind it (indicating ligament connections behind the visible crack tip). AE source locations for mortar specimens, compared to the crack tip location as determined by holographic techniques are shown in Fig. 5 [52]. Others have obtained similar results using AE techniques [21,53,54].

Berthelot and Robert [55-57] also carried out very extensive AE tests. They found that a damage zone appeared to grow in size as the crack progressed, reaching lengths of up to 160 mm and widths of up to

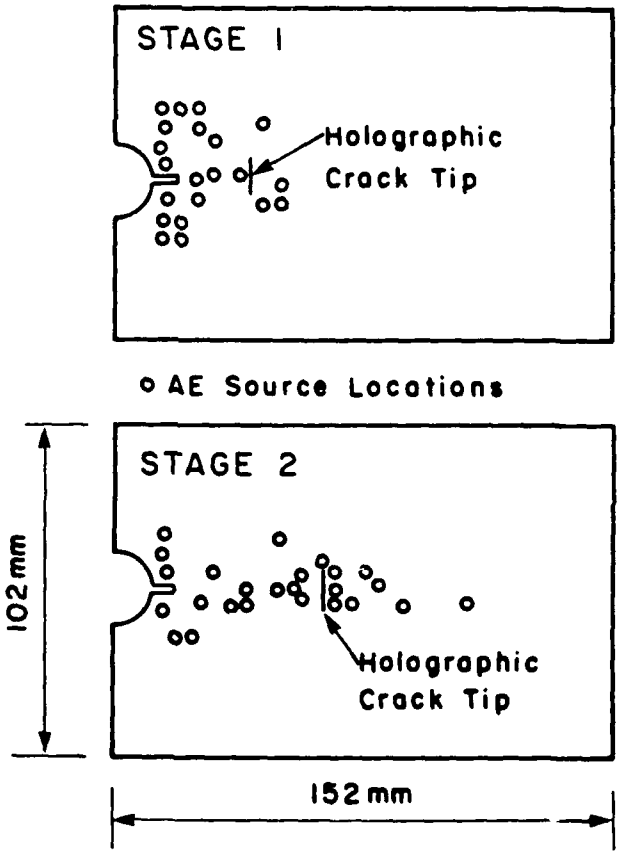

Figure 5. AE source locations for mortar specimen, compared to the location of the crack tip found using holographic techniques, after Maji, Ouyang and Shah [52].

120 mm. Similar results were obtained by Bensouda [58]. Again, however, it is surprising that such extensive damage zones are not readily apparent by microscopic observation.

Results by Rossi [59] and Rossi et al. [60] indicated that there was not a clear transition from the uncracked concrete to the process zone. Overall, a review of the AE literature suggests that the results depend upon the specimen geometry, the sophistication of the instrumentation, and the method of analysis.

5. Indirect Methods

A number of indirect methods have also been devised to estimate the size of the process zone. The earliest of these is the use of **compliance measurements**. That is, from measurements of specimen stiffness (and the location of the visible crack tip) the extent of the process zone can be "guesstimated". Using such techniques, Karihaloo and Nallathambi [61,62] found process zones in the range of 20-40 mm, depending on the specimen size. Compliance techniques were also used by Kobayashi et al. [63], who concluded that the process zone continued to grow as the crack extended, without ever reaching a constant value. In the view of this author, however, because of the impossibility of separating the development of a process zone from slow crack growth, compliance measurements cannot provide a good estimate of the size of the process zone.

An interesting variant on compliance measurements is the use of **multi-cutting techniques**. One such technique [64] involves the cutting of thin strips of the specimen normal to the crack path and measuring their bending stiffness as a function of distance from the visible crack tip. In another version of this technique [65-67], the bridging stresses transferred within the process zone are removed by careful cutting along the plane of the original crack, and determining the compliance of the specimen at each step as the cutting progresses through the process zone. This permits an estimate of the process zone size. Hu and Wittman [65-67] found process zones of up to 43 mm long, but concluded [65] that "the length of the fracture process zone is not a material constant but depends on the actual stress gradient due to the limited specimen geometry".

Demec gauges can be used to determine the average strains in specimens over fairly large gauge lengths. Clearly, this too can only average whatever is taking place within the gauge length. However, it has been found that the use of these gauges can provide similar results to those found from ultrasonic pulse velocity measurements [39,42].

Finally, **numerical methods** (i.e., studies on 'numerical' rather than 'real' concrete) have also been used to try to deduce the size of the process zone [e.g., 68-70]. Clearly, however, the results of such methods depend entirely on the a priori assumptions made in setting up the numerical models, and this cannot provide any definitive answers.

6. Conclusions

From the above brief review, it is clear that the different test techniques provide different information. Some investigators have found no process zone at all; others have found that the process zone size varies from only a few mm to over 500 mm, as summarized in Table I. It would appear, then, that this issue is still far from being resolved. Each different techniques, it seems, is capable of examining only a limited part of the problem. (Indeed, it reminds the author of the old story of a group of blind men trying to describe an elephant.) At

Table I. Fracture process zone dimensions determined using different techniques

Ref. No.	Technique	Process Zone Dimensions (mm)	
		Length	Width
61	Compliance measurements	20-40	
63	Compliance + replica	114	
64	Multi-cutting	30-40	
65-67	"	12-40	
12	SEM	no process zone found	
15	"	no process zone found	
10	"	1-4	
21	Strain gauges	100	10
22	"		14
25	Photoelasticity	5	
39-43	Ultrasonic pulse velocity	20-160	
21	"	100	10
47,49	Acoustic emission	25 ahead of tip >25 behind tip	
53	"	105	
21	"	100	
54	"	500	
56	"	160	120
58	"	160	120
59,60	"		10
27	Interferometry	20-40	
29	"	50	
30	"	no process zone detected	
28	"	zone exists, but dimensions not definable	1/2 aggregate size
32	Moiré interferometry	100	
33	"	20-30	10
70	Numerical techniques	40-80	

present, one can only conclude that the process zone is not a fundamental material property, but depends on the specimen geometry, and the method of measurement.

7. Acknowledgements

This work was supported in part by a grant from the Natural Science and Engineering Research Council of Canada. The authors would also like to thank Dr. Z.P. Bazant, Dr. M.G. Alexander, Dr. A.K. Maji and Dr. S.E. Swartz for their helpful discussions of earlier drafts of this work.

8. References

1. Thouless, M.D. (1988) Bridging and Damage Zones in Crack Growth, **Journal of the American Ceramic Society**, 71 (6) 408-413.
2. Kasperkiewicz, J. (1988) Letter to the author, November 22.
3. Bazant, Z.P. (1988) Letter to the author, October 26.
4. Swartz, S.E. and Go, C-G. (1984) Validity of Compliance Calibration to Cracked Concrete Beams in Bending, **Experimental Mechanics**, 24 (2) 129-134.
5. Pascoal, A., Kharchi, F. and Maso, J.C. (1987) Concerning the Measurement of the Fracture Energy of a Microconcrete according to the Crack Growth in a Three Points Bending Test on Notched Beams, in S.P. Shah and S.E. Swartz (eds.), Proceedings of **SEM-RILEM International Conference on Fracture of Concrete and Rock**, Houston; **Society of Experimental Mechanics**, Bethal CT.
6. Slate, F.O. and Hover, K.C. (1984) Microcracking in Concrete, in A. Carpinteri and A.R. Ingraffea (eds.), **Fracture Mechanics of Concrete: Material Characterization and Testing**, Martinus Nijhoff Publishers, The Hague, pp. 137-159.
7. Slate, F.O. (1983) Microscopic Observation of Cracks in Concrete, with Emphasis on Techniques Developed and Used at Cornell University, in F.H. Wittmann (ed.) **Fracture Mechanics of Concrete**, Elsevier Science Publishers B.V., Amsterdam, pp. 75-83.
8. Slate, F.O. (1983) X-Ray Technique for Studying Cracks in Concrete, with Emphasis on Methods Developed and Used at Cornell University, in F.H. Wittmann (ed.) **Fracture Mechanics of Concrete**, Elsevier Science Publishers B.V., Amsterdam, pp. 85-93.
9. Najjar, W.D. and Hover, K.C. (1988) Modification of the X-Radiography Technique to Include a Contrast Agent for Identifying and Studying Microcracking in Concrete, **Cement, Concrete and Aggregate**, 10 (1) 15-19.
10. Tait, R.B. and Garrett, G.G. (1986) In Situ Double Torsion Fracture Studies of Cement Mortar and Cement Paste Inside a Scanning Electron Microscope, **Cem. Concrete Res.**, 16 (2) 143-155.

11:Baldie, K.D. and Pratt, P.L. (1986) Crack Growth in Hardened Cement Paste, in S. Mindess and S.P. Shah, (eds.), **Cement-Based Composites: Strain Rate Effects on Fracture**, Materials Research Society Symposia Proceedings Vol. 64, Materials Research Society, Pittsburgh, pp. 47-61.
12.Mindess, S. and Diamond, S. (1982) The Cracking and Fracture of Mortar, **Materiaux et Constructions**, 15 (86) 107-113.
13.Mindess, S. and Diamond, S. (1982) A Device for Direct Observation of Cement Paste or Mortar Under Compressive Loading Within a Scanning Electron Microscope, **Cement and Concrete Research**, 12 (569-576).
14.Diamond, S., Mindess, S. and Lovell, J. (1983) Use of a Robinson Backscatter Detector and 'Wet Cell' for Examination of Wet Cement Paste and Mortar Specimens Under Load, **Cement and Concrete Research**, 13 (107-113).
15.Diamond, S. and Bentur, A. (1985) On the Cracking in Concrete and Fibre-Reinforced Cements, in S.P. Shah, (ed.), **Applications of Fracture Mechanics to Cementitious Composites**, Martinus Nijhoff Publishers, Dordrecht, pp. 87-140.
16.Bascoul, A., Ollivier, J.P. and Poushanchi, M. (1989) Stable Microcracking of Concrete Subjected to Tensile Strain Gradient, **Cement and Concrete Research**, Vol. 19, No. 1, pp. 81-88.
17.Bascoul, A., Detriche, C.H., Ollivier, J.P. and Turatsinze, A. (1989) Microscopical Observation of the Cracking Propagation in Fracture Mechanics for Concrete, in S.P. Shah, S.E. Swartz and B. Barr (eds.), **Fracture of Concrete and Rock: Recent Developments**, Elsevier Applied Science, London, pp. 327-336.
18.Eden, N.B. and Bailey, J.E. (1986) Crack Tip Processes and Fracture Mechanism in Hardened Hydraulic Cements, in Proceedings, **8th International Congress on the Chemistry of Cement**, Rio de Janeiro, Vol. III, pp. 382-388.
19.Stroeven, P. (1988) Characterization of Microcracking in Concrete, preprint, **RILEM Conference on Cracking and Durability of Concrete**, Saint Rémy le Chevreuses.
20.Stroeven, P. (1988) Some Observations on Microcracking in Concrete Subjected to Various Loading Regimes, Proc., **International Conference on Fracture and Damage of Concrete and Rock**, Vienna, (in press).
21.Chhuy, S., Cannard, G., Robert, J.L. and Acker, P. (1986) Experimental Investigations into the Damage of Cement Concrete with Natural Aggregates, in A.M. Brandt and I.H. Marshall (eds.), **Brittle Matrix Composites 1**, Elsevier Applied Science, London, pp. 341-354.
22.Reinhardt, H.W. and Hordijk, D.A. (1988) Various Techniques for the Assessment of the Damage Zone Between Two Saw Cuts, presented at the France-U.S. Workshop, **Strain Localization and Size Effect Due to Cracking and Damage**, Cachan, France, September, 12 pp.

23. van Mier, J.G.M. and Nooru-Mohamed, M.B. (1988) Geometrical and Structural Aspects of Concrete Fracture, Proceedings, **International Conference on Fracture and Damage of Concrete and Rock**, Vienna, (in press).
24. van Mier, J.G.M. (1988) Fracture Study of Concrete Specimens Subjected to Combined Tensile and Shear Loading, Proceedings, **International Conference on Measurements and Testing in Civil Engineering**, Lyon-Villeurbanne, 1988 (in press).
25. Stys, D. (1989) Numerical Analysis of the Stress Field Parameters in the Fracture Process Zone in Concrete, in A.M. Brandt and I.H. Marshall (eds.), **Brittle Matrix Composites 2**, Elsevier Applied Science, London, pp. 134-143.
26. Iori, I., Lu, H., Marozzi, C.A. and Pizzinato, E. (1982) Metodo per la Determinazione dei Campi dei Spostamento nei Materiali Eterogenei (Conglomerati Naturali ed Artificiali) a Bassa Resistenza Specifica a Trazione, **L'Industria Italiano Del Cemento**, No. 4, 275-280.
27. Cedolin, L., Dei Poli, S. and Iori, I. (1987) Tensile Behaviour of Concrete, **Journal of Engineering Mechanics**, 113 (3) 431-449.
28. Regnault, Ph. and Brühwiler, E. (1988) Holographic Interferometry for the Determination of Fracture Process Zone in Concrete, in Proceedings, **Int. Conf. on Fracture and Damage of Concrete and Rock**, Vienna, (to be published).
29. Dei Poli, S. and Iori, I. (1986) Osservazioni e Rilievi sul Comportamento a Trazione dei Calcestruzzi: Analisi di Risultanze Sperimentali, **Studi e Ricerche**, Politecnico di Milano, 8 35-62.
30. Ferrara, G. and Morabito, P. (1989) A Contribution of the Holographic Interferometry to Studies on Concrete Fracture, in S.P. Shah, S.E. Swartz and B. Barr (eds.), **Fracture of Concrete and Rock: Recent Developments**, Elsevier Applied Science, London, pp. 337-346.
31. Du, J.J., Kobayashi, A.S. and Hawkins, N.M. (1987) Fracture Process Zone of a Concrete Fracture Specimen, in Proceedings, **International Conference on Fracture Concrete and Rock**, Houston, pp. 280-286.
32. Du, J., Hawkins, N.M. and Kobayashi, A.S. (1989) A Hybrid Analyssi of Fracture Process Zone in Concrete, in Shah, S.P., Swartz, S.E. and Barr, B. (eds.), **Fracture of Concrete and Rock: Recent Developments**, Elsevier Applied Science, London, pp. 297-306.
33. Raiss, M.E., Dougill, J.W. and Newman, J.B. (1989) Observation of the Development of Fracture Process Zones in Concrete, in S.P. Shah, S.E. Swartz and B. Barr, **Fracture of Concrete and Rock: Recent Developments**, Elsevier Applied Science, London, pp. 243-253.
34. Schneider, U. and Diederichs, U. (1983) Detection of Cracks by Mercury Penetration Measurements, in F.H. Wittmann, (ed.), **Fracture Mechanics of Concrete**, Elsevier Science Publishers B.V., Amsterdam, pp. 207-222.
35. Swartz, S.E. and Go, C-G. (1984) Validity of Compliance Calibration to Cracked Concrete Beams in Bending, **Experimental Mechanics**, 24 (2) 129-134.

36. Swartz, S.E. and Refai, T.M.E. (1987) Influence of Size Effects on Opening Mode Fracture Parameters for Precracked Concrete Beams in Bending, in Proceedings, **International Conference on Fracture of Concrete and Rock**, Houston, pp. 403-417.
37. Bascoul, A., Kharchi, F. and Maso, J.C. (1987) Concerning the Measurement of the Fracture Energy of a Micro-Concrete According to the Crack Growth in a Three Point Bending Test on Notched Beams, in S.P. Shah and S.E. Swartz (eds.), **SEM/RILEM International Conference on Fracture of Concrete and Rock**, Houston, pp. 631-643.
38. Luong, M.P. (1986) Infrared Vibrothermography of Plain Concrete, in F.H. Wittmann, (ed.), **Fracture Toughness and Fracture Energy of Concrete**, Elsevier Applied Science Publishers B.V., Amsterdam, pp. 249-257.
39. Alexander, M.G. (1985) Fracture of Plain Concrete - A Comparative Study of Notched Beams of Varying Depth, **Ph.D. Thesis**, University of the Witwatersrand, Johannesburg, South Africa.
40. Alexander, M.G. (1988) Use of Ultrasonic Pulse Velocity for Fracture Testing of Cemented Materials, **Journal of Cement, Concrete and Aggregates**, ASTM, Vol. 10, No. 1, Summer, pp. 9-14.
41. Alexander, M.G., Tait, R.B. and Gill, L.M. (1989) Characterization of Microcracking and Crack Growth in Notched Conrete and Mortar Beams Using the J-Integral Approach, in S.P. Shah, S.E. Swartz and B. Barr (eds.), **Fracture of Concrete and Rock: Recent Developments**, Elsevier Applied Science, London, pp. 317-326.
42. Alexander, M.G. and Blight, G.E. (1986) The Use of Small and Large Beams for Evaluating Concrete Fracture Characteristics, in F.H. Wittmann, (ed.), **Fracture Toughness and Fracture Energy of Concrete**, Elsevier Science Publishers B.V., Amsterdam, pp. 323-332.
43. Alexander, M.G. and Blight, G.E. (1987) Characterization of Fracture in Cemented Materials, **private communication**.
44. Berthaud, Y. (1987) An Ultrasonic Testing Method: An Aid for Material Characterization, in Proceedings, **International Conference on the Fracture of Rock and Concrete**, Houston, pp. 644-654.
45. Berthaud, Y. (1988) Mesure de L'Endommagement du Beton Par Une Methode Ultrasonore, **Ph.D. Thesis**, Univerisité de Paris 6, France.
46. Mindess, S. (1980) Acoustic Emission in V.M. Malhotra and N. Carino (eds.), **Handbook of Nondestructive Testing of Concrete**, CRC Press, Inc., Boca Raton, Florida (in press).
47. Maji, A.K. and Shah, S.P. Process Zone and Acoutic Emission Measurements in Concrete, to be published in Experimental Mechanics (SEM Paper No. 3609).
48. Maji, A.K. and Shah, S.P. (1988) Application of Acoustic Emission and Laser Holography to Study Microfracture in Concrete, **ACI-SP-112 Nondestructive Testing**, American Institute, pp. 83-109.
49. Maji, A.K. and Shah, S.P. (1986) A Study of Fracture Process of Concrete Using Acoustic Emission, Proc., **Soc. Expt. Mech. Spring Conference**, New Orleans, June 8-13.

50. Maji, A. and Shah, S.P. (1988) Initiation and Propagation of Bond Cracks as Detected by Laser Holography and Acoustic Emission, in S. Mindess and S.P. Shah (eds.) **Bonding in Cementitious Materials, Materials Research Society Symposium Proceedings**, Vol. 114, Materials Research Society, Pittsburgh, pp. 55-64.
51. Maji, A.K. (1989) Study of Concrete Fracture Using Acoustic Emission and Laser Holography, **Ph.D. Thesis**, Northwestern University, Evanston, IL, June.
52. Maji, A.K., Ouyang, C. and Shah, S.P. (1990) Fracture Mechanisms of Quasi-Brittle Materials Based on Acoustic Emission, **Journal of Materials Research**, 5 (1) 206-217.
53. Izumi, M. Mihashi, H. and Nomura, N. (1986) Acoustic Emission Technique to Evaluate Fracture Mechanics Parameters of Concrete, in F.H. Wittmann, (ed.), **Fracture Toughness and Fracture Energy of Concrete**, Elsevier Science Publishers B.V., Amsterdam, pp. 259-268.
54. Chhuy, Sok, Baron, J. and Francois, D. (1979) Mecanique de la Rupture Applique au Beton Hydraulique, **Cement and Concrete Research**, 9 (5) 641-648.
55. Berthelot, J.-M. and Robert, J.-L. (1985) Damage Process Characterization in Concrete by Acoustic Emission, presented at the **Second International Conference on Acoustic Emission**, Lake Tahoe, Nevada, October.
56. Berthelot, J.-M. and Robert, J.-L. (1985) Application de l'Emission Acoustique aux Mecanismes d'Enjdommagement du Beton, Bulletin de Liaison des Ponts et Chaussees, 140, Nov.-Dec., 101-111.
57. Berthelot, J.-M. and Robert, J.-L. (1990) Damage Evaluation of Concrete Test Specimens Related to Failure Analysis, Journal of Engineering Mechanics, 116 (3) pp. 587-604.
58. Bensouda, M. (1989) Contribution a L'Analyse par Emission Acoustique de L'Endommagement dans le Beton, **Ph.D. Thesis**, Université du Maine, France.
59. Rossi, P. (1986) Fissuration due Beton: due Materiaux a la Structure, Appliation de la Mecanique Lineaire de Rupture, **Ph.D. Thesis**, Ecole Nationale des Ponts et Chaussees, France.
60. Rossi, P., Robert, J.L., Gervais, J.P. and Bruhat, D. (1989) Acoustic Emission Applied To Study Crack Propagation in Concrete, **Materiaux et Constructions** (Paris), Vol. 22, No. 131, pp. 374-383.
61. Karihaloo, B.L. and Nallathambi, P. (1989) An Improved Effective Crack Model for the Determination of Fracture Toughness of Concrete, **Cement and Concrete Research**, 19 (4) 603-610.
62. Karihaloo, B.L. and Nallathambi, P. (1990) Size Effect Prediction from Effective Crack Model for Plain Concrete, **in preparation**.
63. Kobayashi, A.S., Hawkins, N.M., Barker, D.B. and Liaw, B.M. (1985) Fracture Process Zone of Concrete, in S.P. Shah (ed.) **Applications of Fracture Mechanics to Cementitious Composites**, Martinus Nijhoff Publishers, Dordrecht, pp. 25-50.

64. Foote, R., Mai, Y. and Cotterell, B. (1987) Process Zone Size and Crack Growth Measurements in Fiber Cements, in S.P. Shah and G.B. Batson (eds.) **Fiber Reinforced Concrete Properties and Applications**, SP-105, American Concrete Institute, Detroit, pp. 55-70.
65. Hu, X.Z. and Wittmann, F.H. (1989) Fracture Process Zone and K_r-Curve of Hardened Cement Paste and Mortar, in S.P. Shah, S.E. Swartz and B. Barr (eds.), **Fracture of Concrete and Rock: Recent Developments**, Elsevier Applied Science, London, pp. 307-316.
66. Hu, X.Z. and Wittmann, F.H. (1990) An Experimental Method to Determine the Extension of the Fracture Process Zone, submitted to the **ASCE Journal of Materials in Civil Engineering**.
67. Hu, X.A. and Wittmann, F.H. (1989) An Analytical Method to Determine the Bridging Stress Transferred within the Fracture Process Zone, **private communication**.
68. Schorn, H. and Rode, U. (1987) 3-D Modelling of Process Zone in Concrete by Numerical Simulation," in Proceedings, **International Conference on Fracture of Concrete and Rock**, Houston, pp. 308-316.
69. Alvaredo, A.M., Hu, X.Z. and Wittmann, F.H. (1989) A Numerical Study of the Fracture Process Zone, in S.P. Shah, S.E. Swartz and B. Barr (eds.), **Fracture of Concrete and Rock: Recent Developments**, Elsevier Applied Science, London, pp. 51-60.
70. Gopalaratnam, V.S. and Ye, B.S. (1989) Numerical Studies of the Fracture Process Zone in Concrete, in S.P. Shah, S.E. Swartz and B. Barr (eds.), **Fracture of Concrete and Rock: Recent Developments**, Elsevier Applied Science, London, pp. 81-90.

Characterization of the Fracture Behavior of Ceramics Through Analysis of Crack Propagation Studies

R.W. Steinbrech, R.M. Dickerson, G. Kleist
Research Center Jülich, Institute for Reactor Materials
P.O. Box 19 13, 5170 Jülich , FRG

Abstract

The brittle fracture of structural ceramics, as analyzed from crack propagation studies under conditions of slow, quasi-static crack growth, is described. The experimental results allow one to partition ceramics in to those which have a constant toughness and those which exhibit increasing toughness upon crack extension. The latter effect, known as R-curve behavior is addressed in greater detail for long and short cracks in alumina and MgO-partially-stabilized zirconia. Correlations between microstructure, R-curve behavior and strength are outlined.

1. Introduction

In recent years, important progress has been achieved in the fields of material development and mechanical failure characterization of structural ceramics /1/. The knowledge gathered and accumulated in-service experience enabled a continous widening of the field of application. On the other hand, reliable use of ceramics still demands, for any individual case, knowledge about the interdependencies between application, loading conditions and damage mechanisms.

From the materials and mechanical point of view, characterization of the potential failure mechanisms plays the key role. Specifically, reliable data are needed to avoid catastrophic brittle fracture. Furthermore, information about subcritical crack growth, thermal shock, fatigue, corrosion, creep and high temperature chemical stability are important. Often, the failure of ceramic components is complex because more than one of the forementioned damage mechanisms may act simultaneously.

crack growth can be achieved for materials with steeply rising R-curves over a much wider range. The experimental R-curves of long cracks presented in this section were obtained from single edged notched bend (SENB), double cantilever beam (DCB) and double torsion (DT) specimens (Fig. 6). In section 4, R-curves for short "natural" surface cracks on the tensile surface of bend bars are discussed.

In the SENB-geometry, the depth of the narrow ($\sigma \approx 70$ µm), straight-through notches varied between $a_n/W = 0.2$ and $a_n/W = 0.8$, where W is the width in the direction of crack growth. It should be noted that sharp starter cracks generated by the bridging method /16/ are not appropriate in the case of R-curve behavior because controlled crack propagation starts at an already high resistance level.

The technique used for the propagation studies of long cracks is illustrated in Fig. 7. Load (P), load-point displacement (d) and crack length (a) (monitored with a travelling microscope) were measured simultaneously to generate P-d-a curves; as shown in the lower part of Fig. 7. In addition to continuous experiments under displacement or cross head-position control, tests with several intermediate unloading loading sequences can be run to gain insight into the underlying fracture mechanisms and/or to provide further information for the evaluation of resistance data. Such P-d curves are shown for a coarse grained Al_2O_3 (Fig. 8) and a high toughness Mg-PSZ (Fig. 9). Unloaded, both ceramics reveal a residual displacement (d_r), but they significantly differ with respect to the hysteresis upon reloading. Due to frictional wake effects of rough serrated crack surfaces, hysteresis is very pronounced in Al_2O_3 /17/. Also, the residual displacement can be increasingly reduced by stepwise renotching from notch to crack tip. When the renotch approaches the crack tip, no further d_r is left in Al_2O_3 /17/. In Mg-PSZ, the decrease in d_r depends on the width of the renotch cut /18/, as well. The residual displacement only diminishes if the complete transformation zone is machined away.

2.2 Increasing toughness (R-curve)

In the case of increasing toughness, the fracture stress can increase despite crack growth (Fig. 2b), if toughening overcompensates the strength decrease from crack growth. Ceramics which exhibit this crack propagation behavior are, to a certain extent, "flaw tolerant".

To date, R-curve behavior was predominantly investigated in ZrO_2-containing ceramics /9, 10/ and in coarse grained oxide ceramics /11, 12/. Fig. 5 shows R-curves from measurements using thin, compact tension (CT-) like specimens, which highlight the strong transformation toughening effect of zirconia. The R-curve behavior of both monolithic ceramics is discussed in greater detail in sections 3 and 4.

Although it is out of the scope of this paper it should be mentioned that, in recent years, increasing efforts are under way in materials development to implant R-curve behavior in a large variety of ceramics with initially constant toughness by utilizing second phase toughening. Materials of specific interest are ceramic-ceramic composites /13/ with whisker-, fiber-, platelet reinforcement and ceramic-metal composites /14/.

3.1 Measurement and Evaluation of Crack Resistance

In principle, crack propagation studies of ceramics can be performed with almost all of the testing geometries used in linear elastic fracture mechanics. However, for stable, quasistatic crack extension, specific conditions relating crack growth-associated changes in crack driving and resistance forces must hold /15/. The change in crack driving force (dG/da), which depends on the energy stored in the specimen and the testing device, has to be less than dR/da (< 0 for constant R) to avoid crack instability. When dG/da < dR/da holds, crack propagation is possible only if an additional amount of external work is supplied. In accordance with these considerations, constant toughness materials need a long starter crack (deep notch) which may reduce the available range of crack propagation quite significantly. On the other hand, controlled

mics /6/. In a crude approximation, increases of strength and toughness are positively correlated and the data indicate that a proportionality holds. Using the assumption of surface flaws ($Y \approx 1,3$ /7/) a critical flaw size of about 60 µm could be deduced from the strength-toughness relationships.

However, such an interpretation of Fig. 1 should not be stretched too far, as will be shown by the crack propagation studies described in the following sections. Seperating ceramics into those which have a constant toughness upon crack extension and those which exhibit a rising crack length-dependent crack resistance (R-curve), some general aspects of fracture are outlined next.

2.1 Constant toughness

Upon loading, ceramics typically deform linear elastically until catastrophic failure occurs at crack instability (Fig. 2a) as described by Eq. 1 with the assumption of a constant toughness. In fact, quasi-static crack propagation studies reveal that, for many ceramics, toughness does not change over a wide range of crack extension. Some examples are shown in Fig. 3 for fine grained materials: Si_3N_4 and SiC.

According to Eq. 1, the strength of ceramics can be increased by reducing the critical flaw size. Furthermore, narrowing the flaw size distribution helps to increase reliability (decrease in scatter of strength). The correlation between flaw size and microstructural dimensions urges the processing of fine grained ceramics. This concept of materials development has been sucessfully applied in recent years /8/. However, a more careful control of the individual processing steps is necessary to avoid material inhomogeneities which can act as stress concentrators and cause premature failure. Fig. 4 shows a large graphite inclusion in HIP-SiC and a pore in a Si_3N_4 body. Both were critical flaws for these fine grained non-oxide ceramics in bending strength tests.
The defect sensitivity of fine grained ceramics and their inherent failure potential through local stress concentrations or short overloads, favours an alternative concept of ceramic development which is based on R-curve behavior.

The present paper expands on previous review articles on structural ceramics /1-4/ and focusses on aspects of brittle fracture revealed through crack propagation studies. When using a Griffith-type crack instability criterion, ceramics can be divided into two groups; those which have a constant toughness and those which exhibit increasing toughness upon crack extension. The latter effect, known as R-curve behavior, is addressed here in greater detail for alumina and MgO partially-stabilized zirconia. Correlations between microstructure, R-curve behavior and strength are outlined.

2. Crack instability and toughness behavior

Brittle fracture of ceramics usually is assumed to be determined by pre-existing flaws which become unstable upon loading, thus causing catastrophic failure of the material. Using an energy concept /5/, the point of crack instability is given by the equation

$$\sigma_f = \frac{1}{Y} \sqrt{\frac{E \cdot R}{a_c}} \qquad (1a)$$

which relates fracture stress (σ_f) and material resistance (crack resistance force (R)) to the critical flaw size (a_c). The Young's modulus (E) and the parameter Y, which considers the finite size of components (specimens) with respect to flaw size, are included in Eq. 1a as well.

In the case of linear elastic fracture, the well known equation

$$\sigma_f = \frac{1}{Y} \frac{K_{IC}}{\sqrt{a_c}} \qquad (1b)$$

holds, where K_{IC} is the toughness parameter (critical stress intensity factor), which yields a desciption equivalent to Eq. 1a. In this paper, K and R formulations are used interchangeably, assuming that $K_{IC} = \sqrt{E \cdot R}$.

Using Eq. 1b, the strength (fracture stress in bending) is plotted in Fig. 1 as a function of toughness for various commercial cera-

Which R-curve determination methodology to utilize when analysing mechanical tests, particulary whether residual displacements must be incorporated is currently an unresolved topic of discussion. Most often, the evaluation procedure follows a linear elastic compliance approach, neglecting residual displacement effects. In the case of quasi static crack growth, G = R, and

$$R = \frac{P^2}{2B}\frac{dC}{da} \qquad (2)$$

where B is the width and C the compliance of the specimen.

The three possible methods used in applying Eq. 2 are:

A) from experimental P-d-a data, the experimental compliance function C_{exp} (a_{exp}) is taken

B) a theoretical compliance function C_{th} (a_{th}) is used after calculating a_{th} by equating C_{exp} and C_{th}

C) the experimental crack length is combined with a theoretical compliance function ($C = C_{th}$ (a_{exp})). (Note that this method is equivalent to standard procedures of stress intensity factor determination.)

These three methods can generate different crack resistance curves. For example, due to the wake interaction (discussed in section 3.2.1), alumina is less compliant than theoretically predicted. Thus, the crack length (a_{th}) calculated with method B, is shorter than the physical crack length (a_{exp}) measured with the travelling microscope.

If residual displacement is relevant for the specimen behavior during crack propagation then Eq. 5 has to be modified and extended /15/, which gives

$$R = \frac{P^2}{2B}\frac{dC}{da} + \frac{1}{B}\,P\,\frac{d(d_r)}{da} \qquad (6)$$

where C is a compliance determined from unloading-loading sequences and d_r is the residual displacement on unloading.

Interestingly, in alumina, all 4 analysis methods yield almost the same R-curve over a wide range of crack extension (SENB: 2-3 mm) before significant deviations occur. The details of this comparison will be reported elsewhere /17/. For Mg-PSZ, the initial part of the R-curve is shifted towards a higher resistance if the contribution of residual displacement is considered. The curves from all evaluation methods then approach the same plateau value after about 2-3 mm of crack extension.

(Note that the long crack R-curves shown in this paper were derived either from compliance method A (Mg-PSZ) or B (Al_2O_3, predominantly in SENB geometry).)

3.2 R-Curve behavior

Controlled crack propagation studies using the standard specimens of LEFM allow one to trace the crack-microstructure interaction over a long range of crack extension. Thus, the full potential of a ceramic to resist crack growth can be explored with a long crack R-curve. Some features of the fracture- (resistance-) behavior of Al_2O_3 and Mg-PSZ resulting from such crack propagation studies are discribed in the following two subsections, respectively.

3.2.1 Alumina

In pure alumina, R-curve behavior is more pronounced in coarse-grained than in fine-grained materials (Fig. 10). In summarizing the various R-curve results from different testing geometries and grain sizes, a general shape can be deduced, which is given by an initially rising curve that plateaus out after a certain crack extension. Note, that, in Fig. 10 the specimen size (w = 7 mm) was not large enough to exhibit a plateau-regime. A detailed analysis of the grain size dependence reveals an interesting behavior of the R-curves. Fine grained material starts from a notch tip with a higher initial resistance (R_o) than coarse grained Al_2O_3 but experiences almost no increase, unlike the coarse grained material. This crossing of R-curves, which is confirmed by recent work of Lawn and coworkers /18/, gave rise to some confusion in the past

when K_{IC} values determined from different testing geometries (e.g. SENB and DT) were compared. DT measurements determine the plateau regimes of R-curves /11/ and, therefore, the K_{IC} values so calculated are relatively high. Also, the grain size dependence is inverted compared to K_{IC}-experiments with crack instability in the initial part of an R-curve, e.g. short cracks in SENB.

Crack propagation studies also probe the severe differences in R-curve behavior between the two modes of microfracture (Fig. 11). Nearly pure, coarse-grained alumina fractures predominantly intergranularly and exhibits a steeply rising R-curve. However, the R-curve of a material comparable in grain size but with more glassy phase and transgranular microfracture, is comparatively shallow. Although both curves start at about the same R_o-level, they differ significantly in their slope.
The information gained from crack propagation studies in alumina strongly favour wake controlled crack tip shielding as the basic R-curve mechanism /19, 20/. Our current understanding may be summarized with the aid of the schematic model in Fig. 12. Alumina, due to anisotropy in the thermal expension coefficients, contains residual stresses between neighbouring grains. They depend on grain size and are large for pure coarse grained material. However, when a glassy grain boundary phase is present, the stresses are assumed to be lower. The residual stresses are relieved by the formation of a damage zone of microcracks which is triggered by the stress field of a macrocrack. The microcracks force the macrocrack to generate a rough, tortuous crack surface. In addition, the microcracks became unconstrained when the macrocrack advances, thus generating a layer of dilated material along the crack surfaces. The crack surface roughness and dilation give rise to frictional crack bridging effects which shield the crack tip from the external stresses. The maximum length of such a crack shielding wake zone is reached when the local crack opening displacement is larger than the interaction length of the bridging elements. A constant, steady state size of the wake zone, which obtains thereafter, corresponds with the plateau of the R-curve. In summary, it is important to note that both microstructural properties and crack/specimen geometries determine the actual shape of an R-curve. Quantitative details for the model of the R-curve behavior of Al_2O_3 are reported elsewhere, /17/.

3.2.2 MgO partially stabilized Zirconia

The effectiveness of transformation toughening, the major toughening mechanism in zirconia-containing ceramics, is manifest in the strong R-curve behavior of Mg-PSZ; with plateau toughnesses measured for long cracks of up to 18 MPa $\sqrt{m}$ /21/.

In Mg-PSZ, tetragonal precipitates transform in the crack tip stress field to monoclinic symmetry. The frontal transformation zone thus generated has no effect on the crack tip field /24/. However, upon crack extension, the constraint on the process zone unloads in the wake, giving rise to residual dilatation-associated stresses and crack shielding. A steady state level, which corresponds with the plateau regime of the R-curve, is only attained after substantial crack extension (2-3 mm in high toughness Mg-PSZ /21/).

In the simplified case of supercritical transformation, i.e. all particles within the transformation zone fully transform, the achieveable plateau toughness depends on the size (h) of the zone /23/. A Raman microprobe technique has been developed recently to measure h very accurately /24/ and the zone can be detected easily on polished surfaces (Fig. 13) due to the surface uplifting triggered by the dilatation accompaning the t-m transformation. Nevertheless an exact correlation between the microstructure, zone size, and the R-curve shape cannot be specified to date /1/ yet. Toughnening can be optimized by special heat treatments of Mg-PSZ. Again, crack propagation studies with R-curve measurement probe the effectiveness of a given heat treatment.

Results for a 9.7 mole % Mg-PSZ are shown in Figures 14 and 15. After solution annealing at 1700°C and rapid cooling, samples were annealed at 1400°C for various times up to 10 hours. Additionally, some samples were annealed at 1100°C for up to 2 hours. Figure 14 shows the change in the precipitate microstructure due to the 1400°C heat treatment. The subeutectoid, 1100°C annealing did not change the precipitate size.

The R-curves determined after annealing reveal substantial differences, not necessarily at the beginning (R_o-value), but, with increasing crack extension (Fig. 15).
The R-curve results indicate that, for the given Mg-PSZ, toughening is optimized by annealing at 1400°C followed by 1100°C. The toughness in such samples changes from K_R = 4 MPa $\sqrt{m}$ in the solution annealed material to $K_{plateau} \approx 12$ MPa $\sqrt{m}$ after the treatment.

4. R-curve behavior and strength

The crack propagation studies and R-curve results presented in the previous section are very useful for material development in terms of better understanding the basic mechanisms. However, the high toughness values often cited for modern structural ceramics, which correspond to the plateau of long-crack R-curves, are not really relevant for most structural applications. After failure of ceramic components, no fracture causing cracks of millimeters in length are observed usually. Typically, critical crack sizes are at least one order of magnitude smaller. In order to determine the strength-toughness relationship of ceramics, crack propagation studies should focus on failure relevant short cracks rather than long cracks.

To observe and analyse the propagation of short cracks, stable growth must be achieved. This is possible when R-curve behavior obtains, as was shown by using the energy balance in section 3.1.

To date, only few R-curve measurements for Al_2O_3 and Mg-PSZ with short, failure relevant surface cracks, are published. The short cracks either originated from indentation /12/ or initiated "naturally" on tensile surfaces of bend bars during increasing loading /25, 26/.

Figures 16 and 17 show surface cracks generated by stepwise loading of bend bars in coarse grained Al_2O_3 and high toughness ZrO_2, respectively. In both ceramics, "natural" surface cracks can grow from some tens of microns to several hundred microns. In order to calculate the toughness from such cracks, the crack

profile must be determined. Dye penetrant techniques indicate that the surface cracks are almost semi-circular in Al_2O_3, whereas, serial sectioning in Mg-PSZ reveals that the cracks advance much further at the surface compared to depth (ratio ≈ 5/1). With appropriate Y-functions, determined using the crack profile, K_R is determined in a straightforward manner from Eq. 1b.

The resulting short crack R-curves are plotted for comparison with those of long cracks in Figures 18 and 19.

The short crack R-curves start considerably lower in both ceramics and the plateau toughness level is not reached before instability. Unlike LEFM tests, where the long cracks are forced to initiate from a notch tip, the "natural" surface flaws originate from local heterogeneities, e.g. pores or larger grains. Often, more than one microcrack forms on the tensile surface. In this case, the one with the shallowest R-curve slope becomes unstable first. The fracture stress at instability corresponds to the bending strength as determined from fracture tests with low loading rates. Thus, under technically relevant loading conditions, specimens or components cannot utilize the full potential of R-curve behavior. Clearly, toughness or resistance data referring to the plateau of long crack measurements overestimate the values pertainent for application of a ceramic material.

5. Conclusions

The quasi-static, controlled crack propagation studies reported here enable one to characterize the fracture behavior of structural ceramics in more detail than one parameter descriptions. Furthermore, deeper insight into the correlation between microstructure and mechanical behavior is possible.

Long-crack fracture tests using the standard specimens of LEFM reveal if toughness (equivalent: crack resistance) is a material property constant or increases with crack extension (R-curve behavior). The full potential of a microstructure for toughnening is enabled.

However, for failure relevant fracture characterization and a better understanding of strength-toughness relationship, crack propagation studies have to focus on short cracks. In the case of pronounced R-curve behavior, stable crack growth of natural surface flaws can be achieved experimentally by stepwise loading. As the resulting R-curves are significantly lower than those from long cracks, it must be emphasized that long crack plateau toughness values, often quoted in literature, may overestimate the toughness applicable in components considerably.

Acknowledgements

The authors would like to thank M.J. Readey, A. Reichl, G. Mundry, K.K.O. Bär and G. Dransmann who contributed with their experimental work to the present paper. The R-curve research was funded by the German Research Association (DFG).

Literature

/1/ A.G. Evans, "Perspective on the Development of High-Toughness Ceramics", J. Am. Ceram. Soc., 73 [2] 187-206

/2/ S.W. Freiman, "Brittle Fracture of Ceramics", Ceramic Bulletin, Vol. 67, No. 2, 392-402 (1988)

/3/ T. Fujii and T. Nose, "Evaluation of Fracture Toughness for Ceramic Materials", IJIS International, Vol. 29, No. 9, 717-725 (1989)

/4/ R.O. Ritchie, "Mechanismus of Fatigue Crack Propagation in Metals, Ceramics and Composites: Role of Crack tip Shielding", Mat. Sci. Engng., A 103, 15-28 (1988

/5/ D. Broek, "Elementary Engineering Fracture Mechanics", Noordhoff International Publishing, Leyden (1974)

/6/ Jahrbuch "Technische Keramik", Vulkan Verlag, Essen, (1988)

/7/ C. Mattheck, P. Morawietz, D. Munz, "Stress Intensity Factor at the Surface and at the Deepest Point of a Semi-elliptical Surface Crack in Plates and Stress Gradients", Int. J. Fracture, 23, 201-212 (1983)

/8/ DIA Research Institute, "Advanced Engineering Ceramics - Technology in Japan", Tokyo, July (1987)

/9/ D.J. Green, R.H.J. Hannik, M.V. Swain, "Transformation Toughening of Ceramics" CRC Press, Boca Raton (1989)

/10/ A.H. Heuer, "Transformation Toughening of ZrO_2-Containing Ceramics", J. Am. Ceram. Soc., 70 [10] 689-698 (1987)

/11/ F. Deuerler, R. Knehans and R.W. Steinbrech, "Testing-Methods and Crack Resistance Behavior of Al_2O_3", J. de Physique C1 [2] 617-620 (1986)

/12/ R.F. Cook, C.J. Fairbanks, B.R. Lawn and Y.W. Mai, "Crack Resistance by Interfacial Bridging: Its Role in Determining Strength Characteristics" J. Mater. Res. 2 [3] 345-356 (1987)

/13/ John J. Mecholsky, Jr., "Engineering Research Needs at Advanced Ceramics and Ceramic-Matrix Composites", Ceram. Bull. 68 [2] 367-75 (1989)

/14/ Minoru Taya and Richard J. Arsenault "Metal Matrix Composites - Thermomechanical Behavior", Pergamon Press, Oxford, England (1989)

/15/ A.G. Atkins and Y.W. Mai, "Elastic and Plastic Fracture", Ellis Horwood Limited, Chichester, England (1985)

/16/ R. Warren and B. Johannesson "Creation of Stable Cracks in Hardmetals Using Bridge Indentation", Powder Metallurgy 27 [1] 25-29 (1984)

/17/ H. Nickel and R.W. Steinbrech, Editors, "Mikrobruchvorgänge in Al_2O_3-Keramik", Abschlußkolloquium DFG-Forschungsvorhaben, KFA-Jülich (1990), Proceedings in print.

/18/ R.W. Steinbrech, E. Inghels, A.H. Heuer, "Residual Displacement Effects During Crack Propagation in High Toughness Mg-PSZ", J. Am. Ceram. Soc., in print

/19/ R. Knehans and R.W. Steinbrech, "Memory Effect of Crack Resistance during Slow Crack Growth in Notched Al_2O_3 Bend Specimens", J. Mat. Sci. Letter, 1, 327-329 (1982)

/20/ Y.W. Mai and B. R. Lawn, "Crack-Interface Grain Bridging as a Fracture Resistance Mechanism in Ceramics: II, Theoretical Fracture Mechanics Model", J. Am. Ceram. Soc., 70 [4] 289-294 (1987)

/21/ A.H. Heuer, M.J. Readey and R.W. Steinbrech, "Resistance Curve Behavior of Supertough MgO-Partially-stabilized ZrO_2", Mat. Sci. Engng. A 105/106, 83-89 (1988)

/22/ R.M. McMecking and A.G. Evans, "Mechanics of Transformation Toughening in Brittle Materials", J. Am. Ceram. Sco 65 [5] 242-47 (1982)

/23/ A.G. Evans and R.M. Cannon, "Toughening of Brittle Solids by Martensitic Transformations", Acta Metall. 34 [5] 761-800 (1986)

/24/ R. Dauskardt, D.K. Veirs and R.O. Ritchie, "Spatially Resolved Raman Spectroscopy Study of Transformed Zones in Magnesia-Partially-Stabilized Zirconia", J. Am. Ceram. Soc., 72, [7] 1124-30 (1989)

/25/ D.B. Marshall and M.V. Swain, "Crack-Resistance Curves in Magnesia Partially Stabilized Zirconia", J. Am. Ceram. Soc., 71 [6] 399-407 (1988)

/26/ O. Schmenkel and R.W. Steinbrech, "Crack-Resistance Curves of Surface Cracks in Alumina", J. Am. Ceram. Soc. 71 [5] C-271-273 (1988)

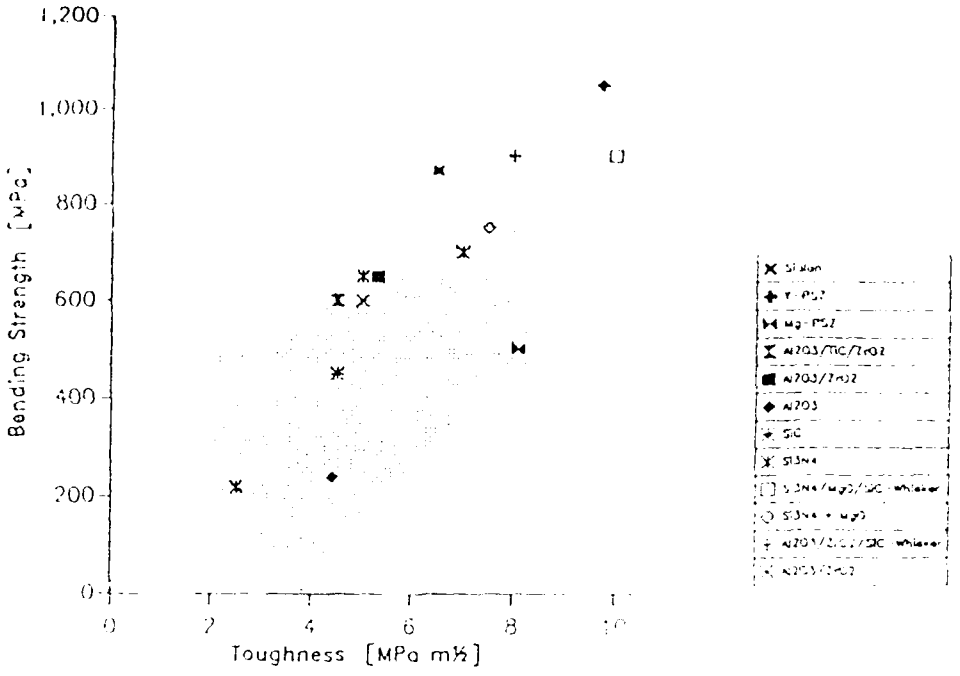

Fig. 1: Strength and toughness of commercial ceramics. Data from /6/

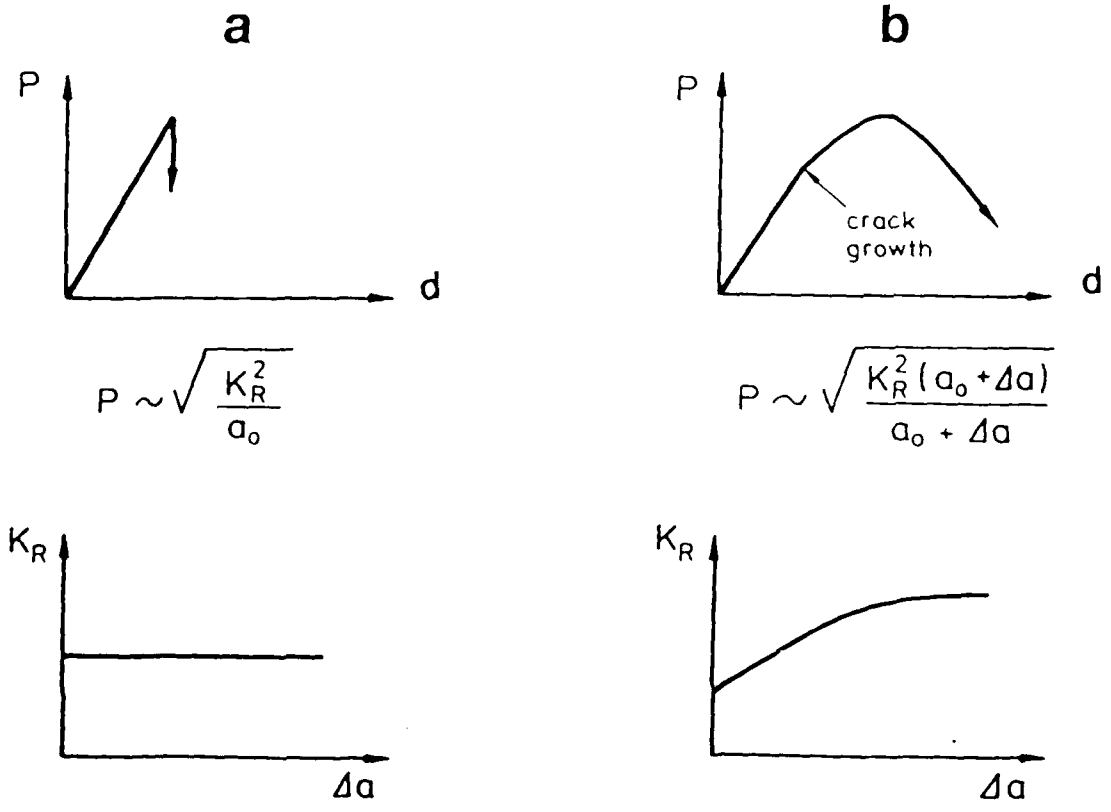

Fig. 2: Loading responses for different crack resistance behaviors (schematic) a) constant toughness b) increasing toughness (R-curve)

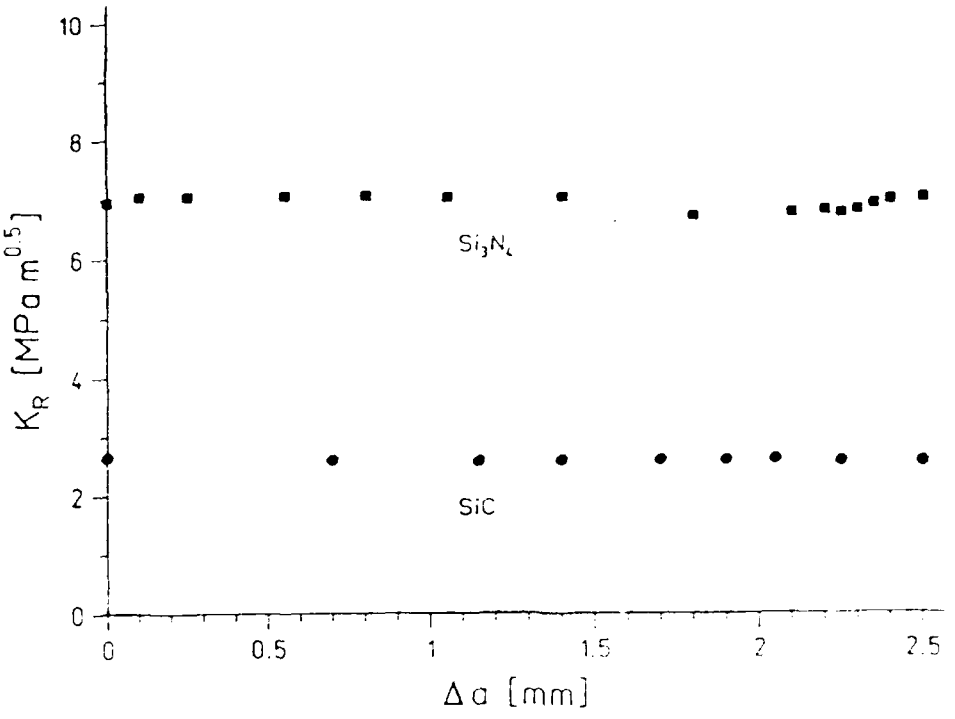

Fig. 3: Resistance behavior of SiC and Si_3N_4

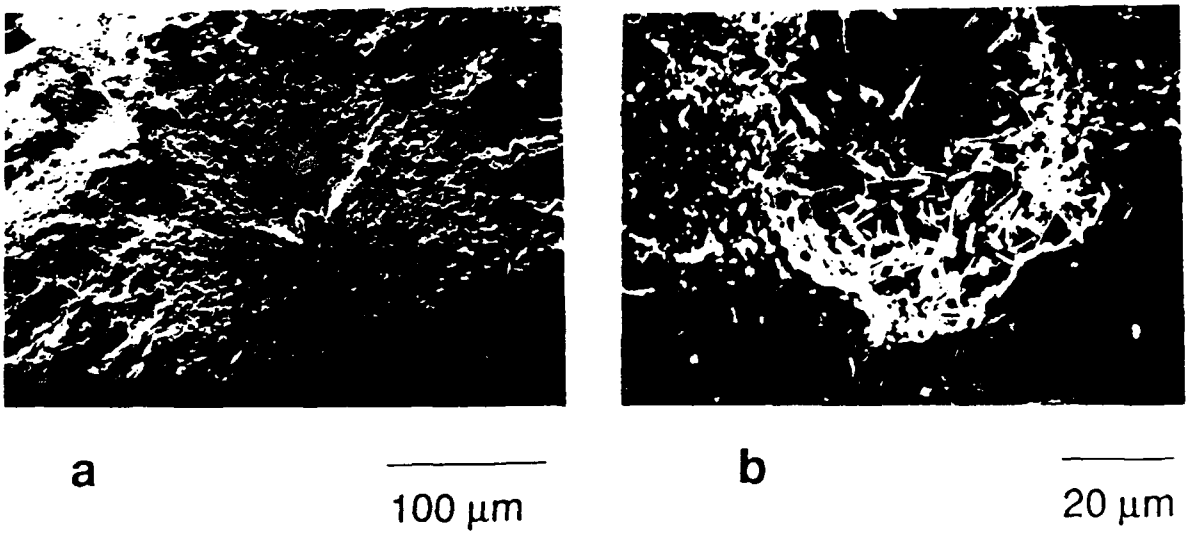

Fig. 4: Critical defects for fine grained non-oxide ceramics
a) graphite inclusion in HIP-SiC
b) pore in Si_3N_4

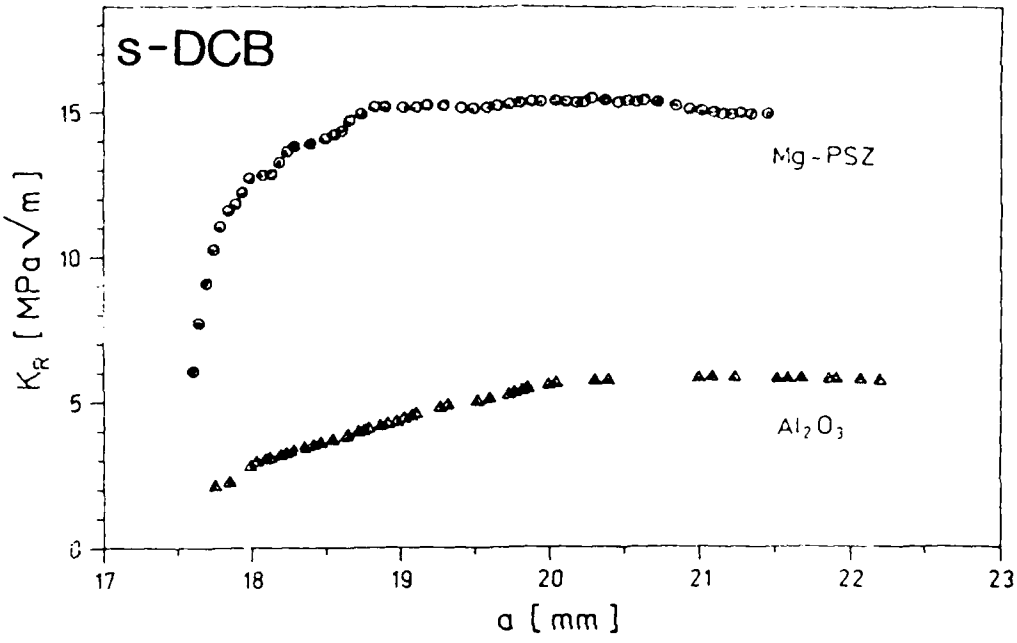

Fig. 5: R-curves of MgO-partially stabilized ZrO_2 and Al_2O_3

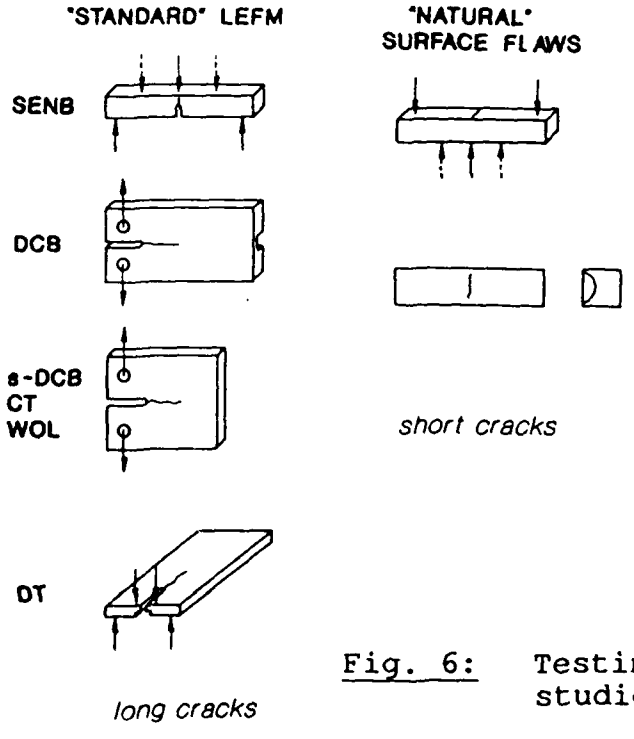

Fig. 6: Testing geometries for propagation studies of long and short cracks

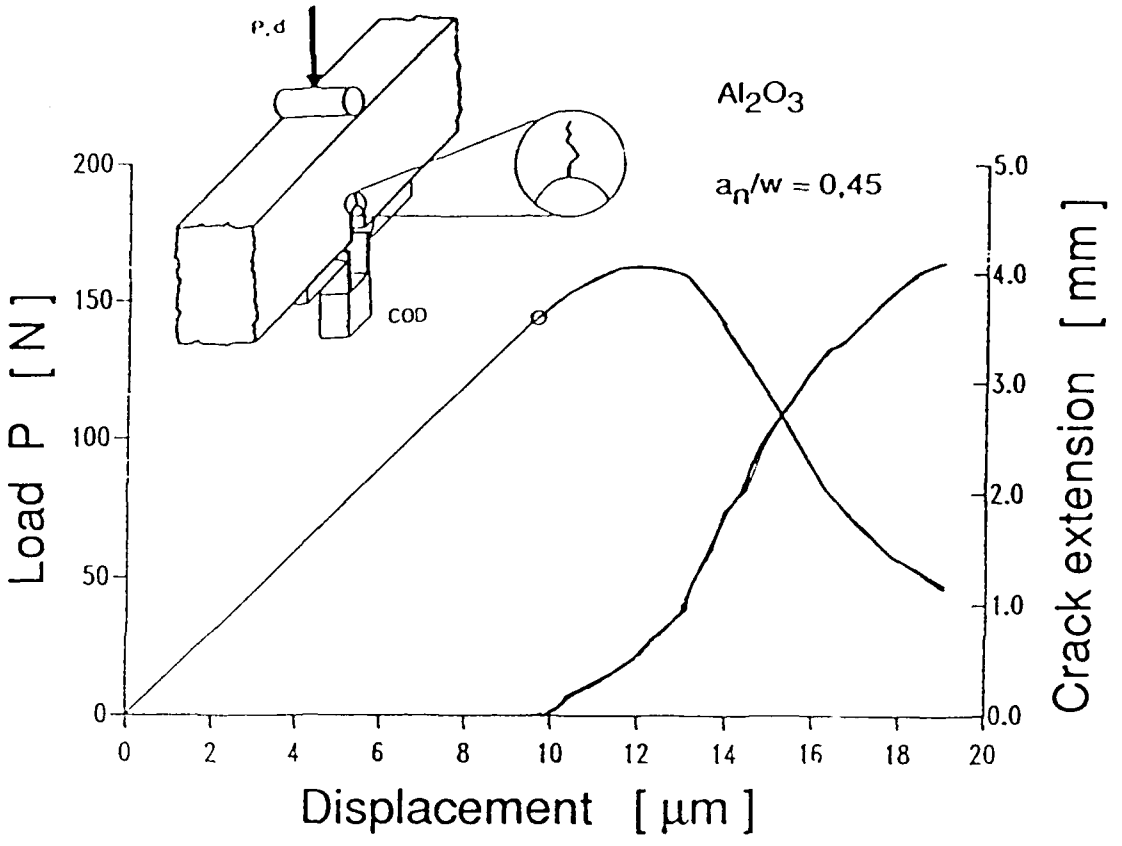

Fig. 7: Experimental technique used for crack propagation studies. Simultaneous measurement of load, load-point displacement and crack length (with travelling microscope)

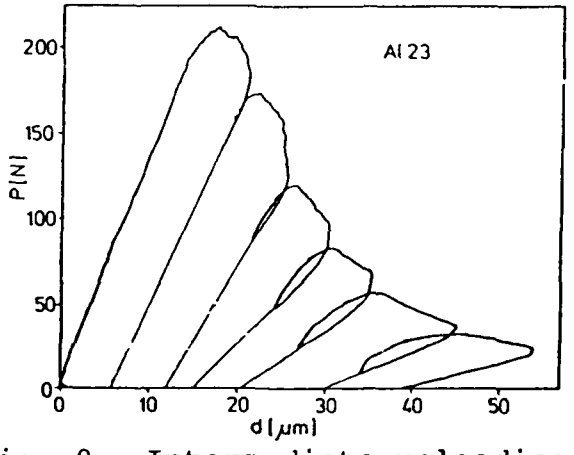

Fig. 8: Intermediate unloading-loading sequences in Al_2O_3

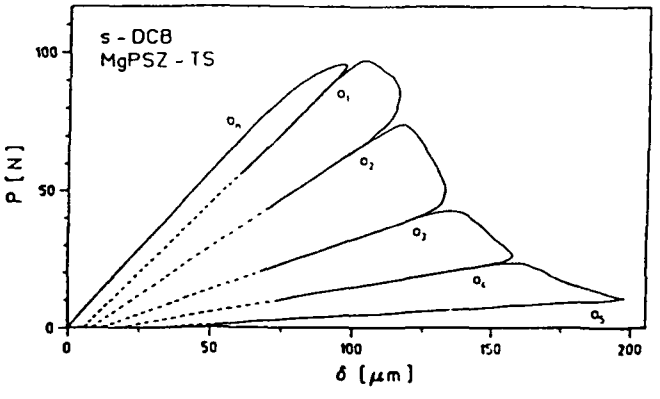

Fig. 9: Intermediate unloading-loading sequences in Mg-PSZ

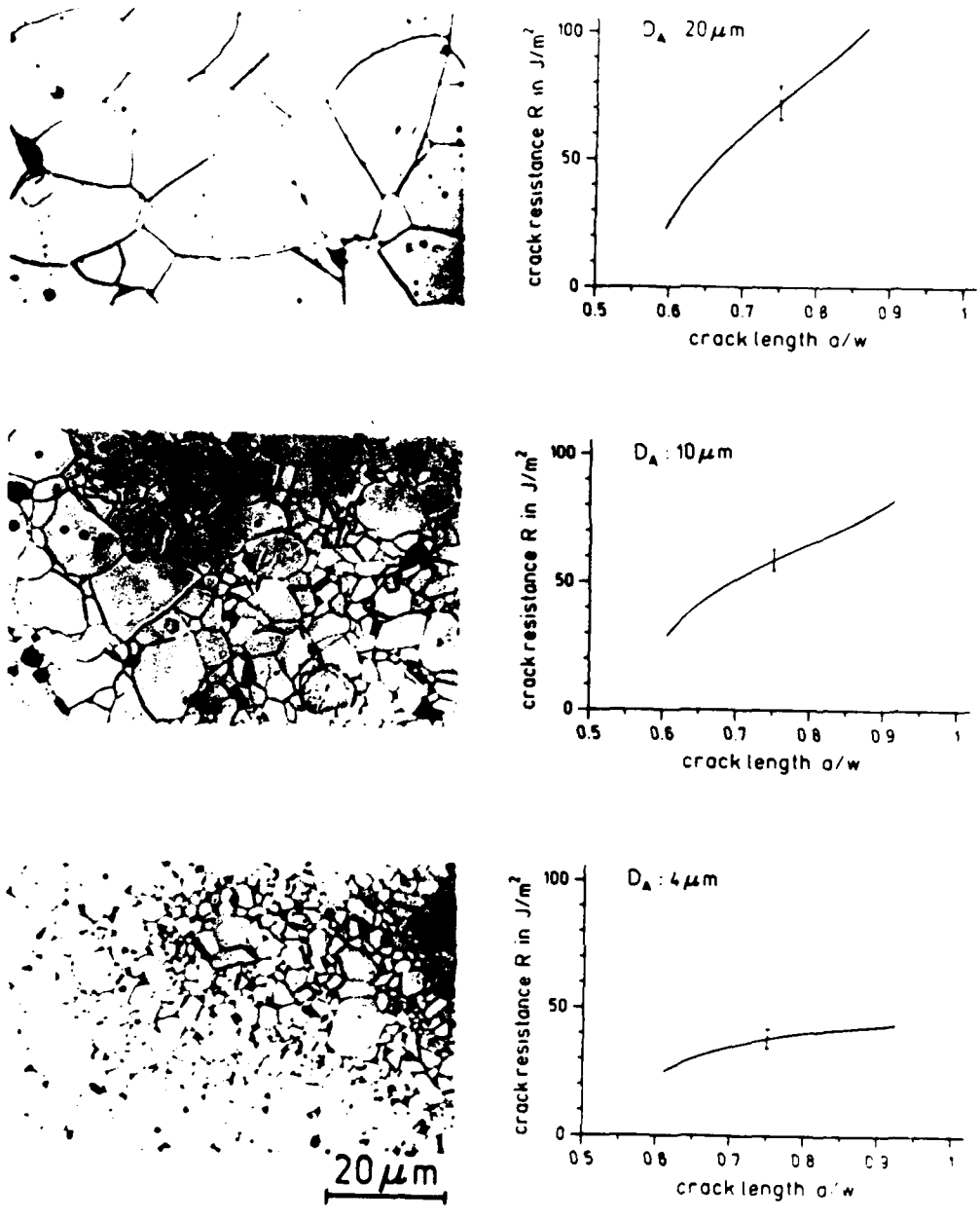

Fig. 10: R-curve behavior of long cracks in Al_2O_3. Intergranular SENB geometry microfracture.

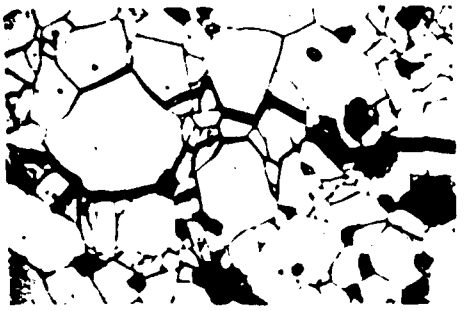

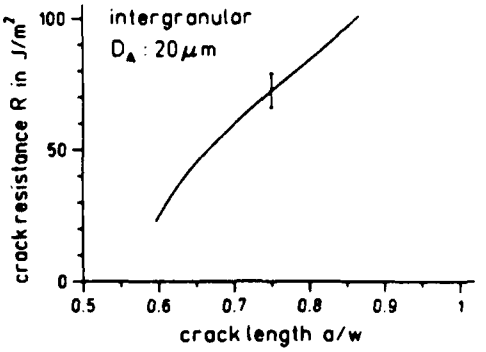

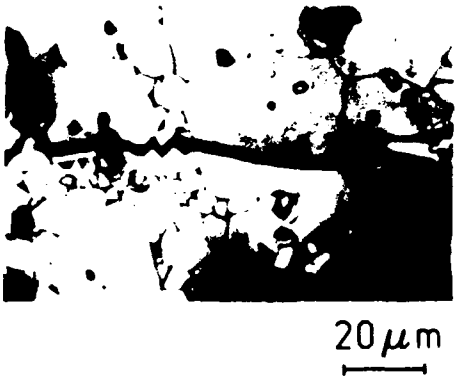

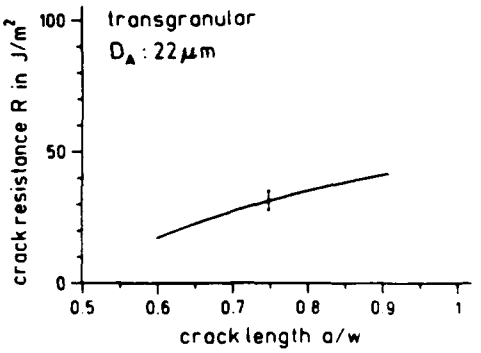

Fig. 11: Influence in mode (transgranular vs. intergranular) of microfracture on R-curve behavior

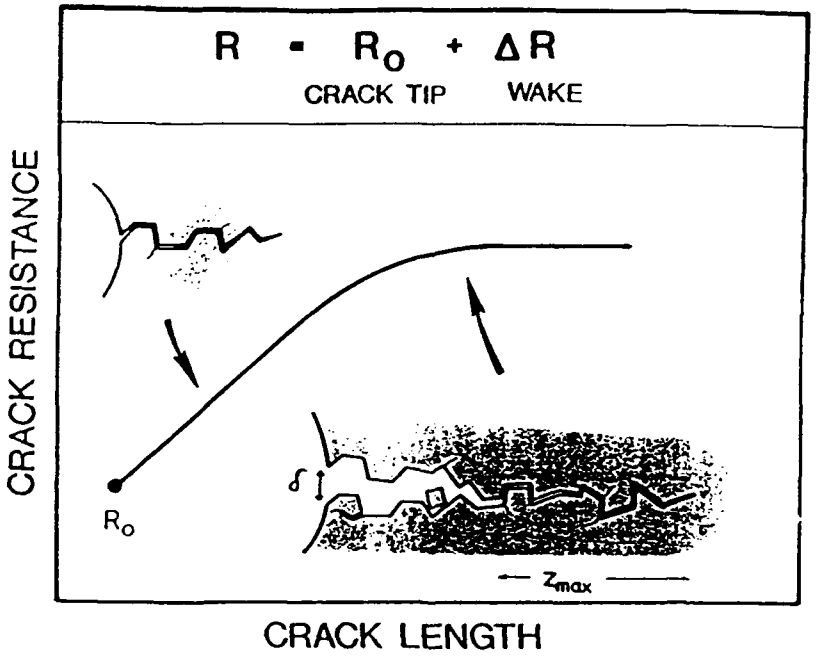

Fig. 12: Qualitative model of R-curve behavior in Al_2O_3

Fig. 13: Surface uplifting (between arrows) showing the transformation zone around crack in Mg-PSZ. The zone between the notch and first arrow was annealed out at 1000°C after precracking

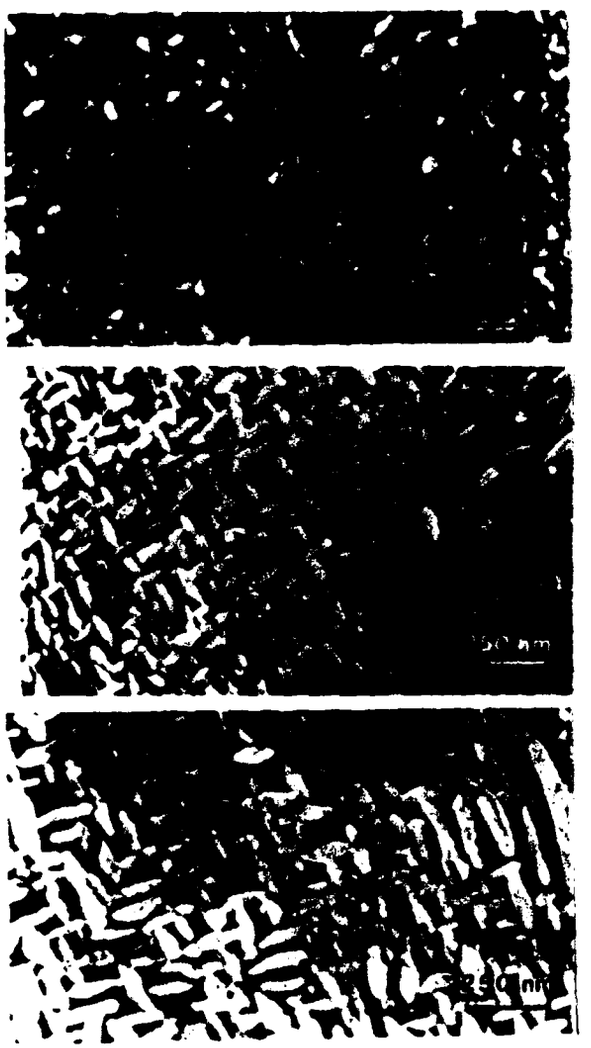

Fig. 14:
Aging of Mg-PSZ precipitates at 1400°C
a) solution annealed
b) 2 h
c) 10 h
SEM-micrographs from etched fracture surfaces

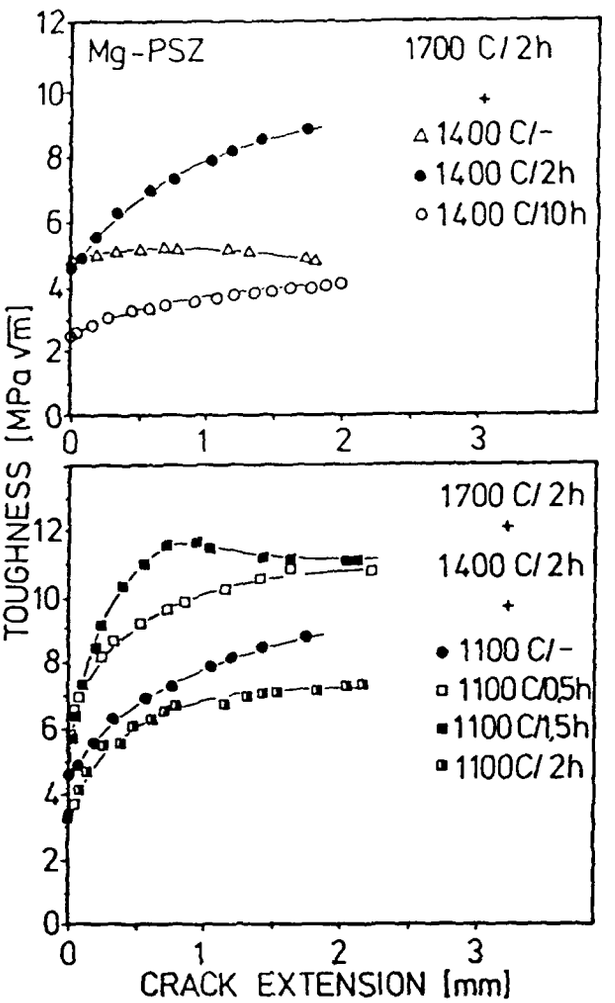

Fig. 15:
Influence of heat treatment on R-curve behavior of Mg-PSZ

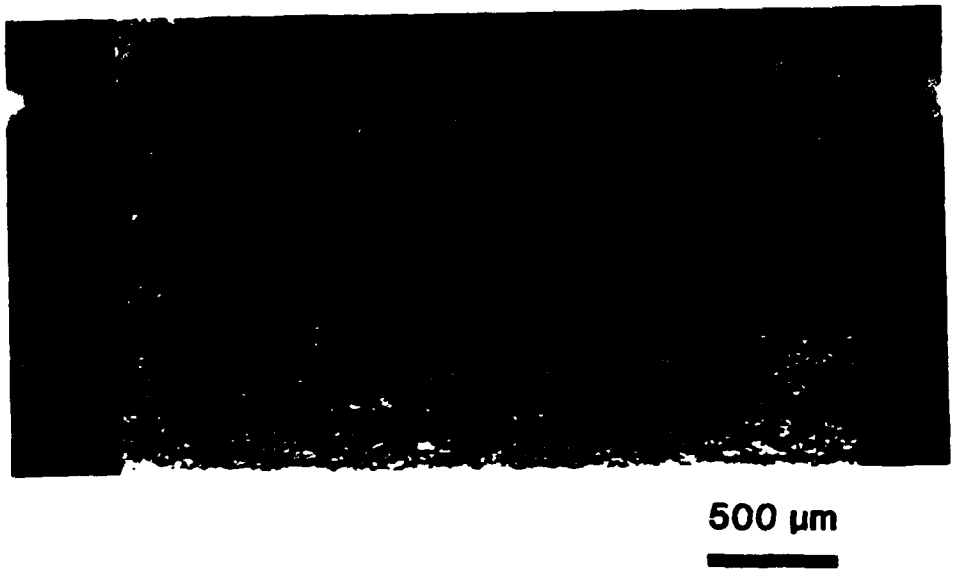

▲ Fig. 17: Surface crack in Mg-PSZ

◀ Fig. 16: Surface crack in Al_2O_3. Micrograph contrast due to oblique illumination

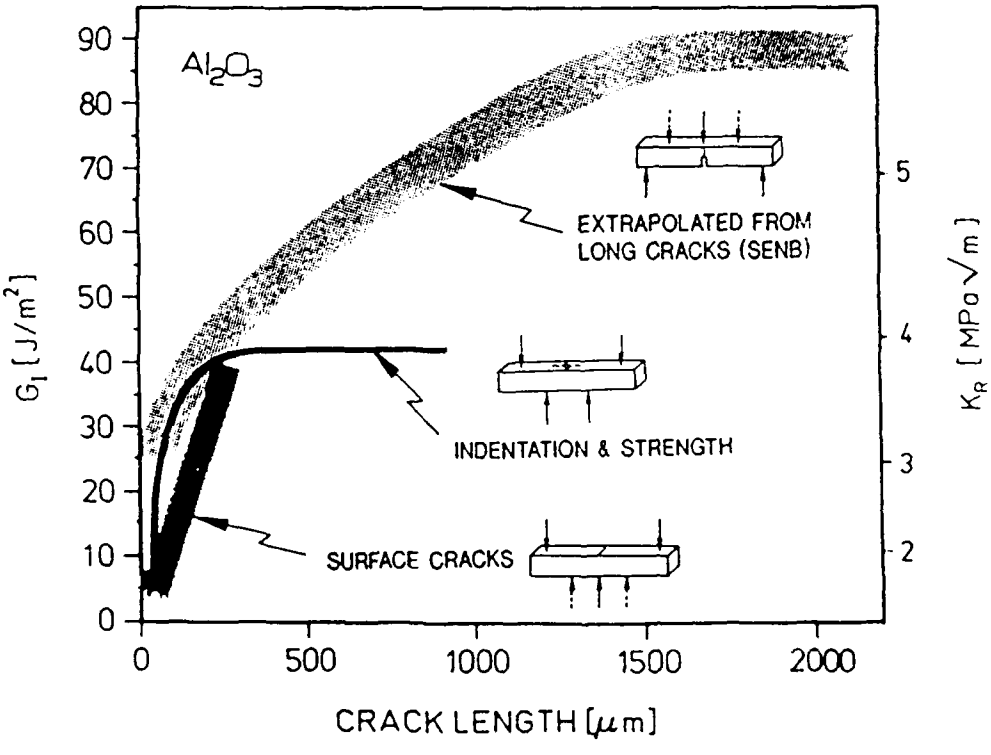

Fig. 18: Comparison of short and long crack R-curve behavior in Al_2O_3. Data for indentation and strength method from /12/

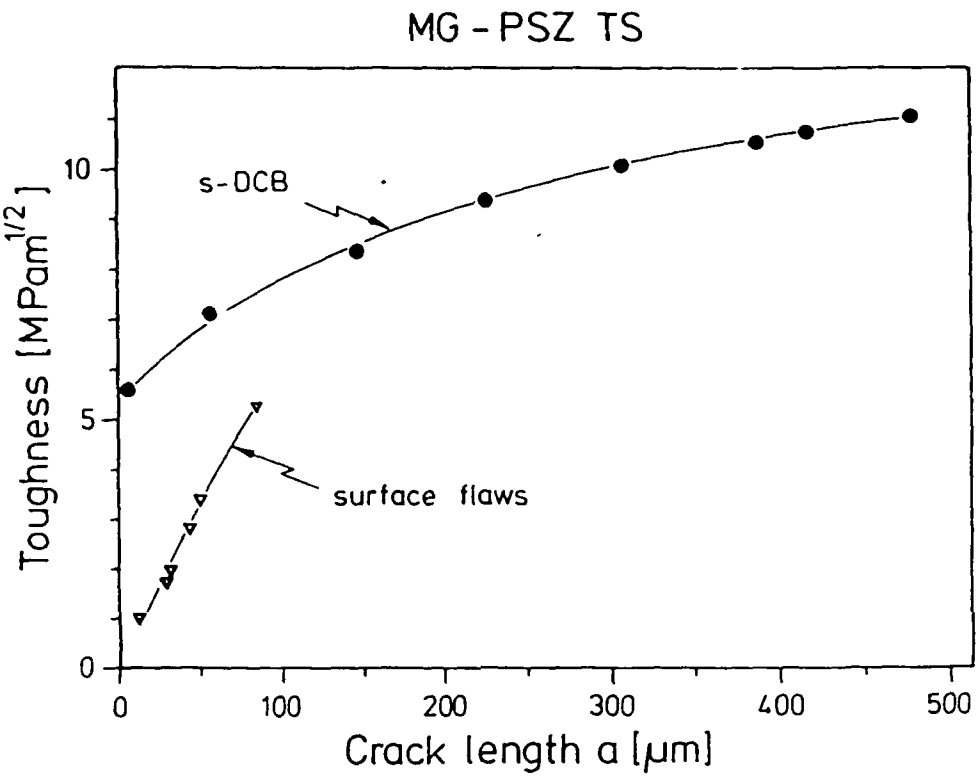

Fig. 19: Comparison of short and long crack R-curve behavior in Mg-PSZ

A REVIEW OF EXPERIMENTAL METHODS TO ASSESS DAMAGE DURING FRACTURE OF ROCK, CONCRETE AND REINFORCED COMPOSITES

Hideaki Takahashi
Research Institute for Fracture Technology
Faculty of Engineering, Tohoku University
Aramaki Aoba, Aobaku
Sendai/980, Japan

ABSTRACT. For quasi-brittle materials like rock, concrete and their composites it is usually adopted that a term of fracture process zone is used as a measure of fracture damage during loading. To assess the fracture damage quantitatively, a significance of acoustic emission and ultrasonic testing have been reviewed.

1. Introduction

For quasi-brittle materials like rock, concrete and advanced cementitious composites it is usually accepted that a term of fracture process zone is commonly used as a measure of fracture damage during loading. However, no physically reasonable explanation of fracture process zone is not made uptil now, because there is no experimental technique to characterize formation and extension of the fracture process zone quantitatively. To investigate the fracture process at the microscopic level, three kinds of NDE methods have been currently developed at Tohoku University. These three techniques are photoelastic coating method, acoustic emission rating method and ultrasonic time difference method. The detail of these techniques are described in Refs [1-5, 8].

2. Intense Microcracking and its Observation by Photo-elastic Coating Technique [1]

2-1. Materials and Photoelastic Coating Technique

The materials examined in this study are rock (a granite with an average grain diameter of 1.3 mm), graphite (a nuclear-grade graphite designated PGX) and mortar. The compositions and mechanical properties of these materials are shown in Table 1.

Rectangular bend specimens (100 x 30 x 28 mm) were cut using a diamond wheel saw. A notch with a root radius of 50 μm was machined into each test specimen.

A transparent ferroelectric ceramic, $(Pb_{0.91}, La_{0.09})(Zr_{0.64}, Ti_{0.34})O_3$ was used as a photoelastic-coating material (designated PLZT).

TABLE 1—COMPOSITION AND MECHANICAL PROPERTIES OF THE MATERIALS USED

Material	Composition	Young's Modulus E (GPa)	Tensile Strength σ_{ult} (MPa)	Fracture Toughness J_{Ic} (J/m²)	$K_{Ic} = \sqrt{E J_{Ic}}$ (MPa m$^{1/2}$)
Granite	Quartz (38 percent), Feldspar (56 percent), Mica (6 percent) average grain size: 1.3 mm	19.4	3.6	68.0	1.15
Graphite	Coke (70 percent), Binder (Pitch) (30 percent) max. grain size of coke: 1.0 mm	6.0	7.2	72.0	0.66
Mortar	Cement (42 percent), Sand (42 percent), Water (16 percent) max. grain size of sand: 2.5 mm	40.4	3.2	11.5	0.68

The material was obtained in the form of a circular disk, 50-cm diameter and 10-mm thick. Thin sections of the PLZT were cut from the disk. The foil thickness was in the range 110-150μm. For light-reflection purposes, an optical mirror was formed on one plane of the ceramic plate by evaporation of chromium. The prepared thin foil was glued with cyanoacrylate to the surface of the three-point-bend specimens. A load frame was designed to permit the specimen to be loaded by high compliance springs on the stage of a polarizing microscope.

Fracture-toughness tests were conducted on the three materials according to the ASTM standard test method using an Instron testing machine. Single-edge-notch specimens were tested in three-point bending.

The averaged load versus J-integral relationship obtained from fracture-toughness tests was used as a calibration to determine the load levels of specimens tested for strain-field observation in terms of J.

The calibration-test for the PLZT was carried out in terms of the relationship between the birefringence Δn and principal-strain difference Δ_ε.

The photoelastic sensitivity of the PLZT, defined as $\Delta n/\Delta_\varepsilon$ is 1.75, which is two or three orders of magnitude higher than common photoelastic-coating materials such as epoxy and Araldite.

2-2. Results and Discussions

Typical test records of load versus load-line displacement (P-V_L) are given in Fig. 1. The three materials exhibit different amounts of nonlinear deformation. The ratio of the secant specimen compliance at peak load to the initial compliance, Csec/Cini, can be taken as a measure of the degree of the nonlinearity (see Fig. 1). The ratio values are 2.22, 1.90, and 2.88 for mortar, graphite, and granite, respectively, indicating that the granite has the highest nonlinearity of deformation.

An example of the interference fringe pattern formed around the notch tip is illustrated for the granite in Fig. 2. The principal-strain difference is determined from the fringe observation using the calibration diagram. Figure 3 shows the distribution of the principal-strain difference along the notch plane at various load levels, where r is the distance from the notch tip, and the J integral is chosen to indicate the load conditions. It is noted that the fringe shape around the notch tip and the strain distribution shown in Figs. 2 and 3 are

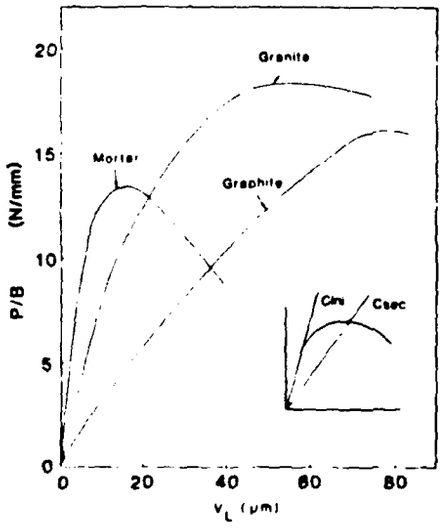

Fig. 1 Load P versus load-line displacement V_L; load is divided by the specimen thickness B

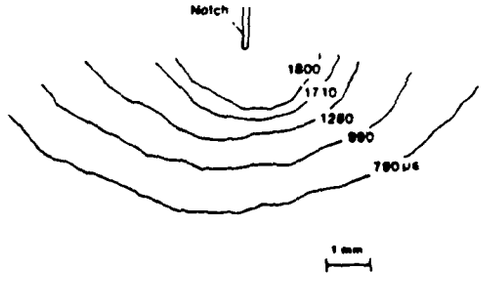

Fig. 2 Sketch of the interference pattern for granite

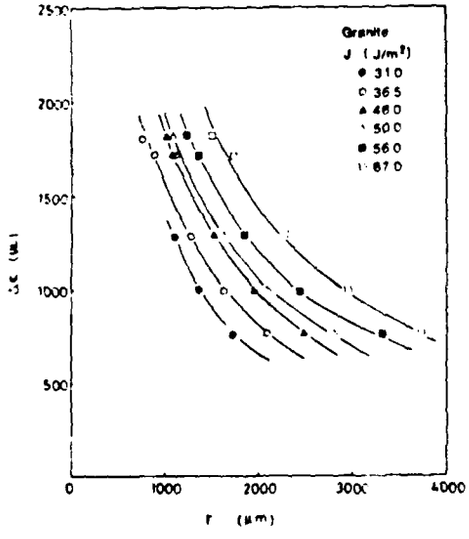

Fig. 3 Notch-tip strain distribution for granite

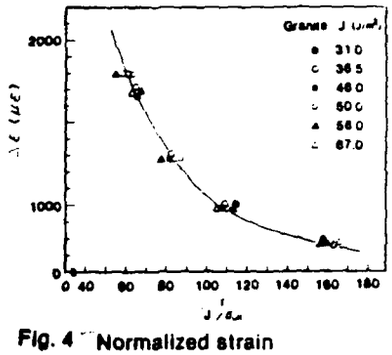

Fig. 4 Normalized strain distribution for granite

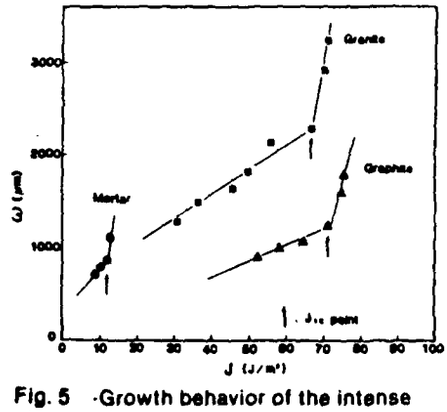

Fig. 5 Growth behavior of the intense microcrack zone

quite different from that observed for linear-elastic materials. The deviation from linear-elastic-deformation behavior is considered to be due to the formation of an extensive microcrack zone ahead of the notch tip.

In order to characterize the strain field within the intense microcrack region, the principal strain difference under several different load conditions is plotted against the nondimensional distance in Fig. 4, where the distance from the notch tip is normalized by the length parameter J/σ_{ult}. It is noted tha the strain distribution around the notch tip is well characterized by the J integral, irrespective of load levels, and the logarithmic plot leads to the following empirical relation.

$$\Delta\epsilon = \Delta\epsilon_0[(J/\sigma_{ult})/r]^m$$

where $\Delta\epsilon_0$ and m are material constants. Looking at the normalized strain distribution, we see that the value of m is close to 1.0 for the three materials, and thus the principal-strain difference ahead of the notch tip has the singularity of r^{-1}, equivalent to that of perfectly rigid plastic materials.

We now examine the extension behavior of the intense microcrack region. Here the length of intense microcrack region ω is taken as the distance from the notch tip where the principal-strain difference exceeds 760 $\mu\varepsilon$. Figure 5 shows the development of the intense microcrack region ω as a function of J. The intense microcrack region increases linearly with increasing J integral at low load levels. Note that the intense microcrack region extends rapidly with increasing load at the point indicated by an arrow. The abrupt increase in ω is interpreted to be due to the effect of macroscopic crack growth. In this study, the J-integral value at the knee point is defined as the critical J-integral value at the onset of macroscopi crack growth, and it is denoted by J_{IC}.

As described above, the crack-tip strain fields in the brittle-microcracking materials show the singularity of r^{-1}, unlike the strain field expressed by the stress-intensity factor K. From this observation the J integral was selected to characterize the strain fields in this study. The fact that the crack-tip strain field and the extension behavior of the intense microcrack region can be characterized by the J-integral supports the use of the J_{IC} criterion for a valid measure of the fracture toughness for these materials.

3. AE Evaluation of Fracture Damage in Rock and Concrete

3-1. Acoustic Emission Characteristics and Determination of Fracture Toughness Evaluation Point in Rock [2, 3]

The load versus displacement record ($P-V_L$) is shown in Fig. 6 for a

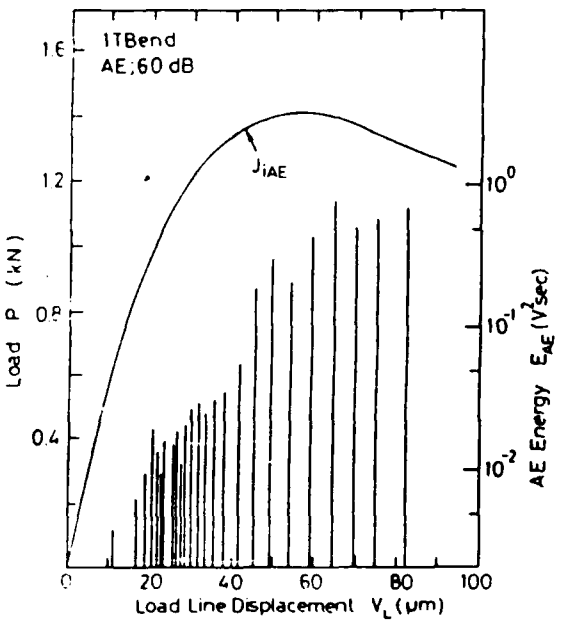

Fig. 6 P-V_L curve and AE behavior

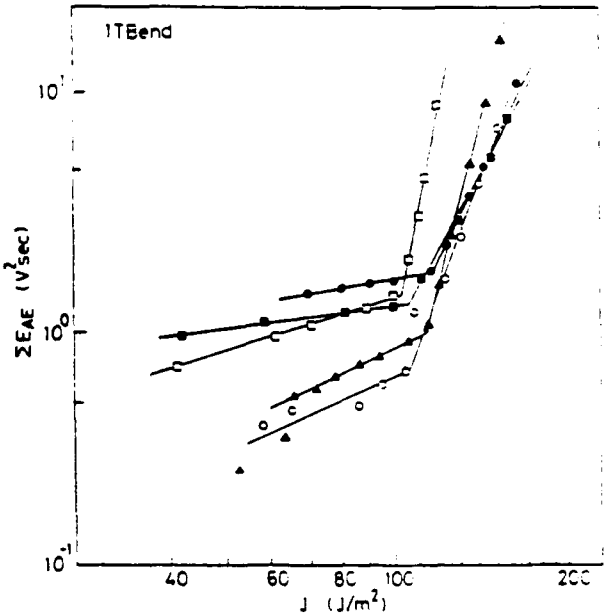

Fig. 7 Accumulated AE energy VS J

small three point bend specimen (1TBend). The granite exhibits significant nonlinear deformation behavior well below the maximum load. The energy of the AE signal, E_{AE} for a 10 s interval at various stage of the bending test is plotted against the load-line displacement. AE signals are detected at early load level. The onset of AE occurs approximately at the load level at which the load-displacement curve becomes nonlinear. The AE activity increases with increasing load and a number of AE signals are emitted prior to the maximum load point. It can be considered from the AE behavior that the development of numberous microcracks around the initial notch tip precedes the macrocrack propagation in the rock. In order to correlate the AE behavior with the fracture process, the E_{AE} was summed with respect to load level, and the accumulated AE energy ΣE_{AE} is shown as a function of J-integral value in Fig. 7. The ΣE_{AE}-J curve can be divided into two regions. The first region, of lower slope, denotes the microcracking with little acoustic activity. The second region of the curve has a high value of slope, and consists of AE events of much higher amplitude than those detected earlier in the test.

To study the correspondence of the AE characteristics shown in Fig. 7 with the microfracture process at the crack tip spectral analyses of AE signals and microscopic observations at the notch tip were made. It is known that the measurement of the frequency spectrum of AE signals enables the identification and separation of individual sources of AE events. The spectral analyses were made on recorded AE signals and the variation in frequency content of the AE signals with respect to load level was examined. The results showed that AE signals observed during the tests can be classified into two groups, type I and II. This

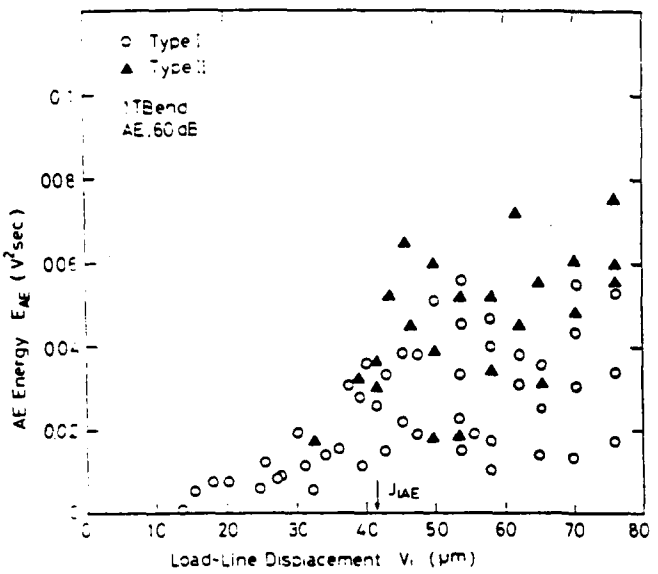

Fig. 8 Emission pattern of the classified AE events

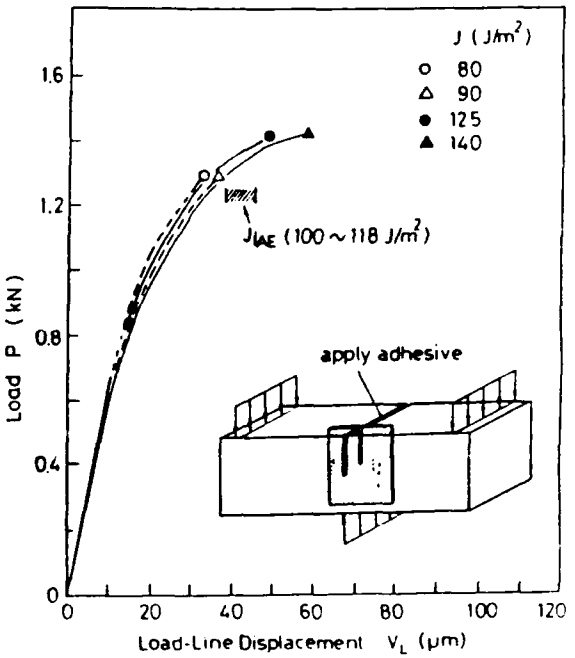

Fig. 9 P-V_L curves for the specimen used for microscopic observation

classification is made on the basis of the difference in low frequency content of AE signal. AE signals of the type II has a predominantly low frequency content in the audible range compared to the type I signal. Peak amplitude of the type II signal is observed to be generally larger than that of the type I. In Fig. 8 is shown the load level at which the classified individual AE event was detected during three-point bend test of the specimen. AE signals of type I with small peak amplitude are emitted at the early loading stage, and then the type II signals start to appear as the load is further increased. The occurrence rates of type I and II signal are seen to be approximately the same after the maximum load level. Similar trend in the emission behaviors has been observed for other tests. It is noted that the abrupt increase in the activity of type II signal corresponds to the knee point as shown in Fig. 8.

Microscopic observations of the notch tip region was made using thin sections prepared as follows. Four three-point bend specimens with identical dimensions(1TBend) were tested for this observation. As shown in Fig. 9 two specimens were loaded to just beyond the load level which corresponds to the J_{iAE} point, and the loads just below the J_{iAE} level were applied to the remaining specimens. The predetermined load was applied to the inverted specimen in such a manner that the precrack mouth was located at the top, and maintained while adhesive (cyanoacrylate) was injected to fix the local opening of fractured zone. After the adhesive was cured the specimen were unloaded. The loaded specimen were sliced off in sections normal to the notch plane, polished and thinned to a thickness of about 20 μm. The thin section was then examined under a polarizing microscope. No crack initiation was identified up to the loading stage of J = 90 J/m^2 , although some

microcracks were observed around the notch tips. However, when the load was further increased to just above the J_{iAE} point crack growth was found to occur from the notch tip throughout the specimen thickness. Based on the observations of the present study, the microfracture processes in the rock can be summarized as follows. On loading the prenotch, a few isolated microcracks are formed due to the heterogeneous nature of rock. On further loading the intensity of microcracking increases and deformation behavior around the crack tip region becomes nonlinear. Finally, macrocrack extension occurs because of the coalescence of microcracks in the nonlinear zone. The acoustic emission characteristics observed in the present experiments support the general picture of the microcrack-controlled fracture processes described above.

Let us discuss the source mechanisms of the classified AE events. The sequence in occurrence of type I and II signals suggests that the emission of type I signal is associated with the formation of microcrack. The coalescence of microcracks is expected to generate elastic stress waves having larger energy since the remaining ligament between microcracks possesses stronger linkage than the neighboring microcrack sites. Hence the intensive microcrack coalescence can be considered to produce the AE signal of type II. The critical event for macroscopic crack growth is the intensive coalescence of microcracks and linkage with the prenotch tip throughout the specimen thickness. We can say that the abrupt increase in the type II activity can pinpoint the critical stage of the notch tip region, and thereby the acoustic emission characteristics as shown in Fig. 7 is used to determine the fracture toughness evaluation point. The J-integral value corresponding to the knee point is hereater called J_{iAE}.

3-2. Effect of Concrete Strength on AE Behavior [4]

Concretes having different compressive strength have been tested in this study. The mix proportions are given in Table 2. Normal Portland Cement was used for all specimens. The maximum size of the coarse aggregate was approximately 20 mm. Water/cement ratio and

Table 2 **Mix proportions of Concretes**

sample	W/C (%)	s/a* (%)	unit weight (kg/m³) water	cement	sand	gravel	silica -fume	w.r.a.** (cc)
A	60	42	188	313	721	1006	0	0
B	47	42	160	340	721	1006	60	12.1
C	25	42	111	444	721	1006	111	41.2

* s : sand, a : sand + aggregate
** w.r.a. : water reducing agent

Table 3 Specimens dimensions of SR, CT and 3PB specimens

specimen	loading configuration	a_o (mm)	W (mm)	B (mm)	Bn (mm)	Ws (mm)	L (mm)	S* (mm)
SR	wedge splitting	90	170	100	60	2	-	-
SR	wedge splitting	105	170	100	60	2	-	-
CT	tension	40	100	100	60	5	-	-
CT	tension	50	100	100	60	5	-	-
CT	tension	60	100	100	60	5	-	-
3PB	bending	50	100	100	-	-	840	780

* S : span

contents of cement and silica-fume were controlled to obtain different strengths. In order to fix the slump, furthermore, water-reducing agent was added into high-strength concrete (B) and very high-strength concrete (C). Each mixture was cast in the rectangular mold for 3 PB specimen and in cylinder mold for SR specimen. All specimens were cured together with the same condition (wet curing). The tests were carried out in wet state on the twenty-eight days of curing time. The average compressive strengths at this curing time were approximately 30, 60 and 95 MPa, respectively.

The geometry of the SR specimen tested is used, together with those of two rectangular specimens; CT and 3PB. The length-to-diameter ratio is set to be the same as that of the conventional compressive test specimen. The specimen dimensions are listed in Table 3. An artificial notch with width of 2 mm was machined into each specimen using a diamond wheel saw. CT specimens were made from remaining halves of tested 3PB specimen.

The wedge splitting method was employed for fracture tests of SR specimens. The load was transmitted to the specimen by means of a wedge and roller bearings. The two roller bearings are fixed to a load box, which was placed on the top of the sample. A clip-gage was located across the load application points, and used to measure and control load-line displacement during tests.

AE signal were classified into eight threshold levels according to the amplitude. AE event distributions plotted on load versus load-line displacement curve of CT test are shown in Fig. 10. In all specimens, the AE occurrence started below the maximum load and continued beyond the maximum load. AE activity during the softening process shows the clear tendency to increase with increasing strength. It can be considered that AE signal was caused by nucleation and propagation of microcrack.

The evidence suggests that a following AE parameter, high energy AE ratio, Rn, can be used as a measure of microfracture resistance.

$$Rn = \frac{\Sigma N_{RI\text{-}AE}}{\Sigma N_{AE}}$$

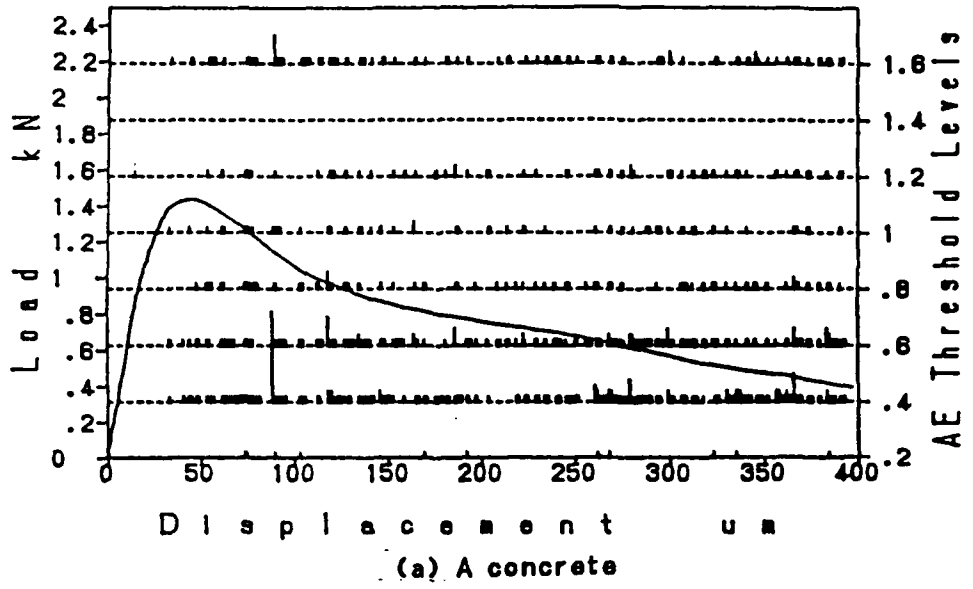

(a) A concrete

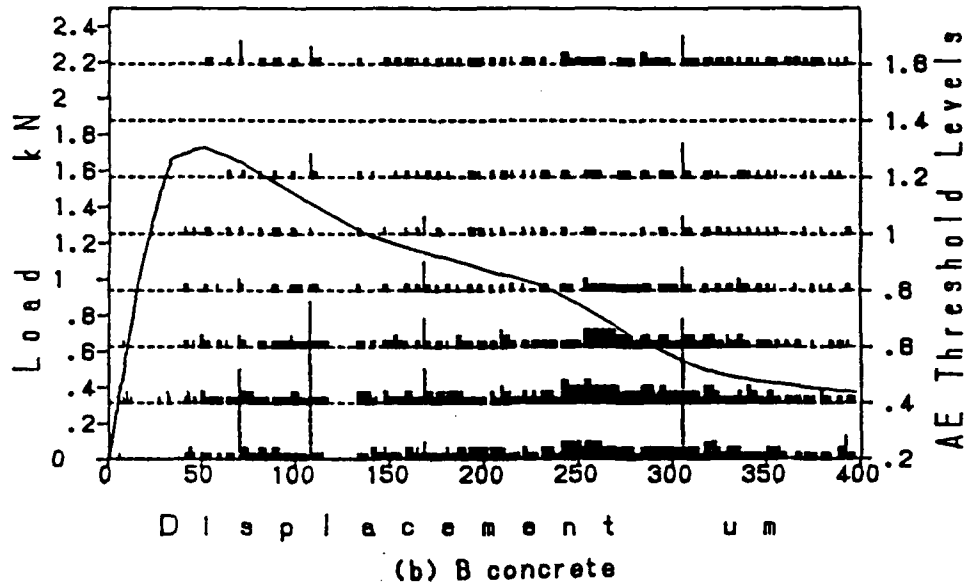

(b) B concrete

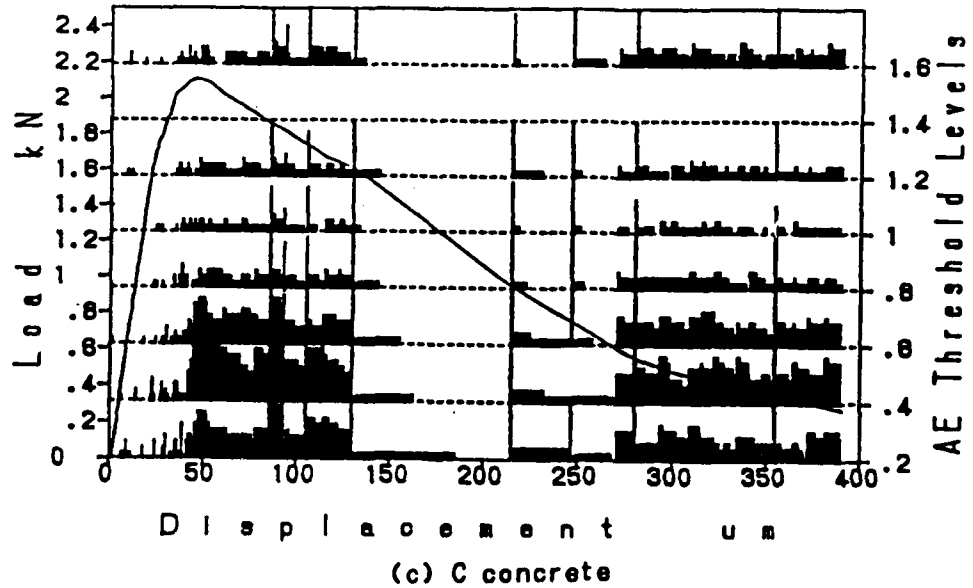

(c) C concrete

Fig. 10 AE event distributions plotted on load-displacement curve

where ΣN_{AE} is AE cumulative count and ΣN_{HI-AE} is cumulative count of AE signal with high energy. AE having energy above 1.6 V was taken as a high energy AE signal. It is considered that the frictional sliding due to crack bridging may produce high energy AE signals.

4. Application of AE to Fracture Evaluation in Advanced Concrete Composites [5]

4-1. Materials and Paper-laminate Composites

Table 4

(a) Starting materials for calcium silicate matrix

Silica	Lime	Cement	Gypsum (wt%)	Pulp fiber P/M(wt%)	Water W/M(wt%)
63	17	17	3	1 or 2	70

M=Silica+Lime+Cement+Gypsum

(b) Laminated spacing, molding process and specimen size

Laminated spacing (mm)	Fiber content in matrix (wt%)	Molding	Specimen size (mm)
—	0	Cast	40x40x160
—	1.0		
2.3			
1.7			
1.4			
—	2.0	Press	20x80x160
1.1			
1.0			
0.9			

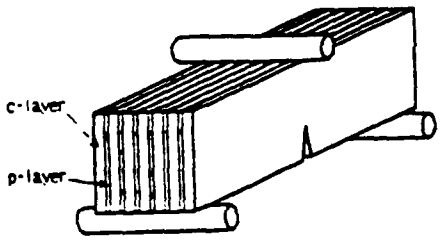

Divider

Fig. 11 Section for fracture toughness test

Paper sheet laminated cementitious composite was made as shown Table 4 (a)(b).

Notched three point bending test with AE method was carried out on the divider section as shown in Fig. 11. On the press molded samples, also the crack growth resistance were measured by un-loading compliance method. The notch cut by carbon blade on the center of the beam had the tip of 0.15 mm curvature radius and one-third depth of the sample width. An AE sensor was glued near the tip of notch. A clip gage for the measurement of the displacement was attached on the shoulder of the notch.

4-2. Results.

A typical compliance curve is shown in Fig. 12. The deformation behavior at un-loading and reloading of calcium silicate/woodpulp laminates, was irreversible similar as that of rocks and concretes. Therefore, the determination of compliance by 10 % unloading measurement, which established to examine the compliance of these laminates. In the case of these laminates, as the deformation at reloading had linear behavior, a gradient at unloading as shown dotted lines in Figure 12 was adopted.

The normalization load-deformation curves of all samples are shown in Fig. 13. The displacement on the shoulder of the notch (Vg) was measured. On the normalization for different sample size, the load was provided by the bending strength, and the deformation by Vg/Vgcal. Vgcal. was calculated by formulas obtained by Tada [6];

J integral values at maximum load, J_{pmax} was more than 30 times larger than that of non-laminate. It is difficult to examine the tendency of J_{pmax} values with laminated spacing because the maximum load point could not be determined as shown in P-Vg curves. Figure 14 shows the relationship between the J integral value and the crack growth length obtained by unloading compliance method on the press-molding laminates (J-R curves).

Khan et al. [7] proposed an AE rating parameter Tac by using AE events energy after the onset of the crack growth and fracture energy, and reported that Tac was an effective parameter evaluating the fracture toughness in various alloys. Tac is defined as follows;

$$Tac = \frac{\Sigma E_{AE} / B}{\Delta J}$$

where ΣE_{AE} is AE cumulative energy and ΔJ is the difference of J integral value after the on-set of the crack growth. The relationship between Tac and the crack growth resistance $\Delta J/\Delta a$ obtained by un-loading

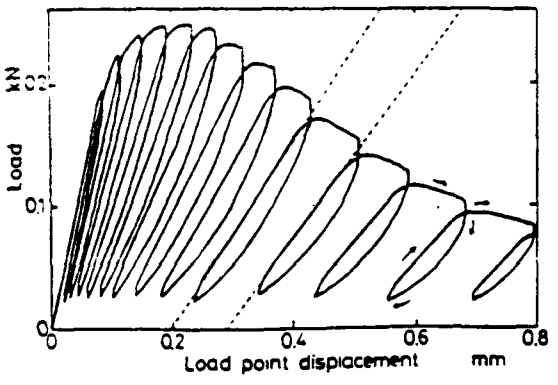

Fig. 12 Typical compliance monitoring curve

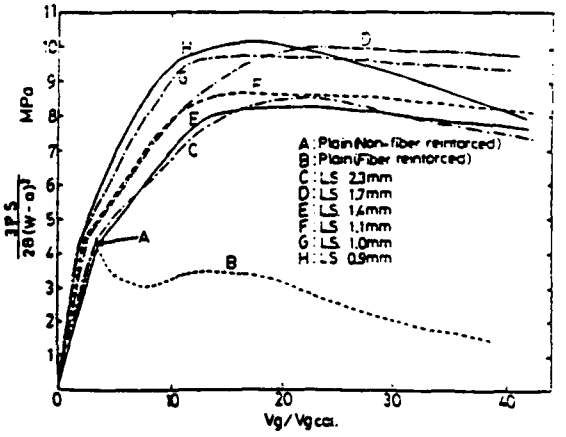

Fig. 13 Load-deformation curves

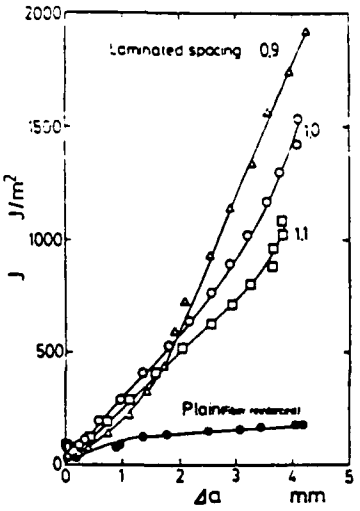

Fig. 14 J-R curves

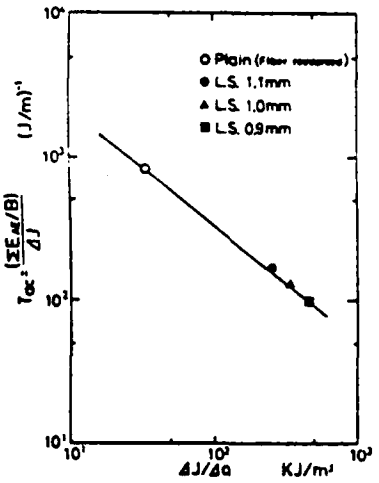

Fig. 15 Relationship between Tac and crack growth resistance

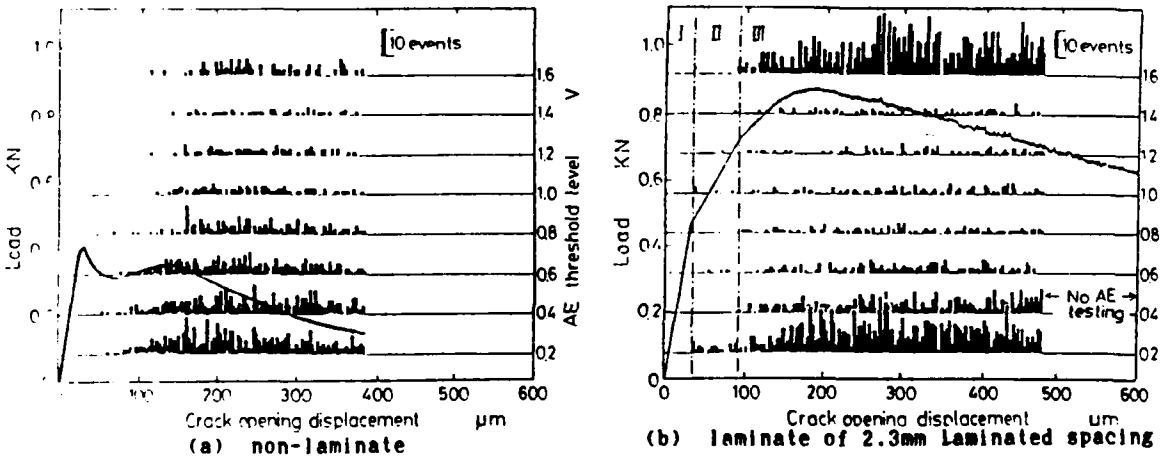

Fig. 16 AE event counts distributions on the load-deformation curves according to threshold level

compliance method (Figure 14) is shown in Figure 15. This figure shows the similar relationship to alloys. Also in calcium silicate/woodfiber comosites, therefore, the crack growth resistance can be predicted by Tac.

The AE event counts distributions plotted on the load-deformation curves according to threshold level were illustrated in Figure 16. These representative illustrations are the nonlaminate and the laminates of 2.3 mm spacing. In the case of laminates, most AE events had low energy in the Area II, while many AE events had high energy in the nonlinear behavior area (Area III). The curves had the load tremble which was caused by the pull-out and/or the failure of the fibers in the non-linear behavior. It was observed that high energy AE events occurred at every short load-drops. Therefore, it is considered that most high energy AE events were caused by the full-out and/or the

failure of the reinforcing fibers.

AE parameters, high AE relative frequency R_E and R_N were defined respectively as follows;

$$R_E = \frac{\Sigma E_{1.6V\text{-}AE}}{\Sigma E_{AE}}$$

and

$$R_N = \frac{\Sigma N_{1.6V\text{-}AE}}{\Sigma N_{AE}}$$

where $\Sigma E_{1.6V\text{-}AE}$ is AE cumulative energy over 1.6 V threshold level and $\Sigma N_{1.6V\text{-}AE}$ and ΣN_{AE} are AE cumulative count over 1.6 V threshold level and AE cumulative count, respectively. The relationships between R_E and crack growth resistance and between R_N and crack growth resistance is shown in Figure 17. The relationship between R_E and crack growth resistance had large dispersion with the difference of AE event rates in low ~ middle threshold levels, because the lower energy AE events were treated lightly in energetic evaluation. On the other hand, R_N increased with increasing of the crack growth resistance. It is suggested that R_N is an effective parameter for reinforcement effect, whether laminating or non-laminating. Figure 18 shows the relationship between R_N and the laminated spacing. R_N clearly increased with decreasing of the laminated spacing. In other words, it is suggested that the crack growth resistance increased with increasing of lamination number. From the other aspect of this figure, R_N values of the laminates asymptotically approached to R_N value of the non-laminate with increasing of laminated spacing. R_N obtained by AE measurement can be used as a measure of effectiveness of lamination reinforcement.

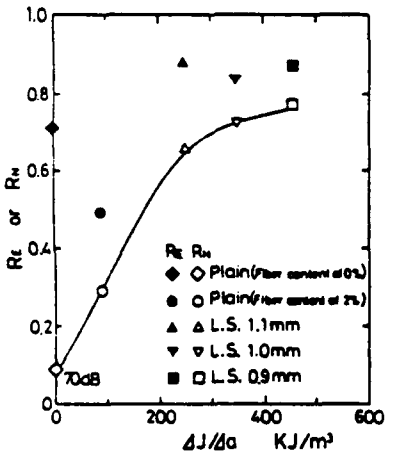

Fig. 17 **Relationship between high AE relative frequency and crack growth resistance**

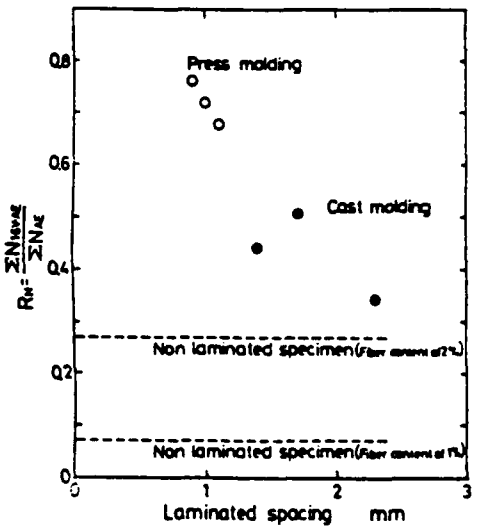

Fig. 18 **Relationship between R_N and laminated spacing**

5. Application of Ultrasomic Timing Method to Fracture Process zone On-line Monitoring in Rock [8]

Labuz et al.[9] and Swanson [10] investigated an extension behavior of the fracture process zone by use of ultrasonic attenuation method, where there exists no quantitative relationship between UT data and process zone size.

In this section the usefulness of ultrasonic timing method for monitoring the formation and extension of the fracture process zone in granite is described. The specimen geomery used is a CT type of 50 mm thickness and 125 mm width.

During the fracture toughness test, the travel time of longitudinal wave prapagation through the specimen is monitored using 500 kHZ transduser as shown in Fig. 19. Based upon an experimental calibration curve of travel time and prenotch length, the extension of fracture process zone can be estimated. Figure 20 shows a typical load-displacement curve and variation of travel time Δt, where the increase of Δt corresponds directly to the length of process zone extension (Δlp). In addition, compliance macrocrack monitoring was also made.

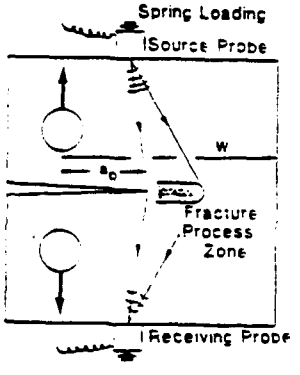

Fig. 19 Illustration of ultrasonic timing method

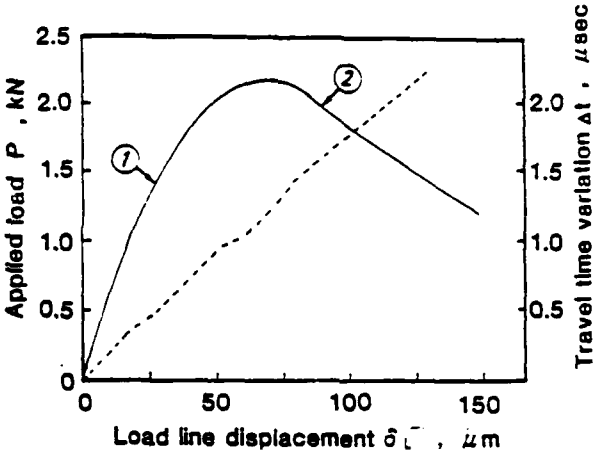

Fig. 20 Load-displacement curve and time-difference (Δt)

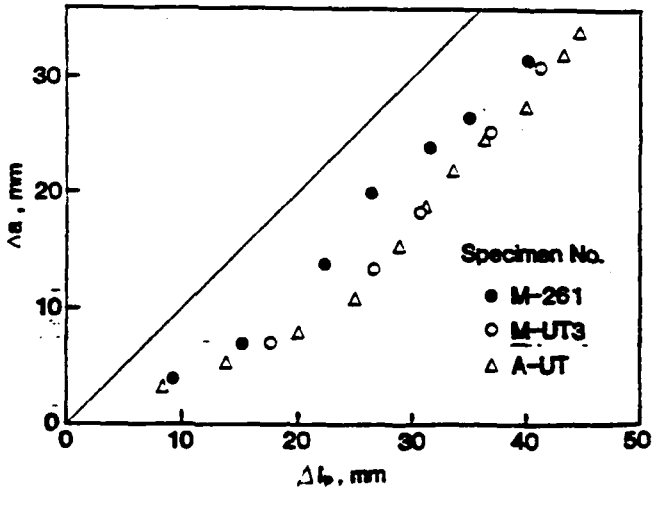

Fig. 21 Macrocrack extension (Δa) vs process (Δlp)

Figure 21 is a relationship between fracture process zone length (Δlp) and the amount of crack growth (Δa). It is clearly shown that although there is a non-linear relation of $\Delta lp - \Delta a$ at an initial loading stage, a linear $\Delta lp - \Delta a$ relation exists during steady propagation stage.

Atkinson proposed an idea of "cloud " of microcracks and macrocrack extension to discuss an extension behavior of the fracture process zone quantitatively, as shown in Fig. 22, where the actual extension of physical macrocrack (Δa) and the length of fracture process zone (Δlp) are indicated.

This illustration is supported by experimental finding that there is nonlinear $\Delta lp - \Delta a$ at the beginning of loading, whereas there exists the unique $\Delta lp - \Delta a$ relation during the macrocrack extension, as shown already in Fig. 21.

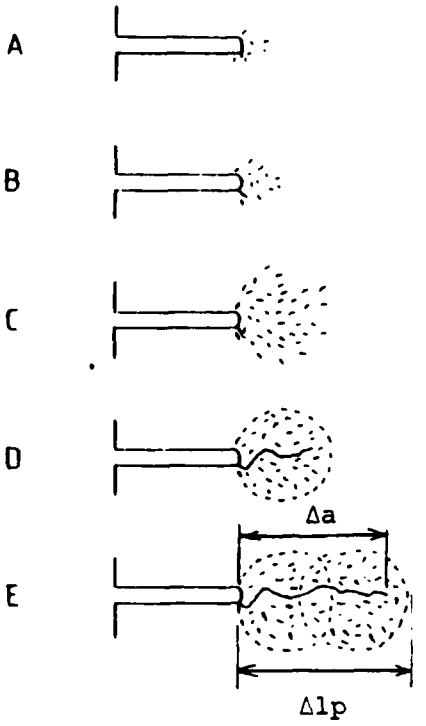

Fig. 22 Sketch of macrocrack growth and process zone extension (modification of the picture by Atkinson [11])

6. Concluding Remarks.

Although there exists several experimental techniques like AE or UT reviewed in this paper to evaluate fracture damage in brittle-microcracking materials, it is still lacking to understand a quantitative relationship between a macroscopic crack extension and microscopic cracking behavior. Extensive efforts for development of reasonable and quantitative NDE procedure to evaluate microcracking behavior in brittle materials are highly encouraged.

Acknowledgements: The author wishes to express his gratitute to Dr. T. Hashida, Tohoku University and Dr. S. Teramura, Onoda ALC Co., for their continuous and fruitsful discussions.

References

[1] Hashida, T. (1989) 'Characterization of Crack-tip Strain Singularity in Brittle-microcracking Materials by Means of the Photoelastic-coating Method', Experimental Mechanics, vol.29, 307-311.

[2] Hashida, T. et al. (1982), 'Determination of Granitic Rock by Means of AE Technique' in M. Onoe, K. Yamaguchi and T. Kishi (eds.), Progress in Acoustic Emission (I), Proc. 6th International

AE symposium, JSNDI, Tokyo, 78-89.

[3] Hashida, T. and Takahashi, H. (1990), 'Significance of AE Crack Monitoring in Fracture Toughness Evaluation and Nonlinear Rock Fracture Mechanics', submitted to Int. J. Rock Mech. Min. Sci. & Geomech. Abstr.

[4] Teramura, S. et al. (1990) 'Development of a Core-based Testing Method for Determining Fracture Energy and Tension-softening Relation of Concrete', Proc. SEM Int. Conf. on Micromechanics of Failure of Quasi-brittle Materials, Albuquerque, (in press).

[5] Teramura, S. and Takahashi, H. (1988) 'Evaluation of Fracture Toughness on Autoclaved Calcium Silicate/Woodfiber Laminate', in K. Yamaguchi, I. Kimpara and Y. Higo (eds.), Progress in Acoustic Emission (IV), Proc. 9th International AE Symposium, JSNDI, Tokyo, 748-756.

[6] Tada, H., Paris, P. and Irwin, G. (1973) 'Stress Analysis of Cracks Handbook', Del Research Co., 2-7.

[7] Khan, M. A., et al., (1982), 'Acoustic Emission Rating Parameter for Prediction of Tearing Instability in Structural Materials', Engineering Fracture Mechanics, vol. 16, 645-658.

[8] Hashida, et al., (1990), 'Ultrasonic Monitoring of the Fracture Process Zone in Fracture Toughness Tests of Granite' (in Japanese), Trans. JSME, Series A, vol. 56, 1177-1182.

[9] Labuz, J. F., Shah, S. P. and Dowding, C. H. (1987), 'The Fracture Process Zone in Granite: Evidence and Effect', Int. J. Rock Mech. Min. Sci. & Geomech. Abstr., vol. 24, 235-246.

[10] Swanson, P. L. (1987), 'Tensile Fracture Resistance Mechanism in Brittle Polycrystals, an Ultrasonic and In-situ Microsocopy Investigation', J. Geophys. Res., vol. 92, 8015-8036.

[11] Atkinson, B. K., (1987), 'Introduction to Fracture Mechanics and its geophysical Applications', in B. K. Atkinson (ed.), Fracture Mechanics of Rock, Academic Press, London, 1-26.

Session 6:

Theoretical Micromechanics Based Models

Chairs:

Dominique Francois
Ecole Centrale de Paris,
France

Wimal Sauris
University of Miami,
U.S.A.

Reporter:

Hideyuki Horii
University of Tokyo,
Japan

A review of some theories of Toughening mechanisms in Quasi-Brittle materials

C. Atkinson
Department of Mathematics, Imperial College, London

May 3, 1990

1 Introduction

To properly account for fracture processes in quasi-brittle materials such as ceramics, rocks or fibre reinforced composites consideration must be given in the first place to the propagation of discrete cracks. However these materials have many microcracks either inherent in the microstructure or created by the inhomogeneous nature of the induced stresses of applied or residual loads produced by fabrication, joining or wear. Thus subsequent steps in the analysis must account for microcrack arrays and statistical methods have been applied to this and other probabilistic aspects of the fracture problem. Although it is important to transfer from analysis of discrete cracks to arrays of cracks, including important interaction effects, we will limit attention here to a single macroscopic crack and discuss various toughening mechanisms in terms of it.

Various toughening possibilities have been suggested which include

(a) Martensitic toughening processes (b) Controlled micro-fracture in a crack tip process zone (c) Ceramic-metallic systems (e.g. cermets such as tungsten carbide cobalt) and (d) Fibre toughening. Although the intrinsic toughness of most ceramics is of the order of 2 to 3 MPa$\sqrt{m}$, the maximum toughness provided by the above mechanisms can be as much as four or five times the intrinsic toughness.

Cases (b), (c) and (d) above have usually been discussed in terms of a mechanism which reduces the effective load seen by the crack. Thus for case (c) the metallic inclusions are assumed to toughen the ceramic by a crack bridging mechanism in which the faces of the advancing crack are pinned together by intact particles for some distance behind the crack tip. These particles provide an additional resistance to the crack opening at the tip hence reducing the effective stress intensity factor of the crack. In case (d) as a crack advances through a fibre composite fibres bridge the crack tip again causing a resistance to the crack opening. For short cracks the fibres may span the whole crack. Each of these situations can be modelled as a crack which in addition to the external applied stress has a compressive internal stress acting on the crack faces which is some function of the crack opening. This stress acts to oppose the external stress and hence reduces the effective crack tip stress intensity factor or an equivalent energy release rate. Such models which have received a fair bit of attention in the last few years have a sentimental interest for the writer because of a review in Applied mechanics reviews (1971) of the paper Atkinson (1970) . The paper considered a penny shaped crack in which the faces of the crack were acted upon by a normal traction which was an arbitrary specified function of the crack opening displacement and subsequently derived a way of solving it by an iterative numerical method. The motivation came from the fibre composites work going on at N.P.L. at the time (1968 when the work was done) but the method wasn't restricted to any particular model and I said so. The review said " Author claims no compelling physical motivation which led him to consider this problem and indeed reviewer fails to see any problem wherein this analysis could be meaningfully applied ". It is a pity that we no longer have published named reviews of papers, Applied mechanics reviews now only publishes abstracts I believe.

Case (a) above, martensitic toughening , is somewhat different to the other cases since here the increased fracture toughness has two fairly distinct ingredients. First there is the work supplied to effect the martensitic transformation which reduces the energy available to produce fracture hence causing an increase in toughness and secondly there is the effect of the transformed inclusions as sources of internal stress. These internal stresses may increase or decrease the effective loads seen by a crack depending on the particular distribution of internal stresses produced. Recently some

models of the interaction of these two effects have been discussed .

It is of course a well known result, for a plane crack with the usual definition of stress intensity factor ($\sigma \sim K/\sqrt{(2r\pi)}$) , that for a non-uniform loading σ^{app} the stress intensity factor can be represented by

$$K = (a\pi)^{-.5} \int_{-a}^{a} (a + x_1)^{.5}(a - x_1)^{-.5}\sigma^{app}(x_1)dx_1 \qquad (1)$$

With this expression and a suitable model leading to the non-uniform loading seen by the crack a number of situations can be considered.Thus the well known Dugdale model has the non-uniform loading as a small "process" zone at the crack tip in which there is a fixed compressive stress resulting from plastic flow in addition to the tensile influence of the applied stress. (We are assuming here that the remote stresses have been subtracted out of the problem so the above formula applies , one can then think of the applied tensile stresses as being equivalent to an appropriate internal pressure acting on the crack faces.) The model then requires that the net stress intensity factor produced by these competing stresses is zero and hence a relation between the extent of a plastic zone to the crack length is obtained. Similar models have been invoked to describe craze formation. For the more sophisticated models considered here the effective stress seen by the crack is not independent of the shape of the crack,thus in general one has to solve a (possibly) non-linear integral equation to determine the crack shape. Models of this kind will be discussed in section 2 where we pay most attention to the problem of a plane crack in plane strain or stress although the case of a penny shaped crack will be considered briefly.

2 Crack bridging by fibres, particulate reinforced ceramics, line spring models.

The cases considered here (b), (c) and (d) of the introduction have in common the fact that the crack can be modelled as reinforced internally by some mechanism which results in a resistance to the crack opening which is some known function of the opening itself. Thus the crack can be imagined as being supported internally by springs which resist its opening in either a linear or non-linear manner and over an extent of the crack which is

localised near the tip or extends over the whole crack. It is , of course, essential to determine the particular relationship between the crack opening and the internal stress acting on the crack from a detailed model of the microstructural processes which are active for particular composites. This will be considered in the next section, here attention is given to the stress analysis of the internally loaded crack.

2.1 Mathematical statement of the discrete crack problem.

(A) THE PENNY SHAPED CRACK.

If the crack is assumed to have a penny shaped planform and the fibres or particles bridge the crack normal to it then using cylindrical polar coordinates (ρ, θ, z) with the crack lying on $z = 0, 0 < \rho < a$ one can write an integral over the crack faces as (Collins (1962))

$$u(\rho) = \frac{2(1-\nu)}{\pi\mu} \int_\rho^a \frac{dt}{(t^2-\rho^2)^{.5}} \int_0^t \frac{w\sigma(w)dw}{(t^2-w^2)^{.5}} \tag{2}$$

this being valid for $0 < \rho < a$. Changing the order of integration we can write this in the form

$$u(\rho) = \frac{2(1-\nu)}{\pi\mu} \left(\int_0^\rho w\sigma(w) I_1(w,\rho)dw + \int_\rho^a w\sigma(w) I_2(w,\rho)dw \right) \tag{3}$$

where

$$I_1(w,\rho) = \int_\rho^a dt/((t^2-\rho^2)^{.5}(t^2-w^2)^{.5}) \tag{4}$$

and

$$I_2(w,\rho) = \int_w^a dt/((t^2-\rho^2)^{.5}(t^2-w^2)^{.5}) \tag{5}$$

In the above integrals u is the half opening of the crack of radius a, and σ is the normal stress acting internally on the crack faces. Thus σ positive means the crack opening up under a given pressure σ negative denotes the resistance to the crack opening due to the micromechanics. The above forms are suitable for the determination of u or equivalently σ once the relationship between u and σ has been determined from the micromechanics. Once σ on the crack has been determined the stress intensity factor follows

as some weighted integral over the crack faces as discussed in the introduction (equation (1)).The corresponding formula for the penny shaped crack can be written as

$$K = 2(a\pi)^{-.5} \int_0^a \frac{\sigma(\rho)\rho d\rho}{(a^2 - \rho^2)^{.5}} \tag{6}$$

As stated above this formulation was originally given by Atkinson (1970), a similar formulation has been presented more recently by Marshall, Cox and Evans (1985) to describe the mechanics of matrix cracking in brittle-matrix fiber composites. The expression they derive for the expression of $\sigma(u)$ has a resistance to the crack opening which is proportional to $\sqrt{u}$. We will return in the next section to the details of their model we merely note that the above equations together with the expression for $\sigma(u)$ enable the calculation of the stress intensity factor of the crack in the composite to be determined and comparing this with the corresponding stress intensity factor of a pure matrix crack or a crack in an assumed composite medium enables the toughening effect to be determined.

(B) THE PLANE CRACK.

As in the penny shaped crack case considered above the crack opening at a given position is determined by the entire distribution of surface tractions and can be written as

$$u(x) = \frac{2(1-\nu)}{\pi\mu}\left(\int_x^a \frac{tdt}{(t^2 - x^2)^{.5}} \int_0^t \frac{\sigma(w)dw}{(t^2 - w^2)^{.5}}\right) \tag{7}$$

Changing the order of integration enables a single integral expression to be obtained with a weak logarithmic singularity i. e.

$$u(x) = \frac{2(1-\nu)}{\pi\mu} \int_0^a \sigma(w)dw \log\left(\frac{(a^2 - x^2)^{.5} + (a^2 - w^2)^{.5}}{\sqrt{(\,|\,(x^2 - w^2)\,|\,)}}\right) \tag{8}$$

Here it has been assumed that the stresses on the crack are symmetric about its centre. An integral equation similar to this is used by Budiansky , Amazigo and Evans (1988) to analyse a model of small scale crack bridging in particulate reinforced ceramics.Essentially the model considers various relationships between u and sigma and for each relationship there results an integral equation to be solved. A number of authors have considered some aspects of this problem e. g. Walton and Weitsman (1984) gave an

analytical and a numerical treatment of the problem when the resistance $\sigma(u)$ was assumed to be linear in u as a model of a craze tip zone also called a "mackeral region". Also Rose (1987) has given a fairly extensive treatment of the linear spring model and given useful asymptotic relations. As part of a "soft" contact theory in colloid science Hughes and White (1979) give an account of some non-linear models. In addition to these fairly extensive treatments it is possible to get some simple results using simple physical arguments and path independent integrals .

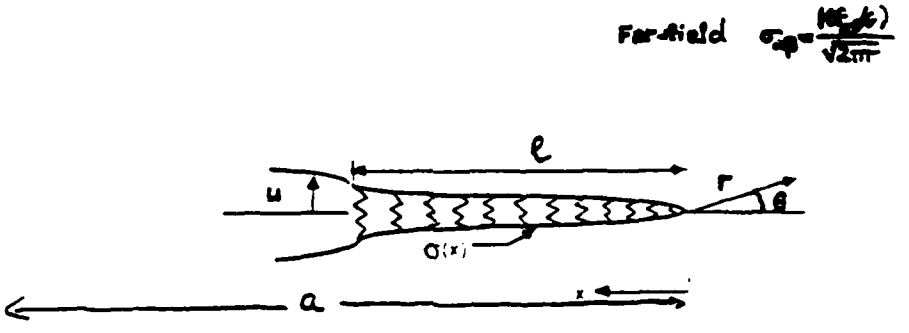

Figure 1: Spring model

2.2 Simple qualitative results

Perhaps the simplest system from which to derive qualitative results is that where a plane crack has a bridged region localised at the crack tip and this region is small compared to the crack length (figure. 1). Since in this case the bridging zone length ℓ is such that $\ell/a \ll 1$ the stress field viewed on a length scale such that a is of order one sees to a first approximation the crack without the bridging zone. The stresses near the crack tip would

then have the distribution

$$\sigma_{\alpha\beta} \approx K f_{\alpha\beta}(\theta)/(2r\pi)^{.5} \tag{9}$$

where K is the stress intensity factor due to the applied loading alone on an unbridged crack and the function f the well known θ dependence of the crack tip stress field. A standard procedure of fracture mechanics is to consider the problem with the bridging zone in a new coordinate system scaled on the zone length ℓ . In this coordinate system in the limit $\ell/a \rightarrow 0$ the crack plus bridged zone appears to be semi-infinite with the stress field (9) as the boundary condition at infinity. This near crack stress distribution can be expressed as

$$\sigma_{\alpha\beta} \approx K_m f_{\alpha\beta}(\theta)/(2r\pi)^{.5} \tag{10}$$

where K_m is now the stress intensity factor of the complete bridged crack problem in the presence of the applied stresses. A relation between K_m . K the "applied" stress intensity factor (i.e. with no bridged zone) and the spring characteristics can be obtained via the J integral (Rice (1968) , Eshelby (1951)) . This can be written as

$$J = \oint (W n_1 - \sigma_{\alpha\beta} u_{\alpha,1} n_\beta) ds \tag{11}$$

taken around the path shown in figure 2 . (Here W is the strain -energy density and u_α components of the displacement vector). The following result is obtained

$$(1-\nu^2)K^2/E = (1-\nu^2)K_m^2/E + \int_0^\ell \sigma u_{,1}\, dx \tag{12}$$

The result on the left of the equation comes from the integral around the large circle which picks up the stress field of (8) , the outer solution, and hence gives the energy release rate (per unit crack advance) of the unbridged crack. The first term on the right of the equation is from the integral around a small contour at the tip giving the bridged crack energy release rate . Further since the crack surfaces are unloaded except in the bridged region where the only non zero stress for mode one deformation is σ_{22} (σin our notation) one gets the second expression on the right of (12) .

(1) LINEAR SPRINGS

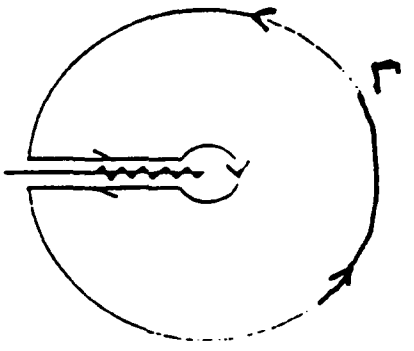

Figure 2: Path for integral

In the special case when the bridged region is modelled by linear springs and the spring stress σ is written as

$$\sigma = kEu/(1-\nu^2) \tag{13}$$

in terms of u (the normal crack tip displacement for mode 1 deformation). Youngs modulus E , Poissons ratio ν and a spring stiffness k, equation (12) reduces to

$$(1-\nu^2)K^2/E = (1-\nu^2)K_m^2/E + (1-\nu^2)\sigma^2(\ell)/(kE) \tag{14}$$

where $\sigma(\ell)$ is the spring stress at the edge (furthest from the crack tip) of the bridged zone (Rose (1987) , Budiansky et al (1988)). An implicit assumption has been made here that $K \geq K_m > 0$ and that the bridged region has opened up with $u > 0$. With this proviso equation (14) provides a relation for the " toughening ratio " $\lambda = K/K_m$ (Budiansky et al (1988))with the following interpretation . It is supposed that K_m represents the critical stress intensity factor for crack growth in the matrix and that new springs connecting the crack faces emanate from the crack tip whenever

the crack propagates i.e. the crack runs into a self similar bridging zone . With the peak spring stress $\sigma(\ell)$ set equal to the spring breaking strength σ_Y crack propagation with simultaneous fracture of the last spring occurs for

$$\lambda = [1 + (\sigma_Y^2 / k K_m^2)]^{1/2} \tag{15}$$

Of course equation (15) is nothing more than a reformulation of (14) since we do not know K_m without solving the integral equation (8) even though k and σ_Y would be specified from the micromechanics. Various expressions are given by Budiansky et al (1988) and Rose (1987) including full numerical solution of the integral equation. A useful alternative is to rewrite equation (14) in the form

$$\lambda = [1 - (\sigma_Y^2 / k K^2)]^{-1/2} \tag{16}$$

since K, the applied stress intensity factor, is easily deduced from the energy input provided from the applied stress field. It is also readily available for a given crack length and loading geometry from handbooks of stress intensity factors. The expression (16) does not require solution of an integral equation it is merely a consequence of the energy balance argument and the assumption that $\ell/a \ll 1$. This is analogous to the situation with the Dugdale model where the condition of no net stress intensity factor enables the length of the plastic zone to be removed from a crack opening displacement growth condition in terms of the ratio of applied load to yield stress. However for comparison with experimental observations of bridging zone lengths relations have been derived which involve this length. Thus Budiansky et al (1988) and Rose (1987) give relations between λ and α defined by

$$\alpha = 4k\ell/\pi \tag{17}$$

which are derived from numerical solution of the integral equation (8). Simple asymptotic solutions which are useful are

$$\lambda \approx (1 + \alpha) \tag{18}$$

for α tending to zero, and

$$\lambda \approx \pi(\alpha/2)^{\frac{1}{2}} \tag{19}$$

for α tending to infinity. The above results equations (13) to (19) are all for the linear spring model whereas equation (12) applied to any stress

displacement law acting in the bridged zone. Thus for application to particulate toughening when plastic yielding of the particles is important other relationships are neccessary, these are considered by the above mentioned authors and outlined below.

(2) ELASTIC PLASTIC SPRINGS

If for increasing u, the springs obey the elastic ideally plastic constitutive law

$$\sigma = kEu/(1-\nu^2),$$

for

$$u < u_Y$$

where

$$u_Y \equiv \sigma_Y(1-\nu^2)/kE$$

and

$$\sigma = \sigma_Y,$$

for

$$u \geq u_Y$$

Then if $u(\ell)$ at the end of the bridged zone exceeds u_Y the result (12) gives

$$(1-\nu^2)K^2/E = (1-\nu^2)K_m^2/E + (1-\nu^2)\sigma_Y^2/(kE) + 2\sigma_Y[u(\ell)-u_Y] \quad (20)$$

If failure of the last spring is now assumed to occur when $[u(\ell)-u_Y]$ attains a critical plastic value u_P, then the toughening ratio becomes

$$\lambda = [1+\sigma_Y^2(1+2u_P/u_Y)/(kK_m^2)]^{1/2} \quad (21)$$

Alternatively writing this in terms of K gives

$$\lambda = [1-\sigma_Y^2(1+2u_P/u_Y)/(kK^2)]^{-1/2} \quad (22)$$

Results from the numerical solution of integral equations which give the lengths of the zones where plastic yielding occurs are given in Budiansky et al (1988).

(3) RIGID PLASTIC SPRINGS

This case follows from the above result when u_P is considered very large the elastic contribution to the spring energy is then ignored and (20) reduces to

$$(1-\nu^2)K^2/E = (1-\nu^2)K_m^2/E + 2\sigma_Y u_P \tag{23}$$

The toughening ratio is now

$$\lambda = [1 + 2E\sigma_Y u_P/(K_m^2(1-\nu^2))]^{1/2} \tag{24}$$

or equivalently

$$\lambda = [1 - 2E\sigma_Y u_P/(K_m^2(1-\nu^2))]^{-1/2} \tag{25}$$

For this case a simple relation can be presented which gives λ in terms of the bridge length ℓ as

$$\lambda = 1 + 2(2/\pi)^{1/2}\sigma_Y L^{1/2}/K_m \tag{26}$$

All of the above results are for the case when the zone length is small compared to the crack length. For situations where the zone extends over the whole crack length such as occurs for short cracks in composites the integral equation formulation is still applicable.

3 Micromechanical models leading to "spring" properties.

We give a rather brief survey of some of the models which have been used to produce stress displacement relations for the region modelled by springs. As we have indicated earlier such considerations are .of course, an essential part of the models. The basis of these models is a more detailed accounting of the deformation processes on the scale of individual fibres or particles and the transfer of this information to concentrations of such fibres or particles. For example in the case of fibre composites models of fibre pull out are used to give a relatioship between σ and u for use in the spring model. Similarly for crack bridging by particles a model relating the average crack opening produced by the particle pinning to the average energy released on a microcrack level can be used to relate average σ values to u values for use together with the spring models for the main macroscopic crack analysis. We give a cursory account of some recent models below.

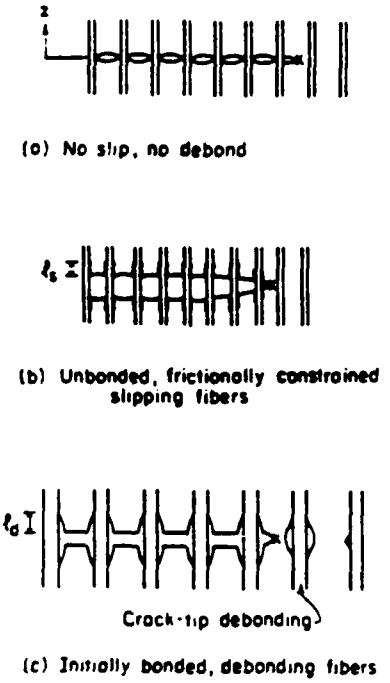

Figure 3: Steady state matrix cracking

3.1 Brittle matrix fiber composites, fibre pullout

The nature of the debonding process between an individual fibre and the matrix can be quite complicated. For example experiments on pulling out a glass rod from a polyeurethane matrix and observing the interface fracture process (e.g. Atkinson et al (1981)) showed a debond to occur initially either at the stress singularity where the rod met the free surface or at a preexisting microscopic flaw at the interface. This latter situation usually occured at the rod base and as the rod was pulled the defect propagated around the interface finally stopping as it met the compressive stresses seen by the rod sides. In this paper the details of the observed failure process was explained in terms of debond fracture mechanics and the induced stress fields. In principle the more detailed the knowledge of this process the more meaningful the application to the spring models . Figure 3 illustrates what might happen to a matrix crack as it proceeds across a fibre composite. If there is enough frictional resisrance no slip will occur at the fibre matrix interface (cf. figure 3 (a)). When slip does occur the situation shown in figure 3 (b) may occur, this is the situation considered below where an

equivalent spring model is derived. We consider a simple model of this here see e.g. (Marshall et al (1985)) . The main assertion is that the application of tractions T to the end of a fibre cause sliding between the matrix and fibre over a distance ℓ_1 say and allows the fibre to pull out of the matrix a distance u. Such behaviour does of course depend on the nature of the matrix bond. For a purely frictional bond the sliding distance is determined by the length over which the interface shear stresses exceed the friction stress τ. Marshall et al (1985) deduce the following approximate relation between T and u.

$$T = 2[uE_f\tau(1+\eta)/R]^{1/2} \tag{27}$$

where $\eta = E_f V_f / E_m V_m$ with E_f and E_m the modulus of fibres and matrix respectively and V_f ,V_m the volume fractions. πR^2 is the fibre cross sectional area. It remains to relate T to σ acting in thespring model. This is done by writing

$$\sigma = TV_f \tag{28}$$

Thus from this model σ is proportional to the square root of u.

The application of the spring model with the above value of σ leads, via solution of the integral equation , to a value for K^L the stress intensity factor of the loaded spring crack model i.e. including both the effect of applied load and the springs. This intensity factor thus characterises the composite stress and strain fields in the region immediately ahead of the matrix crack. Because in this region no relative displacements between fibres and matrix are permitted the matrix and fibre strains must be compatible. Hence

$$\sigma^M / E_m = \sigma / E_c \tag{29}$$

where σ^M is the matrix stress, σ is the composite stress and E_c is the composite modulus

$$E_c = E_m V_m + E_f V_f \tag{30}$$

The matrix and composite stress intensities scale with the stresses such that

$$K^L = K^M E_c / E_m \tag{31}$$

where K^M is the stress intensity in the matrix. The condition for equilibrium crack growth (in the absence of environmental effects) is given by

setting K^M equal to the critical stress intensity factor, K_c^M for the matrix. The criterion for crack growth can then be expressed in terms of K^L as

$$K^L = K_c^L = K_c^M E_c / E_m \tag{32}$$

This model has been further developed recently by Budiansky et al (1986) and Budiansky and Amazigo (1989) and some simpler energy balance arguments such as discussed in the last section apply to this situation also. These authors thus attempt to generalise the earlier model of Aveston et al (1971).

3.2 Particulate toughening

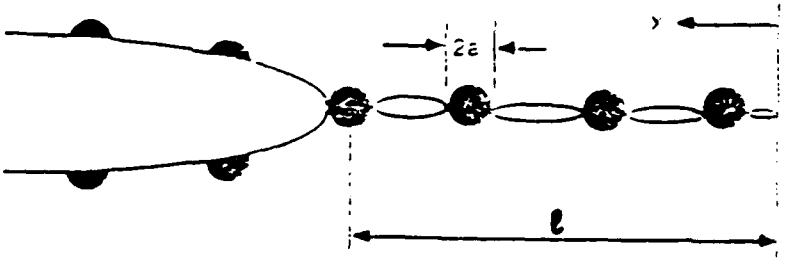

Figure 4: Particulate reinforcement

Budiansky et al (1988) assume spherical particles and suppose that the faces of an advancing plane crack are pinned by particles at their equators. Such an assumption interpreted strictly would require that the matrix area on the bridged zone were reduced by a fraction that exceeds the volume concentration c of particles. As an approximation they assume that the

matrix area concentration on each crack face has the value (1-c) which corresponds to an arbitrary plane cross section of the composite material. To apply the spring models of section 2 the spring stress σ at a given location on the crack plane is identified with smeared out particle stresses $c\sigma_p$ where σ_p is the average stress at that location i.e. the average over all particles in the thickness direction perpindicular to the plane of figure 4 for the plane crack model. The following estimate for the spring constant k is given by Budiansky et al (1988), they write

$$k = (\frac{2c}{a\pi\beta})(\frac{E_m}{1-\nu_m^2})(\frac{1-\nu^2}{E}) \tag{33}$$

where E and ν are the effective elastic constants of the composite material consisting of the ceramic matrix containing a randomly distributed concentration c of particles. a is the particle radius and $\beta(c)$ is given approximately by the formula

$$\beta \simeq (1-c)(1-c^{.5}) \tag{34}$$

The equation (14) denoting the energy balance is modified to

$$(1-\nu^2)K^2/E = (1-c)(1-\nu_m^2)K_m^2/E_m + (1-\nu^2)\sigma^2(\ell)/(kE) \tag{35}$$

Here they argue that since the first term on the right denotes energy release into the real crack tip and this tip advances only into matrix material then e and ν should be replaced by E_m and ν_m and further this term should be multiplied by (1-c) to take into the fact that the bridging particles reduce the the length of the advancing crack front by a factor c. The reader is referred to the original paper for details of comparisons with experiment. The observation is also made by these authors that to be aneffective toughening mechanism a matrix crack should tend to be attracted to the particles and a neccessary condition for this might be that the elastic stiffness of the particles should be less than that of the matrix. Such an effect occurs when one considers the interaction of a plane crack and a circular inclusion of different elastic constants see e.g. Atkinson (1971).

4 Concluding remarks

In this rather brief account of some current theories of toughening we have not treated case (a) of the introduction in any detail .We merely note that

recently Budiansky and Amazigo (1988) have discussed the role of both ductile crack bridging particles and phase transforming particles witha view to the possible enhancement of toughness by these two effects. Rose (1985) has also discussed the transformation toughening problem. It is clear of course that a transforming particle induces an internal stress field in the matrix which will influence crack growth. Precisely how it does this requires the interaction of the spring model and the inclusion problem and a definitive treatment of this perhaps still remains to be done. Although Budiansky and Amazigo (1988) claim to show a synergistic effect in certain parameter ranges. Another interesting paper we have not mentioned hitherto is that of Foote et al (1986) who derive crack growth resistance curves for a fibre cement composite in a double cantilever beam geometry. They look at the effect of various softening indexes (n) of a power law relationship between σ and u .Thus again a σ u relationship holds across the faces of the crack so Atkinson (1970) was not so useless afterall.

4.1 References

Amazigo . J. C. and Budiansky, B., 1988, Interaction of particulate and transformation toughening,J. Mech. Phys. Solids, 36, 581-595

Atkinson, C. , 1970 , An iterative scheme for solving problems relating to cracks opening under a displacement -dependent internal stress , Int. Jnl. of Frac. Mechs. 6, 193 -197.

Atkinson, C. , 1971 , A simple approximation for calculating the effect of inclusions on fracture , Scripta Met , 5, 643-650.

Atkinson, C. , Avila, J., Betz , E. and Smelser, R. E. ,1982, The rod pull out problem .theory and eaperiment., J. Mech. Phys. Solids, 30, 97-120

Aveston, J., Cooper, G. A. and Kelly, A. ,1971 , The properties of fibre composites,15-26, Conference Proceedings, NPL , Guildford., IPC Science and technology press ltd.

Budiansky, B. , Amazigo, J. C. and Evans, A. G. , 1988. Small scale crack bridging and the fracture toughness of particulate-reinforced ceramics, J. Mech. Phys. Solids, 36, 167-187

Budiansky, B. , Hutchinson, J. W. and Evans, A. G. , 1986, Matrix fracture in fiber reinforced ceramics , J. Mech. Phys. Solids, 34, 167-189

Budiansky, B. and Amazigo, J. C. , 1989, Toughening by aligned frictionally constrained fibres,J. Mech. Phys. Solids, 37, 93-109

Collins, W. D. , 1962, The penny shaped crack, Proc. Roy. Soc. A, 266 , 359-386

Eshelby, J. D. , 1951, The force on an elastic singularity, Phil. Trans. Roy. Soc. Lond. ,A 244, 87 -111

Eshelby, J. D. , 1961, Elastic inclusions and inhomogeneities, Prog. Solid. Mech. 2, 89-140

Foote, R. M. L. , Mai, Y. and Cotterell, B. , 1986 , Crack growth resistance curves in strain softening materials,J. Mech. Phys. Solids, 34 , 593-607

Hughes, B. D. and White, L. R. , (1979) , "Soft" contact problems in linear elasticity , Q. J. Mech. Appl. Math. 32, 445-471

Marshall, D. B. , Cox, B. N. and Evans A. G. , 1985 , The mechanics of matrix cracking in brittle-matrix fibre composites. , Acta Met. 33, 2013-2021

Rice, J. R. , 1968 , A path independent integral and the approximate analysis of strain concentration by notches and cracks , J. Appl. Mechs. 35, 379-386

Rose, L. R. F., 1985, Theoretical aspects of reinforcement and toughening, Fundamentals of deformation and fracture (Ed B.A.Bilby et al) C. U. P. Press

Rose , L. R. F. , 1986 , The size of the transformed zone during steady state cracking in transformation toughened materials,J. Mech. Phys. Solids, 34, 609-616

Rose , L. R. F. , 1987 , Crack reinforcement by distributed springs , J. Mech. Phys. Solids, 35 ,383-405

Shah, S. P. (Ed), 1985, Application of fracture mechanics to cementitious composites, Martinus Nijhoff, Dordrecht.

Walton, J. R. and Weitsman, Y. , (1985) , Deformations and stress intensities due to a craze in an extended elastic material, J. Appl. Mechs. 51, 84-92

ON THE FORM OF MICROMECHANICAL MODELS OF THE BRITTLE DEFORMATION OF SOLIDS

by
DUSAN KRAJCINOVIC and MICHAL BASISTA

Mechanical and Aerospace Engineering
Arizona State University, Tempe, AZ 85287-6106

ABSTRACT

The present paper offers a cursory review of the state-of-art in analytical modelling of brittle response. The discussion is formally divided on considerations of dicrete (statistical) and continuum (micromechanical and phenomenological) models. An effort was made to detect the relations between these three classes of models and ascertain the manner of using these relations in improving these models.

INTRODUCTION

The objective of this paper is to review and scrutinize the methodologies for analytical modelling of the response of elastic material weakened by a diffuse ensemble of crack-like micro-defects. The ultimate goal is to examine the methods leading to the establishment of a constitutive relation between the macro-stresses and macro-strains reflecting the physics of irreversible changes of the microstructure of the solid. Since the utility of an analytical model, and its acceptance in engineering practice, are proportional to its simplicity a due consideration must be directed towards the introduction of a set of physically justified simplifying assumptions. Blurring the inconsequential and experimentally not reproducible details of the mechanical response these assumptions emphasize the salient aspects and essential nature of the underlying phenomena. On the other hand, the introduced simplifications by their very nature place limits on the utility and applicability of the model which must be recognized in analyses.

The discussion in this paper is limited to the response of an elastic specimen containing a large number of microcracks distributed over a significant fraction of its volume. It will be assumed that most, if not all, of the energy is dissipated on the formation and propagation of microcracks. Focusing on the predominantly brittle response the macro-strains and attendant deformations may be regarded as infinitesimal rendering the linear theory of elasticity applicable.

For the sake of simplicity assume that all microcracks are planar and elliptical in shape. The stress and strain fields in the specimen containing N of these cracks can be determined, at least in principle, solving N coupled integral equations (Kunin 1983). Naturally, since N is, by definition, a very large number such a strategy will in most cases not be a feasible one. Moreover, in the case of a typical engineering material (such as concrete) the shape of these cracks is irregular and their size and position random. Therefore, a rigorous determination of stress and strain fields within the specimen will not be possible. Additionally, the growth pattern of these microcracks depends not only on the fluctuations of the local stress field but also on the randomness of the material toughness on the microscale. In other words, the evolution of damage (understood herein as a gradual change in the number of cracks and their growth) is a problem with an infinite number of degrees of freedom (Bolotin 1989).

Since a rigorous analytical solution of the problem is not possible it becomes necessary to rely upon a phenomenological theory, construct an approximate micromechanical model or resort to computational methods in conjunction with statistical considerations. First of these strategies, most frequently used in engineering analyses, will be given only a cursory attention within this paper. Even then, phenomenological modelling will be addressed only in relation to the micromechanics. The approximate micromechanical models are commonly based on idealized crack geometry (considering them, for example, penny shaped in form) and involve an averaging (homogenization) process within the framework of the effective continua models (Mura 1982, Kunin 1983, Krajcinovic and Sumarac 1987, Sumarac and Krajcinovic 1988, Ju 1989, etc.). Except for few cases (M. Kachanov 1987), this approach, by its very nature, disregards the irregularities in the microcrack geometry and their interaction leading to tractable, local analytical models involving acceptable levels of computational effort in applications. The last of these three approaches, popular among statistical physicists, fully acknowledges the randomness in the defect morphology and the distribution of fracture energy on the microscale. However, this class of algorithms is purely numerical in form involving numerous and repetitious large scale computations. In fact, the

computations are so extensive that all of the existing analyses were restricted to two-dimensional lattices.

The emphasis of this paper will be placed on the analytical micromechanically based models. The statistical models will be discussed solely in the context of the limitations and possible modifications of the analytical models.

DISCRETE (STATISTICAL) MODELS

For a better understanding of the problem it is, perhaps, advisable to start with a very simple model such as a loose bundle of parallel rods carrying an external tensile load F (Krajcinovic and Silva 1982, Hult and Travnicek 1983, Krajcinovic 1989). The analysis of the parallel bar system, shown in Fig. 1, is based on the following simplifying assumptions:

- all rods are elastic, perfectly brittle and arranged in such a manner that they equally share in carrying the external load F,
- all N rods have identical stiffness K/N and elongation,
- the strengths of the rods are different.

The system is supplied by a rigid beam (bus) at both ends serving as a device preventing unequal elongation of individual bars.

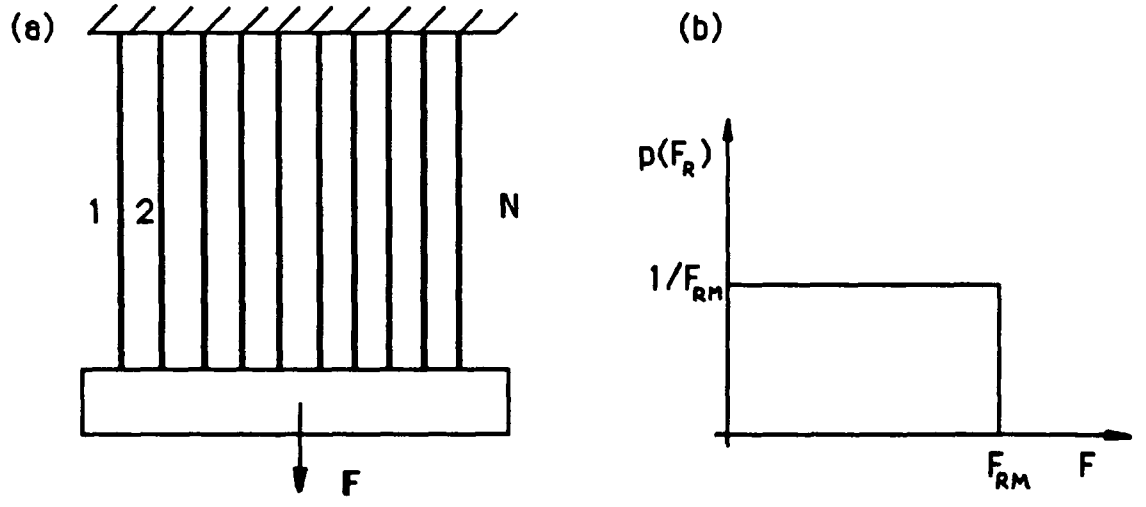

Fig.1. (a) System of parallel loose bars.
(b) Probability density function of bar strengths

Despite the initial (quenched) disorder, introduced by unequal bar strengths, the analysis is thereafter deterministic. It is trivial to prove that the equlibrium is satisfied when

$$F = Kx(1 - D) \tag{1}$$

where x is the elongation of the system and

$$D = (n / N) \tag{2}$$

the damage variable selected as the ratio between the number of the already ruptured bars n and the total number of bars N.

Assuming that the strength probability density function of individual bars is $p(F_R)$, and that the number of bars tends to infinity the equlibrium equation (1) can be recast in form of an integral

$$F = Kx \int_{Kx}^{\infty} p(F_R)\, dF_R \tag{3}$$

The damage variable can now be written as the cumulative probability function P(Kx) of the given strength probability density function $p(F_R)$

$$D = \int_0^{Kx} p(F_R)\, dF_R = P(Kx) = pr(F_R < Kx) \tag{4}$$

In the case when the probability density function of bar strengths is uniform $p(F_R) = (1 / F_{RM})$, where F_{RM} is the strength of the strongest bar, it can readily be demonstrated that

$$D = Kx / F_{RM} \quad \text{and} \quad F = Kx\,[1 - (Kx / F_{RM})] \tag{5}$$

The force-displacement curve is a quadratic parabola with apex at

$$F = F_M = (1/2)\,Kx_M = NF_{RM}/4 \qquad (6)$$

At the apex of the force-displacement curve (Fig.2) the damage is

$$D_M = 0.5 \qquad \text{at} \qquad x = x_M \qquad (7)$$

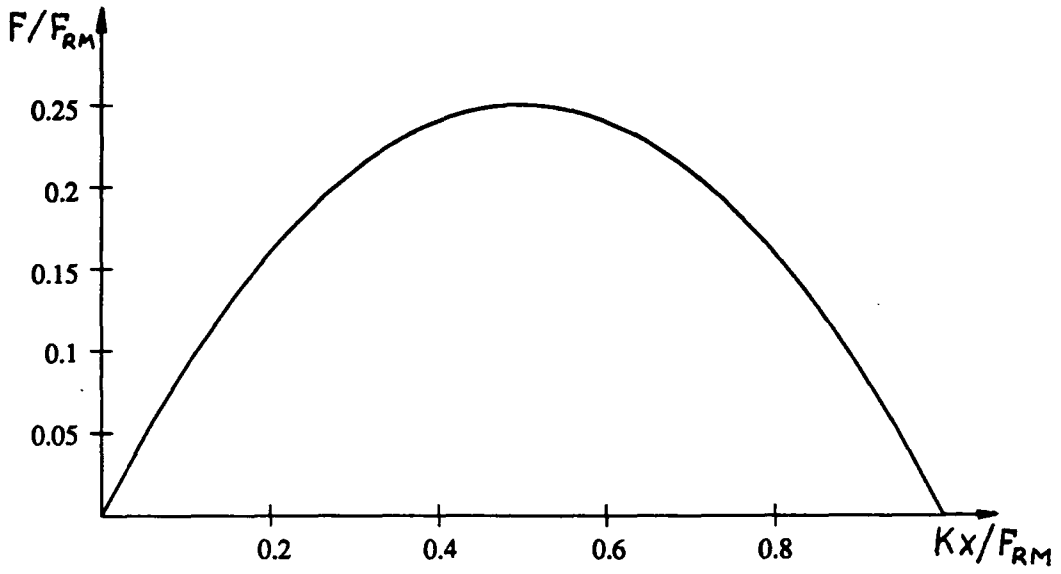

Fig.2. Force-elongation curve for parallel bar model

For different strength distributions the damage at maximum stress and the maximum stress itself will be different (see, Krajcinovic 1989).

Using conventional expressions $F = A_0\sigma$, $\varepsilon = x/L$ and $K = EA_0/L$, where E, A_0 and L are the elastic modulus, initial (undamaged) cross-sectional area and length of the macro-bar, the expressions (5) can be rewritten in the conventional form

$$\sigma = E(1 - D)\varepsilon \qquad \text{and} \qquad D = A_v / A_0 \qquad (8)$$

where A_v is the area initially occupied by the ruptured bars which is not available for the transmission of forces.

A computationally much more intensive problem of a triangular lattice (Fig.3) was lately examined by Herrmann, et al. (1989) and Hansen, et al. (1989). The central idea was to examine the influence of the initial disorder and the size of the lattice on the mechanical

response. The first task was accomplished assigning different strengths to different bars of the lattice and repeating computations for each distribution (initial disorder). In each case the computations of forces in the lattice members for a given displacement of the rigid end members are performed in the routine manner. Naturally, the strength probability density function (taken as uniform as in Fig.1, showing a module of the lattice repeating itself along the horizontal axis) was identical for all cases allowing for a meaningful comparison of results. Computed quantities were then averaged over different lattices keeping the number n of ruptured bars constant ("history" averaging). The influence of the lattice size was then assessed considering lattices for which L (Fig.3) was taken as 4, 8, 16 and 24.

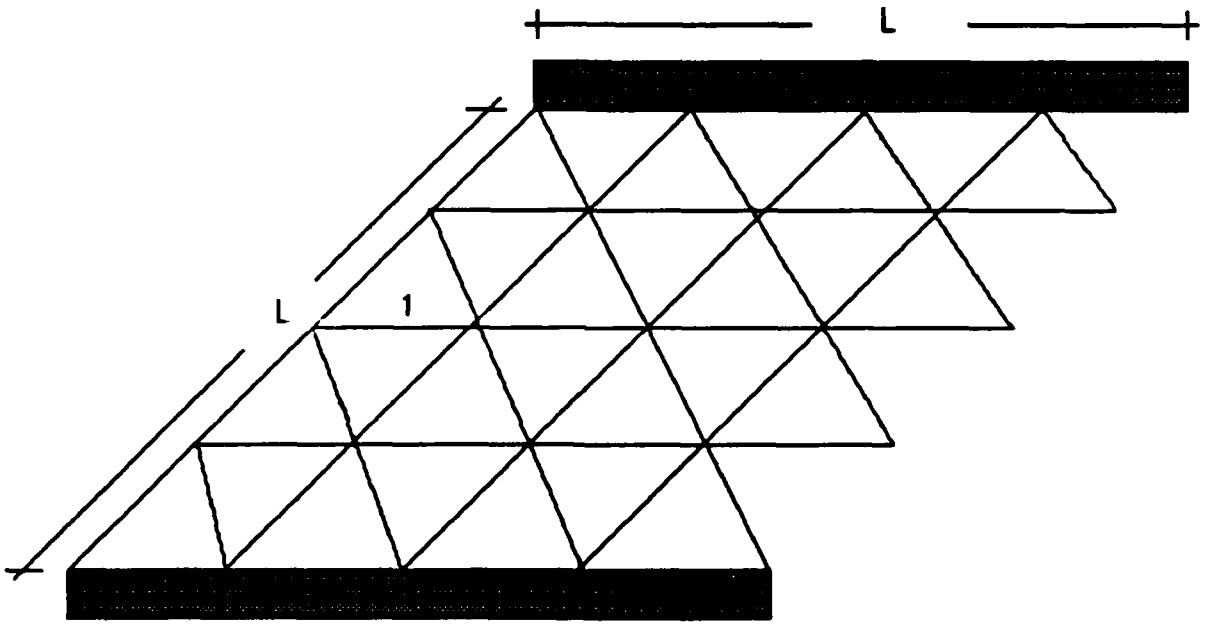

Fig.3. Central-force triangular lattice (L = 4).

According to the reported results of these computations the relationship between macro-stresses and macro-strains (translated into more traditional form) was found to be

$$\sigma = E\varepsilon (1 - \alpha\varepsilon \sqrt{3}) \qquad (9)$$

where the parameter α, proportional to $L^{1/4}$, is determined in such a manner that it fits the results for all lattice sizes equally well. The damage variable can be deduced to be of the form

$$\omega = (3/4)\sqrt{3}\, L^{1/4}\, \varepsilon \qquad (10)$$

It is notable that the corresponding expressions for the loose bundle parallel system and the lattice are identical in form for the pre-critical regime. In other words, the response is not very sensitive to the level of sophistication in modelling.

It is interesting that these computations demonstrate that in the pre-critical regime:

(a) the average stress-strain curves for all four lattice sizes and all distributions of the initial disorder can be collapsed on a single (parabolic) master-curve, and

(b) the relation between damage and strain (10) is linear.

(c) the damage at the apex of the stress-strain curve was again equal to 0.5 as in the previously discussed case of the parallel bar model

In concert with the loose bundle parallel bar system this obviously means that in the pre-critical regime the crack interaction has little influence on the overall response which is well described by simple volume averages of the involved fields. In other words, the pre-critical regime is deterministic by nature. The crack interaction and even the redistribution of stresses is not crucial for the determination of the overall response. The fractality, i.e. dependence of the overall response on the size of the lattice (10) is, perhaps, associated with a rather small number of triangular elements and should disappear for larger lattices. In a sharp contrast, the distribution of forces in the post-peak regime, just before the rupture, is strongly multi-fractal. The inability to identify a single length scaling parameter should be related to the fact that the post-peak regime strongly depends on the distances between the adjacent cracks. It seems reasonable to expect that more than one length parameter must be introduced to model that behavior. Additionally, the post-peak response is found to depend strongly on the initial disorder. Consequently, since the initial disorder in engineering materials is random the post-peak behavior is not deterministic.

It is very important to notice that neither of two models required an additional kinetic law describing the rate of the damage accumulation with either stresses or strains. This law was, indeed, derived from the initial disorder, i.e. assumed distribution of initial defects and fracture strengths. The damage evolution law was, however, found to be different for different strength distributions (Krajcinovic and Silva 1982).

CONTINUUM MODELS

Micromechanical Models

One of the first tasks related to the introduction of an effective continuum is to define the representative volume element (RVE). In a very general sense, a RVE is the smallest volume of material which with respect to a given random variable has the same properties as the macro-specimen. More specifically, the first (n) statistical moments of the distribution of a particular random variable taken over the volume V of the RVE should to a desired level of accuracy equal the corresponding statistical moments of the distribution of the same variable taken over all volumes larger than V. These requirements were further reduced by Nemat-Nasser and Hori (1990) who, roughly speaking, considered a RVE to be statistically representative of the macro-response if the macro-stress is a volume average of micro-stresses corresponding to the same elastic macro-strain. An analogous definition has been advanced by the same two authors for the case of imposed macro-strains.

Assuming that these conditions for the RVE are satisfied it becomes possible to establish a relation between a field on the micro-scale and the same field on the macro-scale. All information regarding the structure of the materials and the defects within the RVE will form the configurational space attached to a material point of the effective continuum. Therefore, the RVE allows for the mapping of the micro-structure of the material on the material point of the continuum. Naturally, since the RVE must contain a statistically valid sample of microcracks a configurational space describing all defects must contain a large number of data. Assuming, for simplicity, all N cracks to be planar and elliptical in shape an all inclusive configurational space should comprise of 8N scalars (2N half-axis lengths, 3N Euler angles and 3N scalars defining the position of the microcrack center). In the case of inhomogeneous state of macro-stress and strain the bookkeeping associated with upgrading the configurational space in every material point of the specimen can obviously present a significant and often unsurmountable problem.

The conventional method of establishing the governing equations is typically prefaced by introducing the Helmoltz $\Phi(\varepsilon)$ and Gibbs $\Psi(\sigma)$ energies of the specimen (or RVE) with volume V such that

$$\Phi(\varepsilon) + \Psi(\sigma) = V(\sigma : \varepsilon) \tag{11}$$

where the bar above the symbol denotes the volume average or, in sense of Nemat-Nasser and Hori (1990) definition, the macro-fields. The macro-stresses and macro-strains are defined as

$$V\,\sigma = \partial\Phi / \partial\varepsilon \qquad \text{and} \qquad V\,\varepsilon = \partial\Psi / \partial\sigma \tag{12}$$

When the elastic strains in the matrix are small, and the concentration of inhomogeneities dilute, the macro-stresses are mapped on the macro-strains by a linearized relation of a general form

$$\varepsilon = \varepsilon^{P}(H) + S(H) : \sigma \tag{13}$$

where H is used to denote a set of scalar and tensor variables defining the irreversible rearrangements of the material microstructure (recorded history). Also, S(H) is a fourth rank tensor known as compliance which, in the present case, depends on the properties of the matrix and the given distribution of microdefects. From equations listed above the compliance is

$$S = (1/V)\,(\partial^2\Psi / \partial\sigma\,\partial\sigma) \tag{14}$$

Additionally,

$$\varepsilon^{P} = \varepsilon(\sigma = 0) \tag{15}$$

is the inelastic (plastic or residual) strain in the specimen.

The incremental form of the relation between the macro-stresses and macro-strains (13) necessary for inelastic analyses is

$$d\varepsilon = d\varepsilon^{P} + S : d\sigma + dS : \sigma \tag{16}$$

The last term on the right hand side of the equation (16) represents the inelastic stress associated with the change in the compliance of the specimen. Naturally, the compliance can change only if the recorded history is changed, i.e. if the energy is dissipated.

Substituting (13) into (11) it also follows that

$$\Psi(\sigma, H) = -\Phi^{o}(H) + V(\sigma : \varepsilon^{p}) + (1/2)\, V(\sigma : S : \sigma) \qquad (17)$$

where Φ^{o} is the locked in energy at vanishing state of stress.

Assuming that the irreversible rearrangement of the microstructure can be described by a finite set of thermodynamic fluxes $d\xi_i$ (i = 1,2,...,n), the inelastic increment of the Gibbs energy can always be written as a scalar product of fluxes and their conjugate thermodynamic forces (Rice 1975),

$$d^{i}\Psi = \Psi(\sigma, H + dH) - \Psi(\sigma, H) = \Sigma\, f_j\, d\xi_j \qquad (j = 1,2,...,n) \qquad (18)$$

Combining (17) and (18) it further follows that

$$\Sigma\, f(\sigma,H)\cdot d\xi = -\, d\Phi^{o}(H) + V(\sigma : d\varepsilon^{p}) + (1/2)\, V(\sigma : dS : \sigma) \qquad (19)$$

Concentrating on the defects in the form of microcracks the history recording set of parameters H consists of data related to the size, shape, orientation and position of all microcracks within the volume V of the RVE. The inelastic change in the Gibbs energy is then (Rice, 1975)

$$d^{i}\Psi = \sum f_j\, d\xi_j = \sum \int_L \left[(G - 2\gamma)\, d\ell\right] dL > 0 \qquad (20)$$

where G is the elastic energy release rate, γ the surface (fracture) energy, and $d\ell$ the local advance of the crack front L in the direction of its normal. The integral in (20) is taken along the perimeter of each active microcrack. The sign of the inequality in (20) is the consequence of the second law of thermodynamics (entropy production). It is important to realize that no energy is dissipated unless the crack size changes ($d\ell > 0$), i.e. unless additional atomic bonds in the material are ruptured.

The energy release rate of a crack embedded in an elastic matrix can be written in form (Rice 1975)

$$G = (\pi/4)\, k_i\, C_{ij}\, k_j \qquad (21)$$

where $\mathbf{k}$ is the vector having the stress intensity factors as components (i = 1,2,3) and C(H) a second rank tensor depending on the elastic properties of the matrix and the recorded history H. From the expressions (19) to (21) the inelastic change in the compliance tensor is now

$$dS_{ijmn} = \frac{1}{V} \sum \int_L \left[\frac{\pi}{2} C_{qr} \frac{\partial k_q}{\partial \sigma_{ij}} \frac{\partial k_r}{\partial \sigma_{mn}} d\ell \right] dL \tag{22}$$

with integration extended over the perimeters of all active cracks within the RVE.

It is important to notice that:

(a) the deformation process is elastic (non-dissipative and reversible dH = 0) in the case when the crack surface area does not change ($d\ell = 0$), regardless of possible changes in the stress and strain fields or even crack opening displacements and/or stress intensity factors,

(b) the overall compliance changes as the history is recorded. Correspondingly, the slopes of the unloading segments at different values of H will not be parallel among themselves or with the initial, elastic part of the loading curve (at H = 0).

The inelastic macro-strain ε^p can readily be derived from the known eigenstrains within the inhomogeneous inclusions (see Mura 1982)

$$\varepsilon^p = \langle \varepsilon^p \rangle = f \varepsilon^{**} = f(\varepsilon^p + \varepsilon^*) \tag{23}$$

where ε^p is the plastic strain and ε^* the eigenstrain within the inclusion. Also

$$f = \Sigma \Omega_\alpha / V \tag{24}$$

is the fraction of the volume occupied by the inhomogeneous inclusions. The sum in (24) is extended over all inhomogeneous inclusions α.

The expressions for the rate of the inelastic change in the compliance tensor can also be derived using the inclusion method in conjunction with averaging (Horii and Nemat-Nasser 1983, Krajcinovic and Fanella 1986, etc.). An elliptical crack is modeled as a limiting case of an ellipsoidal inclusion of vanishing thickness $2a_3$ in the direction of the crack normal. The

eigenstrain can then be written as (Mura 1982, Horii and Nemat-Nasser 1983, Krajcinovic and Sumarac 1987, etc.)

$$\lim_{a_3 \to 0} (a_3 \varepsilon) = \frac{1}{2} \int_A \left\{ \mathbf{n} \otimes [\mathbf{u}] + [\mathbf{u}] \otimes \mathbf{n} \right\} dA \tag{25}$$

In (25) $\mathbf{n}$ is the normal to the crack surface and $[\mathbf{u}]$ the displacement discontinuity across the surface of the crack. The integration is extended over the entire crack surface A. The symbol $\otimes$ in (25) denotes the dyadic (tensor) product of two vectors.

Introducing the expressions relating the stress intensity factors and crack opening displacements (Hoenig 1978) it can be shown that the inelastic change of the compliance can be written (Krajcinovic 1989)

$$dS = \frac{3}{V} \sum \int_L (a \, \mathbf{B} \, \delta a) \, dL \tag{26}$$

where a is a characteristic length (for instance, the length of one of the axes of the ellipse) and $\mathbf{B}(H)$ a fourth rank tensor containing information about the crack sizes and orientations (Euler angles ϕ and θ). Since the components of the tensor $\mathbf{B}$ are computed from the crack opening displacements they, in principle, depend on the presence of other cracks within the RVE. Since the perimeter of the crack can be normalized by the length a from (26) it finally follows that

$$dS = N \, (3/V) < (3 \, a^2 \, \delta a) \, \mathbf{B}(\phi,\theta) > \tag{27}$$

where N is the total number of cracks within the volume V of the RVE. If the crack sizes and orientations are not correlated the expression (27) can be rewritten in a simpler form as

$$dS = \{ \, (N / V) <3 \, a^2 \, \delta a> \, \} <\mathbf{B}(\phi,\theta)> \tag{28}$$

where the term in the first brackets on the right hand side of (28) is the increment of the Budiansky and O'Connell (1976) damage variable. Consequently, expressions (27) and (28) confirm that the change in compliance is nothing but an orientation weighted volume average

(i.e. macro-structural analogue) of the Budiansky-O'Connell damage variable. In all of the above expressions the change of the compliance is inelastic. Since the elastic change of the compliance does not exist it is not considered necessary to use the superscript "i" in equations (26) to (28).

According to the above discussion the constitutive law (21) relating macro-stresses and macro-strains can be written in an explicit form whenever the expressions for the rate of change of the volume averages of the inelastic strains $d\varepsilon^i$ and compliance tensor dS are available. In view of the expressions (21), (22) and (25) this is the case when the geometry, loading and material properties are simple enough to admit analytical solutions for the stress intensity factors, components of the second rank tensor **C** and the crack opening displacements [**u**] (needed to compute the components of the tensor **B**) In general this restricts the analyses to the planar and penny-shaped cracks embedded in a homogeneous isotropic or at most transversely isotropic and infinitely extended elastic matrix. In all other cases the determination of the stress intensity factors and/or crack opening displacements requires use of approximate expressions (Nemat-Nasser and Horii 1982, Fanella and Krajcinovic 1988, Nemat-Nasser and Obata 1988) or nontrivial quadratures of complicated integrals (Mura 1982) unsuitable for the considered problem. The above mentioned restrictions severely limit the applicability of these micromechanical models since the anisotropy will, in a general case, be introduced by microcracks into an otherwise isotropic matrix.

The expressions such as (22) and (28) imply summation of contributions of each of the N microcracks needed to compute the change of the compliance of the RVE mapping on the material point. This process is further complicated by the fact that both the stress intensity factor and the crack opening displacement of the observed crack will be influenced by the presence of the other (N-1) cracks within the RVE. Even though these stress intensity factors and crack opening displacements can be, as already mentioned, determined solving a system of N coupled integral equations, such a strategy is by no means feasible since the computations would have to be repeated for every increment of the stress field (during which the history changes) at each material point.

A much more promising strategy is associated with the application of the effective continuum models discussed at length in Kunin (1983), Nemat-Nasser and Hori (1990) and many other sources. The basic idea of this approach consists in reducing the problem of determining the stresses and strains in an elastic solid weakened by many cracks by a series of much simpler problems of computing the stresses and strains for the case of a single crack

embedded in an effective continuum. The simplest, and most frequently applied, model belonging to this family is based on the so-called self-consistency property. More specifically, the self-consistent model implies that:

(a) the external field of an observed defect weakly depends on the exact location of the other defects within the RVE, and that

(b) the external field of each crack is equal to the average (macro, or far-field) stress in the RVE.

The assumption (b) eliminates the need to solve the system of integral equation while the assumption (a) reduces the configuration space by eliminating from considerations the location of cracks within the RVE. More importantly, it becomes possible to place each crack into the center of the RVE occupied by an effective solid which in the sense of the overall energy reflects the presence of all other cracks. Since a microcrack is typically small compared to the size of the RVE, the stress intensity factors and the crack opening displacements of a given microcrack (assuming it to be penny-shaped or elliptic in form) can readily be determined if the effective solid is either isotropic or transversely isotropic. The simplest solution, to be referred to as the Taylor's model, is to neglect the other cracks altogether and assume that each crack is embedded in the virgin (undamaged) solid. This approximation is, obviously, justified only in the case of a dilute crack concentration. In all of these cases, regardless of the approximation level the overall solution still implies a superposition of a large number of simple problems. The superposition is typically replaced by quadratures introducing the probability density functions for the crack sizes and orientations and integrating over the corresponding space (M. Kachanov 1982, Horii and Nemat-Nasser 1983, Krajcinovic and Fanella 1986, Krajcinovic and Sumarac 1989, etc.).

It is notable that in its conventional form the self-consistent model (Budiansky and O'Connell 1976) predicts that the elastic moduli will vanish at some microcrack density. For example, for the case of isotropic damage (perfectly random orientation of cracks) the elastic modulus vanishes when

$$\omega = (N a^3 / V) = 9/16 \tag{27}$$

It is very interesting, and perhaps not entirely fortuitous, that the damage at the maximum stress is again close to 0.5 as found in the case of the parallel bar model (no interaction) and lattice systems.

This result provided motivation for several modifications and improvements of the original method such as double embedding suggested by Christensen and Lo (1979), a more recent method promoted by Mori and Wakashima (1990). Additionally, the application of the differential scheme (Hashin 1988) attracted substantial interest. All of these models significantly improve the estimates of the elastic moduli for moderate to high microcrack densities defined as the range $0.2 < \omega < 0.5$ of the Budiansky-O'Connell variable (see, Nemat-Nasser and Hori 1990). However, a question remains whether the direct interaction of microcracks at these densities already becomes significant. A more rigorous level of modelling (Kanaun 1974) appears to be too complex to be appealing. An approximation along the lines suggested by M. Kachanov (1987) seems to present a feasible alternative even though the configurational space attached to each material point of the continuum becomes substantially larger since it becomes necessary to keep track of the exact position of each crack within the RVE.

The most difficult problem in the process of the formulation of a continuum theory consist in a rational definition of the kinetic equations, i.e. in prescribing the law describing the advance of the crack front $\delta\ell$ as a function of the stresses. It was already noted that this was not the case utilizing the discrete models discussed above. The kinetic law was just a consequence of the initial disorder, i.e. of the fact that the resistance to the crack growth was not uniform. An essentially similar idea was advanced in Krajcinovic and Fanella (1986), Krajcinovic and Sumarac (1987), Krajcinovic (1989), etc. who considered statistical distribution of strengths based on the microstructural hierarchy of fracture energies, and the morphology of the microstructure itself. The performed computations did not prove to be very sensitive within the considered range of initial disorders. This was to be expected since all performed computations were based on the Taylor's and/or self-consistent models and were, therefore, valid only in the pre-critical regime. The post-critical regime will, in all probability, strongly depend on the morphology of the microstructure (grain size, initial disorder and initial defects).

A rational formulation of kinetic equations, analogous to the procedure commonly adopted in slip theories, was suggested by Krajcinovic and Fanella (1986), Krajcinovic and Sumarac (1987), Krajcinovic (1989), etc.. This formulation is based on the Griffith's criterion, derivable from (20), according to which an observed microcrack will commence its growth ($\delta\ell > 0$) when

$$G - 2\gamma > 0 \tag{28}$$

The elastic energy release rate G of a given crack depends on the crack size a, orientation (Euler angles ϕ), recorded history (accumulated damage) H and the state of stress. Thus, the expressions (28) written for all N cracks within the RVE, represent a family of surfaces in the (a, ϕ, σ, H) space. The inner envelope of this family of surfaces (which contains the unstressed state $\sigma = 0$) represents the locus of points (thermodynamic states) at which the history can change ($\delta \ell > 0$).

The fracture (surface) energy γ must be considered as being a random variable. The distribution of this random variable depends on the morphology of the micro-scale (coarse aggregate grading in concrete, grain size distribution in ceramics, etc.) as well as the hierarchy of strengths of the constituent phases.

The analyses using the described models (see a summary in Krajcinovic 1989, Nemat-Nasser and Obata 1988, or Ju 1989) proved to be reasonably straightforward in the case of simple, homogeneous states of stress. Most, if not all, material parameters were directly identifiable reducing the ambiguity to a minimum. Despite the simplifying assumptions introduced into the model the results proved to be sufficiently accurate for all practical purposes. In all considered cases of uniaxial tension and compression of brittle and semi-brittle materials, time dependent and time independent deformation of polycrystalline ceramics these models were restricted to the pre-critical regime. Nevertheless, by relating the macro-response to the micro-structure of the specimen the micromechanical theories will, eventually, provide rational basis for optimization of materials for a specific set of circumstances. This aspect of the micromechanical modeling was further emphasized in the formulation of an analytical model for the prediction of the gradual degradation of concrete exposed to the sulphate attack, Fig.4 (Krajcinovic, et al., 1990). In this particular case it was possible to go a step further, examine the equations of the chemical reactions, and establish a rational connection between the available volumes of the reactants and the eigenstrains related to the expansion of the reactive products. As a result, the overall strain, and the failure mode, is found to depend on the chemical composition of the concrete, its microstructure (diffusivity and porosity) and the concentration of the diffusing solute. The results, shown below clearly indicate the power of the adopted modelling technique.

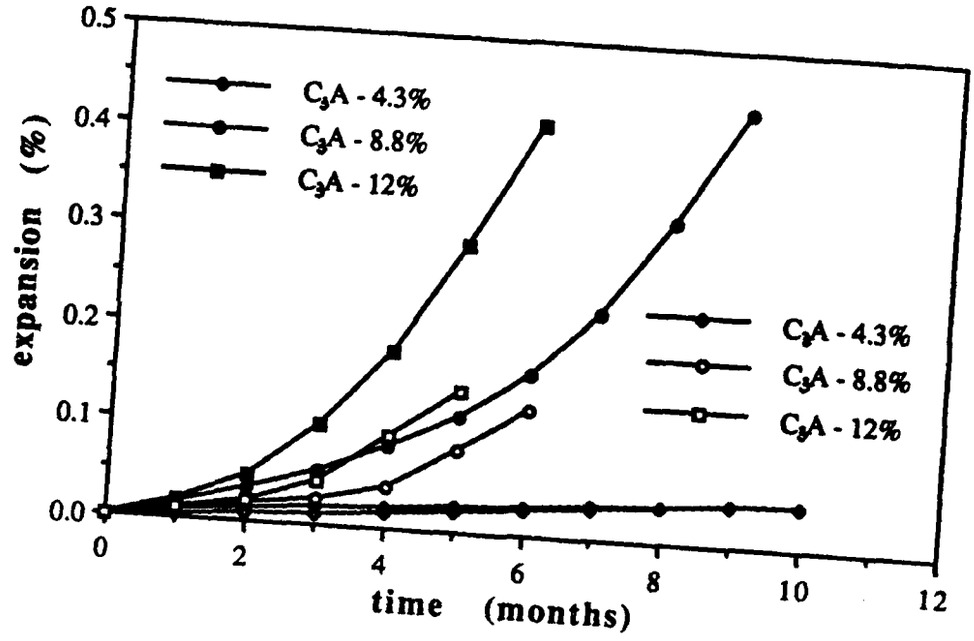

Fig.4. Expansion of mortar bars caused by external sulphate attack (solid symbols - experiments by Ouyang, et al. 1988)

Phenomenological Models

Despite their great advantage in modelling physical reality with a minimum of ambiguity and arbitrariness the micromechanical models are, in general, computationally inefficient for practical applications. Conversely, the ambiguities inherent in macro-modelling of micro-processes often result in emergence of many different and often contradictory phenomenological models. This was certainly true in the case of the damage mechanics (see Krajcinovic, 1984) which was from the very beginning plagued by a plethora of models claiming to be rightful generalizations of the original Kachanov's (1958) model.

It seems, therefore, useful to settle some of the outstanding points using the already known results following from the micromechanics of the analyzed phenomenon. Concentrating on the perfectly brittle processes on the basis of the expression (18) rewritten as,

$$d^i\Psi = Q_i\, dq_j \tag{29}$$

the macro thermodynamic flux written in form of a vector can be defined as

$$dq = \{dS_{1111}, dS_{2222}, ...\} \tag{30}$$

while the corresponding vector of affinities is

$$Q = (1/2)\{\sigma_{11}\sigma_{11}, \sigma_{22}\sigma_{22}, ...\} \tag{31}$$

The micro-fluxes and affinities derived from (20) as

$$f_j = (L/2A)\,(G - 2\gamma)_j \quad \text{and} \quad d\xi_j = (1/V)\,(2A\, dA/L)_j \tag{32}$$

can be related to the corresponding macro fields (31) and (32) in a manner derived in Rice (1971). Thus, as argued in Krajcinovic, et al. (t.a.) the thermodynamic force is the excess energy release rate integrated along the perimeter of the crack and averaged over its surface. Also, the thermodynamic flux is recognized as the increment of the Budiansky-O'Connell damage variable (27).

Following Rice (1971) it can be further shown that if the increase in the surface area of a crack depends on the external stress only via its own affinity $d\xi_n = F(f_n, H)$ the macro-potential (Krajcinovic, et al., t.a.)

$$\Omega(Q, \xi) = \frac{1}{V}\int_0^{f_n(Q,\xi)} \dot{\xi}_m\,(f_m, H)\, df_m \tag{33}$$

can be obtained superimposing all micro-potentials $F(f_n,H)$. The macro-fluxes are then obtained as in the theory of plasticity from the normality property of the macro-potential.

The most important aspect of the outlined micro-to-macro transition, discussed in considerable detail in Krajcinovic, et al. (t.a.) are that the potential exists as long as the propagation of a crack depends only on its own energy release rate. All other cracks influence the observed crack only through the properties of the effective medium. Consequently, the potential exists whenever the self-consistent approximation is justifiable. It is also noticed that while the change of the compliance can be selected as the macro-flux it

is not always possible to identify an instantaneous magnitude of the compliance as the internal variable. This situation is analogous to the theory of plasticity which is also unable to determine the initial value of the plastic strain at the onset of an experiment.

CONCLUSIONS

The objective of the present paper was to review the state-of-art in modelling of brittle response of engineering solids. Without dwelling on details of the discussed models it seems reasonable to conclude that despite the significant progress achieved during the last decade the task of formulating a realistic, reliable and comprehensive analytical model has not as yet been fully accomplished. The mere fact that the three discussed classes of models have not as yet been properly related is just one of the reasons for the above statement.

The statistical (discrete) modelling was limited to expensive computations which will become even more extensive with transition to the three-dimensional problems and more realistic lattices. Nevertheless, the physical insight into the phenomenon of damage evolution and its dependence on the random properties of the microstructure, brought to light with this type of models, should not be underestimated.

The micromechanical modelling seems to work exceedingly well for the homogeneous states of stress and strain and the pre-critical regime. The versatility of this class of models and the ease with which it can be adopted to different types of problems has been established beyond any doubt. The most important accomplishment of these models is associated with their ability to relate the macro-response to the micro-structure and even chemical composition of the solid. The extension of this type of models to the post-critical response (see the papers in Mazars and Bazant, 1989) is still a matter of considerable disagreements. In view of the results of the statistical modelling it appears doubtful whether a deterministic model of the post-peak response presents a realistic objective at all.

It was finally argued that a reasonably simple phenomenological model can be derived from the micromechanical theory in a rigorous manner via a micro-to-macro transition (similar to those establishing connection between the slip and plasticity theories). This approach seems to be very helpful in settling the dispute centering on a "proper" selection of the internal (damage) variable which plagued the adolescent period of the development of the

damage mechanics. However, insufficient data and experience related to the application of this model to a wide spectrum of problems prevents any definitive conclusions and assessments of its utility.

The most far reaching conclusions is, perhaps, that the deterministic nature of the pre-critical response lends itslef well to micromechanical and phenomenological modelling alike. The volume averages of the involved fields are sufficient indicators of the mechanical response and further refinements of these models will lead to an accurate assessment of many related phenomena. The modelling of the response in the post-critical (or softening) regime is an altogether different problem. The response becomes by its nature strongly non-local and non-deterministic. Direct crack interaction takes a dominant role. In the language of the statistical physics the damage is a multifractal involving more than one scale parameter. In view of the random nature of the response, large deviations from the expected values and large skewness of the results the volume averages have much less significance than in the pre-critical regime. Hence, a rational model of this regime of the overall response presents a serious challenge which must be addressed in all of its complexity.

ACKNOWLEDGEMENT

It is a pleasant duty to acknowledge the financial support in the form of research grants from the U.S. Department of Energy, Office of Basic Energy Sciences, Engineering Research Program and the U.S. Air Force Office of Scientific Research, Directorate of Aerospace Sciences, Civil Engineering Program.

REFERENCES

Bolotin, V.V. (1990), "Prediction of Service Life for Machines and Structures" , ASME Press, New York, NY.

Budiansky, B. and R.J. O'Connell, (1976), Int. J. Solids and Structures, 12, p. 81.

Christensen, R.M. and K.H. Lo (1979), J. Mech. Phys. Solids, 27, p. 315.

Fanella, D. and D. Krajcinovic (1988), Eng. Fracture Mech., 29, p. 49.

Hansen, A. S. Roux and H.J. Herrmann (1989), J. Phys. France, 50, p. 733.

Hashin, Z. (1988), J. Mech. Phys. Solids, 36, p. 719.

Herrmann, H.J., A. Hansen and S. Roux (1989), Phys. Rev. B, 39, p. 637.

Hoenig, A. (1978), Int. J. Solids Structures, 14, p. 925.

Horii, H. and S. Nemat-Nasser (1983), J. Mech. Phys. Solids, 31, p. 155.

Hult, J. and L. Travnicek (1983), J. Mec. Theor. Appl., 2, p. 643.

Ju, J.W. (1989), Int. J. Solids Structures, 25, p. 803.

Kachanov, M. (1982), Mech. Mater., 1, p. 19.

Kachanov, M. (1987), Int. J. Solids Structures, 23, p. 23.

Kanaun, S.K. (1974), Isled. po Uprugosti i Plastichnosti, 10, p. 66.

Krajcinovic, D. (1984), Appl. Mech. Rev., 37, p. 1.

Krajcinovic, D. (1989), Mech. Mater., 8, p. 117.

Krajcinovic, D., M. Basista, D. Sumarac and M. Al-Ghaffar (1990), Final Report to AFOSR, Mech. and Aerospace Engng, Arizona State University.

Krajcinovic D., M. Basista and D. Sumarac (to appear) J. Appl. Mech.

Krajcinovic, D. and D. Fanella (1986), Eng. Fract. Mech., 25, p. 585.

Krajcinovic, D. and M.A.G. Silva (1982), Int. J. Solids Structures, 18, p. 551.

Krajcinovic, D. and D. Sumarac (1987), in: D. Krajcinovic and J. Lemaitre eds. "Continuum Damage Mechanics: Theory and Application", Springer-Verlag, Wien, p. 135.

Kunin, I.A. (1983), "Elastic Media with Microstructure II, Three-Dimensional Models", Springer-Verlag, Berlin.

Mazars, J. and Z.P. Bazant (1989), "Cracking and Damage", Elsevier Appl. Sci. Publ., London, UK.

Mori, J. and K. Wakashima (1990), in: G.J. Weng, M. Taya and H. Abe, eds. "Micromechanics and Inhomogeneity - The Toshio Mura Anniversary Volume", Springer-Verlag, New York., p. 269.

Mura, T. (1982), "Micromechanics of Defects in Solids", M. Nijhoff Publ., The Hague.

Nemat-Nasser, S. and M. Hori (1990), in: G.J. Weng, M. Taya and H. Abe, eds: "Micromechanics and Inhomogeneity - The Toshio Mura Anniversary Volume" Springer-Verlag, New York, NY., p. 297.

Nemat-Nasser, S. and H. Horii (1982), J. Geophys. Res., 87, p. 6805.

Nemat-Nasser, S. and M. Obata (1988), J. Appl. Mech., 55, p. 24.

Ouyang, C., A. Nanni and W.F. Chang (1988), Cement and Concrete Res., 18, p. 699.

Rice, J.R. (1971), J. Mech. Phys. Solids, 19, p. 61.

Rice, J.R. (1975), in: A. Argon, ed: "Constitutive Equations in Plasticity" MIT Press, Cambridge, MA., p. 23.

Sumarac, D. and D. Krajcinovic (1987), Mech. Mater., 6, p. 39.

ON THE RELATIONSHIP BETWEEN FRACTURING OF BRITTLE MICROCRACKING SOLID AND ITS EFFECTIVE ELASTIC PROPERTIES

Mark KACHANOV
Department of Mechanical Engineering
Tufts University
Medford, Massachusetts 02155

ABSTRACT

It is argued that, contrary to the spirit of many damage models, there is no simple correlation between fracturing of a brittle microcracking solid and the change of its effective elastic moduli. Physically, the absence of such a correlation is explained by the fact that the fracture-related properties (like stress intensity factors) are determined by local fluctuations of the crack array geometry whereas the effective elastic constants are the volume average quantities, relatively insensitive to such fluctuations.

1. INTRODUCTION

It is discussed whether a correlation exists between the effective elastic moduli of a solid with multiple cracks and the fracture-related properties (like stress intensity factors, SIFs). This discussion is relevant for a number of damage models (see reviews [1,2]) which are aimed at description of fracturing of a brittle microcracking solid but in actuality deal with the effective elastic properties of the solid. Such a substitution is done either explicitly, by assuming that the tensor of effective elastic compliance S_{ijkl} can be used as a damage parameter, or implicitly, by constructing an elastic potential f which is quadratic in stresses (or strains) and contains, in addition, a damage parameter D (scalar, vectorial or tensorial); such a construction, aside from the statement that the derivative $\partial f/\partial D$ can be interpreted as an energy release rate associated with damage, reduces to a certain model for the effective elastic constants. The underlying idea - that progression towards failure can be monitored by the change of effective elastic constants - seems intuitively reasonable; it is particularly tempting due to the fact that the effective elastic moduli can be easily measured.

An objection can be raised that, as is well known, a small crack in a brittle material has a very small impact on the effective elastic constants but drastically reduces the tensile strength. One may argue, however, that, after certain initial set

of cracks has been nucleated and started to grow, the progression towards failure is uniquely correlated to the change of the effective elastic moduli. This idea is examined below from several points of view.

2. "PARADOXICAL" EXAMPLE

To demonstrate that this idea is far from obvious, we start with a simple example when the relation between the SIFs and the effective elastic properties is "paradoxical". Consider a plate containing stacks of parallel cracks (fig.1). Suppose that extra cracks are introduced in-between the neighboring cracks in stacks.

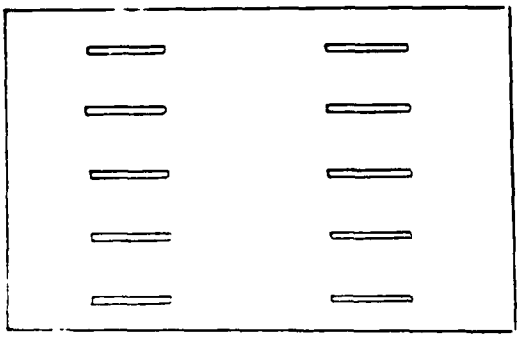

Fig. 1. Crack array with paradoxical relation between SIFs and effective stiffness

Introduction of these new cracks, obviously, reduces elastic stiffness in the direction normal to cracks (since it produces additional displacements at remote boundaries when load is applied) - material elastically "softens". However, the SIFs decrease (due to an increased shielding) so that the critical load at which the cracks start to propagate increases - material is strengthened by new cracks.

3. RANDOM CRACK ARRAYS

It may be argued that the example above does not represent any realistic crack statistics (although such parallel crack patterns occur in rocks and certain composites) and that for the crack arrays that are more "random" the association between progression towards failure and reduction of elastic stiffness is appropriate. To demonstrate that such an association is not obvious even for random arrays, we did the following computer experiments. A number of two-dimensional crack arrays containing randomly oriented cracks of the same length 2l were generated (using the random number generator); statistics of crack centers was also random (subject to the restriction that cracks were not allowed to intersect; this was achieved by generating cracks successively and discarding a newly generated crack if it happened to intersect the already existing ones). For each sample array, using the method of [3], we calculated (1) the effective Young's modulus E_{eff} and (2) maximal, among all the crack tips, value of $K_I^2+K_{II}^2$ induced by a uniaxial loading. (Strictly speaking, the value of $K_I^2+K_{II}^2$ is relevant for the initiation of crack propagation only in the case of rectilinear crack extension; when both K_I and K_{II} are present, a certain linear combination of K_I^2, K_{II}^2 is a relevant parameter. This combination, however, does not differ much from $K_I^2+K_{II}^2$ so that the latter quantity can be

used for an approximate estimate of proximity of a crack to the onset of propagation). We found that, whereas the value of E_{eff} was quite stable, differing by not more than a few percent from one statistical sample to another, the value of Max $(K_I^2+K_{II}^2)$ fluctuated significantly (reaching high values in those samples where two very closely spaced crack tips could be found). The average $\langle \text{Max } (K_I^2+K_{II}^2)\rangle$ over several statistical samples increases with crack density $\rho=Nl^2/A$ (N is the number of cracks in a representative area A) increasing; it may thus seem reasonable to argue that the value of E_{eff} can be used as an indicator of the fracture-related parameter Max $(K_I^2+K_{II}^2)$. (since both quantities are monotonic functions of ρ). It should, however, be mentioned that (1) unlike E_{eff}, the value of $\langle \text{Max } (K_I^2+K_{II}^2)\rangle$ increases not only with ρ but, also, as both the number of cracks N and the representative area A increase while keeping ρ constant (or even decreasing!) and (2) it is unclear whether, in view of a significant fluctuation of Max $(K_I^2+K_{II}^2)$ from one crack array to another, the average (over a number of statistical samples) value of Max $(K_I^2+K_{II}^2)$ can be used as a representative quantity for any given crack array.

4. STRONG AND WEAK INTERACTIONS. CLUSTERING OF CRACKS

As discussed in [4], crack interactions that are strong in terms of their impact on SIFs may be weak in terms of their impact on the effective elastic constants. Indeed, as is well known, contribution of a given crack into the overall strain of a solid with cracks is $\epsilon = (\langle \mathbf{b}\rangle \mathbf{n}+\mathbf{n}\langle \mathbf{b}\rangle)\ (2l/A)$ where $\langle \mathbf{b}\rangle$ is the average displacement discontinuity across the crack line. This implies that the contribution of a given crack into the reduction of the effective stiffness is proportional to $\langle \mathbf{b}\rangle$. In many cases, interaction of a given crack with other cracks will produce a significant increase in SIFs and will, thus, be important from the point of view of fracturing, whereas the average displacement discontinuity $\langle \mathbf{b}\rangle$ and, therefore, the effective moduli, will be affected by interactions insignificantly. (Such situations are typical for the collinear cracks).

A closely related issue is that the maximal values of SIFs attained in a crack array are highly sensitive to clustering of cracks. Fig. 2 illustrates this statement: Max $(K_I^2+K_{II}^2)$ is, typically, substantially higher in the configurations of the type 2b as compared with configurations of the type 2a.

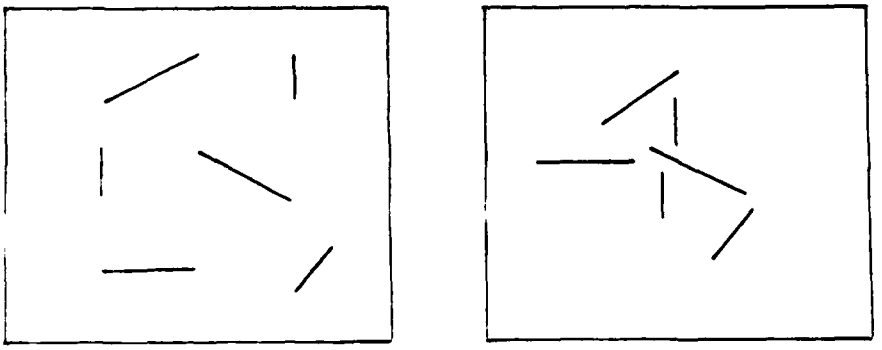

Fig. 2. Clustering of cracks

At the same time, the effective elastic moduli exhibit a low sensitivity to clustering, i.e. the difference between the values of S_{ijkl} for the configurations 2a and 2b is generally insignificant (provided the overall crack density is the same). Thus, monitoring the change in effective elastic constants may not necessarily detect the onset of strong crack interactions and clustering of defects - events that are crucially important from the point of view of progression towards failure.

5. CRACK-MICROCRACK INTERACTION PROBLEM

The absence of correlation between the effective elastic constants and the fracture-related properties of a cracked solid is particularly apparent in the problem of crack-microcrack interactions. As has been found in [5-7], the microcracks located in the short range interaction zone (several microcracks closest to the main crack tip) produce a dominant effect on the SIFs at the main crack tip, as compared with the total impact of all the microcracks located farther away (this can also be seen from two examples considered in [8,9]); due to a high sensitivity of the interaction effect to the exact positions of microcracks in the short range zone, the SIFs at the main crack tip fluctuate significantly and even qualitatively (from "shielding" to "amplification") from one sample of the microcrack statistics to another.

This means that there is no statistically stable effect of stress "shielding"; on the contrary, being conservative, one may conclude that the overall effect of interactions with microcracks is the one of "enhancement", particularly in the 3-D configurations [5,7]. (This does not exclude, of course, other possible mechanisms of toughening due to microcracking, like expenditure of energy on nucleation of microcracks; neither does it exclude the possibility of stress shielding for some special microcrack arrangements, like an extremely dense array of microcracks parallel to the main crack [10]). At the same time, modelling of the microcracked region by an effective elastic material of reduced stiffness would predict that the effect of interactions is the one of stress shielding - the result that appears to be incorrect.

Another important effect of interactions is the appearance of "secondary" modes on the main crack, due to stochastic asymmetries in the microcrack field, i.e. K_{II} under mode I remote loading (or K_I under shear remote loading). Since the appearance of mode II SIF promotes crack kinking, this may be partially responsible for an irregular shape of crack paths in brittle microcracking materials. This effect is obviously, missed if the microcracked zone is modelled by an effective elastic material. This indicates that modelling of the microcracked region (at least, of its short range zone that produces the dominant effect) by an effective elastic material may not be adequate, in the sense that there is no simple correlation between the reduction of stiffness of the damage zone and its impact on the SIFs at the main crack tip.

6. CONCLUSION

It appears that there is no direct correlation between the effective elastic constants and the fracture-related properties of a solid with multiple cracks. Physically, the absence of such correlation has a clear explanation: the fracture-related quantities (like SIFs) are highly sensitive to local fluctuations

of the crack array geometry. The effective elastic constants on the other hand, are the volume average properties which are relatively insensitive to such fluctuations.

ACKNOWLEDGEMENT.

This work was supported by the U.S. Department of Energy (Grant DE-FG02-86ER13607) and by the U.S. Army Research Office (Grant DAAL02-88-K-0027).

REFERENCES

1. D. Krajcinovic, 1989,"Damage Mechanics", Mechanics of Materials, Vol.8, pp. 117-197.
2. M. Kachanov, 1987,"On Modelling of Anisotropic Damage in Elastic-Brittle Materials-a Brief Review", Damage Mechanics in Composites, Winter Annual Meeting of ASME, ed. A. Wang and G.Haritos, pp. 22-105.
3. M. Kachanov, 1987,"Elastic Solids with many Cracks: a Simple Method of Analysis",International Journal of Solids and Structures, Vol.23, pp. 23-43.
4. M. Kachanov and J.-P. Laures, 1989,"Three-Dimensional Problems of Strongly Interacting Arbitrarily Loaded Penny-Shaped Cracks", International Journal of Fracture, Vol.41, pp.289-313.
5. J.-P. Laures and M. Kachanov,1990, "Three-Dimensional Interactions of a Crack Front with arrays of Penny-Shaped Microcracks", International Journal of Fracture, to appear.
6. E. Montagut and M. Kachanov,1988, "On Modelling a Microcracked Zone by Weakened Elastic Material and on Statistical Aspects of Crack-Microcrack Interactions", International Journal of Fracture, Vol. 37 , pp. R55-R62.
7. M. Kachanov, E. Montagut and J.-P. Laures, 1990,"Mechanics of Crack-Microcrack Interactions", Mechanics of Materials, to appear.
8. A. Rubinstein, 1985,"Macrocrack Interaction with a Semi-Infinite Microcrack Array",International Journal of Fracture, Vo. 27, pp. 113-119.
9. A. Rubinstein and H. Choi, 1988,"Macrocrack Interaction with Transverse Array of Microcracks", International Journal of Fracture, Vol. 36, pp. 15-26.
10. A. Chudnovsky and S. Wu, "Effect of Crack-Microcrack Interaction on Energy Release Rates", International Journal of Fracture, to appear.

Session 7:

Fracture Process in Fiber Reinforced Ceramics

Chairs:

Robert Chang
Northwestern University
Evanston, U.S.A

Katherine Faber
Northwestern University
Evanston, U.S.A

Reporter:

Nicholas Pagano
Air Force Materials
Laboratory, Dayton, U.S.A.

THE FRACTURE RESISTANCE AND STRENGTH OF BRITTLE MATRIX COMPOSITES

F. ZOK
Department of Materials
College of Engineering
University of California
Santa Barbara, CA 93106

ABSTRACT. The fracture resistance and fracture strength of brittle matrix components have been examined through a combination of experimental and modelling studies. R-curve measurements on both fiber-reinforced and ductile-reinforced composites have been correlated with models of crack bridging. An important feature of the measurements and calculations is the strong influence of specimen size on fracture resistance. The results are used as a basis for the development of an analytical model to predict the fracture strength of composite materials.

1. Introduction

It has now been well established that many brittle matrix composites exhibit R-curve behavior, i.e. their fracture resistance increases with crack extension. The R-curve is due mainly to bridging processes in the crack wake. Specifically, intact particles or fibers exert closing tractions on the crack faces, thus reducing the stress intensity factor at the crack tip. This behavior has been observed in a broad range of materials including fiber-reinforced ceramics [1-5] and cements [6,7], metal-reinforced ceramics [8-10] and intermetallics [11-12], and some monolithic ceramics [13-19].

The fracture resistance can usually be expressed as the sum of two components,

$$K_R = K_o + K_b \tag{1}$$

where K_o is the initial fracture resistance and is typically of the same order as the fracture toughness of the matrix itself. The term K_b is the component due to the bridging ligaments and is described by [20]

$$K_b = \frac{2}{\sqrt{\pi a}} \int_o^{\Delta a} \sigma(x)\, F\left(\frac{x}{a}, \frac{a}{W}\right) dx \tag{2}$$

where a is the total crack length, x is the distance behind the crack tip, W is the specimen width, Δa is the crack extension, $\sigma(x)$ is the spatial variation in the bridging stress and F is the Green's function applicable to the geometry under consideration. It should be noted that when the crack opening displacement becomes sufficient to break the ligaments furthest from the crack tip, the length L of the bridging zone reaches a saturation level and thus the upper limit on the integral must be replaced by L.

In most cases the stress distribution $\sigma(x)$ cannot be measured directly and so is inferred from experimentally measured R-curves and equations (1) and (2). The bridging stress so obtained is then compared with the results of micromechanical models which take into account the details of the bridging process. To conduct such comparisons, an appropriate expression for F must be selected. It should be noted that the expression applicable to small scale bridging conditions ($F = \sqrt{a / 2x}$) is not valid for specimen geometries in which the bridging zone length is a significant fraction of other in-plane specimen dimensions. This result has not been recognized in some studies [16,17] and has lead to some confusion about both the effects of specimen geometry on R-curve behavior and the magnitude of the bridging stress. Such effects have recently been examined in detail [21].

The purpose of this paper is twofold. First it demonstrates that R-curve behavior is indeed dominated by bridging processes in both fiber-reinforced and ductile reinforced composites. This is accomplished through a combination of experimental measurements, micromechanical modelling and microstructural observations. Emphasis is placed on understanding the effects of specimen geometry on the measured fracture resistance. Furthermore, the effect of reinforcement orientation in *ductile-reinforced* composites is examined. These effects are important in composites containing randomly oriented metal fibers, such as those recently developed by Lange et al. [22]. The second purpose is to illustrate how R-curves can be used to predict the fracture *strength* of composites. In particular, the effects of the spatial variation in the bridging stress, the size of the the reinforcement and the size of the initial flaw are considered.

2. Fracture Resistance

2.1 MEASUREMENTS

Standard testing geometries have been employed for the R-curve measurements, including compact tension specimens and pre-notched 3 point and 4 point bending beams, designed in accordance with ASTM standards [23]. The fracture resistance calculations were based on the usual linear elastic formulations, using the applied loads and the length of the matrix crack. Some tests were interpreted to observe microstructural changes.

A variety of composite materials have been studied, including a metal-reinforced ceramic, a model system consisting of a brittle polymer matrix and metal reinforcements, and a fiber-reinforced glass ceramic. Pertinent details of the microstructures are described in subsequent sections; additional details can be found in Refs. [5], [21] and [24].

2.2 DUCTILE REINFORCED COMPOSITES

Two ductile reinforced composites were examined. The first was Al_2O_3 reinforced with randomly oriented, continuous fibers of an Al 4% Mg alloy, with a metal volume fraction of $\approx 23\%$. The processing route is described in detail in Ref. [22]. The second was a model system consisting of a polymethylmethacrylate (PMMA) and continuous Al wire reinforcements. It was fabricated by aligning the wires between the PMMA sheets and hot pressing at 200°C for several hours. The PMMA/Al composite has numerous advantages, including ease of fabrication and good control of the orientation and volume fraction of reinforcements. Furthermore, the wires can be extracted from the composite by dissolving the matrix and thus the *in-situ* flow properties of the

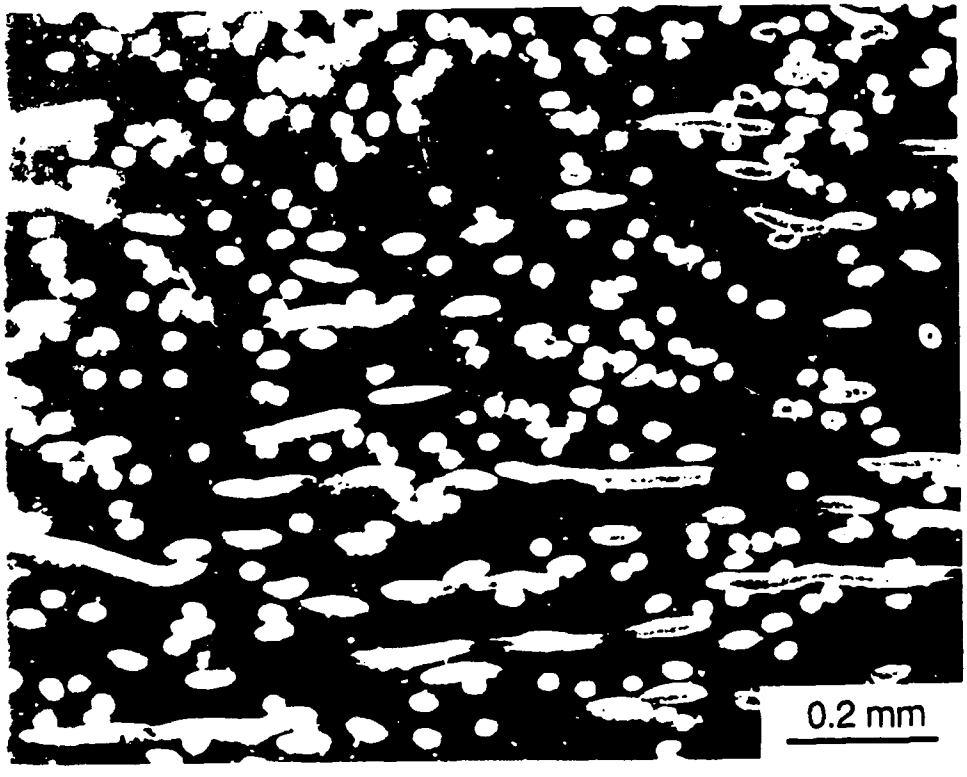

Fig. 1 Micrograph of the Al_2O_3/Al composite.

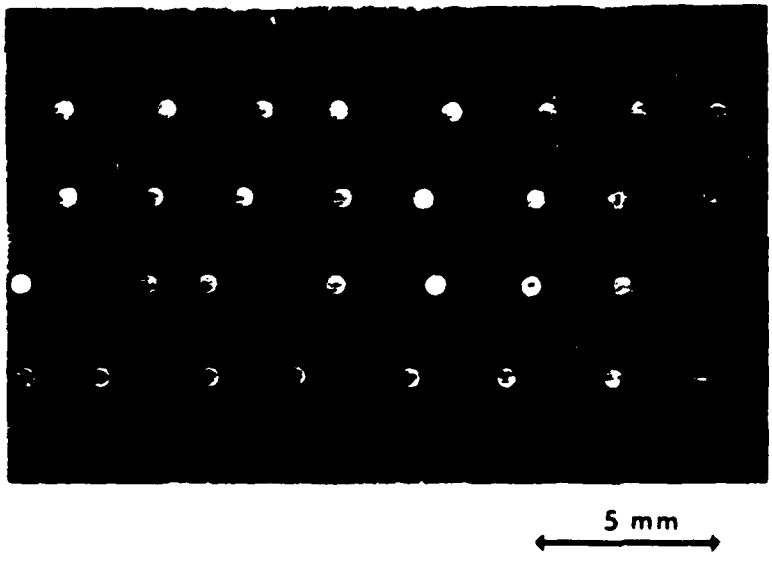

Fig. 2 Transverse section through the PMMA/Al composite ($\theta = 0^0$).

reinforcements can be measured directly. Typical micrographs of both composites are shown in Figs. 1 and 2.

Figures 3 and 4 show the R-curves for the Al_2O_3/Al composite and two of the PMMA/Al composites. The reinforcements in the PMMA/Al composites were aligned perpendicular to the crack plane. The curves for both materials are characterized by an initial fracture resistance K_o equivalent to the fracture toughness of the matrix (3 MPa $\sqrt{m}$ for the Al_2O_3 and 1 MPa $\sqrt{m}$ for the PMMA), an intermediate region where the fracture resistance increases gradually and finally a region in which the resistance apparently increases very rapidly with crack extension. As shown later, the rising portion is symptomatic of large scale bridging and is therefore not representative of the true fracture resistance. Microscopic examinations of the tested specimens reveal the presence of ductile ligaments across the crack faces, an example of which is shown in Fig. 5.

A simulation of the R-curves for the PMMA/Al composites was conducted assuming that the bridging tractions are uniform (as in the Dugdale zone model) and equal to the ultimate tensile strength of the Al wire reinforcements (80 MPa), as measured in a tensile test of the wire itself. The choice of the bridging stress can be justified on the basis that the flow stress of the Al wire increases rapidly from the yield point to the ultimate strength and subsequently remains constant over most of the plastic straining history [21]. Furthermore, the debond length is much larger than the wire radius (Fig. 5) and thus plastic constraint effects can be neglected [25,26]. The fracture resistance is calculated from equations (1) and (2) using an expression for F applicable to the present specimen geometry [20,21]. The agreement between theory and experiment is excellent for composites containing 3% and 10% Al (Fig. 4), thus indicating that the toughness enhancement is indeed attributable to a crack bridging mechanism.

In addition, the computed R-curves for infinitely large specimens of the same material are shown on Fig. 4 for comparison. These correspond to the behavior under small-scale bridging conditions i.e. when the bridging zone length is small relative to all other in-plane specimen dimensions. Evidently the R-curves for the finite specimen geometries are appreciably larger than those corresponding to the infinite specimen, even at relatively small crack extensions. The discrepancy is attributable to *large scale bridging* in the finite geometry and emphasizes the need to account for size effects in interpreting R-curve behavior in composite materials.

A similar simulation was conducted for the Al_2O_3/Al composite, again assuming uniform bridging tractions, and is shown on Fig. 3. In this case, selection of the bridging stress is complicated by the fact that the metal reinforcements are oriented *randomly* in space and thus do not contribute equally to the fracture resistance. Consequently, equations (1) and (2) were used along with the experimental data to infer an average ligament stress of 110 MPa: this corresponds closely to the average between the initial yield stress (70 MPa) and the ultimate tensile strength (170 MPa) of the Al-Mg alloy [21]. The shape of the computed R-curve is in good agreement with the experimental data, provided the finite geometry is taken into account. The R-curve corresponding to small-scale bridging conditions is also shown and again differs substantially from the experimental data obtained on the finite specimen geometry.

Though the R-curve data for the Al_2O_3/Al composite are seemingly described adequately by the Dugdale zone model, cognizance must be taken of the fiber orientation distribution and its role in the crack bridging process. To examine orientation effects in ductile-reinforced composites, a series of PMMA/Al composites containing a symmetric arrangement of *inclined* wires was tested. The composites contained 4 layers of equally spaced wires with a metal volume fraction of $\approx 3\%$. The wires in the two outer layers were aligned parallel to one another but were inclined at an angle 2θ to the wires in the two inner layers. The compact tensions specimens were then machined such

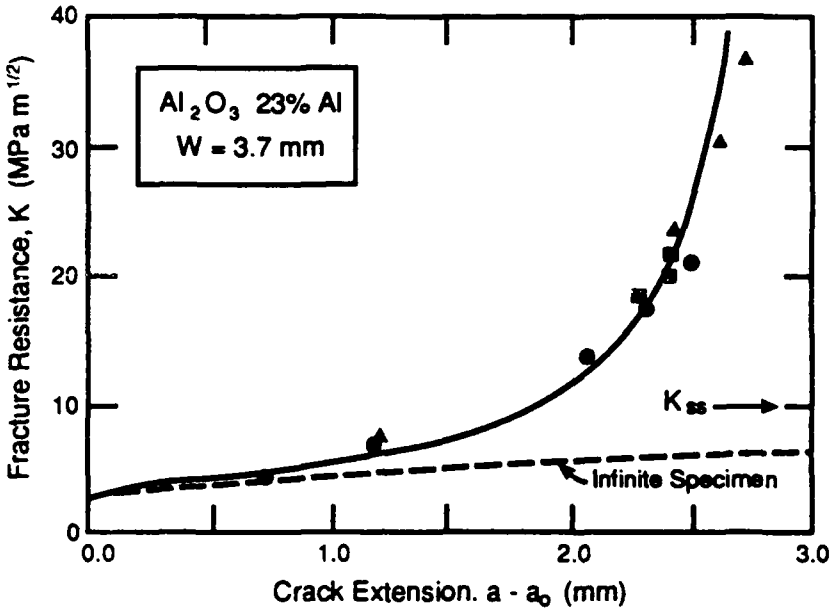

Fig. 3 R-curve for the Al_2O_3/Al composite. The solid line is the computed fracture resistance, taking into account the finite specimen geometry, whereas the dashed line corresponds to the fracture resistance under small-scale bridging conditions. The steady state toughness K_{SS} was determined from the work of rupture test.

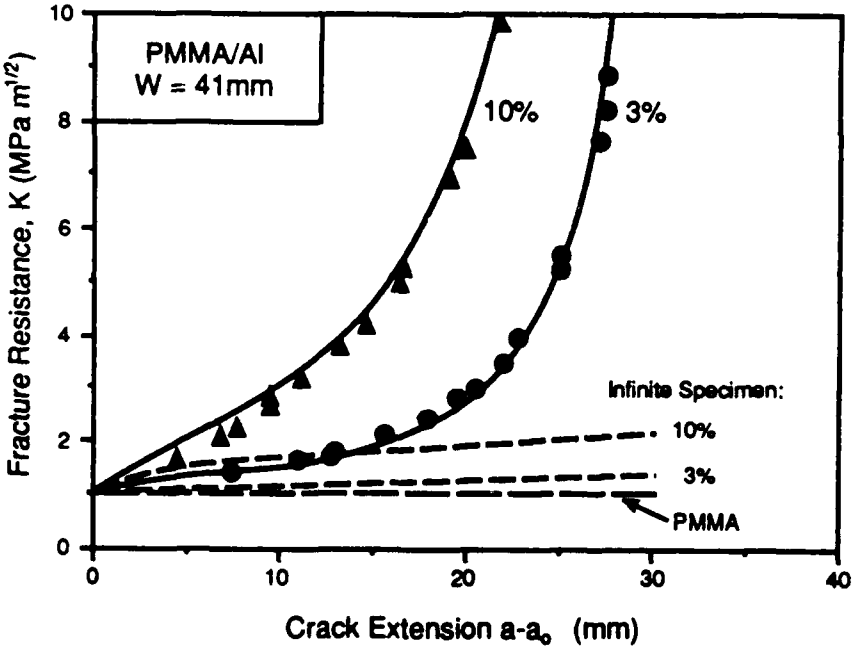

Fig. 4 Measured and calculated R-curves for the PMMA/Al composites containing aligned reinforcements ($\theta = 0^0$).

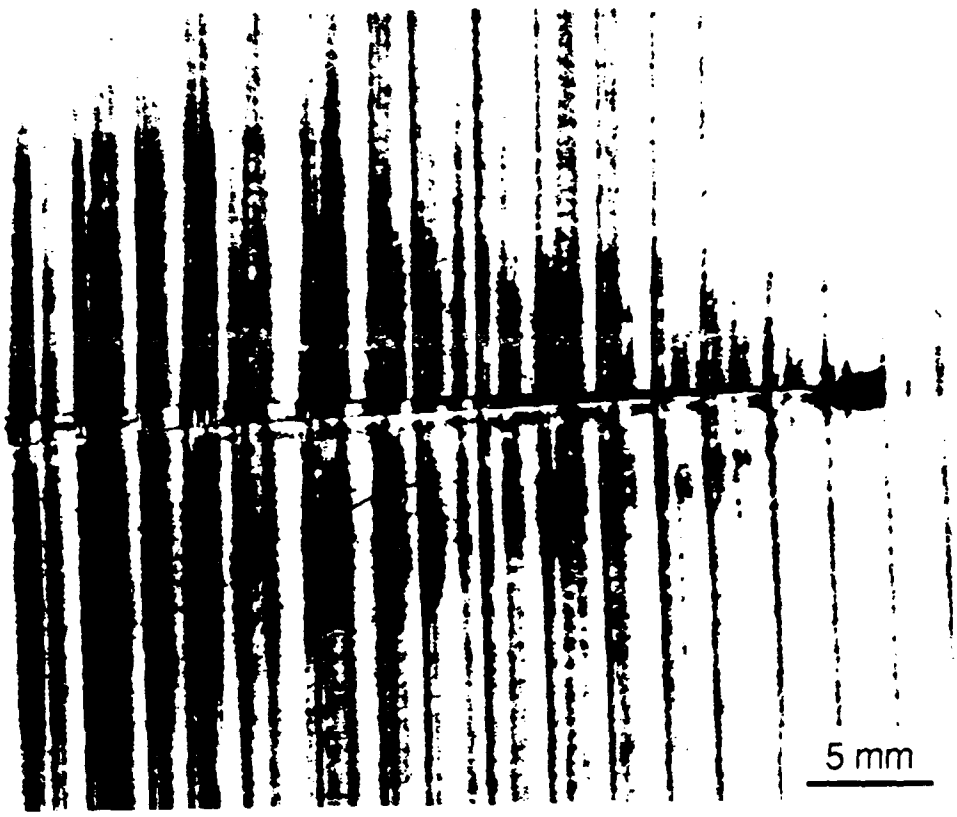

Fig. 5 Macrophotograph of a tested PMMA/Al specimen showing intact Al wires in the crack wake. To observe the degree of debonding at the fiber-matrix interface, a red dye penetrant was inserted into the crack after testing. The debonded region appears dark in the photograph.

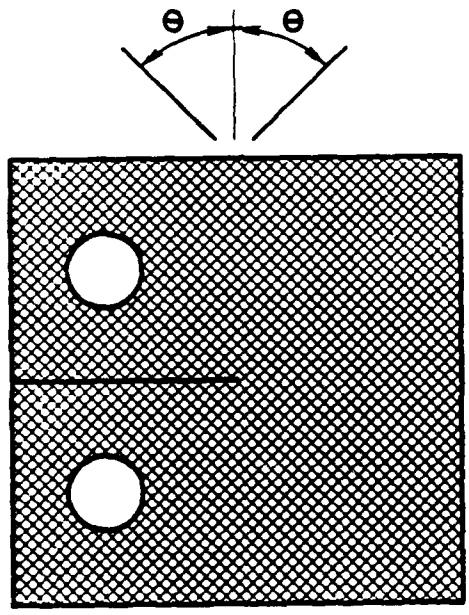

Fig. 6 Schematic diagram of the PMMA/Al specimens containing inclined wires.

that the wires were inclined symmetrically at angles of $\pm\theta$ to the crack plane, as shown schematically in Fig. 6. Figure 7 shows the measured R-curves for values of θ ranging between 0° and 65°. Though they exhibit characteristics of large scale bridging, the curves provide a relative measure of toughening due to bridging since all specimens are the same size. The data show that the toughening contribution K_b decreases substantially with θ: it drops by a factor of ~2 as θ goes from 0° to 45° and is negligible for $\theta \gtrsim 65°$.

The reduction in K_b with θ is attributable to two sources. First, the number of wires intercepted by the crack front per unit area of crack, N_A, *decreases* with θ as:

$$N_A = \frac{f}{\pi R^2} \cos \theta \tag{3}$$

where f is the metal volume fraction and R is the wire radius. Second, the inclined fibers require a smaller load to be plastically deformed than those which are aligned perpendicular to the crack plane because of the imposed bending moment. At the extreme, the wires inclined at a steep angle act essentially as end-loaded cantilever beams and thus contribute minimally to the crack closing tractions and the corresponding toughness K_b. A more detailed examination of orientation effects in both the PMMA/Al and Al_2O_3/Al composites is currently in progress and will be presented elsewhere [24]. For present purposes it is sufficient to note that such effects are important in the fracture resistance behavior of ductile-reinforced composites and must therefore be incorporated into micromechanical models of crack bridging.

An important feature of the present measurements is the absence of a steady-state fracture toughness, K_{SS}, expected to occur when the ligaments furthest from the crack tip begin to fail. This behavior arises because of the large scale bridging effects at large crack lengths. Similar trends have been observed in other materials exhibiting R-curve behavior [16,17] and suggest that the present techniques are not suitable for obtaining steady-state toughness values. An alternate technique, known as the "work of rupture test" [27], was thus employed in this study to evaluate G_{SS} (the steady-state strain energy release rate) for the Al_2O_3/Al composite. The measurements yield an average value of $G_{SS} \approx 400\ Jm^{-2}$, which corresponds to $K_{SS} \approx 10\ MPa\ m^{1/2}$ (assuming an elastic modulus of 250 GPa) [24]. This value is significantly lower than the apparent fracture resistance at large crack lengths (~30 MPa $m^{1/2}$)measured in the previous tests but is likely more representative of the true asymptotic fracture resistance. The magnitude of the discrepancy again demonstrates the problems associated with large scale bridging in the R-curve measurements.

2.3 FIBER REINFORCED CERAMICS

A similar series of R-curve measurements were made on a lithium aluminosilicate (LAS) glass ceramic reinforced with continuous SiC (Nicalon) fibers. The composite contained a symmetric arrangement of 0° / 90° cross plies and a fiber volume fraction of 0.44. Beams suitable for bend testing were machined from the composite plates, with the notch front oriented perpendicular to the plane of the laminate (Fig. 8). The beams were annealed in air at 800° C for periods ranging from 1 h to 16 h [5].

Figure 9 shows a summary of the R-curves for the LAS/SiC composites. The curves are similar to those of the ductile reinforced composites in the sense that they start at a relatively low level of fracture resistance (~5 to 6 MPa $m^{1/2}$) and increase rapidly with crack extension. Once again,

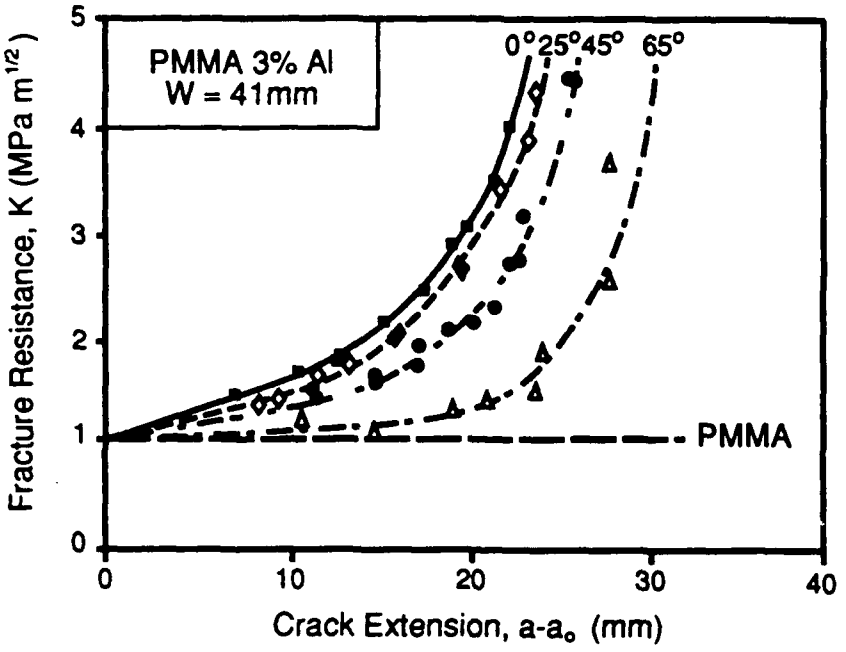

Fig. 7 A diagram showing the effect of orientation on the fracture resistance of the PMMA/Al composite (f = 3%).

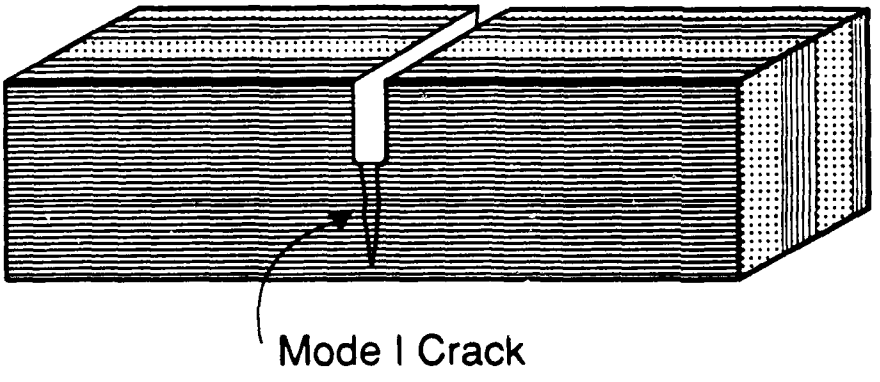

Fig. 8 Schematic diagram showing notch orientation in the LAS/SiC specimens.

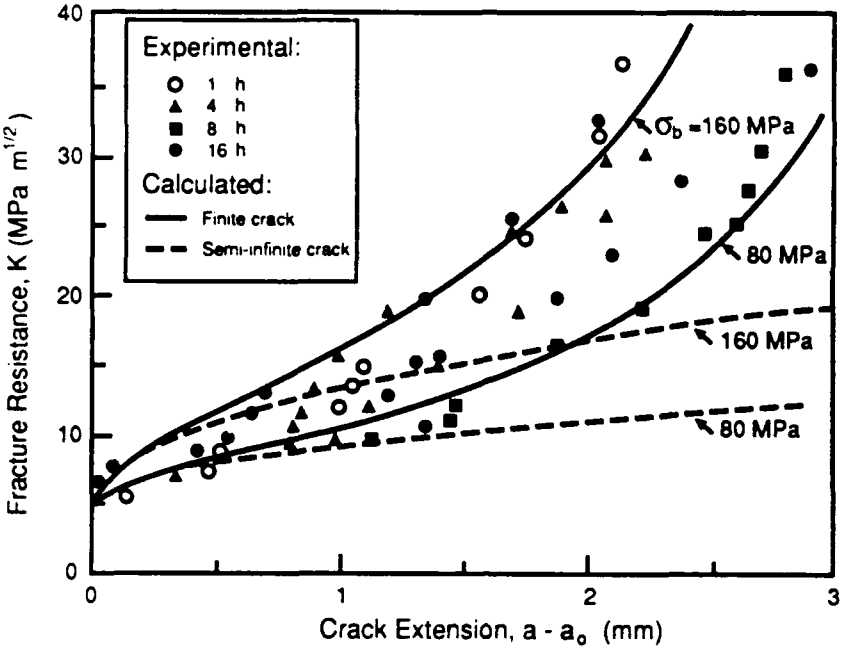

Fig. 9 Measured and computed R-curves for the LAS/SiC composites.

Fig. 10 Micrograph of a notch tip region in the LAS/SiC composite. The arrows show fibers which have failed away from the plane of the matrix crack and subsequently been pulled out of the matrix.

however, the data are influenced by large scale bridging effects, particularly at crack extensions $\gtrsim$ 1mm.

Insight into the origin of the rising R-curve is provided by microscopic observations of the side surfaces of the tested specimens (Fig. 10). Evidently some of the fibers fracture along the plane of the matrix crack whereas others fail at some distance away. Examples of the latter are indicated by arrows in Fig. 10. The embedded fibers are then pulled out of the matrix during crack growth and thus exert tractions on the crack faces.

Near the crack tip the bridging stress associated with fiber pull-out can be expressed as [5]

$$\sigma(x) = \frac{2\tau f h}{R}\left[1-\frac{4\left(1-\nu^2\right)}{Eh}\sqrt{\frac{x}{2\pi}}\,K_o\right] \tag{4}$$

where τ is the sliding resistance of the fiber-matrix interface, h is the average pull-out length, K_O is the critical value of the crack tip stress intensity factor and f is the volume fraction of fibers oriented perpendicular to the crack plane (f = 0.22). Provided the pull-out length is sufficiently large, the second term in the square brackets in equation (4) can be neglected and the bridging stress then taken as

$$\sigma_b \approx \frac{2\tau f h}{R} \tag{5}$$

This approximation allows for a preliminary comparison between theory and experiment, taking into account the large scale bridging effects. Fig. 9 indicates that the measurements are consistent with the computed R-curves for a bridging stress in the range of 80 MPa to 160 MPa. Combining this result with measurements of pull-out length [28], equation (5) gives a sliding stress of ~75 MPa to 250 MPa. These values are broadly consistent with those inferred from pull-out measurements [28], but somewhat higher than those measured by push-through tests [29].

2.4 DISCUSSION

The correlation between the computed and measured R-curves in both the ductile reinforced and fiber reinforced composites indicates that the toughness enhancement is attributable to bridging processes in the crack wake. The important parameters in the resistance behavior are the spatial variation in the bridging stress and the specimen geometry via the function F. In fiber-reinforced composites the bridging stress depends on the interfacial sliding stress and the average pull-out length. In ductile-reinforced composites the bridging stress is governed by the flow characteristics of the metal, the degree of debonding, as well as the orientation of the reinforcements with respect to the crack plane.

An important feature of the present measurements is the marked influence of large scale bridging on fracture resistance. These effects have been incorporated into the simulations through the use of an appropriate Green's function. In general, the magnitude of the large scale bridging effects can be described by the ratio K_b/K_b^∞, where K_b is the increment of toughness due to bridging in the finite specimen and K_b^∞ is the corresponding increment in an infinite specimen. The ratio $K_b/K_b^\infty \rightarrow 1$ when small-scale bridging conditions exist; conversely, $K_b/K_b^\infty >> 1$ when the

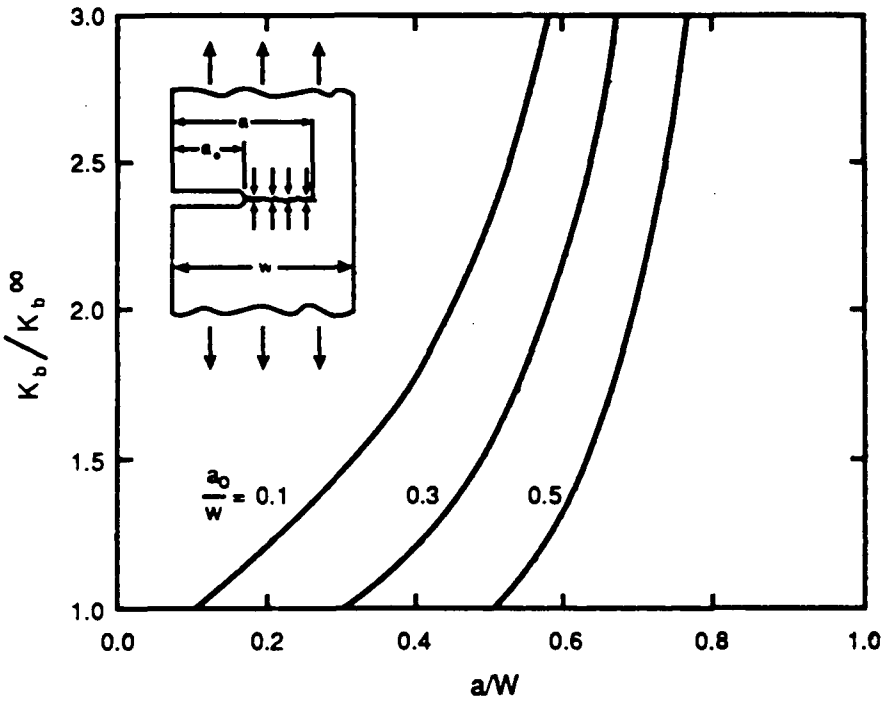

Fig. 11 A diagram showing the effects of large scale bridging, assuming uniform bridging tractions.

bridging zone length is on the same order as the crack length and specimen width. Equation [2] gives

$$\frac{K_b}{K_b^\infty} = \sqrt{\frac{a}{2L}} \int_0^{L/a} F\left(\frac{x}{a}, \frac{a}{W}\right) d\left(\frac{x}{a}\right) \qquad (6)$$

Figure 11 shows a plot of K_b/K_b^∞ against the normalized crack length, a/W, for various values of notch depth, a_o/W, assuming uniform bridging tractions. The curves show a strong dependence of apparent fracture resistance on the relative size of the bridging zone.

It is of interest to note that the preceding calculations can be used in the design of specimen geometries for R-curve measurements, analogous to those of the ASTM Standards for ductile materials. Specifically, the specimen dimensions required to maintain small scale bridging conditions can be determined. First, an estimate of the steady state bridging zone length is required: this is usually available from information about the nature of the bridging process and the scale of the microstructure. From the curves in Fig. 11, appropriate combinations of a and W are then selected such that K_b/K_b^∞ remains below some prescribed level for all resistance measurements up to the saturation level. As a general rule, if the allowable error in K_b is 5 %, i.e. $K_b/K_b^\infty \leq 1.05$, and the initial notch depth a_o/W is between 0.1 and 0.5, then the specimen width should be at least 40 times the bridging zone length. This figure is essentially the same as the minimum ratio of specimen width to *plastic zone* size in ductile materials, as prescribed by ASTM Standard E399 [23].

In addition to the problems of large scale bridging, there exist other effects associated with specimen geometry and mode of loading which may influence resistance measurements in composites. First, the crack opening profile in bending is generally greater than that corresponding to a uniform remote tension, as shown schematically in Fig. 12. Thus, in bending, the bridging stress reaches a maximum at smaller distances from the crack tip, the steady state bridging zone length is shorter, and the slope of the R-curve is higher. Second, the rotational effects in bending result in a crack opening profile which depends on crack length. Specifically, the increase in specimen compliance associated with crack growth causes the crack opening displacement to increase more rapidly with distance from the crack tip, as shown schematically in Fig. 13a. Consequently, the spatial variation in the bridging stress is altered, as is the length of the bridging zone at steady state (Fig. 13b). The resultant R-curve may then exhibit a maximum at the point at which the crack opening effects become larger than those due to large scale bridging (Fig. 16c). Such behavior has recently been observed in TiAl/TiNb composites and has been modelled accordingly [30].

3. Strength

In most recent studies of fracture of composite materials, the emphasis has been focussed mainly on understanding the R-curve behavior and the steady state toughness. In designing structural components with composites, it will also be necessary to understand the relationship between fracture *resistance* K_R and fracture *strength* σ_f. However, this relationship is more complicated than that in monolithic ceramics where the two are linked to the defect length via Griffith's

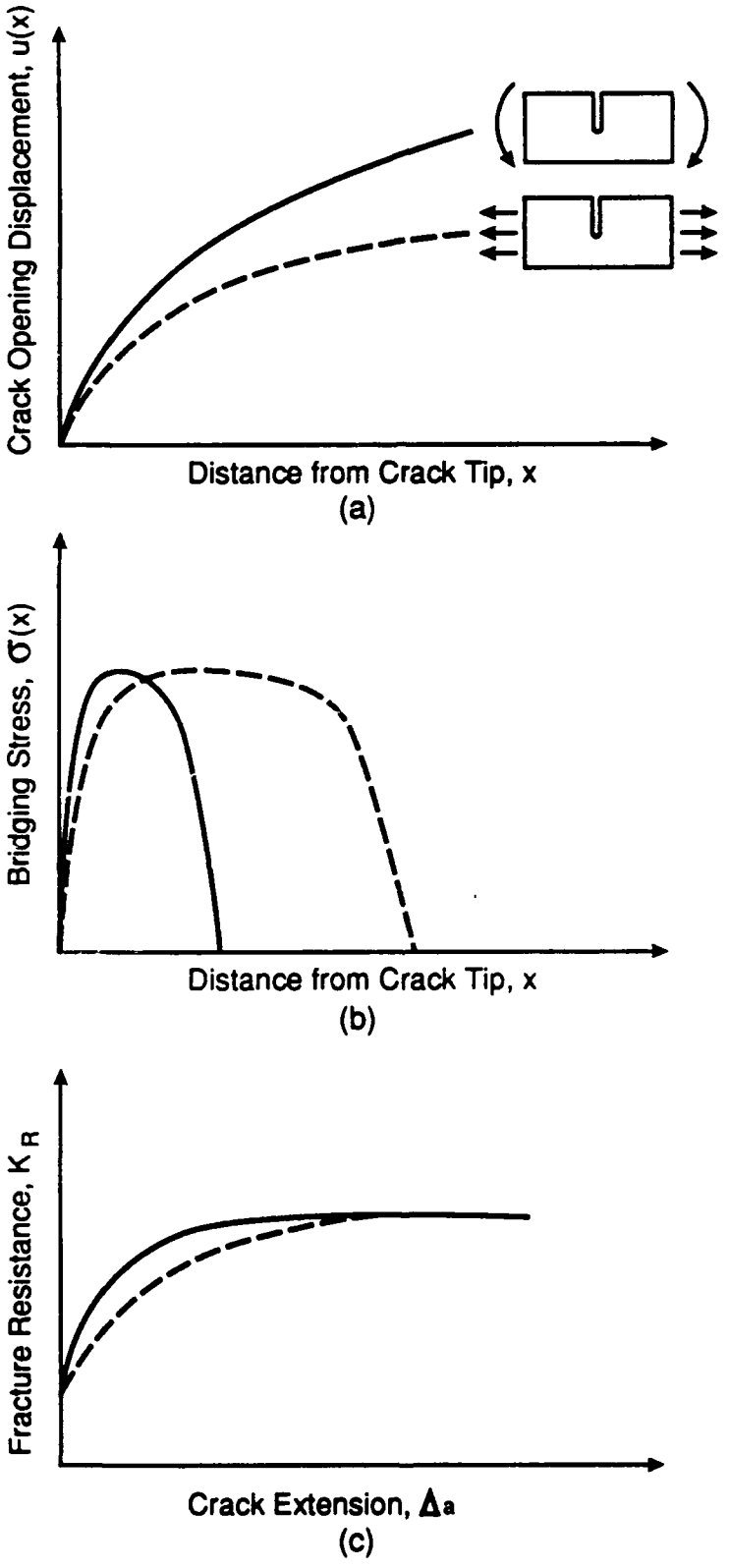

Fig. 12 A schematic diagram showing the effects of mode of loading (tension vs bending) on the crack opening profile, the bridging tractions and the R-curve.

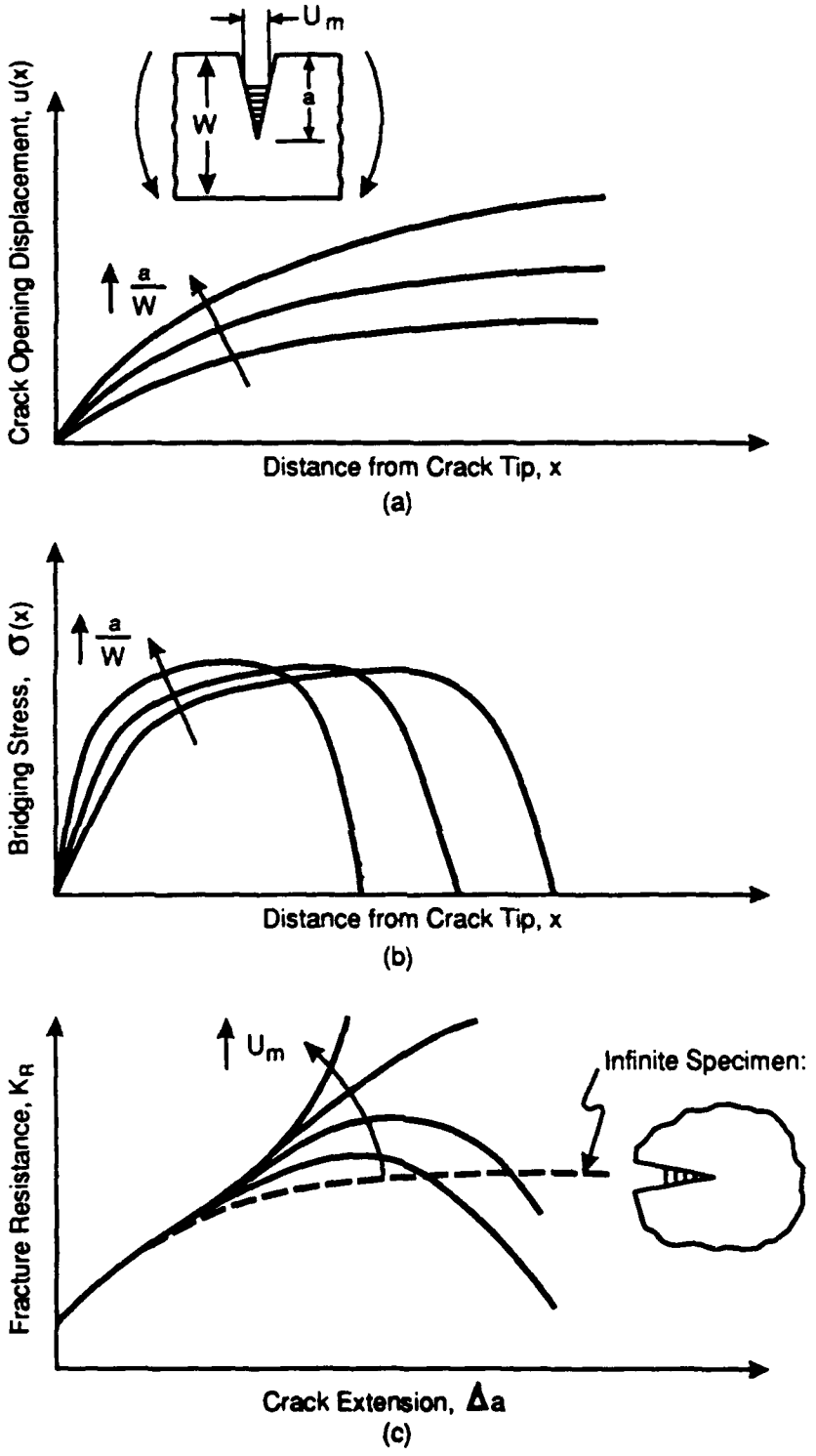

Fig. 13 A schematic diagram showing the influence of crack length on the crack opening profile, the bridging tractions and the R-curve in a bend specimen. Here u_m is the crack opening displacement necessary to fracture the bridging ligaments.

equation. Here the criteria for crack stability involves both the magnitude of K_R and the slope of the K_R - Δa curve. A brief summary of the procedure required to evaluate the fracture strength from the R-curve and some typical results are presented below. The effects of the spatial variation in the bridging stress, the size of the reinforcements and the initial defect length are considered. The results illustrate that the enhancement in strength is appreciably lower than the enhancement in steady state toughness, particularly for short cracks. Furthermore, they demonstrate the need to understand the influence of debonding in ductile-reinforced systems on both the fracture toughness and fracture strength.

3.1 FORMULATION OF THE PROBLEM

The criteria for crack stability under mode I loading conditions are

$$K = K_R \tag{7a}$$

and

$$\frac{dK}{da} = \frac{dK_R}{da} \tag{7b}$$

where K is the mode I stress intensity factor associated with the remote stress σ. A graphical representation of these criteria is presented in Fig. 14. In this diagram, the fracture resistance is plotted against crack extension, Δa, whereas the applied stress intensity factor is plotted against the total crack length, $a_o + \Delta a$. At each level of applied stress, the stress intensity factor is represented by a parabolic curve (shown by the dashed lines). At a critical stress the K curve intersects the K_R curve and the crack begins to grow stably (point A). Further increases in stress result in increases in both K and K_R such that the crack grows stably along the trajectory A-B. Finally, at point B, the incremental increase in K with Δa exceeds the corresponding increment in K_R and hence the crack becomes unstable.

In the present calculations it is assumed that the R-curve is attributable to the bridging tractions, as described by equations (1) and (2). The bridging tractions are assumed to take the form

$$\frac{\sigma}{\sigma_p} = 1 - \left(\frac{u}{u_m}\right)^N \tag{8}$$

where u is the crack opening displacement, u_m is the critical value of u at which the ligaments fail, N is an empirical coefficient which describes the shape of the stress-displacement curve, and σ_p is the peak bridging stress (at u = 0). Three values of N are considered here: 0.1, 1 and 10. The corresponding σ - u curves, shown in Fig. 15, encompass the range of behavior expected in real composite materials. In order to examine the effects of the spatial variation in the bridging fractions, σ_p is selected in such a way that the total work required to fracture the ligaments, $\int_o^{u_m/R} \sigma \, d(u/R)$, is constant. Furthermore, small scale bridging conditions are assumed to exist, so that the crack opening displacement near the crack tip is governed by the local stress intensity factor K_o and increases as $x^{1/2}$.

The results are conveniently expressed in terms of a number of non-dimensional parameters, defined by [33]:

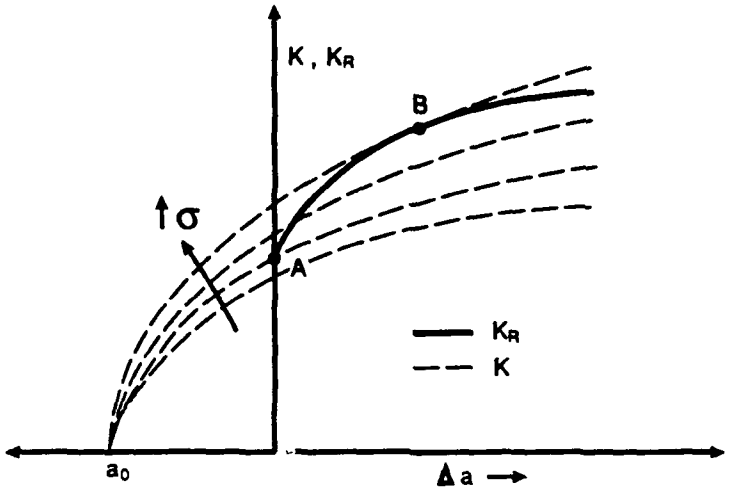

Fig. 14 A diagram showing the crack stability criteria for composite materials.

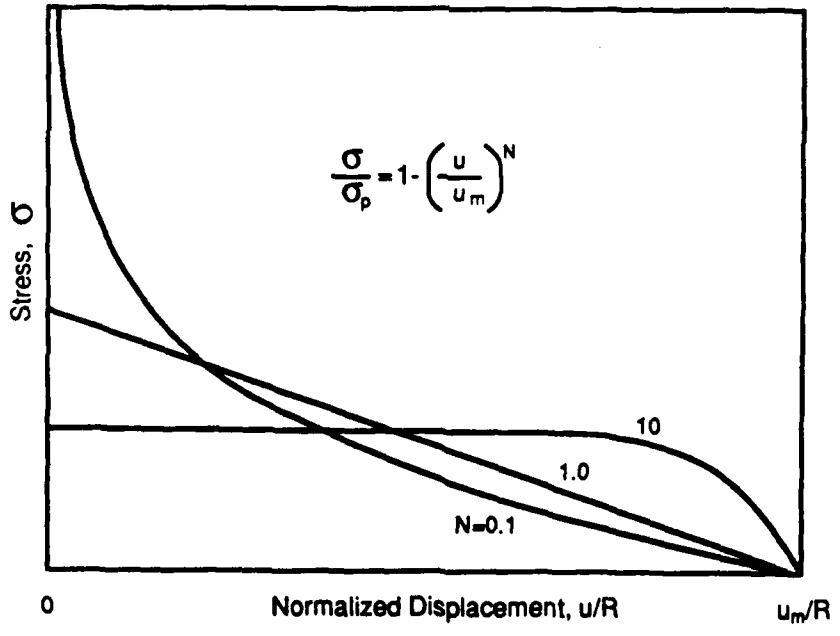

Fig. 15 The effects of the exponent N on the stress-displacement relationship.

$$\rho \equiv R\left[\frac{E}{\left(1-\nu^2\right)K_o}\right]^2 \tag{9a}$$

$$\alpha \equiv a_o\left[\frac{E}{\left(1-\nu^2\right)K_o}\right]^2 \tag{9b}$$

$$\delta \equiv \frac{u_m}{R} \tag{9c}$$

$$\kappa \equiv \frac{K_{ss}}{K_o} \tag{9d}$$

$$\eta \equiv \frac{\sigma_f\sqrt{\pi\, a_o}}{K_o} \tag{9e}$$

$$\omega \equiv \left(\frac{f\ \sigma_p\ u_m}{R}\right)\left(\frac{N}{N+1}\right)\left(\frac{1-\nu^2}{E}\right) \tag{9f}$$

$$\lambda \equiv \frac{a_o}{L} = \frac{32\,\alpha}{\pi\,\delta^2\,\rho^2} \tag{9g}$$

$$\Delta\lambda_c \equiv \frac{\Delta\, a_c}{L} \tag{9h}$$

where Δa_c is the crack extension at the point of instability (point B in Fig. 14) and L is the steady state bridging zone length. The parameters η and κ describe the enhancement in strength and toughness, respectively, while ω represents the work necessary to fracture the ligaments. Furthermore, ρ and α are measures of the particle size and initial crack length, respectively, normalized by an appropriate length parameter.

From equations (1), (2) and (7) - (9), the instability point $\Delta\lambda_C$ is defined by

$$\frac{\rho\,\omega(N+1)\ \Delta\,\lambda^{\frac{N+1}{2}}}{2N}\left[\frac{\lambda}{\Delta\lambda_c^{\frac{N}{2}+1}} - \frac{\lambda}{\Delta\lambda_c} - \frac{N}{N+1}\right] - 1 = 0 \tag{10}$$

The solution for $\Delta\lambda_c$ is obtained through an appropriate numerical method and the strength enhancement η then evaluated from

$$\eta = \frac{\rho\,\omega\,(N+1)\,\lambda^{1/2}}{2N}\left(1+\frac{\lambda}{\Delta\lambda_c}\right)^{1/2}\left(1-\Delta\lambda_c^{N/2}\right) \tag{11}$$

The steady state toughness enhancement is described by

$$\kappa = 1 + \frac{\rho\,\omega}{2} \tag{12}$$

3.2 RESULTS

To establish some of the important trends, the preceding formalisms have been used to calculate η and κ for various values of ρ, λ and N. The results are presented as diagrams with η as the ordinate and κ as the abscissa. In the present calculations ω is taken as 10^{-3} and δ as 1.

Figure 16 shows the effect of the initial defect length (through the parameter α) in the η-κ relationship for N = 1. Also shown is the behavior for an infinitely long crack (or, equivalently, an infinitely steep R-curve): in this case $\eta = \kappa$, as predicted by Griffith's equation. The results show that η initially increases with κ at a rate of unity, but subsequently reaches a steady state value, independent of κ. The steady state value of η increases monotonically with the initial defect length. Thus, for relatively short cracks, the strength enhancement is only a small fraction of the toughness enhancement. In this case, the instability point (B) in Fig. 14 is very near the point of initial crack growth (A) and consequently most of the R-curve is not utilized in improving the fracture strength.

Figure 17 shows a similar η-κ plot for 3 different values of N and $\alpha = 10^6$. At small values of ρ (and consequently small κ), the *shape* of the stress distribution has a negligible effect on the strength enhancement. However, as ρ and κ increase, the strength enhancement decreases with N. This result demonstrates the importance of the bridging stresses very near the crack tip: for a fixed amount of work, ω, it is desirable to concentrate the bridging stress into the region close to the crack tip (as is the case for N = 0.1) rather than distributing it uniformly over the bridging zone. In principle, this can be accomplished by introducing *strongly bonded* ductile particles so that the plastic constraint associated with a small debond length increases the bridging stress near the crack tip. In practice, however, the constraint effects are accompanied by reductions in both the plastic stretch to failure, u_m, and the total work, ω [31], suggesting that there exists an optimal debond length at which η is maximized. Indeed, recent experimental work on lead-glass composites [32] indicates that such an optimum does exist and that it depends on the initial defect length and the particle size.

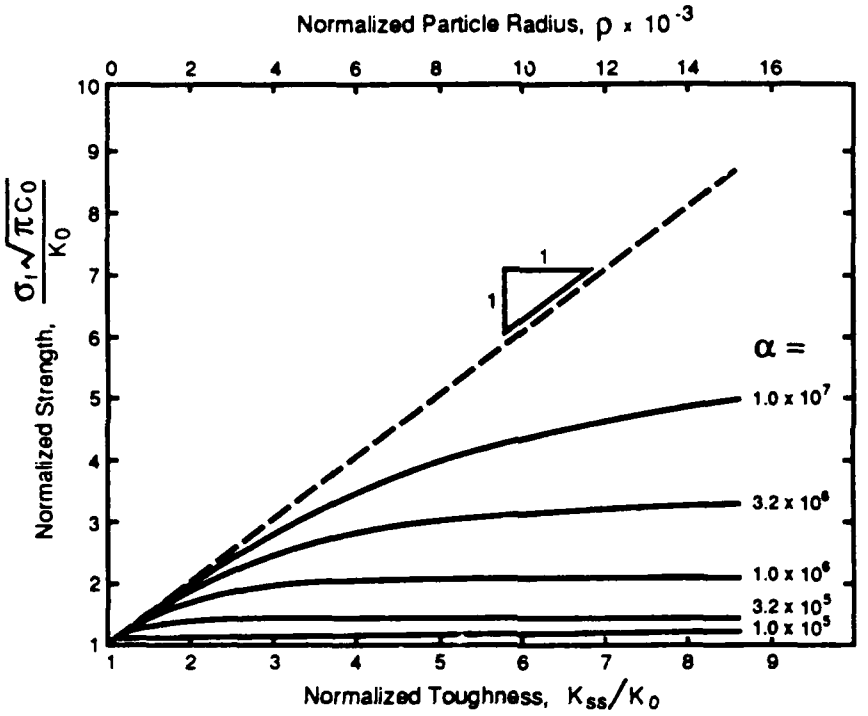

Fig. 16 A plot of the strength enhancen.ent η against toughness enhancement κ for various initial defect lengths. The dashed line corresponds to $\eta = \kappa$.

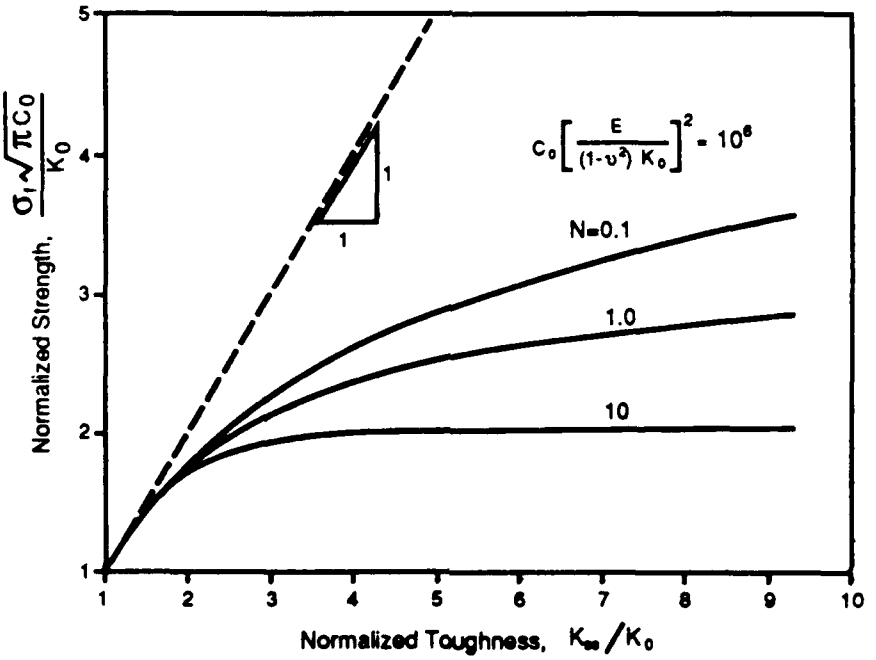

Fig. 17 A diagram showing the effects of the exponent N on the strength enhancement.

4. Conclusions

The results of the present study demonstrate that R-curve behavior in composites is attributable to bridging processes in the crack wake. Good correlation between experiment and theory is obtained when the finite specimen geometry is incorporated into the model of crack bridging. However, issues regarding the effects of fiber orientation and specimen geometry on R-curve behavior still need to be resolved.

The influence of a number of microstructural variables on fracture strength has also been explored. The calculations indicate that the strength enhancement attributable to bridging processes is relatively small for short cracks. Furthermore, they demonstrate the importance of the *shape* of the bridging tractions in crack stability. Trends obtained from these calculations may be useful in designing composite microstructures with optimal strength and toughness characteristics. However, additional experimental evidence relating fracture resistance and fracture strength is required to validate the model.

References

1. A. G. Evans and D. B. Marshall, *Acta Metall.*, **37**, 2567 (1989).
2. J. J. Brennan and K. M. Prewo, *J. Mater. Sci.*, **17**, 2371 (1982).
3. P. F. Becher and G. C. Wei, *Comm. Am. Ceram. Soc.*, C-267 (1984).
4. P. Becher, C. H. Hsueh, P. Angelini and T. N. Tiegs, *J. Am. Ceram. Soc.*, **71**, 1050 (1988).
5. F. Zok, O. Sbaizero, C. L. Hom and A. G. Evans, *submitted to Acta Metall.*, (1990).
6. R. M. L. Foote, Y. Mai and B. Cotterell, *J. Mech. Phys. Solids*, **34**, 593 (1986).
7. B. Cotterell and Y. Mai, *J. Mater. Sci.*, **22**, 2734 (1987).
8. L. S. Sigl and H. E. Exner, *Metall. Trans.*, **18A**, 1299 (1987).
9. L. S. Sigl and H. F. Fischmeister, *Acta Metall.*, **36**, 887 (1988).
10. B. O. Flinn, M. Rühle and A. G. Evans, *Acta Metall.*, **37**, 3001 (1989).
11. H. E. Déve, A. G. Evans, G. R. Odette, R. Mehrabian, M. L. Emiliani and R. J. Hecht, *Acta Metall.*, in press (1990).
12. C. K. Elliott, G. R. Odette, G. E. Lucas, and J. W. Sheckherd, *Mat. Res. Soc. Symp. Proc.*, **120**, 95 (1988).
13. M. Sakai, J. Yoshimura, Y. Goto and M. Inagaki, *J. Am. Ceram. Soc.*, **71**, 509 (1988).
14. M. V. Swain, *J. Mater. Sci. Letters*, **5**, 1313 (1986).
15. H. Wieninger, K. Kromp and R. F. Pabst, *J. Mater. Sci.*, **21**, 411 (1986).
16. R. Knehans and R. Steinbrech, *J. Mater. Sci. Letters*, **1**, 327 (1982).
17. R. Steinbrech and O. Schmenkel, *J. Am. Ceram. Soc.*, **71**, C271 (1988).
18. P. L. Swanson, C. J. Fairbanks, B. R. Lawn, Y. Mai and B. J. Hockey, *J. Am. Ceram. Soc.*, **70**, 279 (1987).
19. Y. Mai and B. R. Lawn, *J. Am. Ceram. Soc.*, **70**, 289 (1987).
20. H. Tada, P. C. Paris and G. R. Irwin, "The Stress Analysis of Cracks Handbook," Del Research Corp., Pennsylvania (1973).
21. F. Zok and C. L. Hom, *Acta Metall.*, in press (1990).

22. F. F. Lange, B. V. Valamakanni and A. G. Evans, *J. Am. Ceram. Soc.*, **73**, 388 (1990).
23. ASTM E399-83, "Plane Strain Fracture Toughness of Metallic Materials," Annual Book of ASTM Standards, ASTM, Philadelphia (1988).
24. F. Zok and B. D. Flinn, unpublished work.
25. M. F. Ashby, F. J. Blunt and M. Bannister, *Acta Metall.*, **7**, 1847 (1989).
26. P. A. Mataga, *Acta Metall.*, in press (1990).
27. H. G. Tattersall and G. Tappin, *J. Mater. Sci.*, **1**, 296 (1966).
28. M. D. Thouless, O. Sbaizero, L. S. Sigl and A. G. Evans, *J. Am. Ceram. Soc.*, **72**, 525 (1989).
29. T. P. Weiks, C. M. Dick and W. D. Nix, *MRS Proceedings*, **120**, 247 (1988).
30. G. R. Odette and G. E. Lucas, unpublished work.
31. M. F. Ashby, F. J. Blunt and M. Bannister, *Acta Metall.*, **37**, 1847 (1989).
32. M. Bannister and M. F. Ashby, *Acta Metall.*, in press (1990).
33. F. Zok, unpublished work (1990).

Session 8:

Fracture Toughness of Fiber-Reinforced Cement Composites

Chairs:

Isaac Daniel
Northwestern University
Evanston, U.S.A

Sidney Mindess
University of British
Columbia, Canada

Reporter:

Methi Wecharatana
New Jersey Institute of
Technology, U.S.A.

Invited Principal Lecture, NATO Advanced Research Workshop on "Toughening Mechanisms in Quasi-Brittle Materials", Northwestern University, July 16-20, 1990

Research Challenges in Fiber Reinforced Concrete

Victor C. Li
Advanced Civil Engineering Materials Research Laboratory
University of Michigan,
Ann Arbor, MI48109-2125

Introduction

Research in fiber reinforced concrete (FRC) has been ongoing for at least two decades. Yet the use of this material at the present time, while growing, is still relatively limited. There are even concerns about the effectiveness of this material in relation to time dependent property deterioration. Although FRC has been repetitedly demonstrated to be an improved structural material over plain concrete, its present commercial 'push' is more on 'reducing shrinkage cracks'. In other words, after curing, the presence of fibers in concrete is not expected to contribute to the properties of this material. The limited volume usage, and its limited functional role raise the question of what has gone wrong in the research and development of this material. A collorary of this question is: Despite the many years of research (certainly earlier than fiber reinforced ceramics), why is it still much less an engineered material than say, fiber reinforced ceramics or polymers?

To answer the above questions may require a full scale investigation by itself, involving an understanding of both the technical deficiencies of and non-technical demands place on FRC, and is surely outside the scope of this paper or this workshop. What could be said at this point is that a great deal of research in FRC are empirical in nature, which makes it difficult to generalize the findings of a piece of research. While often a specific performance of FRC is demonstrated (e.g. flexural capacity), it is not quantitatively related to the fundamental mechanical properties of the material, even less to the material structure. This results in difficulty in furthering the design of FRC. In addition, until in very recent years, the processing of FRC is probably least studied among all modern composites. This probably stems from the fact that the mixing of concrete is relatively simple, and the making of FRC therefore involves just adding fibers into the concrete mix. The drawback of this apparent simplicity in processing is that the material structure is seldom well controlled or even received any critical attention.

Despite these drawbacks, FRC is once again receiving its due attention, partly because of the commercial need of finding substitute materials for asbestoes cement which has been found to be carcinogenic and is being phased out in most industrialized countries, and partly because of the increasing availability of a wide variety of fiber types and geometries for use as reinforcements. In addition, the increasing ease of making high strength concrete and the recognition of the brittleness and difficulty in quality control of this material is begging for a solution in the form of fiber reinforcement.

These recent developments present an opportunity for realizing the structural utilization of fiber reinforced concrete. The lack of understanding in processing, in its linkage to material structure, in its effect on material properties which directly influences the performance of FRC, present immense challenges to the research community. Although it is not the intention of this paper to review the complete picture of performance-property-process-structure relationships, it is still useful to have a brief overview of these relationships to place the more detailed discussions to follow in the context of this framework.

The Performance-Property-Process-Structure Relationship

Performance, property, process and material structure form the apexes of a tetrahedron schematically shown in Figure 1. Their relationship to one another was proposed as a general framework for the study of modern engineered materials by the National Research Council (1990). For our present purpose, we shall restrict the use of this framework to FRC.

The **performance** of FRC may include durability, reliability and safety, manufacturability, sesimic resistance (energy absorption capacity), flexural and shear capacity and other desirable features of the specific structure which ultilize this material. These are elements which the end user and the structural engineer normally would like to see improvements in.

The important **properties** of FRC may include stiffness, strength, fracture toughness and others. In the past, most construction codes are concerned with stiffness and (usually compressive) strength. However, the effectivness of fiber reinforcement in improving these properties are usually insignificant. This may be one of the reasons for the lack of appreciation for the unique structural property which FRC offers. These include for example, the tensile strength and toughness which are expected to influence several of the performance parameters such as reliability, seismic resistance, and shear and flexural

capacities.

As mentioned earlier, until recently, both **processing and material structure** received little attention from researchers. For FRC, the use of pultrusion, intense shear rolling, infiltration, high frequency vibration processing techniques have been attempted with varying successes. They are also responsible for some of the more high performance FRC materials such as SIFCON and reinforced MDF cement, that have surfaced in recent years. The material structure of FRC includes the fibers and their orientation, the cement or concrete matrix and the pores in them, and the fiber/matrix interface. Observational studies of interface microstructure (see e.g. Mindess et al, 1988) have received much attention in recent years, but quantitative links between interface observations and bond properties are rare. These links are needed to relate interface properties to composite properties, and to relate interface structure to processing, and hence processing to composite properties and performances.

Within the framework of the tectrahedron described above, it can be seen that research in FRC is still quite deficient. This framework offers tremendous opportunity for exploration and developmnt of FRC as an engineered composite. The following cites a more specific example of the challenges in FRC research in the context of the performance-property-process-structure framework.

Development of High Strength High Ductility Concrete

In recent years, the strength of concrete has steadily improved such that high strength concrete with compressive strength exceeding 10,000 psi can be readily made in most laboratories. The problem with this material is brittleness and lack of reliability, the latter associated with the increased sensitivity of processing flaws. Thus, its present use is often limited to those structural components requiring additional steel reinforcements or with steel jacketing. The use of additional steel reinforcement defeats the original intent of using less material with less weight for the same structural capacity. The use of steel jacketing restricts the versatility of the application of this material. Thus it is very natural that significant research is currently being pursued in using fibers for regaining some of the lost ductility. If fiber reinforcement is successful, a high performance high strength-high ductility concrete which could be utilized reliably would result.

Unfortunately, the fiber type and volume fraction suitable for reinforcing normal strength concrete becomes inadequate when used for reinforcing high strength concrete. For example, figure 2 (Green, 1989) shows the post-cracking tensile behavior of a high strength mortar reinforced with 0.6 volume percent of a high strength polyethylene fiber

(fiber length = 6.4 mm). Although the fracture energy has been significantly improved, the brittleness of the material remains high due to the rapid drop in strength after peak. For effective reinforcement, it appears necessary that the post cracking strength must be of comparable value to the cracking strength, in addition to having a high fracture energy. Thus it is necessary to understand the origin of the post-cracking strength as a composite property.

It can be shown (Li, 1990) that the post-cracking strength for a 3-D random fiber reinforced brittle matrix composite is given by

$$\sigma_{pc} = \frac{1}{2} V_f \tau \left(\frac{L_f}{d_f} \right) g \tag{1}$$

where τ is the interface bond strength, L_f is the fiber length, d_f is the fiber diameter, V_f is the fiber volume fraction and the snubbing factor g is given by:

$$g = \frac{2}{4 + f^2} \left(1 + e^{\frac{\pi}{2} f} \right) \tag{2}$$

in which f is a snubbing coefficient. The snubbing factor is associated with the additional resistance when fibers are pulled-out at various angle to a matrix crack. In contrast to a continuous fiber composite where the matrix crack plane usually lies in a direction normal to fiber alignment direction, fibers bridging across a matrix crack in a discontinuous randomly oriented fiber reinforced composite can be oriented in any direction. When a flexible fiber is pulled out in this manner, the exiting fiber acts as if it were passing through a friction pulley. The result is a pull-out load which is as much as three times for high angle pull-out compared to that of a straight pull-out of polypropylene monfilaments embedded in a normal concrete matrix (Li et al, 1989, Figure 3a). Pull-out energy of up to four fold has been recorded (Figure 3b). Preliminary result suggests that these increases in pull-out force and energy are limited by the tensile and/or crushing strength of the cement matrix. Surface spalling of normal strength mortar has been observed at high angle pull-out, as is reflected by the large amount of scatter in the high angle data in Figures 3a and 3b. The spalling phenomenon has also been revealed in scanning electron micrograph of fracture surfaces of Spectra (a high strength polyethylene) fiber reinforced normal strength concrete (Figure 4).

The typical range of the snubbing coefficient appears to be between 0 and 1. Figure 5

shows the snubbing factor g plotted against the snubbing coefficient f. At the high end of f, the post cracking strength can be increased by as much as 2.3 times in comparison to the case where no snubbing occurs.

Equation (1) has been used to predict the post-cracking strength of steel and Spectra fiber reinforced concrete. The comparison with experimental data is shown in Figure 6. The Post-Cracking Strength in Figure 6 has been normalized by the interfacial bond strength τ. For the steel FRC (data from Visalvanich and Naaman, 1982), a bond strength of 4 MPa has been assumed. For the Spectra FRC, an interfacial bond strength of 1 MPa (Li et al, 1989) is used. These comparisons suggest that the snubbing coefficient for steel fiber in normal strength mortar is approximately unity, although the well known effect of fiber plastic bending (Morton and Groves, 1974) is not accounted for in this calculation. However Morgan and Groves (1976) suggested that the bending effect is probably small compared to the snubbing effect based on limited pull-out test of steel fibers embedded in an epoxy matrix. For Spectra fibers, the present limited data suggest that f~0.3 in a normal strength matrix and f~0.55 in a high strength matrix (7 day compressive strength of 80MPa). However, pull-out tests based on polypropylene and nylon monofilaments have indicated a snubbing coefficient as high as 0.7 and 0.9 respectively.

Although high strength concrete demands higher post-cracking strength for effective reinforcement, it has been found to have certain advantages over normal concrete in its capability of producing a higher post-cracking strength. For example, Table 1 (Li et al, 1989) shows the effect of matrix strength on pull-out load of nylon monofilaments. In one sample, the fiber was pulled out normal to the matrix crack plane, whereas the other sample involved the fiber pulled out at an angle of 60°. For the normal pull-out case, the average of 8 tests for the higher strength matrix shows a 6.3% increase over that for the normal strength matrix, but the standard deviation was large enough not to attach much significance to this increase. For the 60° pull-out, the average of 8 tests for the higher strength matrix shows a 127% increase over that for the normal strength matrix. This increase was significant in comparison to the standard deviation recorded in the test data, and suggests that while the interface bond strength may not have increased much, if at all, the snubbing effect appears to have been enhanced for the fiber pulled out from the higher strength matrix, presumably due to the better spall resistance of the higher strength matrix. These observations are consistent with that of measured post-cracking strength for Spectra fiber reinforced normal and high strength concrete, discussed above.

Apart from post-cracking strength, another primary property in reducing material brittleness is the fracture energy of the composite. Li et al (1990) derived an expression for the enhanced fracture energy G due to the fiber bridging mechanism in a 3-D random FRC:

$$\tilde{G} = 2\tilde{L}_f^{\,2} F\left(\tilde{L}_f, f\right) \tag{3}$$

where

$$\tilde{G} \equiv \frac{G}{\left(\tau V_f d_f\right)\left(L_c / d_f\right)^2} \tag{4}$$

$$\tilde{L}_f = \frac{L_f / 2}{L_c} \tag{5}$$

and the non-dimensional function F is

$$F = \int_{z'=0}^{1} \int_{\phi=0}^{\cos^{-1}(z')} \left[1 - \frac{z'}{\cos\phi}\right]^2 e^{f\phi} p(\phi) U\left[z' - (1 - \frac{1}{\tilde{L}_f e^{f\phi}})\cos\phi\right] d\phi dz' \tag{6}$$

where the U(g) is the step function and g is defined as:

$$g = z - \left(\frac{L_f}{2} - L_c e^{-f\phi}\right)\cos\phi \tag{7}$$

and p(z) and p(ϕ) are probability density functions of fiber centroidal location z and orientation ϕ for a uniform random distribution of fibers. The step function U has been included in the integrand in (6) in order to discount those fibers of length L_f exceeding twice the critical embedded length L_c. These fibers will be broken instead of pulled out.

Figure 7 shows a plot of the normalized fracture energy as a function of the normalized fiber length, based on equation (3), for different values of f. It is clear that while the snubbing effect increases the fracture energy for short fibers, the maximum attainable fracture energy G_{max} is reduced for increasing f, due to increasing amount of fiber ruptures. Thus, while the snubbing friction assists in attaining a higher post-cracking strength, the maximum attainable fracture energy is simultaneously reduced. This is shown in Figure 8.

From the above discussions, it is clear that the material structure -- in this case the fiber, the matrix, and the interface all play a role in controlling the composite property, specifically the post-cracking strength and the fracture energy.

Apart from the snubbing effect, equations (1) and (3) also elucidate the dependence of the post cracking strength and the fracture energy on the bond strength, the fiber volume fraction and the fiber aspect ratio. They suggest that high fiber volume fraction and high fiber aspect ratio is preferred for high post-cracking strength. However, this route presents a difficulty in material processing. Conventional mixing of fiber in concrete limits the volume fraction to a few (typically less than 2) percent and fiber aspect ratios of less than a few hundred (typically less than 100). Larger fiber volume fraction and longer aspect ratios cause lumping of the fresh mix, resulting in high porosity in the matrix. These large pores tend to act as sites of internal cracks and can lead to significant strength loss. Because high strength concrete typically employs a smaller water/cement ratio, this lumping problem becomes even more serious than conventional concrete. Special processing technique, such as the use of high frequency vibration, may be needed to compact the mix.

Conclusions

Although discussed only very briefly, and using only extremely narrow and specific examples, the above presentation is meant to bring out the inter-dependencies between performance-properties-processing-structure for the development of high strength-high ductility concrete. Successful development of such an engineered material cannot be achieved without appreciating the inter-dependencies and constructing solutions which take advantage of the understanding of these inter-dependencies. In this process, it is also recognized that micromechanics plays a significant role in quatifying the various links, and especially the link between material structure and properties. In addition, the need for studies in material processing is especially emphasized.

The tetrahedron shown in Figure 1 also suggest an approach perhaps foreign to the development of construction materials -- the performance driven approach. If performance criteria (e.g. durability determined by the life expectancy of the structure; or energy absorption capacity determined by expected seismic load which may be imposed on the structure) can be specified, then the required material structure could be developed to achieve certain material properties using a certain processing route. In other words, a material could be engineered to satisfy the required performance of a given structure in a given environment. Certainly our current state of the art is far from this ideal, but that is precisely the challenge we must face in the research and development of high performance engineered FRC.

Acknowledgement

The author would like to acknowledge the many stimulating discussions with S. Backer and Y. Wang. Some of the research results discussed in this paper derives from projects which have received support from the National Science Foundation, the Shimizu Corporation, and the E.I. du Pont Nemours & Co. Inc..

Bibliography

Green, E., *Behavior of High Strength Fiber Reinforced Concrete*, MS Thesis, Civil Engineering, MIT, 1989.

Li, V., "The Scaling Law of Post-Cracking Behavior in Short Fiber Composites", in preparation.

Li, V.C., Y. Wang, and S. Backer, "Effect of Inclining Angle, Bundling, and Surface Treatment on Synthetic Fiber Pull-Out from a Cement Matrix", *Composites*, Vol. 21, 2, pp.132-140, 1990.

Mindess, S. and S.P. Shah, Editors, *Bonding in Cementititous Composites*, MRS Symposium Proceedings, V. 114, 1988.

Morton, J. and G.W. Groves, "The Cracking of Composites Consisting of Discontinuous Ductile Fibers in a Brittle Matrix -- Effect of Fiber Orientation", J. of Materials Science, pp. 1436-1445, 1974.

Morton, J. and G.W. Groves, "The Effect of Metal Wires on the Fracture of a Brittle-Matrix Composites", J. Materials Science, 11, pp.617-622, 1976.

National Research Council, *Materials Science and Engineering for the 1990s*, Pub. National Research Council, 1990.

Visalvanich, K. and A. E. Naaman, "Fracture Modelling of Fiber Reinforced Cementitious Composites", Progress Report for National Science Foundation, Grant ENG 77-23534, 1982.

Table 1: Effect of Matrix Strength on Pull-out of Nylon Monofilament

	Pull-out Load (N)	
	Normal strength HCP	High strength HCP
f = 0°	4.91 (CV = 5.6%)	5.22 (CV = 22.8%)
f = 60°	11.85 (CV = 27.1%)	26.94 (CV = 5.4%)
$P_{60°}/P_{0°}$ =	2.41	5.16

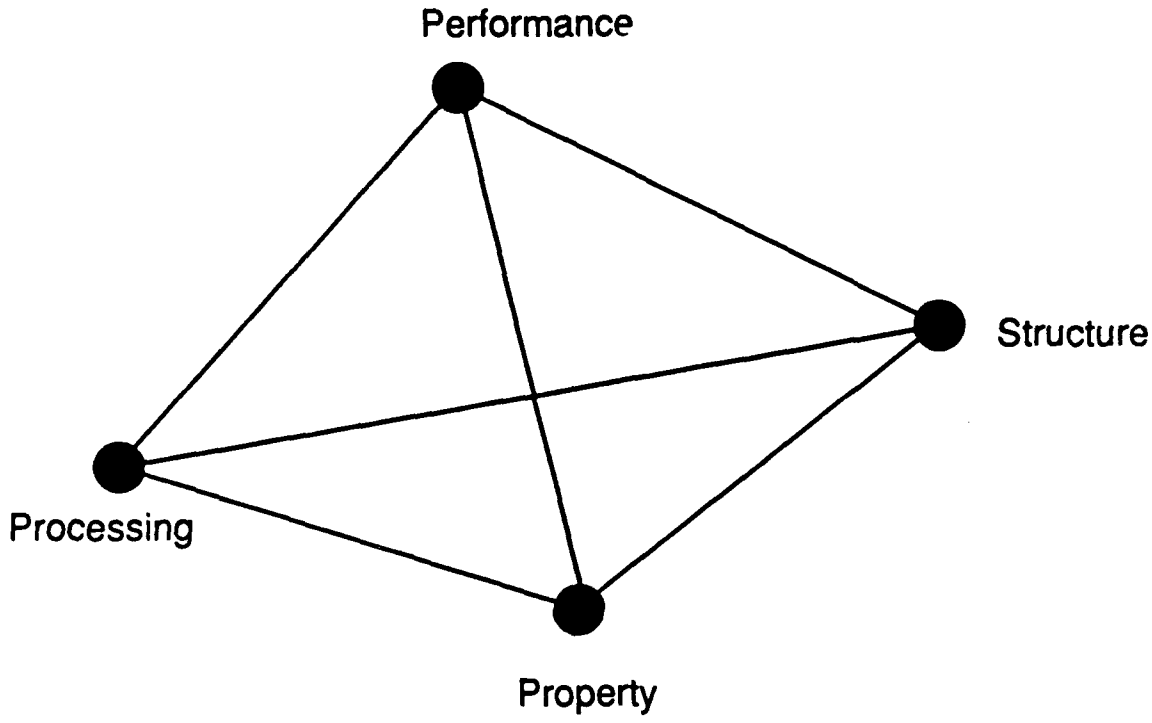

Figure 1: The Tetrahedron: Performance-Property-Processing-Structure Inter-relationship

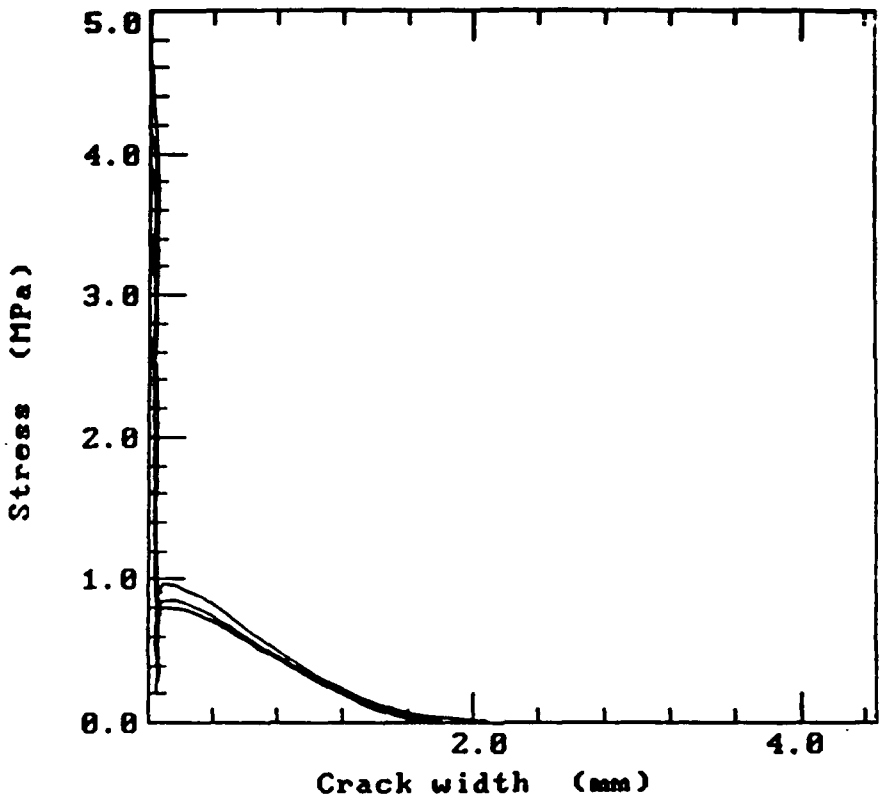

Figure 2: Post-Cracking Tensile Behavior Of Polyethylene Fiber Reinforced High Strength Mortar (Green, 1989)

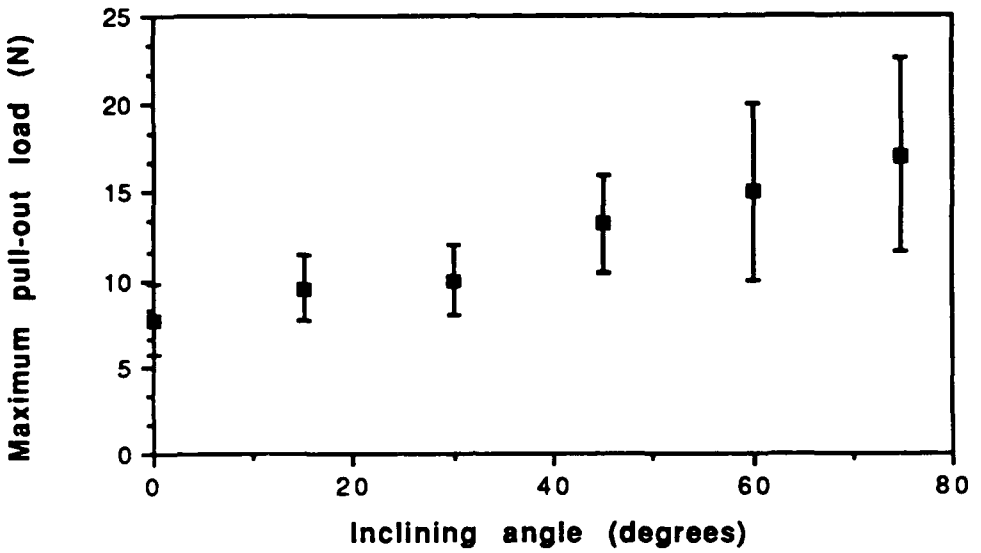

Figure 3a: Maximum Load Vs. Inclining Angle From Angle Pull-Out Test Of Polypropylene Monofils

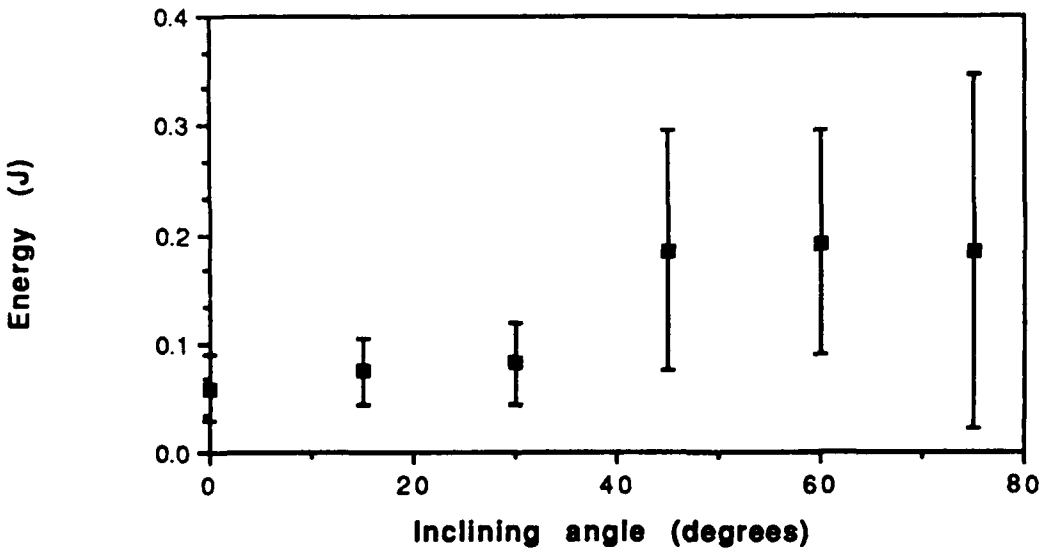

Figure 3b: Pull-out Energy Vs. Inclining Angle For Polypropylene Monofils

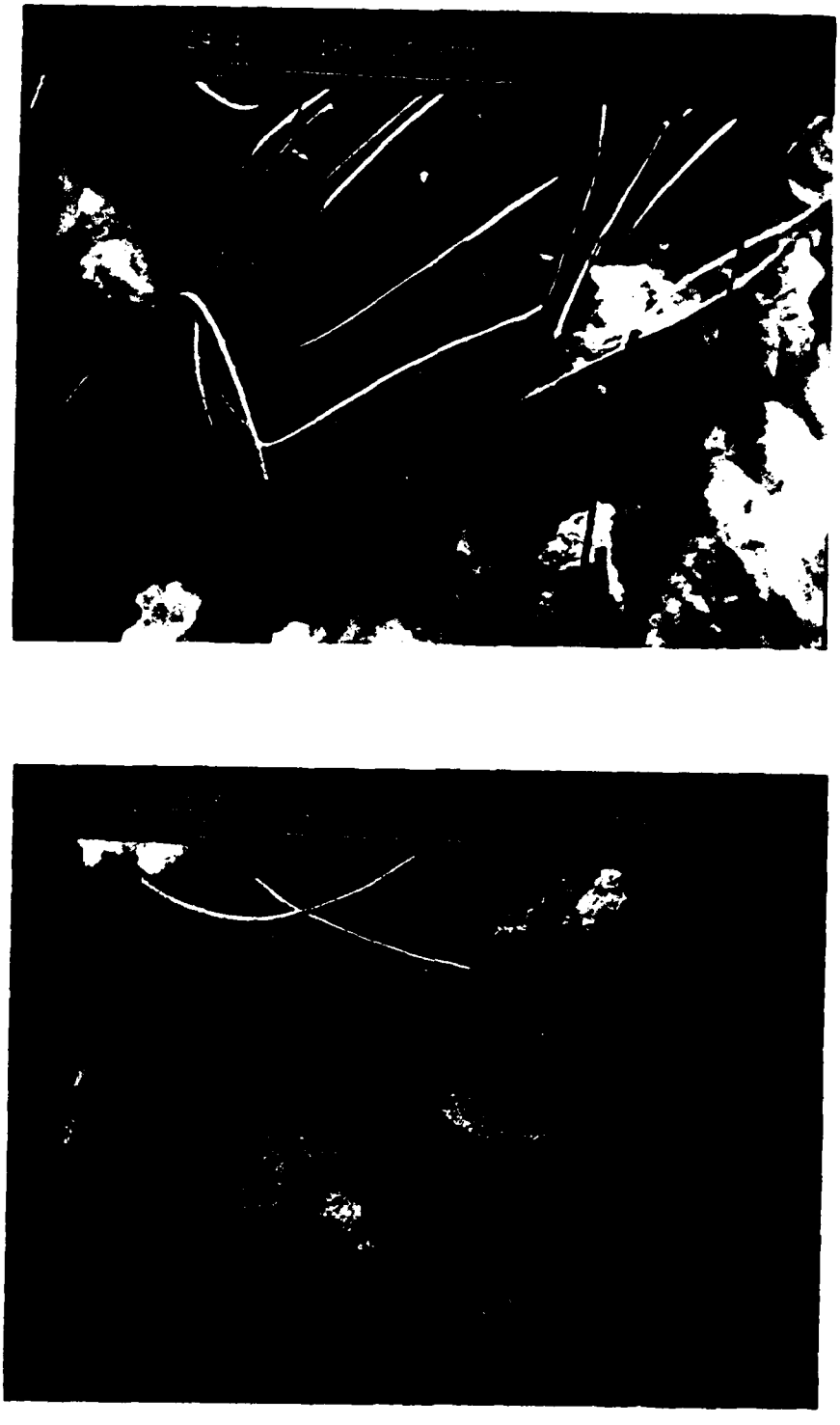

Figure 4: Scanning Electron Photomicrograph of Surface Spalls from the Fracture Surface of Spectra FRC

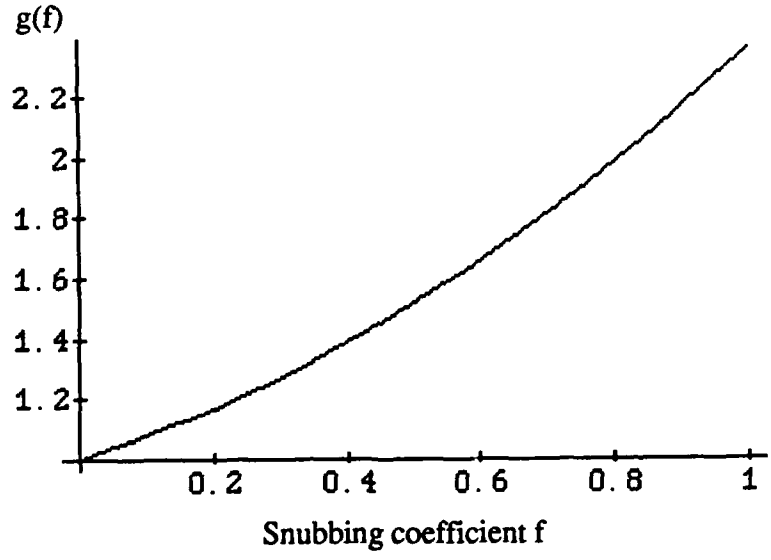

Figure 5: The Snubbing Factor g as a Function of the Snubbing Friction Coefficient

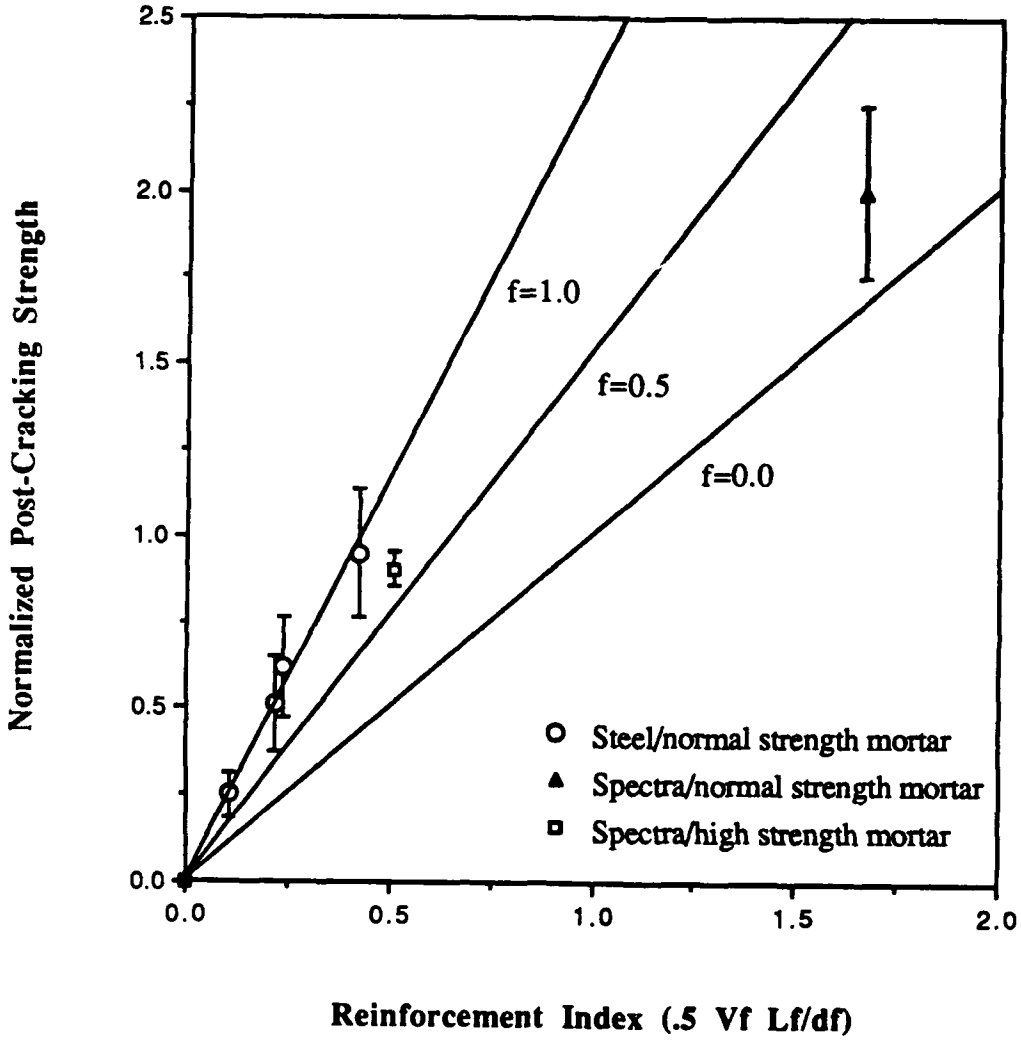

Figure 6: Predicted and Measured Post-Cracking Strength in Steel and Synthetic FRCs.

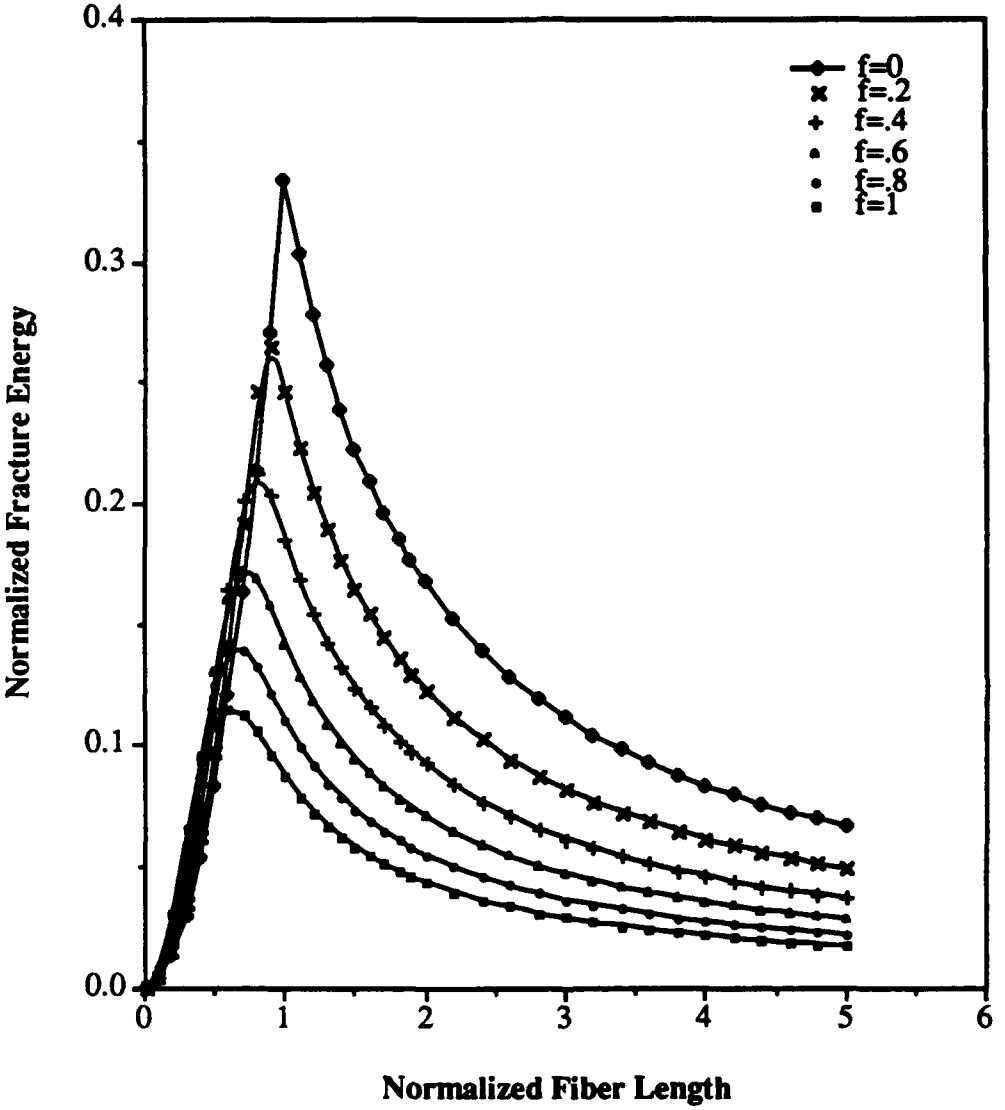

Figure 7: Dependence of Normalized Fracture Energy on Normalized Fiber Length and Snubbing Friction

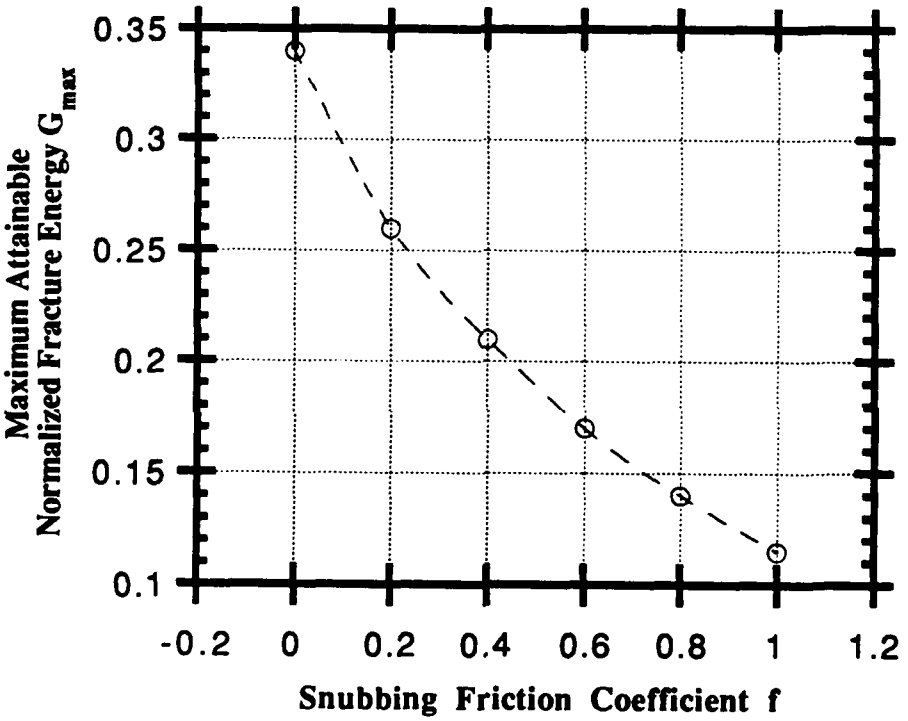

Figure 8: Maximum Attainable Fracture Energy as a Function of Snubbing Friction Coefficient

FAILURE CHARACTERISATION OF FIBRE–REINFORCED CEMENT COMPOSITES WITH R–CURVE CHARACTERISTICS

YIU–WING MAI
Centre for Advanced Materials Technology
Department of Mechanical Engineering
University of Sydney
Sydney, NSW 2006
Australia

ABSTRACT. The failure of fibre–reinforced cement composites can be characterised by the crack–resistance (R) curve approach. In short fibre composites, where the fibres pullout rather than break, theoretical models are presented for the prediction of the R–curve based on the constitutive equation between the closure stress–crack face separation in the fibre–bridging zone at the wake of the crack tip. The influences of specimen size and geometry and the matrix fracture process zone on the R–curve are evaluated and compared to experimental results. Using this crack–face bridging concept the Weibull distribution of the tensile strength of short fibre composites is investigated both theoretically and by computer simulation experiments. It is shown that not only is the crack growth process stabilised but that the Weibull modulus is considerably increased due to the R–curve effect. By including the slow crack growth phenomenon in the theory the time–dependent strengths for short fibre composites with R–curve characteristics are also predicted.

1. Introduction

It is now generally recognised that the failure behaviour of fibre–reinforced cement composites cannot be adequately described by the conventional one–parameter fracture criterion such as the critical potential energy release rate G_c and the critical stress intensity factor K_c. When a crack develops in a short fibre–reinforced composite we have a small matrix fracture process zone (FPZ) at the crack tip region where microcracking activities take place and a fibre bridging zone (FBZ) at its wake where fibre–matrix debonding and fibre pullout occur, Figure 1. The size of these two zones depend largely on the fibre aspect ratio, fibre volume fraction and specimen configuration, Table 1. However, it is the development of the FBZ that gives rise to stable crack growth and the so–called crack–resistance (R) curve usually plotted in the form of stress intensity factor (K_R) versus crack growth (Δa). In these lecture notes only those short fibre cement composites whose failure mechanism is predominantly fibre pullout rather than fibre breakage are considered. Some of the experimental difficulties associated with R–curve and matrix fracture

process zone size measurements are first highlighted (Section 2). Analytical modelling of R–curves consistent with the particular toughening mechanisms are then described in relation to effects of specimen size and geometry and influences of the matrix FPZ (Section 3). The application of R–curve in prediction of tensile strength of short fibre cement composites is finally studied both theoretically and by computer simulation (Section 4).

TABLE 1. Size of fibre bridging and matrix fracture process zones for cementitious materials

Material	Fibre bridging zone (mm)	Fracture process zone (mm)	Reference
Asbestos fibre – cement	~ 125	28	14.48
Cellulose fibre – cement	~ 80	28	4
Steel wire–concrete	> 610	–	17
Steel wire–cement	760	–	48
Glass fibre – cement	–	15	49

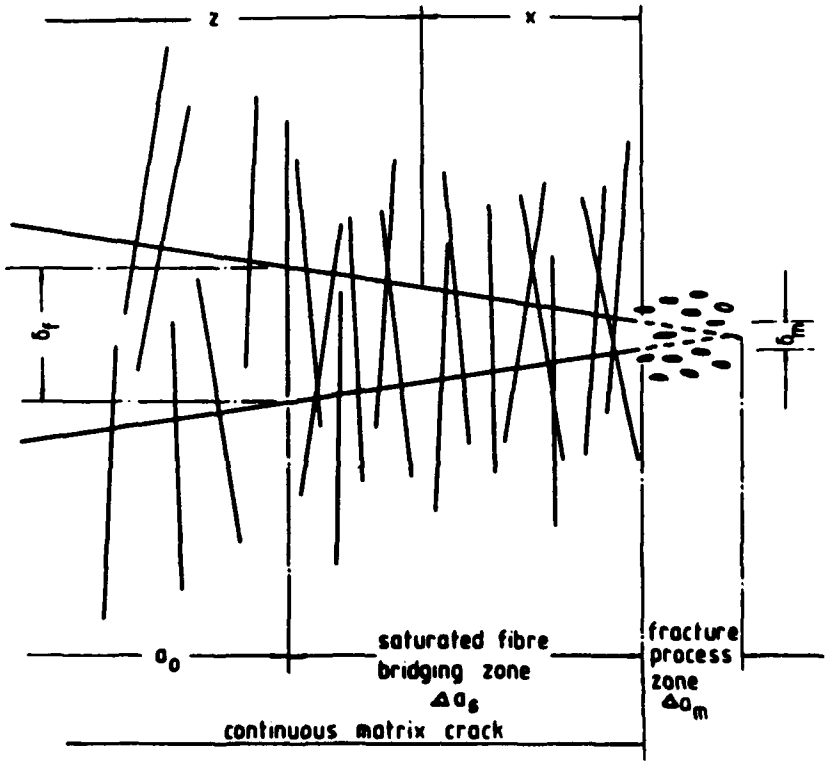

Figure 1. Fibre bridging (FBZ) and fracture process (FPZ) zones at crack tip of a fibre reinforced cement composite.

2. Measurements of FBZ and FPZ for Fibre Cement Composites

In the experimental evaluation of the crack–resistance (R) curve it is required to determine quite accurately the relative sizes of the fibre bridging zone (FBZ) and the matrix fracture process zone (FPZ). Depending on the relative size of the matrix FPZ it may or may not have to be included in the theoretical analysis. Distinction of the exact boundary between the FPZ and the FBZ is always difficult. Many direct and indirect methods have been used to measure either of these two zones. These include optical and scanning electron microscopy techniques, photography, staining and Moire' fringes, replicas, electrical potential difference methods, mercury porosimetry, acoustic emissions and compliance techniques. Foote [1] has given a review of these test methods and their relative merits and usefulness for measurements of the FPZ and FBZ. It is perhaps important to point out that the compliance method, so often employed by the majority of investigators to measure crack length, is not very accurate. The fibres bridging across the crack faces tend to reduce the compliance of a stress–free crack of the same length [2]. Evaluation of crack length from theoretical compliance calculations therefore underestimates its true length (see Figure 2). Recently, Hu and Wittmann [3] have developed a "multi–cutting" technique to measure the FPZ of cementitious matrices and the bridging stresses within this zone. Elegant and simple as this technique may be, it is difficult to extend to fibre cement composites for the separation and measurement of the FPZ and FBZ.

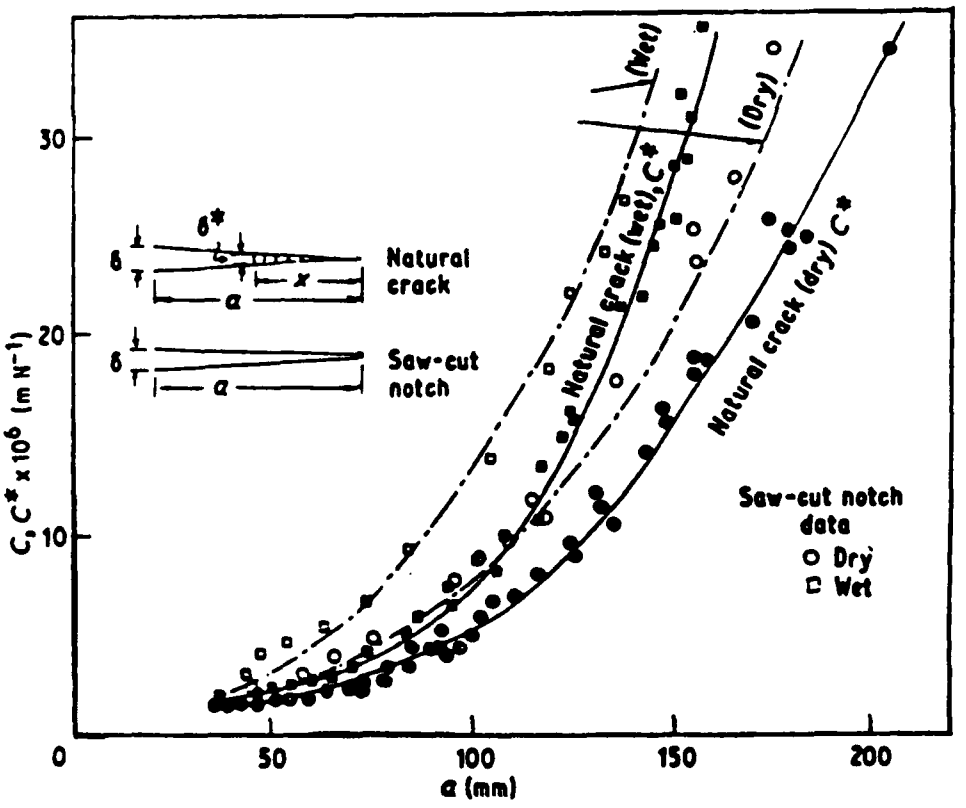

Figure 2. Fibre bridging effect on compliance measurements of a DCB cellulose fibre cement mortar. Compliances C* and C refer to presence and absence of FBZ respectively.

2.1 NEW METHODS FOR FRACTURE PROCESS ZONE SIZE MEASUREMENT AND CRACK GROWTH

The author and his co–workers have developed a new technique to detect the crack tip position and hence to distinguish the boundary of the FBZ and FPZ of fibre cements. An automated method of continuous crack length measurement using a screen–printed conductive grid and a micro–computer is also given. Details of these experimental methods have already been published elsewhere [4]. In the following only the essential features are described.

Figure 3 shows a schematic diagram of the computer aided crack growth monitor system and Figure 4 gives the conductive grid pattern that was used for a compact tension (CT) wood fibre cement composite specimen. There were 64 bars in eight blocks of eight allowing the crack to be measured over a distance of approximately 140 mm. The bars were nominally 1 mm in width and had a repeated distance of 2.14 mm. The conductive ink used consisted of finely divided graphite particles dispersed in a vinyl resin binder and a butyl cellosolve acetate solvent. In operation the computer scanned each bar on the grid serially and tested each for continuity. When a broken bar was detected, indicating the presence of a crack at that location, a voltage corresponding to its number was sent to a plotter and a graphic display of the grid on a monitor showed that bar as broken. With each scan the latest broken bar was detected, plotted and displayed. This permitted the crack growth process to be clearly seen. Both load–time and crack growth–time records could be simultaneously and continuously obtained with this technique until final failure. Figure 5 shows the results obtained for the wood fibre cement CT specimen. The complex nature of crack grwoth was revealed by the bars recording breaks and sometimes closures followed by a second break. The region of bars breaking, or the "activity zone", was approximately 20 mm over the period of crack growth. Table 2 compares the observed crack tip using optical microscopes and the location of the activity zone. Quite clearly, the leading edge of the activity zone gave a good measure of the real crack length and hence a plausible demarcation of the FBZ and FPZ.

In order to measure the size of the matrix fracture process zone narrow strips were cut from the CT specimen after crack growth had taken place. Strips away in the unstressed region were also cut to represent the undamaged material, Figure 6(a). The bending stiffness of crack strip was measured in pure bending with the compressive surface facing the crack growth direction, Figure 6(b), and the location of fracture noted. In strips cut from the cracked (or fibre bridging) region of the specimen, the failure sites would lie along the prolongation of the machined notch. However, in the matrix fracture process zone, the fracture sites were scattered. Figure 7 shows the variation of the normalised bending stiffness with distance from the crack origin and the locations of the failure sites. It is clear that these results support the general concept discussed above. The crack length indicated here is about 80 mm which agrees closely with the optical and computerised electrical methods shown in Table 2. Figure 8 plots the normalised bending stiffness results for four CT specimens as a distance from the crack tip. The matrix FPZ size deduced from this figure varies between 28 mm to 40 mm. Such a size is certainly not negligible and it would seem that it must be properly included in the R–curve modelling. However, as shown later in Section 3.5, its inclusion in the model is not really necessary.

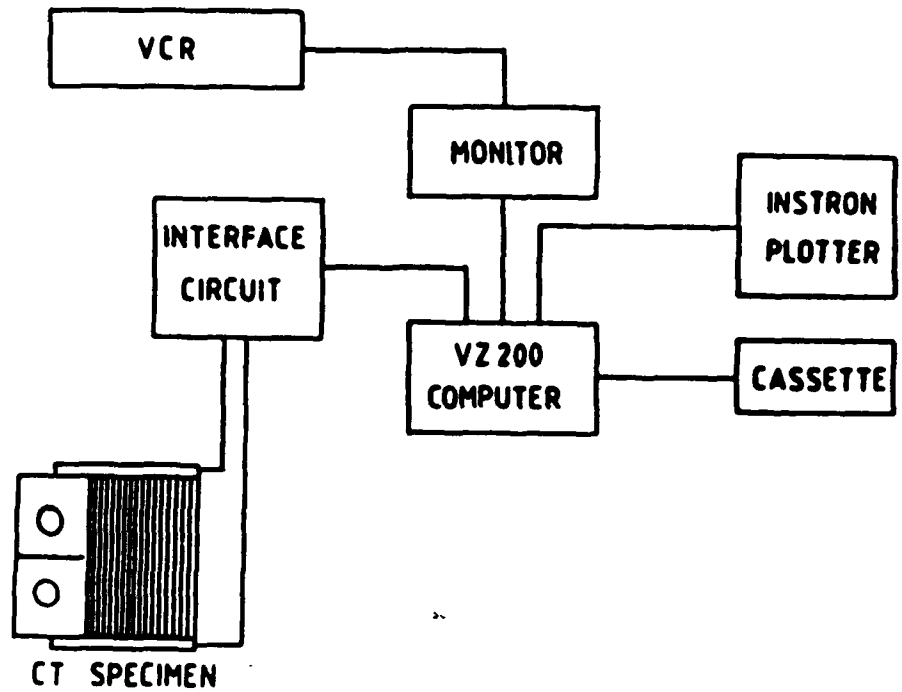

Figure 3. Computer aided crack growth monitoring system.

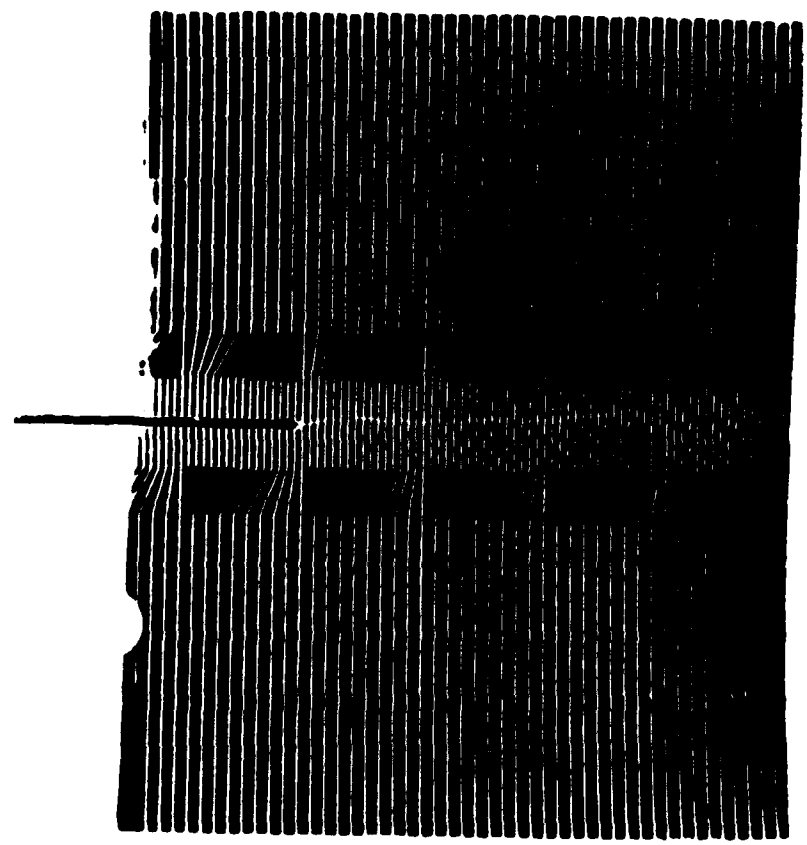

Figure 4. Conductive grid pattern printed on CT specimen.

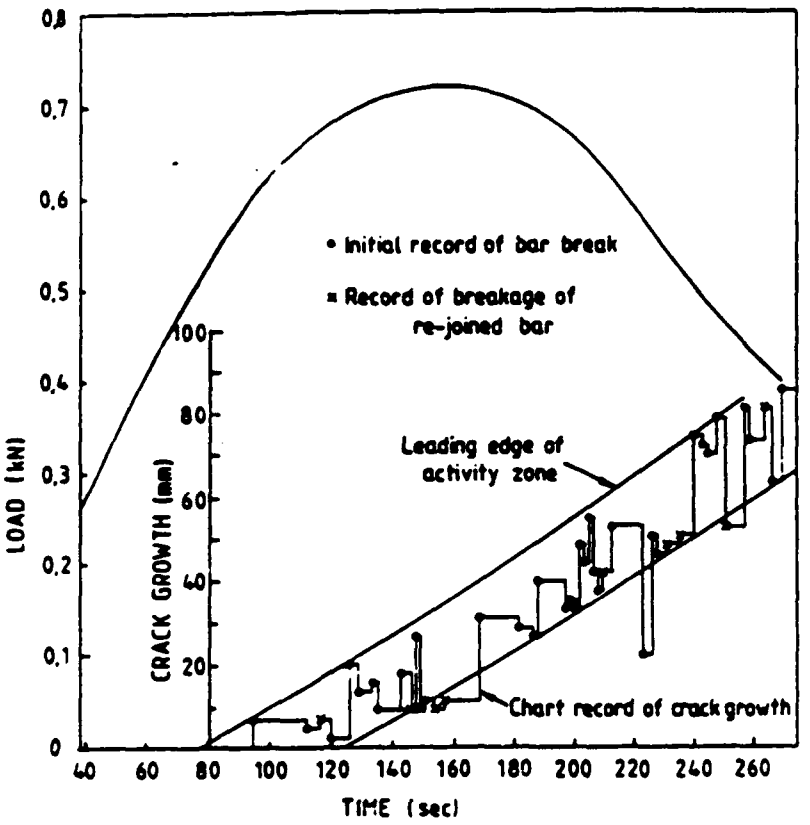

Figure 5. Crack growth/load-time records using the computer-aided system. Activity zone leading edge gives a measure of real crack length.

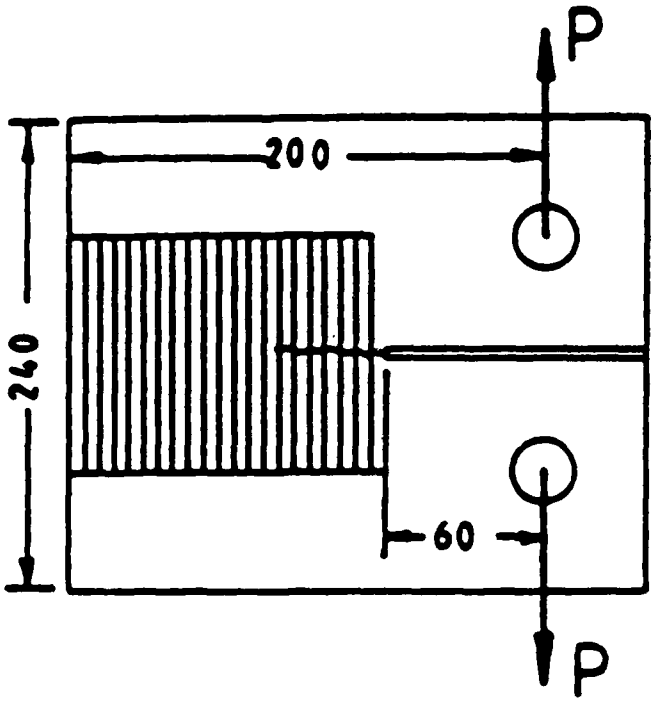

Figure 6(a). Compact tension specimen dimensions in mm and strips cut for bending stiffness tests.

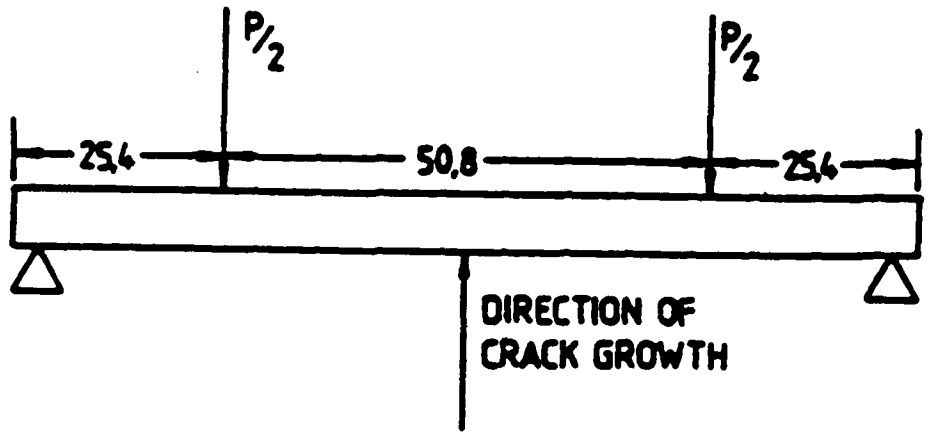

Figure 6(b). Four-point bend tests on damaged strips to evaluate size of the FPZ.

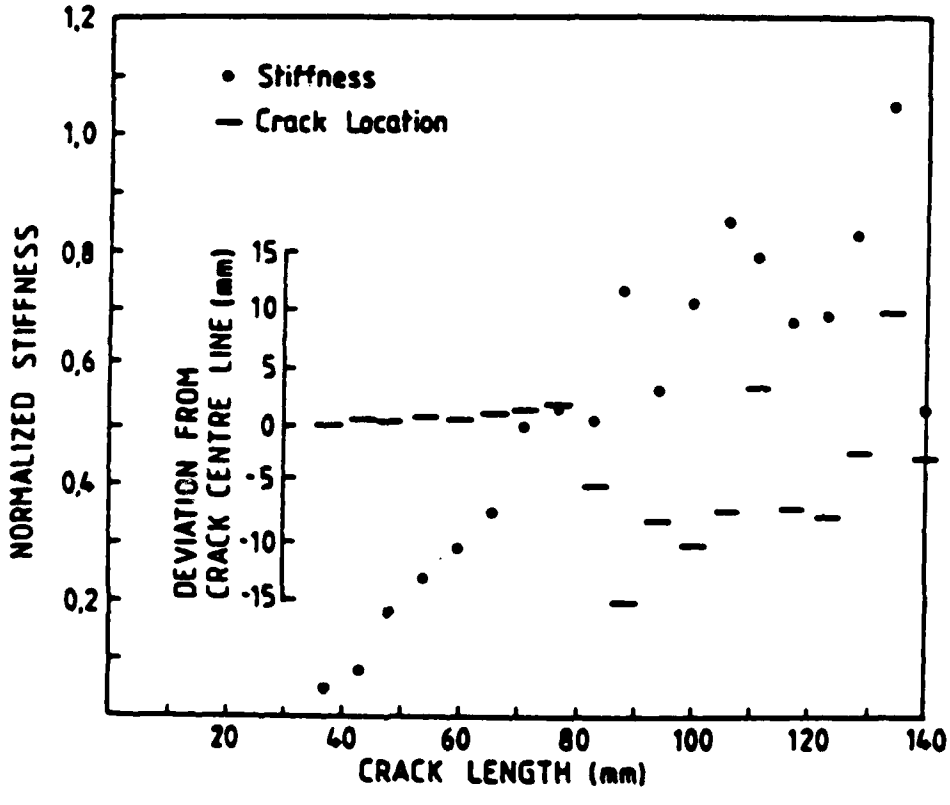

Figure 7. A plot of normalized stiffness versus crack length. Failure sites of sectioned strips are indicated by horizontal bars.

TABLE 2. Crack length measurement using the computerised electrical method and the section and bend stiffness test

Specimen No.	Crack length (mm)		
	Optical method	Electrical conductive bars/activity zone	Bend stiffness measurement
1	78	62–86	77
2	83	56–88	83
3	99	70–105	112

3. Crack–Resistance (R) Curve and Failure Characterisation

The crack–resistance curve is basically controlled by both "intrinsic" and "extrinsic" variables. Intrinsic variables are microstructural in nature and include the level of porosity, the fibre type and its surface treatment, the residual stresses and the matrix properties. By changing these variables it is possible to change the stress–displacement constitutive relations in the FBZ and FPZ. Extrinsic variables are those of specimen geometry, size and loading configuration which would affect the deformation of the FBZ and FPZ and hence the crack tip shielding mechanisms. In the following sub–sections the mechanics of crack–interface bridging and analytical modelling of specimen size, geometry and matrix FPZ effects on R–curves are presented.

3.1 MECHANICS OF CRACK–INTERFACE BRIDGING

In fibre cement composites the single most important variable on the crack–resistance curve is the closure stress (σ)–crack face separation (δ) relationship in the FBZ. Once this relation is known it is possible to predict R–curves for different effects of size and geometry and alternatively the load–deflection or moment–curvature diagrams for various types of structural components. For the very simple situation of fibre debond/pullout the σ–δ relationship can be worked out theoretically. If it can be assumed that the mechanical shear bond strength τ is a material constant then the force F to pullout a fibre is $F = \pi d\tau\ell$, where d and ℓ are the diameter and embedded length of the fibre. When the fracture surfaces have separated a distance δ the maximum possible pullout force is given by $F_m(1-2\delta/L)$ where $F_m = \pi d\tau L/2$ and L is the fibre finite length. The number of fibres per unit area of fracture surface (N) is $\eta V_f/(\pi d^2/4)$, where η is the orientation efficiency factor equal to unity for aligned fibres, $2/\pi$ for 2–D randomness and 1/2 for 3–D randomness; V_f is the fibre volume fraction. Thus, the average closure stress–displacement relationship is as expected linear, i.e.

$$\sigma = [\eta V_f \tau L/d][1 - 2\delta/L]. \qquad (1)$$

However, if it is considered that when the fracture surfaces are separated by an amount δ, then a proportion $2\delta/L$ of the embedded fibres have already pulled out completely. Hence the average stress on the composite is

$$\sigma = [\eta V_f \tau L/d][1 - 2\delta/L]^2 \qquad (2)$$

indicating that the σ–δ relation is parabolic rather than linear. Indeed Ballarine et al [5] have shown that equation (2) is valid for steel fibre reinforced concrete. It may be criticized that neither equations (1) and (2) considers the Poisson's contraction of the fibres and the non–constant shear stress at the fibre–matrix interface. Gao and co–workers [6] have developed σ–δ relationship that incorporates these additional factors from a simple shear lag model.

For many fibre cement composites the complex failure mechanisms in the FBZ make it difficult to derive a rigorous theoretical σ–δ relationship. In these cases experimental methods remain the only solution and both direct and indirect techniques have been developed to measure the σ–δ relationship. In the direct tensile test method a very stiff testing machine or special stiffening devices are required to produce a stable fracture and misalignment has to be eliminated in order to obtain an accurate σ–δ curve [7,8]. Figure 9 shows a schematic tensile stress–displacement curve for a fibre cement composite. In region I the specimen is essentially elastic. In region II the non–linear deformation is largely due to dispersed cracking within the gauge section. When the cracking becomes localised on a future fracture plane the ultimate strength σ_m is achieved. Up till σ_m the deformation is uniform throughout the specimen; but in regions III and IV the deformation is localised in the fracture process and fibre bridging zones. During region III the matrix FPZ develops and when the displacement across it reaches δ_m a continuous matrix crack is established. (see Figure 1). Usually $\delta_m << \delta_f$ so that the stress σ_f is close to the maximum pullout stress. The difference between σ_f and σ_m depends upon V_f and F_m. In region IV the fibres gradually pullout and fracture. Complete fibre pull–out occurs when the crack face separation distance δ_f equals to half the fibre length. The σ–δ relation is therefore that given in regions III and IV as shown in Figure 9. The total specific work of fracture J_∞ in a tension test is given by the sum of the matrix fracture work J_{Ic} and the fibre pull–out work, i.e.

$$J_\infty = J_{Ic} + \eta V_f \tau L^2/6d \qquad (3)$$

if $\delta_m << L/2$. In a sufficiently large notched specimen where the FBZ can be fully established and the crack profile remains unchanged during stable crack growth J_∞ can be obtained and may be identified with the plateau value K_∞ of the crack–resistance curve, i.e. $J_\infty E = K_\infty^2$. The crack resistance J_R prior to J_∞ is therefore

$$J_R(\delta) = \int_0^\delta \sigma(\delta)d\delta = J_{Ic} + \int_{\delta_m}^\delta \sigma(\delta)d\delta \qquad (4)$$

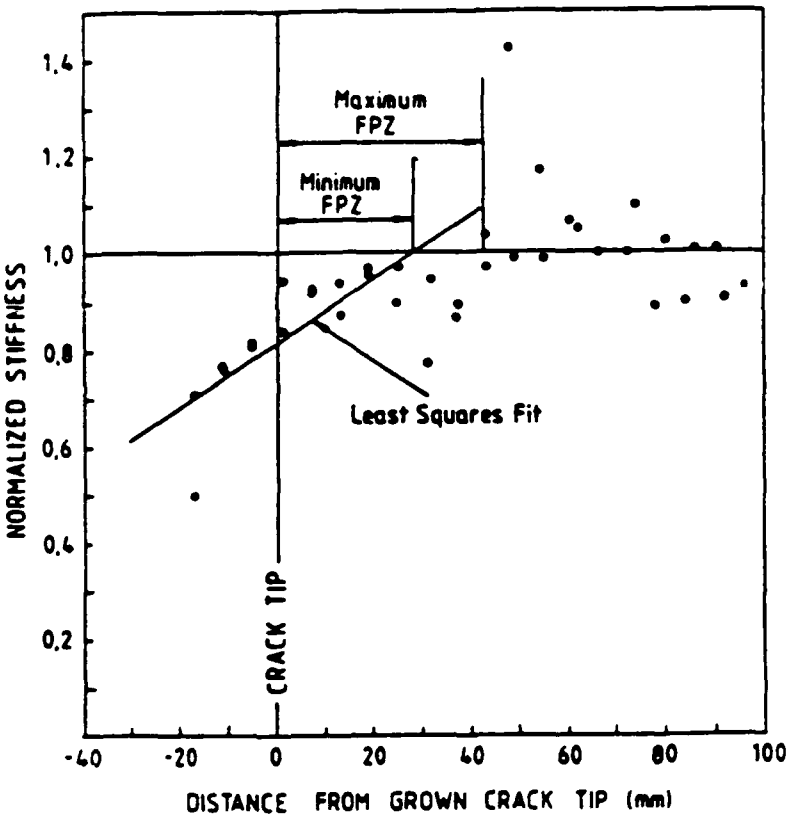

Figure 8. Evaluation of FPZ using normalised stiffness - crack tip distance plot.

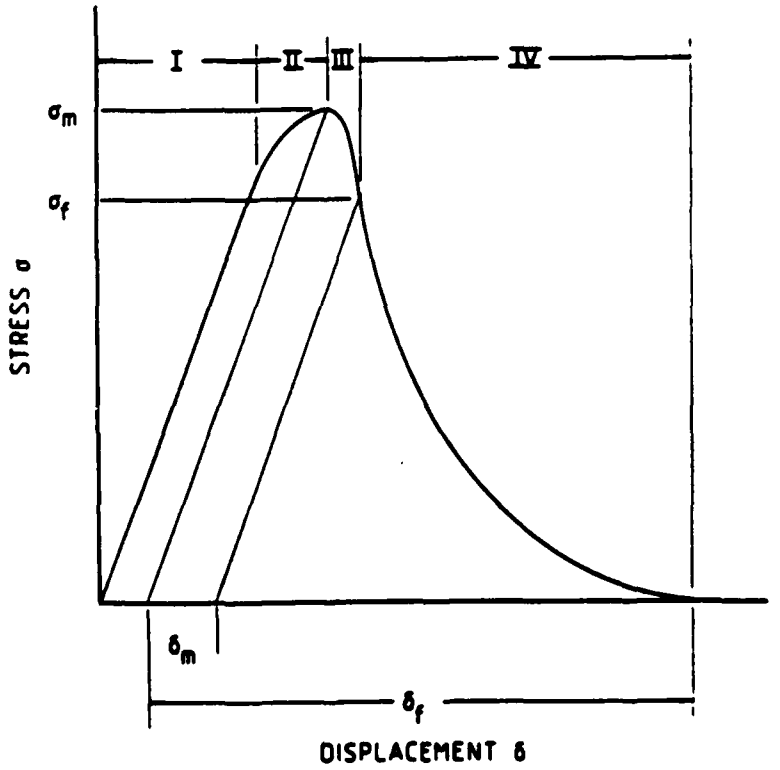

Figure 9. Schematic stress-displacement curve for a fibre cement composite.

Equation (4) has provided a theoretical basis for a simple indirect method to evaluate the σ–δ relationship if the crack–resistance curve $J_R(\delta)$ can be obtained. Using the energetic definition of J it is possible to determine J_R experimentally using specimens of different crack lengths. However, J_R is now evaluated at the load–point or crack mouth opening displacement Δ but not at the leading edge of the FBZ which is δ. For any given specimen geometry Δ and δ can be experimentally related to each other so that

$$\sigma(\delta) = \frac{\partial J_R(\Delta)}{\partial \Delta} \frac{d\Delta}{d\delta}. \tag{5}$$

Li and his co–workers [9,10] have successfully shown the use of equation (5) to determine the $\sigma(\delta)$ functional relationship for concrete and fibre cement composites. Figure 10 shows the σ–δ curves for a range of fibre cementitious materials obtained by Li and Ward [10]. It is interesting to observe that σ–δ is not linear but parabolic as predicted by equation (2). Since crack–resistance curves are usually represented in terms of crack growth Δa and not Δ or δ another version of equation (5) has been derived using the $K_R(\Delta a)$ curves. For the notched crack shown in Figure 11 where Δa is the fibre bridging zone and the initial crack length a_o is much larger than Δa, then

$$K_R(\Delta a) = K_{Ic} + \left[\frac{2}{\pi}\right]^{\frac{1}{2}} \int_0^{\Delta a} \frac{\sigma(x)dx}{\sqrt{x}} \tag{6}$$

and it follows that

$$\sigma(\Delta a) = \left[\frac{\pi}{2}\right]^{\frac{1}{2}} (\Delta a)^{\frac{1}{2}} \frac{dK_R(\Delta a)}{d(\Delta a)} \tag{7}$$

in which $dK_R/d(\Delta a)$ is easily obtained from the $K_R(\Delta a)$ crack–resistance curve. To convert to $\sigma(\delta)$ it is necessary to determine the relationship between Δa and δ either theoretically or experimentally. If it is assumed that the crack profile is an approximate straight line [11] so that

$$\Delta a/\delta = 2\Delta a_s/L \tag{8}$$

where L/2 is the critical fibre pull–out length at the leading edge of the fully developed FBZ of size Δa_s, then

$$\sigma(\delta) = (\pi \Delta a_s \delta/L)^{\frac{1}{2}}\, dK_R(\Delta a)/d(\Delta a). \tag{9}$$

Since the direct tension test method is difficult to use, Chuang and Mai [12] have recently shown that for cementitious matrices the σ–δ relationship can be extracted from the load–displacement or moment–curvature curves of an

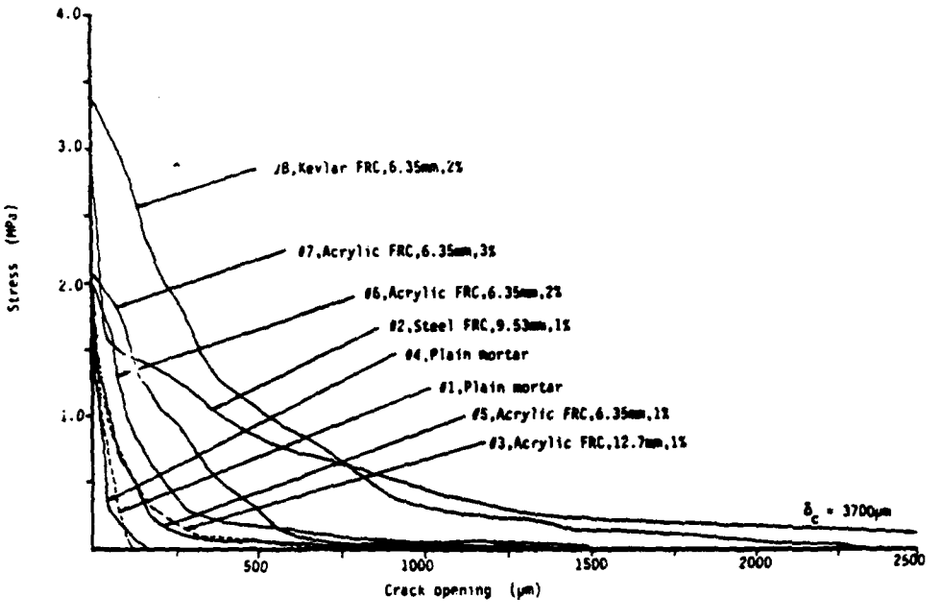

Figure 10. Stress-displacement curves for various fibre cementitious composites. (Taken from Li and Ward, ref. 10).

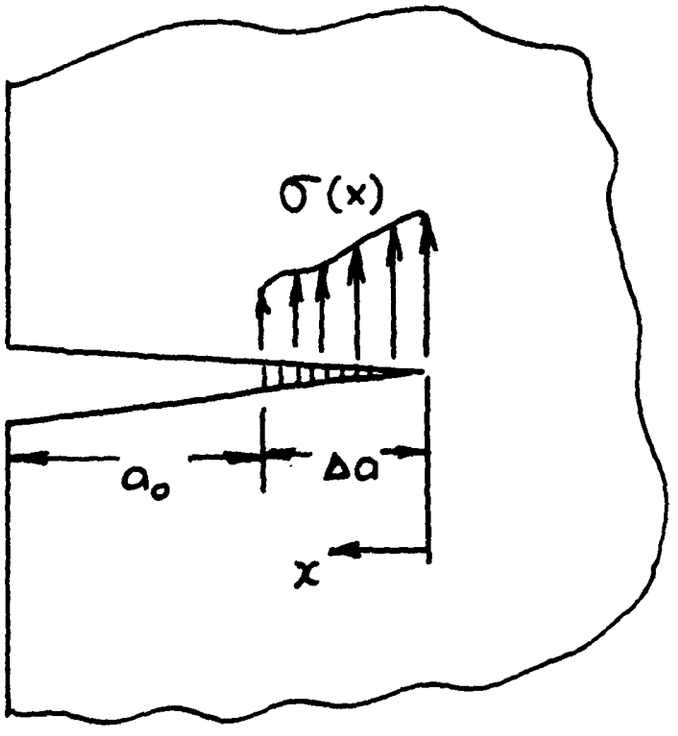

Figure 11. FBZ and stress distribution at wake of crack tip.

unnotched beam in pure bending, provided it is possible to identify the points on these curves for the onset of the FPZ and the initiation of crack growth at the tensile surface. However, this method cannot be readily applied to fibre–reinforced cement composites.

3.2 UNIQUENESS OF CRACK–RESISTANCE (R) CURVE

It is of fundamental interest to ask if the crack resistance (R) curve is a unique material property for fibre cements and other cementitious matrices. If it were to be so then the characterisation of failure would be a simple matter of determining the tangency point on the R–curve due to the applied stress intensity factor K_a–curve (see Section 3.6). The evaluation of the instability point for non–unique R–curves however requires an iterative process. In terms of the crack face separation at the leading edge of the fibre bridging zone equation (4) describes the J_R–δ relationship as the crack resistance increases from a matrix toughness J_{Ic} to a plateau value J_∞ defined by equation (3). Thus, in between these two limits, i.e. for $\delta_m << L/2$ and $\delta > \delta_m$,

$$J_R(\delta) = J_{I_c} + \frac{\eta V_f \tau L^2}{6d}\left\{1 - \left[1 - \frac{2\delta}{L}\right]^3\right\} \tag{10a}$$

or combining with equation (3) this becomes

$$J_R(\delta) = J_{I_c} + (J_\infty - J_{I_c})\left\{1 - \left[1 - \frac{2\delta}{L}\right]^3\right\}. \tag{10b}$$

It is quite obvious from equation (10) that when plotted in terms of δ the crack resistance curve J_R is a unique material property. However, since the relationship between δ and crack growth Δa (or extension of the FBZ) is both specimen geometry and size–dependent, J_R in terms of Δa is generally not invariant with these extrinsic variables. During the evolution of the crack resistance curve expressed in terms of Δa,

$$J_R(\Delta a) = J_{Ic} + \int_0^a \sigma(x)\,\frac{\partial \delta(x,a)}{\partial x}\,dx. \tag{11}$$

Except for a very large specimen the shape of the crack profile changes with crack growth so that $\partial\delta/\partial x \neq -\partial\delta/\partial a$ and $J_R(\Delta a)$ is not unique. A unique crack resistance curve can be obtained in theory if we consider a semi–infinite crack in an infinite sheet and this has indeed been studied by Foote et al [13] using Muskhelishville's method. In this way not only does the crack face profile remain unchanged but that the FBZ is very small compared to the crack length.

3.3 ANALYTICAL MODELLING OF CRACK–RESISTANCE CURVE

Many analytical models for crack growth in fibre cements follow the fictitious crack model of Hillerborg and co–workers [14,15] originally developed for cementitious matrices, e.g. Wecharatana and Shah [16], Ballarine et al [5], Visalvanich and Naaman [17] etc. Because the closure stresses in the FBZ and FPZ are dependent on the crack face separation the problem is a non–linear one and requires an iterative numerical solution [15,16]. To provide a simpler and more general model Jenq and Shah have extended their two–parameter fracture model for concrete [18] to fibre cements [19]. The two parameters are the critical value of δ_m already defined in Figure 1 and the critical stress intensity factor $K_{I_c}^s$ at the tip of the effective or fictitious crack. It is claimed that these parameters are independent of both specimen size and geometry and can be used to predict the crack resistance curve of fibre cementitious composites [20]. A review of these previous fracture models is given by Cotterell and Mai [21].

It appears that the simplest method of analysing crack growth in fibre cements is by superposition of the stress intensity factors due to the applied stresses K_a and the closure stresses in the FBZ, K_r, and the FPZ, K_m. Lenain and Bunsell [22] were the first to use the K–superposition method to model crack resistance in asbestos cements. They assumed that crack growth would commence when the effective K_e at the crack tip was equal to the matrix toughness K_{I_c}. Instead of calculating K_m they assumed K_r to prevail over an effective crack length which included a portion of the matrix fracture process zone. Thus, the equilibrium crack growth criterion becomes:

$$K_e = K_a + K_r = K_{I_c}. \tag{12}$$

The crack resistance is the term K_a which increases as the crack extends and it is usually described by K_R, i.e.

$$K_R(\Delta a) = K_{I_c} - K_r(\Delta a). \tag{13}$$

Lenain and Bunsell further assumed the bridging stresses to be constant and avoided solving the non–linear iterative problem. $K_r(\Delta a)$ can be obtained easily from the expression

$$K_r = -\int G(a,x)\sigma(x)dx \tag{14}$$

where the negative sign is to show that K_r is acting in an opposite sense to the applied K_a and the Green function $G(a,x)$ is dependent on specimen geometry and loading configuration. It is unfortunate that they have used the wrong Green function in their analysis making their results invalid.

The approximations used by Lenain and Bunsell are not realistic and unnecessary. Equations (13) and (14) can be used in conjunction with equation (2) for the σ–δ relationship in the FBZ to obtain an exact solution. Of course, this introduces a non–linear problem, since K_r depends on σ which in turn depends on δ that is the sum of the displacements due to the applied stresses and the fibre bridging forces. Iterations are required to obtain σ that is consistent with δ in the FBZ. For a bridged crack in a uniform stress field σ_∞,

the solution of δ is relatively simple though iterations are still needed. In a non–uniform stress field, such as that in a notched bend (NB) or a double–cantilever–beam (DCB) geometry, the solution of δ is far more complicated. Foote et al [11] have derived a simple equation for δ from stress intensity factors by application of Castigliano's Theorem. Thus, the displacement $\delta(x)$ at a point x from the crack tip (Fig. 12) due to an applied load P acting at a point a away from the tip is given by [11, 23–25]

$$\delta(x) = \frac{2}{E}\int_{a-x}^{a} K_P(u)\left[\frac{\partial K_F}{\partial F}(u-a+x)\right]_{F=0} du \qquad (15a)$$

where F is a fictitious force at x, K_P and K_F are stress intensity factors due to P and F. If the positions of P and F have been interchanged along the crack face $\delta(x)$ can be obtained from a similar expression

$$\delta(x) = \frac{2}{E}\int_{x-a}^{a} K_P(u-x+a)\left[\frac{\partial K_F(u)}{\partial F}\right]_{F=0} du. \qquad (15b)$$

Note that the integration in equation (15) is carried out over the distance between the forces. If P is a unit force the integrals give the displacement coefficients along the crack face which can be used in the iterative scheme to evaluate the exact K_R–curves. It is important to point out here that equation (15) is a powerful tool for crack face separation calculations provided the K–solutions for the applied and fictitious loads P and F are known right to the crack tip for any given geometry.

Foote et al [11,21,23–26] have also developed an approximate method to calculate crack resistance curves for fibre cements. In common with Shah and his co–workers [5,16] the crack faces in the FBZ are assumed to remain straight so that using equations (2) and (8) it can be shown that:

$$\sigma(x)/\sigma_m = \left[1 - \frac{x}{\Delta a_s}\right]^n = \left[1 - \frac{2\delta}{L}\right]^n \qquad (16)$$

where the maximum fibre pull out stress $\sigma_m = \eta V_f \tau L/d$ and n = 2 in this example but it may assume other values depending on the strain–softening characteristics of the material. An iterative solution is still required to determine Δa_s knowing K_{I_c}, E, σ_m and L while satisfying the equilibrium crack growth condition of equation (13). For crack growth less than Δa_s, $\sigma(x)$ is given by equation (16) and K_r calculated from equation (14). No further iterations are necessary. Justifications of the linear crack face profile and the approximate method are shown in Figures 13 and 14 respectively for a wood fibre cement composite and details of these calculations are given in [11,25].

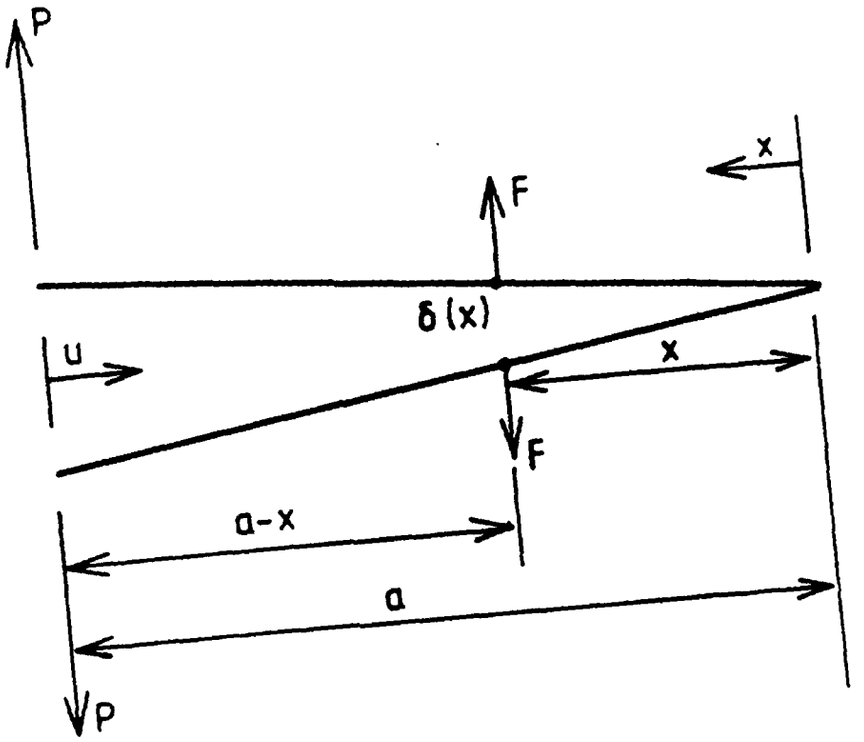

Figure 12. Evaluation of crack face separation (δ) by Castigliano's theorem at the location of the fictitious force (F).

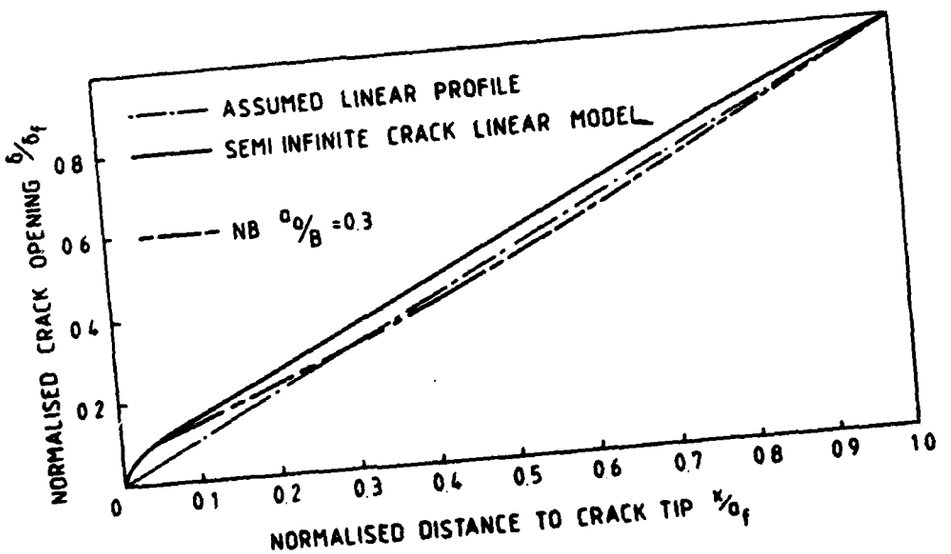

Figure 13. Shape of deformed crack faces for semi-infinite and NB specimens.

3.4 INFLUENCE OF SPECIMEN GEOMETRY AND SIZE ON CRACK RESISTANCE CURVE

It is discussed in Section 3.2 that the crack resistance curve is unlikely to be a unique material property because the FBZ is not small compared to the cracked or uncracked ligament lengths and the crack face profile is not invariant with crack growth. Consequently, specimen size and geometry must have some effects on the R–curve. Foote et al [11,25,27] have studied the size effect of the DCB and NB geometries for asbestos and wood fibre cement composites.

For ease of comparison non–dimensional crack resistance curves, where $\bar{K}_R = K_R/K_\infty$ and $\Delta\bar{a} = \Delta a/(K_\infty/\sigma_m)^2$, are plotted for the DCB geometry in Figure 15 and NB geometry in Figures 16 and 17. In these $\bar{K}_R$–curves a non–dimensional fracture toughness of the matrix $\bar{K}_{Ic} = 0.3$ is assumed which is typical of wood fibre reinforced mortars. K–solutions for the DCB and NB geometries are taken from Foote and Buchwald [28] and Tada et al [29] for use with equation (15) to calculate the crack face separation δ in the FBZ. In the DCB geometry, by keeping $a_o/H = 3$ constant, the crack resistance curves are dependent on the depth of the beam $\bar{H}(= H/(K_\infty/\sigma_m)^2)$ with the length of the fully developed FBZ $\Delta\bar{a}_s$ decreases as $\bar{H}$ decreases but the plateau values K_R are very close to the theoretical limit K_∞, Figure 15. The effect of the notch to depth ratio a_o/H on the crack resistance curve is practically zero, Figure 18. Some very interesting observations can be made for the NB geometry. Keeping the notch to beam depth a_o/B ratio of 0.30 constant it is shown that the size of the beam has a significant effect on the crack resistance curves. When the non–dimensional beam depth $\bar{B}(=B/(K_\infty/\sigma_m)^2)$ is large compared to the FBZ the $\bar{K}_R$ curve reaches a plateau value and indeed the whole crack resistance curve is identical to the DCB geometry when $\bar{H} \to \infty$. For smaller $\bar{B}$ the fully developed FBZ size decreases with specimen size and the crack resistance curve can be much larger than the plateau value K_∞, Figure 16. Also, unlike the DCB geometry, the notch to depth ratio a_o/B has a far greater effect on the $\bar{K}_R$ curves as shown in Figure 17.

It is worth noting that whenever the crack approaches the back–face the crack resistance curve rises rather sharply, such as in NB specimens in Figure 17. In this way small compact tension specimens give similar behaviour. There is no physical reason as to why the fracture resistance should suddenly increase near the back–face other than it is a consequence of the K–solution as the uncracked ligament approaches zero. In fact in cementitious matrices alone the crack resistance curve may decrease as the back–face is reached [30]. This result may be caused by the reduction in the width of the damage zone (a parameter which is not considered in a crack growth model presented in these lecture notes) and the prior damage of the material near the back–face due to precompression [31].

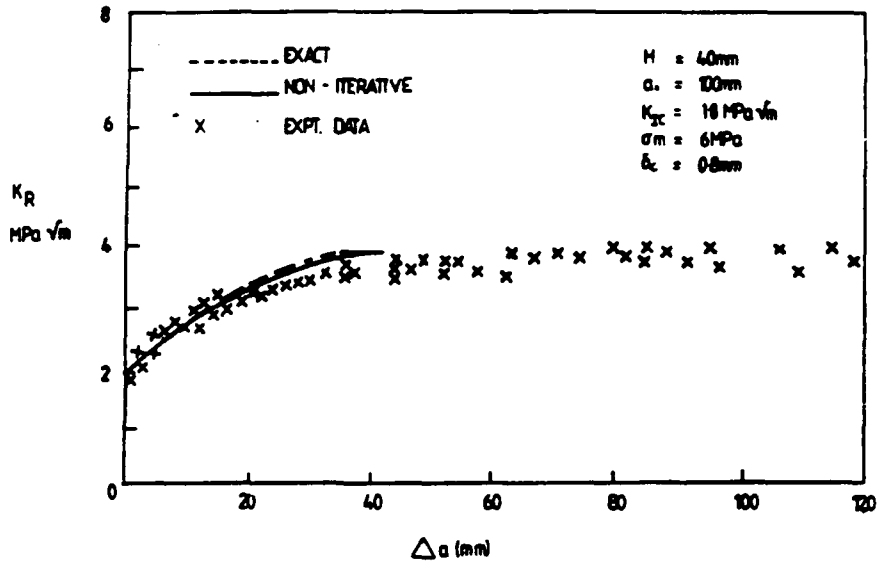

Figure 14. Comparison of 'exact' and approximate crack resistance curves for DCB geometry.

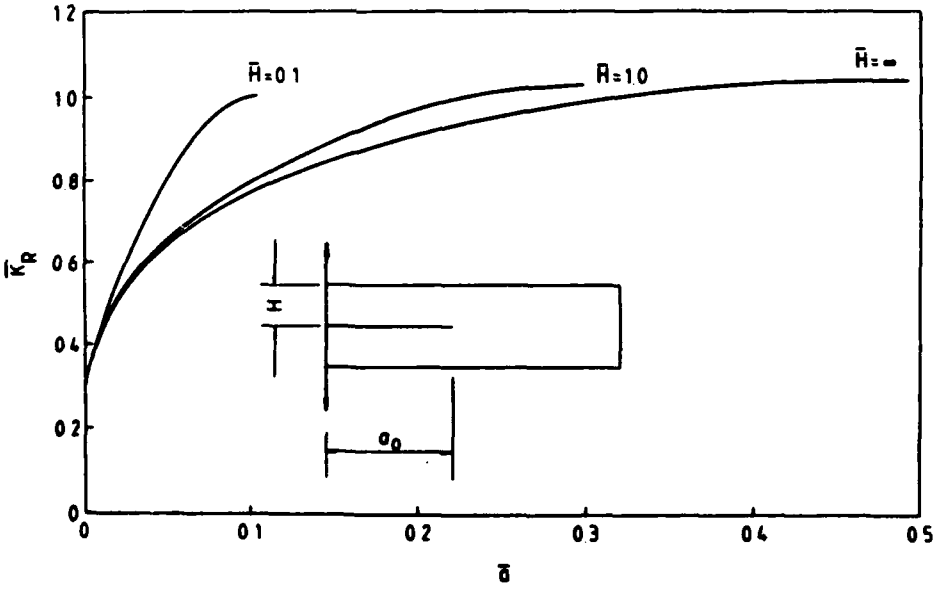

Figure 15. Non-dimensional crack resistance curves for DCB geometry for $a_o/H = 3.0$ and different $\bar{H}$.

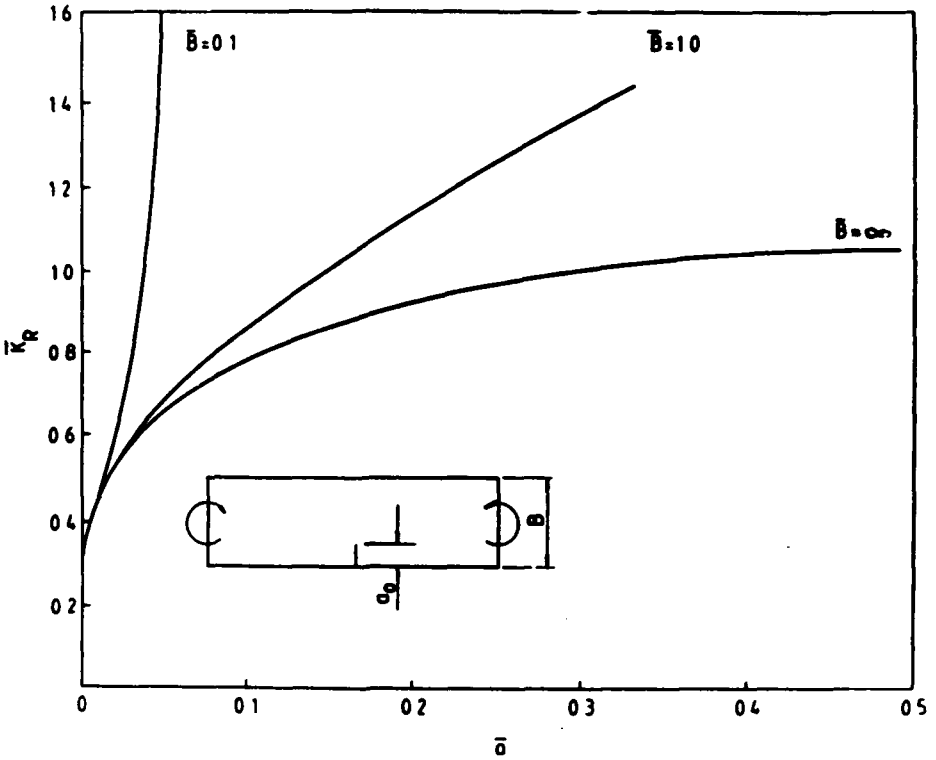

Figure 16. Non-dimensional crack resistance curves for NB geometry for $a_o/B = 0.3$ and different $\bar{B}$.

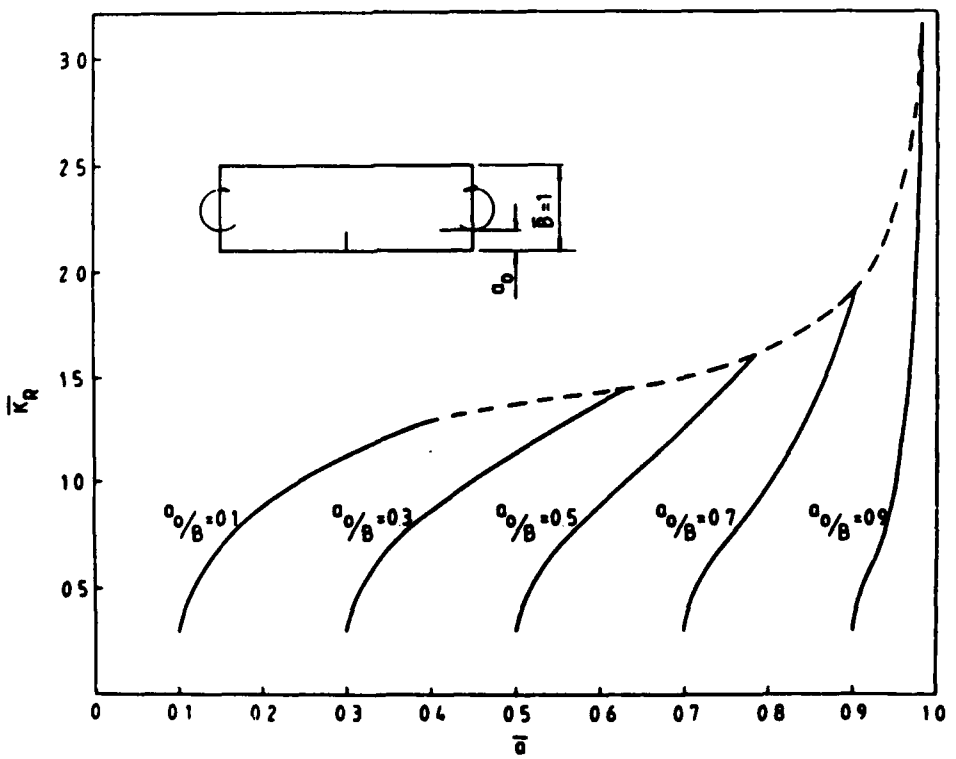

Figure 17. Non-dimensional crack resistance curves for NB geometry for $\bar{B} = 1.0$ and varying a_o/B.

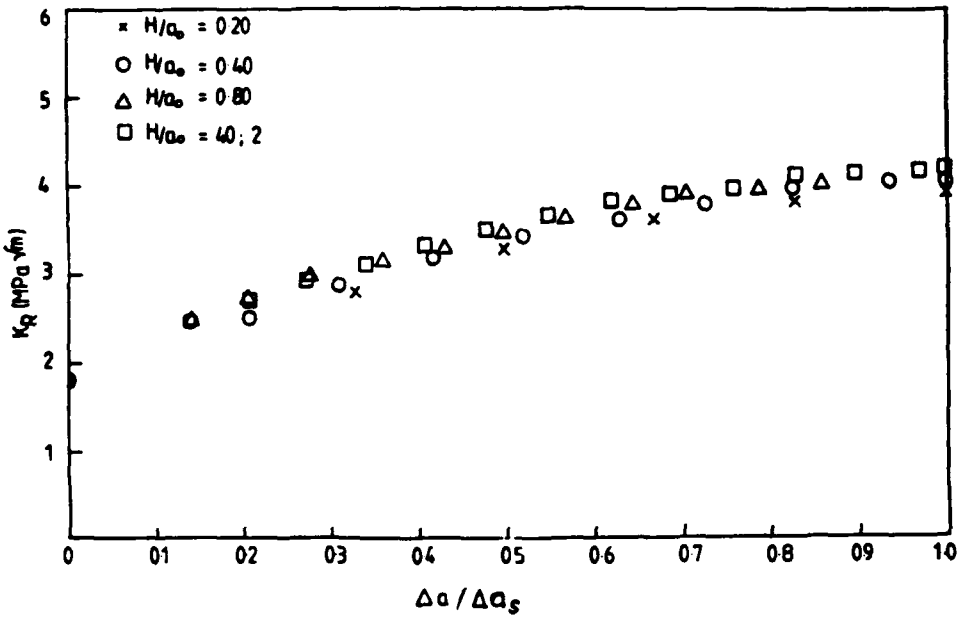

Figure 18. Normalised K_R - $\Delta a/\Delta a_s$ curves for DCB geometry for varying a_o/H ratios.

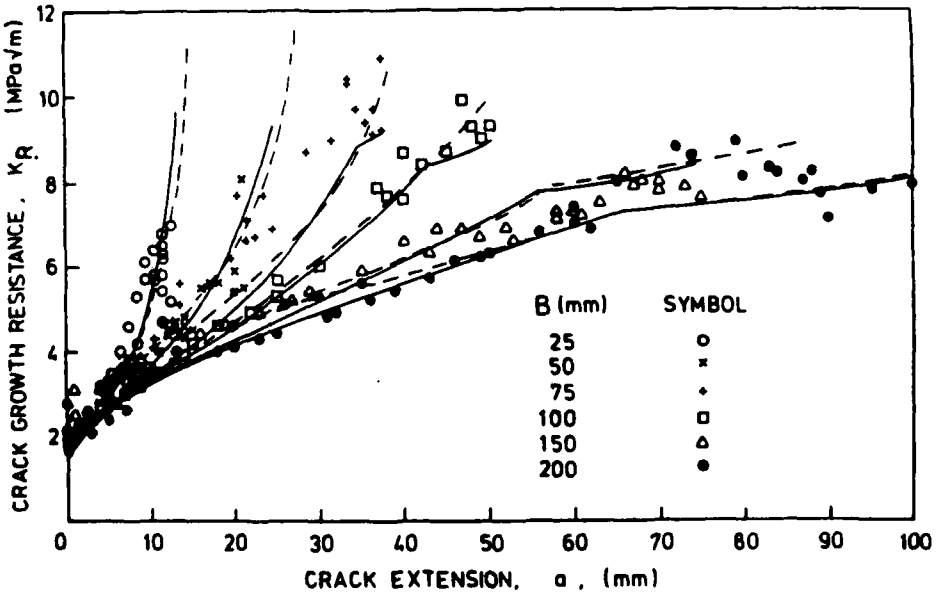

Figure 19. Experimental crack resistance curves for asbestos/cellulose cement mortar NB specimens for $a_o/B = 0.3$ and different beam depth. Theoretical models based on $\sigma_m^o = 10$ MPa, $K_\infty = 5$ MPa$\sqrt{m}$, $K_{IC} = 1.9$ MPa$\sqrt{m}$. —— without FPZ; ------ with FPZ.

Experimental crack resistance curves obtained for an asbestos/cellulose fibre cement mortar [27] for the NB geometry of varying depth and different initial notch length are shown in Figures 19 and 20. The crack growth was in the strong direction of the composite. Table 3 gives the composite and fibre properties. The bond strengths (τ) were not measured directly but selected to give good agreement with the experimental fracture strengths which were dependent on direction of the sheet. The crack resistance values K_{Ic}(= 1.9 MPa$\sqrt{m}$) and K_∞ (= 5 MPa$\sqrt{m}$) were chosen empirically to give the best fit to the K_R curve for the largest NB specimen with B = 200 mm. These parameters were then used to calculate the theoretical crack resistance curves for the smaller NB specimens in Figure 19 and varying initial notch length in Figure 20 using the approximate method outlined in Section 3.3. The agreement with experimental data is very good. An experimental K_R curve for a similar asbestos/cellulose cement mortar for the DCB geometry is given in Figure 14 in which theoretical K_R curves using both the exact iterative and approximate methods are superposed. Crack growth here was in the weak direction. The agreement with experimental data is again excellent.

In concluding this section it is important to point out that there are two levels of modelling. The fundamental level is to start from the closure stress (σ)–crack face separation (δ) relationship and use it to determine $K_r(\Delta a)$ as may be affected by size and geometry of specimen whilst still satisfying the crack growth criterion of equation (13). Since an accurate σ–δ relationship is difficult to obtain for a real composite material, it is appropriate to model crack resistance curves on a more practical level. This involves determining the most appropriate fracture parameters (K_{Ic}, K_∞, E, σ_m) or (K_{I_c}, σ_m, δ_f, E) that give the best fit to the K_R curve of a given geometry and size of specimen. It is also assumed, without any loss of accuracy, n = 1.0 in these calculations. With these parameters the behaviours of other geometries and even full–size structures can be theoretically predicted.

TABLE 3. Properties of asbestos/cellulose fibre cement mortars

(a) Composite properties		
Young's modulus (E)		6 GPa
Matrix toughness (K_{Ic})		1.9 MPa$\sqrt{m}$
Maximum toughness (K_∞)		5.0 MPa$\sqrt{m}$
Fracture strengths (σ_m)		
strong direction		10 MPa
weak direction		5 MPa
(b) Fibre properties		
	Cellulose	Asbestos
Aspect ratio (L/d)	135	80
Fibre length (L)	3.5 mm	2 mm
Volume fraction (V_f)	0.07	0.08
Bend strength (τ)	0.88 MPa	2.0 MPa

3.5 EFFECT OF MATRIX FRACTURE PROCESS ZONE ON CRACK RESISTANCE CURVE

In fibre cements the matrix fracture process zone is not small, (see Table 1 and Figure 8), it is hence necessary to consider what effect the FPZ will have on the crack resistance curve. To model this case equations (12) and (13) are not valid for crack growth. Instead the FPZ is considered as a fictitious extension of the continuous matrix crack and it carries a constant stress equal to σ_m. For equilibrium crack growth the crack opening displacement at the tip of the continuous matrix crack must be equal to the critical value σ_m. In addition since there is a finite stress at the fictitious extension of the continuous crack the sum of the stress intensity factors at the tip of the fictitious extension must be equal to zero, i.e.

$$K_e = K_a + K_r + K_m = 0 . \tag{17}$$

Now K_a is not identical to the crack growth resistance K_R which is calculated at the continuous matrix crack tip but not the fictitious crack. A linearised σ–δ relationship and straight crack face profiles are assumed to hold in the FBZ in modelling crack growth. The method of solution is the same as that given in Section 3.3 except now both Δa_s and Δa_m (the matrix FPZ size) have to be determined by iteration. For Δa less than Δa_s it is still required to determine the current length of the FPZ Δa_m by iteration so that the crack face separation at the continuous matrix crack tip is δ_m. Crack resistances K_R evaluated at the continuous crack tip can now be obtained and plotted against crack extension Δa. These predicted K_R curves are also superposed in Figure 19 and, quite clearly, there is very little difference when they are compared to those K_R curves obtained from the earlier model without the inclusion of the matrix FPZ. In practice the scatter that would be obtained from experimental crack resistance curves is far greater than the difference between the two models. For simplicity therefore it is sufficient to model crack growth in fibre cement composites without considering the matrix FPZ.

3.6 FAILURE CHARACTERISATION OF FIBRE–CEMENTS WITH R–CURVE CHARACTERISTICS

In an earlier review [32] the author has discussed the usefulness of the crack resistance curves in the context of determining the maximum load that can be withstood by a structural component containing a well–defined crack. Certainly, the component may contain many micro–cracks then the application of the crack resistance curve instability analysis is somewhat complex and this is discussed in Section 4.1. The following discussion is limited to the single crack situation.

Mai and Cotterell [33] assumed that if the crack resistance curve were independent of specimen geometry and size it could be approximately represented by a power law function:

$$K_R = \beta(\Delta a)^{\alpha} = \beta(a - a_o)^{\alpha} \tag{18}$$

in which α and β are constants and a_o is the initial crack length. The criteria for crack instability (at maximum load) under load–controlled conditions are:

$$K_a = K_R = K_c \tag{18a}$$

$$\frac{\partial Ka}{\partial a} \geq \frac{dK_R}{d(\Delta a)} \tag{18b}$$

and in general K_a can be expressed as:

$$K_a = PY(a) \tag{19}$$

where P is the applied load and Y(a) is the geometry correction factor for a given specimen geometry and loading configuration [29]. Thus, combining equations (18) and (19) the maximum load K_c value can be obtained.

$$K_c = (\alpha\Phi)^{\alpha}\beta \tag{20}$$

in which $\Phi = Y(a)/Y'(a)$ is a geometry parameter evaluated at the crack length a_c corresponding to the maximum load P_m. Experimentally, it has been established that there exists a linear relationship between a_o and a_c for a range of specimen geometries and sizes [33], i.e.

$$a_c = a_o + \Delta a_c = \gamma a_o \tag{21}$$

so that $\Phi(a_c)$ can be determined easily knowing a_o. Using NB specimens of different sizes on an asbestos/cellulose fibre cement composite Mai and Cotterell [33] have confirmed the validity of equation (20). However, the compact tension geometry data do not fall within the scatter bend of the NB data, Figure 21. This means that α and β are geometry dependent and have to be evaluated separately for different geometries.

There are some fundamental problems with the above approach to obtain solutions for fracture loads. A major difficulty lies with the assumption of a geometry– and size–independent crack resistance curve as defined by equation (18). But as shown in Section 3.4 crack resistance curves generally vary with size and geometry. It appears that equation (18) may be approximately valid for a given geometry up to the maximum load and it is correct if small cracks in infinite plates are considered. The latter may be proven as follows. In general the geometry parameter $\Phi(a_c)$ can be written as the product of a_c and $\theta(a_c)$ which is a constant evaluated at a_c. Thus, using equation (18), (20) and (21), it can be shown that

$$\alpha = (\gamma-1)/\gamma\theta \tag{22}$$

so that the crack resistance curve becomes

$$K_R = \beta(\Delta a)^{(\gamma-1)/\gamma\theta} = \beta(a-a_o)^{(\gamma-1)/\gamma\theta}. \tag{23}$$

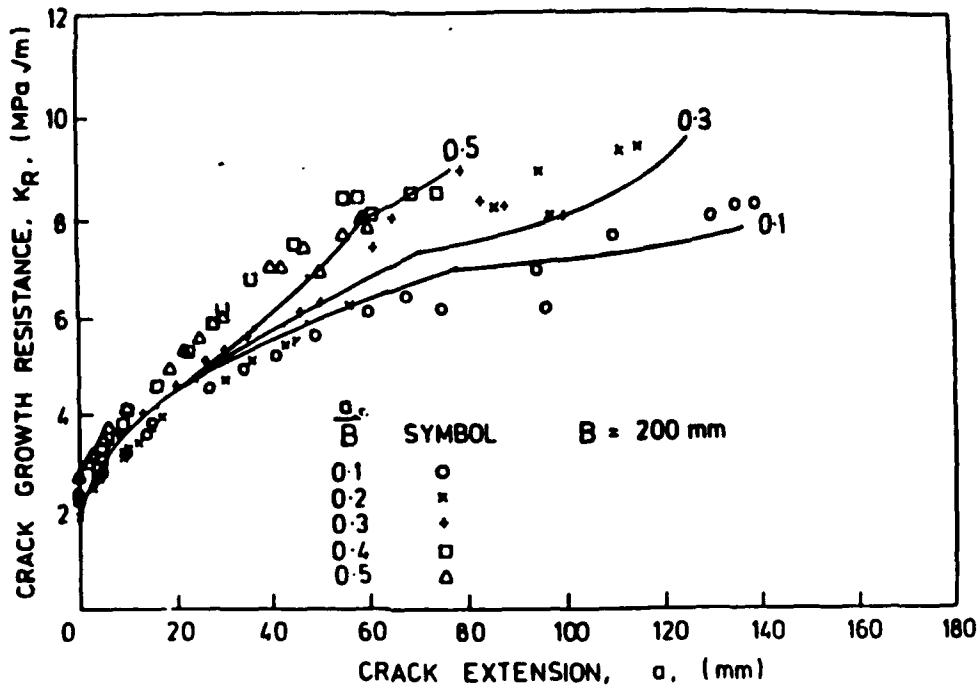

Figure 20. Experimental crack resistance curves for asbestos/ cellulose cement mortar specimens with B = 200 mm. Theoretical model without FPZ and same parameters as in Figure 19.

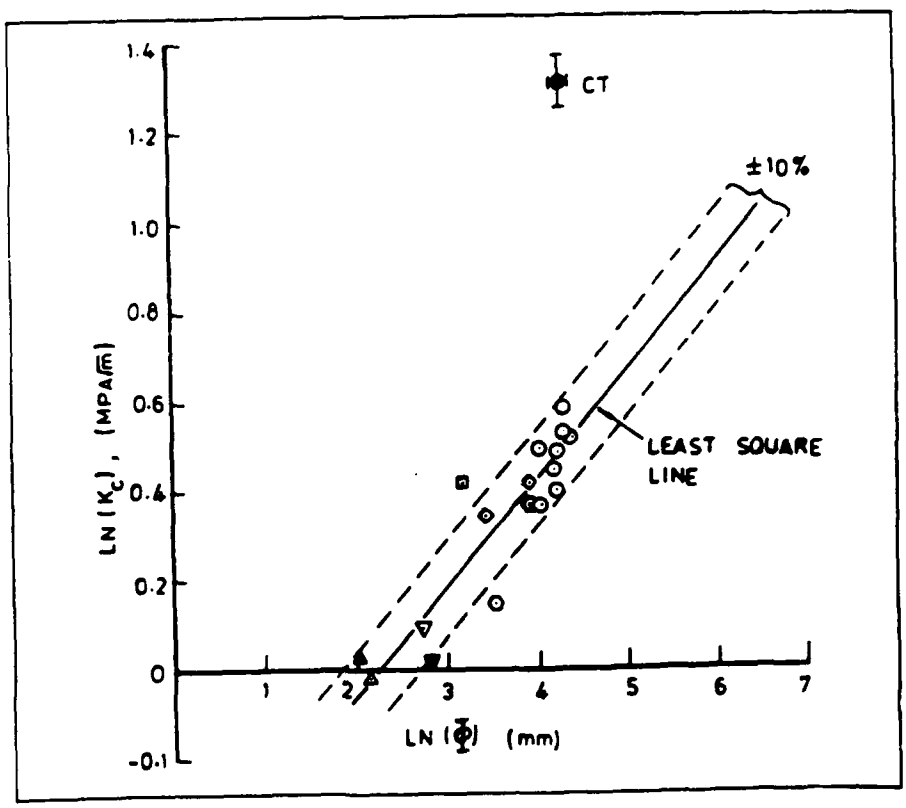

Figure 21. Variation of ℓn K_c versus ℓn Φ for NB and CT asbestos/ cellulose fibre cements according to equation (20).

$\theta(a_c)$ is not only geometry–dependent, but for a given geometry, it also varies with a_c. This suggests that the crack resistance curve is crack length–dependent. In this way the solution for K_c is not self–consistent. However, for small cracks in large sheets, θ is invariant with a_c and equals to 2, i.e.

$$K_R = \beta(\Delta a)^{(\gamma-1)/2\gamma} \tag{24}$$

which is also obtained by Broek [34] and is now a unique material curve.

A similar approach has been used by Mobasher et al [20] for fracture load predictions in cement–based fibre composites. They also used an energy–based R–curve similar to the power–law equation (18) (in which K_R is replaced by R) and assumed equation (21) to apply. The constants β and γ (and hence α) are obtained by solving a set of non–linear integral equations satisfying the following conditions for fracture instability:

$$K_{Ic}^{s} = K_r(a_c) + K_a(a_c) \tag{25}$$

and

$$\delta_m = \delta_r + \delta_a. \tag{26}$$

The two fracture parameters K_{Ic}^{s} and δ_m are to be evaluated from the fracture properties of the unreinforced matrix. It seems that by using K_{Ic}^{s} instead of K_{Ic} in equation (25) the effect of the matrix FPZ is included. But as shown in Section 3.5 this does not really cause any difference in the predicted crack resistance curve. In addition the same comments made above with regard to the Mai and Cotterell approach [33] using a power law R–curve apply. It is also not obvious that K_{Ic}^{s} is geometry and size independent because the length of the matrix FPZ does depend on these variables [24].

In view of the absence of a unique material resistance curve a more rigorous and general approach is to start from the instability equation (18a) and compute the crack resistance curve as Δa is increased in accordance with the procedures outlined in Section 3.3 for any given specimen geometry and size and initial critical crack length. Fracture instability is reached if equation (18b) is satisfied. This solution gives the fracture load and the critical crack length. A numerical iterative scheme is required to solve this problem but it is not difficult. A demonstration of this technique has been given by Cotterell and Mai [35] for cement paste in NB specimens.

4. Studies on Tensile Strength of Short Fibre Cement Composites

Practical cement–based short fibre composites contain many inherent defects which are bridged by fibres so that each individual crack essentially exhibits a R–curve behaviour. The size of these defects is not constant and in the absence of the fibres the Weibull weakest link theory applies, i.e. the tensile strength is predominantly controlled by the largest defect. When fibres are bridging these defects and because the fibres are not uniformly distributed some cracks will have more fibres and others fewer. The tensile strength cannot be determined by the simple weakest link theory and the crack–resistance curve characteristics for each crack has to be considered in any fracture model. Because the fibres exert closure stresses on the crack face a higher applied stress is needed to cause tensile failure of the matrix so that its strength can be increased. Hence, as shown by Andonian et al [36], low modulus fibres like polypropylene and cellulose can indeed reinforce cement mortar with a higher modulus (see Figure 22) because there are many crack–like defects from which fracture initiates. Both the first cracking and final tensile strengths are therefore increased due to the bridging effect of the fibres. In addition, if the matrix material exhibits a time–dependent strength degradation the same will apply to the strength of the fibre cements. These problems and others have been studied both theoretically and with computer simulations by Hu et al [37,38] and Hu [39]. In the following subsections only the essential features of the analytical and computer simulation studies are presented.

4.1 TENSILE STRENGTH OF SHORT FIBRE CEMENT COMPOSITES

Consider a rectangular plate specimen under uniform tension in which the fibre density ρ_f and the fibres of constant aspect ratio (L/d) are randomly distributed throughout the plate but are aligned in the direction of the applied stress. The size of the matrix cracks, which are considered as equivalent Griffith cracks lying normal to the applied stress, varies according to the Pareto distribution:

$$q(a) = (\rho_m\, m/2a_o)(a_o/ \qquad ^{(m+2)/2} \tag{27}$$

for $a > a_o$ and ρ_m is the density of matrix cracks, m is the Weibull modulus of matrix material and a_o is the reference crack size. This choice of q(a) gives the usual Weibull strength distribution equation because

$$F(\sigma) = 1 - \exp\left\{-V\int_{a(\sigma)}^{\infty} q(a)da\right\}$$

$$= 1 - \exp\left\{-V\rho_m\left[\frac{\sigma}{\sigma_o}\right]^m\right\} \tag{28}$$

where V is volume of material under tensile stress, $\sigma_o = K_{Ic}\sqrt{2/\pi a_o}$ and K_{Ic} is the matrix toughness. Crack growth in each individual crack occurs if equation (12) is satisfied, i.e. $K_e = K_a + K_r = K_{Ic}$. The R–curve effect of the matrix

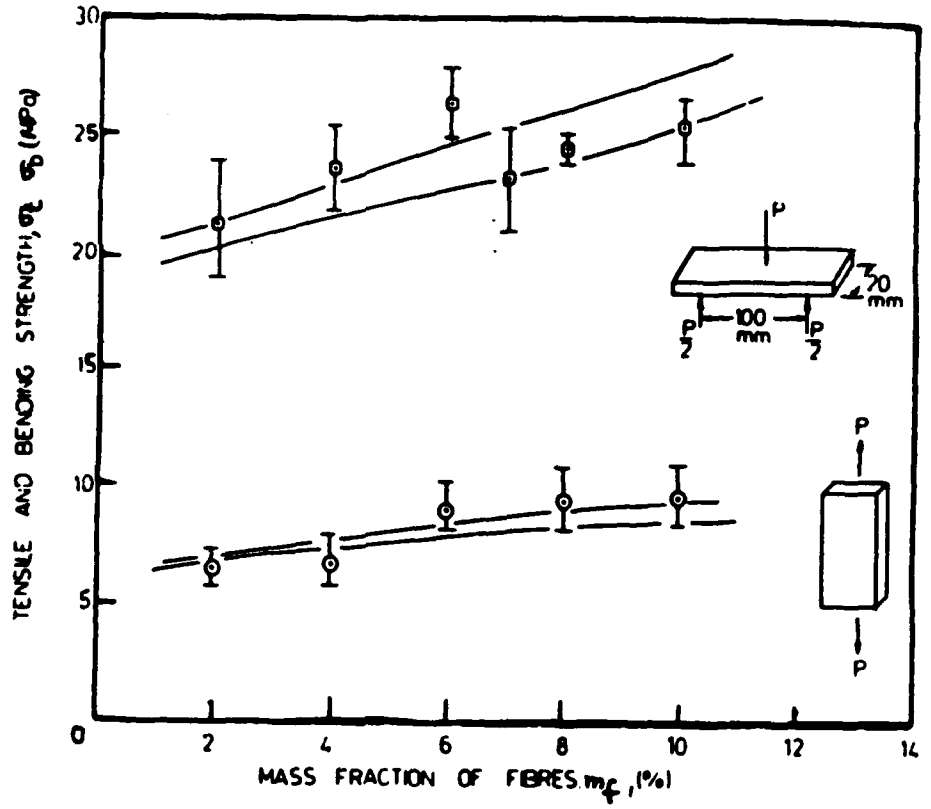

Figure 22. Tensile and bend strengths of cellulose cement mortar composites.

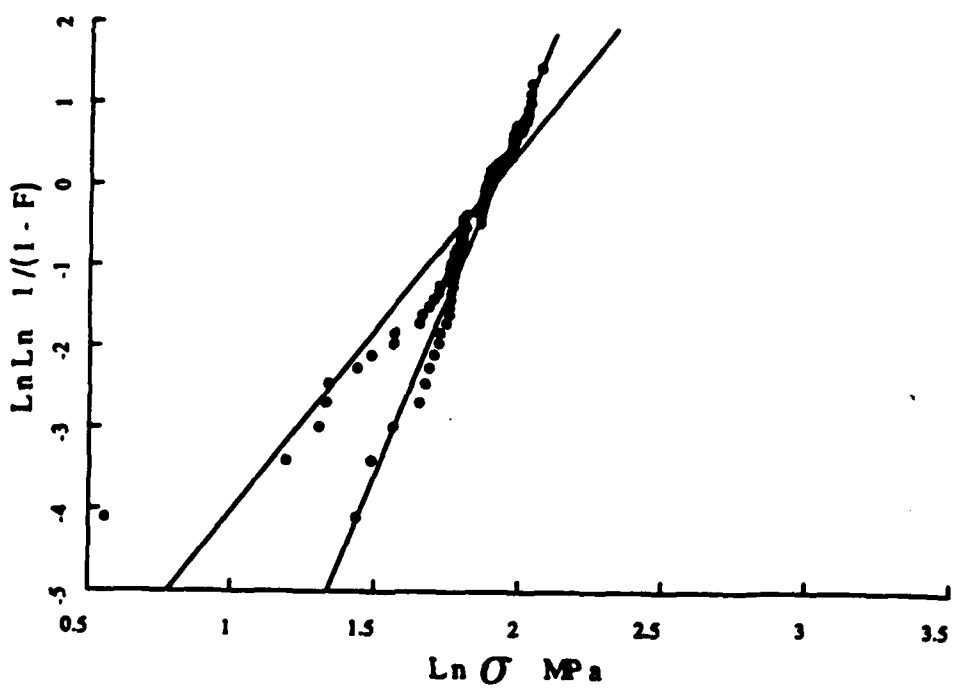

Figure 23. Weibull strength distribution of unreinforced cement matrix.

material is not considered in this crack growth criterion so that it is only necessary to evaluate K_r due to fibres bridging the individual cracks. Failure of the composite is complete when the cracks coalesce and spread across the plate width.

If the fibre density ρ_f is high, the number of fibres bridging a crack is proportional to its length and the effective bridging stress (in this 2–D model)

$$\sigma_{fb} = \pi\tau d\rho_f L^2/4d \tag{29}$$

is the same in each crack being determined by the shortest of the two embedded lengths. Equation (28) then gives the strength distribution of these fibre cement composites if σ is replaced by the effective stress $\sigma_e(=\sigma-\sigma_{fb})$, i.e.

$$F(\sigma) = 1 - \exp\left\{-V\rho_m\left[\frac{\sigma - \sigma_{fb}}{\sigma_0}\right]^m\right\}. \tag{30}$$

In this way the Weibull weakest link theory applies because there is little variation of the bridging stress across the matrix cracks. However, when the fibre density is moderate the number of fibres in defects of a given length is not constant and the bridging stress changes. Unlike the high ρ_f case there will be considerable stable crack growth (Δa) prior to fracture instability due to the stabilization effect of the bridging fibres. Hu et al [38] derived the following failure probability equations:

$$F(\sigma,\Delta a_c) = 1 - \exp\left\{-V\int_{a(\sigma)}^{\infty} Q(a,\Delta a_c)da\right\} \tag{30}$$

for Δa equals Δa_c which is the statistically averaged maximum stable crack growth, and

$$F(\sigma) = 1 - \exp\left\{-V\int_{a(\sigma)}^{\infty} q(a)\sum_{s=0}^{\bar{s}}\frac{(\rho_f La)^s}{s!}\exp(-\rho_f La)da\right\} \tag{31}$$

for first cracking. Q is defined by

$$Q(a,\Delta a) = q(a)\sum_{s=0}^{\bar{s}}\frac{(\rho_f La)^s}{s!}\exp(-\rho La)\times$$

$$\sum_{\Delta s=0}^{\bar{S}-s}\frac{(\rho_f L\Delta a)^{\Delta s}}{\Delta s!}\exp(-\rho_f L\Delta a). \tag{32}$$

$\bar{s}$ is the maximum number of fibres with which a crack of size a can propagate under a stress σ. $\bar{S}$ is the equivalent of $\bar{s}$ when a becomes (a+Δa). It should be noted that when ρ_f becomes zero the Weibull equation (28) is recovered.

To illustrate the application of equations (30) and (31) the properties of a typical steel wire reinforced mortar as shown in Table 4 are used. Equation (31) shows that for $\rho_f = 0$ a constant strength of $\sigma(F=0.5)$ invariant with Δa is obtained. This is consistent with the weakest link theory. For $\rho_f = 0.1$ and 0.2 mm^{-2} equation (30) is used to calculate $\sigma(F=0.5)$ as Δa is increased to Δa_c. These strength results are tabulated in Table 5. For $\rho_f = 0.1$ mm^{-2} the tensile strength is about 9.6 MPa after $\Delta a_c \approx 10$ mm; and for $\rho_f = 0.2$ mm^{-2} this becomes about 13.22 MPa after $\Delta a_c \approx 40$ mm. These strength values should be compared with the matrix strength of 6.71 MPa. Even the first cracking strengths of the fibre–reinforced mortars are larger than the matrix strength. The amount of stable fracture prior to reaching Δa_c is enormous particularly for $\rho_f = 0.2$ mm^{-2}.

TABLE 4. Properties of a fibre reinforced cement mortar composite

(a) Matrix properties

Fracture toughness $K_{Ic} = 0.6$ MPa$\sqrt{m}$
Reference crack size $a_o = 2$ mm
Weibull modulus m = 8
Density of cracks $\rho_m = 0.003$ mm^{-2}
Volume of specimen V = L×W = 100×100 mm^2

(b) Fibre properties

Fibre diameter d = 0.1 mm
Fibre length L = 5 mm
Bond strength $\tau = 4$ MPa
Fibre density $\rho_f = 0.1, 0.22$ mm^{-2}

TABLE 5. Tensile strength of short fibre cement mortar composite

Fibre density ρ_f(mm^{-2})	Crack growth Δa (mm)	Tensile strength (F=0.5) σ(MPa)
0.00	–	6.71
0.10	0	8.51
	1	8.86
	2	9.14
	5	9.52
	10	9.60
	20	9.58
0.20	0	9.67
	1	10.42
	10	12.29
	20	12.74
	30	13.09
	40	13.22

In parallel with the theoretical calculations above computer simulation experiments have also been carried out for these fibre composites. Defects in accordance with the Pareto distribution, equation (27), and distribution of fibres are randomly generated. Incremental stresses are applied and the effective stress intensity factor K_e (due to the applied stress and the fibre closure forces) calculated for each crack. When $K_e = K_{Ic}$ of the mortar matrix crack growth is permitted from fibre to fibre until arrest. This procedure is repeated until complete failure of the specimen. Appropriate stress intensity factors for discrete forces acting on the crack face can be obtained from Tada et al [29]. To avoid stress singularity in K due to a point force acting at a crack tip the closure forces are assumed to act halfway along the shorter half of the bridging fibre and in a symmetrical position on the other side of the crack face. Figures 23 to 25 show the strength distributions for the matrix material and the two fibre cement mortars. Both the first cracking and final failure strengths are shown. Several comments may be made about these results. In Figure 23 the Weibull failure strength distribution obtained from computer simulations is given by:

$$\ln \ln\left[\frac{1}{1-F}\right] = 8.74 \ln\sigma - 16.7 \tag{33}$$

which may be compared to that calculated from Weibull's equation (27) using the properties shown in Table 4, which is:

$$\ln \ln \left[\frac{1}{1-F}\right] = 8 \ln\sigma - 15.56. \tag{34}$$

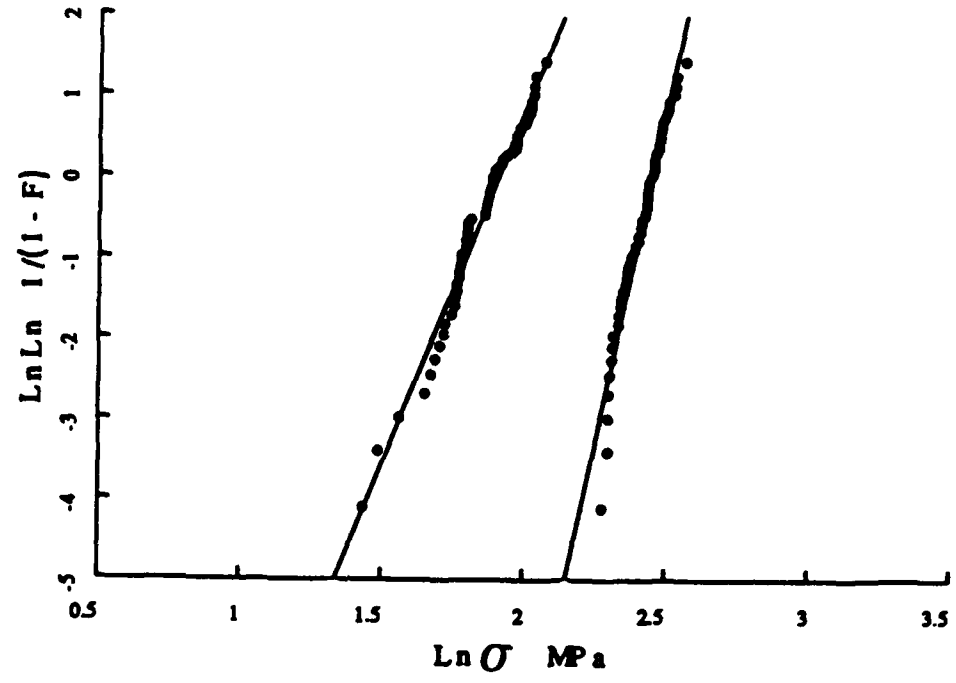

Figure 24. Weibull distribution of first-crack and final failure strengths of fibre cement composites. ρ_f = 0.1 mm^{-2}

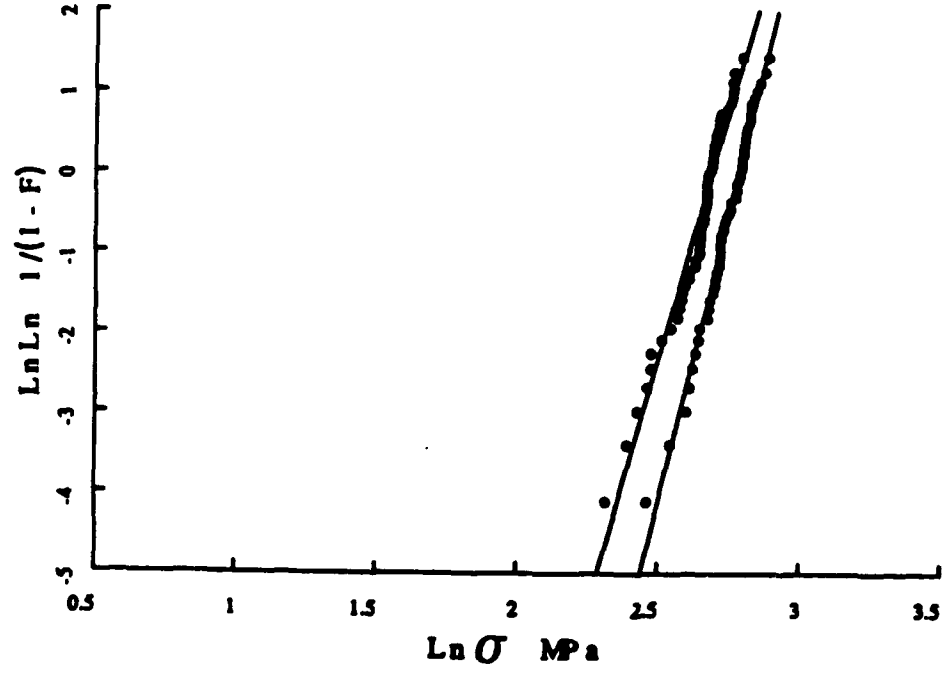

Figure 25. Weibull distribution of first crack and final failure strengths of fibre cement composites. ρ_f = 0.2 mm^{-2} .

The agreement is hence excellent. In Figures 24 and 25 there are considerable increases in the Weibull moduli for the first cracking and final failure strengths, e.g. m = 8.74 and 16.7 for ρ_f = 0.1 mm^{-2}; and m = 12.6 and 14.8 for ρ_f = 0.2 mm^{-2}. Physically, this means that there is much less scatter in strength when the mortar matrix is reinforced with short fibres and this must be caused by the R–curve mechanism in the composite materials. Also, the tensile strengths as expected are increased several times that of the unreinforced mortar matrix.

4.2 TIME–DEPENDENT TENSILE STRENGTH OF SHORT FIBRE CEMENT COMPOSITES

Many cementitious matrices suffer slow crack growth due to the effects of a hostile environment such as water or moisture [40–42]. This phenomenon is usually manifested in terms of strength degradations in constant stressing rate and cyclic loading tests as well as the time under which a sustained stress is applied. The simplest equation to describe slow crack growth in brittle materials is [43]:

$$da/dt = AK_a^p \tag{35}$$

where A and p are constants and K_a is the applied stress intensity factor at the crack tip. Hu et al [44,45] have studied the time–dependent strength behaviour of cementitious matrices by combining their statistical theory of fracture with equation (35) for constant sustained stresses, constant stressing rates and cyclic stresses. In short fibre composites the fibre bridging stresses σ_{fb} must be included in the analysis and are assumed to smear over the crack face. Hence in terms of the effective stress intensity factor K_e equation (35) is recast as:

$$da(t)/dt = AK_e^p = A\{(\sigma-\sigma_{fb})\psi\sqrt{a(t)}\}^p \tag{36}$$

where a(t) is the crack size at time t and is used to distinguish from the initial value a at t = 0. The fibre closure stress σ_{fb} at time t is

$$\sigma_{fb}(t) = \{s(o) + \rho_f L[a(t)-a]\}(\pi L d\tau)/4a(t)d \tag{37}$$

where s(o) is the initial number of bridging fibres. Thus, the time Δt required to extend a distance Δa may be obtained from equation (36), i.e.

$$\Delta t = \int_a^{a+\Delta a} \{A[(\sigma-\sigma_{fb}(t))\psi\sqrt{a(t)}]\}^{-p} da(t)\,. \tag{38}$$

Hence, for any given initial values of s and a, Δt can be obtained for a given Δa or vice versa.

Computer simulation tensile experiments similar to those described in Section 4.1 for tensile strength can be conducted in accordance with equations (37) and (38). The properties of the fibre cement composite are the same as

those given in Table 4 except the following changes: τ = 2 MPa, K_{Ic} = 0.34 MPa$\sqrt{m}$, p = 36, AK_{Ic}^{p} = 0.1359 m/s. These variations are required because of a new matrix material is now selected [40]. Initially a time interval Δt is prescribed and the crack growth Δa is calculated according to equation (36) for all cracks. If no unstable crack propagation occurs and the specimen can still sustain the applied stress, another time interval is assigned and the crack growth calculated again. This procedure is repeated until a crack runs through the specimen. The lifetime to failure t_f at the given stress is the sum of the total time intervals.

Simulations are performed for the matrix material and the fibre composite with ρ_f = 0.1 and 0.2 mm^{-2}. These results are shown in Figure 26 for a 50% failure probability and for a given ρ_f the data can be described by the equation: $\sigma t_f^{p^*}$ = constant [47]. The slope of the log σ–log t_f plot gives a measure of the effective slow crack growth exponent p* of equation (35). Thus, when ρ_f = 0, p* = 33 which compares well with the input value of p = 36. When ρ_f = 0.1 and 0.2 mm^{-2}, p* becomes 125 and 200 respectively. The observed changes in the effective slow crack growth exponent due to the R–curve effect are not uncommon and have also been reported for ceramics with residual stress effects [46,47].

Theoretical evaluation of the time–dependent strength may be obtained from an equation similar to (30), i.e.

$$F(\sigma,\Delta a_c,t_f) = 1 - \exp\left\{-V\int_{a(\sigma,t_f)}^{\infty} Q(a,\Delta a_c,t_f)da\right\}. \qquad (39)$$

$Q(a,\Delta a_c,t_f)$ is more difficult to calculate and is given in [39]. Since no additional physical insight is to be gained from equation (39) the theoretical predictions of σ–t_f–F diagrams are not given here.

5. Concluding Remarks

The fracture behaviour of fibre cementitious composites has been studied using the crack growth assistance curve concept. It is shown that the K_R–curve is not a material property but depends both on specimen geometry and size. In small NB beams the crack resistance does not tend to the limiting plateau value K_∞ as in large DCB specimens. A simple K–superposition method is proposed to model the crack resistance curve. This assumes that crack growth occurs when the effective stress intensity factors K_e at the tip of the continuous matrix crack is equal to the matrix toughness K_{Ic}. Since K_e is the sum of the applied and closure stress intensity factors, K_a and K_r, the modelling reduces to determining K_r due to the fibres bridging across the crack faces. With the

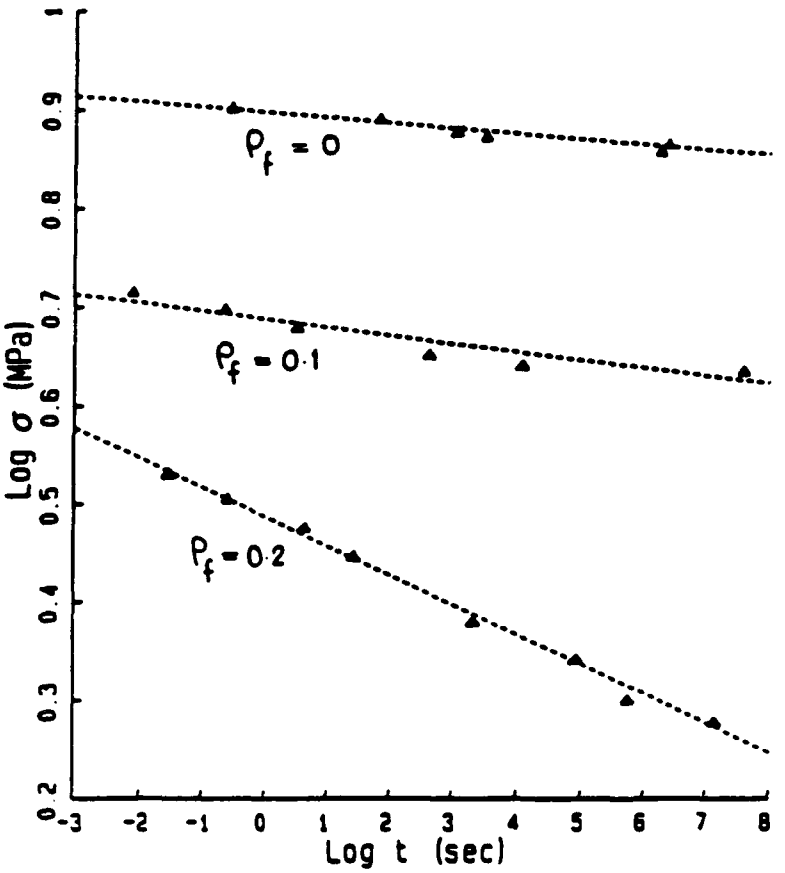

Figure 26. Failure lifetime versus applied stress for plain matrix and fibre cements with ρ_f = 0.1 and 0.2 mm^{-2}.

assumptions of a linearised closure stress (σ)–crack face separation (δ) relationship for the fibre bridges and straight crack flanks in the FBZ the crack resistance curve can be obtained by simple iteration routines. The effect of the exponent n in the stress–displacement equation (16) on the K_R curve is negligible [21]. What matters most are the fracture parameters K_{Ic}, σ_m and K_∞ (or J_∞). As shown in Section 3.4 these parameters can be determined by choosing such values that give the best fit to an experiment crack resistance curve for a given geometry and size. They can be used then to evaluate R–curves for other geometries and sizes.

Failure characterisation of fibre cement composites containing a single dominant crack with a R–curve characteristics may be effected by considering the interaction of the crack resistance curve and the applied stress intensity factor curve and determining the tangency point to evaluate the critical load and critical crack growth. Since the crack resistance curve is not unique iterations are required to solve this problem. Both theoretical and computer

simulation studies on the tensile strength behaviour of short fibre cement composites containing many cracks show that as a consequence of the R–curve characteristics of each individual crack the tensile strength is increased even though low modulus fibres such as cellulose and polyethylene are used. Also, the Weibull modulus of the fibre composite is considerably increased compared to the unreinforced matrix. The time–dependent strength behaviours of short fibre cement composites when subjected to constant applied stresses are also investigated and they show that the effective stress corrosion exponent of the slow crack growth law is increased due to the R–curve effect of the bridging fibres.

A final remark is that whilst these lecture notes deal exclusively with the crack resistance curve – its theoretical modelling and its applications in failure characterisation of cement–based fibre composites – such a concept may not be readily comprehensible to the civil or structural engineers. For practical purposes, once the parameters K_{IC}, K_{∞} and σ_0 are determined, it is desirable to calculate the load to extend a crack and hence to obtain a complete load–deflection curve or a moment–curvature diagram that are of more immediate use. Future work should be directed towards a sensitivity study of these fracture parameters on the shape of the load–deflection curves. Fracture mechanics models can also be extended to investigate the time–dependent strength behaviours of fibre cements particularly for cyclic loading situations.

Acknowledgements

The author wishes to thank the Australian Research Council for financial support. These lecture notes could not have been written without the assistance of many past and present students and colleagues. In particular the contributions in the form of original data and discussion from R. Andonian, B. Cotterell, R.M.L. Foote, X–Z. Hu and B.R. Lawn are much appreciated.

References

1. Foote, R.M.L. (1986) Crack Growth Resistance Curves in Fibre Cements, PhD Thesis, University of Sydney, Sydney.

2. Mai, Y–W. and Hakeem, M.I. (1984) 'Slow crack growth in cellulose fibre cements', J. Mater. Sci. 19, 501–508.

3. Hu, X–Z. and Wittmann, F.H. (1989) 'Fracture process zone and K_r–curve of hardened cement paste and mortar', in S.P. Shah, S.E. Swartz and B. Barr (eds.), Fracture of Concrete and Rock, Elsevier Applied Science, London, pp. 307–316.

4. Foote, R.M.L., Mai, Y–W. and Cotterell, B. (1987) 'Process zone size and slow crack growth measurements in fibre cements', in S.P. Shah and G.B. Barton (eds.), ACI Symposium on Fibre Reinforced Concrete, SP–105, Amer. Concrete Inst., Detroit, pp 55–70.

5. Ballarini, R., Shah, S.P. and Keer, L.M. (1984) 'Crack growth in cement–based composites', Engg. Fract. Mech. 20, 433–445.

6. Gao, Y–C., Mai, Y–W. and Cotterell, B. (1988) 'Fracture of fibre–reinforced composites', ZAMP 39, 550–573.

7. Petersson, P.E. (1981) 'Crack Growth Development of Fracture Zones in Plain Concrete and Similar Materials', Doctoral Dissertation, Lund Institute of Technology, published as Rept TVBM–1006 Division of Bldg. Mats., Sweden.

8. Reinhart, H. (1984) 'Fracture mechanics of an elastic softening material like concrete', Heron 29, 3–42.

9. Li, V.C. (1985) 'Fracture resistance parameters for cementitious materials and their experimental determinations', in S.P. Shah (ed.), Application of Fracture Mechanics to Cementitious Composites, Martinus Nijhoff Publishers, Dorsrecht, pp. 431–449.

10. Li, V.C. and Ward, R. (1988) 'A novel testing technique for post–peak tensile behaviour of cementitious materials', in H. Mihashi (ed.), Proc. Int. Workshop on Fracture Toughness and Fracture Energy: Test Methods for Concrete and Rock, pp. 139–156.

11. Foote, R.M.L., Mai, Y–W. and Cotterell, B. (1986) 'Crack growth resistance curves in strain–softening materials', J. Mech. Phys. Solids 34, 593–607.

12. Chuang, T–J. and Mai, Y–W. (1989) 'Flexural behaviour of strain–softening materials', Int. J. Solids & Structures 25, 1427–1443.

13. Foote, R.M.L., Cotterell, B. and Mai, Y–W. (1980) 'Crack growth resistance curves for cement composites', in D.M. Roy (ed.), Adv. Cement Matrix Coomposites, Materials Research Society, Penn., pp. 135–144.

14. Hillerborg, A., Modeer, M. and Petersson, P.E. (1976) 'Analysis of crack formation and crack growth in concrete by means of fracture mechanics and finite elements', Cement & Conrete Research 6, 773–782.

15. Hillerborg, A. (1983) 'Analysis of one single crack', in F.H. Wittmann (ed.), Fracture Mechanics of Concrete, Elsevier, Amsterdam, pp. 223–249.

16. Wecharatana, M. and Shah, S.P. (1983) 'A model for predicting fracture resistance of fibre reinforced concrete', Cement & Concrete Research 13, 819–823.

17. Visalvanich, K. and Naaman, A.E. (1983) 'Fracture model for fibre reinforced concrete', J. Amer. Concrete Inst. 80, 128–138.

18. Jeng, Y. and Shah, S.P. (1985) 'Two parameter fracture model for concrete', J. Engg. Mech. Div. ASCE III, 1227–1241.

19. Jeng, Y. and Shah, S.P. (1986) 'Crack propagation in fibre–reinforced concrete', J. Struct. Engg. Div. ASCE 112, 19–24.

20. Mobasher, B., Ouyang C. and Shah, S.P. (1990) 'A R–curve approach to predict toughening of cement–based matrices due to fibre reinforcement', to be published.

21. Cotterell, B. and Mai, Y–W. (1988) 'Modelling crack growth in fibre–reinforced cementitious materials', Mater Forum 11, 341–351.

22. Lenain, J.C. and Bunsell, A.R. (1979) 'The resistance to crack growth of asbestos cement', J. Mater. Sci. 14, 321–332.

23. Foote, R.M.L., Cotterell, B. and Mai, Y–W. (1986) 'Analytical modelling of crack growth resistance curves in DCB fibre–reinforced cement specimens', in F.H. Wittmann (ed.), Fracture Toughness and Fracture Energy of Concrete, Elsevier, Amsterdam, 535–544.

24. Cotterell, B. and Mai, Y–W. (1988) 'The effect of a fracture process zone on a model for crack growth in fibre–reinforced cementitious composites', Adv. Cement Research 1, 75–83.

25. Cotterell, B., Mai, Y–W. and Foote, R.M.L. (1988) 'Bounding solutions for crack growth resistance curve in fibre reinforced cement composites", in S.A. Paipetis and G.C. Papanicolaou (eds.), Engineering Applications of New Composites, Omega Scientific, pp. 186–196.

26. Mai, Y–W. (1988) 'Fracture resistance and fracture mechanisms of engineering materials', Mater. Forum 11, 232–267.

27. Mai, Y–W., Foote, R.M.L. and Cotterell, B. (1980) 'Size effects and scaling laws of fracture in asbestos cements', Int. J. Cement Composites 2, 23–34.

28. Foote, R.M.L. and Buchwald, V.T. (1985) 'An exact solution for the stress intensity factor for a double cantilever beam', Int. J. Fract. 29, 125–134.

29. Tada, H., Paris, P.C. and Irwin, G.R. (1973) Stress Intensity Factor Handbook, Del Research Corporation, Hellertown, PA.

30. Hu, X–Z and Wittmann, F.H. (1990) 'Fracture energy and fracture process zone', to be published in Cement & Concrete Research.

31. Hu, X–Z., Mai, Y–W. and Cotterell, B. (1990) 'Crack growth modelling in plain and fibre–reinforced cement composites', to be published in Proc 8th European Fracture Conference, Torino, Italy.

32. Mai, Y–W. 'Fracture measurements of cementitious composites', in S.P. Shah (ed.), Application of Fracture Mechanics to Cementitious Composites, Martinus Nijhoff Publishers, Dordrecht, pp. 399–429.

33. Mai, Y–W. and Cotterell, B. (1982) 'Slow crack growth and fracture instability in cement composites', Int. J. Cement Composites 4, 33–37.

34. Broek, D. (1986) Elementary Engineering Fracture Mechanics, Martinus Nijhoff Publishers, Dordrecht.

35. Cotterell, B. and Mai, Y–W. (1987) 'Crack growth resistance curve and size effect in fracture of cement paste', J. Mater. Sci. 22, 2734–2738.

36. Andonian, R., Mai, Y–W. and Cotterell, B. (1979) 'Strength and fracture properties of cellulose fibre reinforced cement composites', Int. J. Cement Composites 1, 151–158.

37. Hu, X–Z., Mai, Y–W. and Cotterell, B. (1988) 'Computer simulation of fracture behaviour of short–fibre reinforced cement', in R.N. Swamy et. al. (eds.), Proc. 3rd Int. Symp. on Developments in Fibre Reinforced Cement and Concrete, Sheffield, Vol. 2, Paper 6.4.

38. Hu, X–Z., Mai, Y–W. and Cotterell, B. (1988) 'A statistical theory of time–dependent fracture for brittle materials', Phil. Mag. 58, 229–234.

39. Hu, X–Z. (1988) Statistical Fracture of Brittle Materials, PhD Thesis, University of Sydney, Sydney.

40. Mindess, S. and Nadeau, J.S. (1977) 'Effect of loading rate on the flexural strength of cement and mortar', Bull. Am. Ceram. Soc. 56, 429–430.

41. Nadeau, J.S., Mindess, S. and Hay, J.M. (1974) 'Slow crack growth in cement paste', J. Am. Ceram. Soc. 57, 51–54.

42. Mindess, S. (1985) 'Rate of loading effects on the fracture of cementitious materials', in S.P. Shah (ed.), Application of Fracture Mechanics to Cementitious Composites, Martinus Nijhoff Publishers, Dordrecht, pp. 617–636.

43. Atkins, A.G. and Mai, Y–W. (1985) Elastic and Plastic Fracture, Ellis Horwood/John Wiley, Chichester, U.K.

44. Hu, X–Z., Mai, Y–W. and Cotterell, B. (1989) 'A statistical theory of time–dependent fracture for cementitious materials', in S.P. Shah and S.E. Swartz (eds.), Fracture of Concrete and Rock, Springer–Verlag, Berlin, pp. 37–46.

45. Hu, X–Z., Mai, Y–W. and Cotterell, B. (1989) 'A statistical theory of time–dependent fracture for cementitious materials subjected to cyclic loading', J. Mater. Sci 24, 3118–3122.

46. Cook, R.F. and Lawn, B.R. (1984) 'Controlled indentation flaws for construction of toughness and fatigue master maps' in S.W. Friedman (ed.), Methods for Assessing the Structural Reliability of Brittle Materials, ASTM STP 844, pp. 22–42.

47. Fuller, E.R., Lawn, B.R. and Cook, R.F. (1983) 'Theory of fatigue for brittle flaws originating from residual stress concentrations', J. Am. Ceram. Soc. 66, 314–321.

48. Visalvanich, K. and Naaman, A.E. (1982) 'Fracture modelling of fibre reinforced cementitious composites', Program Rept for NSF Grant ENG 77–23534, Department of Materials Engineering, University of Illinois at Chicago Circle.

49. Patterson, W.A. and Chen, H.C. (1975) 'Fracture toughness of glass fibre reinforced cement', Composites 6, 102–104.

Characterization of Interfacial Bond in FRC Materials

Dr. H. Stang
Department of Structural Engineering,
Building 118,
Technical University of Denmark,
DK-2800 Lyngby, Denmark.

Professor S.P. Shah
Director of NSF Center for Science and Technology of
Advanced Cement-Based Materials
Northwestern University, Evanston, Ill. 60208-3109, USA.

Paper to be presented at the NATO-ARW workshop on "Toughening Mechanisms in Quasi-Brittle Materials" at Northwestern University, July 16-20, 1990.

PRELIMINARY VERSION.

ABSTRACT A proper characterization of the fiber/matrix bond in fiber reinforced cementitious – FRC – composites is of great importance not only in the evaluation of the quality of a given fiber/matrix system. Different kinds of fiber/matrix debonding mechanisms are included in many models for the macroscopic mechanical behavior of FRC-materials and the applicability of such models naturally depends on the availability of experimentally determined fiber/matrix bond parameters. The present paper consist of a unified treatment of the fiber/matrix bond models proposed in the literature along with an evaluation of these models from a experimental and theoretical point of view. When dealing with perfectly bonded interfaces, basically two approaches are identified: the stress criterion and the fracture mechanical criterion approach. The results of these two approaches are examined and discussed. Finally some new research directions are proposed.

1 Introduction

Fiber Reinforced Cementitious - FRC - materials are a special type of the so-called *fiber reinforced brittle matrix composites* which again are a special type of *brittle matrix composites*. The latter group of materials consist of composites characterized by the fact that the matrix is very brittle compared to the other phases in the composite material.

Brittle matrix composite materials are designed in order to retain some of the matrix characteristics, typically the stiffness and the mechanical behavior in compression while other characteristics - typically the brittle behavior of the matrix material in tension - are modified.

Fiber reinforced brittle matrix composite materials are the most common of the brittle matrix composite materials. The fiber reinforcement modifies the brittle behavior of the matrix material by stabilizing cracks and microcracks. The crack stabilization takes place both on the so-called *meso-level*, i.e. the level where the characteristic length is in the order of big pores, cement grains, preexisting cracks, and inclusions as well as on the *macro-level*, i.e. the level where the characteristic length is that of the structure and where the cementitious material is treated as a homogeneous continuum.

Looking specifically at cementitious fiber reinforced materials a number of different mechanisms for crack stabilization on the meso- and the macro-level have been identified in the literature including:

- Crack blunting (meso-level), originating in the Cook-Gordon arrest mechanism, (Cook and Gordon, 1964)
- Crack path deviation (meso-level), presumably connected to the Cook-Gordon arrest mechanism, see e.g. Bentur et al. (1985a).
- Crack bridging (meso- and macro-level).Fibers crossing the crack introduce crack closing forces on the entire crack surface (meso-level) or part of the crack surface near the crack tip (macro-level). This effect is probably the most widely recognized crack stabilizing effect identified and modelled by numerous investigators, see e.g. Hillerborg (1980), Korczynskyj *et al.* (1981), Hannant *et al.* (1983), Selvadurai (1983), Mori and Mura (1984), Budiansky *et al.* (1986), Stang (1987), and Budiansky and Amazigo (1989).
- Crack shielding (macro-level), related to the increased formation of cracks on the meso-level. Crack shielding has been dealt with especially in ceramic systems, e.g. Evans (1984), and Hutchinson (1987) but is probably also a significant mechanism in cementitious systems.

In almost all fiber/cementitious matrix systems the bond between the fiber and the matrix is relatively week. It follows as a consequence that all the mechanisms

mentioned above include fiber/matrix debonding to a certain extend. As a further consequence, the magnitude of the fiber/matrix bond – along with the mechanical characteristics of the fibers and the matrix material – has a significant influence on the macroscopical mechanical behavior of the composite material.

Numerus models have been introduced in the literatur dealing with the macroscopical behavior of cementitious fiber reinforced composite materials or brittle matrix composites in general as function of the interfacial fiber/matrix behavior, see e.g. Aveston *et al.* (1971), Hillerborg (1980), Korczynskyj *et al.* (1981), Hannant *et al.* (1983), Budiansky *et al.* (1986), Stang (1987), and Budiansky and Amazigo (1989), and Abudi (1989).

All these models include – implicitly or explicitly – a quantitative characterization of the fiber/matrix bond. The applicability of such models is of course limited if the fiber/matrix bond parameters cannot be determined independently by experiment.

Following this line of thought, the following requirements must be imposed on the parameters used to characterize the fiber/matrix bond:

- The bond parameters should be true "material" parameters in the sense that the magnitude of the parameters should be independent of the loading conditions and the geometrical configuration of the fiber/matrix system.

- The concept behind the parameters should be realistic enough to reflect the significant features of the bond mechanisms and simple enough to allow for application in simplified approaches to complicated composite material systems.

- It should be possible to evaluate the bond parameters directly from relatively simple (pullout) experiments or indirectly from the macroscopical behavior of simple composite material systems. In both cases the magnitude of the bond parameters should be determined by comparing the experimental results with a robust analytical model.

In the following models presented in the literatur will be presented and evaluated with respect to the requirements suggested above. First the different types of interface characterization will be identified from a general point of view. Secondly different types of debonding criteria will be examined and their application to the pullout problem will be investigated. Thirdly different types of experimental investigations will be mentioned and finally conclusions will be drawn on the basis of the findings in the previous sections. Finally some suggestions for future research and investigations will be given.

2 Interface characterization

The volume surrounding the surface separating the fiber and the matrix is usually denoted *the interfacial zone.*

This zone is often idealized as a surface i.e. as a zone with no extension perpendicular to the fiber. In this zone special requirements are then imposed on stresses and displacements – requirements which are different from those imposed in the matrix and fiber volume. These requirement reflects the nature of the interfacial fiber/matrix bond.

There is experimental evidence that this type of modelling *does* represent an idealization. Typically in steel fiber reinforced cementitious composite materials an interfacial *volume* or *transition zone* rather than a *surface* has been described. See Pinchin and Tabor (1978a), Barnes *et al.* (1978), Page (1982), Bentur *et al.* (1985b), and Wei *et al.* (1986). It has been shown that each fiber in the transition zone is surrounded by matrix material which is more porous and less stiff than the bulk matrix material.

Typically the interfacial zone is divided into two parts. One where the original bonding – which can be of a physical and/or chemical nature – between the fibers and the matrix is intact. This part is here denoted as the *perfectly bonded part*, and is usually described by a set of mathematical relations describing continuity of stresses and displacements across the interface.

The other part of the interfacial zone is denoted the *debonded interface.* This zone is usually thought of as a zone created by external thermal or mechanical loading. In the debonded part of the interface a completely new set of mathematical interfacial relations are set up which reflects the ability of the fiber and the matrix volume to experience relative displacements.

2.1 The Perfectly bonded interface

From a continuum mechanics point of view – and accepting the surface idealization of the fiber/matrix interface – the perfectly bonded interface is characterized in the following way.

Using conventional index notation the stress field in the fiber is denoted σ_{ij}^f and the displacement field denoted u_i^f while the stress field and the displacement field in the matrix is denoted σ_{ij}^m and u_i^m.

The constitutive relation in the fiber and the matrix relates – along with the definition of strain – the stress and the displacement fields in each of the two volumes. However, on the perfectly bonded interface it is required that

$$\sigma_{ij}^f n_j = -\sigma_{ij}^m m_j \text{ on } I^b \tag{1}$$

along with

$$u_i^f = u_i^m \text{ on } I^b \tag{2}$$

where I^b represent all points on the perfectly bonded interfacial surface and n_i is the outward unit normal vector to the *fiber* surface while m_i is the outward unit normal vector to the *matrix* surface.

Thus, the perfectly bonded interface is modelled by requiring continuity in the surface tractions and the surface displacements on the interface.

Many analytical models are two dimensional and the analysis may not involve the complete displacement and stress tensor field, however, all models dealing with the perfectly bonded interface set up requirements which can be interpreted as parts or special cases of the equations (1) and (2).

2.2 Debonded interface

On the debonded interface the characterization is changed into a prescribed surface traction boundary condition which is applied to both the fiber surface and the matrix surface in the following way:

$$\sigma_{ij}^f n_j = f_i \text{ on } I^d \tag{3}$$

and

$$\sigma_{ij}^m m_j = -f_i \text{ on } I^d \tag{4}$$

where I^d represent all points on the debonded interfacial surface while f_i represent the prescribed surface traction.

This description obviously allows for displacement discontinuities along the debonded interface, however, it does not give any guarantee that surface overlapping will not occur.

Thus the relations (3) and (4) are only sufficient if:

$$(u_i^m - u_i^f)n_i \leq 0. \tag{5}$$

The surface traction f_i represents frictional stresses which are usually related to surface roughness. Often the frictional surface tractions are assumed to be constant, Lawrence (1972), Laws *et al.* (1973), Bartos (1981), Laws (1982), Gray (1984), Gopalaratman and Shah (1987), Palley and Stevans (1989) Stang, Li, and Shah

(1990), however, if the surface traction is connected to surface roughness it is reasonable to assume some sort of relationship between the surface traction and the displacement discontinuity across the interface:

$$f_i = f_i(u_j^m - u_j^f) \text{ on } I^d \tag{6}$$

see e.g. Wang *et al.* (1988) who used this type of modelling in a fiber pullout investigation involving loading and unloading. In spite of the appealing concepts underlying equation (6), not much work has been done in this direction.

Some models, Budiansky *et al.* (1986) and Gao (1987), Abudi (1989), and Sigl and Evans (1989) deal specifically with the case were the matrix exerts a *compressive* stress on the debonded interface due to thermal mismatch, mechanical loading, or matrix shrinkage. In that case the boundary condition on the debonded interface becomes a complicated mixed type of boundary condition requiring displacement continuity perpendicular to the interface:

$$n_i u_i^f = -m_i u_i^m \text{ on } I^d \tag{7}$$

along with stress continuity *perpendicular* to the interface:

$$n_i n_p n_q \sigma_{pq}^f = -m_i n_p n_q \sigma_{pq}^m \text{ on } I^d \tag{8}$$

However, the surface traction *in* the interface plane is a prescribed frictional surface traction. This condition can be written as:

$$\sigma_{ip}^f n_p - n_i n_p n_q \sigma_{pq}^f = f_i \text{ on } I^d \tag{9}$$

and

$$\sigma_{ip}^m m_p - m_i m_p m_q \sigma_{pq}^m = -f_i \text{ on } I^d \tag{10}$$

assuming a symmetrical stress tensor.

The magnitude of the prescribed frictional surface traction can be assumed to depended on the normal stresses on the interface according to the Coulomb frictional law:

$$\|f\| = c - \mu n_p n_q \sigma_{pq}^f \tag{11}$$

where c is a measure for the cohesion, and μ is the frictional coefficient. The direction of the frictional surface traction can be determined from the direction of the displacement discontinuity rate, as suggested by e.g. Abudi (1989). Thus, the most general type of relationship for the surface traction can be written as:

$$f_i = f_i((u_j^m - u_j^f), n_p n_q \sigma_{pq}^f) \text{ on } I^d \tag{12}$$

Again, many analytical models are two dimensional and the analysis may not involve the complete displacement and stress tensor field, however, all models dealing with the debonded interface set up equations which can be interpreted as parts of or special cases of the above equations.

2.3 Other interface models

A very attractive interface model was suggested by Needleman (Needleman, 1987) originally for use in plastically deforming solids and composite materials. However, it seems obvious to use this kind of interface description in brittle matrix composites as well.

The basic idea of the Needleman interface model – which places it somewhere between the perfectly bonded interface and the debonded interface – is that a separate constitutive relation is postulated relating interface surface traction with displacement discontinuity.

Thus, in this type of model there is no clear distinction between *bonded* and *deboned* interface since a relation of the kind (3), (4), and (6) is governing the interface at *all* times:

$$\sigma_{ij}^f n_j = f_i \text{ on } I \tag{13}$$

and

$$\sigma_{ij}^m m_j = -f_i \text{ on } I \tag{14}$$

and

$$f_i = f_i(u_j^m - u_j^f) \text{ on } I \tag{15}$$

where I means all points on the total interface.

Using a potential formulation the response is specified in terms of three parameters: a maximum tensile surface traction σ_{max} corresponding to a positive interface separation, a maximum positive interface separation δ and the total work of separation, ϕ.

The potential is chosen so that all surface traction components reaches a maximum for increasing interface separation and then drops to zero when the corresponding interface separation component exceeds δ. In case of negative interface separation (interface overlapping) compressive interface tractions build up.

This model has been used in a couple of papers for studying void formation at inclusion boundaries (Nutt and Needleman, 1987) and (Needleman and Nutt, 1989). Tvergaard (1989) modified the model in order to include Coulomb friction and used the modified model to study debonding in whisker-reinforced metals.

The model is somewhat similar to the cohesive crack models by Barenblatt (1962), and Hillerborg *et al.* (1976).

A Needleman type of model was applied to fiber reinforced cementitious matrix composites by Nammur and Naaman (1989) assuming a linear elastic perfectly plastic type of relationship between slip and shear stress at the interface. This relation was assumed to govern shear transfer at the total fiber/matrix interface at all times.

Finally, Leung and Li (1990) mentions the *possibility* of using cohesive crack models to describe the transition zone separating the debonded and perfectly bonded interface in a fiber pullout test.

3 Debonding criteria

Assume that a model for a fiber imbedded in a cementitious matrix has been established including an interface model derived from the general interface description above. If the interface is divided into a perfectly bonded and a debonded interface, a criterion is needed in order to determine weather a point on the perfectly bonded interface is about to change status and becoming a point on the debonded interface.

Basically debonding criteria can be divided into two classes: the stress based predicting onset of debonding when the interface surface traction reaches some critical value.

In general terms the stress based condition for debonding is

$$F(\sigma_{ij}^{I} n_j) = 1 \quad \text{on} \quad I^b/I^d \tag{16}$$

where I^b/I^d means the transition point separating the perfectly bonded and the debonded interface.

The other approach is the fracture mechanical approach which was applied to the fiber pulllout problem by Gurney and Hunt (1967), Outwater and Murphy (1967), Bowling and Groves (1979), Wells and Beaumont (1982), Gray (1984), Piggott *et al.* (1985), Wells and Beaumont (1985), Stang and Shah (1986a), Piggott (1987), Morrison *et al.* (1988), Gao *et al.* 1988.

Basically the fracture mechanical postulate is that given a measure a for the debonded zone A, the debonded zone will increase in size if and only if

$$G = \Gamma \frac{\partial A}{\partial a} \tag{17}$$

where Γ is denoted *the work of fracture* and where

$$G = \frac{\partial W_{ex}}{\partial a} - \frac{\partial W_e}{\partial a} - \frac{\partial W_f}{\partial a} \tag{18}$$

Here W_{ex} is work done by prescribed external forces, W_e is elastic strain energy, and W_f is dissipation in inelastic parts of the structure, e.g. work done by friction on the debonded interface.

If the interface characterization is of the Needleman type no extra criterion is needed in order to determine weather debonding takes place or not.

3.1 The fiber pullout problem

The fiber pullout where a single fiber or a number of fibers are loaded axially and pulled out of a piece of cementitious matrix material with a given geometry as been studied extensively in the literature. The aim of this modelling is to provide a model which can be used to

1. Identify the fiber/matrix bond parameters.
2. Provide a model that can be used for interpretation of a given fiber pullout experiment in order to determine the bond parameters experimentally.

Modelling of the fiber pullout problem involves modelling of the fiber/matrix interface along with a modelling of the matrix geometry and the fiber geometry.

Here, only models which use a perfectly bonded/debonded kind of interface modelling will be considered.

A number of authors, Greszczuk (1969), Lawrence (1972), Laws *et al.* (1973), Bartos (1981), Laws (1982), Gray (1984), Gopalaratman and Shah (1987), Palley and Stevans (1989) Stang, Li, and Shah (1990) have used a simple shear lag type of analysis. The advantages of a simple shear lag approach is that simple closed form analytical expression can be derived and at the same time the model is general enough to be able to identify some of the basic features of the fiber pullout problem.

A typical shear lag solution of the pullout problem based on the description (1), (2), (3), and (4) with a *constant* shear stress at the interface gives the following load/ displacement relation at the end of the fiber (see Stang Li and Shah, 1990):

$$U_f = \frac{P_f - q_f a}{E_f A \omega} \coth(\omega(L-a)) + \frac{P_f - \frac{1}{2} q_f a}{E_f A} a \tag{19}$$

Here, U_f is the displacement of the free fiber end while P_f is the pullout load at the free fiber end . The frictional force per length q_f is acting at the debonded interface which has a length of a. The stiffness and the cross sectional area of the fiber is denoted E_f and A respectively. The quantity ω is given by

$$\omega = \sqrt{\frac{k}{E_f A}} \tag{20}$$

where k is related to the shear stiffness and the geometry of the matrix material.

The total axial displacement field of the fiber $U(x)$ is given by:

$$U(x) = \frac{P_f - q_f a}{E_f A \omega} \frac{\cosh(\omega x)}{\sinh(\omega(L-a))} \qquad 0 \le x \le (L-a)$$

and

$$U(x) = \frac{P_f - q_f a}{E_f A \omega} \coth(\omega(L-a)) - \frac{P_f - q_f L}{E_f A}(L-a) - \frac{q_f}{2E_f A}(L-a)^2 + \frac{P_f - q_f L}{E_f A} x + \frac{q_f}{2E_f A} x^2 \qquad (L-a) < x \le L \tag{21}$$

where L is the total fiber length, $x = L$ is the free fiber end, $x = 0$ is the embedded fiber end, while $x = (L-a)$ correspond to the perfectly bonded/ debonded interface transition.

The fiber force as function of the position in the fiber is given by equations (21) in combined with the constitutive relation for the fiber:

$$P = E_f A U' \tag{22}$$

Solutions of the same nature but introducing the shear stress as function of the normal stress (equation (11)) and furthermore relating the normal stress on the interface to a geometrical misfit due to e.g. matrix shrinkage have been presented by Pinchin and Tabor (1978b, 1978c) and by Beaumont and Aleszka (1978).

More detailed models than the shear lag type are models based on linear elastic analysis of a fiber embedded in an infinite half space, Muki and Sternberg (1970), Sternberg and Muki (1970), Luk and Keer (1979), Phan- Thien (1980), Phan-Thien and Goh (1981), Phan-Thien *et al.* (1982). These models take advantage of the axial symmetry of the pullout problem, thus reducing the 3D problem to 2D. To some extend analytical expressions for stresses and displacements are derived, but only the case where the total interface is perfectly bonded is treated.

Applying finite element or boundary element solutions to the pullout problem allows for a more general type of analysis including modelling of the exact geometry and including more general types of interfacial models. Atkinson *et al.* (1982), Stang (1985), and Morrison *et al.* (1988) presented FEM and BEM solutions based on axial symmetric linear elastic models and used a perfectly bonded, stress free debonded interface model. Marmonier *et al.* (1988) presented an axial symmetrical FEM model but considered only a perfectly bonded interface. Steif and Hoysan (1986) considered a two dimensional FEM analysis of the pullout problem and introduced a interface relation of the kind (13), (14), and (15) governing the interface at *all* times.

3.1.1 Stress based criteria for debonding

As mentioned above the perfectly bonded, debonded interface type of models are not complete until a criterion for continued debonding is established. On the other hand models which do not include the perfectly bonded interface in the analysis, but assume some sort of slip/ stress transfer relation governing the interface at all times (e.g. Nammur and Naaman 1987) do not distinguish between *bonded* and *debonded* and all the bond parameters are already included in the model.

Consider a simple shear lag model for the pullout problem like the Stang Li and Shah (1990) model and apply a maximum shear stress criterion for continued debonding:

$$q = q_{max} \tag{23}$$

where q is the shear force per length at the interface. Then the pullout force as function of the debonded length a is given as

$$P_f = q_f a + \frac{q_{max}}{\omega} \tanh(\omega(L-a)) \tag{24}$$

The load that initiates debonding P_f^0 is given by eq. (24) for $a = 0$:

$$P_f^0 = q_{max} \frac{\tanh(\omega L)}{\omega} \tag{25}$$

Apart from a different interpretation of the factor ω similar expressions were obtained by Lawrence (1972), Laws (1982) and Bartos (1980).

The approach outlined above thus identified two parameters: the maximum shear stress at the perfectly bonded interface, q_{max} and the frictional shear stress at the debonded interface, q_f. However, it is important to note that if the shear lag approach was exchanged with a different type of analysis, e.g. a FEM analysis, then

the magnitude of the maximum shear stresses at the perfectly bonded interface would change significantly.

This is pointed out by e.g. Atkinson *et al.* (1982) and Mamonier *et al.* (1988) reporting singular stresses at the interface in the complete linear elastic solution.

Thus, applying a maximum shear stress criterion to experimental results the bond parameter q_{max} determined would depend on the type of analysis used in the analytical modelling.

3.1.2 Fracture mechanical criteria

The problem of dependency of the magnitude of the bond parameters on the analytical modelling is overcome if a fracture mechanical criterion for continued debonding is applied.

Applying e.g. the fracture mechanical criterion (17) and (18) to the shear lag analysis of Stang, Li and Shah (1990), and identifying the term W_f as the work done by the constant frictional stresses at the debonded interface then the solution for the pullout force as function of the debonded length a reads:

$$P_f = q_f a + \left(\frac{q_f}{2\omega} + \sqrt{\left(\frac{q_f}{2\omega}\right)^2 + 2E_f A p \Gamma} \right) \tanh(\omega(L-a)) \tag{26}$$

or

$$P_f = q_f a + \left(\frac{q_f}{\omega} + \sqrt{2E_f A p \Gamma} \right) \tanh(\omega(L-a)) \tag{27}$$

depending on the approximations done in order to estimate the work done by the frictional stresses. The quantity p designates the perimeter of the fiber.

The solution for the load that initiates the debonding process is readily obtained from the equations (26) and (27):

$$P_f^0 = \left(\frac{q_f}{2\omega} + \sqrt{\left(\frac{q_f}{2\omega}\right)^2 + 2E_f A p \Gamma} \right) \tanh(\omega L) \tag{28}$$

or

$$P_f^0 = \left(\frac{q_f}{\omega} + \sqrt{2E_f A p \Gamma} \right) \tanh(\omega L) \tag{29}$$

A similar solution was derived by Palley and Stevens (1989) for a different geometrical configuration, however, their solution was not presented on an explicit analytical form.

It is interesting to compare the solution obtained from the stress criterion with the two solutions obtained from the fracture mechanical criterion.

Identifying the latter approach as the "true" approach and the first approach as the "approximate" approach it is clear that the approximate parameter q_{max} contains contributions from two real parameters Γ, the work of fracture, and q_f, the interfacial friction. Since q_{max} includes a fracture mechanical parameter it is obvious that q_{max} will depend heavily on the approximations done in the modelling of the approximate stress distribution.

Furthermore, it is observed, that according to the fracture mechanical criterion approach:

$$q_f \leq q_{max} \tag{30}$$

a relation which is not included in the stress criterion approach.

4 Experimental investigations

The most commonly applied experimental setup used for the determination of bond parameters in FRC systems is the fiber pullout experiment where a single or number of fibers simultaneously are pulled out of a block of matrix material while the pullout load and displacement is measured.

Pullout experiments have been used by numerous investigators and a review paper summarizing some of the most commonly used experimental configurations has been prepared by Gray (1983).

In general it is not possible from a conventional pullout experiment to evaluate the validity of a given interfacial modelling scheme, i.e. it is not possible to deduct from a simple pullout test weather a perfect bonding/debonding approach or a more general type of modelling (13)-(15) should be used.

Bien and Stroven (Bień (1986), Bień and Stroeven (1988)) conducted some very detailed studies of a series of pullout tests using a holographic interferometry method combined with a special pullout setup. The experimental setup consisted of a 40x80x20 mmm block of concrete with an embedded steel strip modelling the pull-out of a steel fiber from a cementitious matrix. This setup allowed the displacement fields in the fiber as well as in the matrix to be determined.

Bien and Stroeven clearly identified one interfacial zone with displacement *continuity* and another interfacial zone with displacement *discontinuity*, thus supporting a perfectly bonded/debonded approach to the interface modelling problem.

Applying a perfectly bonded/debonded approach to the interfacial modelling of the fiber pullout problem and furthermore applying either a stress criterion or a fracture mechanical criterion to predict continued debonding the following should be noted:

- According to the fracture mechanical approach the stress criterion parameters

q_{max} and q_f are subjected to the requirement (30). Experimental observations seems to verify this, see Bentur and Mindess (1990), p.62. Bentur and Mindess applies a number of different stress criterion based models to different experimental pullout tests reported in the literature and find with one exception ($q_{max}/p = 9$ MPa and $q_f/p = 11.5$ MPa) that equation (30) holds.

- As pointed out by Leung and Li (1990) it is not possible from a single or a series of pullout tests with the same fiber radius to determine weather a stress criterion or a fracture mechanical criterion is the most appropriate one to use. To determine which of the two approaches to be used a series of tests with different fiber radii should be conducted to test weather the size effect predicted by the fracture mechanical approach can be observed.

- To the authors knowledge no experiments on cementitious matrix/fiber systems have been reported which directly indicate that the perfectly bonded/ debonded type of interface modelling is inadequate. However, only very few experiments allow for microscopic observation of the fiber/matrix interface during loading.

- Finally it should be noted that the displacement measurements done on conventional pullout tests include not only the displacements originating from the strains in the fiber/ matrix system but also the displacements originating from the strains in the free part of the fiber and sometimes part of the testing machine. Simple calculations show that the latter part often can one order of magnitude grater than the first part. This of cause makes a comparison with models which yield only displacements in the fiber/matrix system difficult.

5 Conclusions

From a theoretical point of view characterization of the interface in a cementitious fiber/matrix system consists of one or two steps: Characterization of the interface and if the interface characterization involves a perfectly bonded interface as well a a debonded interface determination of the criterion for continued debonding.

The fiber pullout problem has been investigated with a perfectly bonded/ debonded interface characterization and applying a stress based as well as a fracture mechanical based criterion for continued debonding.

From a theoretical point of view the stress based criterion does not predict true material parameters since the magnitude of the parameters depend heavily on the type of modelling used.

From an experimental point of view a fracture mechanical criterion for continued debonding can only be verified using a test series designed especially to bring out the size effects involved.

6 Future research

On the basis of the investigations above the following suggestions for future research are made:

- Further experimental investigations of the size effects involved in bond characterization (e.g. in connection with pullout tests) in order to verify of reject the size effect predicted by the fracture mechanical approach.
- Further development of advanced pullout test setups which are capable of determining loads and displacements near the matrix surface as well as debonded lengths at different load levels.
- Further work on the implementation in pullout models of interface modelling of the type (13)-(15), either on the whole interface or on part of the interface serving as a transition zone between the debonded and the perfectly bonded interface.

7 Acknowledgements

Dr. Henrik Stang acknowledge the support from the Research Program on Fiber Reinforced Cementitious Composites sponsored by The Danish Council for Scientific and Industrial Research and The Danish Ministry for Industry.

Professor Surendra P. Shah appreciates the support of the NSF Science and Technology Center for Advanced Cement-Based Materials.

8 References

Abudi, J. (1989) "Micromechanical Analysis of Fibrous Composites with Coulomb Frictional Slippage Between the Phases." *Mech. Mat.* 8(2 & 3), 103-115.

Aveston, J., Cooper, G. A., and Kelly, A. (1971) "Single and Multiple Fracture" in *The Properties of Fibre Composites, Conference Proceedings, National Physical Laboratory, 4 November 1971* IPC Science and Technology Press Ltd. 15-26.

Atkinson, C., Avila, J., Betz, E., and Smelser, R. E. (1982) "The Rod Pull Out Problem, Theory and Experiment." *J. Mech. Phys. Solids.* 30(3), 97-120.

Barenblatt, G. I. (1962) "The Mathematical Theory of Equilibrium Cracks in Brittle Fracture" *Adv. Appl. Mech.* 7, 56-129.

Barnes, B. D., Diamond, S., and Dolch, W. L. (1978) "The Contact Zone Between Portland Cement Paste and Glass 'Aggregate'Surfaces" *Cem. Concr. Res.* 8, 233-244.

Bartos, P. (1981) "Review Paper: Bond in Fibre Reinforced Cements and Concretes." *Int. J. Cem. Comp. Ltwt. Concr.* 3, 159-177.

Beaumont, P. W. R. and Aleszka (1978) "Polymer Concrete Dispersed with Short Steel Fibers." *J. Mater. Sci.* 13, 1749-1760.

Bentur, A., Diamond, S., and Mindess, S. (1985a) "Cracking Process in Steel Fiber Reinforced Cement Paste." *Cem. Concr. Res.* 15, 331-342.

Bentur, A., Diamond, S., and Mindess, S. (1985b) "The Microstructure of the Steel Fibre-Cement Interface" *J. Mater. Sci.* 20, 3610-3520.

Bentur, A. and Mindess, S. (1990) *"Fibre Reinforced Cementitious Composites"* Elsevier Applied Science, UK.

Bień, J. (1986) "Holographic Interferometry Study of the Steel Concrete Bond in Pull-Out Testing." *Report 1-86-9*, Delft University of Technology, Stevin Laboratory.

Bień, J. and Stroeven, P. (1988) "Holographic Interferometry Study of Debonding between Steel and Concrete." in *Engineering Applications of New Composites* (eds. S. A. Paipetis and G. C. Papanicolaou). Omega Scientific, 213-218.

Bowling, J. and Groves, G. W. (1979) "The Debonding and Pull-out of Ductile Wires from a Brittle Matrix." *J. Mater. Sci.* 14, 431-442.

Budiansky, B., Hutchinson, J. W., and Evans, A. G. (1986) "Matrix Fracture in Fiber-Reinforced Ceramics." *J. Mech. Phys. Solids* 34(2), 167-189.

Budiansky, B. and Amazigo, J. C. (1989) "Toughening by Aligned, Frictionally Constrained Fibers" *J. Mech. Phys. Solids* 37(1), 93-109.

Cook, J. and Gordon, J. E. (1964) "A Mechanism for the Control of Crack Propagation in all Brittle Systems." *Proc. Roy. Soc.* 282A, 508-520.

Evans, A. G. (1984) "Aspects of the Reliability of Ceramics" *Defect Properties and Processing of High-Technology Nonmetalic Materials* (eds. J. H. Crawford, Y. Chen, and W. A. Sibley) North-Holland, 63-80.

Gao, Y. C. (1987) "Debonding along the Interface of Composites." *Mech. Res. Com.* 14(2), 67-72.

Gao, Y., Mai, Y. W., and Cotterell, B. (1988) *J. Appl. Math. Phys. (ZAMP)* 39, 550.

Gopalaratnam, V. P. and Shah, S. P. (1987) "Tensile Failure of Steel Fiber Reinforced Mortar." *J. Eng. Mech. ASCE* 113, 635-652.

Gray, R. J. (1983) "Experimental Techniques for Measuring Fibre/Matrix Interfacial Bond Strength." *Int. J. Adhesion and Adhesives* 3, 197-202.

Gray, R. J. (1984) "Analysis of the Effect of Embedded Fibre Length on Fibre Debonding and Pull-out from an Elastic Matrix. Part 1. Review of Theories." *J. Mater. Sci.* 19, 861-870.

Greszczuk, L. B. (1969) "Theoretical Studies of the Mechanics of the Fibre-Matrix Interface in Composites." In *Interfaces in Composites.* American Society of Testing and Materials, ASTM STP 452, Philadelphia, 42-58.

Gurney, C. and Hunt (1967) *Proc. Roy. Soc. Lond.* A299, 508.

Hannant, D. J., Highes, D. C., and Kelly, A. (1983) " Toughening of Cement and Other Brittle Solids with Fibres." *Phil. Trans. R. Soc. Lond.* A310, 175-190.

Hillerborg, A. Modéer, M., and Peterson, P.-E. (1976) "Analysis of Crack Formation and Crack Growth by Means of Fracture Mechanics and Finite Elements" *Cem. Concr. Res.* 6(6), 773-781.

Hillerborg, A. (1980) "Analysis of Fracture by Means of the Fictitious Crack Model, Particularly for Fibre Reinforced Concrete." *Int. J. Cem. Comp. Ltwt. Concr.* 2(4), 177-184.

Hutchinson, J. W. (1987) "Crack Tip Shielding by Micro-Cracking in Brittle Solids." *Acta Metall.* 35(7), 1605-1619.

Korczynskyj, Y., Harris, S. J., and Morley, J. G. (1981) "The Influence of Reinforcing Fibres on The Growth of Cracks in Brittle Matrix Composites." *J. Mater. Sci* 16, 1533.

Lawrence, P. (1972) "Some Theoretical Considerations of Fibre Pull-Out from an Elastic Matrix." *J. Mater. Sci.* 7, 1-6.

Laws, V., Lawrence, P., and Nurse, R. W. (1973) "Reinforcement of Brittle Matrices by Glass Fibers" *J. Phys. D.: Appl. Phys.* 6 523-537.

Laws, V. (1982) "Micromechanical Aspects of the Fibre-Cement Bond" *Composites* 13, 145-151.

Leung, K. Y. and Li, V. C. (1990) "Strength-based and Fracture-based Approaches in the Analysis of Fiber Debonding." To be published.

Luk, V.K. and Keer, L.M. (1979) "Stress Analysis for an Elastic Half Space Containing an Axially-Loaded Rigid Cylindrical Rod." *Int. J. Solids Struct.* 15(10), 805-827.

Marmonier, M.F., Desarmot, G., Barbier, B., and Letalenet, J.M. (1988) "A Study of the Pull-out Test by a Finite Element Method." (in French) *J. Theo. Appl. Mech.* 7, 741-765.

Mori, T. and Mura, T. (1984) "An Inclusion Model for Crack Arrest in Fiber Reinforced Materials" *Mech. Mat.* 3, 193-198.

Morrison J.K., Shah S.P., and Jenq Y.-S. (1988) "Analysis of Fiber Debonding and Pullout in Composites." *J. Eng. Mech.* 114(2), 277-294.

Muki, R. and Sternberg, E. (1970) "Elastostatic Load-Transfer to a Half-Space from a Partially Embedded Axially Loaded Rod." *Int. J. Solids and Struc.* 6(1), 69-90.

Nammur, G., and Naaman A.E. (1989) "Bond Stress Model for Fiber Reinforced Concrete Based on Bond Stress-Slip Relationship." *ACI Materials Journal* 86, 45-57.

Needleman, A. (1987) "A Continuum Model for Void Nucleation by Inclusion Debonding" *J. Appl. Mech.* 54, 525-531.

Needleman, A. and Nutt, S. R. (1989) "Void Formation in Short-fiber Composites" In *Advances in Fracture Research* (eds. K. Salama *et al.*) Pergamon Press, 2211-2220.

Nutt, S. R. and Needleman, A. (1987) "Void Nucleation at Fiber Ends in Al-SiC Composites." *Scripta Metall.* 21, 705-710.

Outwater J. D. and Murphy, M. C. (1967) in *Proceedings of the 24th Annual Technical Conference of the reinforced Plastics/Composites Division.* The Society of the Plastics Industry, Washington, D.C. 11.

Page, C. L. (1982) "Microstructural Features of Interfaces in Fibre Cement Composites." *Composites* 13, 140.

Palley, I. and Stevans, D. (1989) "A Fracture Mechanics Approach to the Single Fiber Pull-out Problem as Applied to the Evaluation of the Adhesion Strength Between the Fiber and the Matrix" *J. Adh. Sci. Techn.* 3(2), 141-153.

Phan-Thien, N. (1980) "A Contribution to the Rigid Fibre Pull-Out Problem." *Fibre Science and Technology* 13, 179-186.

Phan-Thien, N. and Goh, C. J. (1981) "On the Fibre Pull-out Problem." *J. Appl. Math. Mech. (ZAMM)* 61, 89-97.

Phan-Thien, N., Pantelis, G. and Bush, M. B. (1982) "On the Elastic Fibre Pull-Out Problem: Asymptotic and Numerical Results." *J. Appl. Math. Phys. (ZAMP)* 33, 251-265.

Piggott, M. R., Chua, P. S., and Andison (1985) *Polym. Composites* 6, 242-248.

Piggott, M. R. (1987) *Comp. Sci. Techn.* 30, 295.

Pinchin, D. J. and Tabor, D. (1978a) "Interfacial Phenomena in Steel Fibre Reinforced Cement I. Structure and Strength of the Interfacial Region" *Cem. Concr. Res.* 8, 15-24.

Pinchin, D. J. and Tabor, D. (1978b) "Inelastic Behavior in Steel Wire Pull-out from Portland Cement Mortar" *J. Mater. Sci.* 13, 1261-1266.

Pinchin, D. J. and Tabor, D. (1978c) "Interfacial Contact Pressure and Frictional Stress Transfer in Steel Fibre Cement" In *Proc. RILEM Conference, Testing and Test Methods of Fibre Cement Composites.* (Ed. R. N. Swamy) The Construction Press, UK. 337-344.

Selvadurai, A. P. S. (1983) "Concentrated Body Force Loading of an Elastically Bridged Penny Shaped Flaw in a Unidirectional Fibre Reinforced Composite" *Int. J. Fracture* 21, 149-159.

Sigl, L. S. and Evans A. G. (1989) "Effects of Residual Stress and Frictional Sliding on Cracking and Pull-out in Brittle Matrix Composites" *Mech. Mat.* 8, 1-12.

Stang, H. (1985) "The Fibre Pull-Out Problem:; An Analytical Investigation." *Series R, No 204.* Department of Structural Engineering, Technical University of Denmark.

Stang, H. and Shah S. P. (1986a) "Failure of Fibre-Reinforced Composites by Pull-Out Fracture." *J. Mater. Sci.* 21, 953-957.

Stang, H. and Shah S. P. (1986b) "Fracture Mechanical Interpretation of the Fibre/Matrix Debonding Process in Cementitious Composites." In *Fracture Toughness and Fracture Energy of Concrete.* (Ed. F. H. Wittmann). Elsevier, 513-523.

Stang, H. (1987) "A Double Inclusion Model for Microcrack Arrest in Fibre Reinforced Brittle Materials" *J. Mech. Phys. Solids.* 35(3), 325-342.

Stang, H., Li, Z., and Shah, S. P. (1990) "The Pullout Problem. The Stress versus Fracture Mechanical Approach." To be published in *J. Eng. Mech. ASCE.*

Steif, P. S. and Hoysan, S. F. (1986) "On Load Transfer Between Imperfectly Bonded Constituents" *Mech. Mat.* 5, 375-382.

Sternberg, E. and Muki, R. (1970) "Load-Absorption by a Filament in a Fiber-Reinforced Material." *J. Appl. Math. Phys. (ZAMP)* 21, 553-569.

Tvergaard, V. (1989) "Effect of Fibre Debonding in a Whisker-reinforced Metal." *DCAMM* Tecnical University of Denmark, Report no. 400.

Wang, Y., Li, V. C., and Backer, S. (1988) "Modelling of Fibre Pull-out from a Cement Matrix." *Int. J. Cem. Comp. Ltwt. Concr.* 10(3), 143-149.

Wei, S., Mandel, J. A., and Said, S. (1986) "Study of the Interface Strength in Steel Fibre Reinforced Cement-based Composites." *J. Am. Concr. Inst.* 83, 597-605.

Wells J. K. and Beaumont P. W. R. (1982) *J. Mater. Sci.* 17, 397-405.

Wells J. K. and Beaumont P. W. R. (1985) *J. Mater. Sci.* 20, 1275-1284.

Session 9:

Strain Rate, Thermal, Time and Fatigue Effects

Chairs:

S. Shyam Sunder
Massachusetts Institute of Technology, U.S.A.

Zdeněk P. Bažant
Northwestern University
Evanston, U.S.A

Reporter:

Stuart Swartz
Kansas State University, U.S.A.

GROWTH OF DISCRETE CRACKS IN CONCRETE UNDER FATIGUE LOADING

DIRK A. HORDIJK
TNO-Institute for Building Materials and Structures
Lange Kleiweg 5, NL-2288 GH Rijswijk, The Netherlands

HANS W. REINHARDT
Institute for Engineering Materials
Stuttgart University
Pfaffenwaldring 4, D-7000 Stuttgart 80, West-Germany

ABSTRACT

Based on the post-peak cyclic tensile behaviour of concrete, a model for the fatigue behaviour of this material is proposed. In order to verify the model, crack opening and closure of a discrete crack under cyclic loading is studied by computer simulation. Input for the model is an appropriate description for alternating stresses in the post-peak tensile region. Results of deformation-controlled uniaxial tensile tests have been used to develop a new model, which consists of continuous functions. This constitutive model was implemented in the FE-code DIANA. It is shown by numerical analysis of a beam under four-point bending, how a crack or softening zone propagates under repeated loading. The fatigue life of this beam for cyclic loading between load-levels 0 and 95 % of its maximum load bearing capacity, is predicted. The results of this preliminary analysis are promising and show good agreement with results that can usually be found in fatigue experiments.

INTRODUCTION

Fatigue of concrete has been studied for many years now. Especially, after the oil crisis in the seventies, research activities in the Netherlands concerning this topic increased considerably. All these investigations yielded an enormous amount of data, like Wöhler curves or S-N curves and Goodman diagrams. Nevertheless, despite all these efforts, the cause and mechanism of the fatigue behaviour of concrete is yet still not fully understood.

Meanwhile, fracture mechanics had entered the research field of concrete structures. Especially the nonlinear fracture mechanics, in which a softening zone ahead of a visible crack tip is assumed, has shed new light on the behaviour of concrete structures (see for instance [1]). By using appropriate material models, the behaviour of most structures can now very well be predicted. It may be obvious that also new achievements in computational techniques and the fact that much more powerful computers became available, has contributed strongly to this progress.

A fatigue model based on nonlinear linear fracture mechanics will be presented. With the model it will be shown that a discrete crack in concrete will grow under cyclic loading. For the sake of clarity, in this paper, a discrete crack is defined to be a visible crack with a softening zone ahead of it, or just a softening zone alone. As soon as the concrete strain reaches the strain that belongs to the tensile strength, which amounts about 100 microstrain, a softening zone is created. It may be obvious that such discrete cracks exist in most concrete structures.

Input for the model is the post-peak cyclic behaviour of concrete under tensile loading. Therefore, deformation-controlled uniaxial tensile tests were performed in the Stevin Laboratory of the Delft University of Technology. Based on the results for post-peak cyclic loading, a new constitutive model was proposed [2]. This model was implemented in the DIANA finite element code and a first fatigue analysis was performed. In this paper, the material model will be presented and some model predictions will be compared with experimental results. Furthermore, the results of the preliminary numerical analysis will be presented and discussed.

APPROACH

From deformation-controlled uniaxial tensile tests on concrete, it is known that a loading cycle in the post-peak region of the σ-δ relation displays a behaviour as sketched in Fig. 1. It appears that after an unloading-reloading cycle, the curve will not return to the same point of the envelope curve where it started from, but to a point which belongs to a lower stress. This phenomenon is due to the damage which is caused in such an unloading-reloading loop. It may be clear that some mismatch of the crack surfaces will occur at

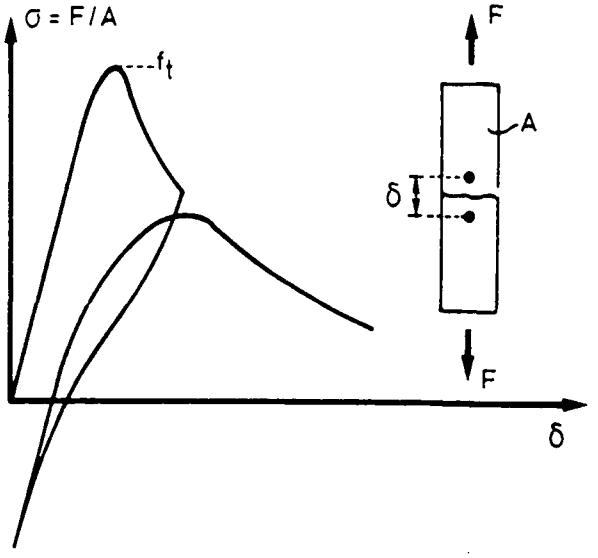

Fig. 1 Post-peak cyclic tensile behaviour of concrete.

unloading, resulting in a propagation of existing microcracks. From the experiments, it was furthermore concluded that the envelope curve is not significantly affected by the cyclic loading [2].

In Fig. 2 the stress-state in front of a visible crack after n loading cycles ($n \geq 0$) is plotted (solid line). Suppose this is part of a total structure which is loaded till a certain load F. If this structure is subjected to another unloading-reloading cycle, then we know by the post-peak tensile behaviour

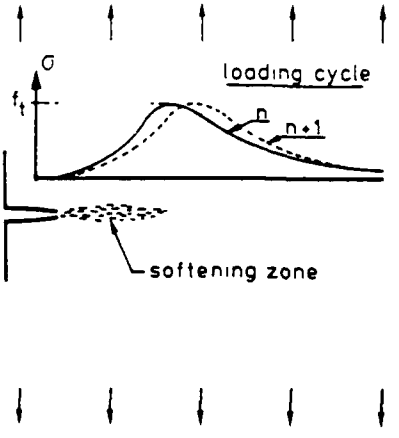

Fig. 2 Assumed stress-distribution near a crack; before and after a loading cycle.

(Fig.1) that the different area in the softening zone cannot attain the same stress as they had at the beginning of this load cycle. This means that for the same maximum external load F, an internal stress-redistribution has to take place. By the dashed line in Fig. 2, a possible stress-distribution after the load cycle is plotted. The actual new stress-distribution depends on the total structure in combination with its load application. Nevertheless, the basic idea is that the softening zone propagates under cyclic or fatigue loading. Furthermore, it can be assumed that deformations increase with the number of load cycles and that this will continue till no longer equilibrium can be found. For the load-deformation relation of the structure, it means that in that case the descending branch is reached. To illustrate this, Fig. 3 shows an assumed load-deformation relation for a certain structure under a continuous increasing deformation. The maximum load bearing capacity is equal to F_{max}. If the same structure is loaded cyclically, probably loops as sketched in Fig. 3 will be found. The loops shift a little to the right, each time a loading cycle is performed. This will proceed till, in a certain cycle, the reloading curve meets the descending branch which is the boundary for combinations of load and deformation that fulfill the requirement of equilibrium. Then failure of the structure occurs.

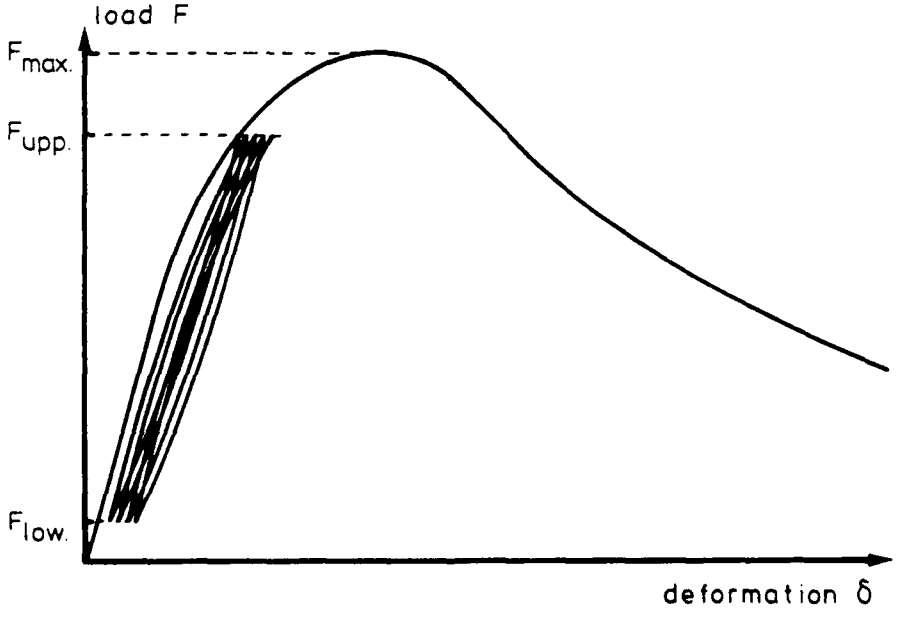

Fig. 3 Schematic representation for the load-deformation relation of a structure loaded under continuous increasing deformation or cyclically loaded between $F_{upp.}$ and $F_{low.}$.

In Fig. 3, it can be seen that for a decreasing upper load level of the cycles, the maximum available increase of deformation, which is equal to the deformation at the descending branch minus the deformation at the ascending branch for that load level, increases. This points to an increasing fatigue life for a decreasing upper load level, which tendency corresponds to that one known from S-N curves (see Fig. 4a). Nevertheless it may be clear that it can only be a minor contribution to the increase of the fatigue life N for a decreasing upper load level. This, namely, yields a S-N relation which is approximately linear, while in reality a logaritmic relation will be found (see Fig. 4a). Therefore, for a decreasing upper load-level of the cycles, the increase in deformation per cycle has to decrease considerably.

Experiments show for the increase of strain (or deformation) at the upper stress-level (or load-level) a relation as schematically plotted in Fig. 4b. It is now interesting to see if such a relation can also be found with a numerical analysis. Finally, the fact that experiments showed that there is a strong relation between the cyclic strain rate in the secondary branch of the ϵ-n relation and the number of cycles till failure [3], supports the existence of a failure criterion based on a maximum deformation as it is included in the proposed model.

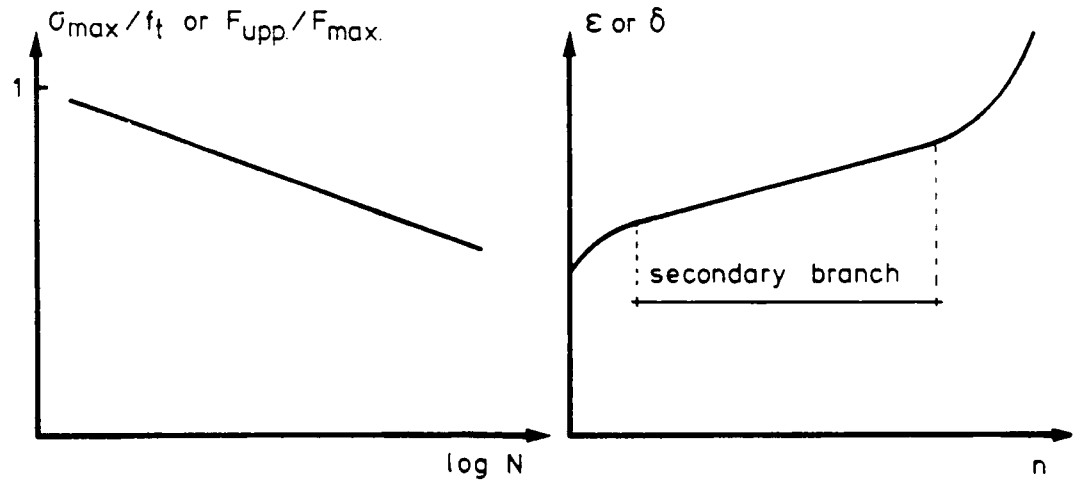

Fig. 4 Typical results for fatigue tests on plain concrete; a) S-N curve or Wöhler curve, b) cyclic creep curve (see also [3]).

The idea as presented above, is not completely new. A similar model was proposed in 1983 by Gylltoft [4]. The material model for the post-peak

behaviour he used, however, deviated strongly from that one that can be found in experiments. In his material model, he did not assume a unique envelope curve. As a result, the deformation at the descending branch did not act as the failure criterion in his model. Nevertheless, the idea of tackling the fatigue behaviour of concrete, starting from a fracture mechanics point of view was the same. Then, at the Stevin Laboratory some preliminary investigations in this direction were performed (see [5]).

CONTINUOUS-FUNCTION-MODEL

For the approach of the fatigue behaviour, as presented above, it was necessary to have an appropriate model for the tensile post-peak cyclic behaviour of concrete. It can be mentioned, however, that such a model is not only required for the fatigue modelling, but for all analyses in which unloading (and reloading) occurs. In this respect it should be noted that a structure may partially unload due to stress-redistributions, while the overall loading increases continuously.

For the post-peak cyclic tensile behaviour of concrete, a limited number of models has been presented in recent years (for a review see [2]). Out of these models, that one by Yankelevsky and Reinhardt [6] simulates appropriately the real material behaviour. It exists of multilinear loops which are constructed by means of so-called "focal-points". A draw back of this model for the fatigue approach is that the increase in crack opening after a loading cycle is independent of the lower stress-level of this loop. As a result, the influence of the lower-stress level of loading cycles on the fatigue life cannot be studied with this material model. Furthermore, for convenience of implementation in numerical programmes, it was preferred to use continuous functions instead of multilinear descriptions. For these reasons, a new model, that can easily be implemented as a mathematical subroutine in numerical programmes, was proposed. The model gives a description for the stress-crack opening relation, while crack opening is defined according to the Fictitious-Crack-Model by Hillerborg et al. [7]. It consists basically of three continuous functions (see Fig. 5) and is therefore called "Continuous-Function-Model" (CFM). Here, the basic equations will be presented. For a complete description of the model, including descriptions for inner loops (reversals within a loop), the reader is referred to [2].

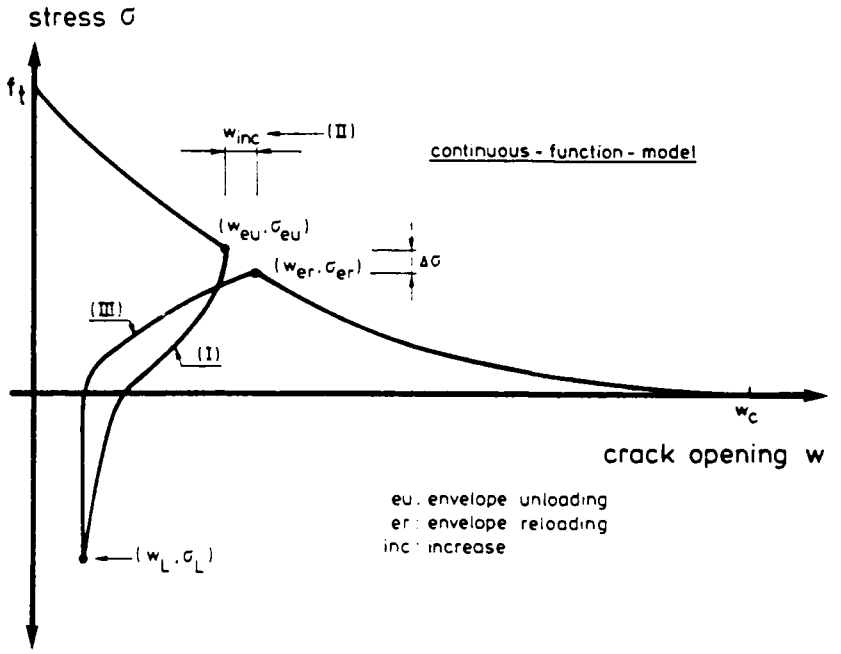

Fig. 5 Set-up for the crack cyclic behaviour model [2].

The three basic equations are, respectively, empirical expressions for the unloading curve (I), the gap in the envelope curve (II) and the reloading curve (III). It has been chosen to use only characteristic points in the σ-w relation $(f_t, w_c, w_{eu}, \sigma_{eu}, \sigma_L)$ as variables in the expressions, while w_c is defined as $5.14G_F/f_t$. The expressions that were chosen are based on a close inspection of the experimental results. The softening relation is described by the following expression:

$$\frac{\sigma}{f_t} = \{1+(c_1\frac{w}{w_c})^3\}\exp(-c_2\frac{w}{w_c}) - \frac{w}{w_c}(1+c_1^3)\exp(-c_2) \qquad (1)$$

with c_1=3, c_2=6.93 and w_c=$5.14G_F/f_t$.

Starting from point (w_{eu}, σ_{eu}) at the envelope curve, the unloading curve is determined by:

$$\frac{\sigma}{f_t} = \frac{\sigma_{eu}}{f_t} + \{\frac{1}{3(w_{eu}/w_c)+0.4}\}[0.014\{\ln(\frac{w}{w_{eu}})\}^5 - 0.57\sqrt{(1-\frac{w}{w_{eu}})}] \qquad (2)$$

When reloading starts from a lower stress level σ_L, the gap in the envelope curve is known by an expression for w_{inc}:

$$\frac{w_{inc}}{w_c} = 0.1\frac{w_{eu}}{w_c}\{\ln(1+3\frac{\sigma_{eu}-\sigma_L}{f_t})\} \qquad (3)$$

The coordinates of the returning point at the envelope curve (w_{er},σ_{er}) can now be found with

$$w_{er} = w_{eu} + w_{inc} \qquad (4)$$

and eq. 1. The reloading curve, starting from the point at the lower stress level (σ_L,w_L) up to point (w_{er},σ_{er}) at the envelope curve, is determined by:

$$\frac{\sigma}{\sigma_L} = 1 + [\frac{1}{c_3}\{\frac{(w-w_L)}{(w_{er}-w_L)}\}^{0.2c_3} + \{1-(1-\frac{(w-w_L)}{(w_{er}-w_L)})^2\}^{c_4}](\frac{c_3}{c_3+1})(\frac{\sigma_{er}}{\sigma_L} - 1) \qquad (5a)$$

with for the coefficients c_3 and c_4:

$$c_3 = 3(3\frac{f_t-\sigma_L}{f_t})^{(-1-0.5\frac{w_{eu}}{w_c})}\{1-(\frac{w_{eu}}{w_c})^{(\frac{0.71f_t}{f_t-\sigma_L})}\} \qquad (5b)$$

$$c_4 = [2(3\frac{f_t-\sigma_L}{f_t})^{-3} + 0.5]^{-1} \qquad (5c)$$

COMPARISONS BETWEEN THE MATERIAL MODEL AND EXPERIMENTAL RESULTS

Predictions by the Continuous-Function-Model have been compared with experimental results of deformation-controlled uniaxial tensile tests. Therefore a test series was performed in which post-peak loops between the envelope curve and five different lower stress-levels (σ_L is approximately 1, 0, -1, -3 and -15 MPa) were performed. For a complete description of these comparisons, the reader is referred to [2]. It could be concluded that the model represents the material behaviour very well. To illustrate this, Fig. 6 shows the results for one experiment. In this figure also the predictions by the Focal-Point-Model are plotted.

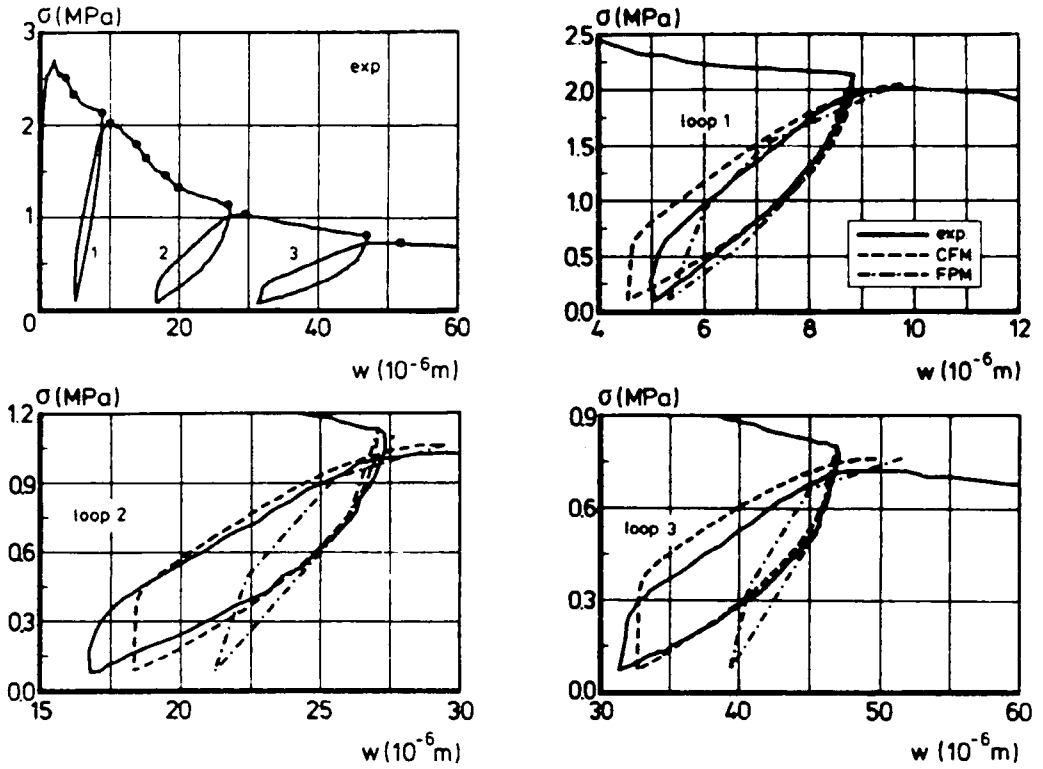

Fig. 6 Experimental stress-crack opening relation and the predictions by the Continuous-Function-Model (CFM) and the Focal-Point-Model (FPM) [2].

As stated above, the relation between the gap in the envelope curve and the lower stress-level should be modelled properly for studying the influence of the lower load-level of the loading cycles on the fatigue life of a structure. The gap in the envelope curve can be represented either by the increase in crack opening w_{inc} or the stress drop $\Delta\sigma$ (see Fig. 5). Fig. 7 shows the comparison between the model predictions and experimental results for the relative stress-drop as function of the relative crack opening. As can be seen, the experiments show the stress drop to increase for a decreasing lower stress level, which is also included in the Continuous-Function-Model. The fact that $\Delta\sigma$ is independent of σ_L in the Focal-Point-Model can also clearly be seen in this figure.

NUMERICAL ANALYSIS OF A BEAM UNDER FATIGUE LOADING

In order to verify the proposed material model, a number of four-point-bending tests on plain notched beams were performed and simulated with the finite element code DIANA. Results of these analyses will be presented in [8]. One of

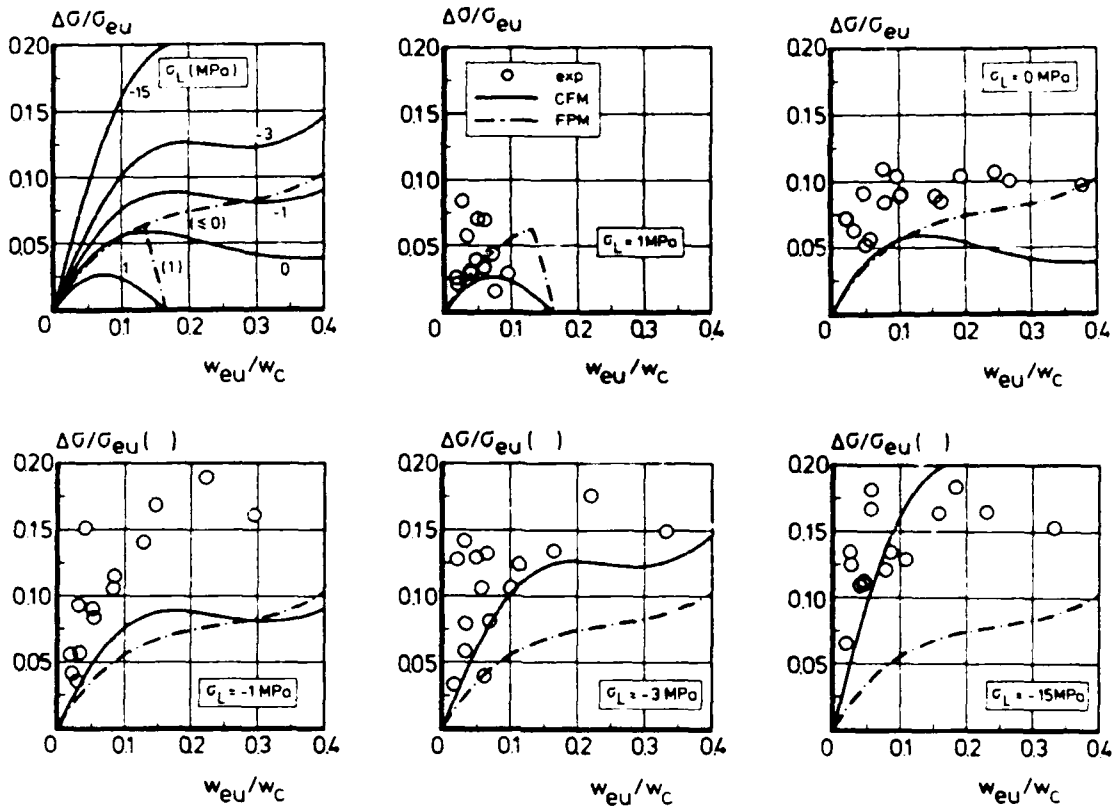

Fig. 7 Experimental results and model predictions for the stress drop $\Delta\sigma$ at the envelope curve [2].

these beams was used to perform a fatigue analysis. Specimen dimensions and loading arrangement are schematically plotted in Fig. 8a. The notch depth was 50 mm which is half of the beam height. Symmetry was used for the applied FE-idealization (see Fig. 8b). For the concrete, eight-noded and six-noded quadratic elements have been used, while six-noded interface-elements were applied to model the crack. For the interface-elements, the vertical displacements of each two nodes that were positioned besides each other were assigned to be equal. In horizontal direction, the Continuous-Function-Model becomes active as soon as the tensile strength is reached. For reasons of comparison with experiments, the vertical displacement of point A (see Fig. 8) was used for the deflection of the beam.

The elastic concrete properties were taken as: Young's modulus E=38000 MPa and Poisson's ratio ν=0.2. The softening parameters, tensile strength and fracture energy were: f_t= 3.0 MPa and G_F=125 J/m^2.

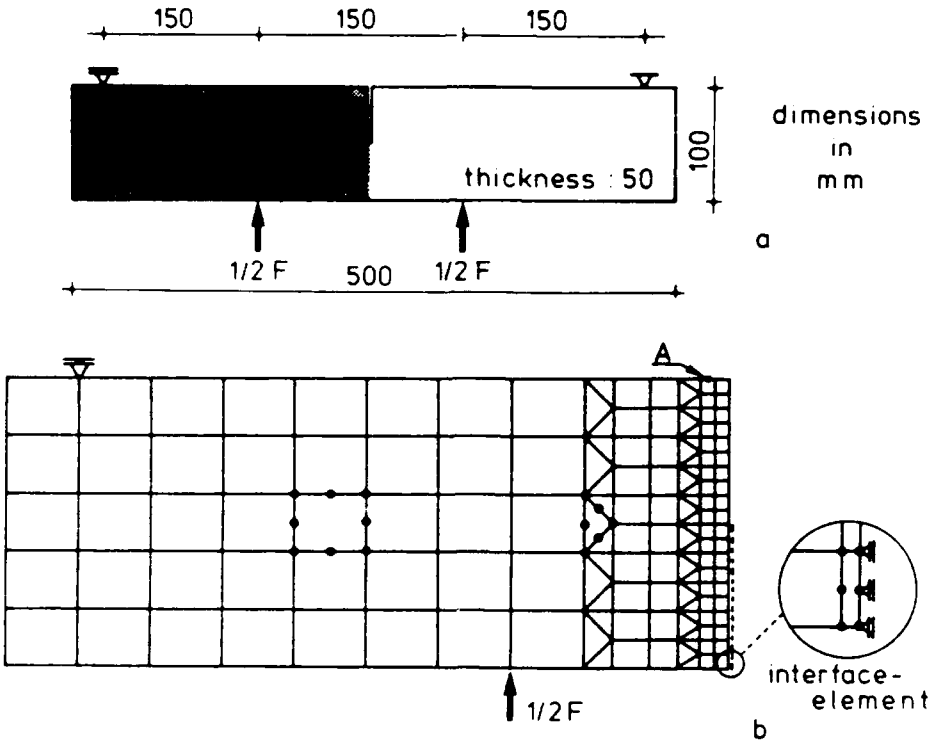

Fig. 8 Specimen dimensions of the four-point bending specimen used for the analysis (a) and applied FE-idealization (b) [8].

Load-deflection relations

First an analysis for a continuous increasing deformation was performed. In this analysis the vertical deformation at the loading point was used as control-parameter. The load-deflection relation that was obtained is plotted in Fig. 9 by the dashed line. Here, only the result up to a deflection of 0.15 mm is plotted. For the force at peak load F_{max}, a value of 1292 N was found.

For the fatigue analysis, the same input was used as for the quasi-static analysis, while in this case the load was applied by load increments (load-controlled). First, load steps up to a maximum of 95% of the peak load were performed. Subsequently, the beam was unloaded till zero load again, followed by a reloading till the same upper value of 0.95 F_{max}. For the unloading as well as for the reloading path, nine load steps of equal size were performed. This procedure was repeated till it was no longer possible to find a new equilibrium. The result of this analysis as far as the load-deflection relation

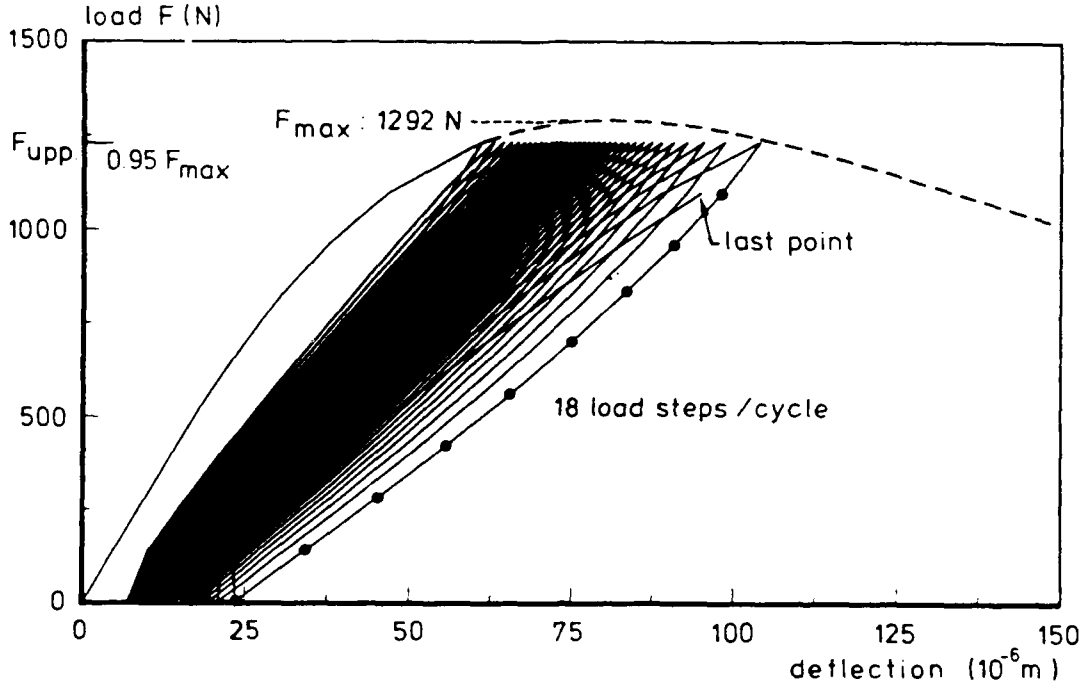

Fig. 9 Load-deflection relations predicted by the FE analyses [8].

is concerned can be seen in Fig. 9. It appeared that 35 unloading-reloading loops could be performed, while in the subsequent reloading part it was not possible to find a solution at the upper load-level. It can be assumed that for smaller loading steps the descending branch as found in the quasi-static analysis would have been reached at a load level smaller than $F_{upp.}$. Therefore, it can be concluded that the descending branch of a quasi-static analysis was an envelope curve and failure criterion for the fatigue loading.

Stress-distributions

For a number of loops, the stress-distributions at the upper ($F=F_{upp.}$) and lower ($F=0$) loading points are plotted in Fig. 10. First of all, it can be seen that the length of the softening zone increases with the number of load cycles. Furthermore, the stress-distributions at zero load show that important residual stresses are active after a preloading till 95% of the maximum load. It appears that the tensile residual stresses in the centre part of the cross-section increase with the number of cycles performed.

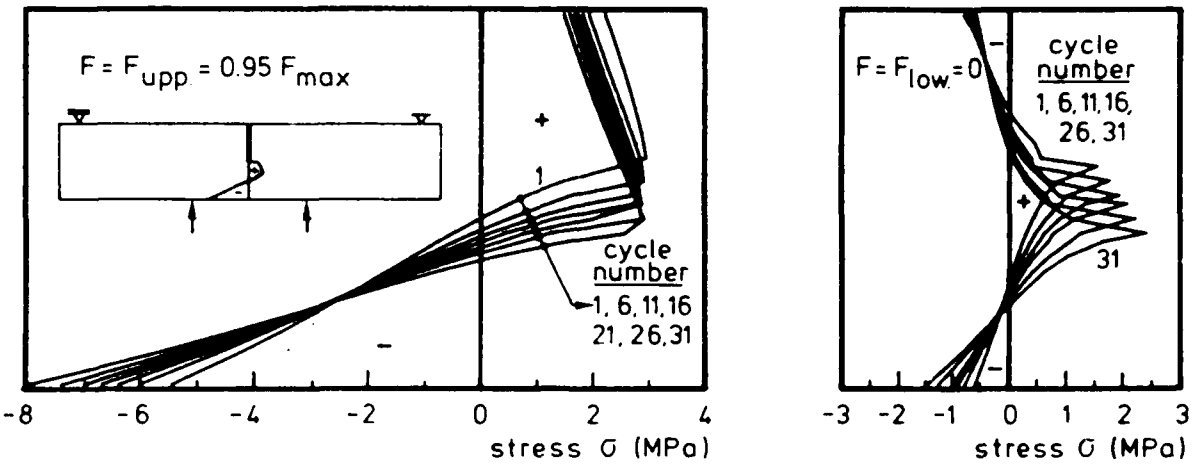

Fig. 10 Stress-distributions at the upper and lower load level for a number of loading cycles [8]

Cyclic creep curve

As already mentioned before, fatigue tests usually show a particular shape for the increase of strain or deformation at the maximum load level as function of the number of cycles performed (Fig. 4b). Normally strain is plotted as function of number of cycles, but it may be obvious that the same holds true for deformation, or, as for this analysis, deflection. Characteristic for a cyclic creep curve is that first the increase of deformation per cycle decreases with increasing n. This first branch of the curve is followed by a secondary branch where this increase is constant. Just before failure occurs, the increase of deformation per cycle increases rapidly.

The deflection as function of number of loading cycles for the performed analysis is plotted in Fig. 11. As can be seen, the shape of the curve resembles very well the cyclic creep curve as found in experiments.

DISCUSSION

In the model for the fatigue behaviour of concrete as presented, starting point is the existence of a softening zone in the structure. This means that if the material of a structure behaves elastically till $F_{upp.}$ and that nosoftening zone existed in advance, the fatigue model will not become active. First of all the authors believe that for most structures, softening zones,

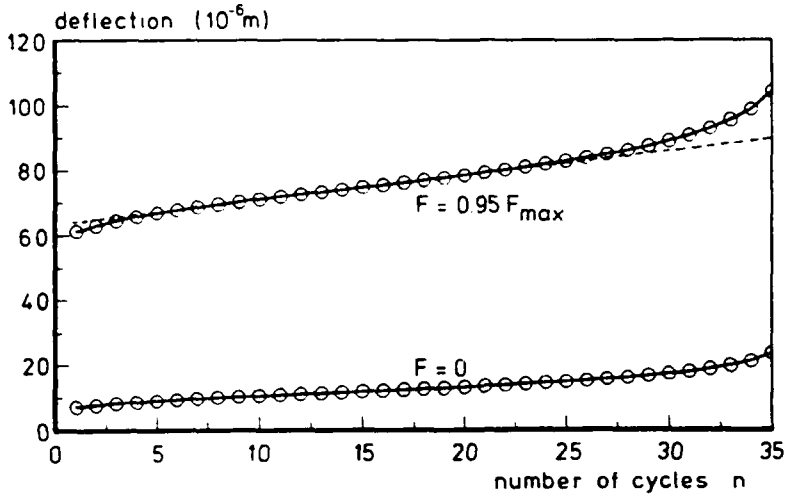

Fig. 11 Deflection as function of number of cycles [8].

for instance, due to differential drying shrinkage, exist in concrete structures. Furthermore, the authors believe that a similar model can also be used to study the fatigue behaviour of a structure without a softening zone as defined above. For that purpose, however, the structure should be modelled at a lower level. In fact, the model was presented at a macro-level. Concrete is treated as a homogeneous isotropic continuum, in which a crack will arise after the strain belonging to the tensile stress is passed. At a lower level, the concrete can be modelled as a two-phase material, in which larger aggregates are embedded in a mortar matrix. In this matrix, softening zones will exist, for instance near aggregates, due to a difference in stiffness between the matrix material and the aggregate (see Fig. 12). It may be obvious that an analysis with a structure modelled in this way demands for extremely powerful computers. Here, however, it is only intended to show that the model can be used at different levels of modelling.

Now the model can further be used to study the relation between F_{max} and N (S-N curve) or the effect of the lower load level on N. The analysis which is presented, however, is very computer-time consuming. Therefore, for such a study a more simplified modelling of the concrete outside the crack area is required. Nevertheless, even then simulating all loadings cycles (thousands or millions) will not be possible. If, however, in one way or another, the secondary branch can be reached directly, then an estimation for the number of cycles till failure can be obtained by simulating only a limited number of cycles. Yet, it looks not to be possible to do this with the presented model. Further study is this direction is required.

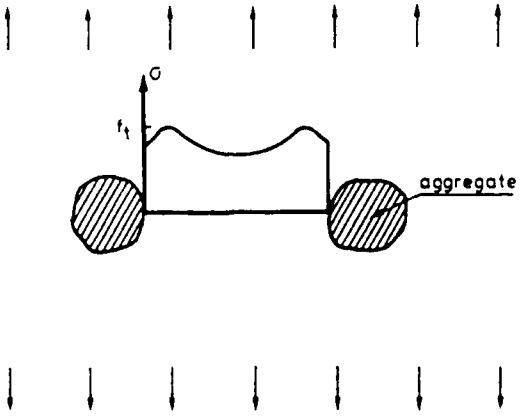

Fig. 12 Assumed stress-distribution between the aggregates in a two-phase model of concrete.

CONCLUSIONS

1 The proposed approach for the fatigue behaviour of plain concrete looks promissing.

2 The constitutive model for the stress-crack opening relation of concrete represents the actual material behaviour, including the relation between stress drop and the lower stress-level of the loading cycle, very well.

3 By numerical simulation, it has been demonstrated that the softening zone will propagate under repeated loading.

4 Failure criterion in the presented modelling is the deformation corresponding to the deformation at the descending branch obtained by a quasi-static analysis.

5 For the increase of deflection as function of number of cycles, a curve was obtained by the numerical analysis which resembles the cyclic creep curves, as usually found in fatigue experiments, very well.

ACKNOWLEDGEMENTS

The experiments were carried out at the Stevin Laboratory of the Delft University of Technology and the calculations have been carried out with the

DIANA finite element code of the TNO Institute for Building Materials and Structures (TNO-IBBC). Regarding the numerical analyses, the authors are indebted to J.G. Janssen who carefully carried out the analyses and to dr. ir. J.G. Rots for his support. This investigation was partly supported by STW (Netherlands Technology Foundation) and by CUR (Netherlands Centre for Civil Engineering, Research, Codes and Specifications).

REFERENCES

1 Elfgren, L. (Ed.), Fracture mechanics of concrete structures; From theory to applications. Report of RILEM TC 90-FMA, Chapman and Hall, 1989, 407 pp.

2 Hordijk, D.A., Doctoral Thesis, in preparation.

3 Cornelissen, H.A.W., State-of-the-art report on fatigue of plain concrete. Stevin report 5-86-3, Delft University of Technology and Chapter 3, CEB Bulletin, 188, "Fatigue of concrete structures".

4 Gylltoft, K., Fracture mechanics models for fatigue in concrete structures. Doctoral thesis, Lulea University of Technology, 1983, 210 pp.

5 Reinhardt, H.W., Cornelissen, H.A.W. and Hordijk, D.A., Tensile tests and failure analysis of concrete. ASCE J. Structural Eng., 112(11), 1986 pp 2462-2477.

6 Yankelevsky, D.Z. and Reinhardt, H.W., Uniaxial behaviour of concrete in cyclic tension. ASCE J. of Structural Eng., 115(1), 1989, pp. 166-182.

7 Hillerborg, A., Modeer, M. and Petersson, P.E., Analysis of crack formation and crack growth in concrete by means of fracture mechanics and finite elements. Cement and Concrete Res., 6, 1976, pp. 773-782.

8 Janssen, J.G., Mode I fracture of plain concrete under monotonic and cyclic loading; Implementation and evaluation of a constitutive model in DIANA. Graduate Thesis, Delft University of Technology, The Netherlands, to be published.

FRACTURE OF CONCRETE AT HIGH STRAIN-RATE

C. Allen Ross

Air Force Engineering and Services Center

Tyndall AFB, Florida 32403-6001

INTRODUCTION

Fracture of concrete at high strain rates, as well as other nonmetallic materials, show a rather similar dependence of tensile fracture strength σ_f upon the strain-rate $\dot{\epsilon}$ to the one-third power. Here the high strain term is used to mean a strain-rate above 1.0/sec. This rather interesting similarity amongst several brittle materials is shown in Figure 1. These several sets of data were experimentally determined by different researchers and collected for comparison by Grady and Lipkin [1]. An analytical approach to determining fracture strength of brittle materials either from a inherent flaw size [1] or an energy method [1-4] leads to the same result. i.e. fracture strength of brittle materials at high strain rates is a function of strain rate to the one-third power. The relationship, based on an inherent flaw size of a penny shaped crack, presented by Grady [1-3] and discussed in detail by Reinhardt [5] is given as

$$\sigma_f = 0.77\pi^{1/3}\left[\frac{EK_{IC}^2}{C_s}\right]^{1/3}\dot{\epsilon}^{1/3} \qquad (1)$$

where E is Young's Modulus, K_{IC} is the fracture toughness, C_s is the elastic shear wave velocity, σ_f is the fracture stress and $\dot{\epsilon}$ is the strain-rate. It is worth noting here that Equation (1) is limited to dynamic loadings or high strain-rates. Apparently the relationship given by Equation (1) holds regardless of the quasistatic cylinder compressive strength f'_{cs}. However, at strain-rates below approximately 1.0/sec and at quasistatic strain-rates, fracture strength is also dependent upon f'_{cs}. Semiempirical curves of various concrete mixes and strengths are presented by Reinhardt [6]. However, the slope of the fracture strength versus strain-rate for the dynamic and static regimes are not sufficient information to determine where strain-rate effects become very large.

Using data presented by Reinhardt [6] a simplified fracture strength versus strain-rate curve may be drawn as shown in Figure 2. For this curve a critical strain-rate $\dot{\epsilon}_{cr}$ may be defined, above which strain rate effects are very important because of the rather large increases in fracture strength with relatively small changes in strain-rate. The critical strain-rate is different for different types of loadings. The normalized strength

compression of tensile and compressive loading of concrete by Ross [7] shows this rather distinct difference in Figure 3. The critical strain rate for tensile fracture of a concrete (f'_{cs} = 48.3 MPa, 7000 psi for 6-inch diameter cylinder) was found to be approximately two orders of magnitude less than that for compressive fracture of the same material. Differences will also exist between flexure and shear, however very little data are available for these comparison but John and Shah [23] show some estimates for various loadings.

Following the same assumptions and development for Equation (1) an expression for concrete fragment size α_f as a function of strain-rate is given by Reinhardt [6] as

$$\alpha_f = 0.147\pi^{1/3}\left[\frac{C_s K_{IC}}{E}\right]^{2/3}\dot{\epsilon}^{-2/3} \qquad (2)$$

Again, the expression of Equation (2) is for high strain-rates. For compressive fracture of a split-Hopkinson pressure bar (SHPB) concrete specimens, the fragment distribution of a sieve analysis by Ross and Kuennen [8] showed considerable difference between a low strain-rate test of 25/sec and high strain rate tests of 100/sec and 200/sec. The size distribution for the SHPB tests is shown in Figure 4. Equation (2), based on an inherent flaw size distribution gives a good estimate of the average experimentally determined high-strain-rate fragment size of Figure 4, but underpredicts the fragment size of the 25/sec test. Fragment size based on an energy criterion equation, similar to Equation 1 predicted much higher post-test average fragments for the SHPB tests of Reference [8].

EXPERIMENTS

Initial studies and experiments of dynamic concrete fracture and increases in compression strength were conducted using impact hammers or dropped weights against short concrete specimens and long bars [9-15]. These early studies (1950-1980) may be classified as dynamic tests as opposed to quasistatic tests, but were mainly conducted in the low to intermediate strain-rates range of 10^{-3}/sec up to 10^{-1}/sec. The disadvantage of dropped weights is they require large drop heights to achieve impact velocities necessary for high strain-rates. Probably the first use of the higher strain-rates generated by a SHPB to test concrete is reported by Sierakowski at al [16], as early as 1977. Gas gun driven or torsional spring loaded SHPB test devices offer an advantage of high velocity impact and high strain rates for compression strength test and fracture of concrete. Several large diameter SHPB devices have been built for compression testing of concrete. A 76-mm (3.0 inch) diameter SHPB is located at the University of Florida and is described in detail by Malvern and Ross [17]. A 64-mm (2.5 inch) diameter SHPB,

described by Felice [18], is located at Los Alamos National Laboratory. A dual mode compression-tension 51-mm (2.0 inch) diameter SHPB is located at the Air Force Engineering and Services Center, Tyndall AFB, FL. and details of this device are given by Ross [7].

Experiments on compression of cement paste at strain-rates up to 0.3/sec were conducted by Harsh et al [45]. The effect of strain-rate on cement paste and mortar show a nonlinear increase up to the maximum strain-rate of 0.3.sec. Harsh also reports increases in Poisson's ratio with strain-rate and decreases in strain capacity with increases in water-cement ratio. The presence of pore fluid and it's movement in saturated cement is shown by Harsh to contribute to strain-rate sensitivity. The higher the porosity the higher the strain-rate sensitivity.

Fracture of concrete in tension at strain-rates above 1.0/sec, by gas gun impact of steel projectiles on concrete rods was reported by Mellinger and Birkimer [19] in 1966. These data showed very large increases in concrete tensile strength; much larger than the 100% and 150% increases in compressive strength that had been reported earlier. Similar experiments were conducted by Griner [20] but the large increases in concrete tensile strength were not evident in the Griner data. A falling weight driven tensile SHPB was developed at Delft University, Netherlands and is described in some detail by Komeling et al [21]. Tensile fracture of uniform cross section concrete bars was accomplished in References [19-20] whereas short notched specimens were fractured in References [7,21] by cementing the specimens to the SHPB. The tensile pulse in the concrete bar specimens [19-20] was generated by reflection of a compressive pulse from the concrete bar free end, as opposed to the direct tension SHPB loading devices of [7 and 21]. High strain-rate tensile fracture of splitting-tensile specimens is also reported by Ross [7] and this data along with other dynamic tensile strength data are shown in Figure 3. A rather novel technique developed by Gran [22] uses axial release waves from an initial compression of a cylindrical concrete rod. The superposition of the two relief waves at the rod midlength place the rod in tension and the rod fails in tension. Tensile strengths found by Gran are not nearly as high as those reported by Millinger and Birkimir [19] and Ross[7].

Experiments specifically designed to study effect of high strain-rate on fracture mechanics parameters are reported by John and Shah [23]. For their experiments crack mouth opening displacement (CMOD) and modulus of rupture (MOR) were measured in a three point bending test specimen mounted in a modified instrumented Charpy impact test device. The highest strain-rate obtained in these tests was 0.4/sec. Using linear elastic fracture mechanics (LEFM) the simplified fracture toughness K_{IC}^{s} and the crack tip opening displacement CTOD can be determined

from the experimentally determined CMOD and MOR of Reference [23]. In similar experiments John and Shah [24] measured crack velocity of concrete at high strain-rates using foil Krak gages, developed by the TTI Division, Hartrun Corp., St. Augustine, FL. These same gages were used by Ross et al [25] to measure crack velocity of splitting tensile concrete specimens in a SHPB.

Bentur et al [26] examined the effect of concrete strength on fracture energy and energy absorption capacity of impact tested flexural beams made of reinforced concrete. Discussion on the operation of this device and analysis of experiment al data is given by Banthia et al [27]. Other dynamic modulus of rupture and flexure tests are reported by Gopalaratnam et al [28-29], as well as the modified Charpy impact data of Sauris and Shah [30], and additional flexural impact experiments by Mindess and Nadeau [31].

It appears that there are no laboratory experiments designed specifically for gathering dynamic shear strength. This was pointed out by Sierakowski [32] in a paper written for this NATO Advanced Research Workshop of 1984 and there still appears to be no specific research in this area. Field tests of scaled reinforced concrete slabs failing by direct shear at the edges are reported by Slawson and Kiger [33]. For these field tests direct shear occurs for very short rise time blast loads and occur at strain-rates of 10/sec. For rise times which are longer, the response and subsequent failure of the slabs is that of flexure.

Laboratory SHPB compression tests of concrete with confining pressure is reported by Malvern and Jenkins [34]. These tests were performed on concrete cylinders of unconfined static f'_{cs} = 48.3 MPa using confining pressures of approximately 3.3 to 10.3 MPa (485-15000 psi). Dynamic tensile tests on concrete with confining pressures are reported by Gran et al [22,35].

DISCUSSION

Fracture of concrete at high strain-rates is significantly different than that found at the lower rates. Figure 5 shows a schematic of the initial compressive fracture of concrete taken from a high speed (10,000 f/sec) film for research reported in Reference [7]. For Figure 5a the strain-rate is approximately 25/sec and the strain-rate of Figure 5b is approximately 130/sec. For both strain-rates the fracture appears as wavy cracks running almost parallel to the longitudinal axis of the specimen. For the lower rate of Figure 5a the number of cracks are less than that of the higher rate of Figure 5b. In addition there appears to be more transverse cracks in Figure 5b which gives smaller fragments which is in agreement with the fragment distribution of similar tests shown in Figure 4. These rather longitudinal

surface cracks appear to be similar to the internal crack patterns, Figure 6, found by Malvern and Jenkins [34] when testing concrete in a SHPB with a limiting strain collar which slightly shorter than the specimen. The crack patterns of Reference [34] were obtained by a special crack enhancement process after sectioning of the cylindrical specimen. These internal cracks of Reference [34] and the surface cracks of Figure 5 are probably the result of tensile straining caused by Poisson effect and tensile stress cracking due to boundary conditions at the interface of the specimen and SHPB. Experimental evidence by Malvern and Ross [17], using circumferential strain gages on a dynamically compressed concrete cylinder in a SHPB, shows that a compressive stress greater than the static compressive strength is evident prior to failure in the circumferential direction. Also, for Reference [17] the ratio of the circumferential strain to the longitudinal strain compared to Poisson's ratio for the concrete material. It is interesting to note here that the onset of high strain-rate effect $\dot{\varepsilon}_{cr}$ for tensile fracture is much less than that of compressive fracture, see Figure 3.

The effect of a static confining pressure on the compressive fracture strength is to increase the compressive strength for a given strain-rate. The combined effect of strain-rate and static confining pressure of 19 confined and 8 unconfined SHPB tests is given in Reference [34] as

$$\sigma_f = A + B\,\dot{\varepsilon}_f + Cp_f$$
$$A = 64.4 \text{ MPa}$$
$$B = 0.388 \text{ MPa's}$$
$$C = 7.59 \qquad (3)$$

where σ_f is the compressive failure stress, $\dot{\varepsilon}_f$ is the strain-rate at failure and p_f is the confining pressure at failure. The expression, Equation 3, was obtained for an unconfined concrete strength of 48 MPa (7,000 psi) at strain-rates of approximately 50/sec to 150/sec and confining pressures of 3.3 MPa (485 psi) to 10.3 MPa (1500 psi). Extrapolation outside these ranges is not recommended. For unconfined tests of References (7,8,17,34) the stress-strain curve rises to a peak and decays very quickly to zero with no elastic recovery and the specimen is reduced to rubble. For the confined tests, the stress-strain curve rises to a plateau and remains relatively constant (resembling a ductile curve) throughout the loading pulse then falls to zero with an apparent elastic unloading. The effect of confinement in the SHPB tests on specimen fracture is to produce an almost intact specimen with one major crack running diagonally across the specimen from one end to the other as opposed to the highly fracture rubble of the unconfined SHPB tests.

Tensile fracture of direct tension SHPB specimen by Ross [7] showed one or more rather clean fractures across the test

specimen. Multiple fractures occur as strain-rate is increased. The experimental data indicates that fracture occurs during the first passage of the tensile stress wave across the specimen. The tensile fracture surface of the 48 MPa compressive strength concrete showed both aggregate pull out and fracture in an approximate one to one proportion. Splitting-tensile SHPB tests[7], of the 48 MPa concrete gave slightly higher tensile strength than that of the direct tension tests. However both the splitting-tensile tests and direct tensions tests show similar strain-rate effects. Large increases in tensile strength show up at lower strain-rates than the compressive data (see Figure 3).

Both photographic and Krak gage data were obtained for crack propagation in the splitting-tensile tests of Reference [7]. Figure 7 shows the crack pattern and the stress associated with these patterns for a SHPB splitting-tensile test. The Figure 7 crack pattern was copied from a Polaroid film taken using an image converter camera running at an equivalent rate of 2000,000 f/sec. The initial crack of Figure 7 appears to start just to the left of the center of the specimen on the side of the incident pulse at a time equivalent to the twice the transit time of the specimen. The pulse then travels in both directions and the specimen fails into two major pieces. Crack velocity measurements for these splitting tension specimens at strain-rates of 1/sec to 10/sec were found to be of 10 to 50% of the 3620 m/sec acoustic velocity of the specimen.

Dynamic analysis, using an ADINA finite element code, of the splitting-tensile cylinder by Tedesco et al [36] shows a build-up of stress distribution very similar to the static stress distribution. A computer generated crack pattern using the specimen loadings of Reference [7] is shown in Figure 8. The bifurcation of the crack shown in Figure 8 was also observed in the experiment. Bifurcation of the crack occurs at the higher strain-rates and appears to be a result of the biaxial compression-tension that occurs off the centerline of the specimen. The failure surface model used in Reference [36] degrades the tensile strength linearly with the presence a compressive principal stress. It is interesting how well the fracture pattern generated using a structural analysis code resembles the fracture pattern observed in the experiments. The differences in times of events of Figures 7 and 8 is due to the difference in crack velocities in the analysis and experiment. In the analysis of Reference 36 the acoustic velocity of a linear elastic material is used in the calculations and in the experiment the crack velocity may be only 10% of the acoustic velocity.

Linear elastic fracture mechanics (LEMF) parameters have been used to predict the effects of strain-rate on the tensile strength and modulus of rupture. John and Shah [23] measured

crack mouth opening displacements (COMD) and used LEMF relationships to predict crack tip opening displacement, (DTOD) and fracture toughness for Mode I fracture, K_{IC}. These values and Young's modulus E may then be used to predict uniaxial tensile strength and splitting-tensile strength. For the higher strain-rate regimes the DTOD is assumed to be the only strain-rate dependent parameter in their calculation. The ratio of dynamic CTOD and quasistatic CTOD of [23] is based on an exponential function using the ratio of dynamic to quasistatic strain-rates. The elastic modulus E and the fracture toughness K_{IC} are assumed to be strain-rate independent but vary with concrete compressive strength f'_{cs}. Strain-rate independence of compressive Young's modulus has been observed in Reference [28] and in experiments of Reference [7]. The compressive module obtained in SHPB work such as [7] is not usually reported as the initial linear portion of the stress-strain occurs during the rise time of the loading pulse, before uniform stress along the specimen length is obtained. Use of the quasistatic fracture toughness in [23] was justified on the basis of the very low crack velocity observed at the higher strain-rates.

The two parameter fracture model of [28] appears to predict the low strain-rate tensile strength data of Cowell [37], Takeda et al [38], Kormeling et al [21] and data presented by Oh [39]. However, it underpredicts experimental data at strain-rates above 1/sec [4,7]. This underprediction of the tensile fracture strength of concrete at high strain-rates, for a predictor based on slightly lower strain-rate data, may be attributed to the steep rise in strain-rate sensitivity on tensile strength shown by Reinhardt [6].

The two parameter fracture model of John and Shah [23] was also used to predict modulus of rupture (MOR) by using CMOD data taken from fracture of three point bend specimens in a modified Charpy device. Again the model agrees well with MOR data taken at strain-rates below 1/sec, but would not be expected to predict MOR for the higher strain-rates.

Probably the highest dynamic tensile strength data reported is by McVay [40]. Dynamic tensile strength increases of over 700% at strain-rates of 100/sec were calculated from spall of a concrete slab subjected to blast from a conventional weapon. These stresses were obtained by back calculating the failure stress from the measured spall plane and the stress wave shape measured at the back of the slab. These data are shown in Figure 3 and fall in the high strain regime predicted by Equation (1).

The observations and data for both low and high strain-rates point out the importance of knowing the fracture strength and fracture processes for the entire strain-rate region of the loading environment. This is especially true for the tensile dominated fractures of uniaxial tension, transverse tensile

fracture of direct compression, splitting-tensile fracture and the tensile fracture of flexure. Models predicting tensile fracture must include the nonlinear portion of the low strain-rate regime and the rather linear and steep slope of the higher strain-rates.

A model presented by Weerheijm and Reinhardt [41], based on an array of penny shaped cracks agrees very well with the concrete tensile date shown in Figure 3. This model, shown as solid lines of Figure 3 predict both the lower strain-rate concrete strength as well as changing slope to predict the concrete strength at the higher strain-rates. This model takes into account the strain-rate dependence of crack speed and fracture energy as well as the effect of compressive concrete strength on tensile strength.

The micromechanical modelling of concrete is based mainly on some distribution of microcracks, microdefects or weak planes. Chen [42] uses a Weibull statistical crack per unit volume distribution which is activated by bulk or volumetric strain based on the mean stress and bulk modulus. The crack distribution is defined in terms of constants taken from experimentally determined fracture stress versus strain-rate data or estimated from Equation (1). In addition the average crack dimension used by Chen [42] is based on a fragment dimension similar to Equation 2. The interaction of the cracks in Chen's model is treated as an internal state variable which represents the accumulation of damage in the material. This damage is assumed to degrade the material stiffness based on equations by Budinasky and O'Connell [43] for an array of penny shape cracks in an isotropic medium. The point here is that modelling of fracture of concrete at strain-rate, whether it be a complicated code such as [42], a single formula for dynamic tensile strength as given by Oh [39] or empirical equations such as Soroushian et al [48], are all based on some form of experimental data.

SUMMARY

Based on experimental observations, fracture strengths of concrete for most all types of loading are dominated by tensile fractures. At the quasistatic and low strain-rates the fracture strength versus strain-rates is nonlinear up to some critical strain-rate. Beyond this critical strain-rate the strength increases rather drastically as a function of the strain-rate to the one-third power. It appears that the critical strain-rate occurs at different strain-rates for the different loadings. It is not that any type of loading is more strain-rate sensitive than another, but that the high strain-rate sensitivity occurs at different strain-rates for different types of loading.

All the modelling of concrete fracture at high strain-rates

at some point in the analysis requires time dependent fracture data. Many times this data is not available and care must be exercised in extrapolating beyond the strain-rate range in which the experimental data was taken.

For the tensile dominated concrete fractures, Mode I fracture appears to occur in the majority of failures. In the low strain-rate compression loading the inherent flaws at the higher stress concentrations grow and relieve the stresses at other sites. Under the low loading rates these activated cracks have time to grow into the weakest areas of the concrete matrix and aggregate. The result is a post-test specimen with very few cracks and large broken pieces. As the compression load rate increases many more of the inherent flaws are activated and forced to grow into the high strength areas of the mortar and aggregates. This results in increased strength, a larger number of much shorter cracks and smaller fragments. At much higher rates the fragments are much smaller and the concrete is reduced to rubble. In the case of tension/compression biaxial or triaxial stress states the tensile failure stress is reduced by the presence of the compressive stress. Hydrostatic confining pressure on concrete inhibit crack growth and fracture at high strain-rates. Continued research into high strain-rate compression of concrete is needed to characterize the crack area and crack pattern for both unconfined and confined loadings.

High strain-rate uniaxial tension specimens usually fail by a single crack plane across the specimen. At high strain-rates multiple cracks form. Experimental direct tension fracture strength at strain-rates higher than 1.0/sec are needed to completely define this area of strain-rate. Data on the effects of confining pressure on tensile strength at higher strain-rates are needed to better understand fracture processes of the compression loading.

Strain-rate effects data on fracture mechanics parameters are scarce and further experimentation is needed. Fracture toughness is a vary fundamental part of the prediction of fracture strength of concrete. Some fundamental high strain-rate experiments in Mode I and Mixed Mode fracture, with and without confining pressures, are needed to determine the extent of strain-rate effects on fracture toughness.

REFERENCES

1. Grady, E. E. and Lipkin, J., "Criteria for Impulsive Rock Fracture", Geophysical Research Letters, Vol. 7, No. 4, April 1980, pp 255-58.

2. Grady, D. E., "The Mechanics of Fracture Under High-Rate Stress Loading", Sandia National Laboratories Report SAND-82-1148C, 1983.

3. Grady, D. E. and Lipkin J., "Mechanisms of Dynamic Fragmentation: Factors Governing Fragment Size", Sandia National Laboratories Report SAND 84-2304C, 1984.

4. Birkimer, D. L., "A Possible Fracture Criterion for the Dynamic Tensile Strength of Rock", Procedures 12th Symposium on Rock Mechanics, G. B. Clark, ed., 573, 1971.

5. Reinhardt, H. W., "Tensile Fracture of Concrete at High Rates of Loading", Application of Fracture Mechanics to Cementation Composites (NATO-ARW), S. P. Shah, ed., 1984 pp 559-90.

6. Reinhardt, H. W. "Dynamic Loading", Fracture Mechanics of Concrete Structures, L. Elfgren, ed. Champman and Hall, Ltd. London, 1989 pp 188-90.

7. Ross, C. A., "Split-Hopkinson Pressure Bar Tests", ESL-TR-88-82, Engineering and Services Laboratory, Air Force Engineering and Services Center Tyndall AFB, FL, 1989.

8. Ross, C. A. and Kuennen, S. T., "Fracture of Concrete at High Strain Rates", Fracture of Concrete and Rock: Recent Developments, S. P. Shah et al, eds. Elsevier Applied Science, London, 1989 pp 152-61.

9. Watstein, D. "Effect of Straining Rate on the Compressive Strength and Elastic Properties of Concrete", ACI Journal, Vol 24, 1953, pp 729-44.

10. Goldsmith, W. Kenner, V. H. and Ricketts T. E., "Dynamic Behavior of Concrete", Experimental Mechanics, Vol. 66, 1966, pp 65-69.

11. Green, H., "Impact Strength of Concrete" Institution of Civil Engineers, Proc., Vol. 28, 1968, pp 731-40.

12. Hughes, B. P., and Gregory, R. "The Impact Strength of Concrete Using Green's Ballistic Pendulum", Institution of Civil Engineers, Proc., Vol 81, 1968, pp 731-40.

13. Atchley, B. L. and Furr, H. L., "Strength and Energy Absorption Capabilities of Plain Concrete Under Dynamic and Static Load", ACI Journal, Nov. 1967, pp 745-56.

14. Hughes, B. P. and Gregory, R., "Concrete Subjected to High Rates of Loading in Compression", Mag. of Concrete Res., Vol 24, 1972, pp 25-36.

15. Hughes, B. P. and Watson, A. J., "Compressive Strength and Ultimate Strain of Concrete Under Impact Loading", Mag. of Concrete Res, Vol. 30, 1978, pp 189-99.

16. Sierakowski, R. L., Malvern, L. E., Collins, J. A., Milton, J. E. and Ross, C. A., "Penetration Impact Studies of Soil/Concrete", Final Report, AFOSR Grant No. 77-3029 and AFATL Tech. Report TR-78-9, University of Florida Gainesville, FL, Nov. 1977.

17. Malvern, L. E. and Ross, C. A., "Dynamic Response of Concrete and Concrete Structures", Two annual reports and a final report for AFOSR Contract F49620-83-K007. University of Florida, Gainesville, FL, Feb. 1984, Feb. 1985, May 1986.

18. Felice, C. W., The Response of Soil to Impulse Loads Using the Split-Hopkinson's Pressure Bar Technique, Ph.D. Dissertation, The University of Utah, 1985.

19. Mellinger, F. M. and Birkimer, D. L., "Measurements of Stress and Strain on Cylindrical Test Specimens of Rock and Concrete Under Impact Loading", Tech. Rep. 4-46 Dept. of Army Ohio River Div. Lab., Apr. 1966.

20. Griner, R. C., Dynamic Properties of Concrete, Thesis for Master of Science Degree in Engineering, University of Florida, Gainesville, FL 1974.

21. Kormeling, H. A., Zielinski, A. J., and Reinhardt, H. W., "Experiments on Concrete Under Single and Repeated Uniaxial Impact Tensile Loading", Stevin Lab. Rept. 5-80-3, Delft University of Technology, 2nd Print, 1981.

22. Gran, J. K., and Seaman, L., "Observations and Analysis of Microcracks Produced in Dynamic Tension Tests of Concrete", Final Dept. AFOSR Contract No. F49620-82-15-0021. SRI International, Merlo Park, CA, 1986.

23. John, R. and Shah, S. P., "Effect of High Strain-Rate of Loading on Fracture Parameters of Concrete", Proc. of Fracture of Concrete and Rock, SEM-RILEM Int. Conf., eds S. P. Shah and S. E. Swartz, Published by Soc. of Ecp. Mech. (SEM), Bethel, CT., 1987, pp 35-52.

24. John, R. and Shah, S. P., "Fracture of Concrete Subjected to Impact Loading", Cement, Concrete and Aggregates, CCAGDP, Vol. 8, No. 1, 1986, pp 24-32.

25. Ross, C. A., Kuennen, S. T., and Tedesco, J. W., "Experimental and Numerical Analysis of High Strain-Rate Concrete Tensile Tests", Proc. Int. Conf. on Micomechanics of Quasi-Brittle Materials, Albuquerque, NM, 1990.

26. Benture, A., Mindess, S. and Banthia, N., "The Behavior of Reinforced Concrete Beams Under Impact: The Effect of Concrete Strength", Pros. of Fracture of Concrete and Rock, SEM-RILEM Int. Conf., eds S. P. Shah and S. E. Swartz, Published by Soc. of Exp. Mech. (SEM), Bethel, CT, 1987, pp 449-58.

27. Banthia, N. P., Mindess, S., and Benture, A., "Energy Balance in Instrumented Impact Tests on Plain Concrete Beams", ibid pp 21-34.

28. Gopalaratnam, V. S. and Shah, S. P., "Properties of Steel Fiber Reinforced Concrete Subjected to Impact Loading", ACI J., Proceedings, V. 83, No. 1, 1985, pp 117-26.

29. Gopalaratnam, V. S., Shah, S. P., and John, R., "A Modified Instrumented Charpy Test for Cement-Based Composites", Exp. Mech., SEM, V. 24, No. 2, 1984, pp 102-11.

30. Sauris, W. and Shah, S. P., "Properties of Concrete Subjected to Impact Loading", Jour. of Struct. Eng., ASCE, Vol. 109, No. 7, 1983, pp 1727-41.

31. Mindess, S. and Nadeau, J. S., "Effect of Loading Rate on the Flexural Strength of Cement and Mortar", Bull. of Amec. Ceramic Soc., Vol. 56, No. 44, 1977, pp 429-30.

32. Sierakowski, R. L., "Dynamic Effects in Concrete Materials", Application of Fracture Mechanics to Cementitious Composites, ed., S. P. Shah, Martinus Mijhoff Publ, Dordrecht, The Netherlands, 1985.

33. Slawson, T. R. and Kiger, S. A., "Dynamic Shear Failure of Shallow-Buried Flat-Roofed Reinforced Concrete Structure Subjected to Blast Loading", Waterways Experiment Station, Vicksburg, MS, Tech. Dept., SL-84-7, 1984.

34. Malvern, L. E. and Jenkins, D. A., "Dynamic Testing of Laterally Confined Concrete", ESL-TR-89-47, Engineering and Services Laboratory, Air Force Engineering and Services Laboratory, Tyndall AFB, FL, 1990.

35. Gran, J. K., Florence, A. L. and Colton, J. D., "Dynamic

Triaxial Tests of High-Strength Concrete", Jour. of Eng. Mech., Vol. 115, 1989, pp 891-904.

36. Tedesco, J. W., Ross, C. A. and Brunair, "Numerical Analysis of Dynamic Split Cylinder Tests", Computers and Structures, Vol. 32, No. 3/4, 1989, pp 609-24.

37 .Cowell, W., "Dynamic Properties of Plain Portland Cement Concrete", Tech. Dept. No. R447, U. S. Naval Engineering Laboratory Post Hueneme, CA, 1966.

38. Takada, J., Tachikawa, H. and Fujimoto, K., "Mechanical Behavior of Concrete Under Higher Rate Loading than in Static Test", in Mechanical Behavior of Materials, Proc. of the Soc. of Material Sciences, Vol. II, 1974.

39. Oh, B. H., "Behavior of Concrete Under Dynamic Tensile Loads", ACI Materials Journal, Jan-Feb 1987, pp 8-13.

40. McVay, M. K., "Spall Damage of Concrete Structures", Tech. Rept-SL-88-22, Waterways Experiment, Corps of Eng., Vicksbury, MS, 1988.

41. Weerheijm, J. and Reinhardt, "Modelling of Concrete Fracture Under Dynamic Tensile Loading", Fracture of Concrete and Rock: Recent Developments, S. P. Shah et al, eds. Elsevier Applied Science, London, 1989, pp 721-28.

42. Chen, E. P., "A Strain Dependent Fracture Model Based on Continuum Damage Mechanics", in Dynamic Constitute/Failure Models, A. M. Rojendran and T. Nicholas eds. AFWAL-TR-88-4229, Univ. of Dayton Res. Inst., Dayton, OH, 1988, pp 212-238.

43. Budiansky, B. and O'Connell, R. J., "Elastic Module of a Cracked Solid", International Journal of Solids and Structures, 12, 81, 1976.

44. Soroushian, P., Choi, K., and Alhamad, A., "Dynamic Constitutive Behavior of Concrete", ACI Journal, Mar-Apr 1986, pp 251-59.

45. Harsh, S., Shen, A. and Darwin, D., "Strain-Rate Sensitive Deformation of Cement Paste and Mortar in Compression", Final Report AFOSR Research Grant, AFOSR-85-0194, University of Kansas, Lawrence, K. S., 1989.

46. Malvern, L. E. and Jenkins, D. A., "Strength and Deformanton of Confined and Unconfined Concrete Under Axial Dynamic Loading", Final Report AFOSR Contract, No. 87-0201, University of Florida, Gainesville, FL, 1988.

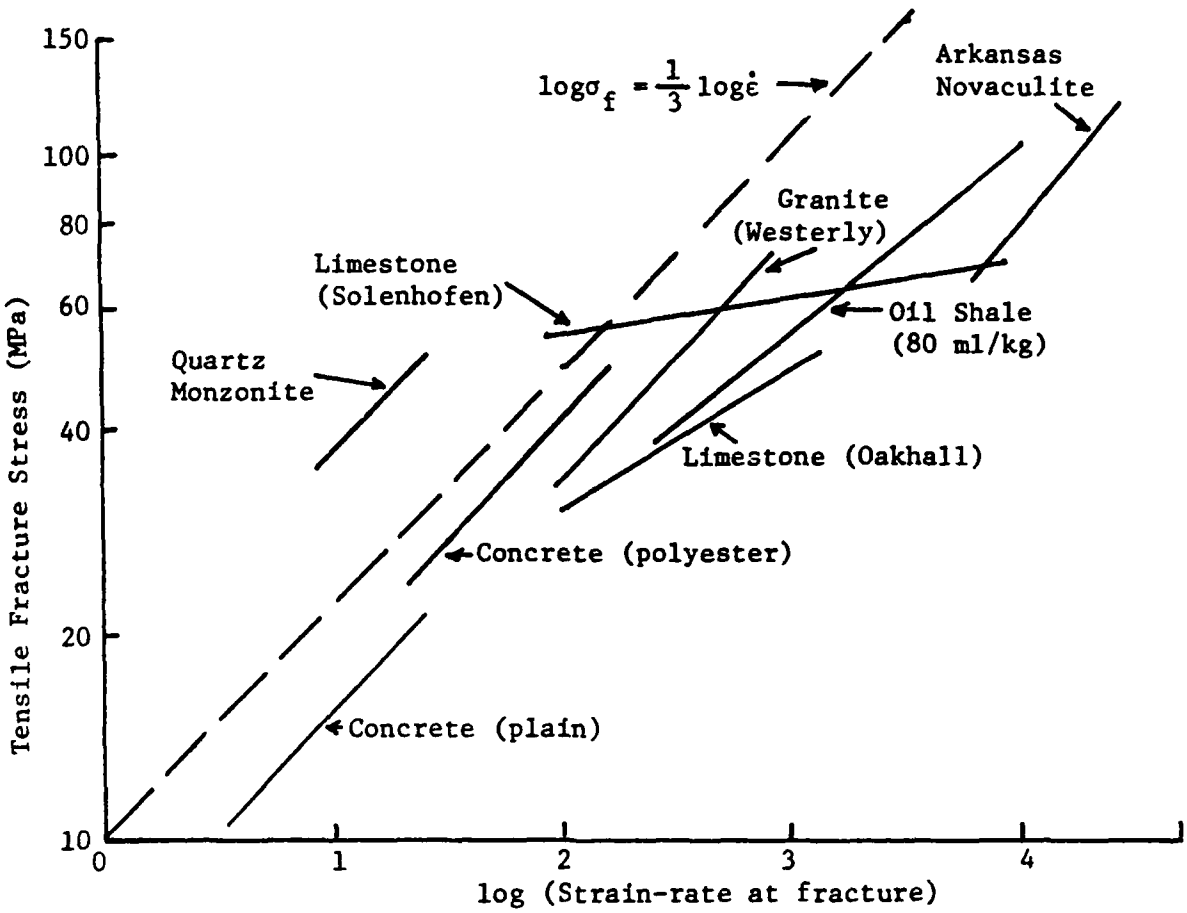

Figure 1. Strain-rate dependence of fracture stress. (Fig. 1 of Ref. [1]) Dotted line added by the author.

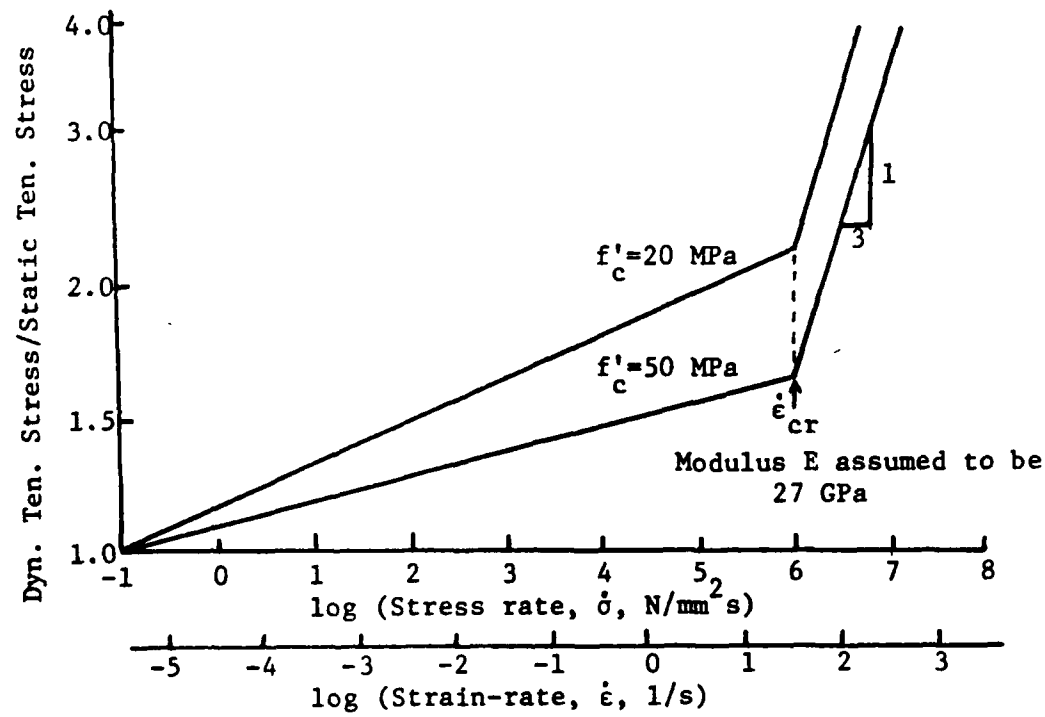

Figure 2. Stress-rate dependence of fracture stress. (Fig. 2 of Ref. [6]) Critical strain-rate $\dot{\varepsilon}_{cr}$ and modulus E added by the author.

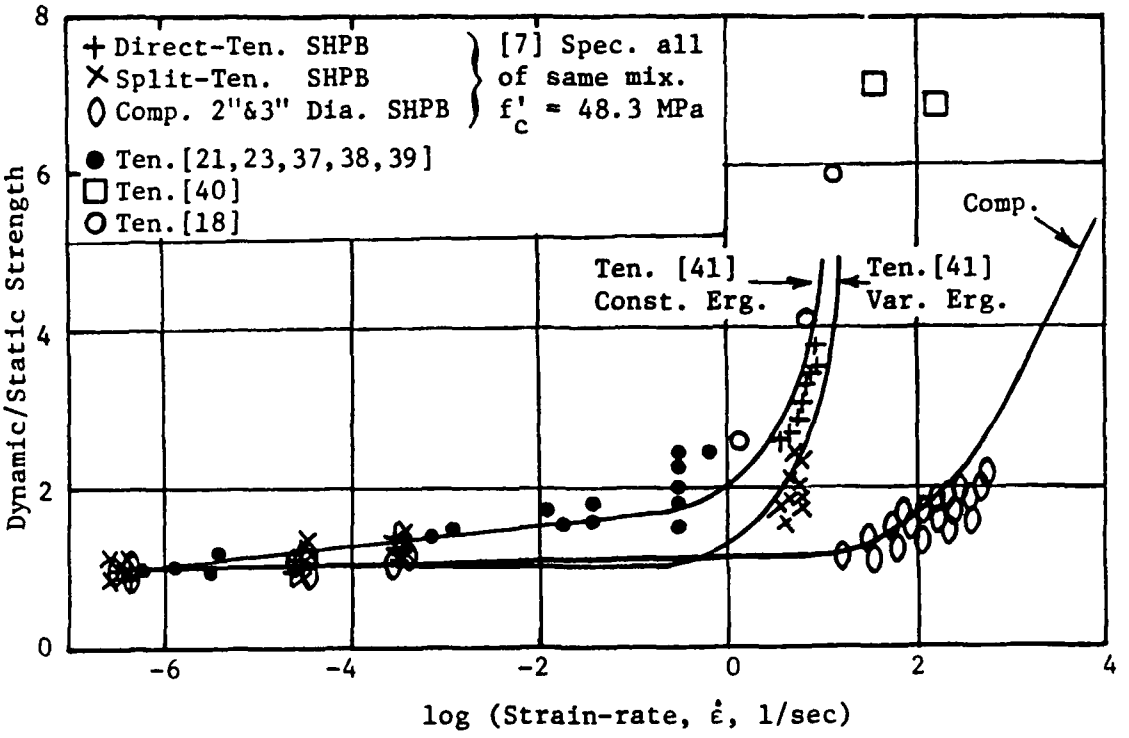

Figure 3. Strain-rate dependence of fracture stress. [7]

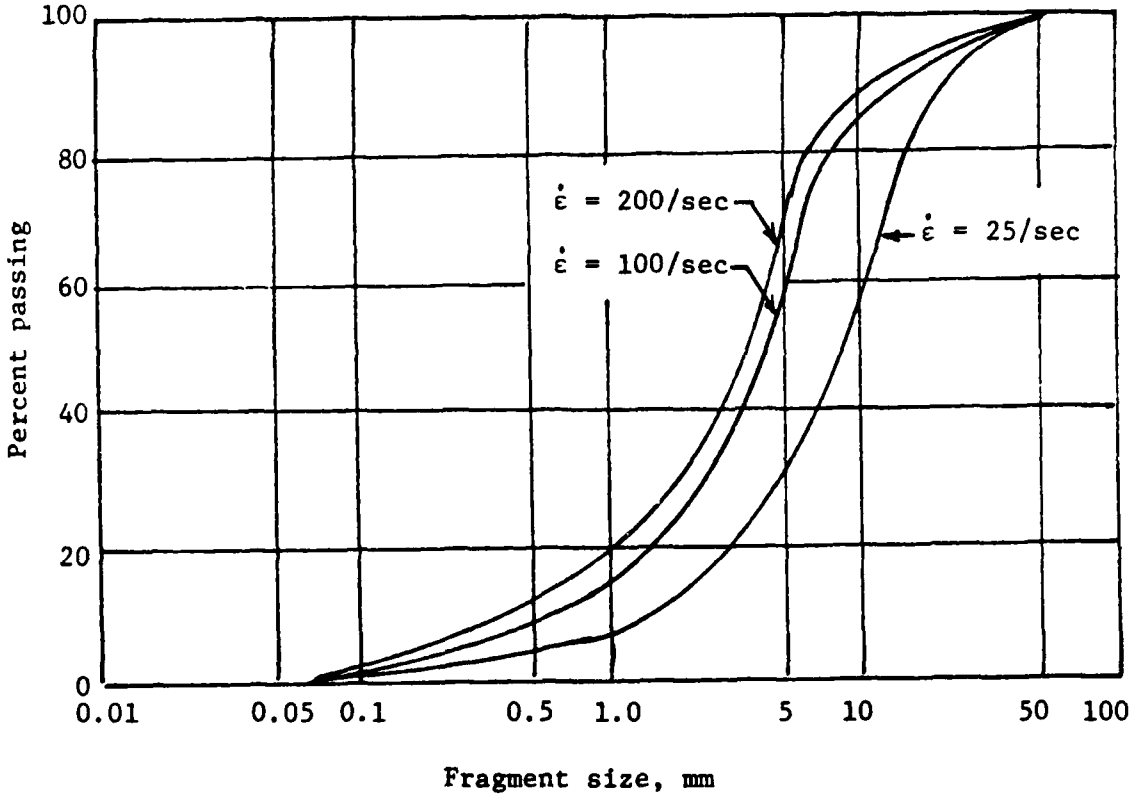

Figure 4. Fragment size distribution from sieve analysis of post-test concrete specimen tested in compressive SHPB. [8]

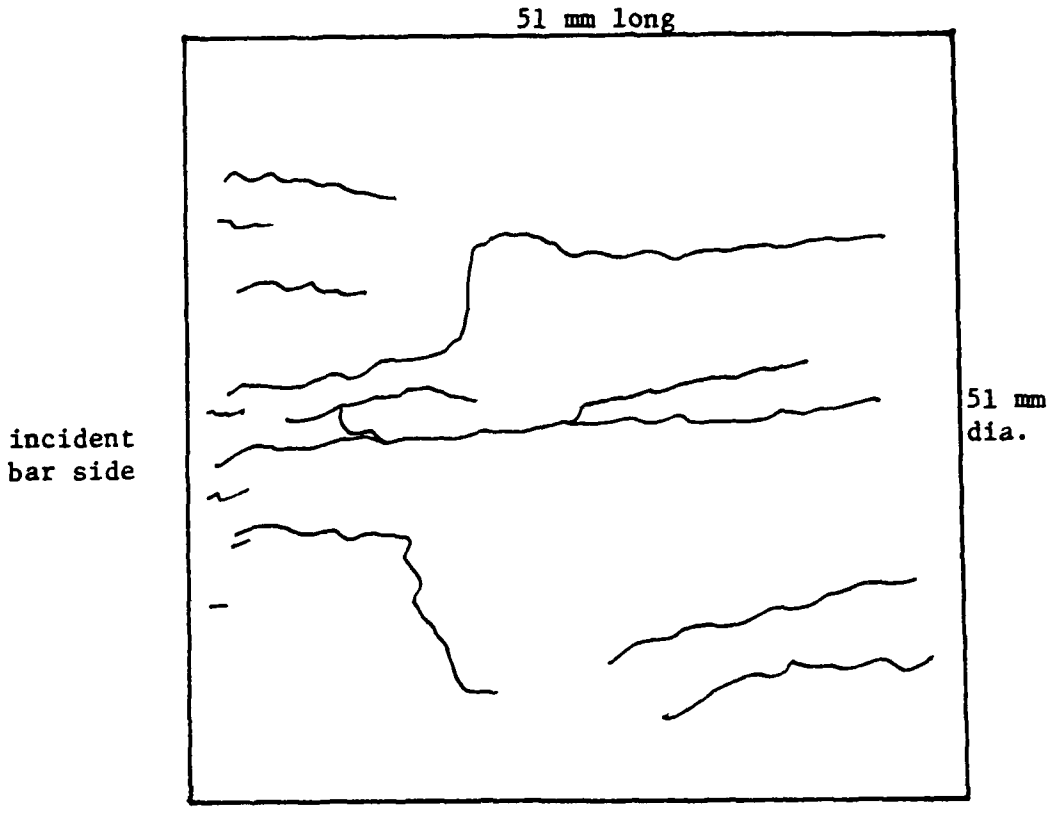

a) $\dot{\varepsilon}$ =30/sec

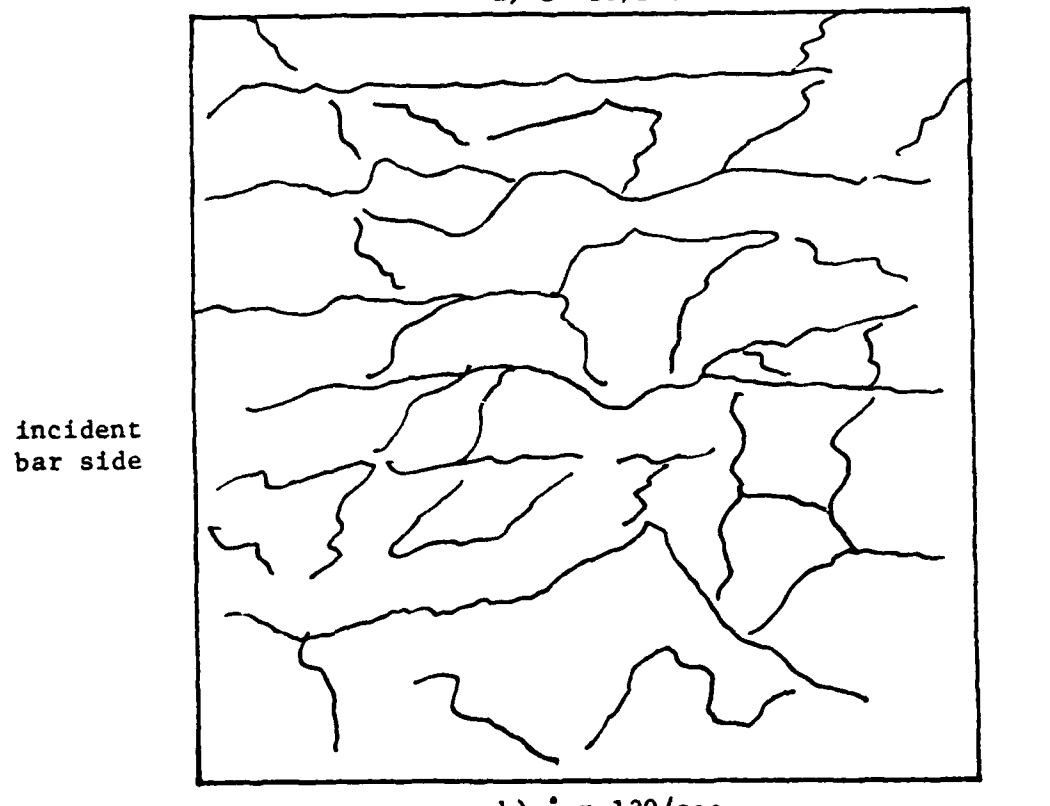

b) $\dot{\varepsilon}$ = 130/sec

Figure 5 Tracing of surface cracks of SHPB concrete compressive specimen taken from high speed film. Time is approximately 200 microsec after arrival of incident pulse.

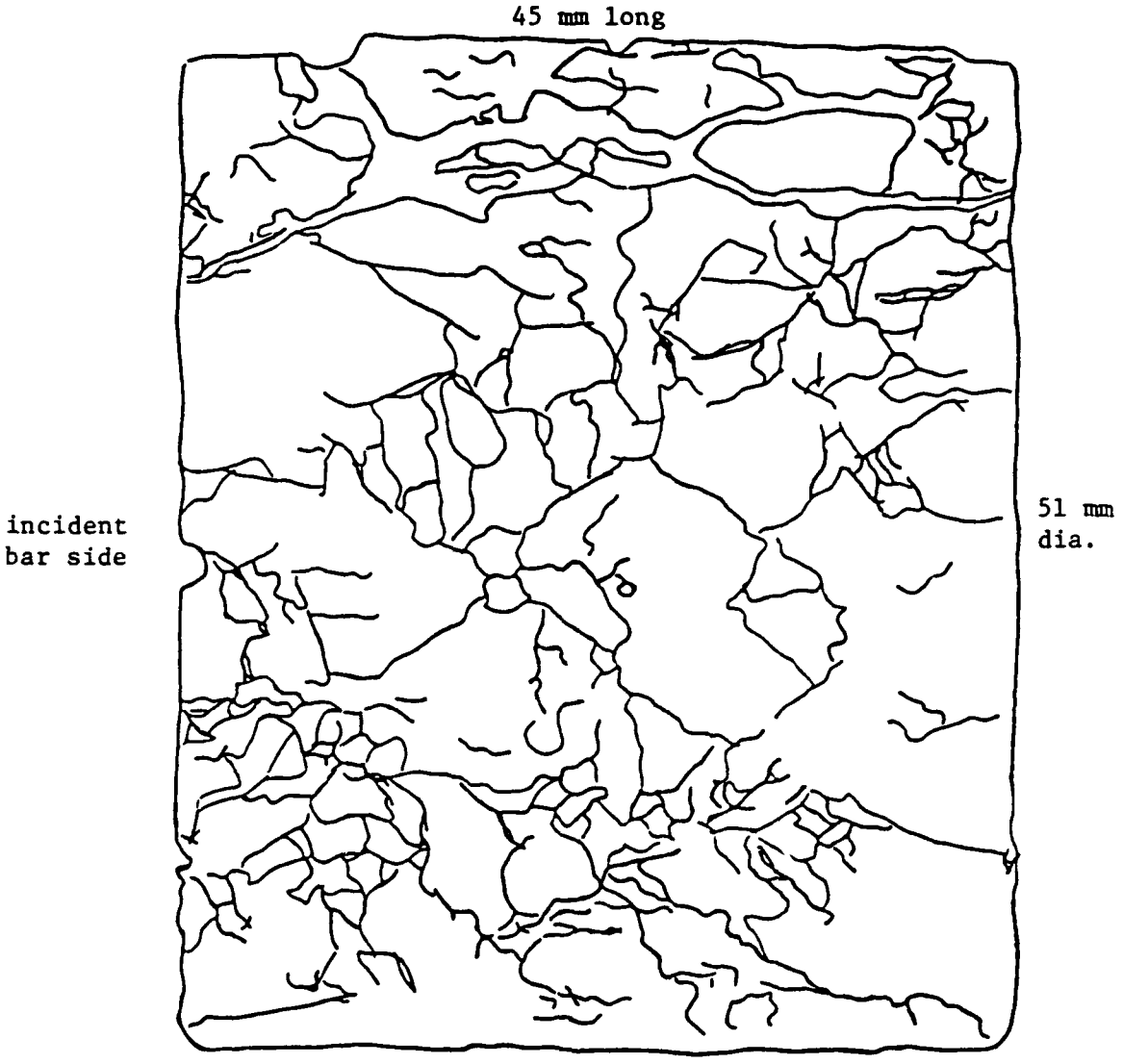

Figure 6. Internal crack pattern of SHPB concrete compressive test with strain limiting collar. Strain-rate 150/sec. Maximum strain of 0.0128 at approximately 150 microsec after arrival of the incident pulse. (Fig. 24 Ref. [46])

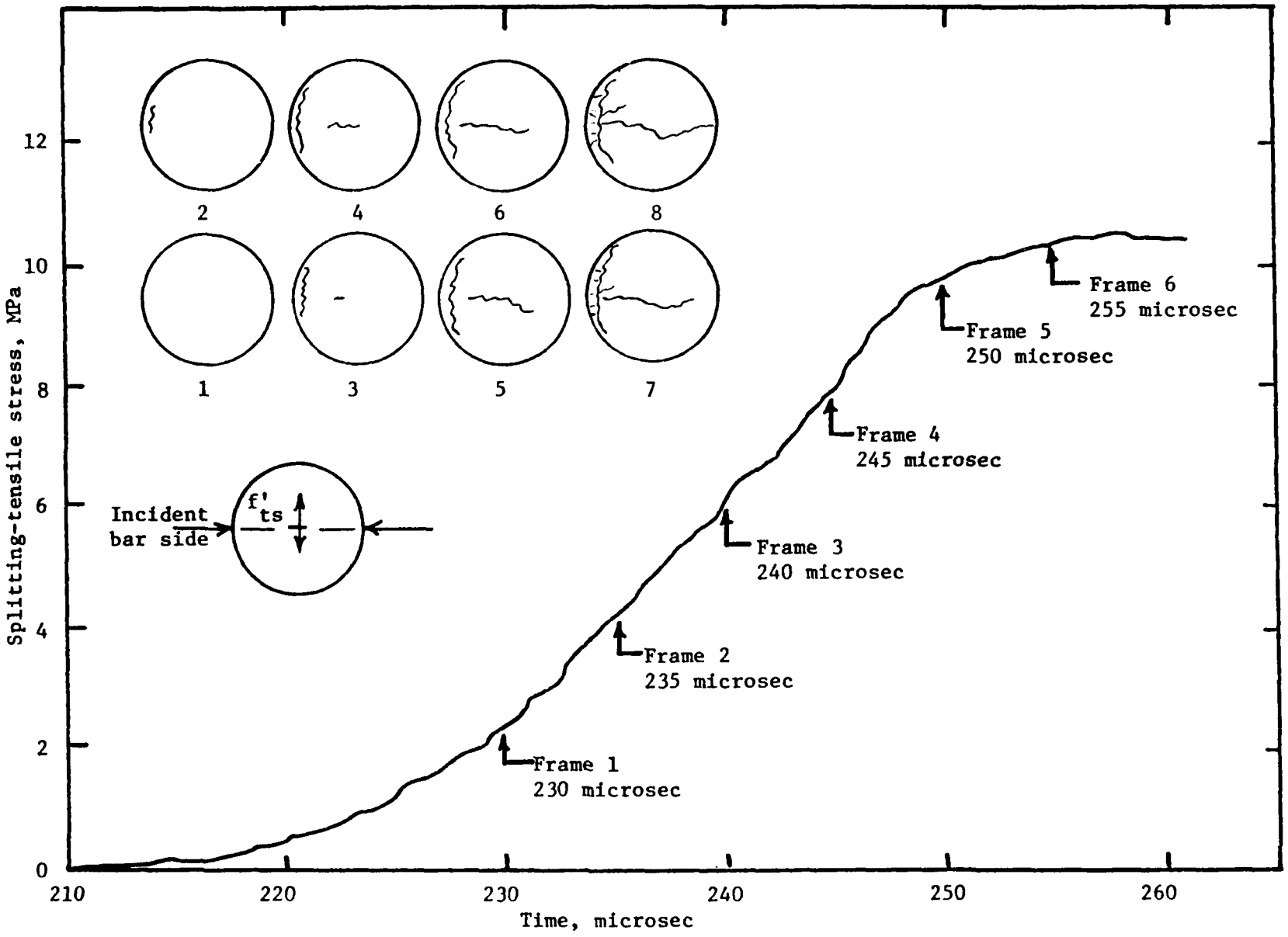

Figure 7. Crack pattern and associated tensile stress for a splitting-tensile SHPB test. Strain-rate approximately 5/sec. 51 mm diameter x 51 mm long specimen. f'_c = 48 MPa. [8]

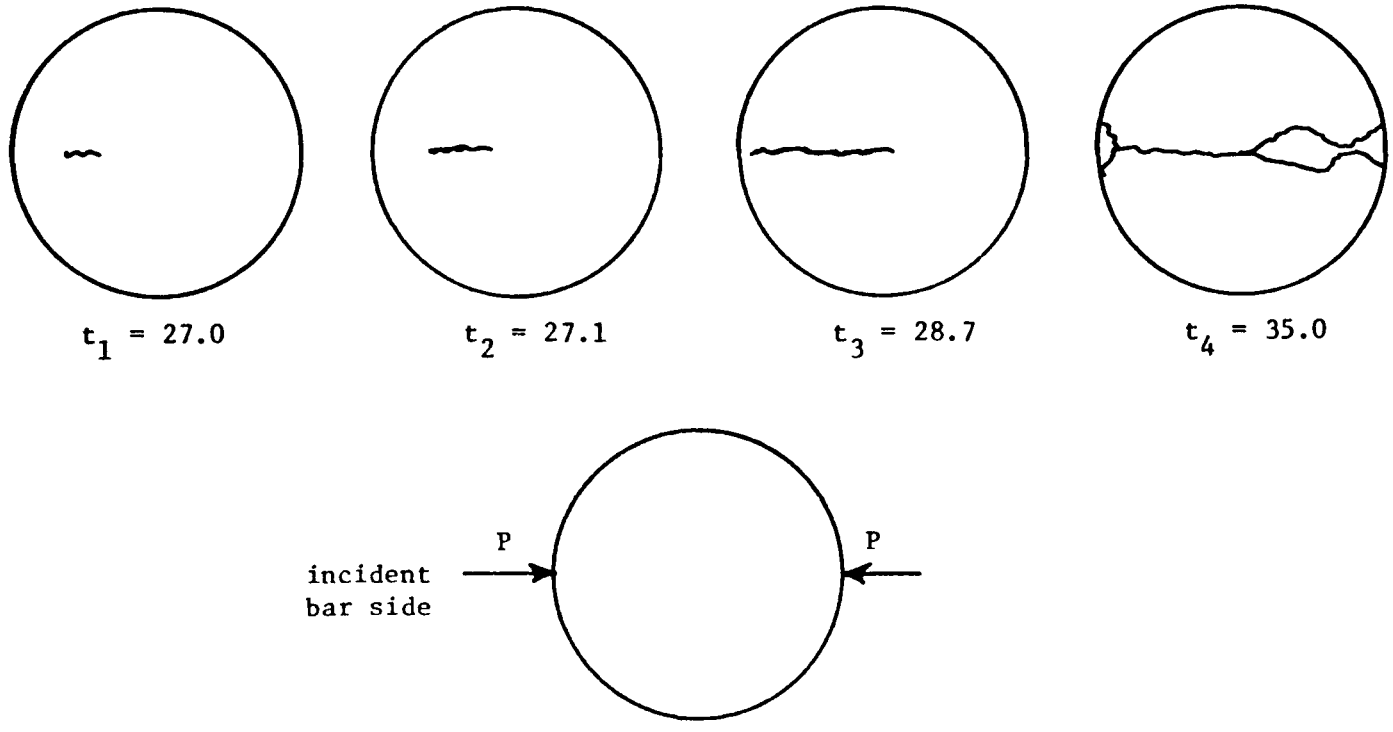

Figure 8. Computer generated crack pattern for splitting-tensile SHPB test. [36] Time given in microsec.